

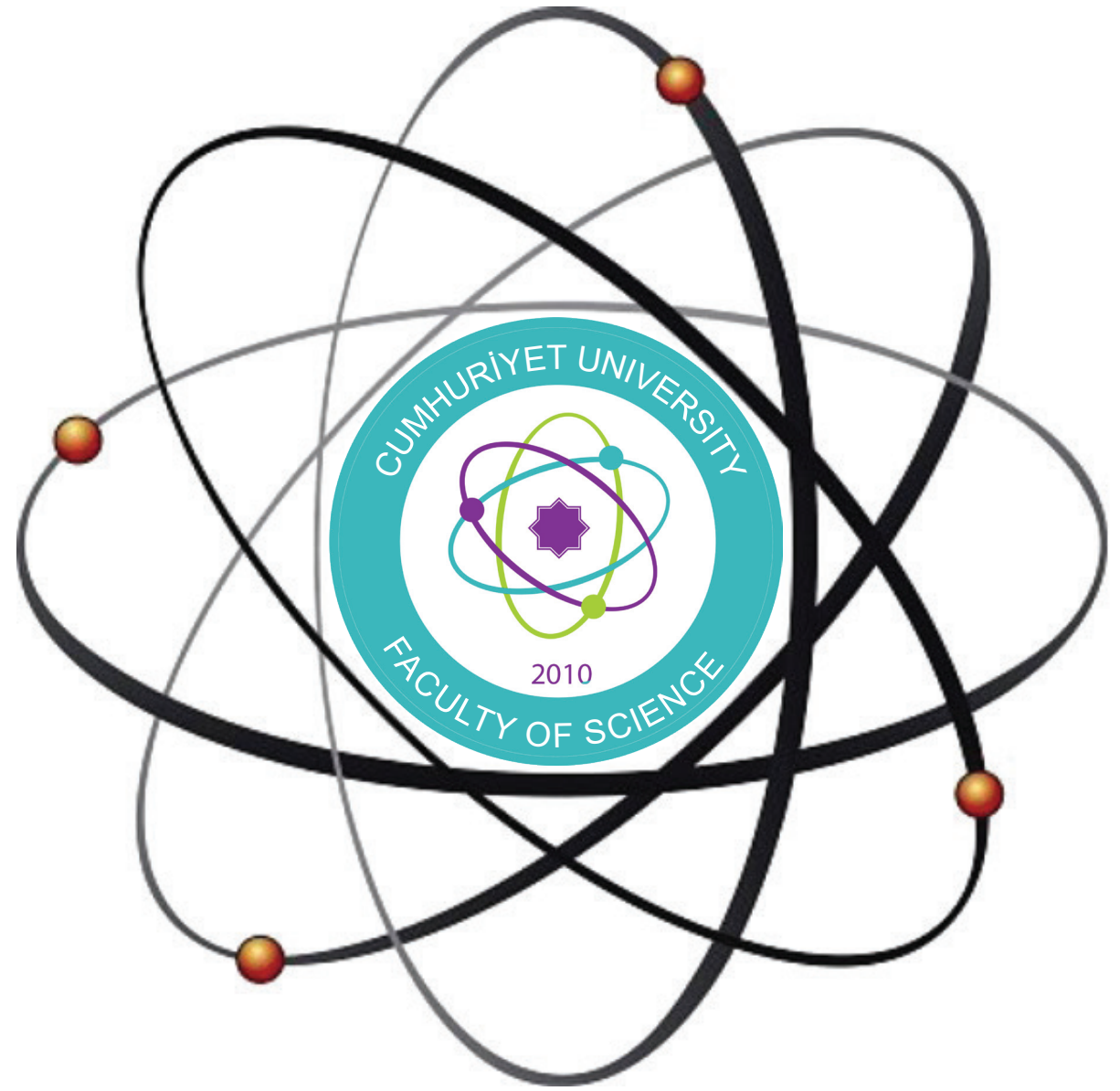


Cumhuriyet University

ISSN : 2587-2680

e-ISSN : 2587-246X

Cumhuriyet Science Journal



Volume : 41

Number : 2

Year : 2020



ISSN: 2587-2680
e-ISSN: 2587-246X
Period: Quarterly
Founded: 2002
Publisher: Cumhuriyet
University

Cumhuriyet Science Journal (CSJ)

Journal Previous Name: Cumhuriyet Üniversitesi Fen-Edebiyat Fakültesi Fen Bilimleri Dergisi

Old ISSN: 1300-1949

Owner on behalf of the Cumhuriyet University, Faculty of Science

Prof. Dr. İdris Zorlutuna (Sivas Cumhuriyet University)

Editor in Chief

Prof. Dr. İdris ZORLUTUNA (Sivas Cumhuriyet University)

Managing Editor

Assoc. Prof. Dr. Adil ELİK (Sivas Cumhuriyet University)

Editors

Prof. Dr. Baki KESKİN

bkeskin@cumhuriyet.edu.tr

Subjects: Mathematics and Statistics

Institution: Sivas Cumhuriyet University

Assoc. Prof. Dr. Adil ELİK

elik@cumhuriyet.edu.tr

Subjects: Chemistry and Chemical Engineering, Environmental Sciences, Basic Sciences (General)

Institution: Sivas Cumhuriyet University

Prof. Dr. Nilüfer TOPSAKAL

ntopsakal@cumhuriyet.edu.tr

Subjects: Applied Mathematics

Institution: Sivas Cumhuriyet University

Prof. Dr. Serkan AKKOYUN

sakkoyun@cumhuriyet.edu.tr

Subjects: Physics and Physical Engineering

Institution: Sivas Cumhuriyet University

Prof. Dr. Hülya KURŞUN

hkursun@cumhuriyet.edu.tr

Subjects: Earth Sciences

Institution: Sivas Cumhuriyet University

Prof. Dr. Birnur AKKAYA

bakkaya@cumhuriyet.edu.tr

Subjects: Molecular Biology and Genetics, Biochemistry

Institution: Sivas Cumhuriyet University

Prof. Dr. Halil İbrahim ULUSOY

hiulusoy@cumhuriyet.edu.tr

Subjects: Chemistry, Analytical Chemistry, Drug Analysis, Pharmacy

Institution: Sivas Cumhuriyet University

Abstracted&Indexing

ULAKBİM TR-Dizin

Index Copernicus (ICI Journals Master List)

Clarivate Analytics Zoological Record

Crossref

Directory of Open Access Journals (DOAJ)

WorldCat

Akademik Dizin

Arastirmax Bilimsel Yayın İndeksi

Bielefeld Academic Search Engine (BASE)

Directory of Research Journal Indexing (DRJI)

Google Scholar

Research Gate

Idealonline

Field Editors

Prof.Dr. Sezai ELAGÖZ (Aselsan)

Prof.Dr. Muhammet BEKÇİ (Sivas Cumhuriyet University)

Assoc.Prof.Dr. Duran KARAKAŞ (Sivas Cumhuriyet University)

Assoc. Prof. Dr. Yaşar ÇAKMAK (Sivas Cumhuriyet University)

Assoc.Prof.Dr. Sevgi DURNA DAŞTAN (Sivas Cumhuriyet University)

Assist. Prof. Dr. Didem ALTUN (Sivas Cumhuriyet University)

Editorial Board

Prof. Dr. Mustafa SOYLAK (Erciyes University)

Prof.Dr. Münevver SÖKMEN (KGTU)

Prof.Dr. Hüseyin MERDAN (TOBB ETU)

Prof.Dr. Chuan Fu Yang (Nanjing University of Science and Technology)

Prof.Dr. Mehmet AKKURT (Erciyes University)

Prof.Dr. Mustafa KAVUTÇU (Gazi University)

Prof.Dr. Abuzar KABIR (International Forensic Research Institute)

Prof. Dr. Mustafa TÜZEN (GOP University)

Prof.Dr. Ali Fazıl YENİDÜNYA (Sivas Cumhuriyet University)

Prof.Dr. Songül KAYA MERDAN (METU)

Prof.Dr. Yeşim SAĞ AÇIKEL (Hacettepe University)

Prof.Dr. Mehmet ŞİMŞİR (Sivas Cumhuriyet University)

Prof.Dr. Atalay SÖKMEN (KGTU)

Prof. Dr. Marcello LOCATELLI (University "G. d'Annunzio" of Chieti-Pescara).

Dr. Ricardo I. JELDRES (Universidad de Antofagasta)

Dr. Jose Javier Valiente-Dobon (INFN-LNL, Padova University)

Prof.Dr. Mustafa YILDIRIM (Sivas Cumhuriyet University)

Assoc.Prof.Dr. Ali DELİCEOĞLU (Erciyes University)

Assoc.Prof.Dr. Tuncay BAYRAM (Karadeniz Technical University)

Assoc.Prof.Dr. Gökhan KOÇAK (Erciyes University)

Dr. Francois VOS (The University of Queensland)

Dr. Nadjet Laouet (Freres Mentouri Constantine-1 University)

Layout Editors:

Research Assistant Esra Merve YILDIRIM

Copyeditors:

Research Assistant Özgür İNCE

Research Assistant Doğa Can SERTBAŞ

Research Assistant Dr. Hacı Ahmet KARADAŞ

Proofreader:

Assist. Prof. Dr. Yener ÜNAL

Assist. Prof. Dr. Tuğba MERT

Publication Type. Peer Reviewed Journal

Cite Type: Cumhuriyet Sci. J.

Contact Information

Faculty of Science Cumhuriyet University 58140

Sivas- TURKEY

Phone: +90(346)2191010-1522

Fax: +90(346)2191186

e-mail: csj@cumhuriyet.edu.tr

<http://dergipark.gov.tr/csj>

CONTENTS	PAGES
Mahmut MAK <i>Some characterizations of timelike rectifying curves in de sitter 3 space</i>	327-343
Koray SAYIN, Majid REZAEIVALA <i>Modelling studies on the investigation of non-linear optical properties of some ExnBox cyclophanes</i>	344-350
Halil İbrahimYOLDAŞ <i>Certain results on Kenmotsu manifolds</i>	351-359
Shyamapada MODAK, Sk SELİM, Md. Monirul ISLAM <i>Common properties and approximations of local function and set operator ψ</i>	360-368
Ezgi NAZMAN , Hülya OLMUŞ <i>Comparison of greedy matching methods on cigarette usage of individuals in Turkey</i>	369-376
Abdulrahman TUKUR, Mustafa Ersin PEKDEMİR, Mehmet COŞKUN <i>Investigation of structural, thermal and dielectric properties of PVC/modified magnetic nanoparticle composites.....</i>	377-385
İdil KARACA AÇARI, Sevgi BALCIOĞLU, Burhan ATEŞ, Süleyman KÖYTEPE, İsmet YILMAZ, Turgay SEÇKİN <i>Synthesis of polyhedral oligomeric silsesquioxane-n-acetylcysteine conjugate with click chemistry and its antioxidant response and biocompatibility</i>	386-396
Seda ÇETİNTAŞ, Deniz BİNGÖL <i>Dissolution kinetics of manganese during nickel recovery from high iron grade laterite by acid leaching combined NaOH-assisted mechanochemical technology</i>	397-406
Muhammet KÖSE, Ozge GUNGÖR, Julide NACAROGLU BALLI, Hilal KIRPIK <i>Structural characterization and DNA binding properties of a new imine compound.....</i>	407-412
Nabih LOLAK, Süleyman AKOCAK <i>Biological evaluation of aromatic bis-sulfonamide Schiff bases as antioxidant, acetylcholinesterase and butyrylcholinesterase inhibitors</i>	413-418
Caner TANIŞ, Buğra SARAÇOĞLU, Coşkun KUŞ, Ahmet PEKGÖR <i>Transmuted complementary exponential power distribution: properties and applications</i>	419-432
Filiz KAHRAMAN ALİÇAVUŞ <i>Spectroscopy of a chemically peculiar delta scuti-type star: 60 tau</i>	433-442
Rauf AMİROV, Yaşar MEHRALİYEV, Nergiz HEYDARZADE <i>On an inverse boundary-value problem for a second-order elliptic equation with non-classical boundary conditions..</i>	443-455
Tufan GÜRAY, Dila ERCENGİZ, Ülkü Dilek UYSA <i>A new spectrophotometric study with ortho hydroxy schiff base for the determination of aluminum in drug</i>	456-461
Hulya BOYRAZ, Emine ÖZTÜRK <i>Electronic features of Gaussian quantum well as depending on the parameters</i>	462-466
Hidayet TAKCI, Kali GURKAHRAMAN, Emre ÜNSAL, Ahmet Fırat YELKUVAN <i>A matching model to measure compliance between department and student.....</i>	467-471
Mohammad Hosein ERSHADİ, Amir BAHARLOUHOUREH <i>Fuzzy control of single-input step-up switched-capacitor- inductor dc-dc converter</i>	472-481
Kasım MERMERDAŞ, Süleyman İPEK, Muhammet Burak BOZGEYİK <i>Experimental evaluation and modeling of the compressive strength of concretes with various strength classes of cements.....</i>	482-492

Ali İrfan MAHMUTOĞULLARI

Two lagrangian relaxation based heuristics for vertex coloring problem 493-505

Cem ERTEK, Fatih CİVELEK

Comparison of functionally graded and ungraded cylinder liners with finite element analysis 506-520

Sefa YILDIRIM

An efficient method for the plane vibration analysis of composite sandwich beam with an orthotropic core 521-526

Yunis TORUN, Sefa MALATYALI

Power analysis of robotic medical drill with different control approaches 527-533

Serdar COŞKUN

Dynamic output-feedback H_{∞} control design for ball and plate system 534-541

Fatih GÜVEN

Post-op bore profile estimation of workpiece clamped using three-jaw chuck..... 542-549

Şükrü Gökhan ELÇİ

Speciation of chromium in beverages and seasoning samples by magnetic solid-phase extraction and microsample injection system flame atomic absorption spectrometry 550-558

Umut ADEM

Ferroelectricity of $\text{Ca}_9\text{Fe}(\text{PO}_4)_7$ and $\text{Ca}_9\text{Mn}(\text{PO}_4)_7$ ceramics with polar whitlockite-type crystal structure..... 559-564



Some characterizations of timelike rectifying curves in de sitter 3-space

Mahmut MAK

Kırşehir Ahi Evran University, The Faculty of Arts and Sciences, Department of Mathematics, Kırşehir / TURKEY

Abstract

De Sitter space is a non-flat Lorentzian space form with positive constant curvature which plays an important role in the theory of relativity. In this paper, we define the notions of timelike rectifying curve and timelike conical surface in De Sitter 3-space as Lorentzian viewpoint. Moreover, we give some nice characterizations and results of a timelike rectifying curves with respect to curve-hypersurface frame in De Sitter 3-space which is a three dimensional pseudo-sphere in Minkowski 4-space.

Article info

History:

Received:08.02.2020

Accepted:26.05.2020

Keywords

Rectifying curve,
Conical surface,
Geodesic, Extremal
curve.

1. Introduction

In Euclidean 3-space R^3 , let $x:I \subseteq R \rightarrow R^3$ be a unit speed regular curve with Frenet-Serret apparatus $\{T, N, B, \kappa, \tau\}$ where nonzero curvature κ and torsion τ of the curve. At each point of the curve, the planes spanned by $\{T, N\}$, $\{T, B\}$ and $\{N, B\}$ are known as the osculating plane, the rectifying plane, and the normal plane, respectively. In R^3 , it is well-known that a curve lies in a plane if its position vector lies in its osculating plane at each point; and it lies on a sphere if its position vector lies in its normal plane at each point. In view of these basic facts, in R^3 , the notion of rectifying curve which is a space curve whose position vector always lie in its rectifying plane, is firstly introduced by Bang-Yen Chen [1]. Thus, the position vector $x(s)$ of a rectifying curve satisfies the equation

$$x(s) - p = c_1(s)T(s) + c_2(s)B(s) \quad (1)$$

such that the fixed point p for some differentiable functions c_1 and c_2 in arc length parameter s [1,2]. It is known that a non-planar (twisted) curve in R^3 is a generalized helix if and only if the ratio τ / κ is a nonzero constant on the curve. However, Chen shows that for any given regular curve in R^3 is satisfied $\tau / \kappa = c_1 s + c_2$ for some constants $c_1 \neq 0$ and c_2 in arc length parameter s iff the curve is congruent to a rectifying curve [1]. Centrode is the path of the instantaneous center of rotation. It plays an important role in mechanics and kinematics. In R^3 , Darboux vector of a regular curve with a nonzero curvature is defined by $D = \tau T + \kappa B$. However, the position vector of a rectifying curve is always in the direction of the Darboux vector which corresponds the instantaneous axis of rotation. Therefore, there is a hard relationship between the centrode and the rectifying curve. In this sense, Chen and Dillen give a relationship between rectifying curves and centrodes of space curves in [3]. They study also rectifying curve as extremal curves and give a classification of curves with nonzero constant curvature and linear torsion in terms of spiral type rectifying curves in [3]. After Chen's articles [1,3], rectifying curves and their characterizations are studied by many authors in different ambient spaces from various viewpoints. In this concept, some remarkable papers are [4,5,6-8]. Moreover, the eq. (1) means that "the straight line that passing through $x(s)$ and the fixed point p , is orthogonal to the principal normal line that starting at point $x(s)$ with the direction of $N(s)$ ". In this sense, Lucas and Yagües give the concept of rectifying curves in three dimensional spherical and hyperbolic space from the viewpoint of Riemannian Space Forms by using this idea in [9,10].

It is well known that De Sitter space is a non-flat Lorentzian space form with positive constant curvature. Also, De Sitter 3-space is called a three-dimensional pseudo-sphere in Minkowski 4-space as a semi-Riemannian

*Corresponding author. Email address: mmak@ahievran.edu.tr

<http://dergipark.gov.tr/csj> ©2020 Faculty of Science, Sivas Cumhuriyet University

hypersurface. Especially, De Sitter space is one of the vacuum solutions of the Einstein equations, so it plays an important role in the theory of relativity.

In this study, as inspiration from [9,10], we introduce the notions of timelike rectifying curve with respect to curve-hypersurface frame and timelike conical surface in De Sitter 3-space as non-flat Lorentzian space form viewpoint. After, we give relationship between timelike rectifying curve and geodesic of timelike conical surface in De Sitter 3-space. Moreover, we obtain a nice characterization with respect to the ratio of geodesic torsion and geodesic curvature for timelike rectifying curves in De Sitter 3-space. However, we have a characterization which determines all timelike rectifying curve in De Sitter 3-space. Finally, in viewpoint of extremal curves, we give a corollary that a timelike curve in De Sitter 3-space, which has non-zero constant geodesic curvature and linear geodesic torsion, congruent to a timelike rectifying curve, which is generated by a spiral type unit speed timelike curve with certain geodesic curvature in 2-dimensional pseudo-sphere, and vice versa.

2. Preliminary

We give the fundamental notions for motivation to differential geometry of timelike curves and timelike surface in De Sitter 3-space and Minkowski 4-space. For more detail and background, see [11-14].

Let R^4 be a 4-dimensional real vector space and a scalar product in R^4 be defined by

$$\langle x, y \rangle = -x_1 y_1 + x_2 y_2 + x_3 y_3 + x_4 y_4,$$

for any vectors $x = (x_1, x_2, x_3, x_4), y = (y_1, y_2, y_3, y_4) \in R^4$. Then the pair $(R^4, \langle \cdot, \cdot \rangle)$ is called Minkowski 4-space (four-dimensional semi Euclidean space with index one), which is denoted by R_1^4 . We say that a nonzero vector $x \in R_1^4$ is called *spacelike*, *timelike* and *null* if $\langle x, x \rangle > 0$, $\langle x, x \rangle < 0$ and $\langle x, x \rangle = 0$, respectively. The *norm* of $x \in R_1^4$ is defined by $\|x\| = \sqrt{|\langle x, x \rangle|}$. The *signature* of a vector x is defined by $\text{sign}(x) = 1, 0$ or -1 while x is spacelike, null or timelike, respectively.

The De Sitter 3-space is defined by

$$S_1^3 = \{x \in R_1^4 \mid \langle x, x \rangle = 1\},$$

which is a three-dimensional unit pseudo-sphere (or a non-flat Lorentzian space form with positive constant curvature one) in R_1^4 .

The wedge product of any vectors $x = (x_1, x_2, x_3, x_4), y = (y_1, y_2, y_3, y_4), z = (z_1, z_2, z_3, z_4) \in R_1^4$ is given by

$$x \times y \times z = \begin{vmatrix} -\mathbf{e}_1 & \mathbf{e}_2 & \mathbf{e}_3 & \mathbf{e}_4 \\ x_1 & x_2 & x_3 & x_4 \\ y_1 & y_2 & y_3 & y_4 \\ z_1 & z_2 & z_3 & z_4 \end{vmatrix},$$

where $\{\mathbf{e}_1, \mathbf{e}_2, \mathbf{e}_3, \mathbf{e}_4\}$ is the standard pseudo-orthonormal basis of R_1^4 . Also, it is clear that

$$\langle w, x \times y \times z \rangle = \det(w, x, y, z), \quad (2)$$

for any $w \in R_1^4$. Hence, $x \times y \times z$ is pseudo-orthogonal to each of the vectors x, y and z . In the tangent space $T_q S_1^3$ at any point $q \in S_1^3$, we can give a cross product is denoted by " \wedge " which is induced from the wedge product " \times " in R_1^4 . Let u, v be tangent vectors (as considered column vectors of R_1^4) in $T_q S_1^3 \subset R_1^4$. Then the cross product $u \wedge v$ in $T_q S_1^3$ is given by

$$u \wedge v = q \times u \times v. \quad (3)$$

By using (2) and (3), it is easy to see that

$$\langle w, u \wedge v \rangle = -\det(q, u, v, w), \quad (4)$$

for every $w \in T_q S_1^3 \subset R_1^4$. Hence, we see that the orientations of a basis $\{u, v, w\}$ in $T_q S_1^3$ and a basis $\{q, u, v, w\}$ in R_1^4 are opposite.

Let $M = \Phi(U)$ be regular surface which is identified by a immersion $\Phi: U \subseteq R^2 \rightarrow S_1^3 \subset R_1^4$ where U is open subset of R^2 . Then, M is called spacelike or timelike surface in S_1^3 , if the tangent plane $T_p M$ at any point $p \in M$ is a spacelike subspace (it contains only spacelike vectors) or timelike subspace (i.e. it contains timelike, spacelike or null vectors) in R_1^4 , respectively.

Let $M = \Phi(U)$ be non-degenerate (spacelike or timelike) surface in S_1^3 , and ξ be unit normal vector field of M such that $\langle \xi, \xi \rangle = \varepsilon = \pm 1$. Then, for any differentiable vector fields $X, Y \in \mathfrak{X}(M) \subset \mathfrak{X}(S_1^3)$, Gauss formulas of M are given by

$$\nabla_x^0 Y = \bar{\nabla}_x Y - \langle X, Y \rangle \Phi, \quad (5)$$

$$\bar{\nabla}_x Y = \nabla_x Y + \varepsilon \langle S(X), Y \rangle \xi, \quad (6)$$

and the Weingarten map (or shape operator) is the map $S: \mathfrak{X}(M) \rightarrow \mathfrak{X}(M)$ defined by

$$S(X) = -\bar{\nabla}_x \xi \quad (7)$$

where Levi-Civita connections of R_1^4 , S_1^3 and M are denoted by ∇^0 , $\bar{\nabla}$ and ∇ , respectively.

Remark 2.1. Let Γ be spacelike (or timelike) three dimensional hyperplane that passing through the origin in R_1^4 , then the surface $\Gamma \cap S_1^3$ is congruent to unit sphere S^2 (or unit pseudo-sphere S_1^2), which is a spacelike (or timelike) totally geodesic surface in S_1^3 . Moreover, let Π be spacelike (or timelike) plane that passing through the origin in R_1^4 , then the curve $\Pi \cap S_1^3$ is congruent to unit circle S^1 (or part of unit pseudo-circle S_1^1), which is a spacelike (or timelike) geodesic in S_1^3 .

Let p and q be distinct non-antipodal S_1^3 , and $\beta = \Pi \cap S_1^3$ be a geodesic that passing through the points p and q in S_1^3 , where $\Pi = Sp\{p, q\}$. Then, for a vector $\omega = q - \langle p, q \rangle p \in R_1^4$, the parametrization of $\beta = \beta(t)$ is given by

(i) If $\langle p, q \rangle > 1$ (i.e. the angle $\theta(p, q) = \operatorname{arccosh}(\langle p, q \rangle)$), then Π is a timelike plane and

$$\beta(t) = \cosh(t)p + \sinh(t) \frac{\omega}{\|\omega\|} \quad (\text{i.e a part of pseudo-circle}) \text{ such that } \operatorname{sign}(\omega) = -1,$$

(ii) If $-1 < \langle p, q \rangle < 1$ (i.e. the angle $\theta(p, q) = \arccos(\langle p, q \rangle)$), then Π is a spacelike plane and

$$\beta(t) = \cos(t)p + \sin(t) \frac{\omega}{\|\omega\|} \quad (\text{i.e a circle}) \text{ such that } \operatorname{sign}(\omega) = 1,$$

(iii) If $\langle p, q \rangle = 1$, then Π is a null plane and $\beta(t) = p + t\omega$ (i.e a straight line) such that $\operatorname{sign}(\omega) = 0$,

(iv) If $\langle p, q \rangle < -1$, then there exists no geodesic joining p and q .

Now, we consider the differential geometry of timelike regular curves in S_1^3 . Let $\alpha: I \rightarrow S_1^3$ be a regular curve where I is an open interval in R . Then, the Gauss formula with respect to α is given by

$$X' \equiv \nabla_{\alpha'}^0 X = \bar{\nabla}_{\alpha'} X - \langle \alpha', X \rangle \alpha, \quad (8)$$

for any differentiable vector field $X \in \mathfrak{X}(\alpha(I)) \subset \mathfrak{X}(S_1^3)$ along the curve α . We say that the regular curve α is spacelike, null or timelike if $\alpha'(t) = d\alpha/dt$ is a spacelike vector, a null vector or a timelike vector, respectively, for any $t \in I$. The regular curve α is said to be a non-null curve if α is a spacelike or a timelike curve. If α is a non-null curve, α can be expressed with an arc length parametrization $s = s(t)$.

Now, we assume that $\alpha = \alpha(s)$ is a unit speed timelike curve in S_1^3 . Then the timelike unit tangent vector of α is given by $T_\alpha(s) = \alpha'(s)$. We assume that the assumption $T_{\alpha'}(s) - \alpha(s) \neq 0$, then the spacelike principal normal vector of α is given by $N_\alpha(s) = \frac{\bar{\nabla}_{T_\alpha(s)} T_\alpha(s)}{\|\bar{\nabla}_{T_\alpha(s)} T_\alpha(s)\|}$, which is pseudo-orthogonal to $\alpha(s)$ and $T_\alpha(s)$. Also, the spacelike binormal vector field of α is given by $B_\alpha(s) = T_\alpha(s) \wedge N_\alpha(s)$ which is pseudo-orthogonal $\alpha(s), T_\alpha(s)$ and $N_\alpha(s)$. Thus, $\{T_\alpha(s), N_\alpha(s), B_\alpha(s)\}$ is called (intrinsic) Frenet frame of non-geodesic timelike curve α in $T_{\alpha(s)} S_1^3$ along the curve α . Also, from the equations (3) and (4), we see that $B_\alpha(s) = \alpha(s) \times T_\alpha(s) \times N_\alpha(s)$ and so we have pseudo-orthonormal frame $\{\alpha(s), T_\alpha(s), N_\alpha(s), B_\alpha(s)\}$ of R_1^4 along α . The frame is also called the *curve- hypersurface frame* of unit speed timelike curve α on S_1^3 . By using Gauss formula (8), under the assumptions $T_{\alpha'}(s) - \alpha(s) \neq 0$, the Frenet equations of α in S_1^3 is given by

$$\bar{\nabla}_{T_\alpha} T_\alpha = \kappa_g N_\alpha, \quad \bar{\nabla}_{T_\alpha} N_\alpha = \kappa_g T_\alpha + \tau_g B_\alpha, \quad \bar{\nabla}_{T_\alpha} B_\alpha = -\tau_g N_\alpha, \quad (9)$$

where the geodesic curvature κ_g and the geodesic torsion τ_g of α is given by

$$\kappa_g(s) = \|\bar{\nabla}_{T_\alpha(s)} T_\alpha(s)\| = \|T_{\alpha'}(s) - \alpha(s)\|, \quad (10)$$

$$\tau_g(s) = \langle \bar{\nabla}_{T_\alpha(s)} N_\alpha(s), B_\alpha(s) \rangle = \frac{\det(\alpha(s), \alpha'(s), \alpha''(s), \alpha'''(s))}{(\kappa_g(s))^2}. \quad (11)$$

By using Gauss formula (8), Frenet equations of α is also given by

$$\nabla_{T_\alpha}^0 T_\alpha = \alpha + \kappa_g N_\alpha, \quad \nabla_{T_\alpha}^0 N_\alpha = \kappa_g T_\alpha + \tau_g B_\alpha, \quad \nabla_{T_\alpha}^0 B_\alpha = -\tau_g N_\alpha, \quad (12)$$

with respect to Levi-Civita connection of R_1^4 .

A non-degenerate curve in S_1^3 is a geodesic iff its geodesic curvature κ_g is zero at all points. By using (8) and (10), we see that the assumption $T_{\alpha'}(s) - \alpha(s) \neq 0$ (or equivalently $\langle \alpha''(s), \alpha''(s) \rangle \neq 1$) corresponds to the curve α is not a geodesic (i.e. $\kappa_g \neq 0$). A non-degenerate curve in S_1^3 is a planar curve iff it lies in a non-degenerate two-dimensional totally geodesic surface (i.e. geodesic torsion τ_g is zero at all point) in S_1^3 . By Remark 2.1, we say that timelike planar curve in S_1^3 , lies fully in two-dimensional unit pseudo-sphere $S_1^2 \subset S_1^3$.

Remark 2.2. Let $M = \Phi(U)$ be non-degenerate surface in S_1^3 with the unit normal vector field ξ , and T_β be the unit tangent vector field of a non-degenerate unit speed curve β which lies on the surface M . Then, β is a geodesic of M iff $\nabla_{T_\beta} T_\beta = 0$. By using (6), we conclude that $\bar{\nabla}_{T_\beta} T_\beta$ is parallel to ξ . Namely, $\bar{\nabla}_{T_\beta} T_\beta$ is orthogonal to the surface M .

Let $p \in S_1^3$ and $w \in T_p S_1^3$. The exponential map $\exp_p : T_p S_1^3 \rightarrow S_1^3$ at $p \in S_1^3$ is defined by $\exp_p(w) = \beta_w(1)$ where $\beta_w : [0, \infty) \rightarrow S_1^3$ is the constant speed geodesic starting from p with the initial velocity $\beta'_w(0) = w$. Also, the property $\exp_p(tw) = \beta_w(1) = \beta_w(t)$ is satisfied for any $t \in \mathbb{R}$. In that case, for any point $\alpha(s)$ in the timelike curve α , the spacelike principal normal geodesic in S_1^3 starting at $\alpha(s)$ is defined by the geodesic curve

$$\exp_{\alpha(s)}(tN_{\alpha}(s)) = \cos(u)\alpha(s) + \sin(u)N_{\alpha}(s),$$

for every $t \in R$.

Let's remind an important property of the parallel transport. A vector field which is pseudo-orthogonal to tangent vector of a geodesic $\beta_w(t) = \exp_p(tw)$ in S_1^3 , is invariant under parallel transport P along the geodesic. Thus, the parallel transport P from $\alpha(s)$ to $\exp_{\alpha(s)}(tN_{\alpha}(s))$ along the spacelike principal normal geodesic satisfies the following statements:

$$P(N_{\alpha}(s)) = -\sin(u)\alpha(s) + \cos(u)N_{\alpha}(s),$$

and

$$P(T_{\alpha}(s)) = T_{\alpha}(s), P(B_{\alpha}(s)) = B_{\alpha}(s).$$

3. Timelike Rectifying Curves in de Sitter 3-Space

In this section, we give the notions of timelike rectifying curve and timelike conical surface S_1^3 . After, we obtain some characterizations for timelike rectifying curves in S_1^3 .

Definition 3.1. Let $\alpha = \alpha(s)$ be a timelike non-geodesic unit speed curve in S_1^3 and p be a fixed point in S_1^3 such that $\{\pm p\} \notin \text{Im}(\alpha)$. Then α is called a timelike rectifying curve in S_1^3 iff the geodesics in S_1^3 that passing through p and $\alpha(s)$ are pseudo-orthogonal to the spacelike principal normal geodesics at $\alpha(s)$ for every s .

From the Definition 3.1, the geodesics that passing through p and $\alpha(s)$ are tangent to the timelike rectifying planes $\text{span}(\{T_{\alpha}(s), B_{\alpha}(s)\})$ of α in $T_{\alpha(s)}S_1^3 \subset R_1^4$. Namely, $\frac{d}{dt}\beta_s(t) \in \text{span}(\{T_{\alpha}(s), B_{\alpha}(s)\})$, and so it is easily seen that rectifying condition is given by

$$\left\langle \frac{d}{dt}\beta_s(t), N_{\alpha}(s) \right\rangle = 0, \quad t \in R,$$

where $\beta_s(t)$ is a geodesic that passing through p and $\alpha(s)$ such that

$$\beta_s(t) = \exp_p(t\alpha(s)) = \cos(t)p + \sin(t)\alpha(s), \quad t \in R.$$

Remark 3.1. The principal normal vector field of any non-degenerate planar curve in S_1^3 is tangent to $S_1^2 \subset S_1^3$ or $S^2 \subset S_1^3$ since its geodesic torsion is zero at all points. So, the tangent vector of geodesic connecting the planar curve with any point which is not element to the curve's image is orthogonal to principal normal vector field of the planar curve (see [9]). Hence, we say that every non-degenerate planar curve in S_1^3 is a rectifying curve. From now on, we will assume that the curve α is a timelike non-geodesic (i.e. $\kappa_g > 0$) and non-planar curve (i.e. $\tau_g \neq 0$) in S_1^3 .

Definition 3.2. Let $M = \Phi(U)$ be a timelike regular surface in S_1^3 via timelike immersion $\Phi: U \rightarrow \Phi(U) \subset S_1^3$ such that open subset $U \subseteq R^2$. Then M is called a timelike conical surface in S_1^3 if and only if M is constructed by the union of all the geodesics that pass through a fixed point (the apex) $p \in S_1^3$ and any point of some regular timelike curve (the directrix) that does not contain the apex. Also, each of those geodesics is called a generatrix of the surface.

Let the fixed point $p \in S_1^3$ be apex of M and γ be the directrix of M , which is a unit speed timelike curve in $S_1^2 \subset T_p S_1^3 \subset R_1^4$. Then the parametrization of timelike conical surface M is given by

$$\Phi(u, v) = \exp_p(v\gamma(u)) = \cos(v)p + \sin(v)\gamma(u), \quad 0 < v. \quad (13)$$

Let P be the parallel transport along the geodesic $\beta_u(t) = \exp_p(t\gamma(u)) = \Phi(u, t)$ that passing through p and $\gamma(u)$. Also, it is known that a vector field which is pseudo-orthogonal to $\frac{d}{dt}\beta_u(t)$, is invariant under parallel transport P along the geodesic β_u . Then the timelike tangent plane of M is spanned by the timelike vectors $\Phi_u(u, v)$ and spacelike vector $\Phi_v(u, v)$ is given by

$$\Phi_u(u, v) = \sin(v)\gamma'(u) = \sin(v)P(\gamma'(u)) \quad (14)$$

$$\Phi_v(u, v) = -\sin(v)p + \cos(v)\gamma(u) = P(\gamma(u)). \quad (15)$$

Coefficients of the first fundamental form of M is

$$E = \langle \Phi_u, \Phi_u \rangle = -\sin^2(v), \quad F = \langle \Phi_u, \Phi_v \rangle = 0, \quad G = \langle \Phi_v, \Phi_v \rangle = 1. \quad (16)$$

The spacelike unit normal vector field $\xi(u, v)$ of M is given by

$$\xi(u, v) = \frac{\Phi_u \wedge \Phi_v}{\|\Phi_u \wedge \Phi_v\|}(u, v) = \frac{\sin(v)}{\sqrt{|EG - F^2|}}(P(\gamma'(u)) \wedge P(\gamma(u))) = -P(N_\gamma(u)) = -N_\gamma(u), \quad (17)$$

where $N_\gamma(u) = \gamma(u) \wedge \gamma'(u)$ is a spacelike unit vector field tangent to $S_1^2 \subset T_p S_1^3$.

Let $S: \mathcal{X}(M) \rightarrow \mathcal{X}(M)$ be the Weingarten map of M , and $\kappa_\gamma = \det(\gamma, \gamma', \gamma'', p)$ be the geodesic curvature of the unit speed timelike curve γ with respect to Sabban frame (curve-surface frame) $\{\gamma, T_\gamma = \gamma', N_\gamma = \gamma \wedge T_\gamma\}$ in $S_1^2 \subset T_p S_1^3$ such that

$$\begin{cases} \bar{\nabla}_{T_\gamma} T_\gamma = \kappa_\gamma N_\gamma, \\ \bar{\nabla}_{T_\gamma} N_\gamma = \kappa_\gamma T_\gamma. \end{cases} \quad (18)$$

Then, we obtain following equations

$$S(\Phi_u) = -\bar{\nabla}_{\Phi_u} \xi = \bar{\nabla}_{T_\gamma(u)} N_\gamma(u) = \frac{\kappa_\gamma(u)}{\sin(v)} \Phi_u,$$

$$S(\Phi_v) = -\bar{\nabla}_{\Phi_v} \xi = -\nabla_{\Phi_v}^0 \xi = 0.$$

by using (7), (14), (17) and (18). Thus, the Gaussian curvature K and the mean curvature H of M is

$$K = K_e + \det(S) = 1, \quad H = \frac{1}{2} \text{tr}(S) = \frac{\kappa_\gamma(u)}{2\sin(v)}$$

where K_e is extrinsic Gaussian curvature of M . Moreover, we obtain the following equations

$$\bar{\nabla}_{\Phi_u} \Phi_u = \sin(v)\cos(v)\Phi_v - \kappa_\gamma(u)\sin(v)\xi, \quad (19)$$

$$\bar{\nabla}_{\Phi_u} \Phi_v = \bar{\nabla}_{\Phi_v} \Phi_u = \cot(v)\Phi_u, \quad (20)$$

$$\bar{\nabla}_{\Phi_v} \Phi_v = 0, \quad (21)$$

by using (5), (14) and (15).

Now, we give the relationship between timelike rectifying curves and timelike conical surface in S_1^3 .

Theorem 3.1. Let $\alpha = \alpha(s)$ be a unit speed timelike curve in S_1^3 , and $p \in S_1^3$ be a fixed point such that $p \notin \text{Im}(\alpha)$. Then, α is a timelike rectifying curve if and only if α is a geodesic of the timelike conical surface M with apex p and timelike director curve γ which is a unit speed timelike curve in 2-dimensional pseudo-sphere $S_1^2 \subset T_p S_1^3$.

Proof. Let $\alpha = \alpha(s)$ be a unit speed timelike rectifying curve in S_1^3 , and $p \in S_1^3$ be a fixed point such that $p \notin \text{Im}(\alpha)$. Then, the parametrization of α can be given by $\alpha(s) = \exp_p(v(s)\gamma(u(s)))$ for some functions $u(s)$ and $v(s)$ such that a unit speed timelike curve $\gamma = \gamma(u)$ in $S_1^2 \subset T_p S_1^3$. By using (13), $\alpha(s) = \Phi(u(s), v(s))$ is a timelike curve on timelike conical surface M which is determined by the apex p and the directrix γ . Hence, the spacelike geodesic that passing through p and $\alpha(s)$ is given by $\beta_s(t) = \Phi(u(s), t)$, and also we get the rectifying condition

$$\langle T_{\beta_s}(v(s)), N_\alpha(s) \rangle = 0, \quad (22)$$

where T_{β_s} is the spacelike unit tangent vector of β_s . So, the timelike tangent plane at point $\alpha(s)$ of M consists of tangent vectors to the generatrix including the point $\alpha(s)$ of M . Namely, $T_{\alpha(s)}M = \{T_{\beta_s}(v(s)), T_\alpha(s)\}$. Then, by using (22), we obtain that $N_\alpha(s)$ is orthogonal to M . Thus, $\bar{\nabla}_{T_\alpha} T_\alpha$ is parallel unit normal vector field of M by using (9), and so α is a geodesic of M by Remark 2.2. On the other hand, let α be a unit speed timelike geodesic of the timelike conical surface M with apex p , and its parametrization be given by $\alpha(s) = \Phi(u(s), v(s))$ with arc length parameter s . Then the spacelike principal normal vector $N_\alpha(s)$ of α is orthogonal to timelike surface M . From here, $N_\alpha(s)$ is also orthogonal to β_s , which is the unit speed spacelike generatrix that passing through $p = \beta_s(0)$ and $\alpha(s) = \beta_s(v(s))$. Thus, we get that the rectifying condition (22), and so α is a timelike rectifying curve.

Now, we give a characterization with respect to the ratio of geodesic torsion and geodesic curvature for timelike rectifying curves in S_1^3 .

Let $\alpha: I \rightarrow M \subset S_1^3$, $\alpha(s) = \Phi(u(s), v(s))$ be a unit speed timelike curve in a timelike conical surface which is given by the parametrization (13) such that some differentiable functions $u = u(s)$ and $v = v(s)$. By using (14) and (15), we obtain that

$$-1 = \langle T_\alpha, T_\alpha \rangle = -(u')^2 \sin^2(v) + (v')^2. \quad (23)$$

Moreover, from (5), we write $\bar{\nabla}_{T_\alpha} T_\alpha = \nabla_{T_\alpha}^0 T_\alpha - \Phi$ for $T_\alpha \in \mathfrak{X}(M)$. Thus, we have the following equation

$$\bar{\nabla}_{T_\alpha} T_\alpha = (u'' + 2u'v' \cot(v))\Phi_u + (v'' + (u')^2 \sin(v) \cos(v))\Phi_v - (u')^2 \kappa_\gamma(u) \sin(v) \xi, \quad (24)$$

by using (16), (19), (20) and (21).

Let α be a geodesic in timelike conical surface M (namely, a timelike rectifying curve in S_1^3). Then, it is easily seen that spacelike principal normal N_α of α is parallel to spacelike unit normal vector field ξ of M from Theorem 3.1, and so we obtain the following differential equation system

$$u'' + 2u'v' \cot(v) = 0, \quad (25)$$

$$v'' + (u')^2 v' \sin(v) \cos(v) = 0, \quad (26)$$

$$-(u')^2 \kappa_\gamma(u) \sin(v) = \kappa_g > 0. \quad (27)$$

with respect to functions $u(s)$ and $v(s)$.

If we take $f(s) = \cos(v(s))$, then we get the following differential equation

$$f''(s) - f(s) = 0,$$

by using (23) and (26). Therefore, the solution is given by

$$f(s) = \lambda_1 \sinh(s + s_0) + \lambda_2 \cosh(s + s_0), \quad (28)$$

and so

$$v(s) = \arccos(\lambda_1 \sinh(s + s_0) + \lambda_2 \cosh(s + s_0)), \quad (29)$$

where some constants λ_1, λ_2 and s_0 . Since $N_\alpha(s)$ is parallel to $\xi(u(s), v(s))$, In without loss of generality, we can write that

$$B_\alpha(s) = \lambda(s)\Phi_u(u(s), v(s)) + \mu(s)\Phi_v(u(s), v(s)),$$

where $\lambda = \frac{\langle B_\alpha, \Phi_u \rangle}{E} = \frac{v'}{\sin(v)}$ and $\mu = \frac{\langle B_\alpha, \Phi_v \rangle}{G} = -u' \sin(v)$. After straightforward calculation, we get that

$$\bar{\nabla}_{T_\alpha} B_\alpha = \lambda' \Phi_u + \mu' \Phi_v + (\lambda u') \bar{\nabla}_{\Phi_u} \Phi_u + (\lambda v' + \mu u') \bar{\nabla}_{\Phi_u} \Phi_v.$$

By using (9), (19) and (20), we obtain that the geodesic torsion which is given by

$$\tau_g = u' v' \kappa_\gamma(u).$$

From the last equation and (27), we get that

$$\frac{\tau_g}{\kappa_g} = \frac{v'}{u' \sin(v)}. \quad (30)$$

Now, by using (25), we obtain

$$u'' \sin^2(v) + 2u' v' \sin(v) \cos(v) = 0,$$

and after changing of variable, we have

$$u' \sin^2(v) = c, \quad (31)$$

for a nonzero constant c . If we consider together the equations (23), (28), (29) and (31), then we get the relation

$$c^2 = \lambda_1^2 - \lambda_2^2 + 1, \quad (32)$$

for the constants λ_1, λ_2 and c . Finally, after required calculations by using (29), (30) and (31), we obtain that

$$\frac{\tau_g}{\kappa_g}(s) = \mu_1 \sinh(s + s_0) + \mu_2 \cosh(s + s_0), \quad (33)$$

for some constants $\mu_1 = \frac{-\lambda_2}{c}$, $\mu_2 = \frac{-\lambda_1}{c}$ and s_0 such that $\mu_2^2 - \mu_1^2 < 1$.

On the other hand, let $\alpha = \alpha(s)$ be a unit speed timelike curve in S_1^3 whose geodesic curvatures satisfying the equation (33) for some constants μ_1 and μ_2 such that $\mu_2^2 - \mu_1^2 < 1$. Let c be a nonzero constant such that

$$c^2 = \frac{1}{\mu_1^2 - \mu_2^2 + 1},$$

and define two constants $\lambda_1 = -\mu_2 c$ and $\lambda_2 = -\mu_1 c$. Let the function $v(s)$ be defined by (29) and the function $u(s)$ be a solution of (31), which is given by

$$u(s) = \tanh^{-1} \left(\frac{\lambda_1 \lambda_2}{c} + \left(\frac{1 + \lambda_1^2}{c} \right) \tanh(s + s_0) \right).$$

Now, let M be the timelike conical surface with apex $p \notin \text{Im}(\alpha) \subset S_1^3$ and timelike director curve γ which is a unit speed timelike curve in $S_1^2 \subset T_p S_1^3$ such that geodesic curvature κ_γ of γ is given by (27). Then, we consider a unit speed timelike curve $\tilde{\alpha}(s) = \exp_p(v(s)\gamma(u(s))) = \Phi(u(s), v(s))$ in M , which is given by the parametrization (13) for some differentiable functions $u = u(s)$ and $v = v(s)$. It is easily seen that $\tilde{\alpha}$ is a geodesic of M , whose geodesic curvatures are the same with geodesic curvatures of the curve α , and so α is congruent to a geodesic in a timelike conical surface. Thus, we show that the equation (33) determines the timelike curves in S_1^3 that are geodesics in a timelike conical surface whose parametrization is $\Phi(u(s), v(s))$. As a result, we say that α is congruent to a timelike rectifying curve in S_1^3 by Theorem 3.1.

Consequently, we obtain the following characterization for timelike rectifying curves in S_1^3 with respect to the ratio of the geodesic curvatures.

Theorem 3.2. Let $\alpha = \alpha(s)$ be a unit speed timelike curve in S_1^3 with geodesic curvature κ_g and geodesic torsion τ_g . Then α is congruent to a timelike rectifying curve iff the ratio of geodesic torsion and geodesic curvature of the timelike curve is given by

$$\frac{\tau_g}{\kappa_g}(s) = \mu_1 \sinh(s + s_0) + \mu_2 \cosh(s + s_0),$$

for some constants μ_1, μ_2 and s_0 such that $\mu_2^2 - \mu_1^2 < 1$.

Now, we give some characterizations for timelike rectifying curves in S_1^3 .

Theorem 3.3. Let $\alpha = \alpha(s)$ be a unit speed timelike curve in S_1^3 and p be the fixed point in S_1^3 such that $p \notin \text{Im}(\alpha)$. Then the following statements are equivalent:

- (i) α is a timelike rectifying curve.
- (ii) p^\perp is the component of p which is orthogonal to T_α in S_1^3 such that

$$\langle p, T_\alpha(s) \rangle = n_1 \sinh(s + s_0) + n_2 \cosh(s + s_0), \quad (34)$$

$$|p^\perp|^2 = n^2, \quad (35)$$

for some constants n_1, n_2, n and s_0 , with $n_1^2 - n_2^2 + n^2 = 1$.

$$(iii) \quad \langle p, N_\alpha(s) \rangle = 0.$$

$$(iv) \quad \langle p, B_\alpha(s) \rangle = \sigma \text{ for some constant } \sigma.$$

$$(v) \quad \langle p, \alpha(s) \rangle = m_1 \sinh(s + s_0) + m_2 \cosh(s + s_0) \text{ for some constants } m_1, m_2 \text{ and } s_0 \text{ such that } m_2^2 - m_1^2 \leq 1.$$

$$(vi) \quad \text{Distance function in } S_1^3 \text{ between } p \text{ and } \alpha(s), \eta(s) = d(p, \alpha(s)), \text{ satisfies}$$

$$\cos(\eta(s)) = k_1 \sinh(s + s_0) + k_2 \cosh(s + s_0),$$

for some constants k_1, k_2 and s_0 such that $k_2^2 - k_1^2 \leq 1$.

Proof. Firstly, let the statement (i) is valid. From Theorem 3.1, we say that $\alpha: I \rightarrow M \subset S_1^3, \alpha(s) = \Phi(u(s), v(s))$ be a geodesic in timelike conical surface M which is given by the parametrization (13) such that some

differentiable functions $u = u(s)$ and $v = v(s)$ which are satisfying (25)-(27). Then, we obtain $\langle p, \alpha(s) \rangle = \cos(v(s))$ and we get statement (v) by using (29) and (32).

Now, let the statement (v) be valid. By using (12) and take into consideration hypothesis, then we obtain

$$\kappa_g(s) \langle p, N_\alpha(s) \rangle + \langle p, \alpha(s) \rangle = \langle p, \nabla_{T_\alpha(s)}^0 T_\alpha(s) \rangle = m_1 \sinh(s + s_0) + m_2 \cosh(s + s_0) = \langle p, \alpha(s) \rangle.$$

From this equation, it must be $\langle p, N_\alpha(s) \rangle = 0$, since $\kappa_g \neq 0$. Thus, we obtain the statement (iii).

Now, let the statement (iii) be valid. Let $\beta_s(t)$ be the spacelike geodesic that passing through $p = \beta_s(0)$ and $\alpha(s) = \beta_s(v(s))$ for some function $v(s)$. From definition of spacelike geodesic in S_1^3 , we can write

$$\beta'_s(t) = f(t)p + g(t)\alpha(s),$$

for some differentiable functions $f(t)$ and $g(t)$ which satisfy the condition $f(t)^2 + g(t)^2 = 1$. Taking into account that hypothesis and $\langle \alpha, N_\alpha(s) \rangle = 0$ by curve-hypersurface frame of α , then we obtain the rectifying condition

$$\langle \beta'_s(v(s)), N_\alpha(s) \rangle = 0.$$

Namely, the statement (i) is obtained. Thus, we say that statements (i), (iii) and (v) are equivalent.

Now, let us show that the statements (iii) and (iv) are equivalent. We suppose that the statement (iii) is valid. After using (12) and hypothesis, we get

$$\frac{d}{ds} \langle p, B_\alpha(s) \rangle = -\tau_g(s) \langle p, N_\alpha(s) \rangle = 0. \quad (36)$$

then the statement (iv) is obtained. Conversely, let the statement (iv) is valid. if we take into consideration that hypothesis and $\tau_g \neq 0$, it has easily seen that by using (36). Hence, we see that (iii) \Leftrightarrow (iv).

Now, let us show that the statements (v) and (vi) are equivalent. Since the position vector of $\alpha(s)$ and the point $p \in S_1^3$ are spacelike, in without lost of generality, we may write $\langle p, \alpha(s) \rangle = \cos(\eta(s))$ for some function $\eta(s)$. Thus, it is easily seen that (v) \Leftrightarrow (vi).

Finally, let us show that the statements (i) and (ii) are equivalent. Now, let the statement (i) be valid. In this case, we say that the statements (iii), (iv) and (v) are hold from the previous results. If we take derivative in (v), we get

$$\langle p, T_\alpha(s) \rangle = m_1 \cosh(s + s_0) + m_2 \sinh(s + s_0),$$

and so the equation (34) is obtained. Moreover, we have

$$|p^\perp|^2 = \langle p, N_\alpha \rangle^2 + \langle p, B_\alpha \rangle^2 = \sigma^2$$

where $p^\perp \in Sp\{N_\alpha, B_\alpha\}$ by using the statements (iii) and (iv). Also, taking into account that T_α is timelike, it is easily seen that

$$1 = \langle p, p \rangle = \langle p, \alpha \rangle^2 - \langle p, T_\alpha \rangle^2 + \langle p, B_\alpha \rangle^2 = m_2^2 - m_1^2 + \sigma^2,$$

for some constants $m_1 = n_2$, $m_2 = n_1$ and $\sigma = n$. Thus the equation (35) is obtained. Namely, we see that (i) \Rightarrow (ii). Conversely, let the statement (ii) is valid. After integrating the equation (34), we have

$$\langle p, \alpha(s) \rangle = n_1 \cosh(s + s_0) + n_2 \sinh(s + s_0) + c_0, \quad (37)$$

for some constant c_0 . Moreover, we have

$$n_1^2 - n_2^2 = \langle p, \alpha \rangle^2 - \langle p, T_\alpha \rangle^2 = 1 - n^2. \quad (38)$$

by using the equation (35). By considering together the equations (34), (37) and (38), then it is easily seen that $c_0 = 0$. Hence, the statement (v) is obtained and so $(v) \Rightarrow (i)$. Consequently, we show that $(i) \Leftrightarrow (ii)$. The proof is complete.

Now, we give the following theorem which characterizes all timelike rectifying curve in S_1^3 .

Theorem 3.4. Let α be a timelike non-planar curve in S_1^3 . Then, α is a timelike rectifying curve if and only if, up to reparametrization, it is given by

$$\alpha(t) = \exp_p(\eta(t)\gamma(t)) = \cos(\eta(t))p + \sin(\eta(t))\gamma(t), \quad (39)$$

where p is the fixed point in S_1^3 such that $p \notin \text{Im}(\alpha)$, $\gamma = \gamma(t)$ is a unit speed timelike curve in $S_1^2 \subset T_p S_1^3$, and $\eta(t) = \arctan(\text{asech}(t + t_0))$ for some constants $a \neq 0$ and t_0 .

Proof. Let $p \in S_1^3$ be a fixed point, $\eta = \eta(t)$ be a positive function and $\gamma = \gamma(t)$ be an unit speed timelike curve in $S_1^2 \subset T_p S_1^3$. If we take as $\alpha(t) = \exp_p(\eta(t)\gamma(t))$ where $p \notin \text{Im}(\alpha)$, then the timelike unit tangent vector field T_α of α is

$$T_\alpha = \frac{\alpha'}{\|\alpha'\|} = \frac{-\eta' \sin(\eta)}{\|\alpha'\|} p + \frac{\eta' \cos(\eta)}{\|\alpha'\|} \gamma + \frac{\sin(\eta)}{\|\alpha'\|} \gamma', \quad (40)$$

where

$$\alpha' = -\eta' \sin(\eta)p + \eta' \cos(\eta)\gamma + \sin(\eta)\gamma',$$

and

$$\|\alpha'\|^2 = \sin^2(\eta) - (\eta')^2 > 0. \quad (41)$$

Moreover, let $s = s(t)$ be the arc length parameter of α such that $\|\alpha'\|(t) = s'(t)$. Then we have

$$\left(\frac{T_{\alpha'}}{\|\alpha'\|} - \alpha \right)(t) = (\kappa_g N_\alpha)(s) \text{ by using (12). It means that } N_\alpha \text{ is parallel to the spacelike vector field } \left(\frac{T_{\alpha'}}{\|\alpha'\|} - \alpha \right).$$

However, let $\{\gamma, \gamma', N_\gamma\}$ be Sabban frame (curve-surface frame) of the unit speed timelike curve γ in $S_1^2 \subset T_p S_1^3$ where geodesic curvature of γ is defined by $\kappa_\gamma = \det(\gamma, \gamma', \gamma'', p)$. Then, by using (18) and Gauss formula, we have

$$\gamma'' = \gamma + \kappa_\gamma N_\gamma \quad (42)$$

where spacelike principal normal $N_\gamma = \gamma \wedge \gamma'$ is tangent to S_1^2 , but normal to p and γ . We get

$$\langle p, \frac{1}{\|\alpha'\|} T_{\alpha'} - \alpha \rangle = \frac{1}{\|\alpha'\|} \left(\frac{\eta'}{\|\alpha'\|} \sin(\eta) \right)' + \cos(\eta).$$

by using (40) and (42). According to the Theorem 3.3, α is a timelike rectifying curve in S_1^3 if and only if

$\langle p, N_\alpha \rangle = 0$. Thus, it must be $\frac{1}{\|\alpha'\|} \left(\frac{\eta'}{\|\alpha'\|} \sin(\eta) \right)' + \cos(\eta) = 0$. After basic calculations, we reach to the differential equation

$$\sin(\eta)\eta'' - 2\cos(\eta)(\eta')^2 + \cos(\eta)\sin^2(\eta) = 0, \quad (43)$$

since N_α is parallel to $\left(\frac{1}{\|\alpha'\|} T_{\alpha'} - \alpha \right)$. Now, we consider a differentiable function $h = h(t)$ such that $\eta(t) = \arctan(h(t))$ for solving the equation (43). In that case, we reach to the equation

$$\frac{1}{(1+h^2)^{3/2}} (hh'' - 2(h')^2 + h^2) = 0.$$

The nontrivial solutions of this differential equation are given by the function $h(t) = a \operatorname{sech}(t + t_0)$ for some constants $a \neq 0$ and t_0 . Thus, we have that $\alpha(t) = \exp_p(\eta(t)\gamma(t))$ is a timelike rectifying curve in S_1^3 iff $\eta(t) = \tan^{-1}(a \operatorname{sech}(t + t_0))$ for some constants $a \neq 0$ and t_0 .

Chen and Dillen give some characterizations for rectifying curves with the viewpoint of extremal curves in Euclidean 3-space [3]. Riemannian viewpoint of this idea is introduced by Lucas and Yagües in Minkowski model of hyperbolic 3-space as Riemannian space form with negative constant curvature [10].

Now, we give some characterizations for Lorentzian version of timelike rectifying curves from the viewpoint of extremal curves in S_1^3 which is Lorentzian space form with positive constant curvature one.

Definition 3.3. Let α be a timelike curve in S_1^3 , is given by $\alpha(t) = \exp_p(\eta(t)\gamma(t))$ where $p \in S_1^3$, $\eta(t) \neq 0$ is an arbitrary function and $\gamma(t)$ is a timelike curve lying in $S_1^2 \subset T_p S_1^3$. Then γ is called the timelike pseudo-spherical projection of α .

The following characterization means that a timelike rectifying curve in S_1^3 is actually an extremal curve which assumes the minimum value of the function $\frac{\|\alpha'\|^4 \kappa_g^2}{\sin^2(\eta)}$ at each point among the curves with the same timelike pseudo-spherical projection.

Theorem 3.5. Let p be a fixed point in S_1^3 and $\gamma = \gamma(t)$ be a unit speed timelike curve with geodesic curvature κ_γ in $S_1^2 \subset T_p S_1^3$. Then, for any nonzero function $\eta(t)$, the geodesic curvature κ_g of a timelike regular curve α in S_1^3 which is given by $\alpha(t) = \exp_p(\eta(t)\gamma(t))$, and κ_γ satisfy the inequality

$$\kappa_\gamma^2 \leq \frac{\|\alpha'\|^4 \kappa_g^2}{\sin^2(\eta)}, \quad (44)$$

with the equality sign holding identically if and only if α is a timelike rectifying curve in S_1^3 .

Proof. Let η be a nonzero function and α be a timelike regular curve in S_1^3 which is given by $\alpha(t) = \exp_p(\eta(t)\gamma(t))$, where γ is a unit speed timelike curve in $S_1^2 \subset T_p S_1^3$. If we consider together the equation

(40) with definition the map \exp_p , and taking account that N_γ is a spacelike vector orthogonal to timelike subspace $\text{span}\{p, \gamma, \gamma'\}$, and so we find that N_γ is orthogonal to both α and T_α . Then, we have

$$N_\gamma = \gamma \wedge \gamma' = \cos(\theta)N_\alpha + \sin(\theta)B_\alpha \quad (45)$$

such that $\theta = \theta(t)$ is a arbitrary function. By differentiating of (45) with respect to t , in addition to applying (12) and (42), we obtain

$$\kappa_\gamma \gamma' = (\|\alpha'\| \kappa_g \cos(\theta))T_\alpha + (\theta' + \|\alpha'\| \tau_g)(-\sin(\theta)N_\alpha + \cos(\theta)B_\alpha) \quad (46)$$

where $\|\alpha'\|$ satisfies the eq. (41). Since $\langle \gamma', \gamma' \rangle = -1$ and $\langle T_\alpha, T_\alpha \rangle = -1$, we have

$$\kappa_\gamma^2 = (\|\alpha'\| \kappa_g \cos(\theta))^2 - (\theta' + \|\alpha'\| \tau_g)^2. \quad (47)$$

Now, we will give the point p with respect to the curve-hypersurface frame $\{\alpha, T_\alpha, N_\alpha, B_\alpha\}$ of α . By using (39), we get

$$\langle p, \alpha \rangle = \cos(\eta), \quad (48)$$

and after differentiating of (48),

$$\langle p, T_\alpha \rangle = -\frac{\eta' \sin(\eta)}{\|\alpha'\|} \quad (49)$$

by using (40). Now, suppose that

$$\gamma' = \sigma_1 T_\alpha + \sigma_2 (-\sin(\theta)N_\alpha + \cos(\theta)B_\alpha)$$

such that

$$\sigma_1 = \frac{\|\alpha'\| \kappa_g \cos(\theta)}{\kappa_\gamma}, \quad \sigma_2 = \frac{\theta' + \|\alpha'\| \tau_g}{\kappa_\gamma}$$

by using (46). Since $\langle p, \gamma' \rangle = 0$ and $\langle p, N_\gamma \rangle = 0$, we obtain linear equation system depending on $\langle p, N_\alpha \rangle$ and $\langle p, B_\alpha \rangle$ by using (45) and (49) and so its solution is given by

$$\langle p, N_\alpha \rangle = \frac{\sigma_1}{\sigma_2} \frac{\eta'}{\|\alpha'\|} \sin(\theta) \sin(\eta), \quad (50)$$

$$\langle p, B_\alpha \rangle = -\frac{\sigma_1}{\sigma_2} \frac{\eta'}{\|\alpha'\|} \cos(\theta) \sin(\eta). \quad (51)$$

From the equations (48)-(51), we get

$$p = \cos(\eta)\alpha - \frac{\eta' \sin(\eta)}{\|\alpha'\|} T_\alpha + \frac{\sigma_1 \eta' \sin(\theta) \sin(\eta)}{\sigma_2 \|\alpha'\|} N_\alpha - \frac{\sigma_1 \eta' \cos(\theta) \sin(\eta)}{\sigma_2 \|\alpha'\|} B_\alpha.$$

Then,

$$1 = \langle p, p \rangle = \cos^2(\eta) + \sin^2(\eta) \left(\frac{\eta'}{\|\alpha'\|} \right)^2 \left(\left(\frac{\sigma_1}{\sigma_2} \right)^2 - 1 \right)$$

and so it must be

$$\left(\frac{\eta'}{\|\alpha'\|}\right)^2 \left(\left(\frac{\sigma_1}{\sigma_2}\right)^2 - 1\right) = 1.$$

Also, if we put σ_1 and σ_2 in this equation, we reach to the equation

$$(\theta' + \|\alpha'\| \tau_g)^2 = \frac{(\eta')^2}{\|\alpha'\|^2 + (\eta')^2} (\|\alpha'\| \kappa_g \cos(\theta))^2. \quad (52)$$

After putting (52) in (47), and also considering the equation (41), we get

$$\kappa_\gamma^2 = \frac{\|\alpha'\|^4 \kappa_g^2 \cos^2(\theta)}{\sin^2(\eta)} \quad (53)$$

which implies inequality (44). It is clear, equality situation of (44), it must be $\sin(\theta) = 0$. Also, take into consideration the equation (45), we get $N_\gamma = \mp N_\alpha$. It means that N_γ and N_α are parallel. Then, by Theorem 3.1, α is a geodesic in timelike conical surface M which is given by the parametrization (13) and so it is a timelike rectifying curve. Therefore, α is a timelike rectifying curve in S_1^3 iff equality situation of (44) is satisfied.

Now, we show that a timelike curve in De Sitter 3-space, which has non-zero constant geodesic curvature and linear geodesic torsion, congruent to a timelike rectifying curve, which is generated by a spiral type unit speed timelike curve with certain geodesic curvature in 2-dimensional pseudo-sphere, and vice versa. Namely, the following corollary is a construction method for timelike spiral type rectifying curves in S_1^3 .

Corollary 3.1. A timelike regular curve α is given by $\alpha(s) = \exp_p(\eta(s)\gamma(s))$ in S_1^3 with nonzero constant geodesic curvature κ_0 and linear geodesic torsion

$$\tau_g(s) = c_1 \sinh(s + s_0) + c_2 \cosh(s + s_0)$$

such that $c_2^2 - c_1^2 - \kappa_0^2 < 0$ for some constants c_1, c_2 and s_0 iff α is congruent to a timelike rectifying curve which is generated by a unit speed timelike spiral type curve $\gamma(t)$ in $S_1^2 \subset T_p S_1^3$ with geodesic curvature

$$\kappa_\gamma(t) = b(\cosh^2(t + t_0) + a^2)^{-3/2} \text{ for some constants } a \neq 0, b \neq 0 \text{ and } t_0.$$

Proof. Let $\alpha = \exp_p(\eta\gamma)$ be a timelike regular curve in S_1^3 with nonzero constant geodesic curvature κ_0 and geodesic torsion $\tau_g(s) = c_1 \sinh(s + s_0) + c_2 \cosh(s + s_0)$ in arc length parameter s where $c_2^2 - c_1^2 - \kappa_0^2 < 0$ for some constants c_1, c_2 and s_0 . Then, α is a timelike rectifying curve by Theorem 3.2. Hence, by using Theorem 3.4, we take $\eta(t) = \arctan(a \operatorname{sech}(t + t_0))$ for some constants $a \neq 0$ and t_0 . Also, taking account of Theorem 3.5, we obtain that $\kappa_\gamma(t) = b(\cosh^2(t + t_0) + a^2)^{-3/2}$ for nonzero constant $b = a(1 + a^2)\kappa_0$.

On the other hand, let $\alpha = \exp_p(\eta\gamma)$ be a timelike rectifying curve in S_1^3 which is generated by a unit speed timelike curve $\gamma = \gamma(t)$ which is lying in $S_1^2 \subset T_p S_1^3$ with geodesic curvature $\kappa_\gamma(t) = b(\cosh^2(t + t_0) + a^2)^{-3/2}$ such that $b \neq 0$. Then, by using Theorem 3.4, we get function $\eta(t) = \arctan(a \operatorname{sech}(t + t_0))$ for some constants $a \neq 0$ and t_0 , and so, we have

$$\frac{\|\alpha'\|^4}{\sin^2(\eta)} = \frac{a(1 + a^2)^2}{(a^2 + \cosh^2(t + t_0))^3}.$$

Since α is a timelike rectifying curve, in accordance with Theorem 3.5,

$$\kappa_\gamma^2 = \frac{\|\alpha'\|^4 \kappa_g^2}{\sin^2(\eta)}.$$

Thus, we obtain that the nonzero constant

$$\kappa_g^2 = \frac{b^2}{a^2(1+a^2)^2}.$$

Finally, if we take into account Theorem 3.2, the proof is complete.

Remark 3.2. We obtain also characterizations for spacelike rectifying curves in S_1^3 by using similar methods which is given in Section 3.

4. Some Examples of Non-Degenerate Rectifying Curves

Now, we give some examples for timelike or spacelike rectifying curve in S_1^3 .

Example 4.1. Let α be a timelike rectifying curve in S_1^3 with geodesic curvature $\kappa_g(s)=10$ and geodesic torsion $\tau_g(s)=2\sinh(s)+2\cosh(s)$. Then, we obtain stereographic projection in Minkowski 3-space which is congruent to α by using numeric methods in Mathematica (see Figure 1)

Example 4.2. Let a timelike pseudo-spherical projection curve be given by

$$\gamma(t) = \left(\frac{15}{8} \cos(17t), 0, \frac{25}{16} \cos(9t) + \frac{9}{16} \cos(25t), \frac{25}{16} \sin(9t) - \frac{9}{16} \sin(25t) \right),$$

in $S_1^2 \subset T_p S_1^3$ (see Figure 2). Then, the parametrization of timelike rectifying curve α is

$$\alpha(t) = \frac{\operatorname{sech}(t)}{16\sqrt{1+\operatorname{sech}^2(t)}} \left(30\cos(17t)\operatorname{sech}(t), \frac{16}{\operatorname{sech}(t)}, 25\cos(9t) + 9\cos(25t), 25\sin(9t) - 9\sin(25t) \right)$$

where the point $p = (0, 1, 0, 0) \in S_1^3$ and the function $\eta(t) = \arctan(\operatorname{sech}(t))$ (see Figure 3).

Example 4.3. Let a spacelike pseudo-spherical projection curve be given by

$$\gamma(t) = \left(\sinh\left(\frac{t}{15}\right), \cosh\left(\frac{t}{15}\right)\cos(t), \cosh\left(\frac{t}{15}\right)\sin(t), 0 \right),$$

in $S_1^2 \subset T_p S_1^3$ (see Figure 4). Then, the parametrization of spacelike rectifying curve α is

$$\alpha(t) = \frac{1}{\sqrt{1+\sec^2(t)}} \left(\sec(t)\sinh\left(\frac{t}{15}\right), \cosh\left(\frac{t}{15}\right), \cosh\left(\frac{t}{15}\right)\tan(t), 1 \right)$$

where the point $p = (0, 0, 0, 1) \in S_1^3$ and the function $\eta(t) = \arctan(\sec(t))$ (see Figure 5).

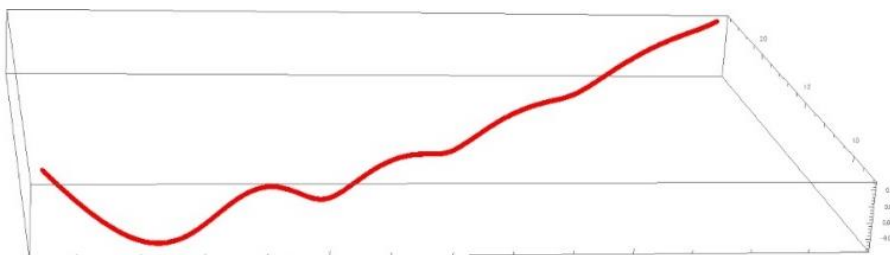


Figure 1. Stereographic projection in Minkowski 3-space of timelike rectifying curve α .

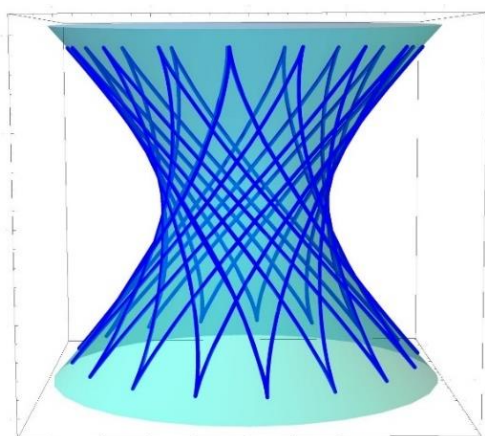


Figure 2. Timelike pseudo-spherical projection curve $\gamma(t)$ in S_1^2 of timelike rectifying curve α

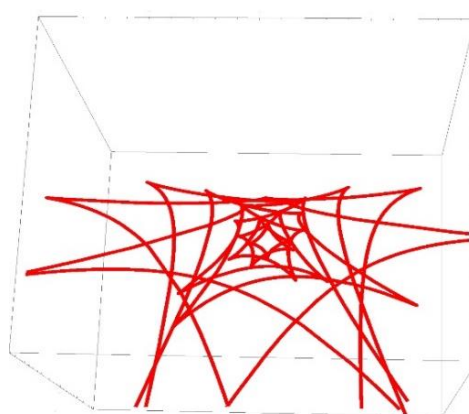


Figure 3. Stereographic projection in Minkowski 3-space of timelike rectifying curve α

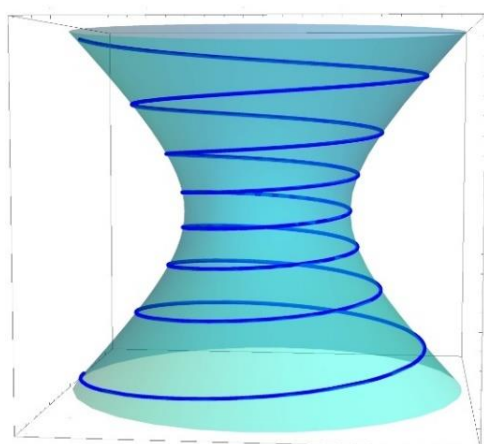


Figure 4. Spacelike pseudo-spherical projection curve $\gamma(t)$ in S_1^2 of spacelike rectifying curve α

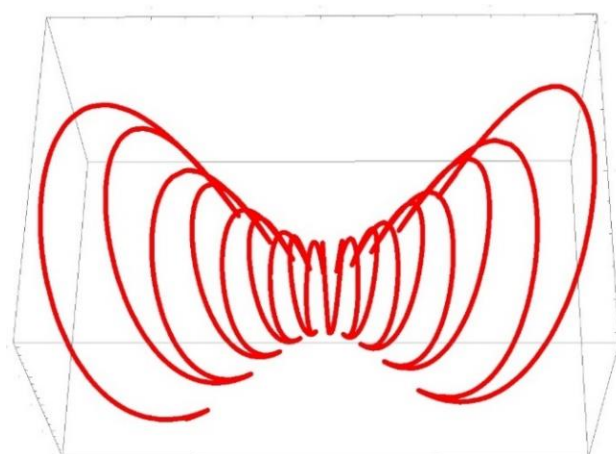


Figure 5. Stereographic projection in Minkowski 3-space of spacelike rectifying curve α

Conflicts of interest

There is no conflict of interest.

References

- [1] Chen B.Y., When does the position vector of a space curve always lie in its rectifying plane? *American Mathematical Monthly*, 110(2) (2003) 147-152.
- [2] Kim D.S., Chung H.S., Cho K.H., Space curves satisfying $\tau/\kappa = as + b$, *Honam Mathematical Journal*, 15(1) (1993) 5-9.
- [3] Chen B.Y., Dillen F., Rectifying curves as centrodes and extremal curves, *Bulletin of the Institute of Mathematics Academia Sinica*, 33(2) (2005) 77-90.
- [4] Chen B.Y., Rectifying curves and geodesics on a cone in the Euclidean 3-space, *Tamkang Journal of Mathematics*, 48(2) (2017) 209-214.

- [5] Deshmukh S, Chen BY, Alshammari SH. On rectifying curves in Euclidean 3-space, *Turkish Journal of Mathematics*, 42(2) (2018) 609-620.
- [6] İlarslan K, Nevsovic E., Some characterizations of rectifying curves in the Euclidean space, *Turkish Journal of Mathematics*, 32(1) (2008) 21-30.
- [7] İlarslan K., Nevsovic E., Petrovic M.T., Some characterizations of rectifying curves in the Minkowski 3-space, *Novi Sad Journal of Mathematics*, 33(2) (2003) 23-32.
- [8] Izumiya S, Takeuchi N., New special curves and developable surfaces, *Turkish Journal of Mathematics*, 28(2) (2004) 153-163.
- [9] Lucas P., Ortega J.Y., Rectifying curves in the three-dimensional sphere, *Journal of Mathematical Analysis and Applications*, 421(2) (2015) 1855-1868.
- [10] Lucas P, Ortega JY. Rectifying curves in the three-dimensional hyperbolic space, *Mediterranean Journal of Mathematics*, 13(4) (2016) 2199-2214.
- [11] Chen L, Takahashi M. Dualities and evolutes of fronts in hyperbolic and de Sitter space, *Journal of Mathematical Analysis and Applications*, 37(1) (2016) 133-159.
- [12] Huang J., Chen L., Izumiya S., Pei D., Geometry of special curves and surfaces in 3-space form, *Journal of Geometry and Physics*, 136 (2019) 31-38.
- [13] Lucas P., Ortega J.Y., Bertrand curves in non-flat 3-dimensional (Riemannian or Lorentzian) space forms, *Bulletin of the Korean Mathematical Society*, 50(4) (2013) 1109-1126.
- [14] O'Neill B., Semi-Riemannian Geometry with Applications to Relativity, London, UK: Academic Press Inc, 1983.

Modelling studies on the investigation of non-linear optical properties of some ExⁿBox cyclophanes

Koray SAYIN^{1,2*} , Majid REZAEIVALA³ 

¹ Sivas Cumhuriyet University, Faculty of Science, Department of Chemistry 58140 Sivas, Turkey

² Sivas Cumhuriyet University, Advanced Research and Application Center (CUTAM) 58140 Sivas, Turkey

³ Hamedan University of Technology, Department of Chemical Engineering, Hamedan 65155, Iran

Abstract

Modelling studies on some ExⁿBox Cyclophanes were performed at HF/6-31G(d) level. Structural properties are examined in detail. Density of state (DOS) spectrum and molecular orbital energy diagram of related compounds at ground state were calculated and contour plots of significant molecular orbitals were investigated in detail. Some quantum chemical descriptors were calculated in the gas phase to examine the non-linear optical properties. Finally, UV-VIS spectrum of the mentioned compounds was calculated and examined in gas phase, toluene, chloroform, ethanol, methanol, 1,2-ethanediol, water and n-methylformamide-mixture. As a result, EX^{2.2}Box⁴⁺ was found as the best candidate to NLO applications.

Article info

History:

Received:11.02.2020

Accepted:06.05.2020

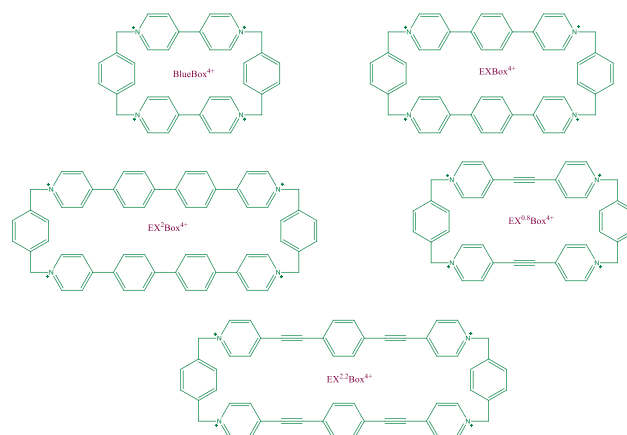
Keywords:

ExⁿBox,
Spectral analyses,
Modeling studies,
Ab-initio,
Optical property.

1. Introduction

Referred [1] to as ExⁿBox⁴⁺ compounds, tetracationic cyclophanes is produced by reacting rigid bipyridyl-based linkers, in which n is the number of p-phenylene spacers having been employed toward various chemistry [2,3]. The recent advent of extended viologen boxes, EXⁿBox⁴⁺ has given rise to the opportunity to construct mechanomolecules out of ever larger recognition units due to the longer dimensions of their cavities. EXBox⁴⁺ has an extraordinary ability to recognize polycyclic aromatic hydrocarbons (PAHs). Even larger EXⁿBoxes possessing viologen extensions are likely to construct, such as p-tertphenylene-hexamethylated for the sake of solubility, dramatically reducing its affinity for guests- as well as bis-p-phenylene-ethylene spacers, resulting in high-yielding preparation of the corresponding host, EX^{2.2}Box⁴⁺. Tetracationic cyclophanes are often used due to the favorable electronic, optical and redox properties and diverse binding ability. These macrocyclic compounds generally possess a two π -deficient cavity on the extended planes and two aromatic linkers [4]. These compounds have been used in the development of axially chiral system, liquid

crystal and nonlinear optical properties [5,6]. The cyclophanes also exhibit optical properties that are influenced by a nonconventional internal charge transfer process, stemming from the strained cyclobutane core. In this project, the attempt is made to investigate CBPQT⁴⁺ (BlueBox⁴⁺), EXBox⁴⁺, EX²Box⁴⁺, EX^{0.8}Box⁴⁺ and EX^{2.2}Box⁴⁺ as computationally techniques were those who synthesized BlueBox⁴⁺, EXBox⁴⁺, EX²Box⁴⁺, EX^{0.8}Box⁴⁺ and EX^{2.2}Box⁴⁺, respectively [7-10]. Schematic structures of these compounds are displayed in Scheme 1.



Scheme 1. Structures of BlueBox⁴⁺, EXBox⁴⁺, EX²Box⁴⁺, EX^{0.8}Box⁴⁺ and EX^{2.2}Box⁴⁺.

*Corresponding author. Email address: krysayin@gmail.com, ksayin@cumhuriyet.edu.tr
<http://dergipark.gov.tr/csj> ©2020 Faculty of Science, Sivas Cumhuriyet University

Quantum chemical analyses of these structures are completed at HF/6-31G(d) level in vacuum. Initially, these structures are optimized at the same level of theory. To investigate the non-linear optical (NLO) properties, their molecular orbital energy diagrams are plotted by selecting the degeneracy threshold as 0.01 a.u. Significant molecular orbitals are determined and their contour diagrams are calculated and examined in detail. Density of state (DOS) spectrum of related compounds is calculated and examined. UV-VIS spectrum of mentioned molecules are calculated at the same level of theory in each area and the wavelength of main band is examined. Finally, some quantum chemical descriptors are calculated in gas phase, toluene, chloroform, ethanol, methanol, 1,2-ethanediol, water and n-methylformamide-mixture.

2. Methods

Theoretical calculations of some ExⁿBox Cyclophanes were performed at HF method with 6-31G(d) basis set in vacuum. Gaussian 5.0.8 [11], Gaussian09 AS64L-G09RevD.01 [12], Chem-Bio Office [13] and GaussSum [14] were used in the whole analyses and structural properties of BlueBox⁴⁺, EXBox⁴⁺, EX²Box⁴⁺, EX^{0.8}Box⁴⁺ and EX^{2.2}Box⁴⁺ were examined. Ultraviolet-Visible (UV-VIS) spectrum of mentioned molecules was calculated in different eight phases which are gas phase ($\epsilon=1$), toluene ($\epsilon=2.3741$), chloroform ($\epsilon=4.7113$), ethanol ($\epsilon=24.852$), methanol ($\epsilon=32.613$), 1,2-ethanediol ($\epsilon=40.245$), water ($\epsilon=78.3553$) and n-methylformamide-mixture ($\epsilon=181.56$). In these calculations, the time-dependent (TD) method was taken into consideration. As for the solvent model, CPCM method was used in solvent calculations. In the determination of NLO properties, urea was selected as a reference material. Some quantum chemical descriptors (QCDs) were used to determine the NLO activity and calculated by using Eq. (1) - (15):

$$I = -E_{HOMO} \quad (1)$$

$$A = -E_{LUMO} \quad (2)$$

$$E_{GAP} = E_{LUMO} - E_{HOMO} \quad (3)$$

$$\eta = \frac{I - A}{2} = \frac{E_{LUMO} - E_{HOMO}}{2} \quad (4)$$

$$\sigma = \frac{1}{\eta} \quad (5)$$

$$\sigma_0 = \frac{1}{E_{GAP}} \quad (6)$$

$$\chi = \frac{|I + A|}{2} = \frac{|-E_{HOMO} - E_{LUMO}|}{2} \quad (7)$$

$$CP = -\chi \quad (8)$$

$$\Delta N_{Max} = -\frac{CP}{\eta} \quad (9)$$

$$\omega = \frac{CP^2}{2\eta} \quad (10)$$

$$N = \frac{1}{\omega} \quad (11)$$

$$\mu = \sqrt{\mu_x^2 + \mu_y^2 + \mu_z^2} \quad (13)$$

$$\alpha = \frac{1}{3}(\alpha_{xx} + \alpha_{yy} + \alpha_{zz}) \quad (14)$$

$$\Delta a = \frac{1}{\sqrt{2}}[(a_{xx} - a_{yy})^2 + (a_{yy} - a_{zz})^2 + (a_{zz} - a_{xx})^2 + 6a_{xz}^2 + 6a_{xy}^2 + 6a_{yz}^2]^{1/2} \quad (15)$$

$$\beta = [(\beta_{xxx} + \beta_{xyy} + \beta_{xzz})^2 + (\beta_{yyy} + \beta_{xxy} + \beta_{yzz})^2 + (\beta_{zzz} + \beta_{xzz} + \beta_{yzz})^2]^{1/2} \quad (16)$$

where Koopmans theorem was taken into consideration in the obtaining of the ionization energy and electron affinities [15]. Calculated in each solvent for studied compounds were related quantum chemical parameters.

3. Results and Discussion

3.1. Molecular structure

BlueBox⁴⁺, EXBox⁴⁺, EX²Box⁴⁺, EX^{0.8}Box⁴⁺ and EX^{2.2}Box⁴⁺ are optimized at HF/6-31G(d) level in vacuum. Optimized structures of mentioned ExⁿBoxes are represented in Fig. 1.

Given the optimized structure of studied molecules, the whole compounds are quite tense. There are a lot of π electrons. Molecular planarity is distorted in each compound. Especially, benzene rings on both sides are nearly perpendicular to other benzene rings. IR spectrum of each studied ExⁿBoxes was calculated and no imaginary frequency was observed in the results. Bond lengths, represented in BlueBox⁴⁺ are calculated as 111°, 112°, 116°, 116° and 115° for BlueBox⁴⁺, EXBox⁴⁺, EX²Box⁴⁺, EX^{0.8}Box⁴⁺ and EX^{2.2}Box⁴⁺, respectively. These angles imply the structural tension.

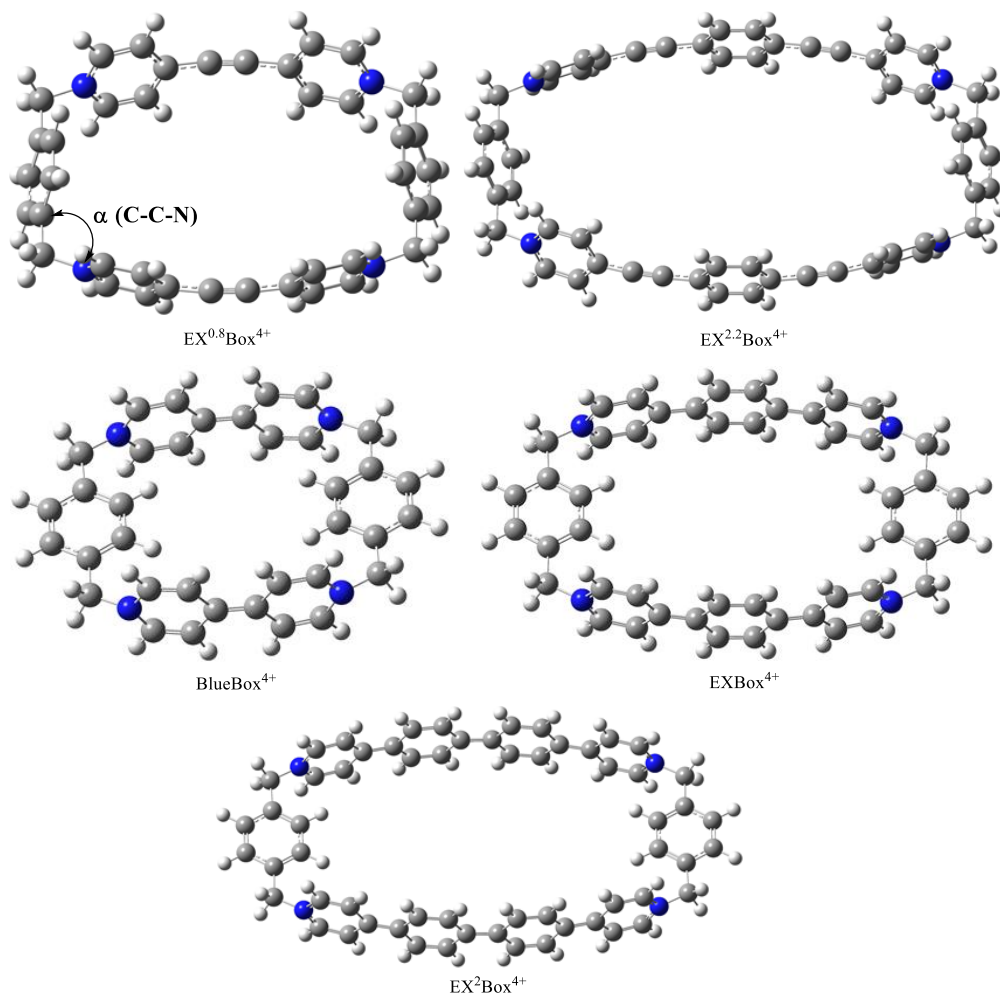


Fig. 1. Ground state structure of studied of some Ex^nBox Cyclophanes.

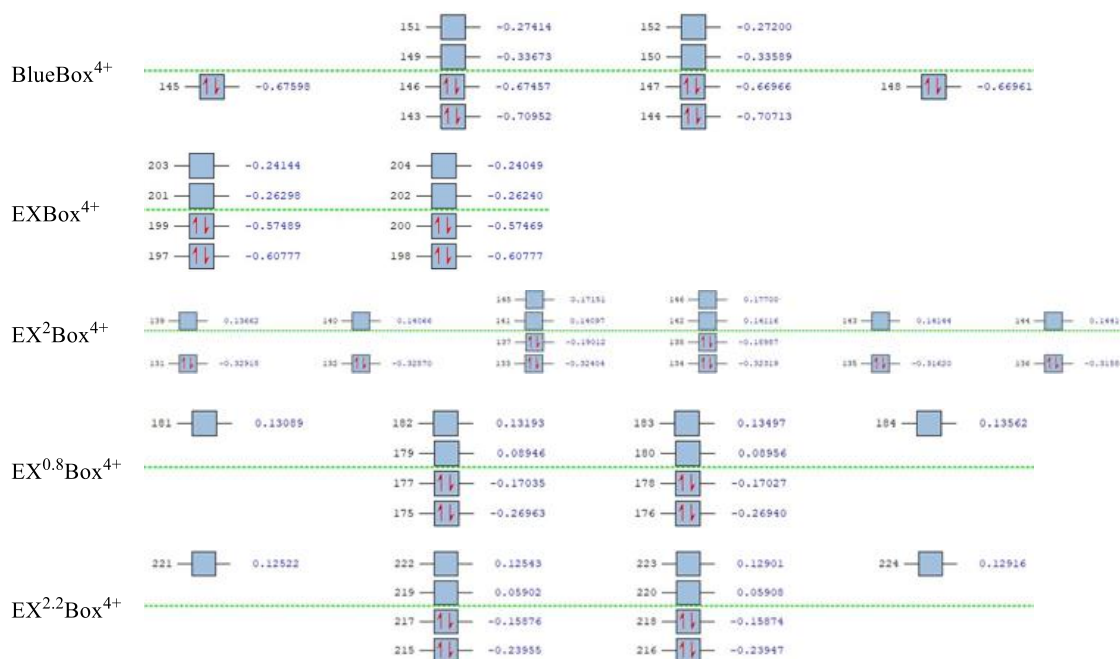


Fig. 2. The molecular orbital energy diagram of mentioned compounds.

3.2. Molecular orbital energy diagram (MOED), contour diagram and density of state (DOS) spectrum

Energy diagram of molecular orbitals (MOEDs) are important to detect the electron fluidity and indirectly to understand the optical property. The lower energy gap means the more electron mobility. Electrons can transfer from ground state to excited state. However, the determination of related molecular orbitals is important. In this stage, MOEDs are calculated by defining the degeneracy threshold as 0.01 a.u, represented in Fig. 2.

Frontier molecular orbitals, the highest occupied molecular orbital (HOMO) and the lowest unoccupied molecular orbitals are important in the determination of electronic properties of compounds. In addition to these molecular orbitals, degenerate molecular orbitals are important in the determination of electronic properties of chemicals, too. Significant molecular orbitals can be seen easily from Fig. 2. For instance, LUMO+1 (150. MO), LUMO (149. MO), HOMO (148. MO), HOMO-1 (147. MO), HOMO-2 (146. MO) and HOMO-3 (145. MO) are important for BlueBox⁴⁺. Contour plots of selected molecular orbitals in BlueBox⁴⁺ are showed in Fig. 3 and selected molecular orbitals in each box are represented in Supplemental Material.

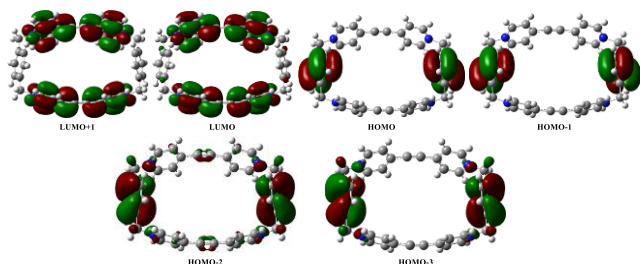


Fig. 3. Contour diagrams of selected MOs in BlueBox⁴⁺.

According to Fig. 2 and Fig. 3, there are red and green loops in contour plots. In occupied molecular orbitals, these loops imply the electron delocalization region. As for the unoccupied molecular orbital, if related compound accepts electron(s), this electron will be delocalized on mentioned loops. There are two electrons in HOMO and these electrons are delocalized on benzene rings where both side on molecule structure. In the determination of optical properties, contour plots of occupied molecular orbitals are more important than those of unoccupied molecular orbitals. Because the optical property is directly proportional to electron mobility. The more the electron mobility, the greater the optical property is expected. Additionally,

the electron mobility is expected to be on the entire molecular surface for the increase of optical property. In BlueBox⁴⁺, electron mobility occurs only both sides on molecule and it is negative advantage for optical properties. As for the other compounds, electrons in occupied molecular orbital are generally delocalized on the entire molecular surface. Therefore, it is supposed that optical properties of EXBox⁴⁺, EX²Box⁴⁺, EX^{0.8}Box⁴⁺ and EX^{2.2}Box⁴⁺ are better than that of BlueBox⁴⁺. DOS spectrum is calculated for studied ExⁿBoxes as represented in Fig. 4.

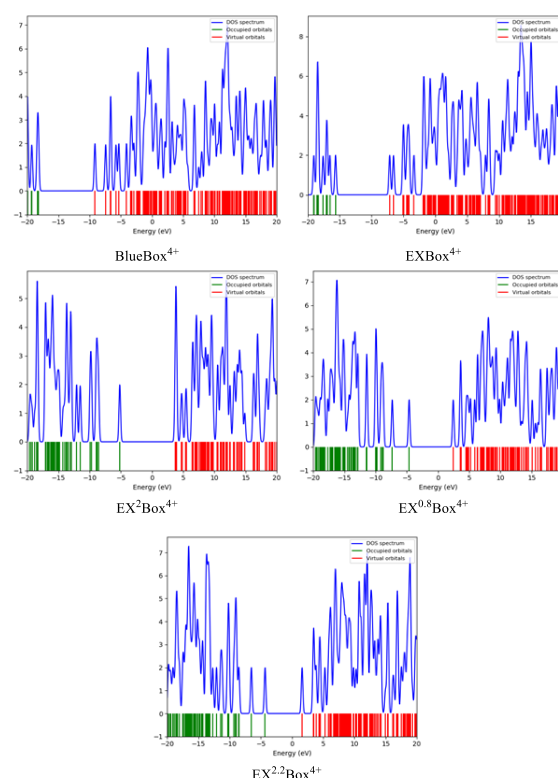


Fig. 4. DOS spectrum of studied of ExⁿBox Cyclophanes

According to Fig. 4, molecular orbitals in the range of (-20.0) – (+20.0) eV are taken into consideration. While green peaks represent the occupied molecular orbitals, red peaks represent the unoccupied molecular orbitals. The more peak number in occupied and unoccupied molecular orbitals means that electrons can be easily transferred from ground state to excited state. In this range, there no more occupied molecular orbitals in BlueBox⁴⁺ and EXBox⁴⁺. Therefore, it is expected that optical properties of EX²Box⁴⁺, EX^{0.8}Box⁴⁺ and EX^{2.2}Box⁴⁺ outperforms than the others.

3.3. Simulated UV-Vis spectrum

UV-VIS spectrum gives significant results about conjugation degree, aromaticity and electronic

transitions. A band in the UV-VIS spectrum consists of many electronic transitions. A lot of bands or shoulder in UV-VIS spectrum means a lot of electronic transitions. Additionally, bigger wavelength value means the lower energy to electronic transitions. UV-

VIS spectrum of mentioned Ex^nBoxes is calculated in gas phase, toluene, chloroform, ethanol, methanol, 1,2-ethanediol, water and n-methylformamide-mixture. The wavelengths of main bands are given in Table 1.

Table 1. Calculated wavelength (nm) of main band of studied Ex^nBoxes in each solvent area

Area	BlueBox ⁴⁺	EXBox ⁴⁺	EX ² Box ⁴⁺	EX ^{0.8} Box ⁴⁺	EX ^{2.2} Box ⁴⁺
Gas Phase	161	171	163	162	279
Toluene	164	172	167	164	171
Chloroform	164	172	167	163	171
Ethanol	163	171	166	163	171
Methanol	163	171	166	162	170
1,2-ethanediol	163	171	166	163	170
Water	163	170	166	162	170
N-Methylformamide-Mixture	163	171	166	163	170

The increasing of the wavelength of main band means the less required energy for electronic transition. According to Table 1, the wavelength of main bands are generally similar to each other in each studied compound except $\text{EX}^{2.2}\text{Box}^{4+}$ for the whole solvents. So, the wavelength was unchanged depending on the solvent. These results affect the optical properties and these properties are similar in each solvent. However, the biggest change occurs in $\text{EX}^{2.2}\text{Box}^{4+}$. The wavelength of main band is calculated as 279 nm in gas phase and nearly 170 nm in the other solvent areas. The wavelength of main band is decreased by the increasing of dielectric constant of solvents. Therefore, the optical property of $\text{EX}^{2.2}\text{Box}^{4+}$ decreases in solvents. As a results, EXBox^{4+} and $\text{EX}^{2.2}\text{Box}^{4+}$ can be

used as an optical material in solvent while $\text{EX}^{2.2}\text{Box}^{4+}$ is the best candidate for NLO application in gas phase.

3.4. Quantum chemical descriptors for NLO properties

Optical properties can be proposed by using quantum chemical descriptors or parameters. The effect of quantum chemical parameters on the NLO activity has been identified in detail in many published theoretical papers [16-19]. Calculated QCDs in gas phase are given in Table 2 while the other results in toluene, chloroform, ethanol, methanol, 1,2-ethanediol, water and n-methylformamide-mixture are given in Supplemental Material.

Table 2. Calculated quantum chemical descriptors for urea and studied Ex^nBoxes in gas phase

Compounds	E_{HOMO}^a	E_{LUMO}^a	I^a	A^a	E_{GAP}^a	η^a	σ^b	σ_{O}^b	χ^a
BlueBox ⁴⁺	-18.221	-9.163	18.221	9.163	9.058	4.529	0.221	0.110	13.692
EXBox ⁴⁺	-15.638	-7.156	15.638	7.156	8.482	4.241	0.236	0.118	11.397
EX ² Box ⁴⁺	-5.167	3.718	5.167	-3.718	8.884	4.442	0.225	0.113	0.725
EX ^{0.8} Box ⁴⁺	-4.633	2.434	4.633	-2.434	7.068	3.534	0.283	0.141	1.099
EX ^{2.2} Box ⁴⁺	-4.320	1.606	4.320	-1.606	5.926	2.963	0.338	0.169	1.357
Urea	-10.988	5.465	10.988	-5.465	16.453	8.227	0.122	0.061	2.761
Compounds	CP^a	ω^a	N^b	ΔN_{Max}	μ^c	α^d	$\Delta\alpha^d$	β^e	
BlueBox ⁴⁺	-13.692	20.696	0.048	3.023	0.093	45.466	114.2771	3.70×10^{-28}	
EXBox ⁴⁺	-11.397	15.314	0.065	2.687	0.000	76.696	185.8248	1.38×10^{-31}	
EX ² Box ⁴⁺	-0.725	0.059	16.925	0.163	0.000	50.704	111.5649	5.46×10^{-32}	
EX ^{0.8} Box ⁴⁺	-1.099	0.171	5.847	0.311	0.000	91.900	216.5514	2.51×10^{-31}	
EX ^{2.2} Box ⁴⁺	-1.357	0.311	3.219	0.458	0.000	158.607	396.4361	1.45×10^{-31}	
Urea	-2.761	0.463	2.158	0.336	1.810	1.898	8.082826	3.81×10^{-28}	

^a in eV,

^b in eV⁻¹,

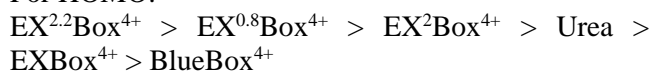
^c in Debye,

^d in Å³,

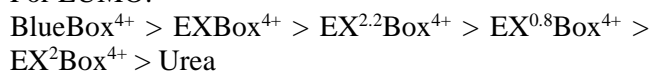
^e cm⁵/esu

According to Table 4, NLO activity ranking should be as follow for mentioned descriptors:

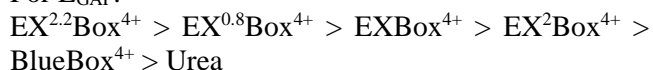
For HOMO:



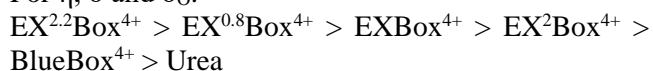
For LUMO:



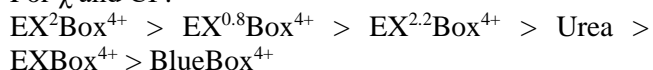
For E_{GAP} :



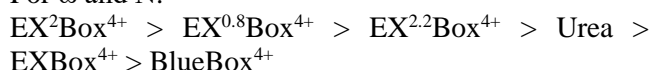
For η , σ and σ_{O} :



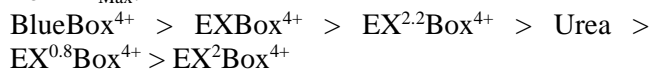
For χ and CP:



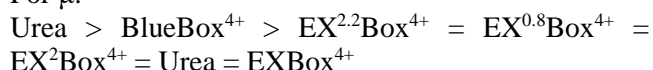
For ω and N:



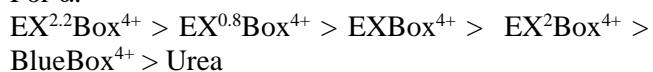
For ΔN_{Max} :



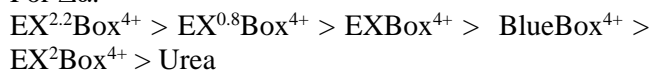
For μ :



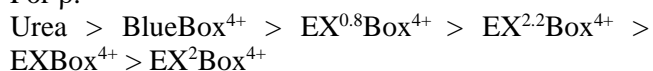
For α :



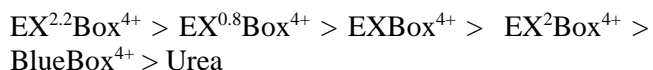
For $\Delta\alpha$:



For β :



According to above rankings, the general activity ranking is given as follow:



In gas phase, $\text{EX}^{2.2}\text{Box}^{4+}$ is determined as the best candidate for NLO applications. Additionally, the same analyses are performed in each area and $\text{EX}^{2.2}\text{Box}^{4+}$ is determined as the best material for NLO application, too. As the final word, the results in quantum chemical parameters are in agreement with contour plots, DOS spectrum, UV-VIS spectrum. It can be said that, $\text{EX}^{2.2}\text{Box}^{4+}$ is the best material respect to all analyzes in this article.

4. Conclusions

We presented the computational investigations of some Ex^nBox Cyclophanes performed at HF/6-31G(d) level in different solvents. Structural and electronic properties of the mentioned compounds underwent scrutiny in detail. The energy diagram of molecular orbitals and contour plots of significant molecular orbitals and counter plots of significant molecular orbitals are calculated and examined. Additionally, density of state (DOS) spectrum was calculated and according to DOS spectrum, electronic mobility in $\text{EX}^{2.2}\text{Box}^{4+}$ and $\text{EX}^{0.8}\text{Box}^{4+}$ is more than the other. UV-VIS spectrum and some quantum chemical descriptors are calculated and $\text{EX}^{2.2}\text{Box}^{4+}$ is found as the best material to NLO applications.

Acknowledgment

The numerical calculations reported in this paper were fully/partially performed at TUBITAK ULAKBIM, High Performance and Grid Computing Center (TRUBA resources). Also, M. R thanks Professor Sir J. Fraser Stoddarts for giving the opportunity to learn this field of Chemistry during the sabbatical time at Northwestern University in 2016.

Conflicts of interest

The authors state that did not have conflict of interests


References

- [1] Barnes J.C., Juricek M., Vermeulen N.A., Dale E.J. and Stoddart J.F., Synthesis of Ex^nBox Cyclophanes. *J. Org. Chem.*, 78 (2013) 11962-11969.
- [2] Dale E.J., Vermeulen N.A., Juricek M., Barnes J.C., Young R.M., Wasielewski M.R. and Stoddart J.F., Supramolecular Explorations: Exhibiting the Extent of Extended Cationic Cyclophanes. *Acc. Chem. Res.*, 49 (2016) 262-273.

- [3] Dale E.J., Ferris D.P., Vermeulen N.A., Hanklis J.J., Popovs I., Juricek M., Barnes J.C., Schneebeli S.T. and Stoddart J.F., Cooperative Reactivity in an Extended-Viologen-Based Cyclophane. *J. Am. Chem. Soc.*, 138 (2016) 3667-3670.
- [4] Fang Q.-S., Chen L. and Liu Q.-L., Template-directed synthesis of pyridazine-containing tetracationic cyclophane for construction of [2] rotaxane. *Chinese Chemical Letters* 28 (2017) 1013-1017.
- [5] Mashraqui S.H., Sangvikar Y.S., Ghadigaonkar S.G., Ashraf M. and Meetsma M., Oxa-bridged cyclophanes featuring thieno[2,3-b]thiophene and C2-symmetric binol or bis-naphthol rings: synthesis, structures, and conformational studies. *Tetrahedron* 64 (2008) 8837-8842.
- [6] Giancarlo L.C. and Flynn G.W., Raising Flags: Applications of Chemical Marker Groups To Study Self-Assembly, Chirality, and Orientation of Interfacial Films by Scanning Tunneling Microscopy. *Acc. Chem. Res.* 33 (2000) 491-501.
- [7] Asakawa M., Ashton P.R., Menzer S., Raymo F.M., Stoddart J.F., White A.J.P. and Williams D.J., Cyclobis(Paraquat-4,4'-Biphenylene)—an Organic Molecular Square. *Chem. Eur. J.*, 2 (1996) 877-893.
- [8] Barnes J.C., Juriček M., Strutt N.L., Frasconi M., Sampath S., Giesener M.A., McGrier P.L., Bruns C.J., Stern C.L., Sarjeant A.A. and Stoddart J.F., ExBox: A Polycyclic Aromatic Hydrocarbon Scavenger. *J. Am. Chem. Soc.*, 135 (2013) 183-192.
- [9] Juriček M., Barnes J.C., Dale E.J., Liu W.-G., Strutt N.L., Bruns C.J., Vermeulen N.A., Ghooray K., Sarjeant A.A., Stern C.L., Botros Y.Y., Goddard W.A. III and Stoddart J.F., Ex2Box: Interdependent Modes of Binding in a Two-Nanometer-Long Synthetic Receptor. *J. Am. Chem. Soc.*, 135 (2013) 12736-12746.
- [10] Asakawa M., Dehaen W., L'abbe G.L., Menzer S., Nouwen J., Raymo F. M., Stoddart J. F. and Williams D.J., Omproved Template-Directed Synthesis of Cyclobis(paraquat-*p*-phenylene). *J. Org. Chem.*, 61 (1996) 9591-9595.
- [11] Dennington II R.D., Keith T.A. and Millam J.M., GaussView 5.0, Wallingford, CT (2009).
- [12] Gaussian 09, Revision D.01, Frisch M. J., Trucks G. W., Schlegel H. B., Scuseria G. E., Robb M. A., Cheeseman J. R., Scalmani G., Barone V., Petersson G. A., Nakatsuji H., Li X., Caricato M., Marenich A. V., Bloino J., Janesko B.G., Gomperts R., Mennucci B., Hratchian H. P., Ortiz J. V., Izmaylov A. F., Sonnenberg J. L., Williams-Young D., Ding F., Lipparini F., Egidi F., Goings J., Peng B., Petrone A., Henderson T., Ranasinghe D., Zakrzewski V. G., Gao J., Rega N., Zheng G., Liang W., Hada M., Ehara M., Toyota K., Fukuda R., Hasegawa J., Ishida M., Nakajima T., Honda Y., Kitao O., Nakai H., Vreven T., Throssell K., Montgomery J.A. Jr., Peralta J. E., Ogliaro F., Bearpark M.J., Heyd J.J., Brothers E.N., Kudin K.N., Starovero, V.N., Keith T.A., Kobayashi R., Normand J., Raghavachari K., Rendell A.P., Burant J.C., Iyengar S.S., Tomasi J., Cossi M., Millam J.M., Klene M., Adamo C., Cammi R., Ochterski J.W., Martin R.L., Morokuma K., Farkas O., Foresman J. B. and Fox D. J. Gaussian, Inc., Wallingford CT, (2009).
- [13] PerkinElmer, ChemBioDraw Ultra Version (13.0.0.3015), CambridgeSoft Waltham, MA, USA (2012).
- [14] O'Boyle N.M., Tenderholt A.L. and Langner K.M.: cclib: A library for package-independent computational chemistry algorithms. *J. Comp Chem*, 29 (2008) 839-845.
- [15] Koopmans T., Über die Zuordnung von Wellenfunktionen und Eigenwerten zu den Einzelnen Elektronen Eines Atoms. *Physica*, 1 (1934) 104-113.
- [16] Tüzün B. and Sayin K., Investigations over optical properties of boron complexes of benzothiazolines. *Spectrochim. Acta A*, 208 (2019) 48-46.
- [17] Uludag N. and Serdaroğlu G., An improved synthesis, spectroscopic (FT-IR, NMR) study and DFT computational analysis (IR, NMR, UVeVis, MEP diagrams, NBO, NLO, FMO) of the 1,5-methanoazocino[4,3-b]indole core structure. *J. Mol. Struct.*, 1155 (2018) 548-560.
- [18] Sayin K., Kariper S.E., Tas M., Alagoz Sayin T. and Karakas D., Investigations of structural, spectral, electronic and biological properties of N-heterocyclic carbene Ag(I) and Pd(II) complexes. *J. Mol. Struct.*, 1176 (2019) 478-487.
- [19] Gungor S.A., Sahin I., Gungor O., Kariper S.E., Tumer F. and Kose M., Pamoic acid esters and their xanthene derivatives: Flourimetric detection of nitroaromatic compounds and non-linear optical properties. *Sensors and Actuators B: Chemical*, 255 (2018) 3344-3354.



Certain results on Kenmotsu manifolds

Halil İbrahim YOLDAŞ 

Mersin University, Department of Mathematics, Mersin/ TURKEY

Abstract

In this paper, we focus on Kenmotsu manifolds. Firstly, we investigate almost quasi Ricci symmetric Kenmotsu manifolds. Then, we study Kenmotsu manifold admitting a Yamabe soliton. We find that if the soliton field V of the Yamabe soliton is orthogonal to the characteristic vector field ξ , then it is Killing and the manifold has constant scalar curvature. Also, we deal with a Kenmotsu manifold which admits a quasi-Yamabe soliton. Finally, we give an example which verify our results.

Article info

History:

Received:19.02.2020

Accepted:12.06.2020

Keywords:

Kenmotsu manifold,
Einstein manifold,
almost quasi Ricci
symmetric manifold,
quasi-yamabe soliton.

1. Introduction

Considering the recent stage of the developments in contact geometry, there is an impression that the geometers are focused on problems in almost contact metric geometry. Many different classes of almost contact structures are defined in the literature such as Sasakian [1], Kenmotsu [2], almost cosymplectic [3], trans-Sasakian [4] and others.

In 1969, Tanno classified connected almost contact metric manifolds whose automorphism groups possess the maximum dimension [5]. For such manifolds, the sectional curvature of plane sections containing ξ is a constant c and it was proved that they can be divided into three classes: *i)* Homogenous contact Riemannian manifolds with $c > 0$. *ii)* Global Riemannian products of a line or a circle with a Kaehler manifold of constant holomorphic sectional curvature if $c = 0$. *iii)* A warped product space $\mathbb{R} \times_f \mathbb{C}$ if $c < 0$. In 1972, Kenmotsu investigated the differential geometric properties of the manifolds of class *iii)* and obtained structure is now as known Kenmotsu structure [2]. After this work, such manifolds have been studied extensively by many mathematicians.

The notion of Yamabe soliton in Riemannian geometry was introduced by Hamilton at the same time as the Ricci flow in 1988 [6]. This notion corresponds to the self-similar solution of Hamilton's Yamabe flow. In dimension $n = 2$ the Yamabe flow is equivalent to the Ricci flow. However, In dimension $n > 2$ the Yamabe and the Ricci flows do not agree, since the Yamabe flow conserve the conformal class of metric the metric but the Ricci flow does not in general. Yamabe soliton is a special solution of the Yamabe flow that moves by one parameter family of diffeomorphisms φ_t generated by a fixed vector field V on a Riemannian manifold M . Also, Yamabe flow is natural geometric deformation to metrics of constant scalar curvature. Therefore, Yamabe solitons have been studied intensively in mathematics as well as physics. For the recent studies on Yamabe solitons, we refer to ([7]-[11]).

A Riemannian manifold (M, g) is called a Yamabe soliton if there exists a real number λ and a vector field $V \in \Gamma(TM)$ such that

$$(L_V g)(X, Y) = (\lambda - r)g(X, Y), \quad (1)$$

where $\Gamma(TM)$ denotes the set of differentiable vector fields on M , $L_V g$ denotes the Lie-derivative of the metric tensor g along vector field V , r is the scalar curvature of M and X, Y are arbitrary vector fields on M . Also, a vector field V as in the definition is called a soliton field for (M, g) . A Yamabe soliton which satisfies (1) is denoted by (M, g, V, λ) . If $L_V g = \rho g$, then the soliton field V is said to be conformal Killing, where ρ is a function. If ρ vanishes identically, then V is said to be Killing. Moreover, if V is zero or Killing in (1), then the Yamabe soliton reduces to a manifold of constant scalar curvature. In addition, a Yamabe soliton is called a gradient if the soliton field V is the gradient of a potential function f (i.e., $V = \nabla f$) and is called shrinking, steady or expanding depending on $\lambda < 0$, $\lambda = 0$ or $\lambda > 0$, respectively.

On the other hand, in 2018, Chen and Deshmukh defined the notion of quasi-Yamabe soliton as a generalization of Yamabe solitons on a Riemannian manifold (M, g) as follows [12]:

$$(L_V g)(X, Y) = (\lambda - r)g(X, Y) + \mu V^*(X)V^*(Y), \quad (2)$$

where V^* stands for the dual 1-form of V , λ is a constant and μ is a smooth function on M . The vector field V is also called soliton field for the quasi-Yamabe soliton. A quasi-Yamabe soliton is denoted by (M, g, V, λ) .

Motivated by the above studies, we concentrate on Yamabe and quasi-Yamabe solitons on Kenmotsu manifolds. Also, we study almost quasi Ricci symmetric Kenmotsu manifolds.

The paper is organized as follows:

Section 1 is devoted to the introduction. In section 2, we give some basic notions which are going to be needed. In section 3, we consider almost quasi Ricci symmetric Kenmotsu manifolds. Then, we study Kenmotsu manifold admitting a Yamabe soliton. Also, we discuss quasi-Yamabe soliton on such a manifold and give some important characterizations. Finally, we give an example to support our results.

2. Preliminaries

In this section, we recall some notions of almost contact metric manifolds from [2], [13] and [14].

A $(2n+1)$ -dimensional smooth manifold M is an almost contact metric manifold equipped with an almost contact metric structure (φ, ξ, g) such that φ is a tensor field of type $(1,1)$, ξ is a vector field (called the characteristic vector field) of type $(1,0)$, 1-form η is a tensor field of type $(0,1)$ on M and the Riemannian metric g satisfies the following relations:

$$\varphi^2 X = -X + \eta(X)\xi, \quad (3)$$

$$\eta(\xi) = 1, \quad (4)$$

$$\varphi\xi = 0, \quad (5)$$

$$\eta \circ \varphi = 0 \quad (6)$$

and

$$g(\varphi X, \varphi Y) = g(X, Y) - \eta(X)\eta(Y), \quad (7)$$

$$g(X, \varphi Y) = -g(\varphi X, Y), \quad (8)$$

$$\eta(X) = g(X, \xi) \quad (9)$$

for any $X, Y \in \Gamma(TM)$.

If the following condition is satisfied for an almost contact metric manifold (M, φ, ξ, g) then it is called a Kenmotsu manifold

$$(\nabla_X \varphi)Y = g(\varphi X, Y)\xi - \eta(Y)\varphi X,$$

where ∇ is the Levi-Civita connection on M . For a Kenmotsu manifold we also have

$$\nabla_X \xi = X - \eta(X)\xi, \quad (10)$$

$$R(X, Y)\xi = \eta(X)Y - \eta(Y)X, \quad (11)$$

$$R(X, \xi)Y = g(X, Y)\xi - \eta(Y)X, \quad (12)$$

$$S(X, \xi) = -2n\eta(X), \quad (13)$$

$$S(\xi, \xi) = -2n, \quad (14)$$

$$Q\xi = -2n\xi, \quad (15)$$

where S and R are the Ricci tensor and Riemann curvature tensor of M , respectively and Q is the Ricci operator defined by $S(X, Y) = g(QX, Y)$.

On the other hand, a Riemannian manifold (M, g) is called η -Einstein if there exists two smooth functions a and b such that its Ricci tensor S satisfies

$$S(X, Y) = ag(X, Y) + b\eta(X)\eta(Y) \quad (16)$$

for any $X, Y \in \Gamma(TM)$. If the function b vanishes identically in (16), then the manifold M becomes an Einstein.

Also, a non-flat semi-Riemannian manifold (M^{2n+1}, g) ($n \geq 1$) is called almost quasi Ricci symmetric manifold if its Ricci tensor field S satisfies [15]

$$(\nabla_X S)(Y, Z) = [A(X) + B(X)]S(Y, Z) - A(Y)S(X, Z) - A(Z)S(X, Y) \quad (17)$$

for any $X, Y, Z \in \Gamma(TM)$, where A and B are non-zero 1-forms. If $A = B$ in (17), then M becomes a quasi Ricci symmetric manifold.

3. Main Results

3.1. Almost quasi Ricci symmetric manifold

In this section, we deal with almost quasi Ricci symmetric Kenmotsu manifold. We begin to this section with the following:

Theorem 1: If M is an almost quasi Ricci symmetric Kenmotsu manifold, then it becomes a quasi Ricci symmetric manifold.

Proof: Let us consider that M is an almost quasi Ricci symmetric Kenmotsu manifold. Putting $Z = \xi$ in (17), we have

$$(\nabla_X S)(Y, \xi) = [A(X) + B(X)]S(Y, \xi) - A(Y)S(X, \xi) - A(\xi)S(X, Y) \quad (18)$$

such that

$$(\nabla_X S)(Y, \xi) = \nabla_X S(Y, \xi) - S(\nabla_X Y, \xi) - S(Y, \nabla_X \xi) \quad (19)$$

for any $X, Y \in \Gamma(TM)$. From (9), (10), (13) and (19), we derive

$$(\nabla_X S)(Y, \xi) = -S(X, Y) - 2ng(X, Y). \quad (20)$$

Using the equality (13) in the right side of (18), then the equation (18) becomes

$$(\nabla_X S)(Y, \xi) = -2n[A(X) + B(X)]\eta(Y) + 2n\eta(X)A(Y) - A(\xi)S(X, Y). \quad (21)$$

Therefore, by combining (20) and (21) we get

$$-S(X, Y) - 2ng(X, Y) = -2n[A(X) + B(X)]\eta(Y) + 2n\eta(X)A(Y) - A(\xi)S(X, Y). \quad (22)$$

Taking $Y = \xi$ in (22) and making use of (4), (13) gives

$$0 = -2n[A(X) + B(X)] + 4n\eta(X)A(\xi)$$

which is equivalent to

$$A(X) + B(X) = 2\eta(X)A(\xi). \quad (23)$$

Replacing X by ξ in (23) yields

$$B(\xi) = A(\xi). \quad (24)$$

Again taking $X = \xi$ in (22) and by virtue of (4), (13) and (24) we find that

$$0 = -2n\eta(Y)A(\xi) + 2nA(Y),$$

namely

$$A(Y) = A(\xi)\eta(Y). \quad (25)$$

From (23) and (25), we obtain

$$A(X) = B(X) = A(\xi)\eta(X).$$

This completes the proof of the theorem.

As a result of the Theorem 1, we can give the following corollary.

Corollary 1: If M is an almost quasi Ricci symmetric Kenmotsu manifold satisfying $A(\xi) \neq 1$, then it is an η -Einstein manifold.

Proof: From (22) and (25), we have

$$-S(X, Y) - 2ng(X, Y) = -2nA(\xi)\eta(X)\eta(Y) - A(\xi)S(X, Y).$$

If we rearrange the last equation, we get

$$S(X, Y) = \frac{2n}{A(\xi)-1} g(X, Y) - \frac{2nA(\xi)}{A(\xi)-1} \eta(X)\eta(Y)$$

which implies that the manifold M is an η -Einstein. Therefore, the proof is completed.

3.2. Quasi-Yamabe solitons on Kenmotsu manifold

In this section, we study quasi-Yamabe solitons on a Kenmotsu manifold and give an important characterization. The first result of this section is the following:

Proposition 1: Let M be a Kenmotsu manifold admitting a Yamabe soliton as its soliton field V . If the vector field V is orthogonal to ξ , then V is Killing on M and the manifold M has constant scalar curvature.

Proof: Since M admits a Yamabe soliton, from (1) we write

$$g(\nabla_X V, Y) + g(\nabla_Y V, X) = (\lambda - r)g(X, Y) \quad (27)$$

for any $X, Y \in \Gamma(TM)$. Substituting $X = Y = \xi$ in (27) gives

$$2g(\nabla_\xi V, \xi) = (\lambda - r). \quad (28)$$

On the other hand, it is easy to see that $g(\nabla_\xi V, \xi) = \nabla_\xi(g(V, \xi))$. Using this equality in (28), we have

$$\nabla_\xi(g(V, \xi)) = (\lambda - r). \quad (29)$$

Now, we assume that the vector field V is orthogonal to ξ . Then, from (29) we get

$$r = \lambda \quad (30)$$

which implies that M is a manifold of constant scalar curvature. Furthermore, using (30) in (27) we obtain

$$(L_V g)(X, Y) = g(\nabla_X V, Y) + g(\nabla_Y V, X) = 0. \quad (31)$$

This means that the vector field V is Killing on M . Thus, the proof of the proposition is completed.

Theorem 2: Let M be a $(2n+1)$ -dimensional Kenmotsu manifold satisfying the condition $R.Q = 0$. If M admits a Yamabe soliton as its soliton field ξ , then the Yamabe soliton is shrinking.

Proof: Let us consider a Kenmotsu manifold M satisfies the condition $(R(X, Y).Q)Z = 0$, that is,

$$R(X, Y)QZ - Q(R(X, Y)Z) = 0 \quad (32)$$

for any $X, Y, Z \in \Gamma(TM)$, where R is the Riemannian curvature of M and Q is the Ricci operator defined by $S(X, Y) = g(QX, Y)$. Replacing Y by ξ in (32), we have

$$R(X, \xi)QZ - Q(R(X, \xi)Z) = 0. \quad (33)$$

With the help of (12), (13), (15) and (33), we derive

$$S(X, Z)\xi + 2n\eta(Z)X + 2ng(X, Z)\xi + \eta(Z)QX = 0. \quad (34)$$

Taking the inner product of (34) with ξ and using (4), (13), we obtain

$$S(X, Z) = -2ng(X, Z). \quad (35)$$

Contracting over X, Z in (35), we get

$$r = -2n(2n+1). \quad (36)$$

On the other hand, from (1) and (10) one has

$$2g(X, Y) - 2\eta(X)\eta(Y) = (\lambda - r)g(X, Y). \quad (37)$$

By setting $X = Y = \xi$ in (37) and from (36), we deduce that $\lambda = -2n(2n+1)$. This implies that the Yamabe soliton is shrinking. This is the desired result.

Now, we are ready to give the main theorem of this section.

Theorem 3: Let M be a Kenmotsu manifold. If M admits a quasi-Yamabe soliton as its soliton field ξ , then M is a manifold of constant scalar curvature.

Proof: Since η is the dual 1-form of the characteristic vector field ξ , the equation (2) becomes

$$(L_\xi g)(X, Y) = (\lambda - r)g(X, Y) + \mu\eta(X)\eta(Y) \quad (38)$$

for any $X, Y \in \Gamma(TM)$. Also, it follows from the definition of the Lie-derivative and from (10), one has

$$\begin{aligned} (L_\xi g)(X, Y) &= g(\nabla_X \xi, Y) + g(\nabla_Y \xi, X) \\ &= 2g(X, Y) - 2\eta(X)\eta(Y). \end{aligned} \quad (39)$$

By combining (38) and (39) we have

$$2g(X, Y) - 2\eta(X)\eta(Y) = (\lambda - r)g(X, Y) + \mu\eta(X)\eta(Y). \quad (40)$$

If we put $X = Y = \xi$ in equation (40), then we get

$$\lambda - r + \mu = 0. \quad (41)$$

On the other hand, let $\{e_1, e_2, \dots, e_{2n+1} = \xi\}$ be an orthonormal basis of the tangent space $T_p M$, at each point $p \in M$. By setting $X = Y = e_i$ in (40) and taking summation over i ($i = 1, 2, \dots, 2n+1$), we deduce

$$4n = (\lambda - r)(2n+1) + \mu. \quad (42)$$

Using the equalities (41) and (42), we obtain

$$\mu = -2. \quad (43)$$

Therefore, from (41) and (43) we have $r = \lambda - 2$ which means that the manifold M has constant scalar curvature. Thus, we get the requested result.

Example 1: [16] We consider the three-dimensional Riemannian manifold

$$M = \{(x, y, z) \in \mathbb{R}^3, (x, y, z) \neq (0, 0, 0)\},$$

and the linearly independent vector fields

$$e_1 = z \frac{\partial}{\partial x}, \quad e_2 = z \frac{\partial}{\partial y}, \quad e_3 = -z \frac{\partial}{\partial z},$$

where (x, y, z) are the Cartesian coordinates in \mathbb{R}^3 . Let g be the Riemannian metric defined by

$$\begin{aligned} g(e_i, e_i) &= 1 \\ g(e_i, e_j) &= 0, \quad i \neq j \end{aligned}$$

and is given by

$$g = \frac{1}{z^2} \{dx \otimes dx + dy \otimes dy + dz \otimes dz\}.$$

Also, let η , φ be the 1-form and $(1, 1)$ -tensor field, respectively defined by

$$\eta(Z, e_3) = 1, \quad \varphi(e_1) = -e_2, \quad \varphi(e_2) = e_1, \quad \varphi(e_3) = 0$$

for any $Z \in \Gamma(TM)$. Therefore, $(M, \varphi, \xi, \eta, g)$ becomes an almost contact metric manifold with the characteristic vector field ξ .

On the other hand, by direct calculations we have

$$[e_1, e_2] = 0, \quad [e_1, e_3] = e_1, \quad [e_2, e_3] = e_2. \quad (44)$$

Using Koszul's formula for the Riemannian metric g , we get:

$$\nabla_{e_1} e_3 = e_1, \quad \nabla_{e_2} e_3 = e_2, \quad \nabla_{e_3} e_3 = 0, \quad \nabla_{e_1} e_1 = \nabla_{e_2} e_2 = -e_3, \quad \nabla_{e_1} e_2 = \nabla_{e_2} e_1 = \nabla_{e_3} e_1 = \nabla_{e_3} e_2 = 0. \quad (45)$$

Thus, $(M, \varphi, \xi, \eta, g)$ is a three-dimensional Kenmotsu manifold. Using the equations (44) and (45), we obtain

$$\begin{aligned} R(e_2, e_1)e_1 &= -e_2, & R(e_3, e_1)e_1 &= -e_3, & R(e_1, e_3)e_3 &= -e_1, & R(e_2, e_3)e_3 &= -e_2, \\ R(e_1, e_2)e_2 &= -e_1, & R(e_3, e_2)e_2 &= -e_3, & R(e_2, e_3)e_1 &= 0, & R(e_1, e_2)e_3 &= 0, & R(e_3, e_1)e_2 &= 0 \end{aligned}$$

which yields

$$S(e_1, e_1) = -2, \quad S(e_2, e_2) = -2, \quad S(e_3, e_3) = -2, \quad S(e_i, e_j) = 0$$

for all $i, j = 1, 2, 3$ ($i \neq j$). Hence, we have

$$r = S(e_1, e_1) + S(e_2, e_2) + S(e_3, e_3) = -6.$$

In this case, the manifold M is a quasi-Yamabe soliton with the soliton field $e_3 = \xi$ which satisfies the equation (2) for $\lambda = -4$ and $\mu = -2$. This result verifies the Theorem 3.

Also, the manifold M is a Yamabe soliton with the soliton field e_1 or e_2 which satisfies the equation (1) for $\lambda = -6$ and this result verifies the Proposition 1.

Conflicts of interest

There is no conflict of interest.

References

- [1] Sasaki, S., On differentiable manifolds with certain structures which are closely related to almost contact Structure. I., *Tohoku Math. J.*, 2(12) (1960) 459-476.
- [2] Kenmotsu, K., A class of almost contact Riemannian manifolds, *Tohoku Math. J.*, 2(25) (1972) 93-103.
- [3] Goldberg, S. I., Yano, K. Integrability of almost cosymplectic structures, *Pacific J. Math.*, 31(1969) 373-382.
- [4] Oubina, J. A., New classes of almost contact metric structures, *Publ. Math. Debrecen*, 32(1985) 187-193.
- [5] Tanno, S., The automorphism groups of almost contact Riemannian manifolds, *Tohoku Math. J.*, 2(22) (1969) 21-38.
- [6] Hamilton, R. S., The Ricci flow on surfaces (Mathematics and General Relativity), *Contemp. Math.*, 71(1988) 237-262.
- [7] Hui, S. K., Mandal, Y. C. Yamabe solitons on Kenmotsu manifolds, *Commun. Korean Math. Soc.*, 34(1) (2019) 321-331.
- [8] Karaca, F., Gradient yamabe solitons on multiply warped product manifolds, *Int. Electron. J. Geom.*, 12(2) (2019) 157-168.
- [9] Suh, Y. J., Mandal, K., Yamabe solitons on three-dimensional $N(k)$ -paracontact metric manifolds, *Bull. Iranian Math. Soc.*, 44(1) (2018) 183-191.
- [10] Blaga, A. M., Some geometrical aspects of Einstein, Ricci and Yamabe Solitons, *J. Geom. Symmetry Phys.*, 52(2019) 17-26.
- [11] Desmukh, S., Chen, B.-Y., A note on Yamabe solitons, *Balkan J. Geom. Appl.*, 23(1) (2018) 37-43.
- [12] Chen, B.-Y., Desmukh, S., Yamabe and quasi-yamabe solitons on Euclidean submanifolds, *Mediterr. J. Math.*, 15(5) (2018) Article 194.

- [13] Blair, D. E., Contact manifolds in Riemannian geometry, Lecture notes in Mathematics, Berlin-Newyork: Springer, 1976.
- [14] Yano, K., Kon, M., Structures on manifolds, Series in Mathematics, World Scientific Publishing: Springer, 1984.
- [15] Kim, J., On almost quasi ricci symmetric manifolds, *Commun. Korean Math. Soc.*, 35(2) (2020) 603-611.
- [16] Yadav, S., Chaubey, K. S., Prasad, R., On Kenmotsu manifolds with a semi-symmetric metric connection, *Facta Universitatis (NIS) Ser. Math. Inform.*, 35(1) (2020) 101-119.

Common properties and approximations of local function and set operator ψ

Sk SELIM¹  Md. Monirul ISLAM²  Shyamapada MODAK^{3,*} 

¹ University of Gour Banga, Department of Mathematics, P.O. Mokdumpur, Malda – 732103, West Bengal, India

² Kaliachak College, Department of Mathematics, Sultanganj, Malda – 732201, West Bengal, India

³ University of Gour Banga, Department of Mathematics, P.O. Mokdumpur, Malda – 732103, West Bengal, India

Abstract

Through this paper, we shall obtain common properties of local function and set operator ψ and introduce the approximations of local function and set operator ψ . We also determined expansion of local function and set operator ψ .

Article info

History:

Received: 08.11.2019

Accepted: 01.04.2020

Keywords: Local function, ψ -operator,

$A = B[\text{mod } \mathcal{I}]$,

compatible ideal, codense ideal.

1. Introduction

The study of ideals on topological spaces was first introduced by K. Kuratowski [1]. The authors, Al-Omari and Noiri [2,3], Modak [4,5,6], Modak and Islam [7,8,9,10], Ekici and Elmali [11], Modak and Mistry [12], Khan and Noiri [13], Csaszar [14], Özbakir and Yildirim [15] have introduced the study of ideals on the generalized topological space. We know from [1] that, a subcollection \mathcal{I} of $\wp(X)$, the powerset of X , is called an ideal on X if (i) for $A, B \subseteq X$ and $A \subseteq B \in \mathcal{I}$, $A \in \mathcal{I}$ (hereditary) and (ii) for $A, B \subseteq X$ and $A, B \in \mathcal{I}$, $A \cup B \in \mathcal{I}$ (finite additivity). Hayashi [16] introduced localization properties of ideal topological space (an ideal \mathcal{I} on a topological space (X, τ) is called an ideal topological space and it is denoted as (X, τ, \mathcal{I})). For a subset A of X , the local function of A in the ideal topological space (X, τ, \mathcal{I}) , is denoted as A^* and defined as:

$A^* = \{x \in X : U_x \cap A \notin \mathcal{I}, U_x \in \tau(x)\}$, where $\tau(x)$ is collection of all open sets of (X, τ) containing x .

In regards of local function, Natkaniec [17] had defined the ψ operator. For an ideal topological space (X, τ, \mathcal{I}) , the ψ operator is defined as follows:

$\psi(A) = X \setminus (X \setminus A)^*$, for every $A \subseteq X$.

Again for its equivalent definition, see [18] and [19].

In this paper, our intension is to study the properties of local function and ψ operator in which topological space, generalized topological space [20], m -space [2], minimal space [21] and supra-topological space [22] etc. are not an essential part. That means we study the properties which hold in any subcollection of $\wp(X)$. We also characterize the Newcomb's idea $A = B[\text{mod } \mathcal{I}]$, τ -boundary [23] and Njastad's compatibility [24]. Secondly, we introduce and study the approximations of local function and the operator ψ . Finally we have

*Corresponding author. Email address: spmodak2000@yahoo.co.in
<http://dergipark.gov.tr/csj> ©2020 Faculty of Science, Sivas Cumhuriyet University

considered the expansion of above two operators. However A. Pavlovic[25] have studied “local function versus local closure function in ideal topological spaces”.

2. Common Properties

In this section, we shall consider the properties of local function and operator ψ which are not dependent on topology, generalized topology, minimal structure etc.

Let X be a set, $\mathcal{A} \subseteq \wp(X)$ and \mathcal{I} be an ideal on X , then we call $(X, \mathcal{A}, \mathcal{I})$ a space.

Definition 2.1. Let $(X, \mathcal{A}, \mathcal{I})$ be a space. A set operator $()^{c*} : \wp(X) \rightarrow \wp(X)$, called the common-local function of \mathcal{I} on X with respect to \mathcal{A} , is defined as: $(A)^{c*}(\mathcal{A}, \mathcal{I}) = \{x \in X : U \cap A \notin \mathcal{I}, \text{ for every } U \in \mathcal{A}(x)\}$, where $\mathcal{A}(x) = \{U \in \mathcal{A} : x \in U\}$.

This is simply called c^* -local function and denoted as A^{c*} , for $A \subseteq X$.

Following is the example of a c^* -local function of a set:

Example 2.2. Let $X = \{a, b, c\}$, $\mathcal{A} = \{\{a\}, \{b\}, \{a, c\}\} \subseteq \wp(X)$ and $\mathcal{I} = \{\emptyset, \{a\}\}$. Take $B = \{b, c\}$. Then $B^{c*} = \{b, c\}$.

Theorem 2.3. Let $(X, \mathcal{A}, \mathcal{I})$ be a space. Then following hold:

1. $(\emptyset)^{c*} = \emptyset$.
2. If $A \subseteq B \subseteq X$, $A^{c*} \subseteq B^{c*}$.
3. If $I \in \mathcal{I}$, then $(I)^{c*} = \emptyset$.
4. If $A \subseteq X$ and $I \in \mathcal{I}$, then $(A \setminus I)^{c*} = (A \cup I)^{c*} = A^{c*}$.
5. For an ideal \mathcal{H} on X with $\mathcal{H} \subseteq \mathcal{I}$, $(A)^{c*}(\mathcal{I}) \subseteq (A)^{c*}(\mathcal{H})$.
6. For an ideal \mathcal{J} on X , $A^{c*}(\mathcal{I} \cap \mathcal{J}) = A^{c*}(\mathcal{I}) \cup B^{c*}(\mathcal{J})$.

Proof. 1. Obvious from the fact that $\emptyset \in \mathcal{I}$.

2. Let $x \in A^{c*}$. Then for all $U \in \mathcal{A}(x)$, $U \cap A \notin \mathcal{I}$. Thus $U \cap B \notin \mathcal{I}$, otherwise $U \cap A \in \mathcal{I}$. Hence the result.

3. It follows from the fact that, for any $U \in \mathcal{A}$, $U \cap I \in \mathcal{I}$, since $I \in \mathcal{I}$.

4. Claim: $A^{c*} \subseteq (A \setminus I)^{c*}$.

Let $x \in (A \setminus I)^{c*}$. Then for all $U \in \mathcal{A}(x)$, $A \cap U \notin \mathcal{I}$. If possible, suppose that $U \cap (A \setminus I) \in \mathcal{I}$. Then for some $J \in \mathcal{I}$, $U \cap (A \setminus I) = J$. Then $(U \cap A) \setminus I = J$, and hence $U \cap A = I \cup J \in \mathcal{I}$, a contradiction.

Claim: $(A \cup I)^{c*} \subseteq A^{c*}$.

Let $x \in (A \cup I)^{c*}$. Then for all $U_x \in \mathcal{A}(x)$, $U_x \cap (A \cup I) \notin \mathcal{I}$. If possible, suppose that $A \cap U_x \in \mathcal{I}$.

Then for some $J \in \mathcal{I}$, $A \cap U_x = J$. Note that $U_x \cap (A \cup I) = (U_x \cap A) \cup (U_x \cap I) = J \cup (U_x \cap I)$. Since $U_x \cap I \subseteq I$, then $U_x \cap (A \cup I) \in \mathcal{I}$, a contradiction.

5. It follows from the fact that every member of \mathcal{H} is also a member of \mathcal{I} .

6. From (5), $A^{c*}(\mathcal{I}) \cup A^{c*}(\mathcal{J}) \subseteq A^{c*}(\mathcal{I} \cap \mathcal{J})$. Let $x \in A^{c*}(\mathcal{I} \cap \mathcal{J})$. Then for all $U \in \mathcal{A}(x)$, $U \cap A \notin \mathcal{I} \cap \mathcal{J}$. Thus $U \cap A \notin \mathcal{I}$ or $U \cap A \notin \mathcal{J}$. This implies that $x \in A^{c*}(\mathcal{I})$ or $x \in A^{c*}(\mathcal{J})$, and hence $x \in A^{c*}(\mathcal{I}) \cup A^{c*}(\mathcal{J})$.

Lemma 2.4. Let $(X, \mathcal{A}, \mathcal{I})$ be a space. Then $\mathcal{A} \cap \mathcal{I} = \{\emptyset\}$ if and only if $X = X^{c*}$.

Proof. Suppose $\mathcal{A} \cap \mathcal{I} = \{\emptyset\}$. It is obvious that $X^{c*} \subseteq X$. For reverse inclusion, let $x \in X$. If possible suppose that $x \notin X^{c*}$. Then there exists $U_x \in \mathcal{A}(x)$ such that $U_x \cap X \in \mathcal{I}$. This implies that $U_x \in \mathcal{I}$, a contradiction.

Conversely, suppose that $X = X^{c*}$ holds. If possible, suppose that $U \in \mathcal{A} \cap \mathcal{I}$, where $x \in U$. Then $U \cap X \in \mathcal{I}$, by hereditary property. Thus $x \notin X^{c*}$, a contradiction.

If an ideal \mathcal{I} satisfies the property $\mathcal{A} \cap \mathcal{I} = \{\emptyset\}$, then the ideal \mathcal{I} is called \mathcal{A} -codense ideal.

This property is similar to Dontchev, Ganster and Rose's [26] 'codense' ideal. An ideal \mathcal{I} in an ideal topological space is called codense ideal if $\mathcal{I} \cap \tau = \{\emptyset\}$. Newcomb [23], Hamlett and Jankovic[18] called such ideal as ' τ -boundary' whereas Dontchev [27] called such spaces as 'Hayashi-Samuel' spaces. In fact such ideals play a very important role in the study of ideals (see: [6,19,28,29,30]).

We define an operator similar to Natkaniec's ψ -operator [17]:

Definition 2.5. Let $(X, \mathcal{A}, \mathcal{I})$ be a space. An operator $\psi_c : \wp(X) \rightarrow \wp(X)$ is defined as follows: for every $A \in \wp(X)$, $\psi_c(A) = \{x \in X : \text{there exists a } U \in \mathcal{A}(x) \text{ such that } U \setminus A \in \mathcal{I}\}$.

Equivalently $\psi_c(A) = X \setminus (X \setminus A)^{c*}$.

Proof. Let $x \in X \setminus (X \setminus A)^{c*}$. Then $x \notin (X \setminus A)^{c*}$, and thus there exists $U \in \mathcal{A}(x)$ such that $U \cap (X \setminus A) \in \mathcal{I}$. So $U \setminus A \in \mathcal{I}$. Hence $x \in \psi_c(A)$.

Let $x \in \psi_c(A)$. Then from definition, there exists $U \in \mathcal{A}(x)$ such that $U \setminus A \in \mathcal{I}$. This implies that $U \cap (X \setminus A) \in \mathcal{I}$. Thus $x \notin (X \setminus A)^{c*}$, and hence $x \in X \setminus (X \setminus A)^{c*}$.

Here we find out the value of ψ_c of a set in a space.

Example 2.6. Let $X = \{a, b, c\}$, $\mathcal{A} = \{\emptyset, \{a, b\}, \{a, c\}\}$ and $\mathcal{I} = \{\emptyset, \{b\}\}$. Take $B = \{a, b\}$. Then $\psi_c(B) = X \setminus (X \setminus B)^{c*} = X \setminus \{c\}^{c*} = X \setminus \{c\} = \{a, b\}$.

Theorem 2.7. Let $(X, \mathcal{A}, \mathcal{I})$ be a space.

1. If $A \subseteq B$, then $\psi_c(A) \subseteq \psi_c(B)$.
2. If $U \in \mathcal{A}$, then $U \subseteq \psi_c(U)$.
3. If $A, B \in \wp(X)$, then $\psi_c(A) \cup \psi_c(B) \subseteq \psi_c(A \cup B)$.
4. If $A \subseteq X$, then $\psi_c(A) = \psi_c(\psi_c(A))$ if and only if $(X \setminus A)^{c*} = ((X \setminus A)^{c*})^{c*}$.
5. If $I \in \mathcal{I}$, then $\psi_c(I) = X \setminus X^{c*}$.
6. If $A \subseteq X$, $I \in \mathcal{I}$, then $\psi_c(A \cup I) = \psi_c(A)$.

7. If $(A \setminus B) \cup (B \setminus A) \in \mathcal{I}$, then $\psi_c(A) = \psi_c(B)$.

Proof. 1. Obvious from Theorem 2.3 (2).

2. Let $x \in U$. Then $x \notin X \setminus U$ and $U \cap (X \setminus U) = \emptyset \in \mathcal{I}$. Thus $x \notin (X \setminus U)^{c*}$. Hence $x \in \psi_c(U)$.

3. Obvious from monotonicity of ψ_c .

4. Suppose $\psi_c(A) = \psi_c(\psi_c(A))$. Then $X \setminus (X \setminus A)^{c*} = \psi_c[X \setminus (X \setminus A)^{c*}]$, and hence $X \setminus (X \setminus A)^{c*} = [X \setminus [(X \setminus A)^{c*}]^{c*}]$. This implies that $(X \setminus A)^{c*} = ((X \setminus A)^{c*})^{c*}$.

5. Obvious from Theorem 2.3 (4).

6. Obvious from 5.

7. Given that $(A \setminus B) \cup (B \setminus A) \in \mathcal{I}$, and let $(A \setminus B) = I$, $(B \setminus A) = J$. Note that $I, J \in \mathcal{I}$ by heredity. Also observe that $B = (A \setminus I) \cup J$. Thus $\psi_c(B) = \psi_c[(A \setminus I) \cup J] = \psi_{c*}(A \setminus I) = \psi_c(A)$.

If we take reverse implication of the above relations, then we get the converse part.

Corollary 2.8. Let $(X, \mathcal{A}, \mathcal{I})$ be a space, then the following properties

are equivalent:

1. $\mathcal{A} \cap \mathcal{I} = \{\emptyset\}$;
2. $\psi_c(\emptyset) = \emptyset$;
3. If $I \in \mathcal{I}$, then $\psi_c(I) = \emptyset$.

Proof. 1 implies 2:

$$\psi_c(\emptyset) = X \setminus X^{c*} = \emptyset, \text{ since } \mathcal{A} \cap \mathcal{I} = \{\emptyset\}.$$

2 implies 3:

$$\psi_c(I) = X \setminus (X \setminus I)^{c*} = X \setminus X^{c*}, \text{ since } I \in \mathcal{I}. \text{ Thus } \psi_c(I) = \emptyset.$$

3 implies 1:

$$\psi_c(I) = \emptyset \text{ gives } X = X^{c*}. \text{ Thus } \mathcal{A} \cap \mathcal{I} = \{\emptyset\}.$$

Definition 2.9. Let $(X, \mathcal{A}, \mathcal{I})$ be a space. We say the \mathcal{A} -structure \mathcal{A} is \mathcal{A} -compatible with the ideal \mathcal{I} , denoted $\mathcal{A} \sim \mathcal{I}$, if the following property holds: for every $A \subseteq X$, if for every $x \in A$ there exists $U \in \mathcal{A}(x)$ such that $U \cap A \in \mathcal{I}$, then $A \in \mathcal{I}$.

Lemma 2.10. Let $(X, \mathcal{A}, \mathcal{I})$ be a space. Then $\mathcal{A} \sim \mathcal{I}$ if and only if $\psi_c(A) \setminus A \in \mathcal{I}$, for every $A \subseteq X$.

Proof. Suppose $\mathcal{A} \sim \mathcal{I}$ holds. Then for $U \setminus A \in \mathcal{I}$, $\psi_c(A) \cap (U \setminus A) \in \mathcal{I}$. This implies that

$$U \cap (\psi_c(A) \setminus A) \in \mathcal{I}, \text{ then from } \mathcal{A} \sim \mathcal{I}, \psi_c(A) \setminus A \in \mathcal{I}.$$

Conversely suppose that $\psi_c(A) \setminus A \in \mathcal{I}$, for every $A \subseteq X$. Let $x \in A$. Also there is $U_x \in \mathcal{A}(x)$ such that

$$U_x \cap A \in \mathcal{I} \text{ for every } x \in A. \text{ Then } x \notin A^{c*}, \text{ and hence } x \in X \setminus A^{c*}. \text{ Thus } A \subseteq X \setminus A^{c*}. \text{ Note that}$$

$$\psi_c(X \setminus A) \setminus (X \setminus A) = [X \setminus (X \setminus (X \setminus A))^{c*}] \setminus (X \setminus A) = (X \setminus A^{c*}) \setminus (X \setminus A) = (X \setminus A^{c*}) \cap A$$

. Therefore $\psi_c(X \setminus A) \setminus (X \setminus A) = (X \setminus A^{c*}) \cap A = A$ (as $A \subseteq X \setminus A^{c*}$). Since $\psi_c(A) \setminus A \in \mathcal{I}$ for every $A \subseteq X$, thus $A \in \mathcal{I}$. Therefore, $\mathcal{A} \sim \mathcal{I}$.

Following example supports the Lemma 2.10.

Example 2.11. Let $X = \{a, b\}$, $\mathcal{A} = \{\{a\}, \{b\}\}$ and $\mathcal{I} = \{\emptyset, \{b\}\}$. Then $\phi^{c*} = \phi, \{a\}^{c*} = \{a\}, \{b\}^{c*} = \phi$ and $X^{c*} = \{a\}$. Then $\psi_c(\phi) = X \setminus X^{c*} = \phi$, $\psi_c(\{a\}) = X \setminus \{b\}^{c*} = X$, $\psi_c(\{b\}) = X \setminus \{a\}^{c*} = \{b\}$ and $\psi_c(X) = X \setminus \phi^{c*} = X$. Then we see that $\psi_c(\phi) \setminus \phi = \phi \in \mathcal{I}$, $\psi_c(\{a\}) \setminus \{a\} = \{b\} \in \mathcal{I}$, $\psi_c(\{b\}) \setminus \{b\} = \phi \in \mathcal{I}$ and $\psi_c(X) \setminus X = \phi \in \mathcal{I}$ and $\mathcal{A} \sim \mathcal{I}$.

Corollary 2.12. Let $(X, \mathcal{A}, \mathcal{I})$ be a space with $\mathcal{A} \sim \mathcal{I}$. Then $\psi_c(\psi_c(A)) \subseteq \psi_c(A)$, for every $A \subseteq X$.

Proof. From above theorem, for any $A \subseteq X$, $\psi_c(A) \setminus A \in \mathcal{I}$. Then $\psi_c(A) \subseteq A \cup I$, for some $I \in \mathcal{I}$. Then $\psi_c(\psi_c(A)) \subseteq \psi_c(A \cup I) = \psi_c(A)$ (from Theorem 2.7 (6)).

We shall give an example against the Corollary 2.12.

Example 2.13. Consider the spsce $(X, \mathcal{A}, \mathcal{I})$, where $X = \{a, b\}$, $\mathcal{A} = \{\{a\}, \{b\}\}$ and $\mathcal{I} = \{\emptyset, \{b\}\}$. Then $\mathcal{A} \sim \mathcal{I}$, by Example 2.11. Now $\phi^{c*} = \phi, \{a\}^{c*} = \{a\}, \{b\}^{c*} = \phi$ and $X^{c*} = \{a\}$ and $\psi_c(\phi) = X \setminus X^{c*} = \phi$, $\psi_c(\{a\}) = X \setminus \{b\}^{c*} = X$, $\psi_c(\{b\}) = X \setminus \{a\}^{c*} = \{b\}$ and $\psi_c(X) = X \setminus \phi^{c*} = X$. Then $\psi_c(\psi_c(\phi)) = \phi = \psi_c(\phi)$, $\psi_c(\psi_c(\{a\})) = X = \psi_c(\{a\})$, $\psi_c(\psi_c(\{b\})) = \{b\} = \psi_c(\{b\})$ and $\psi_c(\psi_c(X)) = X = \psi_c(X)$.

Newcomb has defined $A = B[\text{mod } \mathcal{I}]$ [23] if $(A \setminus B) \cup (B \setminus A) \in \mathcal{I}$.

Definition 2.14. Let $(X, \mathcal{A}, \mathcal{I})$ be a space. A subset B of X is called a Baire set with respect to \mathcal{A} and \mathcal{I} , denoted $A \in \mathbf{B}_r(X, \mathcal{A}, \mathcal{I})$, if there exists a $A \in \mathcal{A}$ such that $B = A[\text{mod } \mathcal{I}]$.

Following example is the existence of Baire set.

Example 2.15. Let $X = \mathbb{R}$, set of real numbers, $\mathcal{A} = \{\emptyset, \mathbb{R}, \mathbb{Q} \cup \{i\}, \mathbb{R} \setminus \mathbb{Q}\}$, and $\mathcal{I} = \wp(\mathbb{Q})$, where \mathbb{Q} is the set of rational numbers and $i \in \mathbb{R} \setminus \mathbb{Q}$. Consider $A = \{i\}$. Then for $B = \mathbb{Q} \cup \{i\}$, $(A \setminus B) \cup (B \setminus A) = \emptyset \cup (\mathbb{Q} \cup \{i\} \setminus \{i\}) = \mathbb{Q} \in \mathcal{I}$. Thus A is a Baire set in $(X, \mathcal{A}, \mathcal{I})$.

Theorem 2.16. Let $(X, \mathcal{A}, \mathcal{I})$ be a space with $\mathcal{A} \sim \mathcal{I}$. If $U, V \in \mathcal{A}$ and $\psi_c(U) = \psi_c(V)$, then $U = V[\text{mod } \mathcal{I}]$.

Proof. Since $U \in \mathcal{A}$, we have $U \subseteq \psi_c(U)$ (from Theorem 2.7 (2)), and hence $U \setminus V \subseteq \psi_c(U) \setminus V = \psi_c(V) \setminus V \in \mathcal{I}$ (by Lemma 2.10). Similarly $V \setminus U \in \mathcal{I}$. Now $(U \setminus V) \cup (V \setminus U) \in \mathcal{I}$ (by finite additivity). Hence $U = V[\text{mod } \mathcal{I}]$.

It is obvious that $A = B[\text{mod } \mathcal{I}]$ is an equivalence relation.

Theorem 2.17. Let $(X, \mathcal{A}, \mathcal{I})$ be a space with $\mathcal{A} \sim \mathcal{I}$. If $A, B \in \mathbf{B}_r(X, \mathcal{A}, \mathcal{I})$, and $\psi_c(A) = \psi_c(B)$, then $A = B[\text{mod } \mathcal{I}]$.

Proof. Let $U, V \in \mathcal{A}$ such that $A = U[\text{mod } \mathcal{I}]$ and $B = V[\text{mod } \mathcal{I}]$. Now $\psi_c(A) = \psi_c(B)$ and $\psi_c(B) = \psi_c(V)$ (by Theorem 2.7 (7)). Since $\psi_c(A) = \psi_c(U)$ implies that $\psi_c(U) = \psi_c(V)$, hence $U = V[\text{mod } \mathcal{I}]$ (by Theorem 2.16). Hence $A = B[\text{mod } \mathcal{I}]$ by transitivity.

Theorem 2.18. Let $(X, \mathcal{A}, \mathcal{I})$ be a space.

1. If $B \in \mathbf{B}_r(X, \mathcal{A}, \mathcal{I}) \setminus \mathcal{I}$, then there exists $A \in \mathcal{A} \setminus \{\emptyset\}$ such that $B = A[\text{mod } \mathcal{I}]$.
2. Suppose $\mathcal{A} \cap \mathcal{I} = \{\emptyset\}$, then $B \in \mathbf{B}_r(X, \mathcal{A}, \mathcal{I}) \setminus \mathcal{I}$ if and only if there exist $A \in \mathcal{A} \setminus \{\emptyset\}$ such that $B = A[\text{mod } \mathcal{I}]$.

Proof. 1. Let $B \in \mathbf{B}_r(X, \mathcal{A}, \mathcal{I}) \setminus \mathcal{I}$. Then $B \in \mathbf{B}_r(X, \mathcal{A}, \mathcal{I})$. If there does not exist $A \in \mathcal{A} \setminus \{\emptyset\}$ such that $B = A[\text{mod } \mathcal{I}]$, we have $B = \emptyset[\text{mod } \mathcal{I}]$. This implies that $B \in \mathcal{I}$, which is a contradiction.

2. Here we prove converse part only. Let $A \in \mathcal{A} \setminus \{\emptyset\}$ such that $B = A[\text{mod } \mathcal{I}]$. Then $A = (B \setminus J) \cup I$, where $J = B \setminus A, I = A \setminus B \in \mathcal{I}$. If $B \in \mathcal{I}$, then $A \in \mathcal{I}$ by heredity and additivity, which contradicts $\mathcal{A} \cap \mathcal{I} = \{\emptyset\}$.

3. Approximation

Approximation is a part of analysis, but in this section, we introduce a method for approximation of local function and set operator ψ with the help of generalized open sets of topological space.

We shall denote ‘Int’ and ‘Cl’ as the ‘interior’ and ‘closure’ operator respectively of topological spaces.

Definition 3.1. Let (X, τ) be a topological space. A subset A of X is called semi-open [31] (resp. preopen [32], semi-preopen [33] ($= \beta$ open [34]), b -open [35]) set, if $A \subseteq Cl(Int(A))$ (resp. $A \subseteq Int(Cl(A))$, $A \subseteq Cl(Int(Cl(A)))$, $A \subseteq Cl(Int(A)) \cup Int(Cl(A))$).

The collection of all semi-open (resp. preopen, semi-preopen, b -open) in a topological space (X, τ) is denoted as $SO(X, \tau)$ (resp. $PO(X, \tau)$, $\beta O(X, \tau)$, $BO(X, \tau)$).

Further $SO(X, x)$ (resp. $PO(X, x)$, $\beta O(X, x)$, $BO(X, x)$) is the collection of all semi-open (resp. preopen, semi-preopen, b -open) sets containing x in a topological space (X, τ) .

From definition, for a topological space (X, τ) , we have $\tau \subseteq SO(X, \tau) \subseteq \beta O(X, \tau) \subseteq BO(X, \tau)$, and $\tau \subseteq PO(X, \tau) \subseteq \beta O(X, \tau) \subseteq BO(X, \tau)$.

Definition 3.2. Let (X, τ, \mathcal{I}) be an ideal topological space. For a subset A of X , we define the following operator: A^{*p} (resp. $A^{*s}, A^{*\beta}, A^{*b}$) $= \{x \in X : A \cap U_x \notin \mathcal{I} \text{ for every } U_x \in PO(X, x) \text{ (resp. } SO(X, x), \beta O(X, x), BO(X, x))\}$.

Theorem 3.3. Let (X, τ, \mathcal{I}) be an ideal topological space. Then

1. for $A \subseteq X$, $A^{*b} \subseteq A^{*\beta} \subseteq A^{*s} \subseteq A^*$.
2. for $A \subseteq X$, $A^{*b} \subseteq A^{*\beta} \subseteq A^{*p} \subseteq A^*$.

Let (X, τ) be a topological space. Then for $A \subseteq X$, we define $sCl(A)$ (resp. $pCl(A)$, $\beta Cl(A)$, $bCl(A)$)
 $= \bigcap \{F \supseteq A : X \setminus F \in SO(X, \tau) \text{ (resp. } PO(X, \tau), \beta O(X, \tau), BO(X, \tau))\}$.

Proposition 3.4. Let (X, τ) be a topological space. Then for any $A \subseteq X$,

- (1) $bCl(A) \subseteq \beta Cl(A) \subseteq sCl(A) \subseteq Cl(A)$,
- (2) $bCl(A) \subseteq \beta Cl(A) \subseteq pCl(A) \subseteq Cl(A)$.

Definition 3.5. Let (X, τ, \mathcal{I}) be an ideal topological space. For a subset A of X , we define the following operator: $\gamma_c(A)$ [3] (resp. $\gamma_{pc}(A), \gamma_{sc}(A), \gamma_{\beta c}(A), \gamma_{bc}(A)$) $= \{x \in X : A \cap Cl(U_x) \text{ (resp. } A \cap pCl(U_x), A \cap sCl(U_x), A \cap \beta Cl(U_x), A \cap bCl(U_x)) \notin \mathcal{I} \text{ for every } U_x \in \tau(x)\}$, where $\tau(x) = \{U \in \tau : x \in U\}$.

Theorem 3.6. Let (X, τ, \mathcal{I}) be an ideal topological space. Then for any $A \subseteq X$,

1. $A^* \subseteq \gamma_c(A) \subseteq \gamma_{sc}(A) \subseteq \gamma_{\beta c}(A) \subseteq \gamma_{bc}(A)$,
2. $A^* \subseteq \gamma_c(A) \subseteq \gamma_{pc}(A) \subseteq \gamma_{\beta c}(A) \subseteq \gamma_{bc}(A)$.

Next we consider following operators:

$$\psi_s(A) \text{ (resp. } \psi_p(A), \psi_\beta(A), \psi_b(A)) = X \setminus (X \setminus A)^{*s} \text{ (resp. } (X \setminus A)^{*p}, (X \setminus A)^{*b}, (X \setminus A)^{*b}).$$

Theorem 3.7. Let (X, τ, \mathcal{I}) be an ideal topological space. Then

1. for $A \subseteq X$, $\psi(A) \subseteq \psi_s(A) \subseteq \psi_\beta(A) \subseteq \psi_b(A)$.
2. for $A \subseteq X$, $\psi(A) \subseteq \psi_p(A) \subseteq \psi_\beta(A) \subseteq \psi_b(A)$.

Definition 3.8. Let (X, τ, \mathcal{I}) be an ideal topological space. For a subset A of X , we define the following operator: $\Gamma_c(A)$ (resp. $\Gamma_{pc}(A), \Gamma_{sc}(A), \Gamma_{\beta c}(A), \Gamma_{bc}(A)$) $= X \setminus \gamma_c(X \setminus A)$ (resp. $\gamma_{pc}(X \setminus A), \gamma_{sc}(X \setminus A), \gamma_{\beta c}(X \setminus A), \gamma_{bc}(X \setminus A)$).

Theorem 3.9. Let (X, τ, \mathcal{I}) be an ideal topological space. Then for any $A \subseteq X$,

1. $\psi(A) \supseteq \Gamma_c(A) \supseteq \Gamma_{sc}(A) \supseteq \Gamma_{\beta c}(A) \supseteq \Gamma_{bc}(A)$,
2. $\psi(A) \supseteq \Gamma_c(A) \supseteq \Gamma_{pc}(A) \supseteq \Gamma_{\beta c}(A) \supseteq \Gamma_{bc}(A)$.

Expansion of local function and set operator ψ have been shown by the following corollaries:

Corollary 3.10. Let (X, τ, \mathcal{I}) be an ideal topological space. Then

1. for $A \subseteq X$, $A^{*b} \subseteq A^{*\beta} \subseteq A^{*s} \subseteq A^* \subseteq \gamma_c(A) \subseteq \gamma_{sc}(A) \subseteq \gamma_{\beta c}(A) \subseteq \gamma_{bc}(A)$.
2. for $A \subseteq X$, $A^{*b} \subseteq A^{*\beta} \subseteq A^{*p} \subseteq A^* \subseteq \gamma_c(A) \subseteq \gamma_{pc}(A) \subseteq \gamma_{\beta c}(A) \subseteq \gamma_{bc}(A)$.

Corollary 3.11. Let (X, τ, \mathcal{I}) be an ideal topological space. Then

1. for $A \subseteq X$, $\Gamma_{bc}(A) \subseteq \Gamma_{\beta c}(A) \subseteq \Gamma_{sc}(A) \subseteq \Gamma_c(A) \subseteq \psi(A) \subseteq \psi_s(A) \subseteq \psi_\beta(A) \subseteq \psi_b(A)$.
2. for $A \subseteq X$, $\Gamma_{bc}(A) \subseteq \Gamma_{\beta c}(A) \subseteq \Gamma_{pc}(A) \subseteq \Gamma_c(A) \subseteq \psi(A) \subseteq \psi_p(A) \subseteq \psi_\beta(A) \subseteq \psi_b(A)$.

4. Conclusion

Anyone can introduce a new type of generalized open set in the topological space and if this collection lies in between the collection of semi-open sets and semi-preopen sets (resp. preopen sets and semi-pre open sets), then we get an another local function whose value lies in between $()^{*\beta}$ and $()^{*s}$ (resp. $()^{*\beta}$ and $()^{*p}$). Similarly we can split the values of ψ_s and ψ_β , ψ_p and ψ_β , γ_{sc} and $\gamma_{\beta c}$, γ_{pc} and $\gamma_{\beta c}$, $\Gamma_{\beta c}$ and Γ_{sc} and $\Gamma_{\beta c}$ and Γ_{pc} .

Conflicts of interest

There is no conflict of interest.

References

- [1] Kuratowski, K., Topology I. Warszawa, 1933.
- [2] Al-omari, A. and Noiri, T., A topology via \mathcal{M} -local functions in ideal m-spaces. *Questions Answers Gen. Topology*, 30 (2012) 105-114.
- [3] Al-omari, A. and Noiri, T., Local closure functions in ideal topological spaces. *Novi Sad J. Math.*, 12(2) (2013) 139-149.
- [4] Modak, S., Grill-filter space. *J. Indian Math. Soc.*, 80 (2012) 313-320.
- [5] Modak, S., Ideal on generalized topological spaces. *Sci. Magna*, 11(2) (2016) 14-20.
- [6] Modak, S., Minimal spaces with a mathematical structure. *J. Assoc. Arab Univ. Basic Appl. Sci.*, 22 (2017) 98-101.
- [7] Modak, S. and Noiri, T., Remarks on locally closed sets. *Acta Comment. Univ. Tartu. Math.*, 22(1) (2018) 57-64.
- [8] Modak, S. and Islam, Md. M., On $*$ and Ψ operators in topological spaces with ideals. *Trans. A. Razmadze Math. Inst.*, 172 (2018) 491-497.
- [9] Islam, Md. M. and Modak, S., Operator associated with the $*$ and Ψ operators. *J. Taibah Univ. Sci.*, 12(4) (2018) 444-449.
- [10] Islam, Md. M. and Modak, S., Second approximation of local functions in ideal topological spaces. *Acta Comment. Univ. Tartu. Math.*, 22(2) (2018) 245-256.
- [11] Ekici, E. and Elmalı, O., On Decompositions via Generalized Closedness in Ideal Spaces. *Filomat*, 29(4) (2015) 879-886.

- [12] Modak, S. and Mistry, S., Ideal on supra topological space. *Int. Journal of Math. Analysis*, 6(1) (2012) 1-10.
- [13] Khan, M., and Noiri, T., Semi-local functions in ideal topological spaces. *J. Adv. Res. Pure Math.*, 2(1) (2010) 36-42.
- [14] Csaszar, A., Modification of generalized topologies via hereditary classes. *Acta Math. Hungar.*, 115(1-2) (2007) 29-36.
- [15] Özbakir, O.B. and Yildirim, E.D., On some closed sets in ideal minimal spaces. *Acta Math. Hungar.*, 125(3) (2009) 227-235.
- [16] Hayashi, E., Topologies defined by local properties. *Math. Ann.*, 156 (1964) 205-215.
- [17] Natkaniec, T., On I-continuity and I-semicontinuity points. *Math. Slovaca*, 36(3) (1986) 297-312
- [18] Hamlett, T.R. and Jankovic, D., Ideals in topological spaces and the set operator ψ . *Bull. U.M.I.*, 7(4-B) (1990) 863-874.
- [19] Modak, S. and Bandyopadhyay, C., A note on ψ - operator. *Bull. Malyas. Math. Sci. Soc.*, 30(1) (2007) 43-48.
- [20] Csaszar, A., Generalized open sets. *Acta Math. Hungar.*, 75(1-2) (1997) 65-87.
- [21] Popa V. and Noiri T., On M-continuous functions. *Anal. Univ. "Dunarea de Jos" Galati, Ser. Mat. Fiz. Mec. Teor. Fasc.II*, 18(23) (2000) 31-41.
- [22] Mashhour, A.S., Allam, A.A., Mahmoud, F.S. and Khedr, F.H., On supra topological spaces. *Indian J. Pure and Appl. Math.*, 14(4) (1983) 502-510.
- [23] Newcomb, R.L., Topologies which are compact modulo an ideal. Ph. D. Dissertation, *Univ. of Cal. at Santa Barbara*, (1967).
- [24] Njastad, O., Remarks on topologies defined by local properties. *Norske Vid-Akad. Oslo (N.S)*, 8 (1966) 1-16.
- [25] Pavlovic, A., Local function versus local closure function in ideal topological spaces. *Filomat*, 30(14) (2016) 3725-3731.
- [26] Dontchev, J., Ganster M., Rose D., Ideal resolvability. *Topology Appl.*, 93 (1999) 1-16.
- [27] Dontchev, J., Idealization of Ganster-Reilly decomposition theorems. *arXIV, Math. Gn/9901017VI*, (1999).
- [28] Modak, S., Some new topologies on ideal topological spaces. *Proc. Natl. Acad. Sci., India, Sect. A Phys. Sci.*, 82(3) (2012) 233-243.
- [29] Bandyopadhyay, C. and Modak, S., A new topology via ψ - operator. *Proc. Natl. Acad. Sci., India, Sect. A Phys. Sci.*, 76(2006) 17-20.
- [30] Jankovic, D. and Hamlett, T.R., New topologies from old via ideals. *Amer. Math. Monthly*, 97(1990) 295-310.
- [31] Levine, N., Semi-open sets and semi-continuity in topological spaces. *Amer. Math. Monthly*, 70 (1963) 36-41.
- [32] Mashhour, A.S., El-Monsef, M.E.A. and El-Deeb, S.N., On precontinuous and weak precontinuous mappings. *Proc. Math. Phys. Soc. Egypt.*, 53 (1982) 47-53.
- [33] Andrijevic, D., Semi-preopen sets. *Math. Vesnik*, 38 (1986) 24-32.
- [34] El-Monsef, M.E.A., El-Deeb, S.N. and Mahmoud, R.A., β -open sets and β -continuous mappings. *Bull. Fac. Sci., Assiut Univ.* 12 (1983) 77-90.
- [35] Andrijevic, D., On b-open sets. *Mat. Vesnik.*, 48 (1996) 59-64.



Comparison of greedy matching methods on cigarette usage of individuals in Turkey

Ezgi NAZMAN^{1,*}  Hülya OLMUŞ² 

¹Sivas Cumhuriyet University, Department of Statistics and Computer Sciences, Sivas/ TURKEY

²Gazi University, Department of Statistics, Ankara/ TURKEY

Abstract

There has been a growing interest in using observational studies to estimate treatment effects on outcomes where treatment selection is often influenced by covariates. Recently, propensity score matching (PSM) method has increasingly being used to reduce bias in estimated treatment effect for observational studies. Greedy Matching (GM), one of the PSM methods, is widely preferred in many studies because of the calculation simplicity of the method. However, GM is still open to be evaluated in terms of bias reduction and classification performances. For this purpose, data including cigarette usage of 17242 individuals in Turkey were used for the comparison of nearest neighbor, caliper, stratification, Mahalanobis metric, and combined propensity score and Mahalanobis metric matching methods in terms of average standardized bias, bias reduction, and accuracy rate. The stratification-matching method should be preferred for not only low standardized bias and high bias reduction, but also high accuracy rate.

Article info

History:

Received: 20.01.2020

Accepted: 28.05.2020

Keywords:

Bias reduction, Greedy matching methods, Standardized bias, Cigarette usage

1. Introduction

The aim of randomized study is to eliminate the effects of confounding and treatment selection bias when using observational data ensuring groups are comparable. However, observational studies cause treatment selection bias. Therefore, propensity score matching (PSM) is a statistical approach to reduce bias in estimated treatment effects. Opposed to randomized study, a subject's probability of receiving a treatment is not known; however, it depends on observed and unobserved covariates in nonrandomized study. The propensity score was first proposed by [1] as a conditional probability of receiving a treatment given that subject's observed covariates [2]. The studies including large data sets are generally observational rather than experimental. Thus, PSM is sensible and more reliable to try to estimate the effects of treatments from such large data sets [3]. Adjustment was indicated based on PSM which can change results if age, sex, education, and income are used as predictors on smoking status [4].

Greedy matching (GM) methods are the most commonly used PSM methods for observational studies due to the application easiness of the methods. Propensity score calculations on cigarette using have been utilized in individual health from different point of views in literature for the observational studies. The effect of in-patient smoking cessation counselling on mortality in patients hospitalized with a heart attack was estimated by [5]. Association between smoking cessation and change in mental health before and after PSM was examined by [6]. The effect of maternal smoking during pregnancy on offspring's initial reactions to cigarettes and alcohol usage was studied by [7]. Multiple potential risk factors for non-smoking related lung cancer among Asian ethnic groups using PSM was investigated by [8]. Smoking's independent contribution to the risk of short-term complication after total joint arthroplasty was studied by [9]. Association of cigarette smoking to cerebral atherosclerosis along with other risk factors was studied by [10].

This study first aims to assess the association of cigarette usage with gender, age group, education level, marital status, employment, income level, chronic disease, Body Mass Index (BMI), tobacco exposure,

*Corresponding author. Email address: ezgicabuk@cumhuriyet.edu.tr.

and alcohol usage in Turkey. In addition, the study compares performances of the greedy matching methods in terms of average standardized bias, bias reduction, and accuracy rate. It is the largest study on cigarette usage of individuals in Turkey up to now that propensity score matching has been applied to reduce bias of the covariates using GM methods.

2. Propensity Matching Method

The propensity score is defined as the conditional probability of assigning a subject to a particular treatment situation when the observed covariates are considered [1, 5]. The propensity score $e(x_i)$ is given in Eq. (1) which can be obtained by using the probit model, discriminant and cluster analysis in addition to the logistic regression model [11].

$$e(x_i) = P(z_i = 1|x_i), \quad 0 < e(x_i) < 1 \quad (1)$$

where z_i is the treatment (1) and control (0) groups, respectively and x_i is the observed covariates vector for i th subject. The propensity score when more than two treatment groups (z_1, \dots, z_n) exist for covariates vector (x_1, \dots, x_n) as in Eq.(2).

$$P(z_1, \dots, z_n|x_1, \dots, x_n) = \prod_{i=1}^N e(x_i)^{z_i} (1 - e(x_i))^{1-z_i} \quad (2)$$

Binary logistic regression is the most commonly used method to estimate the propensity score. The dependent variable is the probability of receiving a particular treatment using logit link function considering all covariates in the propensity score model as independent variables. Then, a propensity score for each subject in the study can be calculated by using the fitted model to estimate the probability of receiving the treatment given that subject's covariates. Once a propensity score for each subject has been estimated, subjects are matched using the propensity scores to create a balanced sample. Logistic regression model considering logit link function is given in Eq. (3).

$$\ln\left(\frac{e(x_i)}{1-e(x_i)}\right) = \ln\left(\frac{P(z_i=1|x_i)}{1-P(z_i=1|x_i)}\right) = \beta_0 + \beta_1 x_1 + \dots + \beta_N x_N \quad (3)$$

The propensity scores of i th subject can be calculated by using as in Eq. (4):

$$e(x_i) = \frac{e^{\beta_0 + \beta_1 x_1 + \dots + \beta_N x_N}}{1 + e^{\beta_0 + \beta_1 x_1 + \dots + \beta_N x_N}} = \frac{1}{1 + e^{-(\beta_0 + \beta_1 x_1 + \dots + \beta_N x_N)}} \quad (4)$$

2.1. Greedy matching methods

In this section, nearest neighbor, caliper, stratification, Mahalanobis, and combined propensity score and Mahalanobis metric matching methods are explained.

2.1.1. Nearest neighbor matching

The control and treatment units are randomly ordered in this method. Then, the smallest absolute value of the difference between the propensity score of the first treatment unit and the control unit are matched [12]. This process is continuous until all units in the treatment group have been generally matched as 1: N , N : 1 and N : N . Nearest neighbor matching was considered as 1:1 in this study. Having more units in the control group than treatment group allows better predictions [13]. In general, matching is described as follow:

$$C(P_i) = \min |P_i - P_j| \quad (5)$$

where $C(P_i)$ is the smallest absolute difference between i th treatment group unit matching the j th control group unit. P_i and P_j are the calculated propensity scores for i th treatment and j th control groups, respectively.

2.1.2. Caliper matching

In this method, units of the control and treatment groups are matched according to the absolute value of the difference between propensity scores and a standard error between predetermined interval values which is often 0.25 as first quantile. Then, the values outside of this range are removed. The fewer the standard error is, the fewer matching units will be [14]. Caliper matching method is as follow:

$$|P_i - P_j| < e \quad (6)$$

where e is the predetermined standard error.

2.1.3. Stratification matching

This method separates the units of treatment and control groups according to their propensity scores and calculates the effect within each interval by taking into account the mean difference between the groups. Within each propensity score stratum, treatment and control units will have roughly similar values of the propensity score [1]. One of the most important problems with this method is to specify number of strata. [15] showed that five strata are often sufficient since it is often enough to reduce 95% of the bias associated with one single covariate.

2.1.4. Mahalanobis metric matching

This method is based on the Mahalanobis metric distance which calculates a multi-dimensional space distances [16]. Mahalanobis metric distance between the treatment and control group units is calculated by starting from the first treatment group unit. Mahalanobis metric distance is shown in Eq. (7):

$$D_{ij} = (x_i - x_j)^T S^{-1} (x_i - x_j) \quad (7)$$

where S^{-1} is the inverse of the covariance matrix for the control units. x_i and x_j are covariate matrices of i th treatment and j th control group subjects. The treatment and control units are matched according to the smallest Mahalanobis metric distance. This process continues until the treatment group matches and unmatched control units are removed from the study [17].

2.1.5. Combined propensity score and Mahalanobis metric matching (Mah-Ps)

This method combines the propensity score and Mahalanobis metric distance for matching [17]. After propensity scores are calculated for all units, these scores are added to the data. Then, units in the treatment group are randomly ordered and Mahalanobis metric distances of the control and treatment groups are calculated by using the combination of covariates and propensity scores [16]. Matching is conducted according to the calculated distance of new Mahalanobis metric.

2.2. Evaluation of matching methods

Inferences from bias reduction (BR) performance of GM methods are calculated to give information on the degree of bias. Percent standardized bias (SB_k) comparing the distribution of each of the variables is defined as in Eq.(8) k th continuous variable.

$$SB_k = \frac{\bar{x}_i - \bar{x}_j}{\sqrt{\frac{s_i^2 + s_j^2}{2}}} \times 100 \quad (8)$$

where \bar{x}_i and \bar{x}_j are the sample means in the treatment and control groups, respectively, and s_i^2 and s_j^2 are the corresponding sample variances. In addition, percent SB_k is defined as in Eq.(9) for each dichotomous variable.

$$SB_k = \frac{\hat{p}_i - \hat{p}_j}{\sqrt{\frac{\hat{p}_i(1-\hat{p}_i) + \hat{p}_j(1-\hat{p}_j)}{2}}} \times 100 \quad (9)$$

where \hat{p}_i and \hat{p}_j denote the prevalence of the dichotomous variable in the treatment and control groups, respectively. [18] mentioned SB_k with more than 10% of a covariate is substantial. The percent BR_k on the k th covariate to evaluate the effectiveness of matching was also calculated as in Eq.(10):

$$BR_k = \frac{|B_{k,beforematching}| - |B_{k,aftermatching}|}{|B_{k,beforematching}|} \times 100 \quad (10)$$

where $B_k = \bar{x}_i - \bar{x}_j$. The percent BR value with more than 80% is acceptable to evaluate effectiveness of GM methods on the covariates [19].

3. Case Study

Turkey Health Survey 2016 administered by TurkStat [20] many indicators on health which have been periodically conducted by TurkStat since 2008 for every two years. Thus, this data set was obtained from TurkStat by special permission. Health Survey 2016 was carried out with 23606 individuals aged 75 and younger. The study was restricted on cigarette using of individuals; thus, the children, who are aged between 0-14, was out of the study. The remained sample included 17242 individuals ignoring children. Gender, age group, education level, marital status, employment, income level, chronic disease, BMI, tobacco exposure, and alcohol usage were specified as the covariates that may related with cigarette using. MASS, Matching, MatchIt, optmatch packages in RStudio were used for data analyses. Individuals are specified as control and treatment groups, respectively as no (non-smokers including never and quit smoking individuals) and yes (smokers including every day and sometimes smoking individuals). Baseline characteristics before matching of the two groups were given in Table1. Categorical variables were explained with the frequencies and percentages whereas BMI was given with mean and standard deviation.

Table 1: Baseline characteristics between control and treatment groups before matching

Variables	Cigarette using		p -value	$ SB_k (\%)$
	No (N=12167)	Yes (N=5075)		
Female	7797 (64.0)	1777 (35.0)	0.001*	60.8
≥ 45 year	5964 (49.0)	1923 (37.9)	0.001*	22.6
Higher Education	1749 (14.4)	815 (16.1)	0.001*	4.7
Married	8255 (67.9)	3657 (72.1)	0.001*	9.2
Working	3667 (30.1)	2790 (55.0)	0.001*	51.9
≥ 2541 TL	3953 (32.5)	1759 (34.7)	0.536	4.6
Chronic Disease	6165 (50.7)	2294 (45.2)	0.018*	11.0
Tobacco Exposure	812 (6.7)	1095 (21.6)	0.001*	43.8
Alcohol	2008 (16.5)	2209 (43.7)	0.001*	62.1
BMI	26.7 \pm 5.3	25.8 \pm 4.7	0.001*	18.0

$|SB_k|$ is the absolute average standardized bias of k -th covariate. Parantes indicates percentage of related baseline characteristic. *shows the significant covariate comparing with p -value=0.05.

As can be seen in Table1, 12167 (71%) individuals are not smokers including 64% female, 49% older than 45 years, 30.1% working, 50.7% having chronic disease, 43.8% being exposed tobacco, and 16.5 % using alcohol. The percent $|SB_k|$ values are also higher than 10% for gender, age, working status, chronic disease, tobacco exposure, alcohol usage, and BMI. According to the binary logistic regression analysis results, only income level is not significant before matching (p-value =0.536).

The baseline characteristics between the control and treatment groups after matching are given in Table 2. According to the results, the percent $|SB_k|$ decreases after matching for all methods. However, nearest (1:1), Mahalanobis, and Mah-Ps matchings cause more than 10% $|SB_k|$ for some of the covariates. On the other hand, caliper and stratified matchings provide $|SB_k|$ less than 10%. Caliper matching method provides the least $|SB_k|$ for gender, marital status, chronic disease, tobacco exposure, and BMI whereas stratified matching generally method reveals the least $|SB_k|$ for age group, working status, alcohol usage. Meantime, Mah-Ps has the least $|SB_k|$ for income level. Stratified and Mahalanobis matching are the lowest for education level with the same $|SB_k|$.

In addition, the percent $|SB|$ results with the average percent BR is shown Table 3. The average standardized bias before matching is 28.9%. The average standardized bias of all matching methods less than 10% whereas caliper (3.2%) and stratified (4.0%) matching methods have the least values. According to the percent BR , caliper and stratified matching methods have the highest value (81.0% and 76.8%) among the other methods. On the other hand, Nearest matching have the lowest average percent BR (56.5%) with 7.8% average percent SB .

The data set was splitted as 70% training and 30% test data to evaluate classification performances of the matching methods. Confusion matrix of binary classification is a two by two table formed by counting of the number of the true positive, false positive, true negative, and false negative of a binary classification method. The most common validation measurements are accuracy, sensitivity, and specificity deriving from the confusion matrix. Accuracy indicates the correctly classification rate of the methods, while sensitivity and specificity assess the accuracy rate. The method can be very specific without being sensitive, or it can be very sensitive without being specific. The accuracy, sensitivity, and specificity rates of the methods are shown in Table 4.

As can be seen, accuracy rate of before matching is almost similar with the rate of stratified matching. Caliper matching has the least accuracy rate among matching methods. Meantime, sensitivity and specificity rates of before matching and stratified matching are high among the other method.

Table 2: Baseline characteristics between control and treatment groups after matching

Methods	Nearest Matching (1:1)			Caliper Matching			Stratified Matching			Mahalanobis Matching			Mah-Ps Matching		
Variables	Cigarette using		$ SB_k $	Cigarette using		$ SB_k $	Cigarette using		$ SB_k $	Cigarette using		$ SB_k $	Cigarette using		$ SB_k $
	No	Yes	(%)	No	Yes	(%)	No	Yes	(%)	No	Yes	(%)	No	Yes	(%)
	(N=5075)	(N=5075)		(N=4436)	(N=4436)		(N=12164)	(N=5075)		(N=5075)	(N=5075)		(N=5075)	(N=5075)	
Female	1984 (39.1)	1777 (35.0)	8.5	1808 (40.8)	1733 (39.1)	3.5	7794 (64.0)	1777 (35.0)	3.7	2207 (43.5)	1777 (35.0)	17.4	2201 (43.4)	1777 (35.0)	17.2
≥45 year	2078 (40.9)	1923 (37.9)	6.3	1810 (40.8)	1741 (39.2)	3.2	5961 (49.0)	1923 (37.9)	1.0	2044 (40.3)	1923 (37.9)	4.9	2008 (39.6)	1923 (37.9)	3.4
Higher Education	938 (18.5)	815 (16.1)	6.4	789 (17.8)	742 (16.7)	2.8	1749 (14.4)	815 (16.1)	0.1	817 (16.1)	815 (16.1)	0.1	822 (16.2)	815 (16.1)	0.4
Married	3704 (73.3)	3657 (72.1)	2.1	3159 (71.2)	3178 (71.6)	1.0	8254 (67.9)	3657 (72.1)	1.9	3628 (71.5)	3657 (72.1)	1.3	3621 (71.3)	3657 (72.1)	1.6
Working	2541 (50.1)	2790 (55.0)	9.8	2173 (49.0)	2250 (50.7)	3.5	3667 (30.2)	2790 (55.0)	1.5	2517 (49.6)	2790 (55.0)	10.8	2427 (47.8)	2790 (55.0)	14.4
≥2541TL	1852 (36.5)	1759 (34.7)	3.8	1590 (35.8)	1549 (34.9)	1.9	3952 (32.5)	1759 (34.7)	3.3	1792 (35.3)	1759 (34.7)	1.4	1791 (35.3)	1759 (34.7)	1.3
Chronic Disease	2346 (46.2)	2294 (45.2)	2.1	2028 (45.7)	2031 (45.8)	0.1	6162 (50.7)	2294 (45.2)	1.4	2304 (45.4)	2294 (45.2)	0.4	2269 (44.7)	2294 (45.2)	1.0
Tobacco Exposure	746 (14.7)	1095 (21.6)	17.9	608 (13.7)	725 (16.3)	7.4	812 (6.7)	1095 (21.6)	8.6	811 (16.0)	1095 (21.6)	14.4	785 (15.5)	1095 (21.6)	15.8
Alcohol	1857 (36.6)	2209 (43.7)	14.6	1592 (35.9)	1679 (37.8)	4.1	2008 (16.5)	2219 (43.7)	0.3	1725 (34.0)	2219 (43.7)	20.1	1694 (33.4)	2219 (43.7)	21.4
BMI	26.1±4.7	25.8±4.7	6.4	25.8 ± 4.8	26.0± 4.7	4.0	26.6 ± 5.3	25.8 ± 4.8	18.0	26.2±4.8	25.8±4.7	8.4	26.0±4.7	25.8±4.7	4.3
$ SB_k $ presents absolute average standardized bias of k -th covariate. Parenthesis indicates percentage of related baseline characteristic.															

Table 3: Average percent standardized bias and bias reduction results

Methods	SB	BR
Before Matching	28.9	-
Nearest Matching (1:1)	7.8	56.5
Caliper Matching	3.2	81.0
Stratified Matching	4.0	76.8
Mahalanobis Matching	7.9	76.0
Mah-Ps Matching	8.1	76.3

Table 4: Classification performances of methods

Methods	Accuracy (%)	Sensitivity (%)	Specificity (%)
Before Matching	75.3	77.9	65.7
Nearest Matching (1:1)	58.3	55.8	64.8
Caliper Matching	52.3	51.6	54.7
Stratified Matching	75.5	77.6	64.8
Mahalanobis Matching	58.3	55.8	64.9
Mah-Ps Matching	58.3	55.8	64.8

4. Discussion

Observational studies have been widely using to estimate treatment effects on outcomes to reduce bias. Greedy Matching methods have generally preferred in many fields because of the calculation simplicity. In this study, nearest, caliper, stratified, and combined propensity score and Mahalanobis metric matching methods are investigated in terms of bias reduction and classification performances on cigarette usage of individuals in Turkey. Results indicated that gender, age group, education level, marital status, working status, chronic disease, body mass index, tobacco exposure, and alcohol usage of individuals are significant on cigarette usage in Turkey. For this reason, sociological and medical effects of these variables should be discussed for future studies in terms of cigarette usage. On the other hand, income levels of individuals do not significantly effect on cigarette usage. It means that individuals in Turkey tend to smoke regardless of their income.

When it comes to the comparison of greedy matching methods, Caliper matching method has the lowest average standardized bias. It also provides the highest average bias reduction. Besides, stratified matching method reveals the second lowest average standardized bias and provides the second highest average bias reduction. It can be mentioned that Caliper method is slightly superior to stratified matching according to the average standardized bias and bias reduction. On the other hand, stratified matching gives the highest accuracy rate whereas caliper matching has low accuracy rate.

Even though before matching provides high accuracy rate, it still produces high average standardized bias. Thus, the necessity and importance of the greedy matching methods is clear in terms of the average standardized bias. Briefly, caliper and stratified matching methods should be preferred if the researchers consider bias reduction whereas stratified matching method should be used in classification studies.

Conflicts of interest

There is no conflict of interest.

References

- [1] Rosenbaum P.R., Rubin, D.B. Assessing Sensitivity to an Unobserved Binary Covariate in an Observational Study with Binary Outcome. *J. R. Stat. Soc. Series B*, 45 (1983) 212–218.
- [2] Morgan C.J. Reducing Bias Using Propensity Score Matching. *J. Nucl. Cardiol.*, 25 (2018) 404-406.

- [3] Rubin D.B. Estimating Causal Effects From Large Data Sets Using Propensity Scores. *Ann. Int. Med.*, 15 (1997) 757-763.
- [4] Larsen M.D. An Analysis of Survey Data on Smoking Using Propensity Scores. *Sankhyā: Ind. J. Stat., Series B*, (1960-2002), (1999) 61.
- [5] Austin P.C. A Tutorial and Case Study in Propensity Score Analysis: An Application to Estimating the Effect of In-hospital Smoking Cessation Counselling on Mortality. *Multivar. Behav. Res.*, 46 (2011) 119-151.
- [6] Taylor G., Girling A., McNeill A., and Aveyard P. Does Smoking Cessation Result in Improved Mental Health? A Comparison of Regression Modelling and Propensity Score Matching. *BMJ Open*, (2015) 5:e008774. doi: 10.1136/bmjopen-2015-008774.
- [7] Bidwell L.C., Palmer R.H.C., Brick L., Madden P.A.F., Heath A.C., and Knopik V.S. A Propensity Scoring Approach to Characterizing the Effects of Maternal Smoking During Pregnancy on Offspring's Initial Responses to Cigarettes and Alcohol. *Behav. Gen.*, 46 (2016) 416-430.
- [8] Lin K.F., Wu H.F., Huang W.C., Tang P.L., Wu M.T., and Wu F.Z. Propensity Score Analysis of Lung Cancer Risk in a Population with High Prevalence of Non-Smoking Related Lung Cancer. *BMC Pulm. Med.*, 17 (2017) 120.
- [9] Sahota S., Lovecchio F., Harold R.E., Beal M.D., and Manning D.W. The Effect of Smoking on Thirty-Day Postoperative Complications after Total Joint Arthroplasty: A Propensity Score-Matched Analysis. *J. Arthroplasty*, 33 (2017) 30-35.
- [10] Song Y., Lee D., Suh D.C., Kim J.G., Kim J.K., Han M., Liu H., Zhao L., Kim E.H., Jung S.C., Lee D.G., Koo H.J., Kim M.J., Baek S., Hwang S.M., Kim B.J., Kim Y.J., Cho H.J., Kim S.J., Jeon S.B., and Kim J.S. Cigarette Smoking Preferentially Affects Intracranial Vessels in Young Males: A Propensity-Score Matching Analysis. *Neurointervention*, 14 (2019) 43-52.
- [11] Rubin D.B., Thomas N. Matching Using Estimated Propensity Scores: Relating Theory to Practice. *Biometrics*, 52 (1996) 249-264.
- [12] Caliendo M., Kopeinig S. Some Practical Guidance for the Implementation of Propensity Score Matching. *J. Econ. Surv.*, 22 (2005) 31-72.
- [13] Ho D.E., Imai K., King G., and Stuart E.A. MatchIt: Nonparametric Preprocessing for Parametric Causal Inference. *J. Stat. Soft.*, 42 (2011) 1-28.
- [14] Stuart E.A., Rubin D.B. Matching with Multiple Control Groups and Adjusting for Group Differences. *J. Ed. Behav. Stat.*, 33 (2008) 279-306.
- [15] Cochran W.G. The Effectiveness of Adjustment by Subclassification in Removing Bias in Observational Studies. *Biometrics*, 24, (1965) 295-313.
- [16] Guo X.S., Fraser M.W. Propensity score analysis: statistical methods and applications. 2nd ed. London, Thousand Oaks: Sage Publications 2015; pp. 100-150.
- [17] Olmos A., Govindasamy P. Propensity Scores: A Practical Introduction Using R. *J. MultiDiscip. Eva.*, 11 (2015) 1-88.
- [18] Normand S.L., Landrum M.B., Guadagnoli E., Ayanian J.Z., Ryan T.J., Cleary P.D., and McNeil B.J. Validating Recommendations for Coronary Angiography Following an Acute Myocardial Infarction in the Elderly: A Matched Analysis Using Propensity Scores. *J. Clin. Epide.*, 54 (2001) 387-398.
- [19] Cochran W.G., Rubin, D.B. Controlling Bias in Observational Studies: A Review. *Ind. J. Stat.*, 35 (1973) 417-446.
- [20] Turkish Statistical Institute. Available at: <http://www.tuik.gov.tr>. Retrieved Oct 23, 2019.

Investigation of structural, thermal and dielectric properties of PVC/modified magnetic nanoparticle composites

Abdulahman TUKUR¹ , Mustafa Ersin PEKDEMİR^{1*} , Mehmet ÇOŞKUN¹ 

¹ Fırat University, Chemistry Department, 23119, Elazığ/ TURKEY

Abstract

Three different composites (5, 10, and 20 wt. %) were prepared using purified PVC and POH-g-N₃PTMS-g-Fe₃O₄. Firstly, 3-azidopropyltrimethoxysilane was synthesized under reflux from 3-chlorotrimethoxysilane and sodium azide. Then, magnetic nanoparticle was bonded with the silane group of 3-azidopropyltrimethoxysilane. After that the 3-azidopropyltrimethoxysilane bearing magnetic nanoparticle undergo click reaction with propargyl alcohol, and then the composites were prepared. Some characterization, including FT-IR spectroscopy, SEM, Differential scanning calorimetry (DSC), vibrating sample magnetometer (VSM), and EDX images was performed to the composites. The DSC measurements showed that the click reaction of the 3-azidopropyltrimethoxysilane graft magnetic nanoparticles (N₃PTMS-g-Fe₃O₄) reduced the glass transition temperature (T_g). Click reaction reduced the thermal stability of N₃PTMS-g-Fe₃O₄. The thermal stabilities of the composites increased by increasing the compositional rate. It was found that the 10% PVC /POH-g-N₃PTMS-g-Fe₃O₄ reached saturation magnetization (M_s) at 5.12 emu/g. The dielectric constant (ϵ') and dielectric loss (ϵ'') of POH-g-N₃PTMS-g-Fe₃O₄ rapidly decreased with increasing applied frequency and then remain more or less constant. Also, the AC conductivity (σ_{ac}) increased sharply with increasing the applied frequency. While the ϵ' decreased slightly for the composites by increasing the applied frequency and the σ_{ac} increase dramatically with an increase in applied frequency at room temperature.

Article info

History:

Received:07.04.2020

Accepted:04.06.2020

Keywords:

PVC,
Fe₃O₄ nanoparticles,
Click reaction,
Composite,
Dielectric.

1. Introduction

The unique electrical, thermal, optical, electronic, and mechanical characteristics properties of metal nanoparticles and nanocomposites make them the subject of extensive researches. Polymers, as ideal host matrices, are good candidates for composite materials [1]. Materials having magnetic properties are of great interest to many possible applications. Amid the number of magnetic nanomaterials, Fe₃O₄ nanoparticles attracted far attention owed to their unique properties [2]. Recently, inorganic-polymer composite has been studied deeply due to their specific use and properties [3], e.g., magnetite/polymer nanocomposite is one of the attractive nanocomposites [4]. Due to its wide applications, poly(vinyl chloride) (PVC) is picked as the host polymer matrix. PVC is a polymer that has lots of characteristics suitable for industrial applications, such as good mechanical properties, good processability, fire retardancy, and good resistance to acidic and basic environments.

Additionally, PVC has a desirable properties, including low cost of production, biocompatibility, and chemical stability [5]. PVC thermal and mechanical properties can be improved by additives addition such as clay, wood fibers and flour, and calcium carbonate [5]. The electrical properties of PVC can be enhanced through incorporating zinc oxide nanorods [6], conjugated polymers (such as polyaniline and polypyrrole) [7], SiO₂ nanoparticle [8], and carbon black [9] embeded in the PVC matrix. The simultaneous presence of Fe₃O₄ nanoparticles, and graphene serve as a nanofiller in the PVC matrix which increases the young's modulus, tensile strength, and conductivity compared to that of pure PVC [10]. These improvements are linked to the synergistic effect of the host polymer and nanometer dimensional dispersion of inorganic nanoparticles. Furthermore, thermal stability studies and dielectric properties of various important polymers and their composites have been studied. Magnetic nanoparticles bonded to PVC with the help of click reaction showed an increase in thermal stability and dielectric constant compared to pure PVC. The saturation magnetization

*Corresponding author. Email address: ersinpkdmr58@gmail.com

<http://dergipark.gov.tr/csj> ©2020 Faculty of Science, Sivas Cumhuriyet University

value revealed that the product is a superparamagnetic [11]. Magnetic nanocomposite prepared by Fe_3O_4 nanoparticles and polystyrene can be used for microelectromechanical systems, since it shows good electrical conductivity [3]. The influence of magnetic nanoparticles was studied for chitin/cashew biopolymer composites, and the results revealed that an increase in thermal stability and the dielectric properties was improved due to the interaction with Fe_3O_4 nanoparticles [12]. Likewise, Fe_3O_4 nanoparticles/polymer composite was studied for polyvinyl butyral/magnetite ($\text{PVB}/\text{Fe}_3\text{O}_4$) and polymethylmethacrylate/magnetite ($\text{PMMA}/\text{Fe}_3\text{O}_4$) composites [13], pectin-magnetite nanocomposite [14], superparamagnetic iron oxide nanoparticles, graphene oxide, chitosan, and poly(vinyl alcohol) biocompatible polymers [15].

In this study, the 3-chloropropyltrimethoxysilane was reacted with sodium azide in the presence of tetraethylammonium bromide to form 3-azidopropyltrimethoxysilane. This is bounded to Fe_3O_4 nanoparticles. The modified magnetic nanoparticle formed undergoes click reaction with propargyl alcohol to form Fe_3O_4 nanoparticles bearing 1,2,3-triazole ring and then, three composites of PVC were prepared by embedding the modified Fe_3O_4 nanoparticles with various concentrations. FT-IR spectroscopy and SEM/EDX were used for structural characterization. DSC and TGA techniques were used for glass transition temperature and thermal stability of the composites. The magnetic property of 10% composite was investigated using vibrating sample magnetometry (VSM). And lastly, dielectric and AC conductivity properties of the modified Fe_3O_4 nanoparticles and composites were studied.

2. Materials and Methods

2.1. Apparatus

T Perkin-Elmer Spectrum one FT-IR spectrometer was used to record Infrared spectra. Morphology studies were performed with the Zeis EVO MA10 scanning electron microscope (SEM). Calorimetric measurements were accomplished using PerkinElmer instruments Sapphire DSC at a heating rate of 20 °C/min under N_2 flow. Thermal stability were recorded using PerkinElmer instruments Pyris Diamond TGA under N_2 flow at a heating rate of 10 °C/min. Dielectric measurements were carried out using QuadTech 7600 precision LCR meter. Magnetic properties was investigated using Quantum Design PPMS-9T.

2.2. Synthesis of 3-azidopropyltrimethoxysilane (N_3PTMS)

NaN_3 (2.14 g, 33.2 mmol), 3-chloropropyltrimethoxysilane (CITMS) (3.30 g, 16.6 mmol), and tetraethylammonium bromide (TEABr) (0.84 g, 4 mmol) were passed into a single neck round bottom flask stocked with reflux condenser containing 50 mL acetonitrile, under argon atmosphere. The reaction continued under reflux for 18 h. The solvent was evaporated after completion, the crude like mixture acquired was diluted in dry hexane and filtered. The solvent was evaporated and the colorless liquid formed is 3-azidopropyltrimethoxysilane [16].

2.3. Bonding of magnetic nanoparticle (Fe_3O_4) to 3-azidopropyltrimethoxysilane (N_3PTMS)

Fe_3O_4 nanoparticles (2.00 g) was homogenized for 30 min in 75 mL absolute ethanol. N_3PTMS (2.00 g) was added and Argon was injected for about 15 min, and the process continued at ambient temperature for 6 h, then under reflux for 48 h. Fe_3O_4 -g- N_3PTMS was separated magnetically, then washed with alcohol, and dried at room temperature followed by vacuum for 24 h at 50 °C.

2.4. Click reaction of N_3PTMS -g- Fe_3O_4 and propargyl alcohol (POH)

In a flask, N_3PTMS -g- Fe_3O_4 (1.00 g) was homogenized for 30 min in 15 mL dimethylformamide (DMF). Then propargyl alcohol (POH) (1.33 g) was added to the solution. After that Cu(I)Br 0.07 g (0.48 mmol) and 5,5'-dimethyl-2,2'-dipyridyl 0.22 g (0.48 mmol) were dissolved in 5 mL DMF in a beaker and poured to the previous solution. Argon was passed for 15 min and continued at 30 °C for 24 h. The product was washed under a magnet with dichloromethane and dried at room temperature for 24 h followed by vacuum at 50 °C for 24 h.

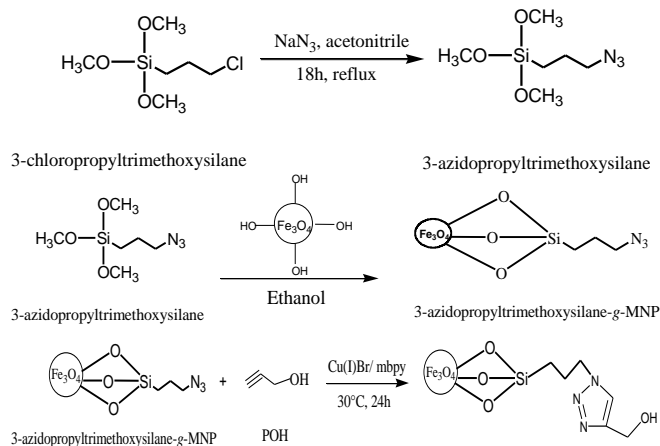
2.5. Preparation of composite of PVC with POH-g- N_3PTMS -g- Fe_3O_4

Firstly, 10 mL tetrahydrofuran (THF) was used to dissolve PVC (0.50 g). 5% (0.025 g) POH-g- N_3PTMS -g- Fe_3O_4 was added to the mixture and sonicated for 45 min. The solution was precipitated in ethanol, filtered, dried at room temperature, and then vacuum for 24 h at 45 °C. The procedure abovementioned was used to prepare 10% (0.05 g) and 20% (0.10 g) composites.

3. Results and Discussion

3.1. FTIR and SEM characterization

3-azidopropyltrimethoxysilane was formed by a nucleophilic substitution reaction of 3-chloropropyltrimethoxy -silane and sodium azide (Scheme 1).



Scheme 1. Reaction pathways in the synthesis of POH-g-N₃PTMS-g-Fe₃O₄

The FT-IR spectrum of 3-azidopropyltrimethoxysilane (Figure 1a) shows an absorption band at 2101 cm⁻¹ which is distinctive and characteristic stretching vibration for -N≡N group. The signal confirms the formation of 3-azidopropyltrimethoxysilane. Other absorption bands are 2843-2944 cm⁻¹ (C-H stretching from aliphatic -CH₂) and 1087 cm⁻¹ (Si-O). The FT-IR spectrum (Figure 1b) of N₃PTMS-g-Fe₃O₄ formed by grafting of Fe₃O₄ to 3-azidopropyltrimethoxysilane shows the characteristic band at 586 cm⁻¹ (Fe-O which indicates the bonding of Fe₃O₄) and 3435 cm⁻¹ (O-H stretch from Fe₃O₄ particle surface). 2923 and 2099 cm⁻¹ bands are for aliphatic C-H and -N≡N stretching vibrations respectively. The product carrying Fe₃O₄ undergoes click reaction with propargyl alcohol (Scheme 1). The FT-IR spectrum (Figure 1c) shows the bands formed from the product of click reaction. 1598 and 1467 cm⁻¹ represent absorption bands respectively for C=C and C-N stretching vibrations from the 1,2,3-triazole ring.

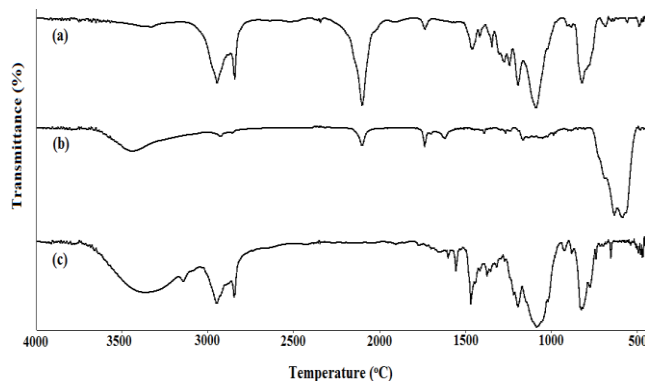


Figure 1. FT-IR spectra of (a) N₃PTMS (b) N₃PTMS-g-Fe₃O₄ and (c) POH-g-N₃PTMS-g-Fe₃O₄

Figure 2a and Figure 3a depict (SEM) images of N₃PTMS-g-Fe₃O₄ and POH-N₃PTMS-g-Fe₃O₄ respectively. The surface morphology of the modified magnetic nanoparticle and composites was examined at 10,000 magnification. It can be deduced that the Fe₃O₄ magnetic nanoparticle (Figure 2a) dominate in the sample and shows good uniformity. After click reaction with propargyl alcohol, the cubic structure of Fe₃O₄ magnetic nanoparticle (Figure 3a) becomes more prominent due to the formation of the 1,2,3-triazole ring. The compositional ratio and the type of constituents was determined using the EDX analysis for the samples shown in Figure 2b and 3b. Fe, C, O, N, Si, and Cl are present in both the samples with different percentages. SEM images of 5 and 20% POH-N₃PTMS-g-Fe₃O₄/PVC composite are respectively depicted in Figures 4a and Figure 5a. The composite showed that most of the POH-N₃PTMS-g-Fe₃O₄ are dispersed well within the PVC matrix with good uniformity and minor irregularities that are more visible on a 20% composite image at the lower part of the sample which is probably due to higher concentration of POH-N₃PTMS-g-Fe₃O₄ in the composite. EDX image in Figures 4b and Figure 5b reveal the presence of Fe, C, Cl, O, N, and Si in both composite samples.

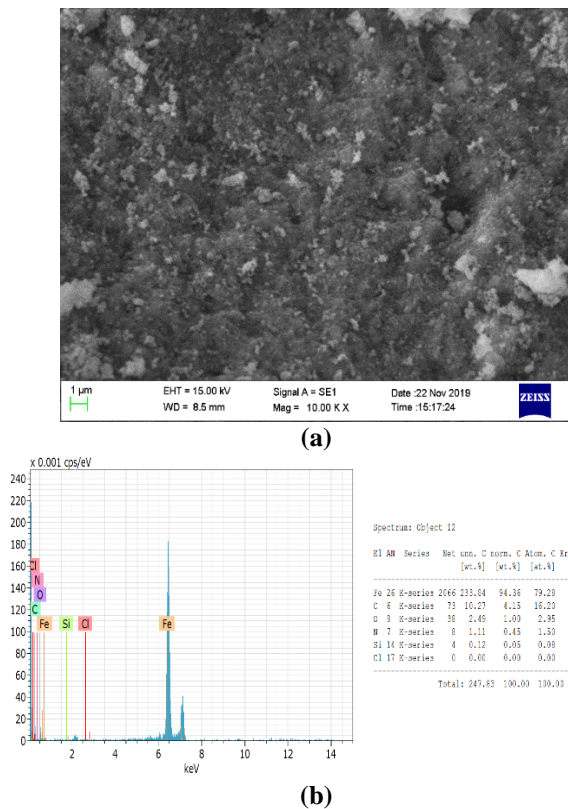


Figure 2. (a) SEM and (b) EDX images of N₃PTMS-g-Fe₃O₄

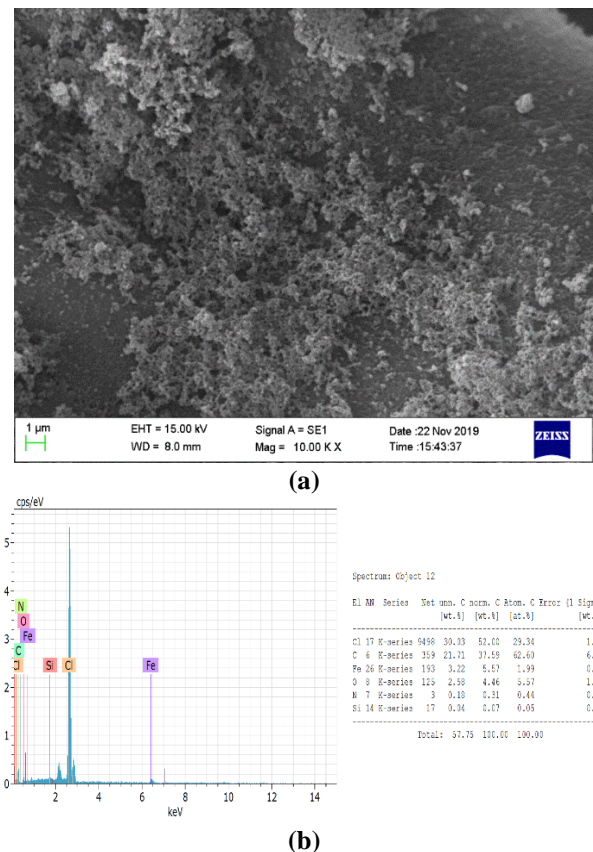


Figure 4. (a) SEM and (b) EDX images of PVC / 5% POH-N₃PTMS-g-Fe₃O₄ composite

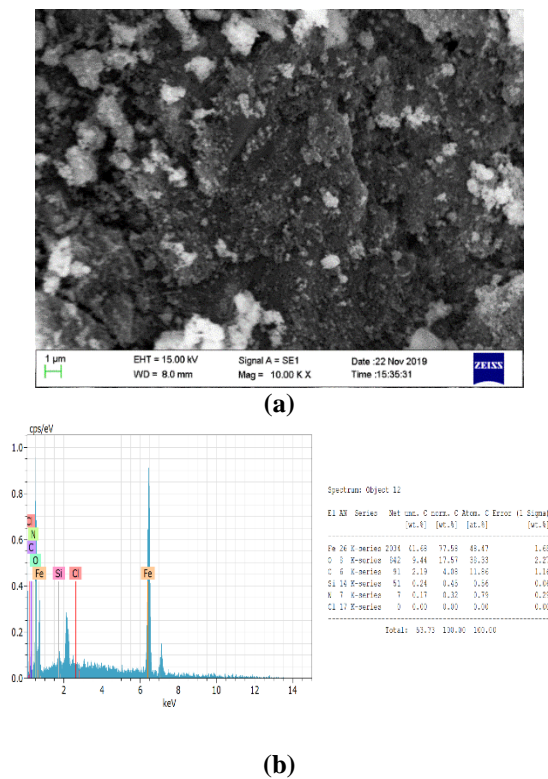


Figure 3. (a) SEM and (b) EDX images of POH-g-N₃PTMS-g-Fe₃O₄

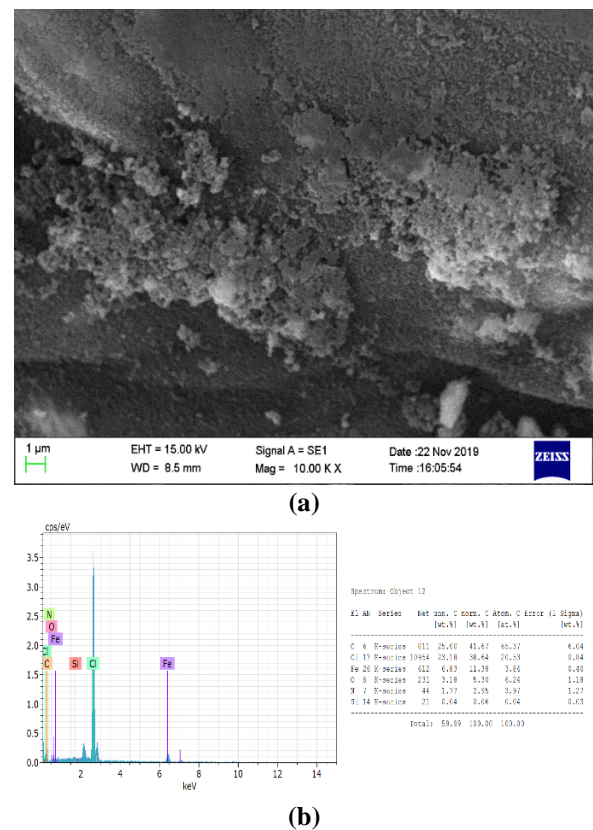


Figure 5. (a) SEM and (b) EDX images of PVC / 20% POH-N₃PTMS-g-Fe₃O₄ composite

3.2. Magnetic investigation

The magnetic property of PVC/10% POH-N₃TMS-g-Fe₃O₄ composite was studied using a vibrating sample magnetometer (VSM) at 300K. From Figure 6, it can be seen that the magnetization curve has s-shaped over the applied magnetic field and the sample, 10% PVC-g-POH-N₃TMS-g-Fe₃O₄ composite showed saturation magnetization (M_s) around 5.12 emu/g which is far lower than M_s values of pure Fe₃O₄ nanoparticle reported in literature. The Fe₃O₄ nanoparticle bonded to PVC with the help of click reaction showed M_s of 41.5 emu/g [11]. The M_s value from the VSM plot is essential evidence of the presence of Fe₃O₄ magnetic nanoparticles within the composite.

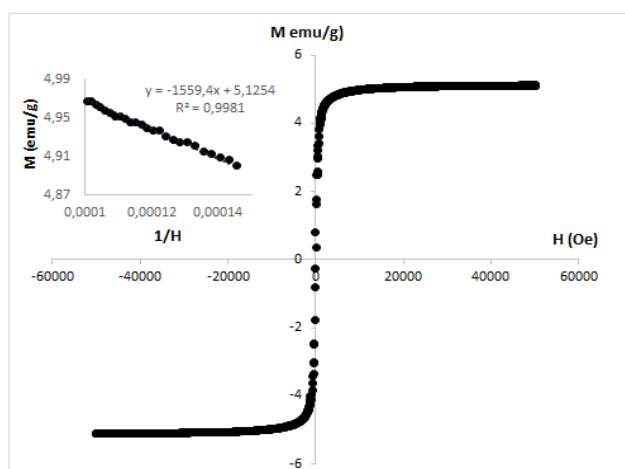


Figure 6. VSM plot of 10% PVC / POH-g-N₃PTMS-g-Fe₃O₄ composite

3.3. Thermal investigation

DSC curves of N₃PTMS-g-Fe₃O₄ and POH-N₃PTMS-g-Fe₃O₄ are depicted in Figure 7. The glass transition temperatures (T_g) determined based on the intermediate of the glass transition region and listed in Table 1. The T_g of 61 °C was recorded before click reaction with propargyl alcohol and the T_g of 57 °C was recorded after click reaction. The T_g was decreased by increasing the chain flexibility of the POH-N₃PTMS-g-Fe₃O₄ as a result of click reaction. TGA curves of N₃PTMS-g-Fe₃O₄ and POH-N₃PTMS-g-Fe₃O₄ are depicted in Figure 8. The initial decomposition temperatures (T_i) of N₃PTMS-g-Fe₃O₄ and POH-N₃PTMS-g-Fe₃O₄ are respectively 226 and 217 °C. The decrease in thermal stability of POH-N₃PTMS-g-Fe₃O₄ related to N₃PTMS-g-Fe₃O₄ is attributed to the formation of the 1,2,3-triazole ring. It can be observed that at 400 °C, the % mass loss of N₃PTMS-g-Fe₃O₄ is 4.6% which is lower than 7.0% for POH-N₃PTMS-g-Fe₃O₄. The friction of mass loss inconsistent also with the formation of the triazole ring through click

reaction. For different temperature readings, the percentage can also be determined. For instance, the residues percent at 800 °C are recorded as 92.4 and 88.5, respectively. The reason for the higher mass loss (%) at 400 °C and a lower % residue at 800 °C for POH-N₃PTMS-g-Fe₃O₄ is probably the click reaction. This is because click reaction increases the linearity of the POH-N₃PTMS-g-Fe₃O₄ which increases the free volume (decrease in T_g). The increase in free volume makes the POH-N₃PTMS-g-Fe₃O₄ susceptible to rapid % mass loss at 400 °C.

Figure 9 depicts the DSC curves of 5, 10, and 20% PVC-g-POH-N₃PTMS-g-Fe₃O₄ composites. When the amount of PVC increased from 5% to 10%, the T_g value increased from 60 to 72 °C. This is because when the PVC percentage is used more than 5%, the distance between the chains does not change much, i.e., when the ratio is exceeded 10%, the distance between the chains decreases, and hence, decreases the free volume in the polymer. The T_g value for 20% composite is 73 °C which was very close to that of 10% composite even though the 20% composite has POH-N₃PTMS-g-Fe₃O₄ contents as twice as the composite contains 10% PVC. In other words, the POH-N₃PTMS-g-Fe₃O₄ added has not considerably affected their T_g temperatures. A worth mentioning outcome from Table 2 is the increase in the T_g temperature of the composites as the POH-N₃PTMS-g-Fe₃O₄ percentage increases in each composite. This result implies that the presence of POH-N₃PTMS-g-Fe₃O₄ within the PVC matrix decreases the free volume of the composite which leads to an increase in the glass transition temperature (T_g) of the composite. TGA curves of 5, 10, and 20% PVC/POH-N₃PTMS-g-Fe₃O₄ composites are shown in Figure 10. The initial decomposition temperatures (T_i) of 5, 10, and 20 % composites are respectively 203, 210, and 217 °C. It can be seen that there is an increase in the thermal stability of the composites due to the increase in POH-N₃PTMS-g-Fe₃O₄ contents within the PVC matrix which is in line with the T_g observed from the DSC curves. Also, the TGA curve at 300 °C shows that the % mass loss is 57 for the 5% composite. The % mass loss increases to 79 for the 10% composite, while this value for 20% composite reaches 44. This implies that the rate of thermal decomposition of the composites is independent of the percentages of POH-N₃PTMS-g-Fe₃O₄ used in the composite preparation. For composites containing 5%, 10%, and 20% PVC, the residue at 450 °C were observed to be 3.2, 7.7, and 11.4, respectively. The observed residue is obviously as a result of the high amount of POH-N₃PTMS-g-Fe₃O₄ in the 20 % composite compared to 5% and 10% composites.

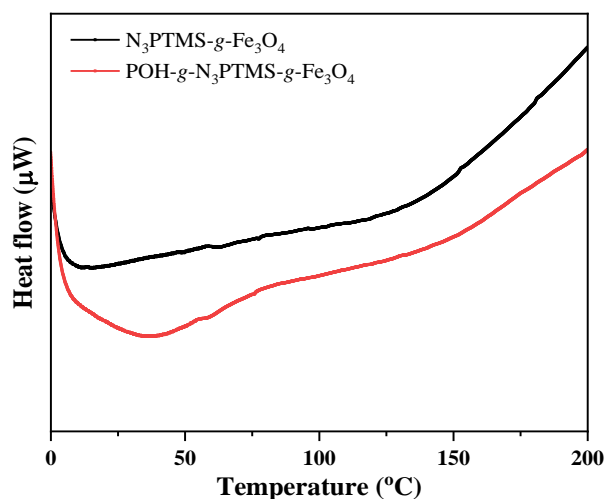


Figure 7. DSC curves of $N_3PTMS-g-Fe_3O_4$ and $POH-g-N_3PTMS-g-Fe_3O_4$

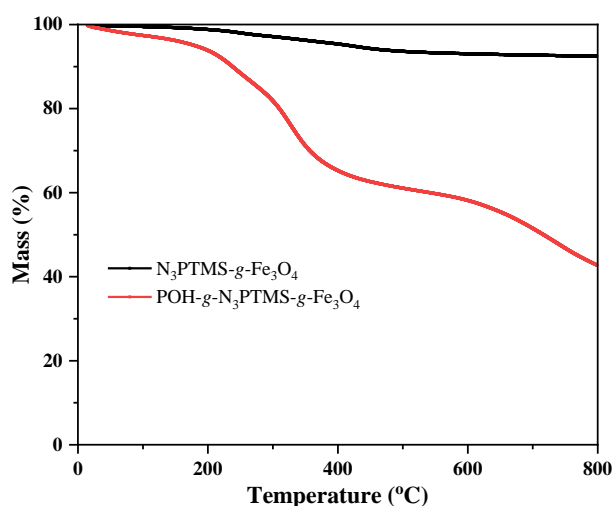


Figure 8. TGA curves of $N_3PTMS-g-Fe_3O_4$ and $POH-g-N_3PTMS-g-Fe_3O_4$

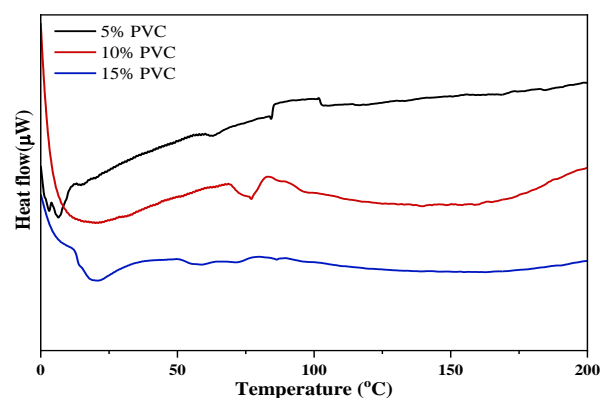


Figure 9. DSC curves of composites containing 5% PVC, 10% PVC, and 20% PVC

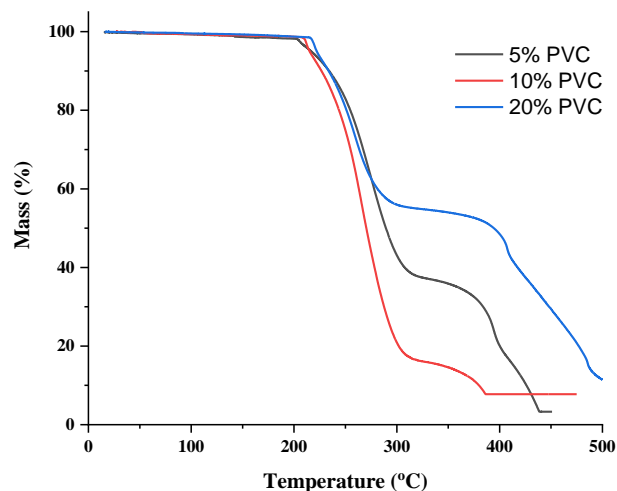


Figure 10. TGA curves of 5%, 10% and 20% PVC- $g-POH-N_3PTMS-g-Fe_3O_4$ composites

Table 1. Thermal investigation of modified Fe_3O_4

Modified Fe_3O_4	T_g (°C)	T_i (°C)	% Mass Loss at 400 °C	% Residue at 800 °C
$N_3PTMS-g-Fe_3O_4$	61	226	4.6	92.4
$POH-g-N_3PTMS-g-Fe_3O_4$	57	217	35.0	43

Table 2. Thermal investigation of PVC- $g-POH-g-N_3PTMS-g-Fe_3O_4$ composites

Composites	T_g (°C)	T_i (°C)	% Mass Loss at 300 °C	% Residue at 450 °C
5% composite	60	203	57	3.2
10% composite	72	210	79	7.7
20% composite	73	217	44	28

3.4. Electrical investigation

The concept of permeability, which is the ratio of dielectric permeability to vacuum permeability, refers to the ability of a material to be polarized. In order for the dielectric constant to be great, the polarization developed by the material in an applied field must be great. Some times, polar polymers need to align the dipoles. At very high frequencies, the dipoles do not have enough time to align before the field direction changes, but at low frequencies they have sufficient time. In the intermediate frequencies, although the dipoles move, they have completed their movements before the field direction changes [11]. Impedance analyzer is a well-known technique used for

characterizing the dielectric properties of the POH-N₃PTMS-g-Fe₃O₄ and its 5, 10, and 20% composites. The dielectric constant (ϵ'), dielectric loss (ϵ'') and AC conductivity (σ_{ac}) are used to characterize the electrical response of a polymer, copolymer, and composite material. They were measured within the same frequency range at room temperature except for the ϵ'' of the composites. Even though mobilization of the dipoles rests on the softness of a material, the dipoles in a polymeric material display a trend to orient in the direction of an applied field [17]. For POH-N₃PTMS-g-Fe₃O₄, ϵ' , ϵ'' , and σ_{ac} are depicted in Figure 11. The variation of dielectric constant (ϵ') with frequency at room temperature is almost the same as that of dielectric loss (ϵ''). At higher frequency, a rapid decrease was observed to a frequency of around 900 Hz, very slowly to a frequency of 5000 Hz, and then continue more or less constant. For the AC conductivity (σ_{ac}) at a higher frequency, it increased rapidly to a frequency of 900 Hz, the increment becomes very slow up to an approximate frequency of 5000 Hz and then continuous more or less linearly with an increase in applied frequency. The inset graphs in Figure 12a depicts the variation of ϵ' of composites with frequency at room temperature. From the graph, it was observed that the ϵ' of the composites increases with increasing POH-N₃PTMS-g-Fe₃O₄. The ϵ' values of 5, 10, and 20% composites are 2.2, 3.0, and 3.9 respectively compared to that of pure POH-N₃PTMS-g-Fe₃O₄ which is 6.0. The main cause in this increase in composites ϵ' seems to be the sequential addition of POH-N₃PTMS-g-Fe₃O₄ into the composite. In this context, effective interaction depends on enhancing the compatibility between POH-N₃PTMS-g-Fe₃O₄ and the PVC matrix through dispersion process which reduces the cohesive forces in the PVC chain leading to an increase in segmental mobility in the composite and hence, more dipoles are developed. The variation of dielectric loss of the composites (Figure 12b) shows an anomalous behavior as the applied frequency is increased at room temperature. Figure 12c demonstrates the variation of σ_{ac} in composites as a function of frequency. The σ_{ac} increases with increasing the applied frequency. Its also observed that the conductivity of the composite increases with an increase in the amount of POH-g-N₃PTMS-g-Fe₃O₄ within the composite.

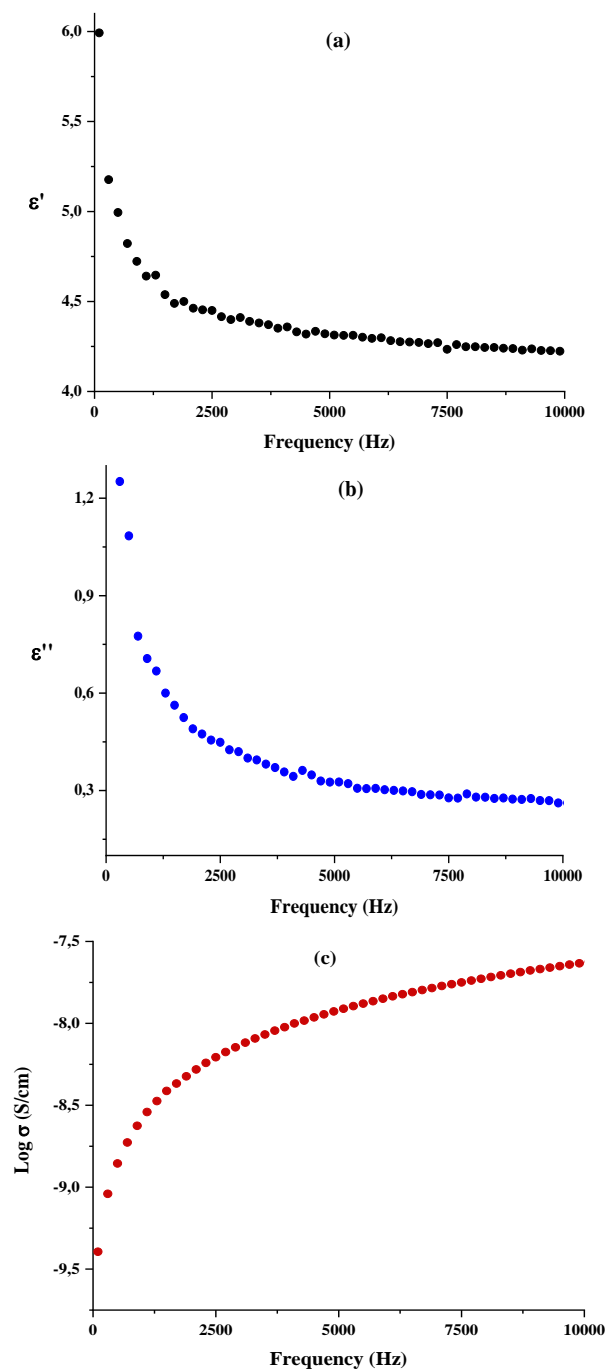


Figure 11. Variation of (a) dielectric constant (b) dielectric loss and (c) AC conductivity of POH-N₃PTMS-g-Fe₃O₄ with frequency at room temperature.

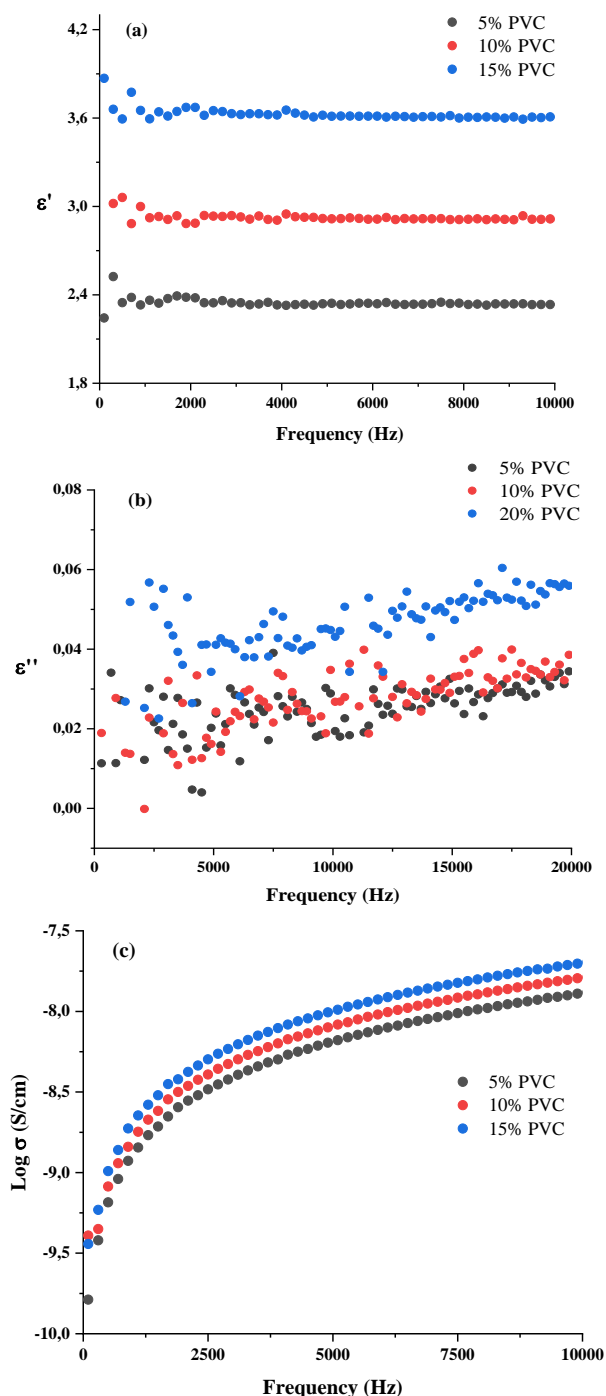


Figure 12. Variation of (a) dielectric constant (b) dielectric loss and (c) AC conductivity of PVC/POH-N₃PTMS-g-Fe₃O₄ composites with frequency at room temperature.

4. Conclusions

The effect on the structure, thermal, and dielectric properties of POH-N₃PTMS-g-Fe₃O₄ obtained by click reaction on 5, 10, and 20% PVC composites were investigated. FT-IR spectroscopy and SEM-EDX techniques were used in the characterization process. The saturation magnetization value (M_s) of the composite was calculated as 5.12 emu/g from the magnetization curve. Thermal analysis of N₃PTMS-g-

Fe₃O₄, POH-N₃PTMS-g-Fe₃O₄, and the PVC/POH-N₃PTMS-g-Fe₃O₄ composites were carried out to investigate the influence of the amount POH-N₃PTMS-g-Fe₃O₄ on the thermal behavior of the composites. It was observed that the glass transition temperature (T_g) value of N₃PTMS-g-Fe₃O₄ is higher than that of POH-N₃PTMS-g-Fe₃O₄ due to the formation of the 1,2,3-triazole ring. Likewise, the T_g of the composites increases as the amount of POH-N₃PTMS-g-Fe₃O₄ is increased. The result implies that the presence of POH-N₃PTMS-g-Fe₃O₄ within the PVC matrix decreases the free volume, and thus, the T_g of the composites increases. Initial decomposition temperature (T_i) was found to be 226 °C and 217 °C for N₃PTMS-g-Fe₃O₄ and POH-N₃PTMS-g-Fe₃O₄ respectively. For the composites, it was observed that the thermal stability of the composites increases with increasing the friction of POH-N₃PTMS-g-Fe₃O₄. Initial decomposition temperature (T_i) were 203 °C for 5%, 210 °C for 10%, and 217 °C for 20% PVC-g-POH-N₃PTMS-g-Fe₃O₄ composites. An increase in the thermal stability of the composites was due to the increase in the amount of POH-N₃PTMS-g-Fe₃O₄ within the PVC matrix, and hence, it conform the T_g results observed from the DSC curves. Also, the residue of N₃PTMS-g-Fe₃O₄ was 92.4% in Table 1, while the residue of POH-N₃PTMS-g-Fe₃O₄ due to the decomposition of both N₃PTMS and POH organic groups in the structure was found to be 43%. The dielectric constant (ϵ') and dielectric loss factor (ϵ'') for POH-N₃PTMS-g-Fe₃O₄ decreased with an increase in applied frequency and for the AC conductivity (σ), it increased rapidly with an increase in applied frequency. For the composites prepared, it was observed that the dielectric constant, dielectric loss factor, and AC conductivity increased as the POH-N₃PTMS-g-Fe₃O₄ percentage increased within the PVC matrix. The ϵ' values of 5, 10, and 20% composites were 2.2, 3.0, and 3.9 respectively.

Acknowledgment

The authors would like to thank the Firat University Scientific Research Projects Coordination Unit (FÜBAP) for the financial support of this research, Elazığ, Turkey, project number FF.18.18.

Conflicts of interest

The authors state that did not have conflict of interests

References

- [1] Wilson J., Poddar P., Frey N., Srikanth H., Mohamed K., Harmon J., Kotha S. and Wachsmuth J. Synthesis and magnetic properties of polymer nanocomposites with embedded iron

- nanoparticles. *Journal of Applied Physics*, 95 (2004) 1439-1443.
- [2] Frounchi M., Hadi M. Effect of synthesis method on magnetic and thermal properties of polyvinylidene fluoride/Fe₃O₄ nanocomposites. *Journal of Reinforced Plastics and Composites*, 32 (2013) 1044-1051.
- [3] Omid M. H., Alibeygi M., Piri F. and Masoudifarid M. Polystyrene/magnetite nanocomposite synthesis and characterization: investigation of magnetic and electrical properties for using as microelectromechanical systems (MEMS). *Materials Science-Poland*, 35 (2017) 105-110.
- [4] Chávez-Guajardo A. E., Medina-Llamas J. C., Maqueira L., Andrade C. A., Alves K. G. and de Melo C. P. Efficient removal of Cr (VI) and Cu (II) ions from aqueous media by use of polypyrrole/maghemite and polyaniline/maghemite magnetic nanocomposites. *Chemical Engineering Journal*, 281 (2015) 826-836.
- [5] Haruna H., Pekdemir M. E., Tukur A. and Coşkun M. Characterization, thermal and electrical properties of aminated PVC/oxidized MWCNT composites doped with nanographite. *Journal of Thermal Analysis and Calorimetry*, (2020) 1-9.
- [6] Qiu F., He G., Hao M. and Zhang G. Enhancing the Mechanical and Electrical Properties of Poly (Vinyl Chloride)-Based Conductive Nanocomposites by Zinc Oxide Nanorods. *Materials*, 11 (2018) 2139.
- [7] Tao Y., Feng W., Ding G. and Cheng G. Polyaniline nanorods/PVC composites with antistatic properties. *Russian Journal of Physical Chemistry A*, 89 (2015) 1445-1448.
- [8] Habashy M. M., Abd-Elhady A. M., Elsad R. and Izzularab M. A. Performance of PVC/SiO₂ nanocomposites under thermal ageing. *Applied Nanoscience*, (2019) 1-9.
- [9] Yazdani H., Hatami K., Khosravi E., Harper K. and Grady B. P. Strain-sensitive conductivity of carbon black-filled PVC composites subjected to cyclic loading. *Carbon*, 79 (2014) 393-405.
- [10] Yao K., Gong J., Tian N., Lin Y., Wen X., Jiang Z., Na H. and Tang T. Flammability properties and electromagnetic interference shielding of PVC/graphene composites containing Fe₃O₄ nanoparticles. *Rsc Advances*, 5 (2015) 31910-31919.
- [11] Tukur A., Pekdemir M. E., Haruna H. and Coşkun M. Magnetic nanoparticle bonding to PVC with the help of click reaction: characterization, thermal and electrical investigation. *Journal of Polymer Research*, 27 (2020) 161.
- [12] Ramesan M., Privya P., Jayakrishnan P., Kalaprasad G., Bahuleyan B. and Al-Maghrabi M. Influence of magnetite nanoparticles on electrical, magnetic and thermal properties of chitin/cashew gum biopolymer nanocomposites. *Polymer Composites*, 39 (2018) E540-E549.
- [13] Kirchberg S., Rudolph M., Ziegmann G. and Peuker U. Nanocomposites based on technical polymers and sterically functionalized soft magnetic magnetite nanoparticles: synthesis, processing, and characterization. *Journal of Nanomaterials*, 2012 (2012).
- [14] Namanga J., Foba J., Ndinteh D. T., Yufanyi D. M. and Krause R. W. M. Synthesis and magnetic properties of a superparamagnetic nanocomposite "pectin-magnetite nanocomposite". *Journal of Nanomaterials*, 2013 (2013).
- [15] Aliabadi M., Shagholani H. Synthesis of a novel biocompatible nanocomposite of graphene oxide and magnetic nanoparticles for drug delivery. *International journal of biological macromolecules*, 98 (2017) 287-291.
- [16] Singh R., Puri J. K., Sharma R. P., Malik A. K. and Ferretti V. Synthesis, characterization and structural aspects of 3-azidopropylsilatrane. *Journal of Molecular Structure*, 982 (2010) 107-112.
- [17] González-Guisasola C., Ribes-Greus A. Dielectric relaxations and conductivity of cross-linked PVA/SSA/GO composite membranes for fuel cells. *Polymer Testing*, 67 (2018) 55-67..

Synthesis of polyhedral oligomeric silsesquioxane-*n*-acetylcysteine conjugate with click chemistry and its antioxidant response and biocompatibility

İdil KARACA AÇARI^{1*} , Sevgi BALCIOĞLU² , Burhan ATEŞ³ , Süleyman KÖYTEPE³ , İsmet YILMAZ³ , Turgay SEÇKİN³ 

¹ Vahap Kucuk Vocational School, Malatya Turgut Ozal University, 44210, Malatya, TURKEY

² Karakocan Vocational School, Fırat University, 23600, Elazığ, TURKEY

³ Department of Chemistry, Faculty of Science, Inonu University, 44280, Malatya, TURKEY

Abstract

In this study, polyhedral oligomeric silsesquioxane-*N*-acetylcysteine (POSS-NAC) conjugate as a potential antioxidant molecule was synthesized from *N*-acetylcysteine (NAC) and amino-functional POSS structure by click chemistry. The chemical structures and thermal properties of the synthesised POSS-NAC conjugate was characterized by spectroscopic and thermal analysis techniques. The antioxidant capacity of the POSS-NAC conjugate was also determined by the 2,2'-azinobis-(3-ethylbenzothiazoline-6-sulfonic acid) (ABTS) radical scavenging activity and reducing power methods. According to the reducing power method, POSS-NAC structure has lower reducing activity than standard ascorbic acid and trolox ($p < 0.001$). It was found from the ABTS radical scavenging activity results that the synthesized POSS-NAC conjugate had a significantly higher radical scavenging effect than the standards ($p < 0.001$). Biocompatibility properties of the POSS-NAC structure were detected *in vitro* cell culture system with 3-(4,5-dimethylthiazol-2-yl)-2,5-diphenyltetrazolium bromide (MTT) test on L-929 mouse fibroblast cells. The synthesized POSS-NAC conjugate exhibits high antioxidant activity and good biocompatibility.

Article info

History:

Received: 11.02.2020

Accepted: 07.05.2020

Keywords:

Polyhedral oligomeric silsesquioxane (POSS), *N*-acetylcysteine (NAC), Antioxidant activity, Biocompatibility.

1. Introduction

Polyhedral oligomeric silsesquioxanes (POSS) carrying eight functional R groups such as alkyl, aryl or epoxide unit are essential structures for modern material design and synthesis studies [1-4]. The R groups connected to the Si atoms in the POSS lattice structure, with the empirical formula $\text{RSiO}_{1.5}$, are suitable for different modifications in advance technological applications [7-19]. It is suitable for use in many fields such as POSS, low dielectric materials, drug delivery system, biosensors, dental composites, tissue engineering, biomedical materials due to its smooth and controllable morphology, functionality with different groups, biocompatible structure, chemical and thermal stability [15-19]. Many POSS compounds have been synthesized in recent years due to these advantageous properties. In particular, the development of molecules with increased activity by binding catalysts, drugs or enzymes on eight functional

groups of the POSS structure is of great importance [20].

N-acetyl-L-cysteine (*N*-acetylcysteine or NAC) as a natural important amino acid is the *N*-acetylated derivative of L-cysteine [21]. NAC is an antioxidant containing thiol and has been used for a long time in clinical treatments [22-24]. In addition, NAC is a powerful free radical scavenger thanks to its nucleophilic reactions with ROS [25]. Therefore, the development of new antioxidant structures connected to the NAC unit is of great importance in clinical and biomedical fields.

In this study, NAC containing POSS-NAC conjugate was synthesized by click chemistry. Click chemistry is particularly important in preparative methods. There is great interest in click chemistry in terms of high yields, short reaction times, selectivities and many functional group tolerances [26-28]. Chemical structure, thermal behaviors and surface morphology of the POSS-NAC conjugate were characterized with nuclear magnetic

*Corresponding author. Email address: idal.karaca@ozal.edu.tr

<http://dergipark.gov.tr/csj> ©2020 Faculty of Science, Sivas Cumhuriyet University

resonance spectroscopy (NMR), fourier transform infrared spectroscopy (FTIR), thermal analysis, scanning electron microscopy (SEM) and energy-dispersive X-ray spectroscopy (EDX) techniques. In addition the radical scavenging activity of synthesised conjugate structure was determined by ABTS and reducing power methods. The antioxidant activity results were compared with ascorbic acid and trolox standard substances. Biocompatibility of the POSS-NAC structure was investigated on L-929 mouse fibroblast cells with *in vitro* cell culture system by MTT test.

2. Materials and Methods

2.1. Materials

Chemicals used in the synthesis of POSS-NAC structure and dimethyl sulfoxide (DMSO) suitable for cell culture study were obtained from the Sigma-Aldrich Chemical Company. Disodium hydrogen phosphate (Na_2HPO_4), sodium hydrogen phosphate dihydrate ($\text{NaH}_2\text{PO}_4 \cdot 2\text{H}_2\text{O}$) and trichloroacetic acid (TCA) used for determination of antioxidant activity were purchased from Merck Chemicals. Fetal Bovine Serum (FBS) was obtained from Biowest. 3-(4,5-dimethylthiazol-2-yl)-2,5-diphenyltetrazolium bromide (MTT) was purchased from AppliChem. Penicillin-Streptomycin was supplied from PAN Biotech. Dulbecco's Modified Eagle Medium (DMEM) was purchased from Capricorn Scientific. Mouse fibroblast cell line (L-929) *Mus musculus mouse fibroblast cell line* were sub cultured from a stock culture obtained from the Hacettepe University Faculty of Science. Other chemicals used in cell culture and antioxidant activity studies were obtained from Sigma-Aldrich Chemical Company.

2.2. Instrumentation

Infrared spectrum of the POSS, NAC and POSS-NAC conjugate were recorded in the range $4000\text{--}650\text{ cm}^{-1}$ with ATR accessory on Perkin Elmer 283 model Fourier transform-infrared spectrometer (FTIR). Verification of the POSS-NAC chemical structure was performed by NMR spectroscopy technique. ^1H -NMR spectrum POSS, NAC and POSS-NAC structures were recorded on Bruker 300 MHz NMR spectrometer and scanned from -0.5 to 13 ppm . DMSO-d_6 was used as a solvent in ^1H -NMR measurements. Surface structure and elemental mapping of obtained amino-functional POSS, POSS-NAC conjugate and NAC molecule were performed via a LEO-EVO 40 model scanning electron microscope and energy dispersive X-ray spectroscopy

(Bruker-125 eV). EDX spectrum measurements were performed in the range of $0.3\text{--}13\text{ keV}$ and ZAF correction was used in these analyzes. In the study, the thermal properties and thermal stability of the obtained POSS-NAC conjugate were determined by thermal analysis methods and compared with the pure NAC and amino-functional POSS structure. As thermal analysis, differential scanning calorimetry (DSC), differential thermal analysis (DTA), and thermogravimetry analysis (TGA) were performed. DTA thermograms were recorded with Shimadzu DTA-50 device at an heating rate of $10\text{ }^\circ\text{C/min}$ in air atmosphere. All DTA measurements were performed with 10 mg sample and Al_2O_3 reference at $20\text{--}800\text{ }^\circ\text{C}$ temperature range. In the thermogravimetric analyses, Shimadzu TGA-50 model thermal analyser was used. The TGA studies were performed at a heating rate of $10\text{ }^\circ\text{C/min}$ at temperature range from 20 to $800\text{ }^\circ\text{C}$ using 10 mg sample in air atmosphere. DSC analysis of amino-functional POSS, NAC and POSS-NAC structure was performed at $5\text{ }^\circ\text{C/min}$ heating rate and under 25 mL/min dynamic nitrogen atmosphere. DSC analyses were carried with 5 mg sample from room temperature to $300\text{ }^\circ\text{C}$. For the determination of antioxidant activity of synthesised POSS-NAC conjugates, BioScan Eon brand 96-well plate microplate reader was used. The inverted microscope systems (Olympus) are used for observing living cells. IKA brand rotary evaporator was used to remove the solvents used in the syntheses.

2.3. Synthesis of the octa(3-aminopropyl)octasilsesquioxane (POSS-NH₂)

For amino-functional POSS (POSS-NH₂) synthesis, 3-aminopropyltriethoxysilane (APS) was used. Firstly, 20 mL of APS was dissolved in 150 mL of methanol. To this solution was added 28 mL of concentrated HCl. The reaction mixture was maintained at $50\text{ }^\circ\text{C}$ for 8 hours. PtCl_4 (0.5% by weight) as catalyst was added in this solution an argon atmosphere. Reaction took place in the thermostat at $50\text{ }^\circ\text{C}$ and a crystalline precipitate formed after one day. The product was filtered and washed with cold methanol. Then obtained POSS-NH₂ precipitate was dried in a vacuum oven at $30\text{ }^\circ\text{C}$. The white product was neutralized by successively washing with 1M NaOH solution ($3 \times 200\text{ mL}$), water ($6 \times 200\text{ mL}$) and methanol ($6 \times 200\text{ mL}$) [29].

2.4. Synthesis of POSS-NAC conjugate

In this study, 1,3-dipolar cycloaddition click reaction between an alkyne and an azide groups, was used. POSS-NAC conjugate was synthesised from azide-

functional POSS structure and alkyne group containing NAC molecules by azide-alkyne Huisgen cycloaddition reaction. These type reactions are of great interest in terms of high yields, short reaction times, selectivities and tolerance of many functional groups [27-28]. These reactions widely used in the synthesis of polymers with many compositions and topologies, from linear to non-linear macromolecular structures [27-28, 30]. POSS-NAC conjugate synthesis was shown in Figure 1 and was carried out in three steps.

Step 1. The azide functional POSS (POSS-N₃) structure was prepared from sodium azide (NaN₃) and octa(3-aminopropyl)octasilsesquioxane with the 1/8 (POSS/ NaN₃) molar ratio. 1 mmol of amino-functional POSS was dissolved in 10 mL of DMSO. 8 mmol NaN₃ was added this solution. After obtaining the appropriate solubility, 0.01 g NH₄Cl was added. The reaction mixture was refluxed for 2 hours at 60 °C. The reaction was continued for 18 hours at room temperature. The active product was obtained by precipitation from the obtained yellow-orange liquid. The product was characterized by FTIR and ¹H-NMR spectroscopic techniques after being washed and removed from its impurities. Thus, the azide-functional POSS structure given in Figure 1 has been obtained.

Step 2. In order to connect NAC groups with the azide-functional POSS structure, the NAC molecule was activated with propargyl bromide. For this reaction, 8 mmol NAC and 8 mmol propargyl bromide were refluxed in 20 mL DMF for 1 h at 100 °C. The reaction was then continued at room temperature for 15 hours. Then, the solvent in reaction mixture was removed from product by rotary evaporator. The product was structurally characterized after being removed from its impurities by washing.

Step 3. In the third step; the products obtained in the first and second steps were allowed to react with each other at room temperature for 24 hours. The POSS-NAC conjugate was obtained as a product according to synthesis scheme in Figure 1. The product was washed to remove impurities and then characterized by different instrumentation techniques.

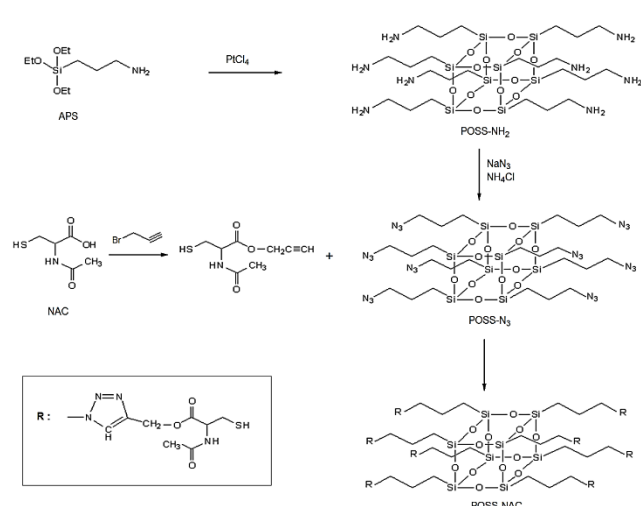


Figure 1. Synthesis scheme of POSS-NAC conjugate with click reaction.

2.5. Antioxidant activity of POSS-NAC conjugate

Radical scavenging activities of antioxidant structures were determined by the widely used ABTS and reduction power methods. The results were compared with ascorbic acid and trolox standard substances. Determination of antioxidant activity by ABTS method and reduction power method was determined respectively in accordance with the methods of Re et al. and Hwang [31-32].

ABTS Method

ABTS was produced by reacting 7.4 mM ABTS with 2.6 mM potassium persulfate in phosphate buffered saline (pH 7.4) and stored at dark for 18 h, and then ABTS was diluted with distilled water to an absorbance of 0.700 at 734 nm. For the experiment, 50 µL of standart and sample solutions were added to the ABTS and incubated for 30 min at dark. Then, absorbance were measured at 734 nm. Finally, ABTS activity was calculated using the equation below. As a standard ascorbic acid and trolox solutions were used (25, 50, 100, 200, 400, 800 and 1000 µM). Polymer samples were adjusted the optimum concentration for linear absorbance graphic and compared with the standarts as the same concentrations.

$$\% \text{ free radical scavenging activity} = [(A_{\text{control}} - A_{\text{sample}}) / A_{\text{control}}] \times 100$$

Reducing Power

In order to determine the ferric-reducing power of polymer samples, first, 0.2 M and 2.5 ml of phosphate buffer and 2.5 mL and 1% potassium ferricyanide were added to 1 mL of standard and sample solutions. Then, they were incubated in a water bath at 50 °C for 20 min followed by adding 2.5 ml 10% of TCA for stopping the reaction. The mixtures were centrifuged at 10000 rpm for 10 min and 2.5 ml of supernatant were taken

and mixed with 3 ml of %0.017 ferric chloride ($\text{FeCl}_3 \cdot 6\text{H}_2\text{O}$). Tubes were mixed for 5 min and the absorbance was measured at 700 nm.

2.6. *In vitro* evaluation of cell viability of POSS-NAC conjugate

In this study, the cytotoxicity values of the synthesized POSS-NAC conjugate, amino-functional POSS structure and pure NAC molecule were determined spectrophotometrically by MTT (thiazole blue tetrazolium bromide) test [33-34]. Mus musculus type mouse fibroblast cells (L-929) were used in the cell viability study. Firstly, the samples were sterilized under UV light for 1 hour by washing with sterile PBS (pH 7.4). Different concentrations of the sample (200, 100, 50, 25, 10 μM) were prepared diluted with DMEM medium and prepared samples were incubated with DMEM medium in an oven containing 5% CO_2 at 37 ° C for 72 hours. The L-929 cell line was proliferated in the DMEM medium for the experiment until it became 80% confluent under the same conditions, then the cells were removed from flasks with a 0.25% trypsin-EDTA solution. Cells taken by centrifugation at 2000 rpm for 5 minutes were then added to 96-well plates as 10^4 cells / well and incubated for 24 hours in an oven containing 5% CO_2 at 37 °C. At the end of the incubation, the samples were exposed to the samples and the medium was incubated for an additional 24 hours under the same conditions. Then, 90 μL of fresh medium was added to the plates by removing the medium from the cells. 10 μL of 5 mg / mL MTT solution prepared in PBS was added and incubated for 4 hours in the same conditions in the dark. Absorbances were measured in the Elisa microplate reader at 540 nm of purple color. The wells that were left in the incubator for 72 hours were added to the control wells and these wells were considered as 100% alive. % Cell viability of the samples compared to the control on L-929 cells was calculated and cell morphologies were determined by JuliFL cell analyzer and % confluent ratios were given. Living cell percentages were obtained based on the absorbance results.

2.7. Statistical analysis

Statistical analyses in antioxidant activity tests of POSS-NH₂, NAC and POSS-NAC conjugate were carried out using Graphpad Prism 5 software. Antioxidant activity test results were presented as mean values \pm standart deviation.

3. Results and Discussion

3.1. Structural characterization of NAC, POSS-NH₂ and POSS-NAC conjugate

Synthesised amino-functional POSS, POSS-NAC conjugate and pure NAC structure were characterized by FTIR and ¹H-NMR spectroscopy techniques. In addition, the thermal, structural and surface properties of these molecules were examined with TGA, DTA, DSC, SEM and EDX techniques. Figure 2 shows FTIR spectra of pure NAC, amino-functional POSS and POSS-NAC conjugate.

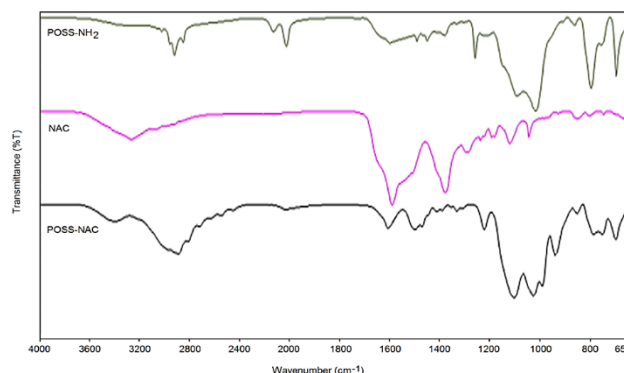


Figure 2. FTIR spectra of POSS-NH₂, NAC and POSS-NAC.

POSS-NAC conjugate as a potential antioxidant molecule was synthesized using amino-functional POSS and NAC structure as antioxidant. The synthesized POSS-NAC molecule structure was interpreted by comparing the FTIR spectra of pure NAC and POSS-NH₂ structures. In Figure 2; In the FTIR spectrum of pure NAC structure, there are symmetrical and asymmetric tensile vibrations of amide, carboxylic acid and thio alcohol groups. -SH group was seen as a wide band between 3100- 3600 cm^{-1} . In addition, amide I peaks at 1560 cm^{-1} and amide II peaks at 1460 cm^{-1} were detected. The carbonyl stress vibration of these amide groups and the carbonyl stress vibration in the carboxylic acid structure coincided to give a wide band at 1600 cm^{-1} . In the NAC structure, aliphatic C-H tensile vibrations were also observed in symmetrical C-H 2800 cm^{-1} and asymmetric C-H 926 cm^{-1} . Three fundamental stress oscillations were observed in FTIR spectra of POSS structure. These are the NH₂ group CH₂ groups and Si-O bonds. These are 3300 cm^{-1} moderate N-H, 2850-2960 cm^{-1} aliphatic C-H tensile vibrations and 1000-1100 cm^{-1} respectively. Stress vibrations of both NAC groups and POSS groups were seen in the FTIR spectrum of the POSS-NAC structure. In particular, the broad band of Si-O-Si groups was seen due to the

POSS group in the structure. Amide I peak in NAC structure was seen in 1560 cm^{-1} and amide II peak in 1425 cm^{-1} , while carbonyl groups were found in 1604 cm^{-1} . In this structure, Si-O-Si and Si-O peaks originating from POSS structure were found at 1056 cm^{-1} and 976 cm^{-1} . As a result, it was proved with FTIR spectra that the desired POSS-NAC structure was obtained. Structural characterization of POSS-NH₂, NAC, POSS-NAC conjugate was also made by ¹H-NMR (Figure 3, 4, 5). NAC, an important antioxidant, was bound to the POSS structure via amino groups. The product structure after this coupling was confirmed by NMR spectra. In ¹H-NMR spectrum, the POSS structure yielded four basic peaks, including NH₂ groups (Figure 3). There are singlet at 8.10 ppm, multiplet at 2.80 ppm, multiplet at 1.72 ppm and multiplet at 0.70 ppm peaks are attributed to -NH₂, -CH₂-N, -CH₂-CH₂-CH₂- and CH₂-Si protons, respectively [35]. Sharp peaks seen at 2.51 and 3.50 ppm are stem from the solvent [35]. In ¹H-NMR spectrum of pure NAC structure, -SH peak at 2.44 ppm, H-C-N proton signal at 4.41 ppm, methyl group C-H peak at 1.98 ppm and CH₂ group C-H multiplet proton peaks at 2.82 ppm are seen (Figure 4). In the NMR spectrum of the POSS-NAC structure, proton peaks arising from the -CH₂-CH₂-CH₂-, NAC structure and 1,2,3-triazole ring groups are seen. First of all, it is understood from the C-H proton in the ring structure of 1,2,3-triazole at 7.68 ppm that the POSS and NAC groups are connected [36]. POSS peaks in the structure of POSS-NAC obtained by a click reaction were observed in 2.51, 1.84 and 0.90. 0.90 ppm (Si-CH₂), 1.84 ppm (CH₂-CH₂-CH₂) and 2.51 ppm (CH₂-N) peaks in the NMR spectrum of the POSS-NAC structure are seen due to POSS functional groups [35]. The NMR spectrum of POSS-NAC in Figure 5 shows 4.20 ppm (H-C-N), 1.26 ppm (CH₂-S), 2.15 ppm (-CH₂-) and 1.85 ppm (-CH₃) peaks due to the NAC structure. Besides these peaks, SH peak at 1.15 ppm proves that NAC group is added to the structure [37]. As a result, acetyl group of NAC at about 1.85 ppm was observed in POSS-NAC, which indicates that NAC was successfully conjugated to the POSS structure [38].

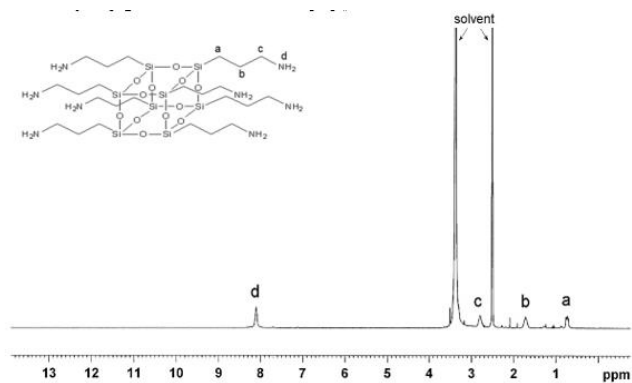


Figure 3. ¹H-NMR spectrum of POSS-NH₂.

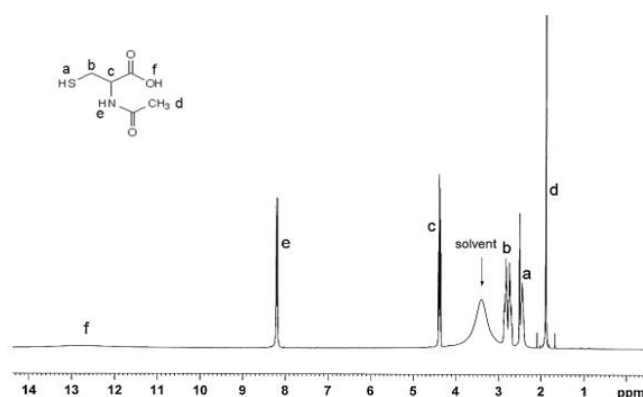


Figure 4. ¹H-NMR spectrum of NAC.

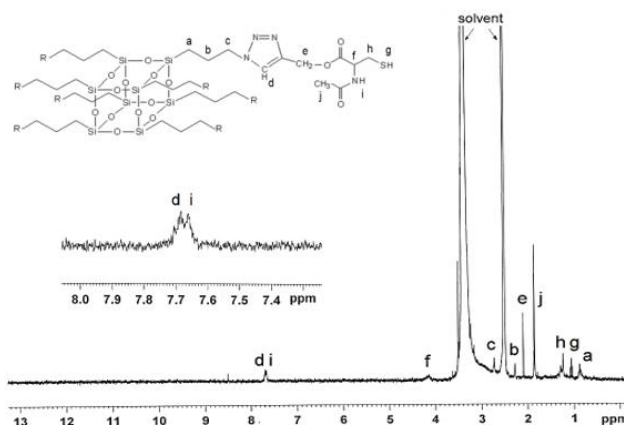


Figure 5. ¹H-NMR spectrum of POSS-NAC conjugate.

3.2. Thermal analysis of POSS-NH₂, NAC and POSS-NAC conjugate

TGA thermograms of amino-functional POSS, NAC and POSS-NAC are given in Figure 6. When these thermograms are examined, it is clearly seen in the thermogram of POSS-NH₂ that the moisture in the structure is removed in the range of 30-100 °C. Structurally, POSS-NH₂ molecule has two basic organic groups as aliphatic CH₂ groups and NH₂ structure. In the thermogram structure, the

decomposition intervals of these two groups are at 105-410 °C and 410-560 °C. Since the NAC structure is a small aliphatic molecule, its thermal stability is low. Although the NAC structure decays to a great extent between 180-225 °C, it can be said that the structure is completely degraded after 225 °C. POSS-NAC structure has gained much more thermal resistance than pure NAC structure. The structure begins to degrade at 285 °C. After this temperature, it is decomposed in two steps by firstly the bound NAC and then aliphatic CH₂ groups. The DTA thermograms of pure NAC, POSS-NH₂ and POSS-NAC are shown in Figure 7.

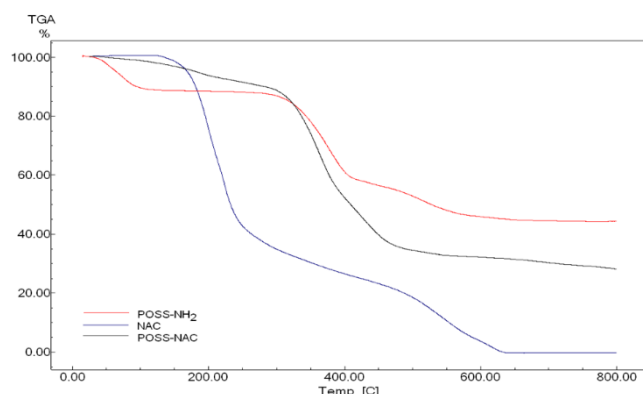


Figure 6. TGA thermograms of POSS-NH₂, NAC and POSS-NAC.

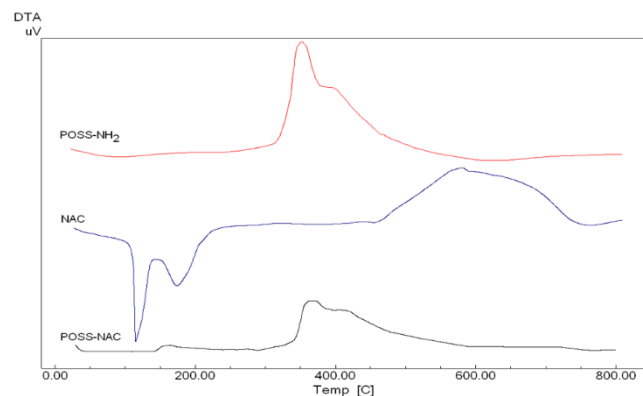


Figure 7. The DTA thermograms of POSS-NH₂, NAC and POSS-NAC.

These thermograms appear to be consistent with TGA results. While POSS-NH₂ structure has a two-stage decomposition band, NAC structure has a melting peak and then thermal decomposition peak. In the POSS-NAC structure, three basic degradation bands are observed. The first band is between 198-300 °C and is caused by a low thermal resistance triazole ring. The second band results from the degradation of NAC groups between 300-390 °C. The final mass loss is the thermal degradation of organic groups due to POSS structure and was observed in the temperature range of 390-580 °C. The DSC thermograms of pure NAC,

POSS-NH₂ and POSS-NAC are shown in Figure 8. In these thermograms there is a band in POSS-NAC structure caused by the removal of moisture in the structure around 100 °C in the range of 30-400 °C, while the degradation of organic side groups around 300 °C is observed. The thermogram of the NAC structure shows a sharp melting peak at 117 °C. In the POSS-NAC structure, the whole thermogram is different. There is no significant melting peak. In addition, the decomposition temperature of the molecule increased and went above 400 °C. These results prove that the desired POSS-NAC structure is obtained thermally stable.

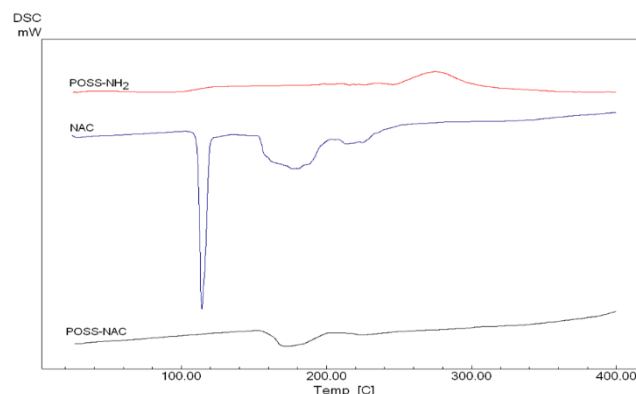


Figure 8. The DSC thermograms of POSS-NH₂, NAC and POSS-NAC.

3.3. Surface analysis of POSS-NH₂, NAC and POSS-NAC conjugate

The surface analysis results of the amino-functional POSS, NAC and POSS-NAC structure were given in Figure 9. Examining Figure 9, we can see that the SEM images of the synthesised POSS-NAC conjugate are different from the initial structures and are more crystalline and planar. POSS-NH₂ structure has morphology in the form of small sharp pieces. The NAC structure shows particulate morphology. The resulting product is different and homogeneous from these structures. The differentiation in the structure proves the formation of a new structure, but homogeneous appearance shows the purity of the product. Figure 10 shows the elemental maps and EDX spectra of pure NAC, amino-functional POSS and POSS-NAC structure. In the POSS amino structure, C, N, O and Si elements originate from the parent structure, while the peaks of the chlorine element are the opposite anions bound to the amines in the end group. In Figure 10(b), in the EDX spectrum of pure NAC structure, C peaks at 0,270 keV, N at 0,290 keV, O at 0,523 keV and S at 0,149 keV and 2,307 keV. These peaks are also evident in POSS-NAC structure. In the POSS-NAC structure, we see the peaks of C element at 0.271 keV, N at 0.290 keV, O at 0.124 keV,

S at 0.130 keV and 2.307 keV, and Si element at 0.090 keV and 1,741 keV due to the POSS structure. This result proves the desired structure. In the EDX mapping images of the conjugate, a quite different surface image was obtained compared to the starting materials. This shows us the formation of a new molecule and the proof of the purity of the structure obtained by the homogeneous distribution of the elements.

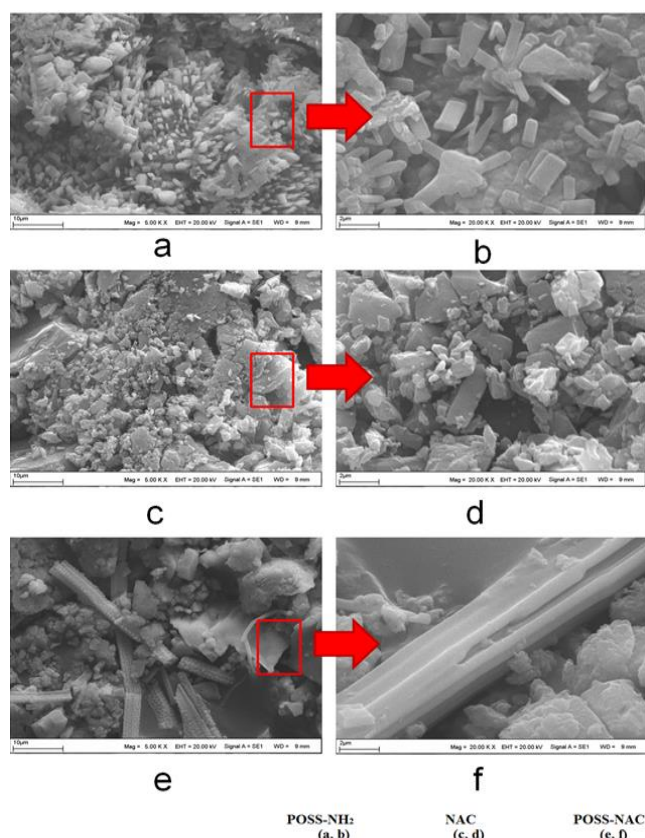


Figure 9. SEM images at different magnification rates for POSS-NH₂, NAC and POSS-NAC.

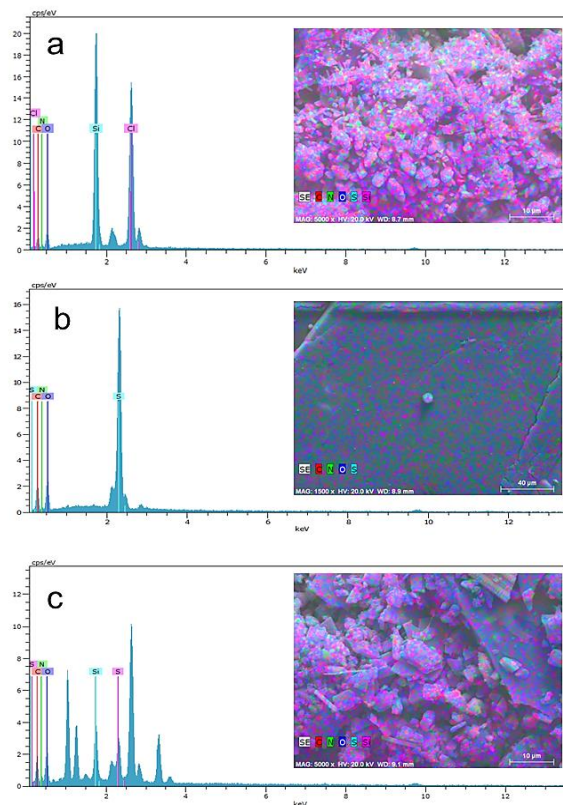


Figure 10. EDX-element mapping images for POSS-NH₂ (a), NAC (b) and POSS-NAC (c).

3.4. Antioxidant activity properties of POSS-NH₂, NAC and POSS-NAC conjugate

Antioxidant activity results were given in Table 1. In ABTS radical scavenging experiment, IC₅₀ values of conjugate and NAC were calculated by using % inhibition graphic and were compared with standart antioxidants such as ascorbic acid and trolox. NAC and POSS-NAC conjugate exhibited very similar IC₅₀ values and these vaules were lower than standard antioxidants. According to the reducing power results, POSS-NAC structures showed more reducing power than amino functional POSS. Wherease, their activities were lower than standard actioxidants. As a result, NAC-functionalized POSS has high antioxidant properties in the compared with amino functional POSS due to conjugation of POSS with NAC.

3.5. Cytotoxicity properties of POSS-NH₂, NAC and POSS-NAC conjugate

The % cell viability values and cell images of cytotoxicity test performed in L-929 fibroblast cells were shown in figures 11 and 12 respectively. We observed that the cell viability was 50% at the concentration of 200 μ M of the amino functional POSS structure, while the cell viability of POSS-NAC conjugates was approximately 100% in the whole

working range. Therefore, the POSS-NAC structure exhibited biocompatible properties. In the POSS-NAC conjugate, cell viability was 100%. Thus, the cell

viability level of the amino functional POSS structure was parallel with POSS-NAC.

Table 1. ABTS radical scavenging activity and reducing power for POSS-NH₂, NAC and POSS-NAC.

	ABTS IC50 (μM)	Reducing Power Abs/mM sample
POSS-NH ₂	>5000	0.007±0.001
POSS-NAC	295.46±3.00	0.160±0.002
NAC	306.20±9.06	0.327±0.004
Ascorbic acid	622.05±12.57	0.474±0.002
Trolox	1070.78±0.03	0.610±0.014

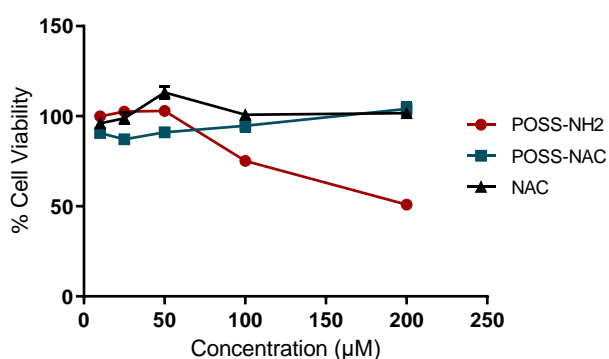


Figure 11. % Cell viability values of POSS-NH₂, POSS-NAC and NAC.

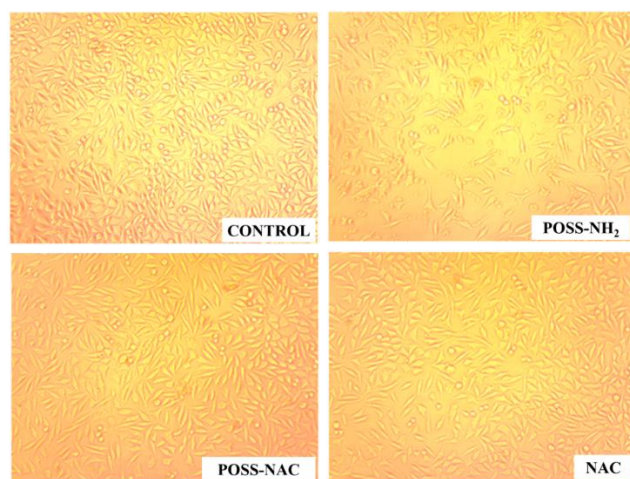


Figure 12. Microscope images of L-929 fibroblast cells incubated for 24 h with 200 μM POSS-NH₂, POSS-NAC and NAC.

4. Conclusions

In the study, POSS-NAC conjugate as a potential antioxidant molecule was synthesized using click chemistry from amino functional POSS and NAC. The

accuracy of the synthesis was checked with FTIR, ¹H-NMR, SEM / EDX and thermal analysis (DTA / TGA / DSC) techniques. Spectrum interpretations for amino functional POSS and NAC are consistent with the literature [39-41]. We understand that POSS-NAC conjugate has been successfully synthesized in the study from the suitable of the characterization results. No articles related to NAC binding to octa(3-aminopropyl)octasilsesquioxane have been found. Navath et al; Dendrimer-NAC conjugates were synthesized using NAM with PAMAM dendrimer poly (amidoamine) dendrimer [42]. Desai et al. Supported chemoprevention in head and neck cancers by encapsulating NAC into poly (DL-lactic-co-glycolic acid) PLGA in their studies [43]. Cheng and colleagues have shown that NAC, an important antioxidant containing thiol, reduces poly (methylmethacrylate) PMMA toxicity [44]. Within the scope of the study, antioxidative activity was gained by NAC binding to amino functional POSS structure. Biocompatibility is very important in assessing the toxicity or irritation potential of the synthesized materials. Biocompatibility of the POSS structure is one of the factors that makes it widely used in various biomedical (drug delivery systems, dental composites, biosensors, biomedical device and tissue engineering) applications [45]. In vitro use of cells is common in assessing biocompatibility. For example; Kim and colleagues have demonstrated the biocompatibility of modified POSS constructs in mouse fibroblast cell (L-929) cells [46]. Punshona et al; mercaptopropyl isobutyl and octahydroxypropyl studied the biocompatibility of POSS constructs in human lens epithelial cells [47]. Skaria et al. performed cell toxicology studies of octaanhydried functional POSS molecule in myoblast (C2C12) and human osteoblast cells (MG63) cells and showed no toxicity [48]. In our study, we observed the high biocompatibility of the POSS-NAC conjugate in vitro in L-929 mouse fibroblast cells. As a result, it is

thought that the synthesized POSS-NAC conjugate with biocompatibility and antioxidative properties has a very high potential for use in many areas (biomaterials, drug delivery systems, biosensors, etc.).

Acknowledgment

The study was financially supported by Inonu University's scientific research projects unit (BAP) with code 2013/157.

Conflicts of interest

The authors state that did not have conflict of interests

References

- [1] Kuo S.W. and Chang F.C. POSS related polymer nanocomposites. *Prog. Polym. Sci.*, 36(12) (2011) 1649–1696.
- [2] Cordes D.B., Lickiss P.D. and Rataboul F. Recent developments in the chemistry of cubic polyhedral oligosilsesquioxanes. *Chem. Rev.*, 110(4) (2010) 2081–2173.
- [3] Shea K.J. and Loy D.A. Bridged polysilsesquioxanes. Molecular-engineered hybrid organic–inorganic materials. *Chem. Mater.*, 13(10) (2001) 3306–3319.
- [4] Ebuloluwa A., Biswajit S. and Paschalis A. Polyhedral Oligomeric Silsesquioxane (POSS)-Containing Polymer Nanocomposites. *Nanomaterials*, 2(4) (2012) 445–475.
- [5] Shockey E.G., Bolf A.G., Jones P.F., Schurab, J.J., Chaffee K.P., Haddad T.S. and Lichtenhan J.D. Functionalized polyhedral oligomeric silsesquioxanes: New graftable POSS hydride, POSS alfa-olefin, POSS epoxy, and POSS chlorosilane macromers and POSS-siloxane triblocks. *Appl. Organomet. Chem.*, 13(34) (1999) 311–327.
- [6] Lichtenhan J.D., Otonari Y.A. and Carr M.J. Linear hybrid polymer building blocks: Methacrylate-functionalized polyhedral oligomeric silsesquioxane monomers and polymers. *Macromolecules.*, 28(24) (1995) 8435–8437.
- [7] Wu J. and Mather P.T. POSS polymers: Physical properties and biomaterials applications. *Polym. Rev.*, 49(1) (2009) 25–63.
- [8] Kanamori K. and Nakanishi K. Controlled pore formation in organotrialkoxy-silane-derived hybrids: from aerogels to hierarchically porous monoliths. *Chem. Soc. Rev.*, 40(2) (2011) 754–770.
- [9] Mantz R.A., Johns P.F., Chaffee K.P., Lichtenhan J.D., Gilman J.W., Ismail I.M.K. and Burmeister M.J. Thermolysis of polyhedral oligomeric silsesquioxane (POSS) macromers and POSS-siloxane copolymers. *Chem. Mater.*, 8(6) (1996) 1250–1259.
- [10] Leu C.M., Reddy G.M., Wei K.H. and Shu C.F. Synthesis and dielectric properties of polyimide-chain-end ethered polyhedral oligomeric silsesquioxane nanocomposites. *Chem. Mater.*, 15(11) (2003) 2261–2265.
- [11] Köytepe S., Demirel M.H., Gültek A., Seçkin T. Metallo-supramolecular materials based on terpyridine functionalized polyhedral silsesquioxane. *Polym Int.*, 63(4) (2014) 778–787.
- [12] Li G.Z., Wang H.N. and Pittman C.U. Polyhedral oligomeric silsesquioxane (POSS) polymers and copolymers. *J. Inorg. Organomet. Polym.*, 11 (3) (2001) 123–154.
- [13] Li G.Z., Yamamoto T., Nozaki K. and Hikosaka M. Crystallization of ladder like polyphenyl silsesquioxane (PPSQ)/isotactic polystyrene (i-PS) blends. *Polymer.*, 42(20) (2009) 8435–8441.
- [14] Liang K., Toghian H., Li G. and Pittman C.U. Synthesis, morphology, and viscoelastic properties of cyanate ester/polyhedral oligomeric silsesquioxane nanocomposites. *J. Polym. Sci.*, 43(17) (2005) 3887–3898.
- [15] McCusker C., Carrol J.B. and Rotello V.M. Cationic polyhedral oligomeric silsesquioxane (POSS) units as carriers for drug delivery processes. *Chem. Commun.*, 28(8) (2005) 996–998.
- [16] Fong H., Dickens S.H. and Flaim G.M. Evaluation of dental restorative composites containing polyhedral oligomeric silsesquioxane methacrylate. *Dent. Mats.*, 21(6) (2005) 520–529.
- [17] Zou Q.C., Yan Q.J., Song G.W., Zhang S.L. and Wu L.M. Detection of DNA using cationic polyhedral oligomeric silsesquioxane nanoparticles as the probe by resonance light scattering technique. *Biosens. Bioelectron.*, 22(7) (2007) 1461–1465.
- [18] Sarkar S., Buriesci G., Wojcik A., Aresti N., Hamilton G. and Seifalian A.M. Manufacture of small calibre quadruple lamina vascular bypass grafts using a novel automated extrusion-phase-inversion method and nanocomposite polymer. *J. Biomech.*, 42(6) (2009) 722–730.
- [19] Ghanbari H., Kidane A.G., Burriesci G., Ramesh B., Darbyshire A. and Seifalian A.M. The anti-calcification potential of a silsesquioxane nanocomposite polymer under in

- vitro conditions: Potential material for synthetic leaflet heart valve. *Acta Biomater.*, 6(11) (2010) 4249-4260.
- [20] Li G., Wang L., Ni H. and Pittman Jr C.U. Polyhedral oligomeric silsesquioxane (POSS) polymers and copolymers: A review. *J. Inorg. Organomet. Polym.*, 11(3) (2002) 123-154.
- [21] Kerkick C. and Willoughby D. The antioxidant role of glutathione and N-acetyl-cysteine supplements and exercise induced oxidative stress. *J. Int. Soc. Sports Nutr.*, 2(2) (2005) 38-44.
- [22] Ater B., Abraham L. and Ercal N. Antioxidant and free radical scavenging properties of N-acetylsysteine amide (NACA) and comparison with N-acetylcysteine (NAC). *Free Rad. Res.*, 42(4) (2008) 372-377.
- [23] Kelly G.S. Clinical applications of N-acetylcysteine. *Altern. Med. Rev.*, 3(2) (1998) 114-127.
- [24] Flanagan R.J. and Meredith T.J. Use of N-acetylcysteine in clinical toxicology. *Am. J. Med.*, 91(3C) (1991) 131-139.
- [25] Auroma O.I., Halliwell B., Hoey B.M. and Butler J. The antioxidant action of N-acetylcysteine: its reaction with hydrogen peroxide, hydroxyl radical, superoxide and hypochlorous acid. *Free Radic. Biol. Med.*, 6(6) (1989) 593-597.
- [26] Kiskan B., Gacal B., Asan M., Gunaydin E.C., Yilmaz I. and Yagci Y. Synthesis and characterization of pyrrole and thiophene functional polystyrenes via "click chemistry". *Polym. Bull.*, 67(4) (2011) 609-621.
- [27] Hein C.D., Liu X-M. and Wang D. Click chemistry, a powerful tool for pharmaceutical sciences. *Pharm. Res.*, 25(10) (2008) 2216-2230.
- [28] Caselli E., Ramognoli C., Vahabi R., Taracila M.A., Bonomo R. and Prati, F. Click Chemistry in Lead Optimization of Boronic Acids as β -Lactamase Inhibitors. *J. Med. Chem.*, 58(14) (2015) 5445-5458.
- [29] Seçkin T., Gültek A. and Köytepe S. Synthesis and Characterization of Novel Hyperbranched Polyimides Based on Silsesquioxane Nanocomposite Networks. *Turk. J. Chem.*, 29(1) (2005) 49-59.
- [30] Zhang X. and Zhang Y. Applications of Azide-Based Bioorthogonal Click Chemistry in Glycobiology. *Molecules*, 18 (6) (2010) 7145-7159.
- [31] Re R., Pellegrini N., Proteggente A., Pannala A., Yang M. and Rice-Evans C. Antioxidant activity applying an improved ABTS radical cation decolorization assay. *Free Radic. Biol. Med.*, 26(10) (1999) 1231-1237.
- [32] Hwang J.Y. Antioxidative activity of roasted and defatted peanut kernels. *Food Res. Int.*, 34(7) (2001) 639-647.
- [33] Wataha JC., Craig RG. and Hanks CT. Precision of and new methods for testing in vitro alloy cytotoxicity. *Dent. Mater.*, 8(1) (1992) 65-70.
- [34] Juciute R., Bukelskiene V., Rutkunas V., Trumpaite-Vanagiene R. and Purienne A. In vitro evaluation of cytotoxicity of permanent prosthetic materials. *Baltic Dent. Maxillofac. J.*, 13(3) (2011) 75-80.
- [35] Hirohara T., Kai T., Ohshita J. and Kaneko Y. Preparation of protic ionic liquids containing cyclic oligosiloxane frameworks. *RSC Adv.*, 7 (2017) 10575-10582.
- [36] Oussadi K., Montembault V. and Fontaine L. Synthesis of poly(oxyethylene phosphate)-g-poly(ethylene oxide) via the "grafting onto" approach by "click" chemistry. *J. Polym. Sci. A Polym. Chem.*, 49 (2011) 5124-5128.
- [37] Mahou R. and Wandrey C. Versatile Route to Synthesize Heterobifunctional Poly(ethylene glycol) of Variable Functionality for Subsequent Pegylation. *Polymers*, 4 (2012) 561-589.
- [38] Kunz S., Maturi M.M., Schrader I., Backenköhler J., Tschurl M. and Heiz U., Same ligand – Different binding: A way to control the binding of N-acetyl-cysteine (NAC) to Pt clusters. *J. Colloid Interface Sci.*, 426 (2014) 264-269.
- [39] Gültek A., Seçkin T. and Adıgüzel H.İ. Design and characterization of amino and chloro functionalized rhombohedral silsesquioxanes. *Turk. J. Chem.*, 29(4) (2005) 391- 399.
- [40] Oehninger L., Stefanopoulou M., Alborzinia H., Schur J., Ledewing S., Naikawa K., Munoz-Castro A., Köster R.W., Baumann K., Wölfl S., Sheldrick W.S. and Ott I. Evaluation of arene ruthenium(II) N-heterocycliccarbene complexes as organometallics interacting with thiol and selenol containing biomolecules. *Dalton Trans.*, 42(5) (2013) 1657-1666.
- [41] Demirel M.H., Köytepe S., Gültek A. and Seçkin T. Synthesis and stimuli- responsive properties of the phenanthroline based metallo-supra molecular polymers. *J. Polym. Res.*, 21(2) (2014) 345-355.
- [42] Navath R.S., Kurtoğlu Y.E., Wang B., Kannan S., Romero R. and Kannan R.M. Dendrimers-drug conjugates for tailored intracellular drug release based on glutathione levels. *Bioconjugate Chem.*, 19(12) (2008) 2446-2455.

- [43] Desai K.G.H., Mallery S.R and Schwendeman S.P. Formulation and characterization of injectable poly(DL-Lactide-co-glycolide) implants loaded with N-Acetylcysteine, a MMP inhibitor. *Pharm. Res.*, 25(3) (2008) 586-597.
- [44] Cheng Y., Yang H.C., Cho J.H., Lee S.H. and Lim B.S. The effect on N- Acetylcysteine addition on the polymerization behavior of PMMA bone cement. *Macromol. Res.*, 20(9) (2012) 928-938.
- [45] Ghanbari H., Cousins BG. and Seifalian AM. A nanocage for nanomedicine: polyhedral oligomeric silsesquioxane (POSS). *Macromol. Rapid Commun.*, 32(14) (2011) 1032-1046.
- [46] Kim SK., Heo SJ., Koak JY., Lee JH., Lee YM., Chung DJ., Lee JI. and Hong S.D. A biocompatibility study of a reinforced acrylic-based hybrid denture composite resin with polyhedraloligosilsesquioxane. *J. Oral. Rehabil.*, 34(5) (2007) 389-395.
- [47] Punshona G., Vara D.S. Sales K.M., Kidane A.G., Salacinski H.J. and Seifalian A.M. "Interactions between endothelial cells and a poly (carbonate-silsesquioxane-bridge-urea)urethane". *Biomaterials.*, 26(32) (2005) 6271-6279.
- [48] Skaria S. and Schricker S.R. Synthesis and characterization of inorganic-organic hybrid materials derived from polysilsesquioxanes (POSS). *J. Macromol. Sci. A: Pure Appl. Chem.*, 47(5) (2015) 381-391.

Dissolution kinetics of manganese during nickel recovery from high iron grade laterite by acid leaching combined NaOH-assisted mechanochemical technology

Seda ÇETİNTAŞ¹ , Deniz BİNGÖL^{1*} 

¹ Kocaeli University, Department of Chemistry, Kocaeli / TURKEY

Abstract

This study investigates the effect of the process involving a combination of sodium-based reagent-assisted mechanochemical conversion (NaOH-MC) and leaching, which was developed to provide highly efficient nickel recovery, on the amount of dissolved manganese during nickel recovery. For this purpose, firstly laterite was treated with NaOH as a reagent and then leaching performed in sulphuric acid medium. Response Surface Methodology (RSM) was successfully used as a statistical approach to determine the effect of parameters for both processes and to optimize processes conditions in terms of dissolved manganese. In optimum conditions determined as 0.5 M H₂SO₄, 55 mL/g liquid to solid ratio, 75 °C and 30 min; dissolution amount of manganese from NaOH-MC treated laterite was achieved as 97.54% ± 1.06 (N = 2) with standard deviation. In addition, the dissolution behavior of manganese was defined by a control mechanism, a combination of chemical reaction and diffusion based on the shrinking core kinetic model. The activation energy of manganese dissolution was found as 35.42 kJ/mol. According to the results, the mechanochemistry contributed positively to the dissolution of manganese due to the increased leachability of laterite at low temperature and in a short time with low acid consumption.

Article info

History:

Received:04.03.2020

Accepted:02.06.2020

Keywords:

Atmospheric acid leaching, Laterite, Manganese recovery, Mechanochemical conversion, Response surface methodology.

1. Introduction

Manganese is a strategically important non-ferrous element used in a wide range of industrial production fields such as steel, ferromanganese, non-ferrous alloys, batteries, fertilizers, food additives, dyestuffs, and other chemicals. Manganese is produced by the electrolysis of manganese sulfate obtained from leaching in sulfuric acid of manganese ore, which is mainly in the form of MnCO₃ and MnO₂ in nature [1]. Manganese is found as an impurity in many hydrometallurgical processes. The manganese-containing industrial waste effluents batteries, catalysts, steel scraps, and mud and slag from could be potentially important manganese sources [2]. The effluents downstream obtained after processing nickel laterite ore and zinc sphalerite ore are also potential manganese sources due to the contains a significant amount of manganese. On the other hand, it has been reported in many studies that manganese can be obtained from these low manganese-containing ores by using leaching with ferrous iron, sulfur dioxide,

cuprous copper, hydrogen peroxide, nitrous acid, organic reductants, and bio- and electro-reductions [3]. In recent years, the increasing nickel demand in the world has created the need to develop new processes for the processing of nickel laterite ores. The applications of mechanochemical processes are innovative procedures that improve the efficiency of mineral processing due to the easy applicable, being economic and eco-friendly process compared to many technologies various technologies such as mechanical activation, alkali roasting, reduction process, microwave irradiation, and ultrasonic assistance. In recently, many researchers aim to obtain high efficiency by improving the leaching process in the field of hydrometallurgy by applying mechanochemical processes [4]. Mechanochemical processes that considerably affect the physical and chemical properties such as calcination temperature, melting point, dissolution rate, etc. of treated materials lead to favorable contributions to reaction kinetics as a result of this are useful technologies for improving the reactivity of minerals [5,6].

*Corresponding author. Email address: denizbingol1@gmail.com, deniz.bingol@kocaeli.edu.tr
<http://dergipark.gov.tr/csj> ©2020 Faculty of Science, Sivas Cumhuriyet University

Determining the effects of the main processing parameters on the response is important to improve the performance of the method and thus make the method economically viable. In this study, RSM preferred for the development of processes is a multivariable optimization technique that includes main steps such as experimental matrix design, model development and validation, and optimization of parameters of processes. It is also possible to describe the complete influence of the parameters in the process combination of mathematical and statistical procedures with this approach. Moreover, RSM does not only evaluate the combined interactions between the independent variables but also providing more information in a short time, and economical [7].

In this study, the dissolution kinetics of manganese with acid leaching (AL) from high iron grade laterite ore which treated by NaOH assisted-mechanochemical process (NaOH-MC) was investigated. Response Surface Methodology (RSM), as a statistical approach was used to improve the process by determining the significance of process parameters in both AL and NaOH-MC, and also to determine the optimum processes conditions for achieving high removal efficiency. Furthermore, the kinetic data were evaluated by the shrinking core model (SCM) to identify the velocity mechanism affecting the manganese dissolution reaction (Figure 1).



Figure 1. Flow chart for AL process following NaOH-MC

2. Materials and Methods

2.1. Laterite

The laterite ore collected from Kayseri/Uzunpinar region of Turkey was used in this study. The ore samples were crushed to below 3.35 mm and ground to $-100\ \mu\text{m}$ to be used in experiments. The ore was characterized as a high-grade iron ore of limonitic type by X-ray diffraction (XRD) and multi-element analysis by Flame Atomic Absorption Spectrometer (FAAS) in our previous study. In our previous study, it was stated that laterite consists of main phases such as clinocllore $((\text{Mg,Fe})_6(\text{Si,Al})_4\text{O}_{10}(\text{OH})_8)$ and quartz (SiO_2), as well as hematite (Fe_2O_3) and goethite $((\text{Fe,Ni})\text{O.OH})$, and contains 32.1% Fe, 1.40% Ni, 0.56% Mn, 3.2% Mg, 11.0% CaO and 30.2% SiO_2 as wt% [8].

In our previous study, the changes and transformations that occurred during mechanochemical conversion in ore mineralogy and the effect of adding NaOH as a

reagent in mechanochemical conversion were demonstrated by analyses such as X-ray diffractometer (XRD, Rigaku Ultima-IV with a Cu-targeted X-ray tube by 2θ scanning), Fourier transform infrared spectroscopy (FTIR, Perkin Elmer 400/Bruker IFS 66/S), scanning electron microscopy (SEM, Quanta 400 F with 1.2 nm resolution) and simultaneously thermogravimetric analysis (TGA, Perkin Elmer/Pyris 1) and differential scanning calorimeter (DSC, Perkin Elmer/Diamond) [9]. The results of XRD analysis for NaOH-MC treated laterite samples obtained from optimum mechanochemical conversion conditions indicated that mechanochemical processes caused amorphization, dehydration and crystal lattice defects as well as the reduction in particle size. In addition, TGA-DSC analysis showed that the dehydroxylation temperature of goethite to hematite had been found lower for NaOH-MC treated samples than other MC treated samples. This situation was explained by the increasing agglomeration power due to the NaOH participation in the formation of structural water produced by OH^- and H^+ ions which are broken down from the mineral structure (hydroxides, oxyhydroxides, clays, etc.) [9].

2.2. Response surface methodology (RSM)

All parameters of both NaOH-MC and leaching processes affecting the leaching kinetics of manganese was determined by using RSM as the statistical design of experiment (DOE) technique. Central composite design (CCD) was employed to optimize the parameters of both NaOH-MC and AL processes and to develop the quadratic mathematical models for processes.

CCD design matrix, widely used for modeling two or more factors, involves of a 2^k factorial (coded to the usual ± 1 notation) augmented by $2k$ axial points $(\pm\alpha, 0, 0)$, $(0, \pm\alpha, 0)$, $(0, 0, \pm\alpha)$ and Co central points $(0, 0, 0)$. The number of experiments required for CCD is defined by the expression $N = 2^k + 2k + \text{Co}$ [9,10]. The value of α for rotatability depends on the number of points in the factorial portion of the design which is given in Eq.1.

$$\alpha = (N_F)^{1/4} \quad (1)$$

where N_F is the number of points in the cube portion of the design ($N_F = 2^k$, k is the number of factors).

Experiments were carried out according to CCD experimental design, which aims to reduce the number of experiments and organize the experiments with

various combinations of independent variables. Minitab statistical tool (Version 16) was used to design the experiment matrix for each process and all the detailed experimental data analysis, modeling and plotting graphics in the visualization of the model. Each obtained response from the design used to develop an empirical model that correlated the response to the parameters of the process using a second-degree polynomial equation given in Eq. 2:

$$y = \beta_0 + \sum_{i=1}^k \beta_i x_i + \sum_{i=1}^k \beta_{ii} x_i^2 + \sum_{1 \leq i < j \leq k} \beta_{ij} x_i x_j + \varepsilon \quad (2)$$

where; x_1, x_2, \dots, x_k are input variables that are effective on response (y); β_0 , is intercept, β_i ($i= 1, 2, \dots, k$), are coefficients of independent process variables, β_{ii} and β_{ij} ($i= 1, 2, \dots, k; j= 1, 2, \dots, k$) are interaction coefficients, ε is random error [11].

The performance of the model is evaluated based on a statistical analysis of the obtained data by analysis of variance (ANOVA). While the determination coefficient (R^2), adjusted determination coefficient (R^2 (adj)) and predicted determination coefficient (R^2 (pred)) were used to evaluate the reliability of the model, the student F test and probability value (P -value) were used to evaluate the statistical significance of both the regression model and each term for the

model. Then later, the selection of the most suitable factor levels for process optimization was carried out by Derringer's desirability approach [9].

2.3. NaOH-assisted mechanochemical conversion

NaOH-MC process was performed in the planetary ball mill (Pulverisette 6 model, Fritsch, Germany) using a 250 mL zirconium oxide grinding jar and 10 mm-diameter zirconium oxide balls. The sodium hydroxide used as a reagent was of analytical grade from MERCK (pellets EMPLURA®, MW: 40.00 g/mol). For *NaOH*-MC experiments, the design matrix consisted of total 31 experimental runs which include 16 factorial points, 8 axial points and 7 replicates at the center points (Table 1). The α value was 2.00 (rotatable). The amount of manganese taken into solution was the experimental response. *NaOH*-MC treated laterite samples obtained from each experiments were subjected to AL under constant conditions (initial acid concentration (C_0) = 0.5 M, liquid to solid ratio (L/S) = 100 mL/g, at room temperature, for leaching time (t) = 30 min).

Table 1. The experimental factors and levels in CCD matrix for *NaOH*-MC process

Factors	Symbol	Factor levels				
		$-\alpha$ (−2.00)	−1	0	+1	$+\alpha$ (+2.00)
rotational time (RT, min)	X_1	30	83	135	188	240
ball to ore ratio (B/O ratio)	X_2	5	10	15	20	25
rotational speed (RS, rpm)	X_3	200	313	425	538	650
ore to reagent ratio (O/R ratio)	X_4	5	10	15	20	25

Run	Coded levels of factors				Actual levels of factors			
	X_1	X_2	X_3	X_4	RT (min)	B/O ratio	RS (rpm)	O/R ratio
1	−1	−1	−1	−1	83	10	313	10
2	+1	−1	−1	−1	188	10	313	10
3	−1	+1	−1	−1	83	20	313	10
4	+1	+1	−1	−1	188	20	313	10
5	−1	−1	+1	−1	83	10	538	10
6	+1	−1	+1	−1	188	10	538	10
7	−1	+1	+1	−1	83	20	538	10
8	+1	+1	+1	−1	188	20	538	10
9	−1	−1	−1	+1	83	10	313	20
10	+1	−1	−1	+1	188	10	313	20
11	−1	+1	−1	+1	83	20	313	20
12	+1	+1	−1	+1	188	20	313	20
13	−1	−1	+1	+1	83	10	538	20
14	+1	−1	+1	+1	188	10	538	20
15	−1	+1	+1	+1	83	20	538	20
16	+1	+1	+1	+1	188	20	538	20
17	−2.00	0	0	0	30	15	425	15
18	+2.00	0	0	0	240	15	425	15
19	0	−2.00	0	0	135	5	425	15
20	0	+2.00	0	0	135	25	425	15
21	0	0	−2.00	0	135	15	200	15
22	0	0	+2.00	0	135	15	650	15
23	0	0	0	−2.00	135	15	425	5
24	0	0	0	+2.00	135	15	425	25
25–31	0	0	0	0	135	15	425	15

2.4. Atmospheric leaching

The manganese dissolution behavior of *NaOH*-MC treated laterite samples was investigated by atmospheric leaching in sulphuric acid medium (H_2SO_4 , 95-98% (w/w) extra pure, Merck). CCD was performed to enhance the dissolution of manganese by optimizing process conditions for leaching of *NaOH*-MC treated laterite. The statistical experimental design produced by CCD was applied to study the combined effect of parameters as initial acid concentration, liquid to solid ratio and temperature on manganese dissolution. The experiments were performed in

accordance with the full factorial CCD matrix included eight factorial points (± 1), six axial points ($\alpha = \pm 1.682$) and six central points (0) (Table 2). The experimental leaching procedure was similar to our previous study [12]. The experiments were carried out in a temperature controlled water bath by mechanically mixing ore and acid solution in a 600 mL beaker with a Teflon mixer at 200 rpm. The reflux system was connected to prevent evaporation at high temperatures. After the leaching time (30 min), the leachate was filtered using a syringe filter (0.45 μ m) and analyzed for Mn(II) using FAAS (PerkinElmer/AAnalyst 800).

Table 2. The experimental factors and levels in CCD matrix for the leaching process

Factors	Symbol	Factor levels				
		$-\alpha (-1.682)$	-1	0	+1	$+\alpha (+1.682)$
acid concentration (Co, M)	X_1	0.5	0.8	1.25	1.70	2.00
liquid to solid ratio (L/S, mL/g)	X_2	10	28	55	82	100
temperature (T, °C)	X_3	25	39	60	81	95

Run	Coded levels			Actual levels		
	X_1	X_2	X_3	Co (M)	L/S ratio (mL/g)	T (°C)
1	-1	-1	-1	0.80	28	39
2	+1	-1	-1	1.70	28	39
3	-1	+1	-1	0.80	82	39
4	+1	+1	-1	1.70	82	39
5	-1	-1	+1	0.80	28	81
6	+1	-1	+1	1.70	28	81
7	-1	+1	+1	0.80	82	81
8	+1	+1	+1	1.70	82	81
9	-1.68	0	0	0.50	55	60
10	+1.68	0	0	2.00	55	60
11	0	-1.68	0	1.25	10	60
12	0	+1.68	0	1.25	100	60
13	0	0	-1.68	1.25	55	25
14	0	0	+1.68	1.25	55	95
15-20	0	0	0	1.25	55	60

2.5. Kinetic evaluation of leaching process

The shrinking core model (SCM) has been applying for determining the rate-limiting mechanism of the laterite leaching process. This model assumes that the solid particle that maintains the bulk size gradually shrinks during the reaction that leads to the formation of a porous layer on the surface of the unreacted core [13]. SCM considers that the reaction mechanism of consists of three rate-determining steps as film diffusion control, ash layer diffusion control, and surface chemical reaction control [14]. The following equations of the shrinking core model are used to describe the dissolution kinetics:

If the reaction is controlled by a chemical reaction on the surface,

$$1 - (1 - \alpha)^{1/3} = k_s \cdot t \quad (3)$$

If the reaction is controlled by diffusion through a liquid film or through a liquid-solid layer,

$$1 - (1 - \alpha)^{2/3} = k_f \cdot t \quad (4)$$

$$1 - \frac{2}{3} \alpha - (1 - \alpha)^{2/3} = k_d \cdot t \quad (5)$$

If the reaction is controlled by a combination of both chemical and diffusion,

$$1 - 2(1 - \alpha)^{1/3} + (1 - \alpha)^{2/3} = k_m \cdot t \quad (6)$$

where α is the fraction of reacted, t is the reaction time, and k_s , k_f , k_{dif} and k_m are the rate constants.

Evaluations regarding the explanation of kinetic data by SCM models were made according to the correlation coefficients of fitting curves obtained by applying the data to model equations. The reaction rate

constants predicted by the models are determined from the slopes of curves (k_s , k_t , k_{dif} and k_m) [14].

The activation energy (E_a , kJ/mol) for the reaction is determined based on Arrhenius relation (Eq. 7) with using the rate constant. The fact that the E_a is lower than 20 kJ/mol defines diffusion-controlled processes while E_a is higher than 40 kJ/mol for chemical reaction controlled processes [13].

$$\ln k = \ln A - \frac{E_a}{RT} \quad (7)$$

where k is the rate constant (1/min), A is the frequency factor (1/min), R (8.314 J/K mol) is the ideal gas constant and T (K) is temperature. E_a is calculated from the slope of the Arrhenius plot ($\ln k$ vs $1/T$).

3. Results and Discussion

3.1. Optimization of NaOH-MC conditions

ANOVA results for *NaOH*-MC based on manganese recovery with AL were summarized in Table 3. The effects of terms such as $X_4^*X_4$ (P -value: 0.273) of square interaction and $X_1^*X_2$ (P -value: 0.183), $X_1^*X_4$ (P -value: 0.050), $X_2^*X_4$ (P -value: 0.250) and $X_3^*X_4$ (P -value: 0.246) of 2-Way interaction, were found not be statistically significant on the amount of manganese taken into solution due to higher P -values than 0.05.

Table 3. ANOVA results based on manganese recovery for *NaOH*-MC with AL

Source	DF	Adj SS	Adj MS	F-Value	P-Value	VIF
Model	14	13051.5	932.25	31.89	0.000	
Linear	4	8533.4	2133.34	72.97	0.000	
X_1 : rotational time (RT, min)	1	340.7	340.69	11.65	0.001	1.00
X_2 : ball/ore ratio (B/O ratio)	1	2207.0	2207.03	75.49	0.000	1.00
X_3 : rotational speed (RS, rpm)	1	5449.0	5448.97	186.37	0.000	1.00
X_4 : ore/reagent ratio (O/R ratio)	1	536.7	536.67	18.36	0.000	1.00
Square	4	2385.1	596.26	20.39	0.000	
$X_1^*X_1$	1	626.1	626.13	21.42	0.000	1.03
$X_2^*X_2$	1	719.2	719.25	24.60	0.000	1.03
$X_3^*X_3$	1	1502.6	1502.55	51.39	0.000	1.03
$X_4^*X_4$	1	36.0	35.98	1.23	0.273	1.03
2-Way Interaction	6	2133.1	355.52	12.16	0.000	
$X_1^*X_2$	1	53.5	53.46	1.83	0.183	1.00
$X_1^*X_3$	1	486.1	486.10	16.63	0.000	1.00
$X_1^*X_4$	1	118.1	118.12	4.04	0.050	1.00
$X_2^*X_3$	1	1395.5	1395.50	47.73	0.000	1.00
$X_2^*X_4$	1	39.6	39.61	1.35	0.250	1.00
$X_3^*X_4$	1	40.3	40.32	1.38	0.246	1.00
Error	47	1374.2	29.24			
Lack-of-Fit	10	1233.8	123.38	32.53	0.000	
Pure Error	37	140.3	3.79			
Total	61	14425.7				
Model Summary	: S = 5.41 $R^2 = 90.47\%$ R^2 (adj) = 87.64% R^2 (pred) = 81.19%					
Reduced Model Summary	: S = 1.52 $R^2 = 99.11\%$ R^2 (adj) = 98.92% R^2 (pred) = 98.60%					

The surface and contour plots presented in Figures 2 and 3, respectively, show the effects of factors on the *NaOH*-MC process based on the amount of manganese taken into solution by AL. It was seen that manganese dissolution was almost unchanged with increasing O/R ratio for changing levels of B/O ratio and RS. The dissolution rate of manganese increased with increasing B/O ratio and RS but it remained stable after certain levels of factors (B/O ratio = 16 and RS = 425 rpm). While increasing the B/O ratio causes a continuous increase in manganese dissolution, it was determined that the model predicts high B/O ratios for the best recovery. Because, the increase in B/O ratio during the mechanochemical process leads to cause

amorphization and structural disordering in laterite, as well as the decrease in particle size [15]. In addition, it indicated that the dissolution rate of manganese increased by increased rotational time up to 135 min, but it decreased by increased rotational time above 135 min.

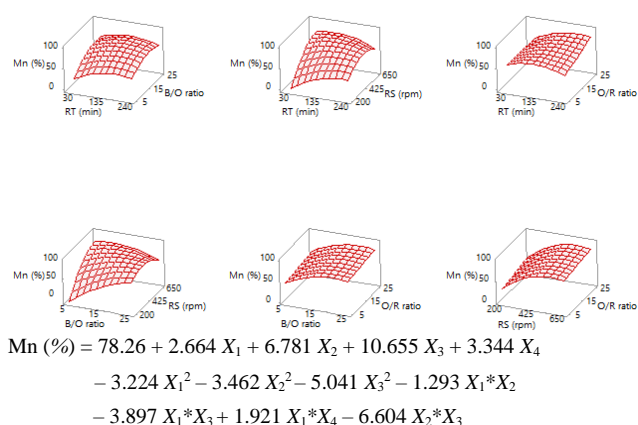


Figure 2. Response surface plots for *NaOH*-MC based on manganese recovery with AL. (Hold values: RT = 135 min, B/O ratio = 15, RS = 425 rpm and O/R ratio = 15)

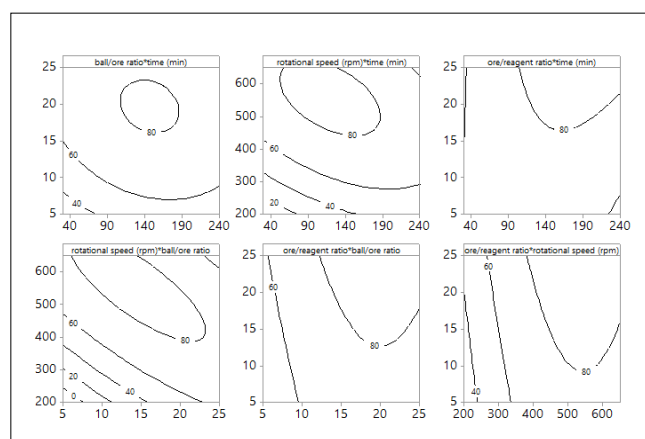


Figure 3. Contour plots for *NaOH*-MC based on manganese recovery with AL. (Hold values: RT = 135 min, B/O ratio = 15, RS = 425 rpm and O/R ratio = 15)

Table 4. ANOVA results for manganese recovery with AL following *NaOH*-MC

Source	DF	Adj SS	Adj MS	F-Value	P-Value	VIF
Model	9	2841.77	315.75	21.63	0.000	
Linear	3	1803.10	601.03	41.17	0.000	
X_1 : acid concentration (Co, M)	1	93.27	93.27	6.39	0.017	1.00
X_2 : liquid to Solid ratio (L/S, mL/g)	1	228.07	228.07	15.62	0.000	1.00
X_3 : temperature (T, °C)	1	1481.76	1481.76	101.51	0.000	1.00
Square	3	880.08	293.36	20.10	0.000	
$X_1 * X_1$	1	2.26	2.26	0.15	0.697	1.02
$X_2 * X_2$	1	830.54	830.54	56.90	0.000	1.02
$X_3 * X_3$	1	91.80	91.80	6.29	0.018	1.02
2-Way Interaction	3	158.59	52.86	3.62	0.024	
$X_1 * X_2$	1	22.29	22.29	1.53	0.226	
$X_1 * X_3$	1	15.74	15.74	1.08	0.307	
$X_2 * X_3$	1	120.56	120.56	8.26	0.007	
Error	30	437.92	14.60			
Lack-of-Fit	5	354.80	70.96	21.34	0.000	
Pure Error	25	83.12	3.32			
Total	39	3279.68				
Model Summary	: S = 3.82 R^2 = 86.65% R^2 (adj) = 82.64% R^2 (pred) = 72.96%					
Reduced Model Summary:	S = 0.27 R^2 = 99.92% R^2 (adj) = 99.90% R^2 (pred) = 99.88%					

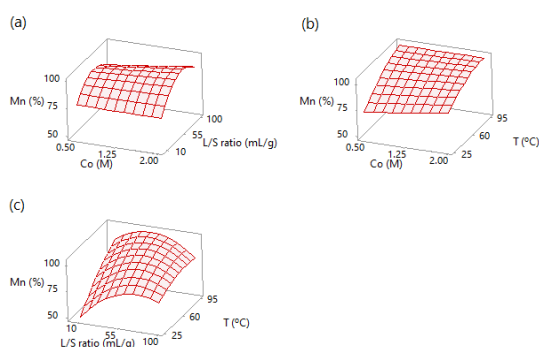
The optimum conditions determined for high-efficiency nickel recovery considering the amount of nickel dissolution were RT = 135 min, B/O ratio = 15, RS = 425 rpm and O/R ratio = 18 for *NaOH*-MC process. In these conditions, the predicted and the experimental manganese recoveries with standard deviations were found as $80.27\% \pm 1.52$ (N = 2) and $82.30\% \pm 0.93$ (N = 2), respectively.

3.2. Optimization of AL conditions

ANOVA results for AL following *NaOH*-MC were evaluated based on the amount of manganese taken into solution (see Table 4). The terms which have statistically insignificant effects on the amount of manganese taken into solution were neglected in the model due to high *P*-values. The reduced model equation was obtained by gradually neglecting the terms (*P*-value: 0.697 for $X_1 * X_1$). The model equation indicated that temperature (*F*-value: 101.51 and *P*-value: 0.000) was the most effective factor for the amount of manganese taken into solution.

The surface and contour plots for manganese recovery with AL following *NaOH*-MC were given in Figures 4 and 5, respectively. Figure 4a clearly showed that the leaching rate of manganese increases initially with increases of the L/S ratio, then the leaching rate decreases with increasing the L/S ratio. The optimum manganese recovery was achieved with an efficiency of over 95% at the L/S of 55 mL/g.

In addition, it was seen that the effect of Co was insignificant, the leaching rate of manganese remained almost stable with increasing Co. While the difference in obtained manganese dissolution for the levels of Co ranging from 0.50 to 2.00 M at constant L/S ratio (55 mL/g) was only 3% for the temperature was 70 °C and above, it was 15% for the temperature below 70 °C. Figures 4b and 4c indicated that the leaching of manganese increased with increasing temperature. While the temperature was changing from 25 to 95 °C, the amount of manganese taken into solution increased from 53.02% to 87.72% for 10 mL/g, increased from 84.95% to 88.59% for L/S ratio of 100 mL/g at constant Co (0.50 M). The optimum leaching conditions following *NaOH*-MC were determined as Co = 0.50 M, L/S ratio = 55 mL/g and T = 75 °C. Under these conditions, the predicted and the experimental manganese recoveries with standard deviations were found as $98.03\% \pm 0.27$ (N = 2) and $97.54\% \pm 1.06$ (N = 2), respectively.



$$\text{Mn (\%)} = 95.53 + 1.848 X_1 + 2.890 X_2 + 7.365 X_3 - 5.340 X_2^2 - 1.757 X_3^2 + 1.180 X_1 * X_2 - 0.992 X_1 * X_3 - 2.745 X_2 * X_3$$

Figure 4. Response surface plots for manganese recovery with AL following *NaOH*-MC (Hold values: Co = 1.25 M H₂SO₄, L/S ratio = 55 mL/g and T = 60 °C)

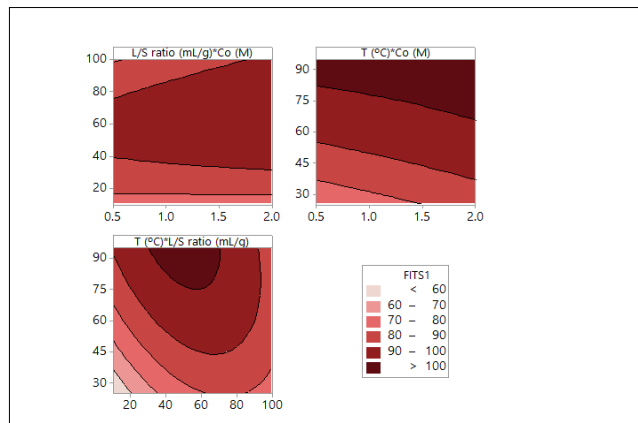


Figure 5. Contour plots for manganese recovery with AL following *NaOH*-MC (Hold values: Co = 1.25 M H₂SO₄, L/S ratio = 55 mL/g and T = 60 °C)

3.3. Kinetic analysis of leaching

The rate-limiting control mechanism of manganese dissolution reactions was investigated based on SCM assumptions. The graphs obtained by fitting the data to SCM model equations were also given in Figure 6. Significant model constants calculated using these graphs were summarized in Table 5.

The Eq. 4 related to the combination of chemical reaction and diffusion mechanisms had the best correlation with experimental data. The model with high R^2 value indicates that the manganese dissolution reaction rate was affected by both the chemical reaction on the surface and the diffusion throughout the product layer [16,17]. The reaction rate constants calculated from the model clearly showed that the dissolution rate of manganese increased with the increase in temperature. The reaction was approximately ten times faster when the temperature was raised from 25 °C to 95 °C. In addition, the activation energy of manganese dissolution from *NaOH*-MC treated laterite was calculated as 35.42 kJ/mol based on the Arrhenius equation (Figure 7). Generally, it is known that the diffusion-controlled reaction has a typical activation energy of less than 20 kJ/mol whereas it has over 40 kJ/mol for the chemical controlled reaction [18]. The calculated activation value in this range confirmed the control mechanism.

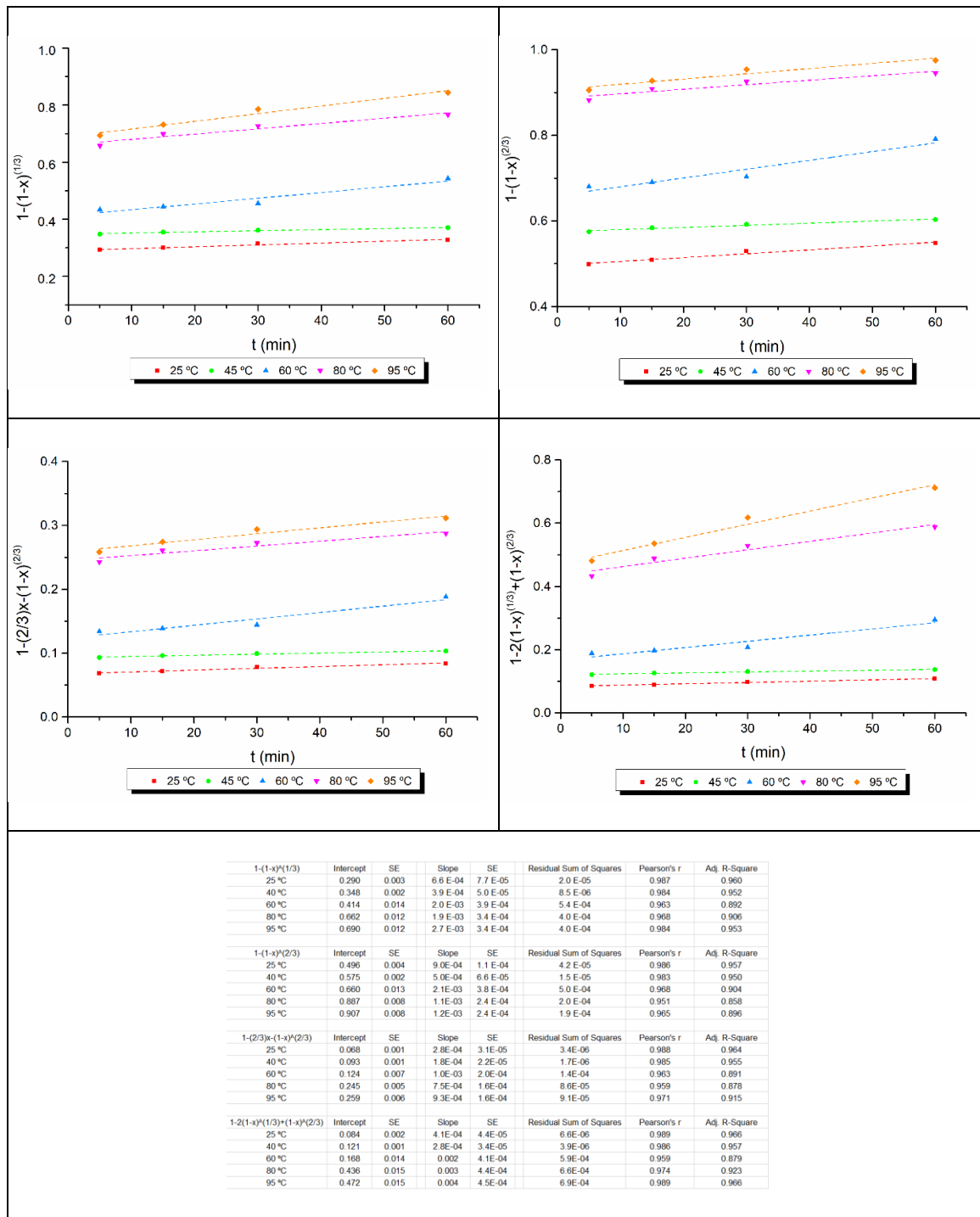
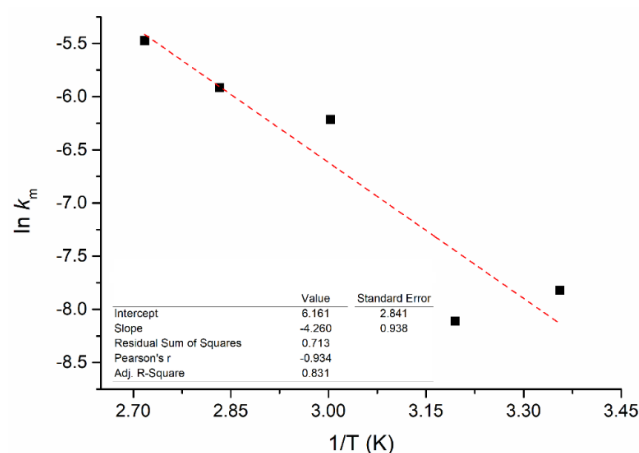


Figure 6. Fitting curves of SCM kinetic models

Table 5. Correlation coefficients (R^2) and reaction rate constants of the kinetic models in different temperatures for manganese dissolution

Mechanisms of SCM	Constants	T (°C)				
		25	40	60	80	95
Surface reaction $1-(1-\alpha)^{1/3}$	k_s (1/min)	0.0007	0.0004	0.0020	0.0019	0.0027
	R^2	0.96	0.95	0.89	0.91	0.95
Film diffusion $1-(1-\alpha)^{2/3}$	k_f (1/min)	0.0009	0.0005	0.0021	0.0011	0.0012
	R^2	0.96	0.95	0.90	0.86	0.90
Diffusion from product layer $1-2/3\alpha - (1-\alpha)^{2/3}$	k_d (1/min)	0.0003	0.0002	0.0010	0.0008	0.0009
	R^2	0.96	0.96	0.89	0.88	0.92
Combination of chemical reaction and diffusion $1-2(1-\alpha)^{1/3}+(1-\alpha)^{2/3}$	k_m (1/min)	0.0004	0.0003	0.0020	0.0030	0.0040
	R^2	0.97	0.96	0.88	0.92	0.97

**Figure 7.** Determination of activation energy for manganese dissolution (Hold values: Co = 0.5 M H₂SO₄ and L/S ratio = 55 mL/g)

4. Conclusions

In this study, the effect of the process developed to provide high-efficiency nickel recovery, which is a combination of a sodium-based reagent-assisted mechanochemical conversion and leaching, on the amount of manganese dissolved during nickel recovery was investigated. The results obtained from the studies were presented below:

- The optimum conditions of both *NaOH*-MC and AL were determined by CCD and the manganese recovery was obtained over 95% with the proposed method.
- High determination coefficients above 95% showed that RSM models can be used as a reliable method for predicting responses in both mechanochemical conversion and leaching processes conditions.
- Manganese recovery obtained from raw ore at 4 h leaching time (3.08 M H₂SO₄, 27.9 mL/g of

L/S ratio, 95 °C) was achieved from *NaOH*-MC treated laterite at only 30 min (0.50 M H₂SO₄, 55 mL/g of L/S ratio, 75 °C) following *NaOH*-MC. This is an obvious result of the positive effect of mechanochemical processes on the leachability of minerals.

- Moreover, the results indicated that the quantitative manganese recovery achieves with less acid consumption at lower temperatures and shorter times due to easier mass transfer. That is, *NaOH*-MC processes contributed to the leachability of laterite by facilitating the dissolution reaction of both laterite and manganese as a result of caused deformations, phase transformations and increase of new reactive surfaces.
- The mineralogical and structural transformations occurring through as a result of mechanochemical processes identified by the characterization of *NaOH*-MC treated laterites

supported the positive effect of *NaOH*-MC on the leachability of laterite ore and indirectly on the dissolution of manganese.

- The results of leaching kinetics evaluations indicated that the mechanism of manganese dissolution reaction rate for AL following *NaOH*-MC was controlled by a combination of chemical and diffusion reactions based on SCM.

Consequently, the results indicate that the proposed method for achieving high-efficiency nickel recovery can also improve the dissolution of manganese. The high amount of manganese above 95% achieved with less acid consumption at low temperatures and short times, due to the increased leachability of laterite.

Acknowledgment

This work was supported by the Scientific and Technological Research Council of Turkey (TÜBİTAK) [Grant Number 116M076].

Conflicts of interest

The authors state that did not have conflict of interests

References

- [1] Xin B., Li T., Li X., Dan Z., Xu F., Duan N., Zhang Y. and Zhang H. Reductive dissolution of manganese from manganese dioxide ore by autotrophic mixed culture under aerobic conditions. *J. Cleaner Prod.*, 92 (2015) 54-64.
- [2] Zhang W., Cheng C.Y. and Pranolo Y. Investigation of methods for removal and recovery of manganese in hydrometallurgical processes. *Hydrometallurgy*, 101 (2010) 58-63.
- [3] Zhang W., Cheng C.Y., Manganese metallurgy review. Part I: Leaching of ores/secondary materials and recovery of electrolytic/chemical manganese dioxide, *Hydrometallurgy*, 89 (2007) 137-159.
- [4] Zhang Y., Chen X., Chu W., Cui H. and Wang M. Removal of vanadium from petroleum coke by microwave and ultrasonic-assisted leaching. *Hydrometallurgy*, 191, (2020) 105168.
- [5] Li C., Liang B., Study on the mechanochemical oxidation of ilmenite, *J. Alloys Compd.*, 459 (2008) 354-361.
- [6] Baláz P., Mechanical activation in hydrometallurgy, *Int. J. Miner. Process.*, 72 (2003) 341-354.
- [7] Nayak A.K., Pal A., Statistical modeling and performance evaluation of biosorptive removal of Nile blue A by lignocellulosic agricultural waste under the application of high-strength dye concentrations. *J. Environ. Chem. Eng.*, 8(2) (2020) 103677.
- [8] Çetintaş S., Bingöl D., Response surface methodology approach to leaching of nickel laterite and evaluation of different analytical techniques used for the analysis of leached solutions, *Anal. Methods.*, 8 (2016) 3075-3087.
- [9] Abrouki Y., Anouzla A., Loukili H., Bennazha J., Lotfi R., Rayadh A., Bahlaoui M.A., Sebti, S., Zakarya D. and Zahouily M. Experimental design-based response surface methodology optimization for synthesis of β -mercapto carbonyl derivatives as antimycobacterial drugs catalyzed by calcium pyrophosphate. *Int. J. Med. Chem.*, (2014) doi: <http://dx.doi.org/10.1155/2014/586437>.
- [10] Montgomery D.C., Design and analysis of experiments, 7th ed. John Wiley & Sons, New York, 2008.
- [11] Lundstedt T., Seifert E., Abramo L., Thelin B., Nyström Å., Pettersen J., Bergman R. Experimental design and optimization. *Chemometr. Intell. Lab. Syst.*, 42 (1998) 3-40.
- [12] Çetintaş S., Yildiz U. and Bingöl D. A novel reagent-assisted mechanochemical method for nickel recovery from lateritic ore. *J. Cleaner Prod.*, 199 (2018) 616-632.
- [13] MacCarthy J., Nosrati A., Skinner W. and Addai-Mensah J. Atmospheric acid leaching mechanisms and kinetics and rheological studies of a low grade saprolitic nickel laterite ore. *Hydrometallurgy*, 160 (2016) 26-37.
- [14] Dehghan R., Noaparast M. and Kolahdoozan M. Leaching and kinetic modelling of low-grade calcareous sphalerite in acidic ferric chloride solution. *Hydrometallurgy*, 96(4) (2009) 275-282.
- [15] Tunç T., Yıldız K., Effects of ball-to-mass ratio during mechanical activation on the structure and thermal behavior of Turkish lateritic nickel ore, *TOJSAT.*, 3 (2013) 80-85.
- [16] Ayanda O.S., Adekola F.A., Baba A.A., Fatoki O.S. and Kimba B.J. Comparative study of the kinetics of dissolution of laterite in some acidic media. *JMMCE.*, 15 (2011) 1457-1472.
- [17] Petrovski A., Načevski G., Dimitrov A.T. and Paunović P. Kinetic models of nickel laterite ore process. *Inter. Sci. J. Mach. Technol. Mater.*, 13 (2019) 487-490.
- [18] Liu K., Chen Q., Yin Z., Hu H. and Ding Z. Kinetics of leaching of a Chinese laterite containing maghemite and magnetite in sulfuric acid solutions. *Hydrometallurgy*, 125 (2012) 125-136.

Structural characterization and DNA binding properties of a new imine compound

Özge GÜNGÖR^{1*} , Jülide NACAROĞLU BALLI¹ , Hilal KIRPIK¹ , Muhammet KÖSE^{1*} 

¹ Kahramanmaraş Sutcu Imam University, Chemistry Department, Kahramanmaraş, Turkey

Abstract

In this study, a new imine compound (M) was prepared from the reaction of *o*-vanillin and 4-isopropylaniline. The structure of the compound was characterized by the spectroscopic and analytical methods. Single crystals of the compound were grown and solid-state structure of the compound was further characterized by X-ray diffraction study. The UV-Vis absorption and emission properties of the compound were studied in different solvents. Moreover, DNA binding ability of the compound was investigated and compared with the standard DNA binding agents. The compound showed similar binding constant ($4 \times 10^5 \text{ M}^{-1}$) to those spermine and ethidiumbromide.

Article info

History:

Received:22.07.2019

Accepted:17.04.2019

Keywords:

Imine,
Absorption,
Emission,
X-ray,
DNA binding

1. Introduction

Imine compounds also called as Schiff bases contain a characteristic C=N double bond. They are prepared from the reaction of primary amines with an aldehyde or a ketone [1]. Imine compounds are the nitrogen analogue of an aldehyde or ketone in which the carbonyl group has been replaced by an imine group. They are widely used as organic compounds and their chemistry attracts great attention due to their ability to form complexes with metal ions and have a wide variety of applications in many fields such as analytical, biological and inorganic chemistry. Some of them have pharmacological properties including toxicity against bacterial/fungal growth, anticancer and antitumor activity [2-5].

DNA chains are composed of units called genes that are responsible for synthesizing specific proteins. DNA is an important biomolecule and has crucial roles in biological process such as long-term storage of information, identification of hereditary characteristics, and reproduction of genetic information [6].

The linking and interaction of newly synthesized small molecules with DNA is also important in the design of new drugs as well as in the development of DNA detection methods [7]. The interaction of DNA with drug molecules is particularly important to determine

the interaction with drug molecules with anticarcinogenic properties of a specific molecule [8].

2. Method

2.1. General

Starting materials (4-isopropylaniline and *o*-vanillin) and solvents were purchased from Sigma Aldrich and used as received. FT-IR spectra were measured on a Perkin Elmer Spectrum 100 FT-IR. The electronic spectra were taken on a Perkin Elmer Lambda 45 spectrophotometer. The fluorescence spectra were obtained on a Perkin Elmer LS55 luminescence spectrometer.

2.2. Synthesis of the compound (M)

4-isopropylaniline (1 mmol) and *o*-vanillin (1 mmol) were mixed in ethanol (40 mL). The resulting red-clear solution was refluxed for two hours. The completion of the reaction was followed by T.L.C. and the volume of the solution was reduced 20 mL on a rotary evaporator. The red-coloured crystals were obtained from slow evaporation in a few days.

M: C₁₇H₁₉NO₂: Yield: 82 %, color: red, melting point: 52 °C. Elemental Analysis (%): Found (Calcd.): C, 75.62 (75.81%); H, 6.81 (7.11%); N, 5.03(5.20). ¹H-NMR (ppm; CDCl₃): 13.25 (*b*, 1H, OH), 8.44 (*s*, 1H, CH=N), 6.87-7.55 (*m*, 7H, Ar-H), 3.83 (*s*, 3H, OCH₃),

*Corresponding author. Email address: muhammetkose@ksu.edu.tr, muhammetkose0146@gmail.com
<http://dergipark.gov.tr/csj> ©2020 Faculty of Science, Sivas Cumhuriyet University

2.72 (septet, 1H, CH₃isopropyl), 1.25 (d, 6H, CH₃isopropyl), ¹³C-NMR (d, ppm; CDCl₃): 160.11 (-C=N), 115-150 (Ar-C), 58.73 (OCH₃), 34.2 and 22.2 (C₃isopropyl). FT-IR (ATR): 2958-2866, 1616, 1593, 1461, 1443, 1410, 1359, 1273, 1249, 1200, 1178, 1075, 968, 851, 778, 735, 563 cm⁻¹.

2.3. X-ray structure solution and refinement for the compound

Single crystals for X-ray diffraction study were grown by recrystallization of a chloroform solution of the compound. A single crystal of dimensions 0.26 × 0.25 × 0.10 mm³ was mounted on the diffractometer. Data were collected at 293(2) K on a Bruker ApexII CCD diffractometer using Mo-Kα radiation (λ = 0.71073 Å). The structure was solved by direct methods and refined on *F*² using all the reflections [9, 10]. All the non-hydrogen atoms were refined using anisotropic atomic displacement parameters and hydrogen atoms bonded to carbon atoms were inserted at calculated positions using a riding model.

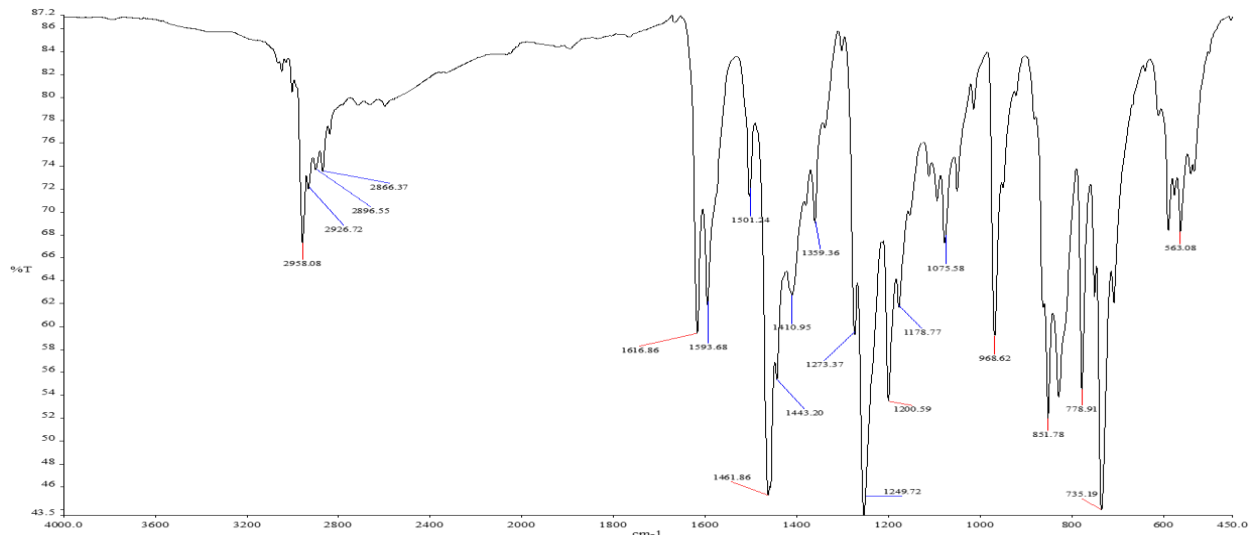


Figure 2. FT-IR spectrum of compound.

Single crystals of the compound were obtained from slow evaporation of ethanol solution of the compound. Thus, structure of the compound was determined by X-ray diffraction study. X-ray crystallographic data for the compound is listed in Table 1. Bond lengths and angles are given in Table 2 and Table 3. X-ray structure of the compound is shown in Figure 3.

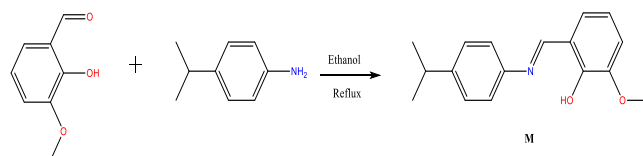


Figure 1. Synthesis of the compound (M).

3. Results and Discussion

In the course of this work, a new imine compound was prepared and its DNA binding ability was determined by spectroscopic method. The compound (Figure 1) was prepared by Schiff base condensation reaction of one equivalent *o*-vanillin and one equivalent 4-isopropylaniline in ethanol. The compound was characterized by the spectroscopic and analytical methods. FT-IR spectrum of the compound is shown in Figure 2. The characteristic ν(C=N) bond stretching was observed as a sharp peak at 1616 cm⁻¹ confirming the formation of the compound. The stretching's in the range of 2866-2926 cm⁻¹ are due to the ν(C-H) stretching's.

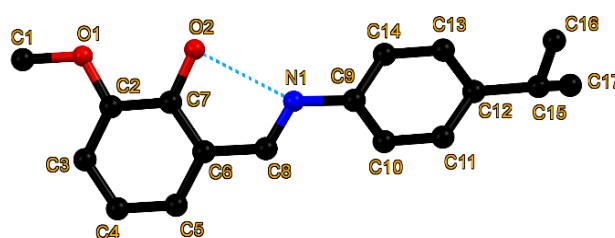


Figure 3 X-ray structure of the compound.

X-ray crystallographic data revealed that the asymmetric unit contain a molecule with no crystallographically imposed symmetry. In the structure of the compound, the N1-C8 bond distance is 1.277(5) Å and within the range of C=N bond distance.

This confirms that the compound favours the enol-imine tautomeric form in the solid state. In the structure of the compound, as expected, a phenol-imine intramolecular hydrogen bond (O2···N1) was observed. The phenyl and phenol rings are located in trans conformation with respect to the imine bond. The intermolecular contacts which stabilise crystal structure of the compound were investigated by using Hirshfeld surface analysis. The 2D fingerprints plot of the compound showing the different intermolecular contacts are shown in Figure 4. The fingerprint plot showed high intensities for di and de values between 1.2 and 1.8 Å. The main contribution comes from H···H contacts followed by C···H/H···C and O···H/H···O contacts. The O···H/H···O contacts were observed as red-spots in the dn surface of the compound (Figure 5).

Table 1. Crystallographic data for the compound.

Identification code	M
Empirical formula	C ₁₇ H ₁₉ NO ₂
Crystal size/mm ³	0.12×0.11×0.09
Formule weight	269.33
Crystal system	Monoclinic
Space group	P2 ₁ /n
Unit cell	a/Å
b/Å	7.5355(7)
c/Å	14.6976(13)
α/°	90
β/°	90.426(5)
γ/°	90
Volume/Å ³	1502.0(2)
Z	4
Abs. Coeff. (mm ⁻¹)	0.078
Refl. collected	25987
R1, WR2 [I>=2σ(I)]	0.0990, 0.1756
R1, WR2 [all data]	0.1579, 0.2011
Largest diff. peak/hole/eÅ ⁻³	0.20/-0.26
CCDC number	1905445

Table 2 Bond lengths for compound

Bond	Length/Å	Bond	Length/Å
O(1)-C(1)	1.422(5)	C(6)-C(8)	1.445(5)
O(1)-C(2)	1.365(4)	C(9)-C(10)	1.385(5)
O(2)-C(7)	1.349(4)	C(9)-C(14)	1.376(5)
N(1)-C(8)	1.277(5)	C(10)-C(11)	1.370(5)
N(1)-C(9)	1.413(5)	C(11)-C(12)	1.382(5)
C(2)-C(3)	1.374(5)	C(12)-C(13)	1.391(5)
C(2)-C(7)	1.391(5)	C(12)-C(15)	1.513(6)
C(3)-C(4)	1.380(6)	C(13)-C(14)	1.374(5)
C(4)-C(5)	1.363(6)	C(15)-C(16)	1.463(7)
C(5)-C(6)	1.401(5)	C(15)-C(17)	1.487(6)
C(6)-C(7)	1.398(5)		

Table 3 Bond angles for compound.

Bond	Angle/°	Bond	Angle/°
C(2)-O(1)-C(1)	116.8(3)	N(1)-C(8)-C(6)	123.2(3)
C(8)-N(1)-C(9)	121.1(3)	C(10)-C(9)-N(1)	124.1(4)
O(1)-C(2)-C(3)	124.6(4)	C(14)-C(9)-N(1)	117.8(3)
O(1)-C(2)-C(7)	115.6(3)	C(14)-C(9)-C(10)	118.1(4)
C(3)-C(2)-C(7)	119.8(4)	C(11)-C(10)-C(9)	120.6(4)
C(2)-C(3)-C(4)	120.5(4)	C(10)-C(11)-C(12)	122.0(4)
C(5)-C(4)-C(3)	120.4(4)	C(11)-C(12)-C(13)	117.0(4)
C(4)-C(5)-C(6)	120.6(4)	C(11)-C(12)-C(15)	121.6(4)
C(5)-C(6)-C(8)	120.0(4)	C(13)-C(12)-C(15)	121.4(4)
C(7)-C(6)-C(8)	118.7(4)	C(14)-C(13)-C(12)	121.2(4)
C(7)-C(6)-C(8)	121.3(3)	C(13)-C(14)-C(9)	121.1(3)
O(2)-C(7)-C(2)	118.4(3)	C(16)-C(15)-C(12)	113.1(4)
O(2)-C(7)-C(6)	121.6(3)	C(16)-C(15)-C(17)	114.7(5)
C(2)-C(7)-C(6)	120.0(4)	C(17)-C(15)-C(12)	111.7(4)

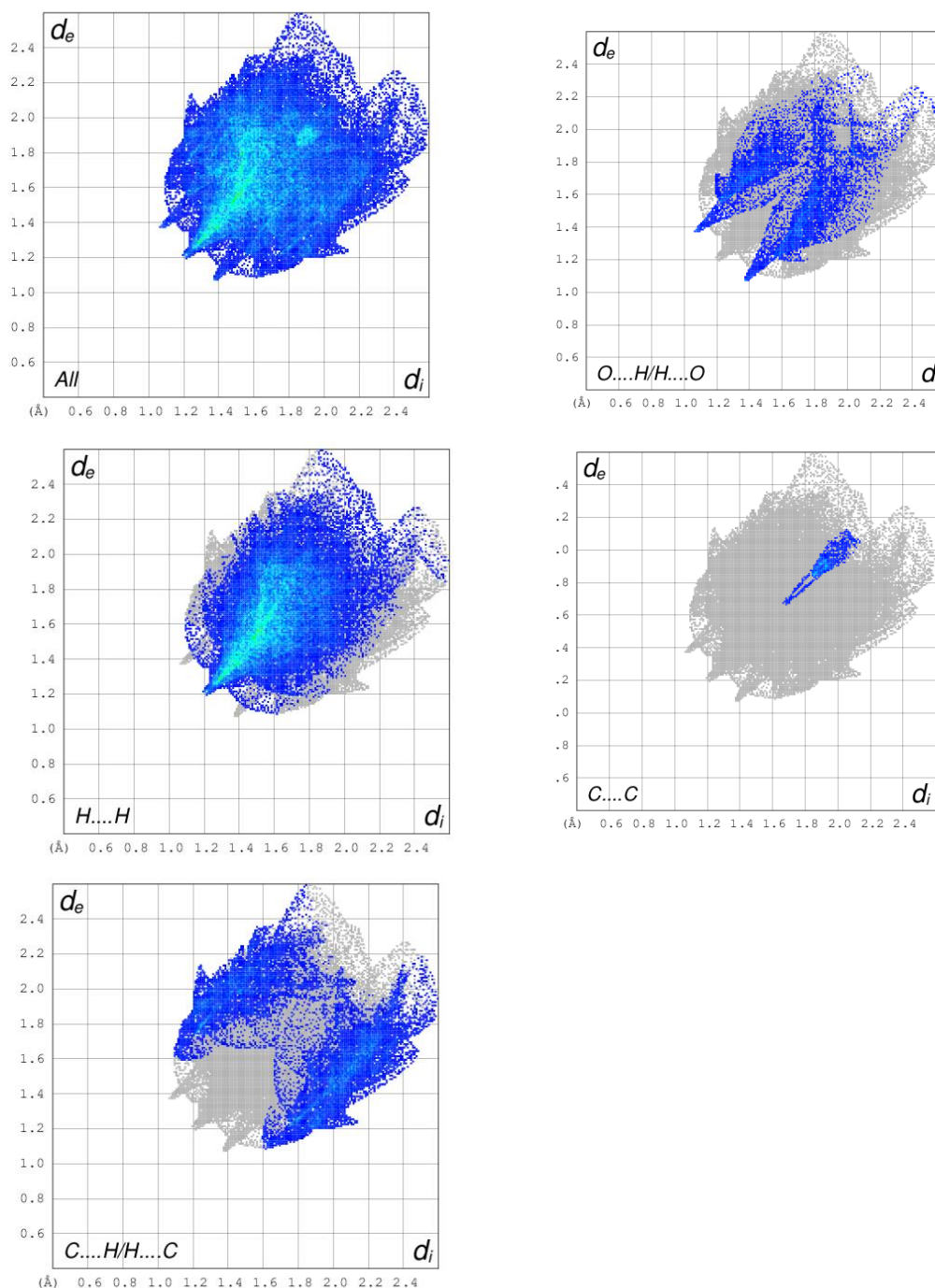


Figure 4. The 2D fingerprints plot of the compound showing the different intermolecular contacts.

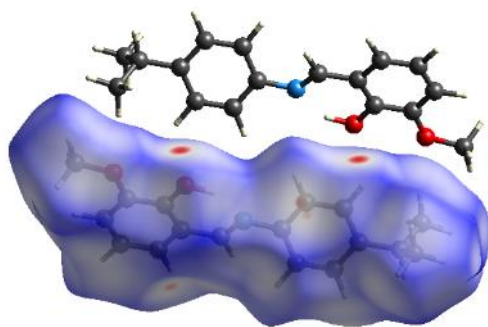


Figure 5 The d_n surface of the compound.

UV-Vis. absorption spectra of the compound were studied in four different solvent at 5×10^{-5} M concentration. The compound showed two absorption bands in 250-400 nm range. The first band in the range of 250-300 nm can be assigned to π - π^* electronic transition due to the π -electrons in the structure of the compound. The latter band in the range of 300-350 nm can be attributed to the n - π^* electronic transitions. The absorption bands slightly shifted to longer wavelengths when solvent polarity increases. In methanol, a weak broad absorption band at 400-500 nm range may be

due to the shift from phenol-imine tautomeric form to keto-amine form [11]. *o*-Hydroxy Schiff bases can exist in two tautomeric forms (enol and keto forms) in both solutions and the solid state. The conversion from one tautomeric form to another depends on several factors such as temperature, the substituent structure and solvent polarity etc. The computational data indicates that the Gibbs free energies of these two forms are close and they can, easily, convert to each other. The enol-keto tautomeric transformation has an influence on their photo-physical and photochemical properties. Due to their intrinsic enol-keto tautomeric transformation also known as intramolecular proton

transfer tautomerism, *o*-hydroxy Schiff bases have found applications in higher energy radiation detectors, memory storage devices.

The compound showed a strong emission band when excited at around 300 nm. The increase in solvent polarity caused a blue shift in the emission band of the compound and the highest intensity was observed in DMF solution. The absorption and emission maximums are given in Table 4. Absorption and emission spectra of the compound are shown in Figure 6.

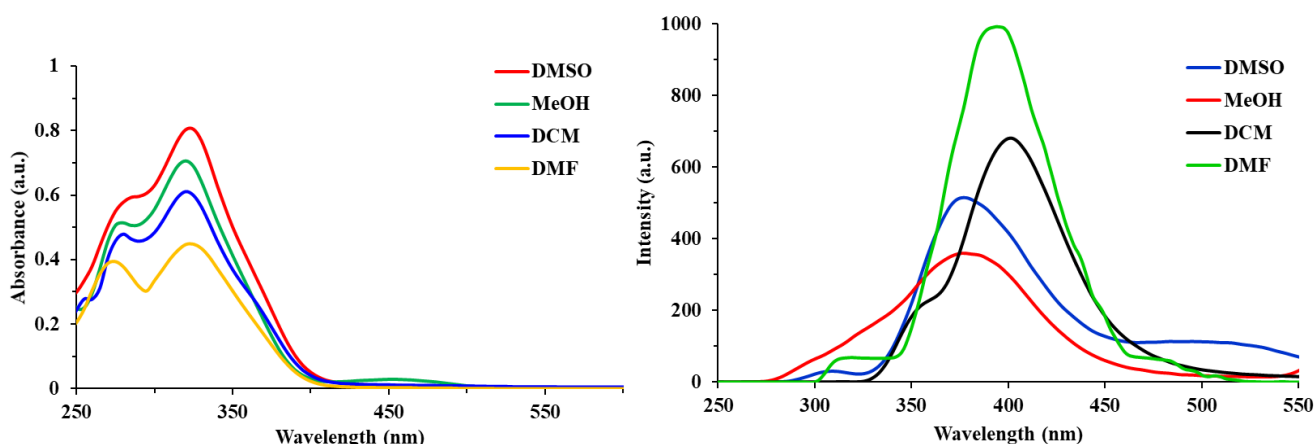


Figure 6. UV-Vis. and photoluminescence spectra of the compound

Table 4. UV-Vis. and photoluminescence data for the compound.

Solvent	UV-vis absorption (nm)	Photoluminescence		Stokes Shift (nm)
		Exc.(nm)	Em.(nm)	
DMSO	280, 325	288	377	89
MeOH	280, 320, 450	278	377	99
DCM	255, 280, 320	334	401	67
DMF	275, 325	302	394	92

3.1. DNA binding studies

To examine the interaction between the synthesized molecule and FSdsDNA (fish sperm double strand DNA), UV-Vis. spectra of the compound was followed upon addition different concentration of DNA. It was observed that the absorption band of the compound at around 250-300 nm increased incremental addition of the DNA solution (Figure 7). This increase showed a linear curve (1×10^{-5} and 5×10^{-5} M DNA concentration range). Moreover, the addition of DNA to the solution of the compound (M) caused a red shift in the absorption bands. The DNA binding constant for

the compound was then calculated using the equation given below.

$$[DNA] / (\epsilon_a - \epsilon_f) = [DNA] / (\epsilon_b - \epsilon_f) + 1 / K_b(\epsilon_a - \epsilon_f)$$

where $\epsilon_a = A_{obs}/[Complex]$, ϵ_a =Absorptivity coefficient of the selected wavelength of the complex and ϵ_b =Absorbency coefficient of wavelength selected by DNA of complex, respectively. In plots $[DNA]/(\epsilon_b/\epsilon_f)$ versus $[DNA]$, K_b is binding constant.

The binding constant with FSdsDNA was found to be as $K_b = 4 \times 10^5 \text{ M}^{-1}$. The binding constant of the

compounds are close to those standard DNA binders (K_b value of spermine and ethidium bromide are 2.1×10^5 and 8.1×10^4 , respectively) [12-14].

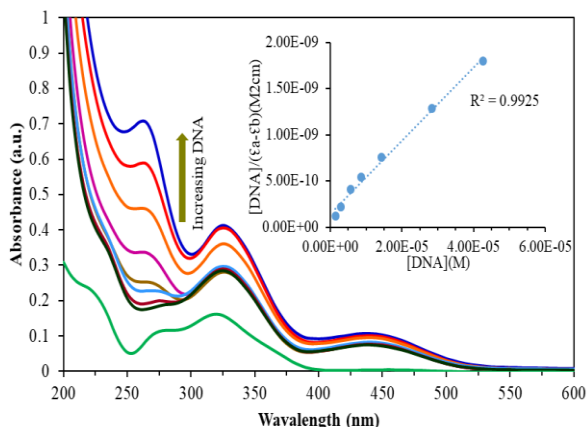


Figure 7. UV-Vis. spectra of the compound upon addition of FSdsDNA.

4. Conclusions

A new imine compound was prepared and its structure was characterized by spectroscopic and analytical methods. The structure of the compound was determined by X-ray diffraction analysis and intermolecular interactions within the crystal structure were investigated by Hirshfeld surface analysis. Finally, the DNA binding properties of the compound was investigated by the spectroscopic method. The compound showed similar binding constant to those spermine and ethidiumbromide.

Conflicts of interest

The authors state that did not have conflict of interests

References

- [1] Ceyhan G, Köse M., Tümer M. and Demirtaş I. Anticancer, photoluminescence and electrochemical properties of structurally characterized two imine derivatives. *Spectrochimica Acta Part A: Molecular and Biomolecular Spectroscopy*, 149 (2015) 731-743.
- [2] Al Zoubi W. and Ko, Y. G. Schiff base complexes and their versatile applications as catalysts in oxidation of organic compounds: part I. *Applied Organometallic Chemistry*, 31 (2017) 3574.
- [3] Al Zoubi W., Kandil F. and Chebani, M. K. Solvent extraction of chromium and copper using Schiff base derived from terephthaldialdehyde and 5-amino-2-methoxy-phenol. *Arabian Journal of Chemistry*, 9 (2016) 526-531.
- [4] Kandil F., Al Zoubi W. and Chebani M. K., The synthesis and characterization of new Schiff bases and investigating them in solvent extraction of chromium and copper. *Separation Science and Technology*, 47 (2012) 754-1761.
- [5] Köse M., Ceyhan G., Tümer M., Demirtaş I., Gönül I. and McKee V. Monodentate Schiff base ligands: Their structural characterization, photoluminescence, anticancer, electrochemical and sensor properties. *Spectrochimica Acta Part A: Molecular and Biomolecular Spectroscopy*. 137 (2015) 477-485.
- [6] Oliveira-Brett A. M., Diclescu V. and Piedade J. A. P. Electrochemical oxidation mechanism of guanine and adenine using a glassy carbon microelectrode. *Bioelectrochemistry*, 55 (2002) 61-62.
- [7] Kuetche V. An initio bubble-driven denaturation of double-stranded DNA: selfmechanical theory. *Journal of Theoretical Biology*, 401 (2016) 15-29.
- [8] Sammriski E., Schwartz D. and Pablo J., A mesoscale model of DNA and its renaturation. *Biophysical Journal*, 96 (2009) 1675-1690.
- [9] Sheldrick G.M., A short history of SHELX, *Acta Crystallogr. Sect. A Found. Crystallogr.*, 64 (2007) 112-122.
- [10] Sheldrick G.M., Crystal structure refinement with SHELXL, *Acta Crystallogr. Sect. C: Struct. Chem.*, 71 (2015) 3-8.
- [11] Gözel A., Kose M., Karakaş D., Atabey H., McKee V. and Kurtoglu M., Spectral, structural and quantum chemical computational and dissociation constant studies of a novel azo-enamine tautomer. *Journal of Molecular Structure*, 1074 (2014) 449-456.
- [12] Strekowski L., Harden D. B., Wydra R. L., Stewart K. D. and Wilson W. D. Molecular basis for potentiation of bleomycin-mediated degradation of DNA by polyamines. Experimental and molecular mechanical studies. *Journal of Molecular Recognition*, 2 (1989) 158-166.
- [13] Chaires J. B., A thermodynamic signature for drug-DNA binding mode. *Archives of biochemistry and biophysics*, 453 (2006) 26-31.
- [14] Strekowski L. and Wilson B. Noncovalent interactions with DNA: an overview. *Mutation Research/Fundamental and Molecular Mechanisms of Mutagenesis*, 623 (2007) 3-13.

Biological evaluation of aromatic bis-sulfonamide Schiff bases as antioxidant, acetylcholinesterase and butyrylcholinesterase inhibitors

Nebih LOLAK¹ , Suleyman AKOÇAK^{1*} 

¹ Adıyaman University, Faculty of Pharmacy, Department of Pharmaceutical Chemistry, 02040, Adıyaman, Türkiye

Abstract

Aromatic/heterocyclic Schiff bases are one of the most investigated and studied scaffold for many pharmaceutical applications. For this reason, in the current work, a series of aromatic bis-sulfonamide Schiff bases (7-15) were re-synthesized by reacting aromatic bis-aldehydes and aromatic sulfonamides in ethanol and assayed for antioxidant properties by using different bioanalytical methods such as DPPH free radical scavenging assay, ABTS cation radical decolorization, cupric reducing antioxidant capacity (CUPRAC) and metal chelating methods. The acetylcholinesterase (AChE) and butyrylcholinesterase (BChE) inhibition profiles were also assessed. In general, the synthesized compounds showed weak antioxidant activity against all tested methods, but two compounds (12 and 15) showed good CUPRAC activity at 10, 25 and 50 μ M concentrations. The weak inhibition potency was obtained against AChE and moderate activity was observed against BChE enzymes at 200 μ M.

Article info

History:

Received:23.07.2019

Accepted:17.04.2020

Keywords:

Sulfonamide,
Schiff base,
Antioxidant,
Anticholinesterase.

1. Introduction

Schiff bases (R-C=N-R) are one of the most versatile ligands which are synthesized from the condensation of primary amines with active carbonyl groups [1]. The imine group of the Schiff bases is an interesting core for medicinal chemistry applications. In literature, Schiff base derivatives shown to have broad biological properties such as antimicrobial, antifungal, diuretics and antitumor activities [2-8]. More specifically, aromatic/heterocyclic mono and bis sulfonamide Schiff bases were investigated as carbonic anhydrase inhibitors (CAIs) [9-12] and histamine Schiff bases as carbonic anhydrase activators (CAAs) by several groups and us [13-15]. Although mono type of sulfonamide Schiff bases was extensively investigated for many different biological applications, bis type of sulfonamide Schiff base derivatives was not yet investigated, the best of our knowledge, as an antioxidant and cholinesterase inhibitors.

More recently, our group showed the efficient carbonic anhydrase inhibition profile on aromatic bis-sulfonamide Schiff base derivatives [9]. The nanomolar potency was obtained against human carbonic anhydrase IX and XII (hCA IX and XII), which are tumor-overexpressed membrane-bound isozymes of carbonic anhydrase enzyme [9]. Since the

potent inhibition profile of these compounds, in the present study, prompted by these potent biological activities, we re-synthesized and assessed these aromatic bis-sulfonamide Schiff bases as antioxidant and cholinesterase (AChE and BChE) inhibitors.

2. Material and Methods

2.1. Chemistry

General synthetic route for the preparation of aromatic bis-sulfonamide Schiff bases (7-15) were depicted in Figure 1. These compounds were synthesized and characterized previously by us as an efficient carbonic anhydrase inhibitors [9]. As a general procedure for the synthesis of aromatic bis-sulfonamide Schiff bases, the aromatic sulfonamides were conjugated with aromatic bis-aldehydes in ethanol in the presence of a few drops of formic acid as a catalyst and then refluxed. The obtained compounds were washed with ice-cold methanol/ethanol and collected by filtration. The final compounds (7-15) were dried under vacuum and characterized by physicochemical and spectroscopic methods as previously described by us [9].

*Corresponding author. Email address: sakocak@adiyaman.edu.tr

<http://dergipark.gov.tr/csj> ©2020 Faculty of Science, Sivas Cumhuriyet University

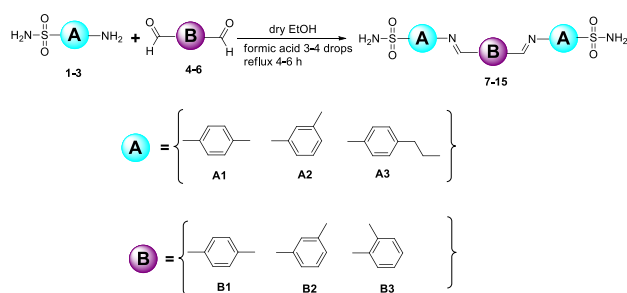


Figure 1. General synthetic route for the synthesis of bis-sulfonamide Schiff bases (7-15) [9].

2.2. Determination of antioxidant and anticholinesterase activity of bis-sulfonamide schiff bases (7-15)

2.2.1 DPPH radical scavenging ability

The DPPH (2,2-diphenyl-1-picrylhydrazyl) radical scavenging activity of the synthesized compounds was determined by spectrophotometric method based on the reduction of an ethanol solution of DPPH [16]. 2, 5, 10, 20 μL of 1 mM stock solution of each compound was completed to 40 μL with the DMSO and mixed with 160 μL of 0.1 mM of DPPH free radical solution. The mixture was led to stand for 30 min in the dark and the absorbance was then measured at 517 nm against a blank. Inhibition of free radical, DPPH, in percent (I %) was calculated according to the formula:

$$I \% = (A_{\text{control}} - A_{\text{sample}}) / A_{\text{control}} \times 100;$$

where A_{control} is the absorbance of the control reaction (containing all reagents except for the tested compounds), and A_{sample} is the absorbance of the test compounds. Tests were carried out in triplicate. BHA, BHT and α -Toc were used as positive control.

2.2.2. ABTS cation radical decolorization

The percent inhibition of decolorization of ABTS (2,2'-azino-bis(3-ethylbenzothiazoline-6-sulfonic acid)) cation radical is obtained as a function of time and concentration, and evaluated by comparison with the BHT, BHA and α -Toc compounds used as standard [17, 18]. The tested compounds at different concentrations are added to each well and 160 μL of 7 mM ABTS solution is added. After 6 min at room temperature, the absorbances were measured at 734 nm. ABTS cation radical decolorization activities were determined by using the equation below:

$$\% \text{Inhibition} = (A_{\text{control}} - A_{\text{sample}}) / A_{\text{control}} \times 100$$

where A is the absorbance. Tests were carried out in triplicate. BHA, BHT and α -Toc were used as positive control.

2.2.3. Metal Chelate

The chelating ability of synthesized compounds was examined according to the method of Dinis et al. [19]. The tested compounds at different concentrations were added to each well and 4 μL of 2 mM ferrous (II) chloride was added. Then 8 μL of 5 mM ferrozine was added and the reaction was started. After 10 min at room temperature, the absorbance was measured at 562 nm against blank. The results were expressed as percentage of inhibition of the ferrozine- Fe^{2+} complex formation. The percentage inhibition of the ferrozine - Fe^{2+} complex formation was calculated using the formula given below:

$$\text{Chelating ability (\%)} = (A_{\text{control}} - A_{\text{sample}}) / A_{\text{control}} \times 100$$

where A is the absorbance. Tests were carried out in triplicate. EDTA was used as a positive control.

2.2.4. Cupric reducing antioxidant capacity (CUPRAC) method

CUPRAC method comprises the reduction of Cu(II)-Neocuproine into its colored form Cu(I)-Neocuproine chelate in the presence of antioxidant compounds [20, 21]. The tested compounds at different concentrations were added to each well and 61 μL of CuCl_2 , Neocuproine and NH_4OAc solutions were added. After 1 hour at room temperature, the absorbance was measured at 450 nm. The absorbance values were compared with the standard molecules BHA, BHT and α -Toc. Each of samples was applied three times.

2.2.5. Anticholinesterase activity of the bis-sulfonamide Schiff bases

The inhibitory effect of bis-sulfonamide Schiff base derivatives (7-15) on AChE and BChE activities was determined according to the slightly modified spectrophotometric method of Ellman et al. [22]. All compounds were dissolved in DMSO to prepare stock solutions at 4 mM concentration. Aliquots of 150 μL of 100 mM sodium phosphate buffer (pH 8.0), 10 μL of sample solution and 20 μL AChE (or BChE) solution were mixed and incubated for 15 min at 25 $^\circ\text{C}$, and DTNB (5,5'-Dithio-bis(2-nitro-benzoic)acid) (10 μL) is added. The reaction was then initiated by the addition of acetylthiocholine iodide (or butyrylthiocholine iodide) (10 μL). The final

concentration of the tested compounds' solution was 200 μM .

$$\% \text{Inhibition} = (A_{\text{control}} - A_{\text{sample}}) / A_{\text{control}} \times 100$$

where A is the absorbance. Tests were carried out in triplicate. Galantamine was used as positive control. IC_{50} values were calculated from the equation of the curve obtained from the concentration-inhibition graph. The value of IC_{50} is the value found when we write fifty instead of inhibition in the equation of the obtained curve.

2.3. Statistical analysis

The results of the antioxidant and anticholinesterase activity assays are expressed as the mean \pm SD of three parallel measurements. The statistical significance was estimated using a Student's t-test, where p-values < 0.05 were considered significant.

3. Results and Discussion

In the current study, we report the antioxidant, acetylcholinesterase and butyrylcholinesterase inhibition activities of a series of bis-sulfonamide Schiff base derivatives (7-15). These compounds were re-synthesized as described in our previously published work. In the present study, the main idea was to assess antioxidant and cholinesterase activities of these potent carbonic anhydrase inhibitors.

Schiff bases and their metal complexes were extensively studied as a potential antioxidant reagents [23, 24]. Specifically, a histamine Schiff bases were recently evaluated as an antioxidant and cholinesterase inhibitors by us [20]. Among the series, most of the compounds showed moderate antioxidant activity with IC_{50} values ranging from 249.63 to 945.23 μM for DPPH activity, from 89.18 to 868.89 μM for ABTS activity, and from 70.34 to 296.25 μM for metal chelating activity. Another study from the Khan et al. [25], demonstrated the IC_{50} values within the range of 15.16-48.26 μM for in vitro free radical scavenging activity by using Schiff bases of 4-amino-1,5-dimethyl-2-phenylpyrazolones. Aslam et al. [26], showed also DPPH antioxidant activity of Schiff bases that synthesized from the condensation of 2-aminophenol and various chloro- and nitro-benzaldehydes. The good antioxidant activity was observed from these compounds with IC_{50} values ranging from 17.2 to 33.1 μM having much better potential when compared with the standard BHA [26].

The antioxidant capacities of synthesized bis-sulfonamide Schiff base derivatives (7-15) are determined by using four different antioxidant methods, including DPPH free radical scavenging, ABTS cation radical decolorization, cupric reducing (CUPRAC) and metal chelating methods. Acetylcholinesterase and butyrylcholinesterase inhibition activities were also investigated.

The results revealed that bis-sulfonamide Schiff base derivatives (7-15) showed no significant activity in case of DPPH free radical scavenging method with IC_{50} values of >1000 μM . In the present work, all compounds were less active than the standard BHA (61.72 μM), BHT (232.11 μM), and α -Toc (56.86 μM) (Table 1) in case of DPPH free radical scavenging method. The ABTS cation radical scavenging activities of synthesized compounds was assayed and compared with BHT, BHA, and α -Toc used as standards and IC_{50} values of compounds were summarized in Table 1. All compounds showed weak activity with IC_{50} values of <1000 μM , except the compounds 12 (A2B3) and 13 (A3B1) displayed moderate activity with IC_{50} values of 964.82 and 355.77 μM , respectively (Table 1).

The metal chelating effect of the bis-sulfonamide Schiff base derivatives on iron (II) ions was presented in Table 1 and compared with standard EDTA. It was considered that compounds 13 (A3B1) and 15 (A3B3) were the most active compounds with IC_{50} values of 92.31 and 70.32 μM , respectively. Interestingly, both of these compounds have 4-(2-aminoethyl) benzenesulfonamide moiety. These compounds showed close chelating activity to standard EDTA (IC_{50} = 52.35 μM). The remaining compounds showed moderate chelating activity with IC_{50} values ranging from 101.43 to 268.56 μM , except the compound 12 (A2B3), which displayed no chelating activity with IC_{50} value of >1000 μM .

The cupric reducing antioxidant capacity (CUPRAC) method was also applied to identify the antioxidant activity of the prepared bis-sulfonamide Schiff base derivatives (7-15). As expected, the activity of the compounds increased with increasing concentration (10 to 100 μM) as shown in Table 2. The results of the CUPRAC test of the synthesized compounds at 10, 25, 50 and 100 μM were compared with standards BHT, BHA and α -Toc. In the current study, the compounds 12 (A2B3) and 15 (A3B3) showed a better CUPRAC activity than standard α -Toc at 10, 25 and 50 μM . Specifically, the compound 12 had better activity at 10 μM of concentration than all three standards (BHT, BHA and α -Toc). Interestingly, these two active compounds (12 and 15) have 1,2-disubstituted phenyl (B3) with different sulfonamides (A2 and A3).

Table 1. DPPH radical scavenging, ABTS cation radical decolorization and metal chelating activities of aromatic bis-sulfonamide Schiff base derivatives (7-15) and controls BHA, BHT, α -Toc, and EDTA.

Comp.	A	B	IC ₅₀ (μ M) ^a		
			DPPH Free Radical Scavenging Activity	ABTS Cation Radical Scavenging Activity	Metal Chelating Activity
7	A1	B1	>1000	>1000	101.43 \pm 1.24
8	A1	B2	>1000	>1000	144.51 \pm 1.91
9	A1	B3	>1000	>1000	120.55 \pm 0.06
10	A2	B1	>1000	>1000	268.56 \pm 1.04
11	A2	B2	>1000	>1000	109.90 \pm 1.14
12	A2	B3	>1000	964.82 \pm 0.94	>1000
13	A3	B1	>1000	355.77 \pm 0.50	92.31 \pm 0.26
14	A3	B2	>1000	>1000	181.34 \pm 1.78
15	A3	B3	>1000	>1000	70.32 \pm 2.26
BHA ^b	--	--	61.72 \pm 0.85	45.40 \pm 1.08	-
BHT ^b	--	--	232.11 \pm 3.01	26.54 \pm 0.18	-
α -TOC ^b	--	--	56.86 \pm 0.77	34.12 \pm 0.41	-
EDTA ^b	--	--	-	-	52.35 \pm 1.15

^a IC₅₀ values represent the means (standard deviation of three parallel measurements (p < 0.05).^b Reference compounds.**Table 2.** Absorbance values for the cupric ion reducing antioxidant capacity (CUPRAC), of the aromatic bis-sulfonamide Schiff base derivatives (7-15) and controls BHA, BHT, and α -Toc.

Comp.	Absorbance Values ^a					
	A	B	10 μ M	25 μ M	50 μ M	100 μ M
7	A1	B1	0.076 \pm 0.001	0.083 \pm 0.005	0.090 \pm 0.012	0.097 \pm 0.002
8	A1	B2	0.086 \pm 0.002	0.177 \pm 0.002	0.288 \pm 0.001	0.398 \pm 0.005
9	A1	B3	0.085 \pm 0.002	0.090 \pm 0.004	0.117 \pm 0.004	0.222 \pm 0.004
10	A2	B1	0.084 \pm 0.004	0.085 \pm 0.003	0.087 \pm 0.003	0.101 \pm 0.003
11	A2	B2	0.088 \pm 0.002	0.178 \pm 0.003	0.281 \pm 0.001	0.399 \pm 0.005
12	A2	B3	0.277 \pm 0.001	0.391 \pm 0.005	0.494 \pm 0.003	0.512 \pm 0.002
13	A3	B1	0.121 \pm 0.085	0.277 \pm 0.002	0.383 \pm 0.001	0.395 \pm 0.006
14	A3	B2	0.082 \pm 0.003	0.077 \pm 0.002	0.084 \pm 0.002	0.099 \pm 0.003
15	A3	B3	0.377 \pm 0.004	0.479 \pm 0.000	0.583 \pm 0.002	0.791 \pm 0.003
BHA ^b	--	--	0.288 \pm 0.015	0.572 \pm 0.046	1.026 \pm 0.013	1.984 \pm 0.035
BHT ^b	--	--	0.303 \pm 0.010	0.610 \pm 0.010	1.167 \pm 0.024	2.000 \pm 0.173
α -TOC ^b	--	--	0.179 \pm 0.001	0.296 \pm 0.012	0.482 \pm 0.017	0.912 \pm 0.065

^a Values expressed are means \pm SD of three parallel absorbance measurements (p<0.05)^b Reference compounds

In this study, a series of aromatic bis-sulfonamide Schiff bases were assessed against cholinesterase (AChE and BChE) enzyme. None of the compounds from the series showed better activity than standard drug galantamine (Table 3). Specifically, only three compounds 13, 14 and 15, showed some activity against AChE with % inhibitions about 16.19, 5.42 and 24.00, respectively. Interestingly, these three compounds have A3 (4-(2-aminoethyl)benzenesulfonamide) substitution with different linker types (B1, B2 and B3). Slightly better activity was observed against BChE, which all compounds had some activity with % inhibitions ranging from 5.44 to 26.19 at 200 μ M. Specifically,

compounds 7, 8 and 15 showed moderate activity against BChE with % inhibition rates 26.19, 24.40 and 21.17, respectively. The remaining compounds showed weak inhibition activity against BChE enzyme with % inhibition values ranging from 5.44 to 13.69 depending on the nature of the compounds (Table 3).

Table 3. Anticholinesterase activity of the aromatic bis-sulfonamide Schiff base derivatives (**7-15**) at 200 μ M and standard drug galantamine.

Comp.	A	B	AChE (Inhibition %) ^a	BChE (Inhibition %) ^a
7	A1	B1	NA	26.19 \pm 0.33
8	A1	B2	NA	24.40 \pm 0.25
9	A1	B3	NA	6.97 \pm 0.24
10	A2	B1	NA	7.40 \pm 0.32
11	A2	B2	NA	6.12 \pm 0.20
12	A2	B3	NA	10.20 \pm 0.72
13	A3	B1	16.19 \pm 0.57	13.69 \pm 0.37
14	A3	B2	5.42 \pm 0.79	5.44 \pm 0.92
15	A3	B3	24.00 \pm 0.78	21.17 \pm 0.36
Galantamine ^b	--	--	84.20 \pm 0.74	87.86 \pm 0.24

^a 200 μ M^b Standart madde

NA: Not Active

4. Conclusions

In the current study, a series of aromatic bis-sulfonamide Schiff bases (7-15) were re-synthesized from the condensation reaction of aromatic sulfonamides (A1, A2, and A3) and aromatic bis-aldehydes (B1, B2 and B3). The antioxidant properties of the bis-sulfonamide Schiff base derivatives were investigated by DPPH free radical scavenging assay, ABTS cation decolorization, cupric reducing antioxidant capacity (CUPRAC) and metal chelating methods. The acetylcholinesterase (AChE) and butyrylcholinesterase (BChE) inhibition profiles were also determined. In general, weak DPPH, ABTS and metal chelating activity were observed. On the other hand, two compounds (12 and 15) showed good CUPRAC activity at 10, 25 and 50 μ M concentrations. Some of the compounds did not show any activity against AChE (compounds 7-12). In general, a weak to moderate activity were obtained against AChE and BChE enzymes with % inhibition values ranging from 5.42 to 26.9 at 200 μ M concentration.

Acknowledgment

This work was partially funded by The Scientific and Technological Research Council of Turkey (TUBITAK) with Grant nos. 215Z484, 315S103, and 216S907.

Conflicts of interest

The authors state that did not have conflict of interests

References

- [1] Rani, A., Kumar, M., Khare, R., Tuli, H.S., Schiff bases as an antimicrobial agents: A review, *J. Biol. Chem. Sci.*, 2 (2015), 62-91.
- [2] Sridhar, S.K., Saravanan, M., Ramesh, A., Synthesis and antibacterial screening of hydrazones, Schiff and Mannich bases of isatin derivatives, *Eur. J. Med. Chem.* 36 (2001), 615-625.
- [3] Panneerselvam, P., Nair, R.R., Vijayalakshmi, G., Subramanian, E.H., Sridhar, S.K., Synthesis of Schiff bases of 4-(4-aminophenyl)-morpholine as potential antimicrobial agents, *Eur. J. Med. Chem.*, 40 (2005), 225-229.
- [4] Lam, P.L., Lee, K.K.H., Kok, S.H.L., Gambari, R., Lam, K.H., Ho, C.L., Ma, X., Lo, Y.H., Wong, W.Y., Dong, Q.C., Bian, Z.X., Chui, C.H., Antifungal study of substituted 4-pyridylmethylene-4'-aniline Schiff bases, *RSC Adv.*, 106 (2016), 104575-104581.
- [5] Nizami, G., Sayyed, R., Antimicrobial, electrochemical and thermodynamic studies of Schiff base complexes and their potential as anticarcinogenic and antitumor agents: A review, *IOSR J. Appl. Chem.*, 10 (2017), 40-51.
- [6] Raquel, S.A., Pessoa, C., Lourenco, M.C.S., de Souza, V.N.M., Lessa, A.J., Synthesis, Antitubercular and Anticancer activities of p-nitrophenylethylenediamine derived Schiff bases, *Med. Chem.* 13 (2017), 391-397.
- [7] Dhar, D.N., Taploo, C.L., Schiff bases and their applications, *J. Sci. Ind. Res.* 41 (1982), 501-506.
- [8] Gupta, S.D., Revathi, B., Mazaira, G.I., Galigniana, M.D., Subrahmanyam, C.V.S.,

- Gowrishankar, N.L., Raghavendra, N.M., 2,4-dihydroxy benzaldehyde derived Schiff bases as small molecule Hsp90 inhibitors: Rational identification of a new anticancer lead. *Bioorg. Chem.*, 59 (2014), 97-105.
- [9] Akocak, S., Lolak, N., Nocentini, A., Karakoc, G., Tufan, A., Supuran, C.T., Synthesis and biological evaluation of novel aromatic and heterocyclic bis-sulfonamide Schiff bases as carbonic anhydrase I, II, VII and IX inhibitors, *Bioorg. Med. Chem.*, 25 (2017), 3093-3097.
- [10] Durgun, M., Turkmen, H., Ceruso, M., Supuran, C.T., Synthesis of 4-sulfamoylphenyl-benzylamine derivatives with inhibitory activity against human carbonic anhydrase isoforms I, II, IX and XII, *Bioorg. Med. Chem.*, 24 (2016), 982-988.
- [11] Sarikaya, B., Ceruso, M., Carta, F., Supuran, C.T., Inhibition of carbonic anhydrase isoforms I, II, IX and XII with novel Schiff bases: Identification of selective inhibitors for the tumor-associated isoforms over the cytosolic ones, *Bioorg. Med. Chem.*, 22 (2014), 5883-5890.
- [12] Durgun M, Turkes C, Isik M, Demir, Y., Sakli, A., Kuru, A., Guzel, A., Beydemir, S., Akocak, S., Osman, S.M., AlOthman, Z., Supuran, C.T., Synthesis, characterization, biological evaluation, and in silico studies of novel series sulfonamide derivatives. *J. Enzyme Inhib. Med. Chem.* 35 (2020), doi:10.1080/14756366.2020.1746784.
- [13] Akocak, S., Lolak, N., Vullo, D., Durgun, M., Supuran, C.T., Synthesis and biological evaluation of histamine Schiff bases as carbonic anhydrase I, II, IV, VII and IX activators, *J. Enzyme Inhib. Med. Chem.*, 32 (2017), 1305-1312.
- [14] Akocak, S., Lolak, N., Bua, S., Nocentini, A., Karakoc, G., Supuran, C.T., α -Carbonic anhydrases are strongly activated by spinaceamine derivatives, *Bioorg. Med. Chem.*, 27 (2019), 800-804.
- [15] Akocak, S., Lolak, N., Bua, S., Nocentini, A., Supuran, C.T., Activation of human α -Carbonic anhydrase isoforms I, II, IV and VII with bis-histamine Schiff bases and bis-spinaceamine substituted derivatives, *J. Enzyme Inhib. Med. Chem.*, 34 (2019), 1193-1198.
- [16] Blois, M.S., Antioxidant determinations by the use of a stable free radical, *Nature*, 181 (1958), 1199-1200.
- [17] Pellegrini, R.R.N., Proteggente, A., Pannala, A., Yang, M., Rice-Evans, C., Antioxidant activity applying an improved ABTS radical cation decolorization assay, *Free Rad. Bio. Med.*, 26 (1999), 1231-1237.
- [18] Akocak, S., Boga, M., Lolak, N., Tuneg, M., Sanku, R.K.K., Design, synthesis and biological evaluation of 1,3-diaryltriazeno-substituted sulfonamides as antioxidant, acetylcholinesterase and butyrylcholinesterase inhibitors, *J. Turk Chem. Soc. Sec. A: Chem.*, 6 (2019), 63-70.
- [19] Dinis, T.C.P., Maderia, V.M.C., Almedia, L.M., Action of phenolic derivatives (acetoaminophen, salicylate and 5-aminosalicylate) as inhibitors of membrane lipid preoxidation and as peroxy radical scavengers, *Arch. Biochem. Biophys.*, 315 (1994), 161-169.
- [20] Akocak, S., Lolak, N., Tuneg, M., Boga, M., Antioxidant, acetylcholinesterase and butyrylcholinesterase inhibition profiles of histamine Schiff bases, *J. Turk Chem. Soc. Sec. A: Chem.*, 6 (2019) 157-164.
- [21] Apak, R., Guclu, K., Ozyurek, M., Karademir, S.E., Novel total antioxidant capacity index for dietary polyphenols and vitamins C and E, using their cupric ion reducing capability in the presence of neocuproine: CUPRAC Method, *J. Agric. Food Chem.*, 52 (2004), 7970-7981.
- [22] Ellman, G.L., Courtney, K.D., Andres, V., Featherstone, R.M., A new and rapid colorimetric determination of acetylcholinesterase activity, *Biochem. Pharmacol.*, 7 (1961), 88-95.
- [23] Mohapatra, R.K., Das, P.K., Pradhan, M.K., Maihub, A.A., El-ajaily, M.M., Biological aspects of Schiff base-metal complexes derived from benzaldehydes: an overview, *J. Iran. Chem. Soc.* 15 (2018), 2193-2227.
- [24] Al Zoubi, W., Al-Hamdani, A.A.S., Kaseem, M., Synthesis and antioxidant activities of Schiff bases and their complexes: a review, *Appl. Organometal. Chem.*, 30 (2016), 810-817.
- [25] Khan, M., Khan, M., Taha, M., Salar, U., Hameed, A., Ismail, N.H., Jamil, W., Saad, S.M., Perveen, S., Kashif, S.M., Synthesis of 4-amino-1,5-dimethyl-2-phenylpyrazolone derivatives and their antioxidant activity, *J. Chem. Soc. Pak.*, 37 (2015), 802-810.
- [26] Aslam, M., Anis, I., Mehmood, R., Iqbal, L., Iqbal, S., Khan, I., Chishti, M.S., Perveen, S., Synthesis and biological activities of 2-aminophenol-based Schiff bases and their structure-activity relationship, *Med. Chem. Res.*, 25 (2016), 109-115

Transmuted complementary exponential power distribution: properties and applications

Caner TANIŞ¹, Buğra SARAÇOĞLU^{1,*}, Coşkun KUŞ¹, Ahmet PEKGÖR²

¹ Selcuk University, Department of Statistics, Konya/ TURKEY

² Necmettin Erbakan University, Department of Statistics, Konya/ TURKEY

Abstract

In this study, we introduce a new lifetime distribution by using quadratic rank transmutation map. The some properties of this new distribution is provided. Furthermore, the parameters of this new distribution are estimated by the maximum likelihood method. The performances of the estimates are examined according to bias and mean squared errors (MSEs) criteria through a Monte Carlo simulation study. Finally, two applications with real data are presented to evaluate the fits of introduced distribution.

Article info

History:

Received: 25.12.2019

Accepted: 24.03.2020

Keywords:

Maximum likelihood estimation, Monte Carlo simulation, Transmuted distribution.

1. Introduction

In reliability analysis, every statistical tools are presented based on assumption of the distribution of lifetimes. Therefore, lifetime distributions are hearts of survival and reliability theory. Nowadays, introducing the new lifetime distributions is gaining much more attention. There are a lot of distributions introduced in last two decades. One of the them is complementary exponential power (CEP) distribution suggested by [1] using exponential power (EP) distribution introduced in [2]. The probability density function (pdf) and cumulative distribution function (cdf) of CEP distribution are given, respectively, by

$$g(x; \gamma) = \frac{\beta \theta x^{\beta-1}}{\alpha^\beta} \exp \left\{ 1 + \left(\frac{x}{\alpha} \right)^\beta - \exp \left\{ \left(\frac{x}{\alpha} \right)^\beta \right\} \right\} \times \left\{ 1 - \exp \left(1 - \exp \left\{ \left(\frac{x}{\alpha} \right)^\beta \right\} \right) \right\}^{\theta-1} I_{\mathbb{R}_+}(x) \quad (1)$$

and

$$G(x; \gamma) = \left[1 - \exp \left(1 - \exp \left\{ \left(\frac{x}{\alpha} \right)^\beta \right\} \right) \right]^\theta, \quad (2)$$

where $I_A(x)$ is indicator function on set A , $\gamma = (\alpha, \beta, \theta)$ is parameter vector, $\alpha > 0$ is a scale parameter, $\beta > 0$ and $\theta > 0$ are shape parameters.

In this study, we aim to introduce a new distribution named transmuted complementary exponential power (TCEP) using Quadratic Rank Transmutation Map (QRTM) proposed by [3]. In the literature, there are many lifetime distributions generated by QRTM such as [4], [5], [6] and [7]. The pdf and cdf of QRTM family are given by

$$f(x; \delta) = g(x; \gamma) [1 + \lambda - 2\lambda G(x; \gamma)] \quad (3)$$

and

*Corresponding author. Email address: bugrasarac@selcuk.edu.tr

$$F(x; \delta) = (1 + \lambda)G(x; \gamma) - \lambda G(x; \gamma)^2, \quad (4)$$

where G and g are cdf and corresponding pdf of any lifetime, γ is parameter vector of distribution with cdf G and $\lambda \in [-1, 1]$ is extra parameter beside $\delta = (\gamma, \lambda)$. Hence, new distribution includes a parameter to baseline distribution G . For more information on QRTM, see [3].

In this paper, a new lifetime distribution is introduced by QRTM family. In Section 2, the pdf and cdf of distribution are described. The raw moments are derived under a condition, quantile, survival and hazard functions are also given. In Section 3, the point and interval estimations are discussed by maximum likelihood (ML) methodology. A simulation study is conducted to observe the behaviours of ML estimates (MLEs) in Section 4. In Section 5 and Section 6, two numerical examples are also provided to close the paper.

2. TCEP Distribution

In this study, we introduce a new lifetime distribution obtained by using Eqs. (1-2) in Eqs. (3-4). Then pdf and cdf of introduced distribution are given, respectively, by

$$f(x; \delta) = \frac{\beta \theta x^{\beta-1}}{\alpha^\beta} \exp \left(1 + \left(\frac{x}{\alpha} \right)^\beta - \exp \left\{ \left(\frac{x}{\alpha} \right)^\beta \right\} \right) \times \left[1 - \exp \left(1 - \exp \left\{ \left(\frac{x}{\alpha} \right)^\beta \right\} \right) \right]^{\theta-1} \left[1 + \lambda - 2\lambda \left[1 - \exp \left(1 - \exp \left\{ \left(\frac{x}{\alpha} \right)^\beta \right\} \right) \right] \right]^\theta I_{\mathbb{R}_+}(x) \quad (5)$$

and

$$F(x; \delta) = (1 + \lambda) \left[1 - \exp \left(1 - \exp \left\{ \left(\frac{x}{\alpha} \right)^\beta \right\} \right) \right]^\theta - \lambda \left[1 - \exp \left(1 - \exp \left\{ \left(\frac{x}{\alpha} \right)^\beta \right\} \right) \right]^{2\theta}, \quad (6)$$

where $\delta = (\alpha, \beta, \theta, \lambda)$ is parameter vector, $\lambda \in [-1, 1]$, $\alpha, \beta, \theta \in \mathbb{R}_+$ are parameters. The distribution with pdf (5) and cdf (6) is called Transmuted Complementary Exponential Power (TCEP) (δ) distribution. When $\lambda = 0$, TCEP (δ) reduces to CEP(γ). In Fig. 1, the pdf of TCEP (δ) are plotted for some selected parameter values.

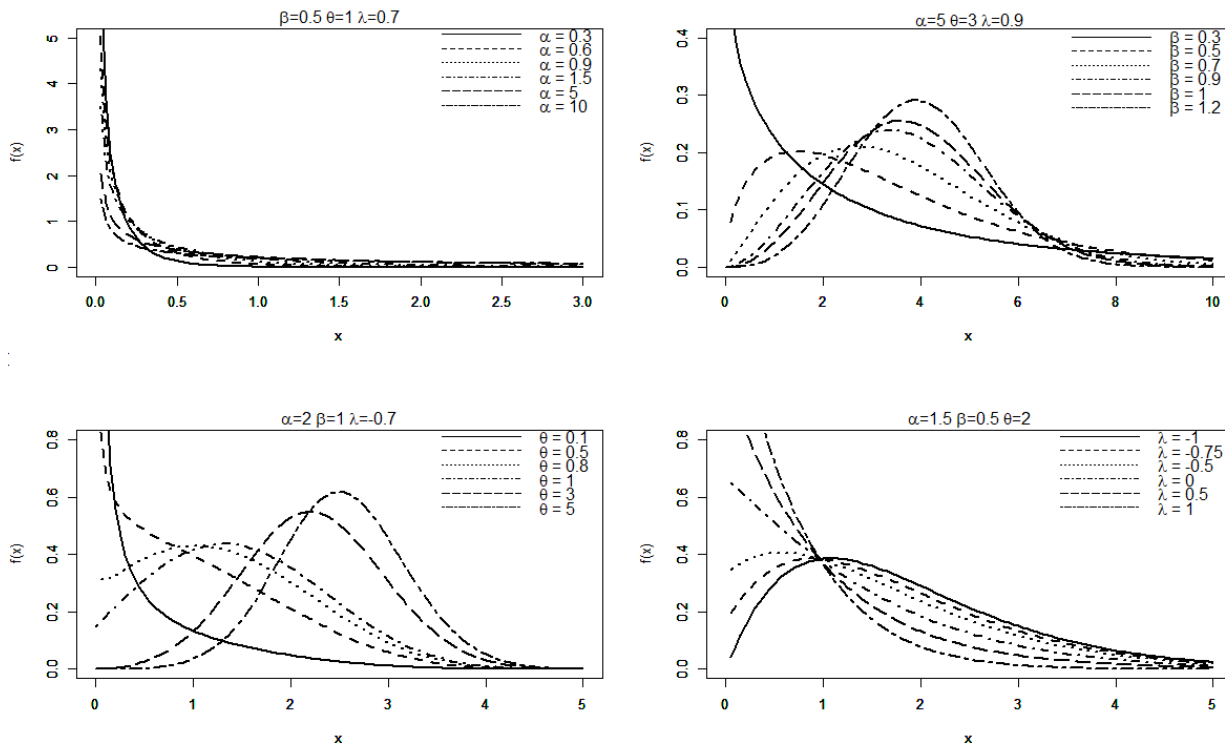


Figure 1. TCEP density functions

2.1. Moments

In this subsection, the raw moments of the TCEP(δ) distribution are derived, explicitly. We obtain the raw moments using following lemma under the condition that r/β is an integer.

Lemma 1 For $\nu, \mu > 0$ and $m \in \mathbb{N}$

$$\int_1^{\infty} x^{\nu-1} (\log x)^m \exp(-\mu x) dx = \frac{\partial^m \mu^{-\nu} \Gamma(\nu, \mu)}{\partial \nu^m}, \quad m=0,1,2,\dots \quad (7)$$

where $\Gamma(a, x) = \int_x^{\infty} t^{a-1} \exp\{-t\} dt$ is the incomplete gamma function [8]. Using Lemma 1, following theorem gives the raw moments of TCEP(δ) distribution.

Theorem 1

If r/β is an positive integer, the r th moments of TCEP(δ) distribution are given by

$$E(X^r) = (1+\lambda)\alpha^r \sum_{j=0}^{\infty} \frac{(-1)^j \Gamma(\theta+1) \exp(j+1)}{\Gamma(\theta-j) j!} \left(\frac{\partial^m}{\partial \nu^m} (j+1)^{-\nu} \Gamma(\nu, j+1) \Big|_{\nu=1} \right) - \lambda \alpha^r \sum_{j=0}^{\infty} \frac{(-1)^j \Gamma(2\theta+1) \exp(j+1)}{\Gamma(2\theta-j) j!} \left(\frac{\partial^m}{\partial \nu^m} (j+1)^{-\nu} \Gamma(\nu, j+1) \Big|_{\nu=1} \right), \quad (8)$$

where $r=1,2,\dots$ and $\Gamma(\alpha) = \int_0^{\infty} t^{\alpha-1} \exp(-t) dt$ is the well-known gamma function.

Proof. Using pdf in Eq. (5), the raw moments can be written by

$$E(X^r) = \frac{(1+\lambda)\beta\theta}{\alpha^\beta} \int_0^\infty x^{r+\beta-1} \exp\left\{1 + \left(\frac{x}{\alpha}\right)^\beta - \exp\left\{\left(\frac{x}{\alpha}\right)^\beta\right\}\right\} \left(1 - \exp\left\{1 - \exp\left\{\left(\frac{x}{\alpha}\right)^\beta\right\}\right\}\right)^{\theta-1} dx$$

$$- \frac{2\lambda\beta\theta}{\alpha^\beta} \int_0^\infty x^{r+\beta-1} \exp\left\{1 + \left(\frac{x}{\alpha}\right)^\beta - \exp\left\{\left(\frac{x}{\alpha}\right)^\beta\right\}\right\} \left(1 - \exp\left\{1 - \exp\left\{\left(\frac{x}{\alpha}\right)^\beta\right\}\right\}\right)^{2\theta-1} dx$$
(9)

for $\theta > 0$. Let us consider the identity

$$(1-z)^{\theta-1} = \sum_{j=0}^{\infty} \frac{(-1)^j \Gamma(\theta) z^j}{\Gamma(\theta-j) j!}.$$
(10)

By using expansion (10) in (9), we can write

$$\mu'_r = \frac{(1+\lambda)\Gamma(\theta+1)\beta}{\alpha^\beta} \sum_{j=0}^{\infty} \frac{(-1)^j e^{j+1}}{\Gamma(\theta-j) j!} \int_0^\infty x^{r+\beta-1} \exp\left\{\left(\frac{x}{\alpha}\right)^\beta\right\} \exp\left\{-(j+1)\exp\left\{\left(\frac{x}{\alpha}\right)^\beta\right\}\right\} dx$$

$$- \frac{\lambda\Gamma(2\theta+1)\beta}{\alpha^\beta} \sum_{j=0}^{\infty} \frac{(-1)^j e^{j+1}}{\Gamma(2\theta-j) j!} \int_0^\infty x^{r+\beta-1} \exp\left\{\left(\frac{x}{\alpha}\right)^\beta\right\} \exp\left\{-(j+1)\exp\left\{\left(\frac{x}{\alpha}\right)^\beta\right\}\right\} dx.$$
(11)

Using transformation of $y = \exp\left\{\left(\frac{x}{\alpha}\right)^\beta\right\}$ in integrals in (11), we get

$$\mu'_r = (1+\lambda)\alpha^r \Gamma(\theta+1) \sum_{j=0}^{\infty} \frac{(-1)^j e^{j+1}}{\Gamma(\theta-j) j!} \int_0^\infty y^{1-1} (\log y)^{\frac{r}{\beta}} \exp\{-(j+1)y\} dy$$

$$- \lambda \alpha^r \Gamma(2\theta+1) \sum_{j=0}^{\infty} \frac{(-1)^j e^{j+1}}{\Gamma(2\theta-j) j!} \int_0^\infty y^{1-1} (\log y)^{\frac{r}{\beta}} \exp\{-(j+1)y\} dy$$
(12)

By using Lemma 1 in (12), the proof is completed.

2.2. Quantile function and random number generation

The quantile function of TCEP(δ) distribution is obtained by solving $F(x; \delta) = p$ for $p \in (0, 1)$ and it is given by

$$x_p = \alpha \left[\log \left(1 - \log \left(1 - \left(\frac{1 + \lambda - \sqrt{(\lambda+1)^2 - 4\lambda p}}{2\lambda} \right)^{1/\theta} \right) \right) \right]^{1/\beta},$$
(13)

where $F(x; \delta)$ is given in (6).

2.3. Reliability and hazard functions

The reliability function and hazard function of TCEP(δ) distribution are given, respectively, by

$$R(t) = 1 - \left[(1+\lambda) \left[1 - \exp \left(1 - \exp \left\{ \left(\frac{t}{\alpha} \right)^\beta \right\} \right) \right]^\theta - \lambda \left[1 - \exp \left(1 - \exp \left\{ \left(\frac{t}{\alpha} \right)^\beta \right\} \right) \right]^{2\theta} \right]$$
(14)

and

$$h(t) = \frac{g(t; \alpha, \beta) \left[1 - \exp \left(1 - \exp \left\{ \left(\frac{t}{\alpha} \right)^\beta \right\} \right) \right]^{\theta-1} \left[1 + \lambda - 2\lambda \left[1 - \exp \left(1 - \exp \left\{ \left(\frac{t}{\alpha} \right)^\beta \right\} \right) \right]^\theta \right]}{1 - \left[(1 + \lambda) \left[1 - \exp \left(1 - \exp \left\{ \left(\frac{t}{\alpha} \right)^\beta \right\} \right) \right]^\theta - \lambda \left(\left[1 - \exp \left(1 - \exp \left\{ \left(\frac{t}{\alpha} \right)^\beta \right\} \right) \right]^\theta \right)^2 \right]}, \quad (15)$$

where

$$g(t; \alpha, \beta) = \frac{\beta \theta t^{\beta-1}}{\alpha^\beta} \exp \left(1 + \left(\frac{t}{\alpha} \right)^\beta - \exp \left\{ \left(\frac{t}{\alpha} \right)^\beta \right\} \right).$$

Fig. 2 presents the shapes of the hazard function of TCEP(δ) distribution for selected parameter values.

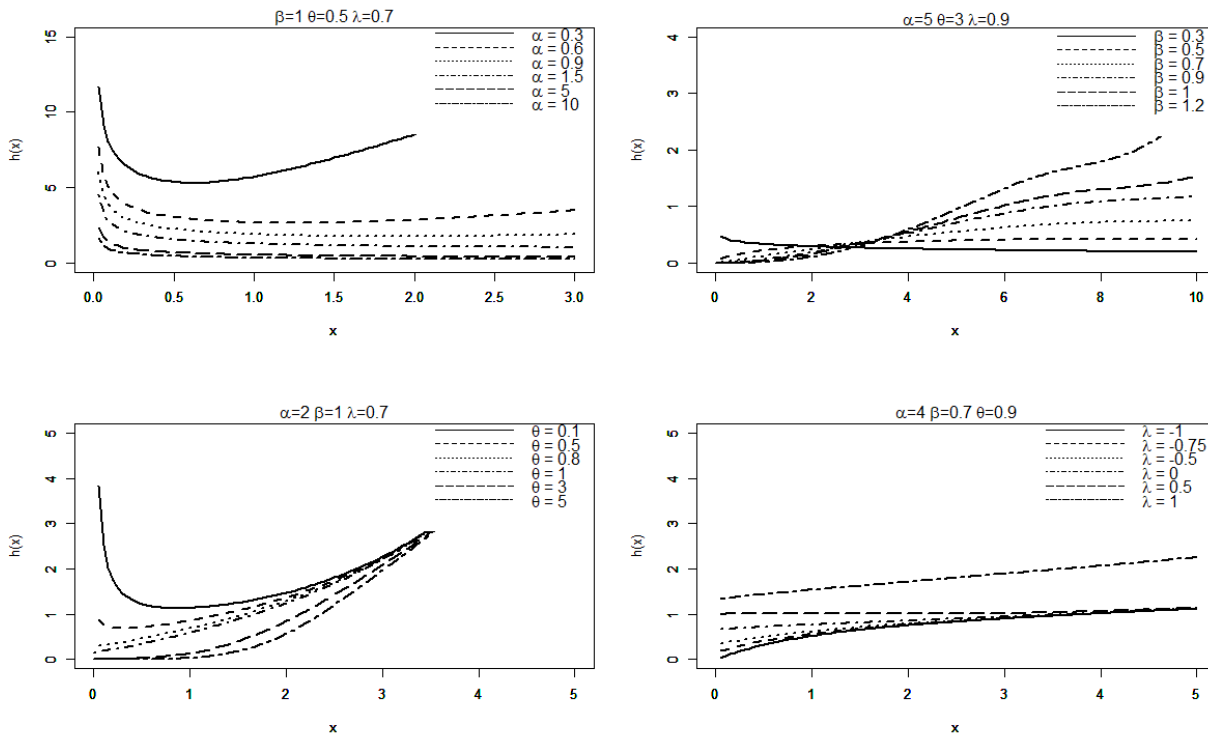


Figure 2. TCEP hazard functions

3. Maximum Likelihood Estimation and Asymtotic Confidence Intervals

Let X_1, X_2, \dots, X_n be the independent random variables having TCEP(δ) distribution. The log-likelihood function based on this sample is given by

$$\begin{aligned}\ell(\boldsymbol{\delta} | \mathbf{x}) = & n(1 + \log(\beta) + \log(\theta) - \beta \log(\alpha)) \\ & + (\beta - 1) \sum_{i=1}^n \log(x_i) + \sum_{i=1}^n \left(\frac{x_i}{\alpha}\right)^{\beta} - \sum_{i=1}^n \exp\left(\left(\frac{x_i}{\alpha}\right)^{\beta}\right) \\ & + \sum_{i=1}^n \log \left[\left(1 - \exp \left(1 - \exp \left\{ \left(\frac{x_i}{\alpha}\right)^{\beta} \right\} \right) \right)^{\theta-1} \left(1 + \lambda - 2\lambda \left(1 - \exp \left(1 - \exp \left\{ \left(\frac{x_i}{\alpha}\right)^{\beta} \right\} \right) \right)^{\theta} \right) \right]\end{aligned}\quad (16)$$

and associated gradients found to be

$$\begin{aligned}\frac{\partial \ell(\boldsymbol{\delta} | \mathbf{x})}{\partial \alpha} = & \frac{2\lambda\theta(\theta-1) \left[\sum_{i=1}^n \log(k(x, \alpha, \beta)) (k(x, \alpha, \beta))^{\theta} \right]}{k(x, \alpha, \beta)} \\ & + \frac{(\theta-1) \left(\frac{1}{2} + \frac{\lambda}{2} - \lambda (k(x, \alpha, \beta))^{\theta} \right) \beta \left(\frac{x_i}{\alpha} \right)^{\beta} \exp \left(\left(\frac{x_i}{\alpha} \right)^{\beta} \right) (1 - k(x, \alpha, \beta))}{k(x, \alpha, \beta)} \\ & + \frac{\beta}{\alpha} \left[\sum_{i=1}^n \left(\frac{x_i}{\alpha} \right)^{\beta} \exp \left(\left(\frac{x_i}{\alpha} \right)^{\beta} \right) + \left(n + \frac{\sum_{i=1}^n x_i}{\alpha} \right) \right]\end{aligned}\quad (17)$$

$$\begin{aligned}\frac{\partial \ell(\boldsymbol{\delta} | \mathbf{x})}{\partial \beta} = & \frac{n}{\beta} - n \log(\alpha) + \sum_{i=1}^n \log(x_i) + \left(\frac{\sum_{i=1}^n x_i}{\alpha} \right)^{\beta} \\ & + \log \left(\frac{\sum_{i=1}^n x_i}{\alpha} \right) - \sum_{i=1}^n \left(\frac{x_i}{\alpha} \right)^{\beta} \log \left(\frac{x_i}{\alpha} \right) \exp \left(\left(\frac{x_i}{\alpha} \right)^{\beta} \right) \\ & - 2\lambda\theta \sum_{i=1}^n \left(\frac{x_i}{\alpha} \right)^{\beta} \log(k(x, \alpha, \beta)) (k(x, \alpha, \beta))^{\theta} \\ & - \frac{(\theta-1) \left(\frac{1}{2} + \frac{\lambda}{2} - \lambda (k(x, \alpha, \beta))^{\theta} \right) \exp \left(\left(\frac{x_i}{\alpha} \right)^{\beta} \right) \log \left(\frac{x_i}{\alpha} \right)}{k(x, \alpha, \beta)}\end{aligned}\quad (18)$$

$$\frac{\partial \ell(\boldsymbol{\delta} | \mathbf{x})}{\partial \theta} = n \left(1 + \frac{1}{\theta} + \lambda \right) - 2\lambda \sum_{i=1}^n (k(x, \alpha, \beta))^{\theta} + 2\lambda(\theta+1) \log(k(x, \alpha, \beta)) (k(x, \alpha, \beta))^{\theta} \quad (19)$$

$$\frac{\partial \ell(\boldsymbol{\delta} | \mathbf{x})}{\partial \lambda} = \sum_{i=1}^n \log \left((k(x, \alpha, \beta))^{\theta-1} (1 - 2(k(x, \alpha, \beta))^{\theta}) \right), \quad (20)$$

where

$$k(x, \alpha, \beta) = 1 - \exp \left(1 - \exp \left(\left(\frac{x_i}{\alpha} \right)^{\beta} \right) \right).$$

The log-likelihood function $\ell(\boldsymbol{\delta} | \mathbf{x})$ can be maximized by using numerical methods such as Nelder-Mead. Let $\hat{\boldsymbol{\delta}}$ denote the MLEs of $\boldsymbol{\delta}$. Under some mild regularity conditions, one can write

$$\sqrt{n}(\hat{\boldsymbol{\delta}} - \boldsymbol{\delta}) \xrightarrow{d} N(\mathbf{0}, I^{-1}(\boldsymbol{\delta})),$$

where

$$I(\boldsymbol{\delta}) = \begin{pmatrix} -E\left[\frac{\ell^2(\boldsymbol{\delta}|\mathbf{x})}{\partial\alpha^2}\right] & -E\left[\frac{\ell^2(\boldsymbol{\delta}|\mathbf{x})}{\partial\alpha\partial\beta}\right] & -E\left[\frac{\ell^2(\boldsymbol{\delta}|\mathbf{x})}{\partial\alpha\partial\theta}\right] & -E\left[\frac{\ell^2(\boldsymbol{\delta}|\mathbf{x})}{\partial\alpha\partial\lambda}\right] \\ -E\left[\frac{\ell^2(\boldsymbol{\delta}|\mathbf{x})}{\partial\beta\partial\alpha}\right] & -E\left[\frac{\ell^2(\boldsymbol{\delta}|\mathbf{x})}{\partial\beta^2}\right] & -E\left[\frac{\ell^2(\boldsymbol{\delta}|\mathbf{x})}{\partial\beta\partial\theta}\right] & -E\left[\frac{\ell^2(\boldsymbol{\delta}|\mathbf{x})}{\partial\beta\partial\lambda}\right] \\ -E\left[\frac{\ell^2(\boldsymbol{\delta}|\mathbf{x})}{\partial\theta\partial\alpha}\right] & -E\left[\frac{\ell^2(\boldsymbol{\delta}|\mathbf{x})}{\partial\theta\partial\beta}\right] & -E\left[\frac{\ell^2(\boldsymbol{\delta}|\mathbf{x})}{\partial\theta^2}\right] & -E\left[\frac{\ell^2(\boldsymbol{\delta}|\mathbf{x})}{\partial\theta\partial\lambda}\right] \\ -E\left[\frac{\ell^2(\boldsymbol{\delta}|\mathbf{x})}{\partial\lambda\partial\alpha}\right] & -E\left[\frac{\ell^2(\boldsymbol{\delta}|\mathbf{x})}{\partial\lambda\partial\beta}\right] & -E\left[\frac{\ell^2(\boldsymbol{\delta}|\mathbf{x})}{\partial\lambda\partial\theta}\right] & -E\left[\frac{\ell^2(\boldsymbol{\delta}|\mathbf{x})}{\partial\lambda^2}\right] \end{pmatrix}$$

is expected Fisher information matrix. $I(\boldsymbol{\delta})$ can be approximated by $I(\hat{\boldsymbol{\delta}})$ which is observed Fisher Information Matrix. Using asymptotic normality of MLEs, we can write the approximate confidence intervals (CIs)

$$P\left(\hat{\delta}_i - z_{\frac{\eta}{2}}\sqrt{Var(\hat{\delta}_i)} < \delta_i < \hat{\delta}_i + z_{\frac{\eta}{2}}\sqrt{Var(\hat{\delta}_i)}\right) = 1 - \eta, i = 1, 2, 3, 4, \quad (21)$$

where $Var(\hat{\delta}_i)$ is (i, i) (diagonal) elements of $I^{-1}(\hat{\boldsymbol{\delta}})$, $\boldsymbol{\delta} = (\delta_1, \delta_2, \delta_3, \delta_4) = (\alpha, \beta, \theta, \lambda)$ and $\hat{\boldsymbol{\delta}} = (\hat{\delta}_1, \hat{\delta}_2, \hat{\delta}_3, \hat{\delta}_4) = (\hat{\alpha}, \hat{\beta}, \hat{\theta}, \hat{\lambda})$.

4. Simulation Study

In this section, Monte Carlo simulation study is performed in order to compare the performances of the MLEs of $\boldsymbol{\delta}$ according to MSE and bias. In the simulation study, the biases and MSEs of the MLEs are empirically estimated by 1000 trials. The sample sizes are fixed as 50, 100, 250, 500, 750, 1000, 5000 and four different parameter settings are considered. The bias and MSEs of MLEs are given in Table 1 while the average lengths (AL) and coverage probabilities (CPs) of MLEs for TCEP($\boldsymbol{\delta}$) are presented in Table 2.

According to Table 1, when the sample size increases, the MSEs and bias of MLEs decrease for all selected parameters settings. On the other hand, it is observed that the CPs of confidence intervals approach to nominal level 0.95 and AL of intervals decrease when the sample size increases for all the parameters.

Table 1. Biases and MSEs of MLEs for TCEP(δ) parameters

α	β	θ	λ	n	$\hat{\alpha}$		$\hat{\beta}$		$\hat{\theta}$		$\hat{\lambda}$	
					bias	MSE	bias	MSE	bias	MSE	bias	MSE
1	0.4	0.5	0.2	50	0.3767	1.0402	0.3563	0.3860	-0.0253	0.2618	-0.0370	0.2322
				100	0.3976	0.8813	0.2401	0.1978	-0.0832	0.0744	-0.0249	0.2307
				250	0.3694	0.8274	0.1470	0.0937	-0.0739	0.0341	-0.0100	0.1889
				500	0.2476	0.5415	0.0859	0.0469	-0.0439	0.0228	-0.0069	0.1152
				750	0.2005	0.3822	0.0658	0.0300	-0.0370	0.0162	0.0079	0.0865
				1000	0.1567	0.2944	0.0511	0.0230	-0.0282	0.0134	0.0051	0.0642
				5000	0.0505	0.0511	0.0134	0.0029	-0.01	0.0028	0.0103	0.0135
0.5	0.7	0.8	-0.5	50	0.1391	0.0696	0.8293	2.4541	-0.1237	0.2535	0.3079	0.3827
				100	0.0896	0.0455	0.4032	0.9083	-0.0723	0.1339	0.1925	0.2941
				250	0.0685	0.0234	0.1779	0.1976	-0.0784	0.0568	0.1264	0.2003
				500	0.0470	0.0133	0.1037	0.0778	-0.0561	0.0380	0.0778	0.1330
				750	0.0309	0.0067	0.0613	0.0322	-0.0463	0.0267	0.0360	0.0912
				1000	0.0265	0.0041	0.0485	0.0164	-0.0329	0.0211	0.0472	0.0707
				5000	0.0066	0.0005	0.0104	0.0013	-0.0187	0.0076	-0.0106	0.0193
0.2	0.3	0.4	0.3	50	0.1110	0.0909	0.2334	0.1456	-0.0536	0.1047	-0.0963	0.2066
				100	0.1124	0.0790	0.1472	0.0741	-0.0629	0.0434	-0.0715	0.2099
				250	0.1062	0.0651	0.0952	0.0368	-0.0554	0.0214	-0.0324	0.1345
				500	0.0781	0.0384	0.0620	0.0198	-0.0361	0.0137	0.0100	0.0784
				750	0.0547	0.0276	0.0422	0.0133	-0.0228	0.0106	-0.0018	0.0619
				1000	0.0429	0.0213	0.0322	0.0100	-0.0175	0.0088	-0.0072	0.0470
				5000	0.0122	0.0035	0.0089	0.0016	-0.0066	0.0019	0.0049	0.0092
0.3	0.5	0.6	-0.2	50	0.1157	0.0596	0.5440	0.8602	-0.0728	0.3321	0.1192	0.2737
				100	0.1124	0.0469	0.3407	0.3864	-0.1340	0.0768	0.0939	0.2586
				250	0.0714	0.0275	0.1523	0.1123	-0.0872	0.0386	0.0447	0.1833
				500	0.0391	0.0123	0.0766	0.0398	-0.0586	0.0207	0.0116	0.1166
				750	0.0265	0.0076	0.0480	0.0223	-0.0467	0.0145	-0.0163	0.0905
				1000	0.0241	0.0052	0.0400	0.0136	-0.0370	0.0108	0.0110	0.0700
				5000	0.0034	0.0007	0.0055	0.0013	-0.0048	0.0015	0.0024	0.0113

Table 2. ALs and CPs of approximate CIs for TCEP(δ) parameters

				α			β		θ		λ	
α	β	θ	λ	n	AL	CP	AL	CP	AL	CP	AL	CP
1	0.4	0.5	0.2	50	3.6072	0.6150	1.1817	0.5910	1.6266	0.6170	2.2592	0.8660
				100	3.5897	0.6340	1.0703	0.6690	1.0541	0.6820	1.9235	0.7900
				250	2.9860	0.6940	0.8319	0.7300	0.7323	0.7580	1.5404	0.7540
				500	2.3293	0.7470	0.6178	0.7910	0.5688	0.8090	1.2633	0.8190
				750	1.9973	0.7890	0.5281	0.8120	0.4747	0.8480	1.0483	0.8450
				1000	1.7505	0.8190	0.4572	0.8340	0.4230	0.8490	0.9403	0.8710
				5000	0.8132	0.9270	0.1954	0.9320	0.1990	0.9320	0.4342	0.9430
0.5	0.7	0.8	-0.5	50	0.9020	0.8130	2.7776	0.8280	2.1747	0.7710	2.3373	0.8520
				100	0.6988	0.8890	1.7721	0.8960	1.6363	0.8540	1.9090	0.8570
				250	0.5046	0.9410	1.0998	0.9630	1.0700	0.8890	1.5006	0.8550
				500	0.3435	0.9440	0.6911	0.9680	0.7879	0.9200	1.1748	0.8720
				750	0.2611	0.9560	0.4650	0.9730	0.6515	0.9210	0.9884	0.8540
				1000	0.2316	0.9620	0.4105	0.9790	0.5813	0.9300	0.9291	0.8820
				5000	0.0835	0.9510	0.1363	0.9610	0.2905	0.9130	0.4720	0.8800
0.2	0.3	0.4	0.3	50	1.0002	0.5600	0.6802	0.4830	1.0916	0.5180	2.1066	0.9210
				100	0.9593	0.5970	0.6419	0.5910	0.8196	0.6170	1.7801	0.8400
				250	0.7696	0.6350	0.5399	0.6640	0.5735	0.6890	1.3525	0.8000
				500	0.7097	0.6850	0.4583	0.7100	0.4927	0.7440	1.1476	0.8340
				750	0.5561	0.7170	0.3819	0.7590	0.4127	0.7880	0.9511	0.8190
				1000	0.4816	0.7400	0.3214	0.7780	0.3558	0.8000	0.8254	0.8440
				5000	0.2211	0.8890	0.1482	0.8910	0.1710	0.8920	0.3818	0.9150
0.3	0.5	0.6	-0.2	50	0.8327	0.6900	1.6557	0.6850	1.6997	0.6600	2.3687	0.8480
				100	0.7394	0.8030	1.3941	0.8130	1.0630	0.7440	1.9961	0.7930
				250	0.5439	0.9000	0.9379	0.9100	0.7644	0.8480	1.5755	0.8260
				500	0.3764	0.9370	0.5872	0.9440	0.5535	0.8870	1.2496	0.8800
				750	0.2855	0.9450	0.4248	0.9550	0.4371	0.8940	1.0186	0.8860
				1000	0.2587	0.9540	0.3786	0.9610	0.3810	0.9080	0.9058	0.9170
				5000	0.0984	0.9400	0.1330	0.9390	0.1500	0.9490	0.3973	0.9550

5. Real Data Analysis I

In this section, an application with real data is provided to compare the fitting ability of TCEP(δ) distribution with some lifetime distributions such as Complementary Exponential Power (CEP) [1], Log-Kumaraswamy (LKw) [9], Weibull and Exponentiated Exponential (EE) [10]. The pdfs of these distributions are given by

$$LKw: f(x) = \alpha\beta e^{-x} (1 - e^{-x})^{\alpha-1} \left[1 - (1 - e^{-x})^{\alpha} \right]^{\beta-1} I_{\mathbb{R}_+}(x)$$

$$Weibull: f(x) = \frac{\alpha}{\beta^{\alpha}} x^{\alpha-1} e^{-\left(\frac{x}{\beta}\right)^{\alpha}} I_{\mathbb{R}_+}(x)$$

$$EE: f(x) = \alpha\beta (1 - e^{-\beta x})^{\alpha-1} e^{-\beta x} I_{\mathbb{R}_+}(x)$$

where $\alpha, \beta > 0$ are parameters. We have considered the comparison criteria as the $-2 \times \log$ -likelihood value, Akaike's Information Criterion (AIC), Kolmogorov-Smirnov test statistics (KS) and its (p-value) as comparison criteria. The data related to the failure stresses of single carbon fibers (length 1mm) is considered in the analysis. Note that this data firstly analyzed by [11]. The MLEs and the selection criteria statistics are given in Table 3. Furthermore, Fig. 3 presents the fitted cdfs to real data.

Table 3. Selection criteria statistics and MLEs for carbon fibres data					
	Weibull	TCEP	LKw	EE	CEP
LogL	-71.0240	-69.9704	-72.0352	-73.7699	-70.0187
-2LogL	142.0479	139.9408	144.0705	147.5399	140.0375
AIC	146.0479	147.9408	148.0705	151.5399	146.0375
BIC	150.1340	156.1130	152.1566	155.6260	152.1666
CAIC	146.2701	148.7100	148.2927	151.7621	146.4903
HQIC	147.6359	151.1168	149.6585	153.1279	148.4195
K-S	0.0859	0.0576	0.0803	0.0967	0.0603
A*	0.3882	0.1521	0.4354	0.6913	0.1595
W*	0.0591	0.0212	0.0729	0.1067	0.0227
p-value(K-S)	0.7618	0.9859	0.8273	0.6261	0.9777
p-value (A*)	0.8598	0.9985	0.8124	0.5655	0.9978
p-value (W*)	0.8219	0.9961	0.7359	0.5545	0.9941
$\hat{\alpha}$	4.5752	4.0176	68.7284	114.5288	3.5979
$\hat{\beta}$	5.5930	1.5294	1.7687	1.2421	1.3105
$\hat{\theta}$	-	5.7577	-	-	7.5679
$\hat{\lambda}$	-	0.3693	-	-	-
LB for α	4.3507	1.9357	47.7744	15.5453	2.0178
LB for β	4.4972	0.0795	1.0788	1.0039	0.2921
LB for θ	-	-4.7440	-	-	-5.2705
LB for λ	-	-1.1059	-	-	-
UB for α	4.7998	6.0995	89.6825	213.5122	5.1779
UB for β	6.6887	2.9793	2.4587	1.4804	2.3290
UB for θ	-	16.2593	-	-	20.4064
UB for λ	-	1.8444	-	-	-
SE of $\hat{\alpha}$	0.1146	1.0622	10.6910	50.5027	0.8062
SE of $\hat{\beta}$	0.5591	0.7397	0.3520	0.1215	0.5196
SE of $\hat{\theta}$	-	5.3581	-	-	6.5503
SE of $\hat{\lambda}$	-	0.7526	-	-	-

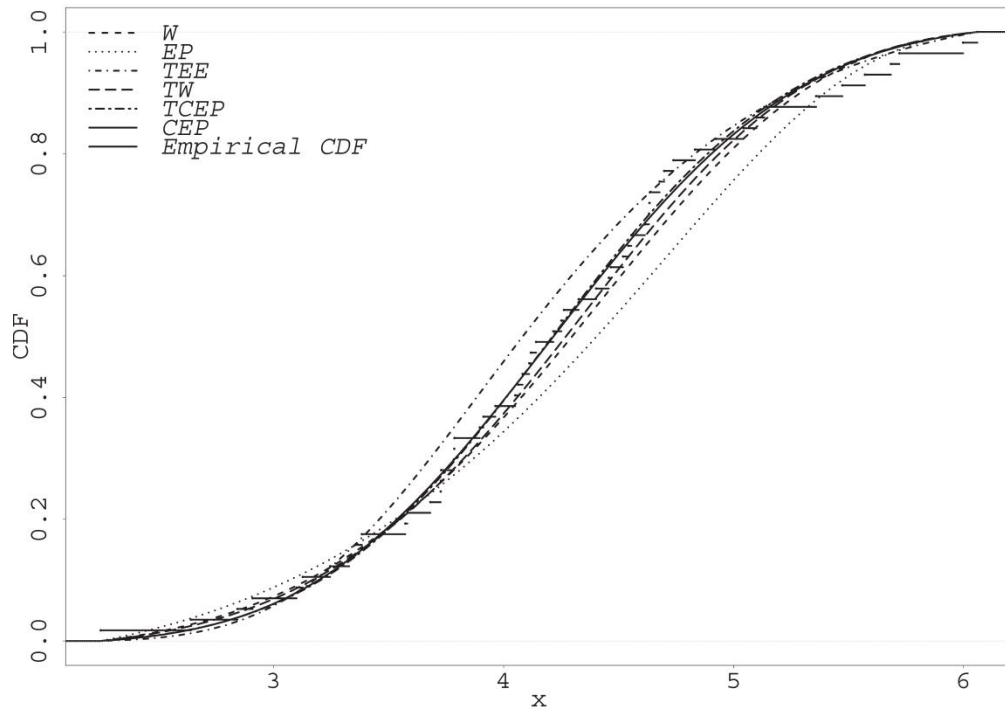


Figure 3. Fitted cdfs and empirical cdf for carbon fibres data

From Table 3 and Fig. 3, it can be said that the TCEP(δ) distribution is candidate to fitting the real data and it is competitor to the other existing models according to all criteria discussed here.

6. Real Data Analysis II

Let us consider lifetime regression analysis and let $Y = \log(X)$. Then cdf and pdf of Y is given by

$$F_1(y; \kappa) = (1 + \lambda) \left[1 - \exp \left(1 - \exp \left\{ \exp \left(\frac{y - \mu}{\sigma} \right) \right\} \right) \right]^\theta - \lambda \left[1 - \exp \left(1 - \exp \left\{ \exp \left(\frac{y - \mu}{\sigma} \right) \right\} \right) \right]^{2\theta}, \quad (22)$$

and

$$f_1(y; \tau) = \frac{\theta}{\sigma} \exp \left(\frac{y - \mu}{\sigma} \right) \exp \left(1 + \exp \left(\frac{y - \mu}{\sigma} \right) - \exp \left\{ \exp \left(\frac{y - \mu}{\sigma} \right) \right\} \right) \times \left[1 - \exp \left(1 - \exp \left\{ \exp \left(\frac{y - \mu}{\sigma} \right) \right\} \right) \right]^{\theta-1} \times \left[1 + \lambda - 2\lambda \left[1 - \exp \left(1 - \exp \left\{ \exp \left(\frac{y - \mu}{\sigma} \right) \right\} \right) \right]^\theta \right] I_{\mathbb{R}}(y) \quad (23)$$

where $\kappa_1 = (\mu, \sigma, \theta, \lambda)$ is parameter vector. Let $\mu = 0$ and $\sigma = 1$ in Eq. (22). Then, Eq. (22) is reduce to

$$F_1(z; \kappa) = (1 + \lambda) \left[1 - \exp \left(1 - \exp \left\{ \exp(z) \right\} \right) \right]^\theta - \lambda \left[1 - \exp \left(1 - \exp \left\{ \exp(z) \right\} \right) \right]^{2\theta}. \quad (24)$$

Let us consider regression model

$$\mathbf{Y} = \boldsymbol{\mu} + \sigma \mathbf{Z},$$

where $\mathbf{Y} = (Y_1, Y_2, \dots, Y_n)^T$ random vector and Y_1, Y_2, \dots, Y_n are iid random variables (they are also called dependent variables) with cdf (22). $\mathbf{Z} = (Z_1, Z_2, \dots, Z_n)^T$ is a random error vector and Z_1, Z_2, \dots, Z_n are iid random variables with cdf (24) and $\sigma > 0$. Assume that location is linked to covariates by $\boldsymbol{\mu} = \mathbf{X}\boldsymbol{\beta}$, where \mathbf{X} is $n \times (p+1)$ matrix consist of covariates (First coloumn is $\mathbf{1}$) and $\boldsymbol{\beta} = (\beta_0, \beta_1, \dots, \beta_p)^T$. Let $T_i = \min(Y_i, c_i)$ and c_i is censoring time for i th individual or any component. Then the log-likelihood function is written by

$$\ell(\boldsymbol{\kappa}) = \sum_{i=1}^n \left\{ \omega_i \log(f_1(t_i; \boldsymbol{\kappa})) + (1 - \omega_i) \log(1 - F_1(t_i; \boldsymbol{\kappa})) \right\}, \quad (25)$$

where ω_i is the indicator function given by

$$\omega_i = \begin{cases} 1 & , \quad t_i \leq c_i \\ 0 & , \quad t_i > c_i \end{cases}$$

Let us consider the data given in page 335 in [12]. [13] carried out an experiment and obtained a data on the lifetime of specimens of solid epoxy electrical-insulation in an accelerated voltage life test. 20 specimens were put on a life test at each of three voltage levels: 52.5, 55.0, and 57.5 kV. Failure times were measured in minutes. Six lifetimes of specimens are censored at a random. Based on the data, the log-likelihood (25) is maximized and the MLEs of parameters, AIC criteria are presented in Table 4 for TCEP regression. For a comparison Weibull and TLGBXII (see [14]) regression results are also given in Table 4. From the Table 4 and Fig. 4, it can be conclude that TCEP regression can be alternative lifetime regression analysis to Weibull and TLGBXII regression.

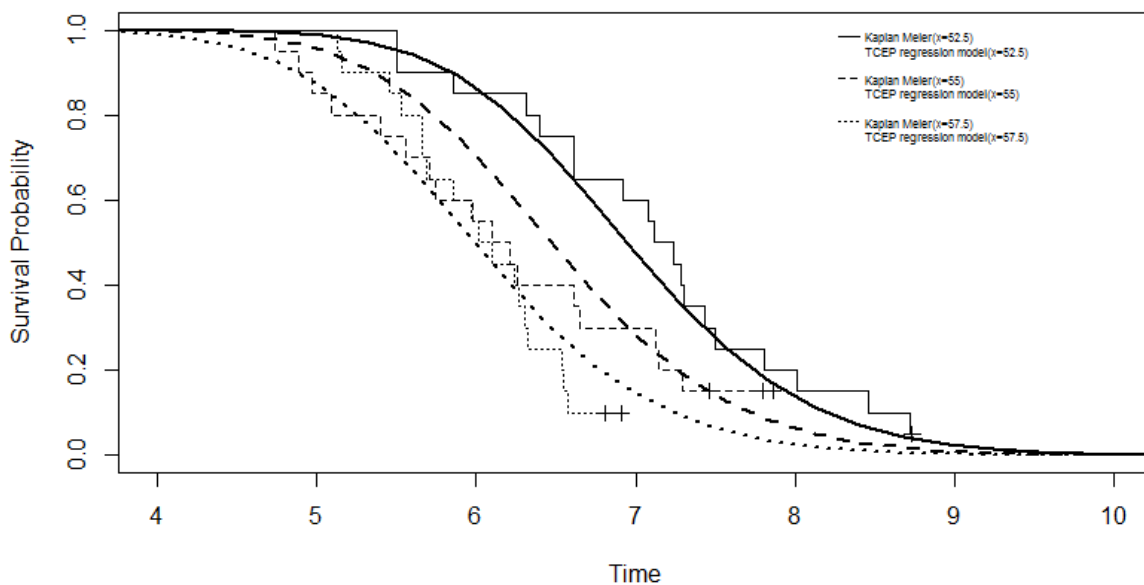


Figure 4. Fitted survival functions and the empirical survivals

Table 4. Lifetime regression analysis results: MLEs of the parameters, standard errors in second line, p-values in [·]) and the AIC statistics.

Model		θ	β	β_0	β_1	σ	$-\ell$	AIC
TCEP	$\lambda = 0.6184$	126.8443		11.3612	-0.19132	9.9420	78.3754	166.7
	0.5023	257.2796		6.6557 [0.0878]	0.0598 [0.0014]	5.8034		
TLGBXII	$\gamma = 0.6860$	7.7247	0.7089	14.4513	-0.1790	0.8024	78.2	168.4
	0.685	7.027	0.984	4.876	0.074	0.827		
Weibull				22.000	-0.274	0.845	83.7	173.4
				3.046	0.055	0.09		

In the lifetime regression analysis, 1000 initial parameters are generated uniformly and the best ten solutions (in the likelihood manner) are presented in Table 5. The estimates are treated MLEs which gives maximum likelihood. In Table 5, Method “1” indicates Nelder-Mead whereas Method “2” indicates BFGS.

Table 5. First 10 best solutions with initial values for TCEP regression

Trial	Method	$-\ell$	$\hat{\beta}_0$	$\hat{\beta}_1$	$\hat{\sigma}$	$\hat{\theta}$	$\hat{\lambda}$	se ($\hat{\beta}_0$)	se ($\hat{\beta}_1$)	se ($\hat{\sigma}$)	se ($\hat{\theta}$)	se ($\hat{\lambda}$)	$\beta_0^{(0)}$	$\beta_1^{(0)}$	$\sigma^{(0)}$	$\theta^{(0)}$	$\lambda^{(0)}$
359	1	-78.375	11.361	-0.191	9.942	126.844	0.619	6.656	0.060	5.803	257.279	0.502	26.936	-0.357	0.845	0.620	0.366
971	1	-78.455	12.328	-0.192	8.719	86.939	0.464	3.994	0.059	2.617	70.926	0.640	21.215	-0.225	0.840	0.894	0.685
262	2	-78.483	13.115	-0.198	8.318	72.457	0.509	4.963	0.059	3.688	101.625	0.570	27.251	-0.048	0.670	0.905	0.892
309	2	-78.494	13.225	-0.199	8.221	69.651	0.510	4.904	0.059	3.610	96.054	0.565	16.533	-0.096	1.146	0.541	0.103
631	2	-78.497	13.205	-0.198	8.216	69.078	0.517	4.868	0.059	3.579	93.937	0.556	15.586	-0.073	1.352	0.733	0.910
487	2	-78.513	12.499	-0.186	8.287	70.057	0.523	4.481	0.059	3.122	79.607	0.532	27.940	-0.330	1.276	0.640	0.161
727	2	-78.521	13.492	-0.200	8.003	63.720	0.509	4.872	0.059	3.541	87.711	0.558	22.355	-0.118	1.386	0.138	0.374
218	1	-78.528	12.926	-0.193	8.255	67.090	0.587	4.058	0.059	2.715	60.461	0.473	26.250	-0.356	0.991	0.727	0.879
781	2	-78.535	13.363	-0.197	7.946	61.167	0.521	4.547	0.059	3.182	73.457	0.541	19.195	0.260	1.329	0.730	0.276
890	1	-78.537	12.225	-0.196	8.658	102.473	0.090	4.362	0.085	2.547	138.953	3.308	23.208	-0.295	0.839	0.903	0.297

Conflicts of interest

There is no conflict of interest.

References

- [1] Barriga, G. D., Louzada-Neto, F., Cancho, V. G. The complementary exponential power lifetime model. *Computational Statistics and Data Analysis*, 55 (3) (2011) 1250-1259.
- [2] Smith, R. M., Bain, L. J. An exponential power life-testing distribution. *Communications in Statistics-Theory and Methods*, 4 (5) (1975) 469-481.
- [3] Shaw, W. T., Buckley, I. R. The alchemy of probability distributions: beyond Gram-Charlier expansions, and a skew-kurtotic-normal distribution from a rank transmutation map. (2009) *arXiv preprint arXiv:0901.0434*
- [4] Aryal, G. R. Transmuted log-logistic distribution. *Journal of Statistics Applications and Probability*, (2013), 2-1 11-20.
- [5] Aryal, G. R., Tsokos, C. P. Transmuted Weibull distribution: A generalization of the Weibull probability distribution. *European Journal of Pure and Applied Mathematics*, 4 (2) (2011) 89-102.
- [6] Khan, M. S., King, R., Hudson, I. L. Transmuted Kumaraswamy Distribution. *Statistics in Transition new series*, 17 (2) (2016) 183-210.

- [7] Merovci, F. Transmuted exponentiated exponential distribution. *Mathematical Sciences and Applications E-Notes*, 1-2, (2013) 112-122.
- [8] Gradshteyn, I., Ryzhik, I. M. Table of integrals, series, and products. Academic Press, San Diego, 6th edition, 2000.
- [9] Lemonte, A. J., Barreto-Souza, W., Cordeiro, G. M. The exponentiated Kumaraswamy distribution and its log-transform. *Brazilian Journal of Probability and Statistics*, 27-1, (2013) 31-53.
- [10] Gupta, R. D., Kundu, D. Exponentiated exponential family: an alternative to gamma and Weibull distributions. *Biometrical Journal: Journal of Mathematical Methods in Biosciences*, 43 (1) (2000) 117-130.
- [11] Crowder, M.J., Kimber, A.C., Smith, R.L. and Sweeting, T.J. The Statistical Analysis of Reliability Data. Chapman and Hall, London, 1991.
- [12] Lawless, J. F. Statistical models and methods for lifetime data (Vol. 362). John Wiley & Sons, 2011.
- [13] Yousof, H.M., Altun, E., Rasekhi, M., Alizadeh, M., Hamedani G. G., Ali, M.M. A new lifetime model with regression models, characterizations and applications. *Communications in Statistics - Simulation and Computation*, 48(1), (2019) 264-286.

Spectroscopy of a chemically peculiar δ Scuti-type star: 60 Tau

Filiz KAHRAMAN ALIÇAVUŞ^{1,2} 

¹Çanakkale Onsekiz Mart University, Faculty of Sciences and Arts, Physics Department, 17100, Çanakkale/Turkey

²Nicolaus Copernicus Astronomical Center, Bartycka 18, PL-00-716 Warsaw/Poland

Abstract

In this study, a detailed spectroscopic analysis of 60 Tau is presented. 60 Tau is known to be a metallic-line (Am) star which exhibit δ Scuti-type pulsations. The pulsation mechanism of the δ Scuti stars have been thought to be well understood and it was also suggested that metallic-line stars did not exhibit pulsations. However, in recent studies, particularly after *Kepler* and *TESS* data have been released, many metallic-line δ Scuti stars have been found and it turned out that the current pulsation mechanism of δ Scuti stars including the metallic-line ones has not completely understood. Therefore, to make a reliable investigation for the driving mechanism of the δ Scuti variables, we need to know precise fundamental stellar (mass, radius) and atmospheric (T_{eff} , $\log g$, ξ) parameters of these variables. Hence in this study, the atmospheric parameters, projected rotational velocity and the chemical abundances of 60 Tau were obtained by using the high-resolution and high signal-to-noise spectra. The position of the star is shown in the H-R diagram and the δ Scuti instability strip using the Gaia luminosity.

Article info

History:

Received:06.01.2020

Accepted:24.05.2020

Keywords:

Stars, chemically peculiar, spectroscopy, atmospheric parameters.

1. Introduction

Interior structures of stellar systems can be deeply investigated by using asteroseismology. Asteroseismology is a method which uses the stellar oscillations to probe the stellar interior structure [1]. There are many pulsating variables located in different parts of the Hertzsprung-Russell (H-R) diagram. These variables are the main targets of asteroseismology and they allow us to examine stars in different evolutionary stages.

The δ Scuti stars are one of the most known targets of asteroseismology. These variables exhibit radial, non-radial pressure, gravity and mixed-mode pulsations which are believed to be driven by the κ mechanism [1]. Pulsation frequency of the δ Scuti stars mostly ranges from 5 to 50 d⁻¹ [2], but it was shown that most δ Scuti stars also exhibit low-frequency regime [3]. δ Scuti-type variations can be found in chemically normal and peculiar stars. There are many δ Scuti stars which exhibit chemical peculiarities in their atmospheres. However, previously it was thought that chemically peculiar stars did not oscillate [4, 5] but recent discoveries showed that those stars can also pulsate [6, 7].

Chemically peculiar stars have a spectral type ranging from late-B to early-F and they show atmospheric chemical abundance different than solar. The chemically peculiar stars are divided into different groups by taking into account their magnetic field strength and weak or strong absorption lines [8]. Among these chemically peculiar stars, there are metallic-line (Am) stars. These stars show weak CaK lines, rich iron-peak elements and also weak magnetic field [9, 10]. Am stars can be easily distinguished by a spectral classification. In their spectral classifications, we define earlier spectral type from CaK lines relative to hydrogen and metal lines. Considering the difference of spectral types between CaK and metal lines, Am stars are classified as classical and marginal Am stars. If the spectral-type from CaK and metal lines differ at least five subtypes, these Am stars are defined as classical Am stars, while others are called to be marginal Am stars.

Am stars are mostly a member of short-period binary systems [11,12]. They are also known to be slow rotators. It is thought that the reason for slow rotation is the effect of the binarity. However, it was shown that there are some single Am stars which probably was born originally as slowly rotating stars [13, 14].

*Corresponding author. Email address: filizkahraman01@gmail.com

<http://dergipark.gov.tr/csj> ©2020 Faculty of Science, Sivas Cumhuriyet University

60 Tau (HD 2728, $V=5.71$ mag) is known as a δ Scuti-type Am star. This object was classified to be a classical Am star by [15] and its δ Scuti-type pulsations were first found by [16] during the photometric observations of the Hyades. A detailed photometric study for 60 Tau was given by [17]. In this study, five nights photometric observations of the star are presented. As a result, [17] found two pulsation frequencies of 13.0364 and 11.8521 d^{-1} . The star is also a single-lined spectroscopic binary. For years, lots of radial velocity measurements of the system were done [11, 18, 19]. The last radial velocity measurements and analysis were given by [20]. In this analysis, orbital parameters (such as orbital period, periastron passage time) of the system were determined.

60 Tau has a spectroscopic study [21] in which atmospheric parameters of the system were obtained. However, to understand the real pulsation mechanism occurring in the pulsating Am stars, a more detailed spectroscopic study with higher-resolution spectra is needed. Therefore in this study, I focus on the detailed spectroscopic analysis of a metallic-line (Am) δ Scuti pulsator. The study is organised as follows. Information about the spectroscopic data is given in Sect.2.1. The spectral classification is presented in Sect.2.2. The details about the spectroscopic study are given in Sect.2.3. Consequently, the results and discussions are introduced in Sect. 3.

2. Materials and Methods

2.1. Observational data

There are five public spectra of 60 Tau in archives. One HARPS spectrum is available in the European Southern Observatory (ESO) archive (<http://archive.eso.org>). HARPS is an échelle spectrograph mounted on the 3.6-m telescope at ESO (La Silla, Chile). It has a resolving power of 115000 and supplies spectra with a wavelength range of about 378 – 690 nm [22]. There is also one SOPHIE spectrum of 60 Tau. SOPHIE is an échelle spectrograph attached on the 1.93-m telescope at the Haute-Provence Observatory (OHP, France). The system offers spectra with two different resolving powers of 39000 and 75000 in a wavelength range of 380 – 680 nm [23]. The SOPHIE spectrum of 60 Tau was taken with 39000 resolving power. 60 Tau also has three ELODIE spectra. ELODIE is an échelle spectrograph installed on the 1.93-m telescope at the OHP (France). ELODIE supplies a resolving power of 42000 with a spectral window of 385 – 680 nm [24]. The information for the instruments and the spectra are given in Table 1. All available spectra of 60 Tau were reduced by the dedicated pipelines for each spectrograph. They were normalized manually by using the IRAF *continuum* task [25].

Table 1. Information for the spectroscopic data.

Instrument	Observation dates	Number of spectra	S/N ratio
ELODIE	October, 2003,	3	150
	October, 2004,		220
	September, 2005		100
HARPS	December, 2014	1	160
SOPHIE	October, 2006	1	350

2.2. Spectral classification

The spectral classification is an easy way to estimate the initial information for the atmospheric parameters (such as effective temperature T_{eff} , surface gravity $\log g$) and chemical anomalies in stars' atmosphere. To obtain this information for a star, even a low-resolution spectrum is enough. In the spectral classification, the spectra of observed stars are compared with the spectra of spectral classification standard stars. During this comparison, depending on the searching spectral type (e.g. A0, F0), there are a few important lines which should be checked [26].

As 60 Tau is a δ Scuti star, it should have a spectral type of A – F. Therefore, A – F type spectral type standard stars [27] were used and they were compared with all available spectra of 60 Tau. Detailed information about spectral classification can be found in the study of [28].

During the comparison, three different line groups, CaK, hydrogen and metal lines in the wavelength range of $\sim 380 - 450$ nm, were taken into account. The spectral types determined from these lines should agree with each

other for a chemically normal star. If a star is a metallic-line star as suggested for 60 Tau, these lines give different spectral types, especially there should be a significant difference between the determined spectral types from CaK and metal lines. By applying this analysis, I determined the spectral and luminosity type of 60 Tau to be kA5hF0mF0IV. This classification shows that the spectral type from CaK lines (k) is A5 while the spectral type from hydrogen (h) and metal (m) lines is F0. This result confirms the Am feature of 60 Tau. The obtained spectral classification slightly differs than the literature A3m classification [21].

2.2. Determination of the atmospheric parameters

The atmospheric parameters (T_{eff} , $\log g$ and microturbulence ξ) of the star were determined using the hydrogen and metal lines. In the spectroscopic analysis, the spectrum synthesis method was used and the final parameters were derived considering the minimum difference between the synthetic and observed spectra.

Before starting to spectroscopic analysis, to have initial information about the atmospheric parameters, uvby β colors and the spectral energy distribution (SED) of the star were used. First, the uvby β colors were taken from [29]. The T_{eff} and $\log g$ parameters were calculated from uvby β using the method of [30]. During the analysis, E(b-y) value was obtained as 0.0 mag. The interstellar reddening E(B-V) value was also calculated taking into account the galactic coordinates and Gaia parallax [31] of 60 Tau. In the calculation, the galactic extinction maps published in [32] was used. As a result, E(B-V) was determined as 0.0 mag.

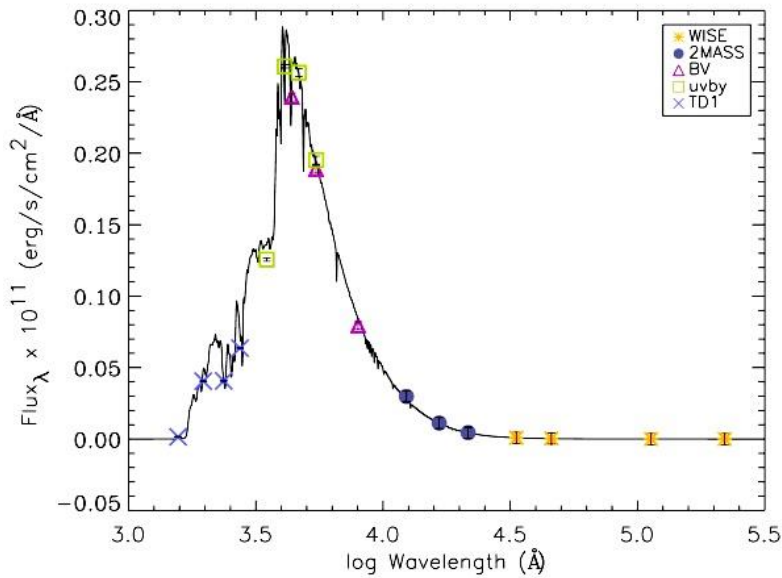


Figure 1. SED fit for 60 Tau.

The SED was constructed by using the E(B-V), Johnson [33], 2MASS [34], uvby β [29], the Ultraviolet Sky Survey Telescope (TD1) [35, 36] and the Wide-field Infrared Survey (WISE) [37] colors. In the analysis, the Kurucz model fluxes [38] were used. The final SED T_{eff} was determined considering the minimum difference between the model and color fluxes. During the calculation, $\log g$ and metallicity values were fixed as 4.0 and solar, respectively. The SED fit for 60 Tau is illustrated in Fig. 1. The T_{eff} values calculated from the SED analysis and uvby β colors are given in Table 2.

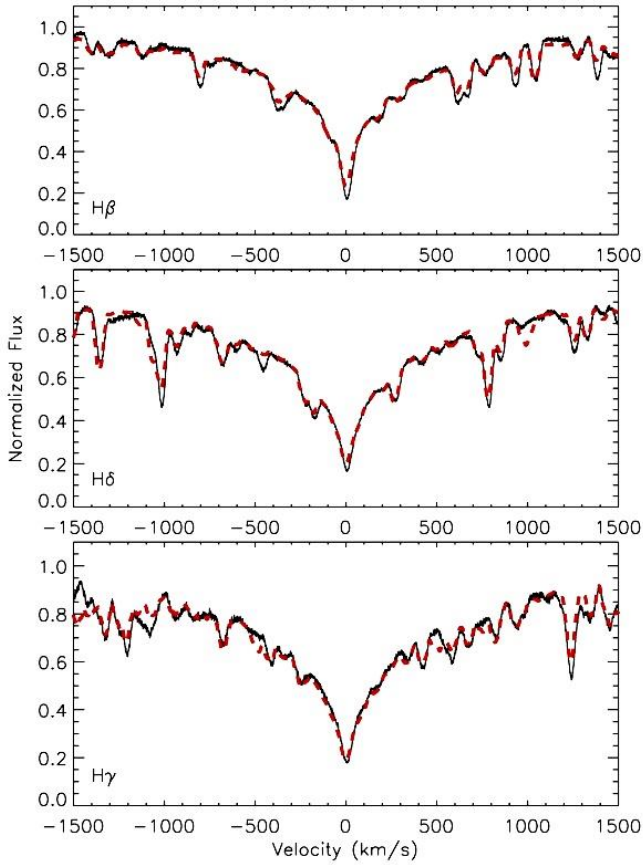


Figure 2. Theoretical hydrogen lines (red dashed) fit to the observed hydrogen (black solid) lines.

After the initial atmospheric parameters were estimated, these values were used as input in the spectroscopic analysis. First, hydrogen lines were taken into account to derive T_{eff} value of 60 Tau. Hydrogen lines are very sensitive to T_{eff} and less sensitive to $\log g$ for the stars which have T_{eff} lower than 8000 K [12]. Therefore, hydrogen lines, H_{β} , H_{γ} and H_{δ} were only used to determine T_{eff} and in this analysis $\log g$ was fixed to be 4.0. In the hydrogen lines analysis and the further spectroscopic analysis, ATLAS9 model atmospheres [38] and SYNTHE code [39] were used. The hydrogen T_{eff} values were determined using the minimization method described by [40]. The theoretical hydrogen lines fit to the observed ones (for HARPS spectrum) are demonstrated in Fig. 2 and the resulting hydrogen T_{eff} value is given in Table 2. The errors in T_{eff} was estimated using the same method given in [41].

Table 2. Resulting atmospheric parameters, projected rotational velocity and iron abundance.

Parameters	Value
$T_{\text{eff}}^{\text{uvby}}$ (K)	7285 ± 220
$\log g_{\text{uvby}}$ (K)	4.08 ± 0.20
$T_{\text{eff}}^{\text{SED}}$ (K)	7190 ± 230
$T_{\text{eff}}^{\text{Hydrogen}}$ (K)	7100 ± 200
$T_{\text{eff}}^{\text{final}}$ (K)	7000 ± 100
$\log g_{\text{final}}$	4.10 ± 0.10
ξ (km/s)	2.4 ± 0.1
V_{ini} (km/s)	32 ± 1
Fe/H (dex)	7.73 ± 0.18

The final atmospheric parameters were determined depending on the excitation and ionization equilibrium of metal lines. In this analysis, iron (Fe) lines were used because they are more abundant for the searching T_{eff} value ($\sim 6800 - 7400$ K). Therefore, all available Fe lines (~ 200 lines) in the HARPS spectrum were taken into

account. I used the HARPS spectrum in the analysis because it has a higher resolving power. Higher-resolution spectra are more useful in the analysis of slowly rotating stars and from the literature, it is known that 60 Tau is a slowly rotating star [~ 31 km/s, 21].

To determine the final atmospheric parameters the method explained in the study of [41] was used. The uncertainties in the obtained atmospheric parameters were also estimated by the same method given in the same study. The obtained final atmospheric parameters and their errors are listed in Table 2.

After accurate atmospheric parameters were determined, the atmospheric chemical abundances of 60 Tau was be obtained. Taking into account the final atmospheric parameters as input, chemical abundances of individual elements were determined using the spectrum synthesis method explained in [41]. In the analysis individual lines and very narrow spectral windows (~ 0.5 nm) were analysed and the chemical abundances of individual elements and the projected rotational velocity ($V \sin i$) were obtained. The resulting abundances and $V \sin i$ parameter were obtained considering the average values. The $V \sin i$ value and Fe abundance are given in Table 2, while the abundances of the individual elements are listed in Table 3. The uncertainties in the abundances were calculated using the same method presented by [41]. The theoretical fits obtained in the abundance analysis are compared with the observed ones in Fig. 3.

Table 3. Chemical abundances of individual elements.

Symbol of the elements	Abundance (dex)	Number of the analyzed spectral parts
C	8.13 ± 0.10	3
Na	6.63 ± 0.14	4
Mg	7.76 ± 0.24	8
Si	7.25 ± 0.44	20
S	7.85 ± 0.26	2
Ca	5.86 ± 0.26	19
Sc	2.45 ± 0.20	4
Ti	5.06 ± 0.35	54
V	4.40 ± 0.45	13
Cr	6.04 ± 0.27	53
Mn	5.52 ± 0.17	21
Fe	7.73 ± 0.18	186
Co	5.39 ± 0.24	6
Ni	6.72 ± 0.17	58
Cu	4.44 ± 0.27	2
Zn	4.63 ± 0.25	1
Sr	3.28 ± 0.49	4
Y	3.11 ± 0.25	11
Zr	3.30 ± 0.25	5
Ba	3.61 ± 0.30	2
La	1.72 ± 0.50	3
Ce	2.48 ± 0.20	8
Pr	1.24 ± 0.10	3
Nd	1.89 ± 0.26	6
Eu	1.35 ± 0.27	1
Gd	2.50 ± 0.35	1
Dy	1.72 ± 0.30	1

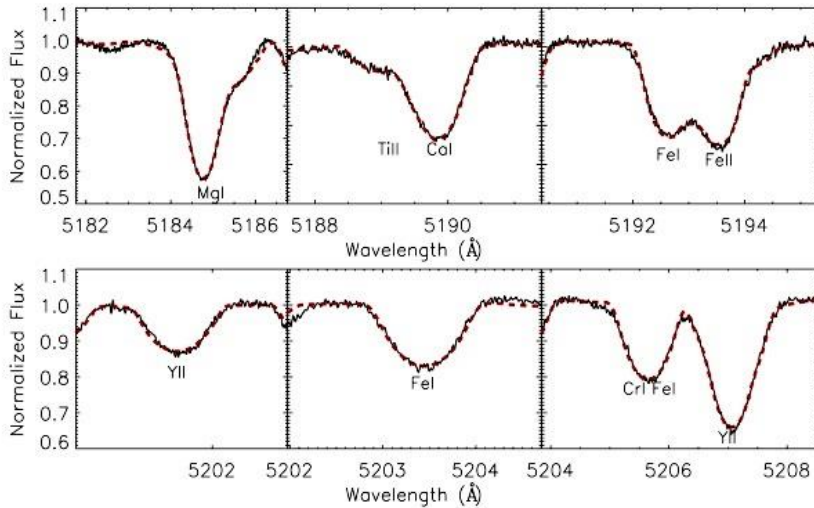


Figure 3. Comparison the theoretical lines fits (red dashed) with the observed (black solid) lines.

3. Results and Discussion

60 Tau was previously classified to be a metallic-line star and its spectral type was given as A3m [21]. According to the result of the spectral classification presented in this study, the star has a spectral type of kA5hF0mF0IV. This result confirms the Am feature of the star. However, this classification is slightly different than the previous one.

To precisely confirm the Am feature of 60 Tau, a detailed spectroscopic analysis was carried out. First, the atmospheric parameters were derived and they were found to be consistent with the spectral classification. The chemical abundances were obtained as well. The chemical abundance distribution for 60 Tau is given in Fig. 4. The Am stars exhibit overabundant iron-peak elements and some heavy elements such as Zn, Sr and Ba. Additionally, they typically show underabundant Ca and Sc [26]. According to this definition and the chemical abundance distribution of 60 Tau, Am feature of the star is confirmed.

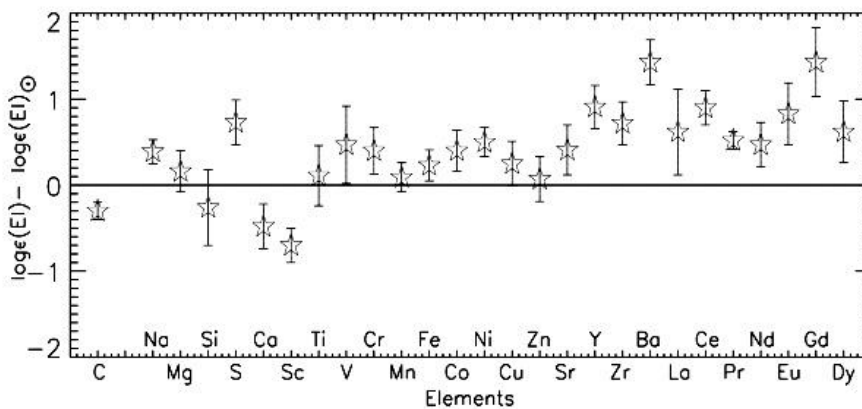


Figure 4. Chemical abundance distribution of 60 Tau relative to solar abundance [42].

In the literature, there is a spectroscopic study of 60 Tau [21]. In this study, the atmospheric parameters and $V \sin i$ parameters are given. While T_{eff} , $\log g$ and $V \sin i$ values are consistent with the results obtained in the current study within error, the ξ value differs around 1.3 km/s. This is probably the effect of the resolving power of the used instruments. In the present study, a higher resolution spectrum ($R \sim 115000$) was used and for such slowly-rotating stars, higher resolution spectra are more suitable to be used in a comprehensive spectroscopic analysis.

The position of the star in the δ Scuti instability strip was found. The Gaia luminosity of 60 Tau was calculated using the bolometric corrections for the star's T_{eff} value [43], Gaia parallax [31] and extinction coefficient. As a result, the location of the star in the H-R diagram and in the δ Scuti instability strip is demonstrated in Fig. 5. [44] found that pulsating Am stars mostly confine a specific area in the H-R diagram and 60 Tau is also found in this region.

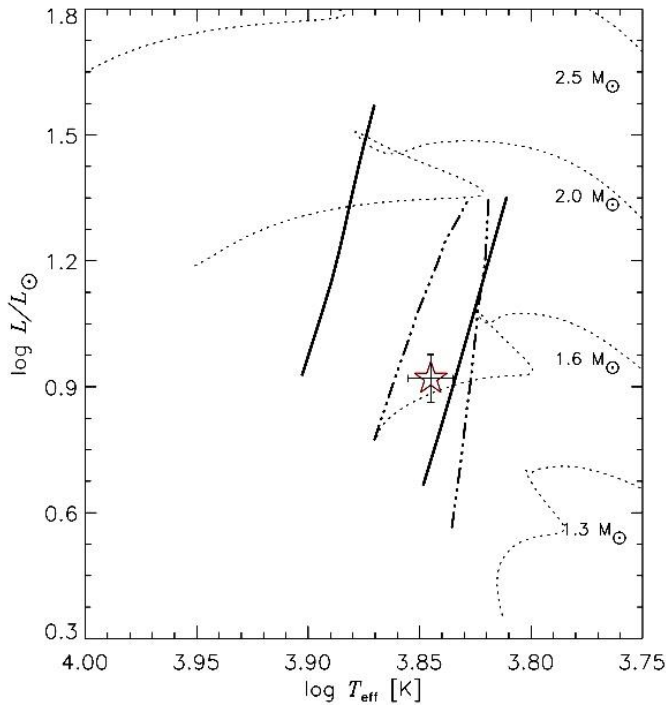


Figure 5. The position of 60 Tau in the H-R diagram. Solid and dashed-pointed lines represent the δ Scuti and γ Doradus instability strips [45], respectively. The evolutionary tracks (dotted lines) were taken from [41].

In this study, the Am characteristic of 60 Tau was confirmed with a comprehensive spectroscopic study. An updated spectral classification of the system was obtained. The T_{eff} , $\log g$, ξ and $V \sin i$ parameters were derived and the star was found to be a slowly-rotating object as expected for the Am stars. The obtained chemical abundance distribution of 60 Tau also exhibit a typical Am feature.

The current pulsation mechanism in the δ Scuti stars unfortunately is not completely understood. Especially, the driving mechanism in the pulsating chemically peculiar stars is needed more explanations. Therefore, accurate fundamental stellar and atmospheric parameters of this kind of objects are needed. This study will supply good input data for the future theoretical studies to understand the available pulsation mechanism in the normal and chemically peculiar δ Scuti stars.

Acknowledgment

I thank the Polish National Center for Science (NCN) for supporting the study through grant 2015/18/A/ST9/00578. The calculations have been carried out in Wrocław Centre for Networking and Supercomputing (<http://www.wcss.pl>), grant No. 214. This research has made use of the SIMBAD database, operated at CDS, Strasbourg, France. The study has been carried out based on observations made with ESO Telescopes at the La Silla Paranal Observatory under programme ID 094.D-0596. This work has made use of data from the European Space Agency (ESA) mission Gaia (<http://www.cosmos.esa.int/gaia>), processed by the Gaia Data Processing and Analysis Consortium (DPAC, <http://www.cosmos.esa.int/web/gaia/dpac/consortium>).

Conflicts of interest

The author states that did not have conflict of interests.

References

- [1] Aerts C., Christensen-Dalsgaard J. And Kurtz D. W., *Asteroseismology*, 10th ed., Berlin, Springer, 2010; pp 50 – 52.
- [2] Chang S. -W., Protopapas P., Kim D. -W. and Byun Y. -I., Statistical Properties of Galactic δ Scuti Stars: Revisited, *The Astronomical Journal*, 145 (2013) 132 – 142.
- [3] Balona L. A., Catanzaro G., Abedigamba O. P., Ripepi V. and Smalley B., Spots on Am stars, *Monthly Notices of the Royal Astronomical Society*, 448 (2015) 1378 – 1388.
- [4] Breger M., Metallic-Line a Stars and Pulsation, *Astrophysical Journal*, 162 (1970) 597 – 604.
- [5] Kurtz D. W., Metallicity and pulsation: an analysis of the Delta Delphini stars, *Astrophysical Journal*, 32 (1976) 651 – 680.
- [6] Bowman D. M., Buysschaert B., Neiner C., Pápics P. I., Oksala M. E. and Aerts C., K2 space photometry reveals rotational modulation and stellar pulsations in chemically peculiar A and B stars, *Astronomy and Astrophysics*, 616 (2018) 1 – 40.
- [7] Nemec J. M., Balona L. A., Murphy S. J., Kinemuchi K. and Jeon Y.-B., Metal-rich SX Phe stars in the Kepler field, *Monthly Notices of the Royal Astronomical Society*, 466 (2017) 1290 – 1329.
- [8] Preston G. W., the chemically peculiar stars of the upper main sequence, *Annual Rev. Astron. Astrophys.*, 12 (1974) 257 – 277.
- [9] Roman N. G., Morgan W. W. and Eggen O. J., The Classification of the Metallic-Line Stars, *Astrophysical Journal*, 107 (1948) 107 – 109.
- [10] Titus J., Morgan W. W., On the Classification of the Stars. I. The Spectral Types of the Brighter Members of the Hyades Cluster, *Astrophysical Journal*, 92 (1940) 256 – 261.
- [11] Abt H. A., The Frequency of Binaries among Metallic-Line Stars, *Astrophysical Journal Supplement*, 6 (1961) 37 – 76.
- [12] Smalley B., Observations of convection in A-type stars, The A-Star Puzzle, held in Poprad, Slovakia, Cambridge, Cambridge University Press, 2004; pp 131 – 138.
- [13] Balona A., Pulsation frequency distribution in δ Scuti stars, *Monthly Notices of the Royal Astronomical Society*, 452 (2015) 3073 – 3084.
- [14] Smalley B., Southworth J., Pintado O. I., Gillon M., Holdsworth D. L., Anderson D. R., Barros S. C., Collier Cameron A., Delrez L., Faedi F., Haswell C. A., Hellier C., Horne K., Jehin E., Maxted P. F. L., Norton A. J., Pollacco D., Skillen I., Smith A. M. S., West R. G., Wheatley P. J., Eclipsing Am binary systems in the SuperWASP survey, *Astronomy & Astrophysics*, 564 (2014) 20 – 32.
- [15] Kurtz D. W., Metallicity and pulsation: the marginal metallic line stars, *Astrophysical Journal*, 21 (1978) 869 – 880.
- [16] Horan S., A photometric survey of the Hyades for delta Scuti variables, *Astronomical Journal*, 84 (1979)

1770 – 1774.

- [17] Zhiping L., Pulsation behavior of classical Am star 60 Tauri, *Astronomy and Astrophysics*, 360 (2000) 185 – 188.
- [18] Margoni R., Munari U. and Stagni R., Spectroscopic orbits of AM stars. I. Seven field stars, *Astronomy and Astrophysics*, 93 (1992) 545 – 552.
- [19] Plaskett J. S., Harper W. E. and Young R. K., Fourth list of spectroscopic binaries, *Journal of the Royal Astronomical Society of Canada*, 13 (1919) 372 – 378.
- [20] Griffin R. F., Photoelectric Radial Velocities, Paper XVIII Spectroscopic Orbits for Another 52 Binaries in the Hyades Field, *Journal of Astrophysics and Astronomy*, 33 (2012) 29 – 200.
- [21] Gebran M., Vick M., Monier R. and Fossati L., Chemical composition of A and F dwarfs members of the Hyades open cluster, *Astronomy and Astrophysics*, 523 (2010) 13 – 29.
- [22] Mayor M., Pepe F., Queloz D., Bouchy F., Rupprecht G., Lo Curto, G., Avila, G., Benz, W., Bertaux, J. -L., Bonfils X., Dall Th., Dekker H., Delabre B., Eckert W., Fleury M., Gilliotte A., Gojak D., Guzman J. C., Kohler D., Lizon J. -L., Longinotti A., Lovis C., Megevand D., Pasquini L., Reyes J., Sivan J. -P., Sosnowska D., Soto R., Udry S., van Kesteren A., Weber L., Weilenmann U., Setting new standards with HARPS, *The messenger*, 114 (2003), 20 – 24.
- [23] Perruchot S., Bouchy F., Chazelas B., Díaz R. F., Hébrard G., Arnaud K., Arnold L., Avila G., Delfosse X., Boisse I., Moreaux G., Pepe F., Richaud Y., Santerne A., Sottile R., Tézier D., Higher-precision radial velocity measurements with the SOPHIE spectrograph using octagonal-section fibers, *Proceedings of the SPIE*, 8151 (2011) 1 – 12.
- [24] Moultağa J., Ilovaisky S. A., Prugniel P., Soubiran C., ELODIE-SOPHIE: Spectroscopic archive. SF2A-2004: Semaine de l'Astrophysique Française, meeting held in Paris, France, June 14-18, 2004. Edited by F. Combes, D. Barret, T. Contini, F. eynadier and L. Pagani. Published by EdP-Sciences, Conference Series.
- [25] Tody D., The IRAF data reduction and analysis system, *IN: Instrumentation in astronomy*, 627 (1986) 733 – 753.
- [26] Gray R. O., Corbally C. J., *Stellar Spectral Classification*, Princeton University Press, 2009; pp 120-140.
- [27] Gray R. O., Corbally C. J., Garrison R. F., McFadden M. T. and Robinson P. E., Contributions to the Nearby stars (NStars) Project: Spectroscopy of Stars Earlier than M0 within 40 Parsecs: The Northern Sample. I., *The Astronomical Journal*, 126 (2003) 2048 – 2059.
- [28] Kahraman Aliçavuş F., Niemczura E., Polińska M., Helminiak K. G., Lampens P., Molenda-Żakowicz J., Ukita N., Kambe E., High-resolution spectroscopy and abundance analysis of δ Scuti stars near the γ Doradus instability strip, *Monthly Notices of the Royal Astronomical Society*, 470 (2017) 4408 – 4420.
- [29] Paunzen E., A new catalogue of Strömgren-Crawford uvby β photometry, *Astronomy and Astrophysics*, 580 (2015) 23 – 25.
- [30] Moon T. T., Dworetzky M. M., Grids for the determination of effective temperature and surface gravity of B, A and F stars using uvbybeta photometry, *Monthly Notices of the Royal Astronomical Society*, 217 (1985) 305 – 315.
- [31] Gaia Collaboration, Brown A. G. A., Vallenari A. et al., Gaia Data Release 2. Summary of the contents and survey properties, *Astronomy and Astrophysics*, 616 (2018) 1 – 22.
- [32] Amores E. B., Lepine J. R. D., Models for Interstellar Extinction in the Galaxy, *The Astronomical Journal*,

130 (3005) 659 - 673.

- [33] Röser S., Schilbach E., Piskunov A. E., Kharchenko N. V., Scholz R. -D., A deep all-sky census of the Hyades, *Astronomy and Astrophysics*, 531 (2011) 92 – 104.
- [34] Cutri R. M., Skrutskie M. F., van Dyk S., et al., 2MASS All Sky Catalog of point sources, The IRSA 2MASS All-Sky Point Source Catalog, NASA/IPAC, 2003.
- [35] Boksenberg A., Evans R. G., Fowler R. G., Gardner I. S. K., Houziaux L., Humphries C. M., Jamar C., Macau D., Malaise D., Monfils A., Nandy K., Thompson G. I., Wilson R., Wroe H., The ultra-violet sky-survey telescope in the TD-1A satellite, *Monthly Notices of the Royal Astronomical Society*, 163 (1973) 291 – 332.
- [36] Thompson G. I., Nandy K., Jamar C., Monfils A., Houziaux L., Carnochan D. J., Wilson R., Catalogue of stellar ultraviolet fluxes : a compilation of absolute stellar fluxes measured by the Sky Survey Telescope (S2/68) aboard the ESRO satellite TD-1, 1978.
- [37] Cutri R. M., Wright E. L. and Conrow T., Explanatory Supplement to the WISE All-Sky Data Release Products. Explanatory Supplement to the WISE All-Sky Data Release Products, 2012.
- [38] Kurucz R. L., ATLAS9 Stellar Atmosphere Programs and 2 km/s grid, Kurucz CD-ROM No. 13. Cambridge, Mass.:Smithsonian Astrophysical Observatory, 13, 1993.
- [39] Kurucz, R. L., Avrett, E. H., Solar Spectrum Synthesis. I. A Sample Atlas from 224 to 300 nm, *SAO Special Report*, 391 (1981) 391.
- [40] Catanzaro G., Leone F. and Dall T. H., Balmer lines as T_{eff} and $\log g$ indicators for non-solar composition atmospheres. An application to the extremely helium-weak star HR 6000, *Astronomy and Astrophysics*, 425 (2004) 641 – 648.
- [41] Kahraman Aliçavuş F., Niemczura E., De Cat P., Soyduğan E., Kołaczowski Z., Ostrowski J., Telting J. H., Uytterhoeven K., Poretti E., Rainer M., Suárez J. C., Mantegazza L., Kilmarin P., Pollard K. R., Spectroscopic survey of γ Doradus stars - I. Comprehensive atmospheric parameters and abundance analysis of γ Doradus stars, *Monthly Notices of the Royal Astronomical Society*, 458 (2016) 2307 – 2322.
- [42] Asplund M., Grevesse N., Sauval A. J. and Scott P., the Chemical Composition of the Sun, *Annual Review of Astronomy and Astrophysics*, 47 (2009) 481 – 522.
- [43] Flower P. J., Transformations from Theoretical Hertzsprung-Russell Diagrams to Color- Magnitude Diagrams: Effective Temperatures, B-V Colors, and Bolometric Corrections, *Astrophysical journal*, 469 (1996) 355 – 365.
- [44] Smalley B., Antoci V., Holdsworth D. L., Kurtz D. W., Murphy S. J., De Cat P., Anderson D. R., Catanzaro G., Cameron A. C., Hellier C., Maxted P. F. L., Norton A. J., Pollacco D., Ripepi V., West R. G., Wheatley P. J., Pulsation versus metallicity in Am stars as revealed by LAMOST and WASP, *Monthly Notices of the Royal Astronomical Society*, 465 (2017) 2662 – 2670.
- [45] Dupret M.-A., Grigahcène A., Garrido R., Gabriel M., Scuflaire R., Convection- pulsation coupling. II. Excitation and stabilization mechanisms in δ Sct and γ Dor stars, *Astronomy and Astrophysics*, 435 (2005) 927 – 939.

On an inverse boundary-value problem for a second-order elliptic equation with non-classical boundary conditions

Rauf AMİROV^{1,*}  Yaşar MEHRALİYEY²  Nergiz HEYDARZADE² 

¹Sivas Cumhuriyet University, Department of Mathematics, Sivas/ TURKEY

²Baku Statet University, Faculty of Mathematics, Baku/ AZERBAIJAN

Abstract

An inverse boundary value problem for a second-order elliptic equation with periodic and integral condition is investigated. The problem is considered in a rectangular domain. To investigate the solvability of the inverse problem, we perform a conversion from the original problem to some auxiliary inverse problem with trivial boundary conditions. By the contraction mapping principle we prove the existence and uniqueness of solutions of the auxiliary problem. Then we make a conversion to the stated problem again and, as a result, we obtain the solvability of the inverse problem.

Article info

History:

Received: 04.02.2020

Accepted: 18.04.2020

Keywords:

Inverse boundary value problem, elliptic equation, Fourier method, classical solution.

1. Introduction

Determination of differential equations according to the supplementary information about their solutions are called inverse problems for differential equations. Inverse problems arise in different scientific areas such as seismology, mineral exploration, biology, medicine, quality control of industrial products etc. so that it makes them one of the most important problems of modern mathematics. Different inverse problems for special types of partial differential equations have been studied in many works. Let us note here, first of all, A. N. Tikhonov's [1], M. M. Lavrentiev's [2,3], V. K. Ivanov's [4] and their students' works. You can find more detailed information about it in the A. M. Denisov [5] monography.

The aim of this study is to prove the uniqueness and existence of the solution of stated inverse boundary problem for a second-order elliptic equation with periodic and integral conditions.

2. Main Results

Let us consider the equation

$$u_{tt}(x, t) + u_{xx}(x, t) = p(t)u(x, t) + f(x, t) \quad (1)$$

and state it an inverse boundary value problem in the domain $D_t = \{(x, t): 0 \leq x \leq 1, 0 \leq t \leq T\}$.

The inverse problem has non-local conditions

$$u(x, 0) = \varphi(x) + \int_0^T M_1(t)u(x, t)dt,$$
$$u_t(x, T) = \psi(x) + \int_0^T M_2(t)u(x, t)dt \quad (0 \leq x \leq 1), \quad (2)$$

Neumann boundary condition

$$u_x(1, t) = 0 \quad (0 \leq t \leq T), \quad (3)$$

*Corresponding author. Email address: emirov@cumhuriyet.edu.tr
<http://dergipark.gov.tr/csj> ©2020 Faculty of Science, Sivas Cumhuriyet University

non- classical boundary condition

$$u_{xx}(0,t) - bu_x(0,t) + au(0,t) = 0 \quad (0 \leq t \leq T), \quad (4)$$

and the additional condition

$$u(x_0, t) = h(t) \quad (0 \leq t \leq T), \quad (5)$$

where a, b are positive constants, $x_0 \in (0,1)$ is a fixed number, $f(x,t), \varphi(x), \psi(x), M_1(t), M_2(t), h(t)$ are given functions, $u(x,t)$ and $p(t)$ are the unknown functions.

Definition. By classical solution of (1)-(5) inverse boundary value problem we shall understand the $\{u(x,t), p(t)\}$ pair of functions, if $u(x,t) \in C^2(D_T)$, $p(t) \in C[0, T]$ and relations are satisfied in the usual sense.

For the study of (1)-(5) firstly we reduce the considered problem to the equivalent problem:

$$y''(x) + \lambda y(x) = 0, \quad (0 < x < 1) \quad (6)$$

$$y'(1) = 0, \quad (a - \lambda)y(0) = by'(0), \quad a > 0, b > 0. \quad (7)$$

The following lemma is valid:

Lemma 1. Suppose that $p(t) \in C[0, T], M_1(t) \in C[0, T], M_2(t) \in C[0, T]$,

$$\|p(t)\|_{C[0, T]} \leq R = \text{const}$$

Moreover,

$$T\|M_1(t)\|_{C[0, T]} + T^2(\|M_2(t)\|_{C[0, T]} + \frac{1}{2}R) < 1. \quad (8)$$

Then the problem (6), (7) has a unique trivial solution.

Proof: It is easy to see that boundary value problem (6),(7) is equivalent to the integral equation

$$y(t) = \int_0^T (tM_2(\tau) + M_1(\tau) + p(\tau)G(t, \tau))y(\tau)d\tau, \quad (9)$$

where

$$G(t, \tau) = \begin{cases} -t, & t \in [0, \tau], \\ -\tau, & t \in [\tau, T]. \end{cases}$$

Let us introduce the following denotations

$$Ay(t) = \int_0^T (tM_2(\tau) + M_1(\tau) + p(\tau)G(t, \tau))y(\tau)d\tau, \quad (10)$$

and write integral equation (9) as

$$y(t) = Ay(t). \quad (11)$$

We shall investigate (11) in the space $C[0, T]$. It's obvious that the operator A is continuous in the space $C[0, T]$.

Let us show that the operator A is contracting in the space $C[0, T]$. Indeed, for arbitrary $y(t), \bar{y}(t) \in C[0, T]$ we have

$$\|Ay(t) - A\bar{y}(t)\|_{C[0, T]} \leq (T\|M_1(\tau)\|_{C[0, T]} + T^2\|M_2(\tau)\|_{C[0, T]} + \frac{T^2}{2}\|p(t)\|_{C[0, T]})\|y(t) - \bar{y}(t)\|_{C[0, T]} \quad (12)$$

From (12) by (8), it follows that operator A is contracting in the space $C[0, T]$. Therefore, in the space $C[0, T]$, the operator A has a single fixed point $y(t)$, which is the solution of the equation (11). Thus, integral equation (9) has unique solution in $C[0, T]$. Since, boundary value problem (6), (7) also has unique solution in $C[0, T]$. As $y(t) \equiv 0$ is the solution of (6), (7). So, the boundary value problem (6), (7) has a unique trivial solution. The proof is complete.

Besides with inverse boundary value problem (1)-(5) let's consider the following auxiliary inverse boundary value problem. It is required to determine the pair $\{u(x, t), p(t)\}$ of functions $u(x, t) \in C(D_T)$ and $p(t) \in C[0, T]$ from the relations (1)-(4) and

$$h''(t) + u(x_0, t) = p(t)h(t) + f(x_0, t) \quad (0 \leq t \leq T). \quad (13)$$

The following theorem is valid:

Theorem 1. Assume that $f(x, t) \in C(D_T)$, $\varphi(x), \psi(x) \in C[0, T]$, $M_1(t), M_2(t) \in C[0, T]$, $h(t) \in C^2[0, T]$, $h(t) \neq 0$ ($0 \leq t \leq T$) and the compatibility conditions

$$\begin{aligned} \varphi(x_0) &= h(0) - \int_0^T M_1(t)h(t)dt \\ \psi(x_0) &= h'(T) - \int_0^T M_2(t)h(t)dt \end{aligned} \quad (14)$$

hold. Then the following assertions are valid:

- 1) Each classical solution $\{u(x, t), p(t)\}$ of problem (1)-(5) is also the solution of (1)-(4), (13);
- 2) Each solution $\{u(x, t), p(t)\}$ of problem (1)-(4), (13) satisfying

$$T\|M_1(t)\|_{C[0, T]} + T^2(\|M_2(t)\|_{C[0, T]} + \frac{1}{2}\|p(t)\|_{C[0, T]}) < 1 \quad (15)$$

is a classical solution of (1)-(5).

Proof. Let $\{u(x, t), p(t)\}$ be classical solution of (1)-(5). Taking into consideration $h(t) \in C[0, T]$ and twice differentiating (5), we find:

$$u_t(x_0, t) = h'(t), u_{tt}(x_0, t) = h''(t), \quad (0 \leq t \leq T). \quad (16)$$

Setting $x = x_0$ in the equation (1), we have

$$u_{tt}(x_0, t) + u_{xx}(x_0, t) = p(t)u(x_0, t) + f(x_0, t) \quad (0 \leq t \leq T). \quad (17)$$

Hence by (5) and (16) we conclude that (13) is valid.

Now, assume that $\{u(x, t), p(t)\}$ is a solution of (1)-(4), (13), and the compatibility conditions (14) are satisfied. Then from (1) and (17) we get

$$\frac{d}{dt^2}(u(x_0, t) - h(t)) = a(t)(u(x_0, t) - h(t)) \quad (0 \leq t \leq T). \quad (18)$$

Furthermore, by (2) and the compatibility conditions (14) we have

$$\begin{aligned} u(x_0, t) - h(t) - \int_0^T M_1(t)(u(x_0, t) - h(t))dt &= u(x_0, t) - \int_0^T M_1(t)u(x_0, t)dt - (h(t) - \\ &- \int_0^T M_1(t)h(t)dt) = \varphi(x_0) - (h(t) - \int_0^T u_1(t)h(t))dt = 0 \\ u(x_0, T) - h(T) - \int_0^T M_2(t)(u(x_0, t) - h(t))dt &= u(x_0, T) - \int_0^T M_2(t)u(x_0, t)dt - (h(T) - \\ &- \int_0^T M_2(t)h(t)dt) = \varphi(x_0) - (h(T) - \int_0^T M_2(t)h(t))dt = 0. \end{aligned} \quad (19)$$

From (18) (19) and by virtue of Lemma 1, we conclude that the condition (5) is satisfied.

The theorem is thus proved.

Let us consider the following spectral problem

$$y''(x) + \lambda y(x) = 0 \quad 0 \leq x \leq 1 \quad (20)$$

$$y'(1) = 0 \quad (a - \lambda)y(0) = by'(0) \quad (21)$$

[9], with positive the coefficients a and b . Eigenfunctions of this problem has the form

$$y_k(x) = \sqrt{2} \cos(\sqrt{\lambda_k}(1-x)), \quad k = 0, 1, 2, \dots$$

with positive eigenvalues λ_k from characteristic equation

$$tg\sqrt{\lambda} = \frac{a - \lambda}{b\sqrt{\lambda}}.$$

We assign zero index to any pre-selected eigenfunction, and number all the reminded by increasing order of eigenvalues.

It is known from [6-10]:

Lemma 2. Beginning from a certain number N the following estimations holds true:

$$0 \leq \sqrt{\lambda_k} - \frac{\pi}{2} - \pi(n-1) < \frac{b}{\frac{\pi}{4} + \pi(k-1)}.$$

Now let us compare the system, $\{y_k(x)\}$ without function $y_0(x)$ to a known system,

$\{v_k(x)\}$, $v_k(x) = \sqrt{2} \cos\sqrt{\mu_k}(1-x)$ where $\sqrt{\mu_k} = \frac{\pi}{2} + \pi(k-1)$, $k = 1, 2, \dots$, which is orthonormal basis in $L_2(0,1)$.

In analogous manner [6-10], we have

$$\sum_{k=N}^{\infty} \|y_k(x) - v_k(x)\|_{L_2(0,1)}^2 < b^2 \sum_{k=N}^{\infty} \frac{2}{3(\frac{\pi}{4} + \pi(k-1))^2}, \quad (22)$$

which we get convergence of the series from the left hand side of this inequality.

Let us suppose that $\eta_k(x) = \sqrt{2} \sin(\sqrt{\lambda_k}(1-x))$, $\xi_k(x) = \sqrt{2} \sin(\sqrt{\mu_k}(1-x))$

then the inequality

$$\sum_{k=N}^{\infty} \|\eta_k(x) - \xi_k(x)\|_{L_2(0,1)}^2 < b^2 \frac{2}{3(\frac{\pi}{4} + \pi(k-1))^2} \quad (23)$$

hold.

It's known [9] that functions of biorthogonally conjugate system $\{z_k(x)\}$ to the system $\{y_k(x)\}$, $k = 1, 2, \dots$ are defined by the equality

$$z_k(x) = \sqrt{2} \left(\cos(\sqrt{\lambda_k}(1-x)) - \frac{\cos(\sqrt{\lambda_k}) \cos(\sqrt{\lambda_0}(1-x))}{\cos(\sqrt{\lambda_0})} \right) / \alpha_k, \quad (24)$$

$$\text{where } \alpha_k = 1 + \frac{\cos^2(\sqrt{\lambda_k})}{b} + \frac{a \cos^2(\sqrt{\lambda_k})}{b \lambda_k}$$

Here it's also known that $\{y_k(x)\}$ $k = 1, 2, \dots$ form a basis Riess in space $L_2(0,1)$.

Suppose that $g(x) \in L_2(0,1)$. Then by (22), we get

$$\left(\sum_{k=1}^{\infty} \left(\int_0^1 g(x) y_k(x) dx \right)^2 \right)^{\frac{1}{2}} \leq M \|g(x)\|_{L_2(0,1)} \quad (25)$$

where

$$M = \left(\frac{N(1+N)}{2} + b \sum_{k=N}^{\infty} \frac{2}{3(\frac{\pi}{4} + \pi(k-1))^2} + 2 \right)^{\frac{1}{2}}$$

Similar to (25), by (23), we find:

$$\left(\sum_{k=1}^{\infty} \left(\int_0^1 g(x) \eta_k(x) dx \right)^2 \right)^{\frac{1}{2}} \leq M \cdot \|g(x)\|_{L_2(0,1)}$$

Since, the functions $\{y_k(x)\}$, $k = 1, 2, \dots$ are the basis of Riess in $L_2(0,1)$ space, then it's known [10] that for any function $g(x) \in L_2(0,1)$

$$g(x) = \sum_{k=1}^{\infty} g_k y_k(x)$$

holds true, where

$$g_k = \int_0^1 g(x) z_k(x) \quad (k = 1, 2, \dots)$$

It is not difficult to see that

$$|g_k| \leq \sqrt{2} \left(\int_0^1 g(x) y_k(x) dx + \frac{1}{|\cos \sqrt{\lambda_0}|} \cdot \frac{b \sqrt{\lambda_k}}{|a - \lambda_k|} \cdot \int_0^1 |g(x)| dx \right)$$

From here, by virtue of (25), we have

$$\left(\sum_{k=1}^{\infty} g_k^2 \right)^{\frac{1}{2}} \leq M_0 \|g(x)\|_{L_2(0,1)} \quad (27)$$

where

$$M_0 = 2 \left[M + \frac{b}{\cos \sqrt{\lambda_0}} \cdot \sup_k \left(\frac{\lambda}{|a - \lambda_k|} \right) \left(\sum_{k=1}^{\infty} \frac{1}{\lambda_k} \right)^{\frac{1}{2}} \right].$$

Assume that $g(x) \in C[0,1]$, $g'(x) \in L_2(0,1)$.

$$J(g) \equiv g(x) + \frac{b}{\cos \sqrt{\lambda_0}} \int_0^1 g(x) \cos \sqrt{\lambda_0} (1-x) dx \equiv 0$$

Then we have

$$\begin{aligned} g_k &= \frac{\sqrt{2}}{\alpha_k} \int_0^1 g(x) (\cos(\sqrt{\lambda_k} (1-x)) - \frac{\cos \sqrt{\lambda_k}}{\cos \sqrt{\lambda_0}} \cos(\sqrt{\lambda_0} (1-x))) dx = \\ &= \frac{\sqrt{2}}{\alpha_k} \cdot \frac{a}{b \lambda_k} g(0) \cos \sqrt{\lambda_k} + \frac{\sqrt{2}}{\alpha_k} \cdot \frac{1}{\sqrt{\lambda_k}} \int_0^1 g'(x) \sin(\sqrt{\lambda_k} (1-x)) dx \end{aligned} \quad (28)$$

Hence by (26) we have

$$\left(\sum_{k=1}^{\infty} (\lambda_k g_k)^2 \right)^{\frac{1}{2}} \leq m_0 |g(0)| + 2M \|g'(x)\|_{L_2(0,1)}, \quad (29)$$

where

$$m_0 = \frac{2a}{b} \left(\sum_{k=1}^{\infty} \frac{1}{\lambda_k} \right)^{\frac{1}{2}}$$

Now suppose that $g(x) \in C^1[0,1]$, $g'''(x) \in L_2(0,1)$, $J(g) = 0$, $g'(1) = 0$. Then from (28) we get

$$\begin{aligned} g_k &= \frac{\sqrt{2}}{\alpha_k} \cdot \frac{1}{a - \lambda_k} \cdot \frac{1}{\sqrt{\lambda_k}} (a g(0) - b g'(0) \sin \sqrt{\lambda_k} + \frac{\sqrt{2}}{\alpha_k} \cdot \frac{1}{\lambda_k \sqrt{\lambda_k}} \cdot \\ &\cdot \int_0^1 g''(x) d \sin(\sqrt{\lambda_k} (1-x)) - \frac{\sqrt{2}}{\alpha_k} \cdot \frac{1}{a - \lambda_k} \cdot \frac{a}{\lambda_k \sqrt{\lambda_k}} g''(0) - \\ &- \frac{\sqrt{2}}{\alpha_k} \cdot \frac{1}{\lambda_k \sqrt{\lambda_k}} \int_0^1 g'''(x) \sin(\sqrt{\lambda_k} (1-x)) dx. \end{aligned} \quad (30)$$

From here we find:

$$\left(\sum_{k=1}^{\infty} (\lambda_k \sqrt{\lambda_k} |f_k|^2)^{\frac{1}{2}}\right)^2 \leq m_1 a |g''(0)| + 2M \|g'''(x)\|_{L_2(0,1)} \quad (31)$$

where

$$m_1 = 2 \sup_k \frac{\lambda_k}{|a - \lambda_k|} \left(\sum_{k=1}^{\infty} \frac{1}{\lambda_k}\right)^{\frac{1}{2}}.$$

Now suppose that $g(x) \in C^2[0,1]$, $g'''(x) \in L_2(0,1)$, $J(g) = 0$, $g'(1) = 0$, $g''(0) - bg(0) + ag(0) = 0$. Then from (29) we get

$$g_k = -\frac{\sqrt{2}}{\alpha_k} \cdot \frac{1}{a - \lambda_k} \cdot \frac{a}{\lambda_k \sqrt{\lambda_k}} g''(0) - \frac{\sqrt{2}}{\alpha_k} \cdot \frac{1}{\lambda_k \sqrt{\lambda_k}} \int_0^1 g'''(x) \sin(\sqrt{\lambda_k}(1-x)) dx. \quad (32)$$

From (32) we find:

$$\left(\sum_{k=1}^{\infty} (\lambda_k \sqrt{\lambda_k} |g_k|^2)^{\frac{1}{2}}\right)^2 \leq m_1 a |g''(0)| + 2M \|g'''(x)\|_{L_2(0,1)}. \quad (33)$$

Denoted by $B_{2,T}^{\frac{3}{2}}$, the set of all the functions $u(x, t)$ of the form

$$u(x, t) = \sum_{k=1}^{\infty} u_k(t) y_k(x),$$

is considered D_T , where each function $u_k(t)$ is continuous on $[0, T]$ and

$$\left\{ \sum_{k=1}^{\infty} (\lambda_k \sqrt{\lambda_k} \|u_k(t)\|_{C[0,T]})^2 \right\}^{\frac{1}{2}} < +\infty.$$

We define the norm on this set as follows:

$$\|u(x, t)\|_{B_{2,T}^{\frac{3}{2}}} = \left\{ \sum_{k=1}^{\infty} (\lambda_k \sqrt{\lambda_k} \|u_k(t)\|_{C[0,T]})^2 \right\}^{\frac{1}{2}}.$$

Denoted by $E_T^{\frac{3}{2}}$ the space that consist of the topological product

$$B_{2,T}^{\frac{3}{2}} \times C[0, T].$$

The norm of the element $z = \{u, p\}$ is defined by the formula

$$\|z\|_{E_T^{\frac{3}{2}}} = \|u(x, t)\|_{B_{2,T}^{\frac{3}{2}}} + \|p(t)\|_{C[0,T]}.$$

It is known that $B_{2,T}^{\frac{3}{2}}$ and $E_T^{\frac{3}{2}}$ are Banach spaces.

We shall seek for the first component $u(x, t)$ of $\{u(x, t), p(t)\}$ in the form

$$u(x, t) = \sum_{k=1}^{\infty} u_k(t) y_k(x), \quad (34)$$

where

$$u_k(t) = \int_0^1 u(x, t) z_k(x) dx \quad (k = 1, 2, \dots),$$

and

$$y_k(x) = \sqrt{2} \cos(\sqrt{\lambda_k}(1-x)).$$

By applying method of separation of variables, from (1), (2) we have

$$u_k''(t) - \lambda_k u_k(t) = F_k(t, u, p) \quad (k = 1, 2, \dots; 0 \leq t \leq T), \quad (35)$$

$$u_k(0) = \varphi_k + \int_0^T M_1(t) u_k(t) dt, \quad (36)$$

$$u_k'(T) = \psi_k + \int_0^T M_2(t) u_k(t) dt \quad (k = 1, 2, \dots) \quad (37)$$

where

$$F_k(t, u, p) = f_k(t) + p(t) u_k(t), \quad f_k(t) = \int_0^1 f(x, t) y_k(x) dx,$$

$$\varphi_k = \int_0^1 \varphi(x) z_k(x) dx, \quad \psi_k = \int_0^1 \psi(x) z_k(x) dx \quad (k = 1, 2, \dots)$$

Solving problem (35)-(37) we obtain

$$\begin{aligned} u_k(t) = & \frac{ch(\lambda_k(T-t))}{ch(\lambda_k T)} \left(\varphi_k + \int_0^T M_1(t) u_k(t) dt \right) + \frac{sh(\lambda_k(T-t))}{\lambda_k ch(\lambda_k T)} \left(\psi_k + \int_0^T M_2(t) u_k(t) dt \right) + \\ & + \frac{1}{\lambda_k} \int_0^T G_k(t, \tau) F_k(\tau, u, p) d\tau, \quad (k = 1, 2, \dots) \end{aligned} \quad (38)$$

Where

$$G_k(t, \tau) = \begin{cases} \frac{sh(\sqrt{\lambda_k}(T-(t+\tau))) - sh(\sqrt{\lambda_k}(T+t-\tau))}{2ch(\sqrt{\lambda_k}T)}, & t \in [0, \tau] \\ \frac{sh(\sqrt{\lambda_k}(T-(t+\tau))) - sh(\sqrt{\lambda_k}(T-(t-\tau)))}{2ch(\sqrt{\lambda_k}T)}, & t \in [\tau, T] \end{cases}$$

After substitution the expression (38) in (34), by the definition of the component $u(x, p)$ of problem, we get (1)-(4), (13)

$$\begin{aligned} u(x, t) = & \sum_{k=1}^{\infty} \left[\frac{ch(\lambda_k(T-t))}{ch(\lambda_k T)} \left(\varphi_k + \int_0^T M_1(t) u_k(t) dt \right) + \right. \\ & \left. + \frac{sh(\lambda_k(T-t))}{\lambda_k ch(\lambda_k T)} \left(\psi_k + \int_0^T M_2(t) u_k(t) dt \right) + \frac{1}{\lambda_k} \int_0^T G_k(t, \tau) F_k(\tau, u, p) d\tau \right] y_k(x). \end{aligned} \quad (39)$$

Now, from (13), by (34) we have

$$p(t) = [h(t)]^{-1} \left\{ h''(t) - f(x_0, t) - \sqrt{2} \sum_{k=1}^{\infty} \lambda_k u_k(t) \cos \sqrt{\lambda_k} (1 - x_0) \right\}. \quad (40)$$

In order to get the equation for the second component $p(t)$ of solution $\{u(x, t), p(t)\}$ of problem (1)-(4), (13) we substitute the expression (38) in (40):

$$p(t) = [h(t)]^{-1} \left\{ h''(t) - f(x_0, t) - \sqrt{2} \sum_{k=1}^{\infty} \lambda_k \left[\frac{ch(\lambda_k(T-t))}{ch(\lambda_k T)} \left(\varphi_k + \int_0^T M_1(t) u_k(t) dt \right) + \right. \right. \\ \left. \left. + \frac{sh(\lambda_k(T-t))}{\lambda_k ch(\lambda_k T)} \left(\psi_k + \int_0^T M_2(t) u_k(t) dt \right) + \frac{1}{\lambda_k} \int_0^T G_k(t, \tau) F_k(\tau, u, p) d\tau \right] \cos \sqrt{\lambda_k} (1 - x_0) \right\} \quad (41)$$

Thus, the solution of problem (1)-(4), (13) was reduced to the solution of the system (39), (41) respectively to unknown function $u(x, t)$ and $p(t)$

Now let us consider the operator $\Phi(u, p) = \{\Phi_1(u, p), \Phi_2(u, p)\}$ in the space $E_T^{3/2}$, where

$$\Phi_1(u, p) = \tilde{u}(x, v) \equiv \sum_{k=1}^{\infty} \tilde{u}_k(v) \cdot y_k(x), \quad \Phi_2(u, p) = \tilde{p}(v), \quad \text{a } \tilde{u}_k(v) \quad (k = 1, 2, \dots)$$

and $\tilde{p}(v)$ are equal to the right-hand side parts of (38) and (41) respectively.

It is obvious that

$$\frac{ch(\lambda_k(T-t))}{ch(\lambda_k T)} < 1, \quad \frac{sh(\lambda_k T)}{ch(\lambda_k T)} < 1, \quad \frac{sh(\lambda_k(T+t-\tau))}{ch(\lambda_k T)} < 1 \quad (t \in [0, \tau]), \\ \frac{sh(\lambda_k(T-(t+\tau)))}{ch(\lambda_k T)} < 1, \quad \frac{sh(\lambda_k(T-(t-\tau)))}{ch(\lambda_k T)} < 1 \quad (t \in [\tau, T]).$$

Using these relations, and simple transformations we find

$$\left(\sum_{k=1}^{\infty} (\lambda_k \sqrt{\lambda_k} \|\tilde{u}_k(t)\|_{C[0,T]})^2 \right)^{\frac{1}{2}} \leq \sqrt{6} \left(\sum_{k=1}^{\infty} (\lambda_k \sqrt{\lambda_k} |\varphi_k|^2) \right)^{\frac{1}{2}} + \sqrt{6} \left(\sum_{k=1}^{\infty} (\lambda_k |\psi_k|^2) \right)^{\frac{1}{2}} + \\ + \sqrt{6T} \|M_1(t)\|_{C[0,T]} \left(\sum_{k=1}^{\infty} \lambda_k \sqrt{\lambda_k} \|u_k(t)\|_{C[0,T]}^2 \right)^{\frac{1}{2}} + \sqrt{6T} \|M_2(t)\|_{C[0,T]} \left(\sum_{k=1}^{\infty} \lambda_k \|u_k(t)\|_{C[0,T]}^2 \right)^{\frac{1}{2}} + \\ + \sqrt{6T} \left(\int_0^T \sum_{k=1}^{\infty} (\lambda_k |f_k(\tau)|^2) d\tau \right)^{\frac{1}{2}} + \sqrt{6T} \|p(t)\|_{C[0,T]} \left(\sum_{k=1}^{\infty} \lambda_k \sqrt{\lambda_k} \|u_k(t)\|_{C[0,T]}^2 \right)^{\frac{1}{2}} \quad (42)$$

$$\|\tilde{p}(t)\|_{C[0,T]} \leq \| [h(t)]^{-1} \|_{C[0,T]} \left\{ \|h''(t) - f(x_0, t)\|_{C[0,T]} + \left(\sum_{k=1}^{\infty} \lambda_k^{-1} \right)^{\frac{1}{2}} \left[\left(\sum_{k=1}^{\infty} (\lambda_k \sqrt{\lambda_k} |\varphi_k|^2) \right)^{\frac{1}{2}} + \right. \right. \\ \left. \left. + \left(\sum_{k=1}^{\infty} (\lambda_k |\psi_k|^2) \right)^{\frac{1}{2}} + T \|M_1(t)\|_{C[0,T]} \left(\sum_{k=1}^{\infty} (\lambda_k \sqrt{\lambda_k} \|u_k(t)\|_{C[0,T]}^2 \right)^{\frac{1}{2}} + T \|M_2(t)\|_{C[0,T]} \right] \right\}$$

$$\cdot \left(\sum_{k=1}^{\infty} (\lambda_k \sqrt{\lambda_k} \|u_k(t)\|_{C[0,T]})^2 \right)^{\frac{1}{2}} + \sqrt{T} \left(\int_0^T \sum_{k=1}^{\infty} (\lambda_k |f_k(\tau)|)^2 d\tau \right)^{\frac{1}{2}} + T \|p(t)\|_{C[0,T]} \cdot \left. \cdot \left(\sum_{k=1}^{\infty} (\lambda_k \sqrt{\lambda_k} \|u_k(t)\|_{C[0,T]})^2 \right)^{\frac{1}{2}} \right\} . \quad (43)$$

Suppose that the data of (1)-(4), (13) satisfy the following conditions:

1. $\varphi(x) \in C^2[0,1], \varphi'''(x) \in L_2(0,1), J(\varphi) = 0, \varphi'(1) = 0, \varphi''(0) - b\varphi'(0) + a\varphi(0) = 0,$
2. $\psi(x) \in C^1[0,1], \psi''(x) \in L_2(0,1), J(\psi) = 0, \psi'(1) = 0,$
3. $f(x,t), f_x(x,t), f_{xx}(x,t) \in L_2(D_T),$
 $J(f) = 0, f_x(1,t) = 0 \quad (0 \leq t \leq T)$
4. $a > 0, b > 0, M_1(t), M_2(t) \in C[0,T], h(t) \in C^2[0,T], h(t) \neq 0 \quad (0 \leq t \leq T)$

Then from (42) and (43), by (30) and (32), we find

$$\begin{aligned} & \left(\sum_{k=1}^{\infty} (\lambda_k \sqrt{\lambda_k} \|\tilde{u}_k(t)\|_{C[0,T]})^2 \right)^{\frac{1}{2}} \leq \\ & \leq \sqrt{6} [m_1 a |\varphi''(0)| + 2M \|\varphi'''(x)\|_{L_2(0,T)}] + \sqrt{6} (m_1 (a|\psi(0)| + b|\psi'(0)|) + \sqrt{b} M \|\psi''(x)\|_{L_2(0,1)}) + \\ & + \sqrt{b} T (\|M_1(t)\|_{C[0,T]} + \|M_2(t)\|_{C[0,T]}) \left(\sum_{k=1}^{\infty} (\lambda_k \sqrt{\lambda_k} \|u_k(t)\|_{C[0,T]})^2 \right)^{\frac{1}{2}} + \\ & + \sqrt{6T} [m_1 (a\|f(0,t)\|_{C[0,T]} + b\|f_x(0,t)\|_{C[0,T]}) + 2M \|f_{xx}(x,t)\|_{L_2(D_T)}] + \\ & + \sqrt{6T} \|p(t)\|_{C[0,T]} \left(\sum_{k=1}^{\infty} (\lambda_k \sqrt{\lambda_k} \|u_k(t)\|_{C[0,T]})^2 \right)^{\frac{1}{2}}, \quad (44) \\ & \|\tilde{p}(t)\|_{C[0,T]} \leq \| [h(t)]^{-1} \|_{C[0,T]} \left\{ \|h''(t) - f(x_0, t)\|_{C[0,T]} + \right. \\ & + \left(\sum_{k=1}^{\infty} \frac{1}{\lambda_k} \right)^{\frac{1}{2}} [m_1 a |\varphi''(0)| + 2M \|\varphi'''(x)\|_{L_2(0,T)} + m_1 (a|\psi(0)| + b|\psi'(0)|) + \\ & + \sqrt{b} M \|\psi''(x)\|_{L_2(0,1)} + T (\|M_1(t)\|_{C[0,T]} + \|M_2(t)\|_{C[0,T]}) \left(\sum_{k=1}^{\infty} (\lambda_k \sqrt{\lambda_k} \|u_k(t)\|_{C[0,T]})^2 \right)^{\frac{1}{2}} + \\ & + \sqrt{T} [m_1 (a\|f(0,t)\|_{C[0,T]} + b\|f_x(0,t)\|_{C[0,T]}) + 2M \|f_{xx}(x,t)\|_{L_2(D_T)}] + \\ & \left. + T \|p(t)\|_{C[0,T]} \left(\sum_{k=1}^{\infty} (\lambda_k \sqrt{\lambda_k} \|u_k(t)\|_{C[0,T]})^2 \right)^{\frac{1}{2}} \right\} \quad (45) \end{aligned}$$

Let us introduce the denotations

$$\begin{aligned} A_1(T) = & \sqrt{6} [m_1 a |\varphi''(0)| + 2M \|\varphi'''(x)\|_{L_2(0,1)}] + \sqrt{6} [m_1 (a|\psi(0)| + b|\psi'(0)|) + \sqrt{b} M \|\psi''(x)\|_{L_2(0,1)}] + \\ & + \sqrt{b} T [m_1 (a\|f(0,t)\|_{C[0,T]} + b\|f_x(0,t)\|_{C[0,T]}) + \sqrt{b} M \|f_{xx}(x,t)\|_{L_2(D_T)}] \end{aligned}$$

$$\begin{aligned}
 B_1(T) &= \sqrt{6}T, \quad D_1(T) = \sqrt{6}T(\|M_1(t)\|_{C[0,T]} + \|M_2(t)\|_{C[0,T]}), \\
 A_2(T) &= \left\| [h(t)]^{-1} \right\|_{C[0,T]} \left\{ \|h''(t) - f(x_0, t)\|_{C[0,T]} + \right. \\
 &\quad + \left(\sum_{k=1}^{\infty} \frac{1}{\lambda_k} \right)^{\frac{1}{2}} [m_1 a |\varphi''(0)| + 2M \|\varphi'''(x)\|_{L_2(0,1)} + m_1 (a |\psi(0)| + b |\psi'(0)|) + 2M \|\psi''(x)\|_{L_2(0,1)} + \\
 &\quad + \sqrt{T} [m_1 (a \|f(0, t)\|_{C[0,T]} + b \|f_x(0, t)\|_{C[0,T]}) + 2M \|f_{xx}(x, t)\|_{L_2(D_T)}] \Big\} \\
 B_2(T) &= \left\| [h(t)]^{-1} \right\|_{C[0,T]} \left(\sum_{k=1}^{\infty} \frac{1}{\lambda_k} \right)^{\frac{1}{2}} T,
 \end{aligned}$$

$$D_2(T) = \left\| [h(t)]^{-1} \right\|_{C[0,T]} \left(\sum_{k=1}^{\infty} \frac{1}{\lambda_k} \right)^{\frac{1}{2}} T (\|M_1(t)\|_{C[0,T]} + \|M_2(t)\|_{C[0,T]}).$$

and write the estimations (44) and (45) as follows

$$\|\tilde{u}(x, t)\|_{B_{2,T}^{\frac{3}{2}}} \leq A_1(T) + B_1(T) \|p(t)\|_{C[0,T]} \|u(x, t)\|_{B_{2,T}^{\frac{3}{2}}} + D_1(T) \|u(x, t)\|_{B_{2,T}^{\frac{3}{2}}}, \quad (46)$$

$$\|\tilde{p}(t)\|_{C[0,T]} \leq A_2(T) + B_2(T) \|p(t)\|_{C[0,T]} \|u(x, t)\|_{B_{2,T}^{\frac{3}{2}}} + D_2(T) \|u(x, t)\|_{B_{2,T}^{\frac{3}{2}}}. \quad (47)$$

From the inequalities (46) and (47) we conclude:

$$\|u(x, t)\|_{B_{2,T}^{\frac{3}{2}}} + \|\tilde{p}(t)\|_{C[0,T]} \leq A(t) + B(T) \|p(t)\|_{C[0,T]} \cdot \|u(x, t)\|_{B_{2,T}^{\frac{3}{2}}} + D(T) \|u(x, t)\|_{B_{2,T}^{\frac{3}{2}}}, \quad (48)$$

where

$$A(T) = A_1(T) + A_2(T), \quad B(T) = B_1(T) + B_2(T), \quad D(T) = D_1(T) + D_2(T).$$

The following theorem can be proved.

Theorem 2. If conditions (1)-(4) and the condition

$$(B(T)(A(T) + 2) + D(T))(A(T) + 2) < 1 \quad (49)$$

hold. Then problem (1)-(4), (13) has a unique solution in the ball $K = K_R$ ($\|z\|_{E_T^{\frac{3}{2}}} \leq R = A(t) + 2$) of the space $E_T^{\frac{3}{2}}$.

Proof. In the space $E_T^{\frac{3}{2}}$, we consider the equation

$$z = \Phi z \quad (50)$$

where $z = \{u, p\}$, the components $\Phi_i(u, p)$ ($i = 1, 2, \dots$) of operator $\Phi(u, p)$ is defined by the right sides of equations (39), (41).

Consider the operator $\Phi(u, p)$ in $K = K_R$ of the space $E_T^{\frac{3}{2}}$. Similar to (48) we get that for any $z, z_1, z_2 \in K_R$ the following inequalities hold:

$$\begin{aligned}
 \|\Phi z\|_{E_T^{\frac{3}{2}}} &\leq A(T) + B(T) \|p(t)\|_{C[0,T]} \|u(x, t)\|_{B_{2,T}^{\frac{3}{2}}} + D(T) \|u(x, t)\|_{B_{2,T}^{\frac{3}{2}}} \leq A(T) + B(T) \cdot \\
 &\cdot (A(T) + 2)^2 + D(T)(A(T) + 2) = A(T) + (B(T)(A(T) + 2) + D(T))(A(T) + 2)
 \end{aligned} \quad (51)$$

$$\begin{aligned} \|\Phi z_1 - \Phi z_2\|_{E_T^{3/2}} &\leq B(T)R(\|P_1(t) - P_2(t)\|_{C[0,T]} + \|u_1(x,t) - u_2(x,t)\|_{B_{2,T}^{3/2}}) + \\ &+ D(T)\|u_1(x,t) - u_2(x,t)\|_{B_{2,T}^{3/2}} \end{aligned} \quad (52)$$

Then by (49) from (51) and (52), it follows that the operator Φ acts in the sphere $K = K_R$ and is contracting. Therefore in the sphere $K = K_R$ operator Φ has only unique fixed point $\{u, p\}$, which is the solution of the equation (50), i.e. $\{u, p\}$, is the unique solution of the system (39), (41) in the sphere $K = K_R$.

Then the function $u(x, t)$, as an element of $B_{2,T}^{3/2}$, is continuous and has continuous derivatives $u_x(x, t)$ and $u_{xx}(x, t)$ in D_T .

Furthermore, from (38) it is obvious that $u_k''(t) \in C[0, T]$ and

$$\begin{aligned} \left(\sum_{k=1}^{\infty} (\sqrt{\lambda_k} \|u_k''(t)\|_{C[0,T]})^2\right)^{\frac{1}{2}} &\leq \sqrt{3} \left(\sum_{k=1}^{\infty} (\lambda_k \sqrt{\lambda_k} \|u_k(t)\|_{C[0,T]})^2\right)^{\frac{1}{2}} + \sqrt{3} \left(\sum_{k=1}^{\infty} \sqrt{\lambda_k} \|f_k(t)\|_{C[0,T]}\right)^{\frac{1}{2}} + \\ &+ \sqrt{3} \|p(t)\|_{C[0,T]} \left(\sum_{k=1}^{\infty} \lambda_k \sqrt{\lambda_k} \|u_k(t)\|_{C[0,T]}\right)^{\frac{1}{2}} \end{aligned}$$

or considering (29) we find:

$$\begin{aligned} \left(\sum_{k=1}^{\infty} (\sqrt{\lambda_k} \|u_k''(t)\|_{C[0,T]})^2\right)^{\frac{1}{2}} &\leq \sqrt{3} (m_0 \|f(0, t)\|_{C[0,T]} + 2M \|f_x(x, t)\|_{C[0,T]}) + \\ &+ \sqrt{3} (1 + \|p(t)\|_{C[0,T]}) \left(\sum_{k=1}^{\infty} (\lambda_k \sqrt{\lambda_k} \|u_k''(t)\|_{C[0,T]})^2\right)^{\frac{1}{2}} \end{aligned}$$

This implies that $u_{tt}(x, t)$ is continuous in D_T . It is easy to verify that equation (1) and conditions (2), (3), (4) and (13) are satisfied in the usual sense.

Consequently, $\{u(x, t), p(t)\}$ is the solution of (1)-(4), (13). The proof is complete.

With the aid of Theorem 1 the following theorem was proved.

Theorem 3. Suppose that all conditions of Theorem 2

$$T \|M_1(t)\|_{C[0,T]} + T^2 (\|M_2(t)\|_{C[0,T]} + \frac{1}{2} (A(T) + 2)) < 1$$

and the compatibility condition (14) hold. If

$$\varphi(x_0) = h(0) - \int_0^T M_1(t) h(t) dt,$$

$$\varphi(x_0) = h'(T) - \int_0^T M_2(t) h(t) dt.$$

then problem (1)-(5) has a unique classical solution in $K = K_R$ of $E_T^{3/2}$.

Conflicts of interest

There is no conflict of interest.

References

- [1] Tikhonov A.N., On stability of inverse problems, , [in Russian], *Dokl. AN SSSR*, 39(5) (1943) 195– 198..
- [2] Lavrent'ev M.M., On an inverse problem for a wave equation, [in Russian], *Dokl. AN SSSR*, 157(3) (1964) 520–521.
- [3] Lavrent'ev M.M. Romanov V.G. Shishatsky S.T., Ill-posed problems of mathematical physics and analysis, [in Russian], M., Nauka, 1980.
- [4] Ivanov V.K. Vasin V.V. Tanana V.P., Theory of linear ill-posed problems and its applications, [in Russian], M., Nauka, 1978.
- [5] Denisov A.M., Introduction to theory of inverse problems, , [in Russian], M. MGU, 1994.
- [6] Iskenderov A. D., The inverse problem of determining the coefficients of an elliptic equation, *Journal of Differential Equations*, 15(5) (1979) 858-867.
- [7] Aliyev R. A., On determining the coefficients of a linear elliptic equation, *Sib. Journal of industry Mathematics*, 19(2) (2016) 17-28
- [8] Solovyev V. V., Inverse problems for elliptic equations on a plane. *Journal of Dif. Equations*, 42(8) (2008) 1106-1114.
- [9] Megraliyev Y. T., The inverse boundary value problem for second- order elliptic equation with an additional integral condition, *Bulletin of the Udmurt University, Mathematics, Mechanics, Computer Science*, 1 (2012) 32-40.
- [10] Khudaverdiyev K. I. Veliyev A. A., The study of a one- dimensional mixed problem for one class of third- order pseudo-hyperbolic equations with nonlinear operator right- hand side, Baku: Chashiogly, 2010, 168P.

A new spectrophotometric study with ortho hydroxy schiff base for the determination of aluminum in drug

Tufan GÜRAY¹ , Dila ERCENGİZ² , Ulku Dilek UYSAL^{3*} 

¹ Eskisehir Osmangazi University, Faculty of Arts and Science, Department of Chemistry, Eskisehir, Turkey

² Eskişehir Technical University, Graduate School of Sciences, Eskişehir, Turkey

³ Eskişehir Technical University, Science Faculty, Department of Chemistry, Eskişehir, Turkey

Abstract

In this study, a Schiff base called (*E*)-2-((2- hydroxy -3- methoxy benzylidene)amino)-5- methylphenol (L) was used as a ligand. Spectrophotometric properties of the ligand have been defined and the optimum conditions for determining aluminium by complex by UV-Vis. spectrophotometry. The absorbance of Al(III)-L complex obeys Beer's law between 1.4 µg mL⁻¹ and 13.5 µg mL⁻¹ for the aluminium in the optimum conditions. Under optimum conditions, the determination of aluminium in Kompensan® drug was done successfully. The LOD and LOQ values of the developed method were 0.01139 µg mL⁻¹ and 0.0345 µg mL⁻¹, respectively for the ligand.

Article info

History:

Received:23.02.2020

Accepted:05.06.2020

Keywords:

Aluminium,
Schiff base,
UV- Vis
spectrophotometry,
Kompensan®.

1. Introduction

Aluminium is used in many areas, so it can enter the living body through inhalation, contact and nutrition. Searches have shown that aluminum has toxic effects in humans. Certain diseases are thought to be associated with high aluminium content in human tissues. Although there are many ways of exposure to aluminum, nutrition is seen as the main source of intaking aluminum. It is estimated that 20% of the aluminum taken into the body in one day comes from cooking and preserving containers. Certain antacid drugs used for stomach disorders contain significant amounts of aluminium compounds. For these reasons, it is important to determine aluminium [1, 2]. AAS [3-5], Chromatography [6, 7], Fluorescence [8], X-ray fluorescence spectrometry [9], Voltametry [10], Polarography [11], and ICP-MS [12, 13] methods are used for the determination of aluminium apart from UV-Vis. method. Although these methods give positive results for the qualitative and quantitative analysis, they need an expert and extra pre-treatment. UV-visible method has been the choice for this study because of less cost and ease-of-use in comparison to the other methods. Certain spectrophotometric methods have been proposed for the determination of aluminium in the last decade [14-22]. Although the azo compound-based methods have high sensitivity and

selectivity, they have certain disadvantages such as difficulties in the synthesis of azo compounds and low synthesis efficiency [14-17]. Schiff bases are known to be a particular class of chelating ligands for metal ions and they are widely used as receptors due to their easy synthesis with a high yield [23]. Moreover, the structures of Schiff bases can be easily characterized. Schiff bases have attracted much attention of researchers due to their certain properties such as nonlinear optical properties, polymerization, metal bond formation abilities and superior biological activities [24, 25]. Schiff bases derived from aromatic o-hydroxyaldehydes have received attention due to their biological properties. These properties are antifungal, antibacterial, antimalarial, antiproliferative, anti-inflammatory, antiviral, antipyretic, herbicide properties and anti-tumor activity [24-28]. The purpose of the study is to develop a new UV-Vis. method to determine aluminium. To the best of our knowledge, (*E*)-2-((2- hydroxy -3- methoxy benzylidene)amino)-5- methylphenol (L) has not been used for the determination of aluminium (Fig. 1).

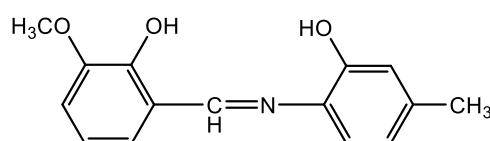


Figure 1. Chemical structure of (*E*)-2-((2- hydroxy -3- methoxy benzylidene)amino)-5- methylphenol (L).

*Corresponding author. Email address: duysal@eskisehir.edu.tr

<http://dergipark.gov.tr/csj> ©2020 Faculty of Science, Sivas Cumhuriyet University

2. Materials and Methods

2.1. Chemical and instruments

All the reagents used were ACS grade with $\geq 95\%$. These chemicals were purchased from Sigma, Merck and Alfa Aesar. Their solutions were prepared with bi-distilled deionized water. A stock solution of aluminium solution of 1000 mg L^{-1} (ICP, Merck) was used. By dissolving 0.2032 g of ligand in 500 mL of deionized water, it was prepared [29]. The solution is stable for a one month at ambient temperature. Shimadzu UV-3150 UV-Vis spectrophotometry (Shimadzu Corporation, International Marketing Division, Tokyo, Japan) using a 1.00 cm quartz cell was used for the spectrophotometric measurements. Mettler Toledo Inlab Expert Pro-ISM pH meter (Mettler-Toledo GmbH, Analytical CH-8603 Schwerzenbach, Switzerland) was used for the pH measurements.

2.2. General procedure

The Al (III)-(E)-2-((2-hydroxy -3-methoxy benzylidene)amino)-5-methylphenol complex has been formed in optimum conditions detailed in 'Results and discussion' section. Transfer Al (III) solution (last concentration was in the range of $1.4\text{--}13.5 \text{ } \mu\text{g mL}^{-1}$) into a 10 mL calibrated flask. Add 1 mL $1.0 \times 10^{-3} \text{ M}$ ligand and dilute to the mark with pH 5 buffer solution. Measure the absorbance at 413.5 nm against the reagent blank. Since the concentration of ligand affects the formation of the complex, the concentration of the ligand was identical in blank and tests solutions. The ligand solution, whose concentration and pH were the same with those of the complex, has been used as a blank. A calibration curve is obtained and the unknown amount of Al (III) is determined with similar method.

2.3. Analytical applications of the method

2.3.1. Determination of aluminium in artificial mixture

The developed method was successfully applied to the artificial mixture. The artificial mixture was prepared as in the below:

$$0.54 \text{ mg Al}^{3+} + 0.30 \text{ mg Mn}^{2+} + 0.13 \text{ mg Cr}^{3+}$$

The mixture was diluted with pH 5 buffer solution up to 100 mL. The aliquot parts of the solution was taken, then 1.0 mL of $1.0 \times 10^{-3} \text{ M}$ ligand was added into the solution. The mixture was diluted to the appropriate volume with pH 5 buffer solution. The absorbances of the solution was measured.

2.3.2. Application of the method to drug

Kompensan® is a tablet. It includes 62.826 mg of aluminum in per g of tablet. A stock solution of the tablet was prepared by complying the pharmacopeia procedure (USP XXIV) [30]. The aliquot part of this solution (last concentration was in the range of $1.4\text{--}13.5 \text{ } \mu\text{g mL}^{-1}$) and a $1.0 \times 10^{-3} \text{ M}$ ligand (1.5 mL) reagent were added. Then, the mixture was diluted up to 10 mL with a buffer solution of pH 5. The absorbance of the solution was measured at 413.5 nm.

3. Results and Discussion

3.1. Working wavelength and pH

The selection of the measurement wavelength is the most important step of the determination of metals using UV-Vis spectrophotometry. Due to all the experimental measurements performed at the false selected wavelength, all experimental results are negative affected.

In this work, the UV-Vis. spectra of $\text{Al}^{3+}\text{-L}$ complex at different pH values were examined against water and ligand. This complex gave maximum absorbance at 420.0 nm and pH 9. Since Aluminium can precipitate or forms hydroxyl complex in alkaline medium, pH 5 was selected as an optimum pH and 413.5 nm was selected as working wavelength (Fig. 2 and Table 2).

Table 2. Absorbance values of the aluminium complex of the ligand at different pH (the standard for comparison: ligand)

	pH											
	1	2	3	4	5	6	7	8	9	10	11	12
Abs	0.619	0.796	0.730	0.745	0.824	-	-	-	0.887	0.705	0.700	0.425

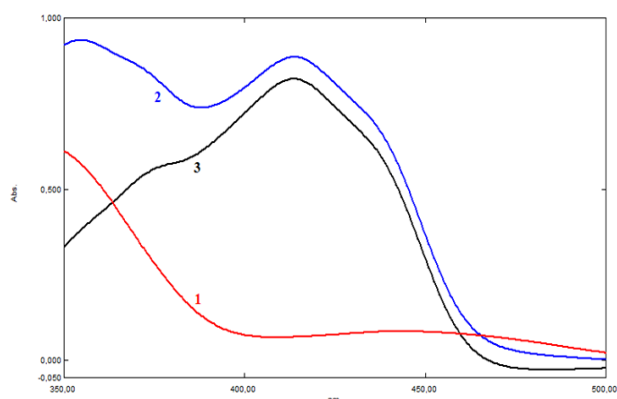


Figure 2. Absorption spectra, pH=5; (1) ligand (comparison standard: water), $C_L=2.0 \times 10^{-4}$ M; (2) Al-L complex (comparison standard: water), $C_{Al}=5.0 \times 10^{-5}$ M, $C_L=2.0 \times 10^{-4}$ M; (3) Al-L complex (comparison standard: ligand), $C_{Al}=5.0 \times 10^{-5}$ M, $C_L=2.0 \times 10^{-4}$ M, $l=1$ cm.

3.2. The ligand concentration

The absorbance of the Al^{3+} -L complex increased by increasing concentrations of ligand at constant metal concentration, and the absorbance of the complex became constant on the 1.5×10^{-4} mol L^{-1} ligand at 413.5 nm. So, the 1.5×10^{-4} mol L^{-1} ligand was used in this study.

3.3. Temperature and time on complex formation

The data concerning complex formation depending on the time and temperature was given in the slight. The complex is stable up to 40 min. All the studies were done at room temperature. The complex was stable for more than 30 minutes.

3.4. Complex stoichiometry

Job's method of continuous variation and mole-ratio methods were used for determining the molar composition of the complex. The stoichiometry of the complex was determined as (M:L) is 1:2 by Job method (Figure 3). The conditional stability constant (K) was computed as 2.68×10^6 by Job's method.

3.5. Calibration curve

Absorbance of the Al^{3+} -L complex obeys Beer's law between $1.4 \mu g mL^{-1}$ and $13.5 \mu g mL^{-1}$ for the aluminium in the optimum conditions. The molar absorption coefficient of aluminium was $1.47 \times 10^4 L mol^{-1} cm^{-1}$. The Sandell's sensitivity [31, 32] is computed for the developed method and it was $1.84 \times 10^{-3} \mu g cm^{-2}$. The correlation coefficient for the Al^{3+} -L is 0.9964. The values of slope are 0.0579 and the

intercept is + 0.0062. Thus, the calibration equation was $y = 0.0579x + 0.0062$.

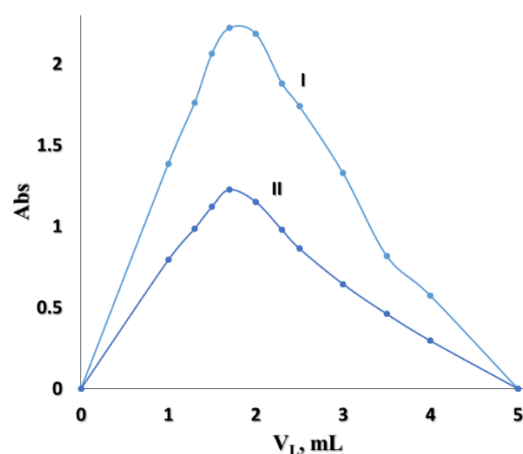


Figure 3. Determination of Al-L Complex formation stoichiometry by Job method, 413.50 nm, comparison standard: ligand, $l=1$ cm, pH=5; (I) $C_L=C_{Al}=1.0 \times 10^{-3}$ M, (II) $C_L=C_{Al}=5.0 \times 10^{-4}$ M

3.6. The investigation of interfering species

The possible interference effects on the determination of aluminium were investigated under the optimum conditions and the quantities did not cause any interfering effects. In the complexization study using the ligand, the ligand, it was masked with iron (III) and bismuth (III) ascorbic acid, copper (II) thiourea, mercury (I) urea, and manganese (II) KSCN (Table 4.2).

3.7. Analytical performance

The developed method was successfully applied on the three artificial mixtures. The artificial mixtures include aluminium with spiked aluminium (Section 2.4.1). The results are summarized in Table 4. The values of standard deviation, absolute and relative errors were acceptable levels. Then, the developed method was applied to the 'Kompensan®' drug. The developed method has high accuracy. There is no meaningful difference ($|\bar{X} - X_{true}| < \frac{ts}{\sqrt{N}}$) (Table 5).

Table 3. Interference effects for the determination of Al^{3+} with ligand at pH=3.5, 485 nm

Interfering species (I)	Limiting mass ratio (Al^{3+} : I)	Interfering species (I)	Limiting mass ratio (Al^{3+} : I)
K^+	1:385	NO_3^-	-
Na^+	1:85	CH_3COO^-	1:35
Pb^{2+}	-	SO_4^{2-}	1:420
Mg^{2+}	1:4	MnO_4^-	-
Zn^{2+}	1:160	NaO_2^{3-}	1:155
Bi^{3+}	-	SCN^-	1:74
Ni^{2+}	1:14	$\text{B}_4\text{O}_7^{2-}$	1:300
Cd^{2+}	1:27	NaO_3^-	1:305
Cu^{2+}	-	Thio Urea	1:370
Cr^{3+}	1:4	Ascorbic Acid	1:370
Fe^{3+}	-	Tartaric Acid	-
Hg^+	-	Urea	1:740
Sr^{2+}	1:150	EDTA	-
Co^{2+}	1:17	Cr^{3+} + Urea	-
As^{3+}	1:210	Cu^{2+} + Urea	-
Sn^{2+}	-	Cd^{2+} + Urea	-
Mn^{2+}	-	Bi^{3+} + Urea	-
Ag^+	-	Cr^{3+} + Thio Urea	-
Ga^{3+}	1:0,300	Ni^{2+} + Urea	-
In^{3+}	1:1	Zn^{2+} + Urea	-
NH_4^+	-	Fe^{3+} + Ascorbic Acid	1:5
F^-	-	Bi^{3+} + Ascorbic Acid	1:30
Cl^-	1:350	Cu^{2+} + Thio Urea	1:19
Br^-	1:245	Hg^+ + Urea	1:25
I^-	1:565	Mn^{2+} + KSCN	1:240

Table 4. Determination of aluminium in artificial mixture ((0.54 mg Al^{3+} +0.30 mg Mg^{2+} +0.13 mg Cr^{3+})/100 mL) (n=5).

Taken, sample (A), mL	Amount of Al^{3+} , μg 10 mL^{-1}	Added standard Al^{3+} , μg 10 mL^{-1}	Found, Al^{3+} , \bar{X} , μg 10 mL^{-1}	Standard deviation, s	Absolute Error, AE ^a	Relative Error, % (RE%) ^b
1.0	5.400	-	5.540	0.151	0.140	2.593
1.0	5.400	2.700	8.230	0.059	0.130	1.605
1.5	8.100	-	8.020	0.192	0.070	0.865
1.5	8.100	2.700	10.750	0.270	0.040	0.370

^a Absolute error, AE = $|\bar{X} - X_{\text{true}}|$ ^b Relative error, %, (RE%) = $\frac{|\bar{X} - X_{\text{true}}|}{X_{\text{true}}} * 100$ **Table 5.** Determination of aluminium in drug suspension (Kompensan®)

Certified value of Al (\bar{X}_{true}), mg	Found Al, (\bar{X}), (CL)	Standard deviation, s	Relative standard deviation (RSD%) ^a	Relative Error, %	$ \bar{X} - X_{\text{true}} $	ts/ \sqrt{N}
62.800	62.750± 0.067	0.054	0.089	0.080	0.050	0.067

4. Conclusions

A new UV–Vis. spectrophotometry has been developed to determine aluminium. In the range of 1.4–13.5 $\mu\text{g ml}^{-1}$ Al(III) , the method obeys Beer's

law. The developed method is an alternative method with molar extinction coefficient of the Al(III)-L complex (M:L;1:2) is $1.474 \times 10^4 \text{ L mol}^{-1} \text{ cm}^{-1}$. The developed method has high selectivity

and sensitivity. The developed method is an alternative to the present methods [14, 18, 19, 21]. In the certain spectrophotometric methods, the synthesis of azo compounds has difficulties for the determination of aluminum and some others have low reaction efficiency. So, our developed method has certain advantages in terms of the use of easily synthesized ligand and the high reaction efficiency compared to the other methods [14-17]. It does not require any separation technique in this study. Our method; neither surfactant nor time consuming extractant solvent usage in dispersive liquid-liquid microextraction or immobilization procedure [20, 22] requires to increase the selectivity and sensitivity. As a conclusion, the proposed method is simple, reproducible, easy and sensitive to determine aluminium. Moreover, the method can be successfully applied on artificial mixture and drug suspension to determine aluminium.

Acknowledgment

We kindly acknowledge to Anadolu University Scientific Research Projects (No:1509F633) for its support to this study.

Conflicts of interest

The authors state that did not have conflict of interests

References

- [1] Farndon, J. The elements. Aluminum. Benchmark Books, 2001, New York.
- [2] Nayak, P. Aluminium: impacts and disease. *Environmental Research*, 89(2) (2002) 101–115.
- [3] Santarossa, D. G., Talio, M. C. and Fernández, L. P. Aluminium traces determination in biological and water samples using a novel extraction scheme combined with molecular fluorescence. *Microchem. J.*, 129 (2016) 274–280.
- [4] Minshall, C., Nadal, J. and Exley, C. Aluminium in human sweat. *J.Trace Elem. Med. and Bio.*, 28 (1) (2014) 87–88.
- [5] Antoine, J. M. R., HooFung, L. A., Grant, C. N. Assessment of the potential health risks associated with the aluminium, arsenic, cadmium and lead content in selected fruits and vegetables grown in Jamaica. *Toxicology Reports*, 4 (2017) 181–187.
- [6] Frankowski, M. Aluminium and Its Complexes in Teas and Fruity Brew Samples, Speciation and Ions Determination by Ion Chromatography and High-Performance Liquid Chromatography–Fluorescence Analytical Methods. *Food Anal. Met.*, 7 (5) (2014) 1109–1117.
- [7] Kalogria, E., Varvaresou, A., Papageorgiou, S., Protopapa, E., Tsaknis, I., Matikas, A. and Panderi, I. Pre-Column Derivatization HPLC Procedure for the Quantitation of Aluminium Chlorohydrate in Antiperspirant Creams Using Quercetin as Chromogenic Reagent. *Chromatographia*, 77 (19-20) (2014) 1275–1281.
- [8] Hydes, D. J. and Liss, P. S. Fluorimetric Method for the Determination of Low Concentrations of Dissolved Aluminium in Natural Waters. *Analyst*, 101 (1976) 922–931.
- [9] Pedrozo-Peñafiel, M.J., Doyle, A., Mendes, L.A.N., Tristão, M.L.B., Saavedra, A. and Aucelio, R.Q. Methods for the determination of silicon and aluminum in fuel oils and in crude oils by X-ray fluorescence spectrometry. *Fuel*, 243 (2019) 493–500.
- [10] Qiong, L., Lirong, W., Danli, X. and Guanghan L. Determination of trace aluminum in foods by stripping voltammetry. *Food Chem.*, 97(1) (2006) 176–180.
- [11] Ritchie, G.S.P., Posner, A.M., and Ritchie, I.M. The determination of trace levels of aluminum by differential pulse polarography. *Anal. Chim. Acta*, 117, (1980) 233–239.
- [12] Eroglu E. I., Gulec, A. and Ayaz A. Determination of aluminium leaching into various baked meats with different types of foils by ICP-MS. *J. Food Process. Preserv.*, 42 (12) (2018) 1–9.
- [13] Fairman, B. and Sanz-Medel, A. Flow injection-mini-column technique with ICP-AES detection for the isolation and preconcentration of the fast reactive aluminium fraction in waters. *Fresenius J. Anal. Chem.*, 355 (1996) 757–762.
- [14] Huseyinli A.A., Alievaa R., Hacıyevaa S. and Guray T. Spectrophotometric determination of aluminium and indium with 2,2',3,4-tetrahydroxy-3',5'-disulphoazobenzene. *J. Hazard. Mat.*, 163 (2-3) (2009) 1001–1007.
- [15] Guray T., Uysal U.D., Gedikbey T. and Huseyinli A.A. 2,2',3,4-Tetrahydroxy-3'-sulpho-5'-nitroazobenzene for spectrophotometric determination of aluminium in pharmaceutical suspensions and granite. *Anal. Chim. Acta*, 545 (2005) 107–112.
- [16] Guray T., Ogretir C., Gedikbey T. and Huseyinli A.A. Synthesis and spectrophotometric determination of acidity constants of 2,3,4,6'-tetrahydroxy-3'-sulfoazobenzene and their use

- in determination of aluminum. *Turk. J. Chem.*, 35 (2011) 291–305.
- [17] Huseyinli A.A. and Aliyeva R.A. A new tetrahydroxyazon SC analytical reagent for the spectrophotometric determination of Al(III), In(III), and Ga(III). *Anal. Sci.*, 17 (2001) 1683–1685.
- [18] Ahmed, M.J., Hoque, M.R., Khan, S.H. and Bhattacharjee, S.C. A simple spectrophotometric method for the determination of aluminum in some environmental, biological, soil and pharmaceutical samples using 2-hydroxynaphthaldehydebenzoylhydrazone. *Eurasian J. Anal. Chem.*, 5(1) (2010) 1-15.
- [19] Saritha, B. and Reddy, T.S. Direct Spectrophotometric determination of Aluminum (III) using 5-Bromo-2-hydroxy-3-methoxybenzaldehyde-P-hydroxybenzoic hydrazine. *IOSR J. Applied Chem.*, 7 (2) (2014) 5-10.
- [20] Khajehsharifi, H., Solhjoo, A. and Bordbar M. M. Design of an Optical Sensor for Aluminium(III) Determination Based on Immobilization of Eriochrome Cyanine R on a Triacetylcellulose. *Iranian J. Anal. Chem.*, 3 (2) (2016) 145-152.
- [21] Zhou, T., Huang, Y., Yuan, D., Feng, S., Zhu, Y., Ma, J. A sensitive flow-injection analysis method with iminodiacetate chelation and spectrophotometric detection for on board determination of trace dissolved aluminum in seawater. *Analytical Methods*, 8(22) (2016) 4473-4481.
- [22] Lima, L. C., Papai and R., Gaubeur, I. Butan-1-ol as an extractant solvent in dispersive liquid-liquid microextraction in the spectrophotometric determination of aluminium. *J. Trace Elements Med. Bio.*, 50 (2018). 175-181.
- [23] Oter O., Ertekin K., Kılınçarslan R., Ulusoy M. and Cetinkaya B. Photocharacterization of a novel fluorescent Schiff Base and investigation of its utility as an optical Fe^{3+} sensor in PVC matrix. *Dyes and Pigments*, 74(3) (2007) 730-735.
- [24] Baran N.Y. and Saçak M. Synthesis, characterization and molecular weight monitoring of a novel Schiff base polymer containing phenol group: Thermal stability, conductivity and antimicrobial properties. *J. Mole. Struc.*, 1146 (2017) 104-112.
- [25] Ejidike I.P. and Ajibade P.A. Transition metal complexes of symmetrical and asymmetrical Schiff bases as antibacterial, antifungal, antioxidant, and anticancer agents: Progress and prospects. *Rev. Inorg. Chem.*, 35(4) (2015) 191–224.
- [26] Napier I., Ponka P., Richardson Des R., Iron trafficking in the mitochondrion: novel pathways revealed by disease, *Blood*, 105(5) (2005) 1867-1874.
- [27] Percino M.J., Cerón M., Castro M.E., R Ramírez R., Soriano G. and Chapela V.M. (E)-2-[(2-hydroxybenzylidene)amino]phenylarsonic acid Schiff base: Synthesis, characterization and theoretical studies. *J. Mol. Struc.*, 1081 (2015) 193-200.
- [28] Al-Shemary R.K., Al-khazraji A.M.A., Niseaf A.N. Preparation, spectroscopic study of Schiff base ligand complexes with some metal ions and Evaluation of antibacterial activity. *The Pharma Innovat. J.* 5(1) (2016) 81-86.
- [29] Uysal U.D., Güray T., Berber H., Ercengiz D., Aydoğdu A., 2018, Synthesis of Certain Schiff Bases Formed Substituted 2-Aminophenol and Substituted Hydroxy Benzaldehyde, Spectroscopic Study and Investigation of Their Applications on Metal Determination in Different Samples, Anadolu University Scientific Research Projects (No:1509F633).
- [30] The United States Pharmacopeia-National Formulary, United States Pharmacopeial Convention, Rockville, MD, 1999.
- [31] Suresha S., Silwadi M.F. and Syed A.A. Sensitive and selective spectrophotometric determination of Hg(II), Ni(II), Cu(II) and Co(II) using iminodibenzyl and 3-chloroiminodibenzyl as new reagents and their applications to industrial effluents and soil samples, *Int. J. Environ. Anal. Chem.*, 82 (2002) 275-289.
- [32] Khopkar S.M., Basic Concepts of Analytical Chemistry, 3rd edition ed., New Age Science, 2008, pp. 211-240.

Electronic features of Gaussian quantum well as depending on the parameters

Hülya BOYRAZ , Emine ÖZTÜRK* 

¹Sivas Cumhuriyet University, Department of Physics, 58140, Sivas/TURKEY

Abstract

In this study, the electronic characteristics of Gaussian quantum well have been examined as dependent on the parameters such as the concentration ratio, the even power parameter and Gaussian potential range. The energy levels and the wave functions in Gaussian quantum well (GQW) under effective mass approach were concluded by Schrödinger equation solution. According to our results, all parameters have a great impact on the electronic characteristics of GQW. These characteristics have practical interest in the design of adjustable semiconductor devices using such structures.

Article info

History:

Received:06.03.2020

Accepted:13.05.2020

Keywords:

Gaussian quantum well, Electronic properties, Concentration ratio, Adjustable parameters.

1. Introduction

The electronic characteristics of the low-dimensional structures (LDSs) are extremely reliant on the shape of the potential profile of a semiconductor quantum well (QW). Superior interest has been motivated on GaAs/Al_xGa_{1-x}As heterostructures due to their direct band gap for Al concentration x -factor below (0.40–0.45). The studies on quantum heterostructures open a new field in fundamental physics, and also offer a wide range of potential applications for optoelectronic devices [1-2]. GaAlAs / GaAs QW systems are applied in modern photo-electronics and high-speed electronic devices, the electrical and optical properties of the related systems have been widely investigated under both the pressure and external fields [3-9]. There is no direct experimental method for defining the confinement potential. The confinement potentials are frequently modeled by rectangular potential well or the parabolic potential [10]. It was noted that, the conventional rectangular QW has basic, but unrealistic form owing to the non-parabolic shape at the center of the QW. On the other hand, the parabolic potential is inappropriate to describe the experimental results due to its infinite depth and range [10]. Based on the experimental results, Xie [11] has pointed that the real confinement potential is not parabolic but Gaussian quantum well (GQW) potential which possesses the

finite depth and range. Based on GQW potential, a lot of studies have been conducted investigated the electronic and optical properties of heterostructures [12-13].

This study focused on the theoretical research of the electronic qualities of Ga_{1-x}Al_xAs/GaAs GQW depending on the x -concentration (where x represents the contribution rate of Al in GQW) and the structure parameters. The paper is organized as follows: In Section 2, the theoretical material and method is outlined. In Section 3, we discuss the results of our calculations. In particular, we compare the potential shape and the energy levels according to structure parameters. Section 4 is allocated to a brief conclusion of the study.

2. Material and Method

With the effective-mass approach, the wave functions and the energy levels for electrons in GQW could be accomplished by solving the one-dimensional Schrödinger equation.

$$\left(-\frac{\hbar^2}{2m^*} \frac{d^2}{dz^2} + V(z)\right) \Psi(z) = E \Psi(z) \quad (1)$$

*Corresponding author. Email address: eozturk@cumhuriyet.edu.tr
<http://dergipark.gov.tr/csj> ©2020 Faculty of Science, Sivas Cumhuriyet University

where $V(z)$ is the confined potential, m^* is the effective mass of electron, and E and $\Psi(z)$ are the eigen-energy and eigen-function of the Eq. (1) solution.

The confinement potential of GQW for the electron z -direction is given by

$$V(z) = V_0 \left\{ -\text{Exp} \left[-\left(\frac{2z}{\beta} \right)^p \right] + 1 \right\} \quad (2)$$

The discontinuity in the conduction band edge of $\text{Ga}_{1-x}\text{Al}_x\text{As}/\text{GaAs}$ [9, 13, 15]

$$V_0 = 0.6 (1.155 x + 0.37 x^2) \quad (3)$$

Where x denotes the concentration of Al in the structure, p is the even power parameter [13], β is the Gaussian potential range (in nm unit).

3. Results and Discussion

It has been notionally examined the electronic features of $\text{Ga}_{1-x}\text{Al}_x\text{As}/\text{GaAs}$ GQW structure as depending on the changeable parameters. In this study, the well width is $L = 10$ nm and $m^* = 0.067 m_0$ (m_0 is the free electron mass).

For different two p -values, Fig. 1 and Fig. 2 demonstrate the variation of the confinement potential related to x -concentration for $\beta = 0.5$ and $\beta = 1$ value, respectively. As understood from these figures, when the x -concentration increases, the height of the confined potential increases. For $\beta = 0.5$, all enclosed potentials at $p = 2$ value yield the Gaussian potential profile, while at $p = 6$ rate these profiles approach towards square well potential profiles (see Fig. 1). For $\beta = 1$, while at $p = 2$ the quantum well potentials both with less depth and behave more like parabolic quantum wells appear, whereas for $p = 6$ value shows almost square quantum well profiles (Fig. 2). It can be understood from here that by changing the Gaussian potential parameters, quantum well shapes similar to parabolic and square well potential profiles can be obtained from the Gaussian potential profile. Such different profiles describe the diffusion process [16] which is used in order to realize a desired configuration of the energy levels (for example, a group of equidistant levels). A change in the p -parameter leads to an adjustment of the confinement potential shape from the Gaussian well for $p = 2$ to the parabolic or square quantum well for $p > 2$. Thus, the elasticity of the present approach in treating the confined carriers in a QW is guaranteed [17].

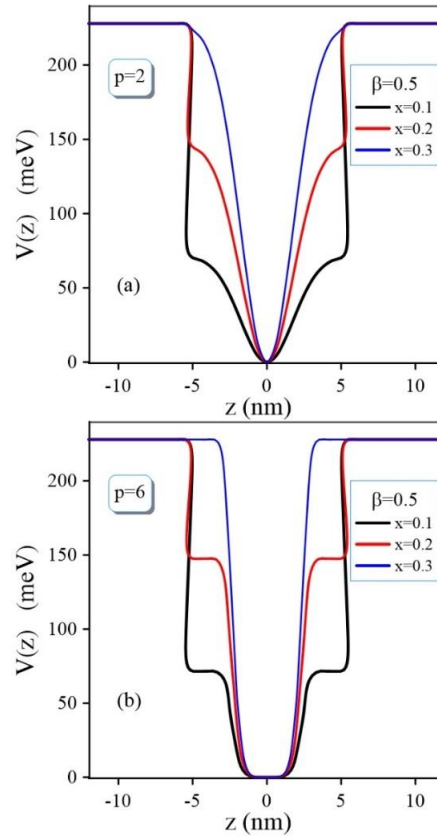


Figure 1. For $\beta = 0.5$, the change of confined potential of GQW related to the x -concentration for a) $p = 2$, b) $p = 6$.

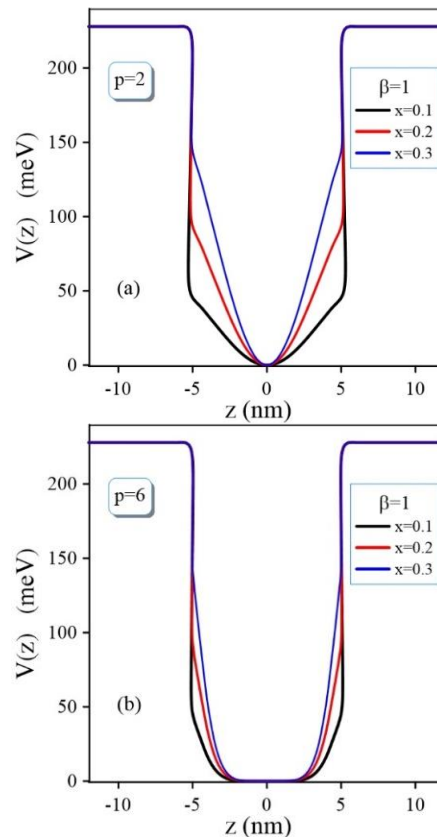


Figure 2. For $\beta = 1$, the change of confined potential of GQW related to the x -concentration for a) $p = 2$, b) $p = 6$.

For three different x -values, Fig. 3 exhibits the confinement potential, the bound energy levels and squared wave functions referred to these energy levels for $\beta = 0.5$ and $p = 2$. The major difference for these values is the depth and width of the Gaussian potential. As estimated, for $x = 0.1$ the energy levels with lower Gaussian potential height is continuously lower than the energy levels of $x = 0.1$ and 0.3 values. As can be seen from these figures, there are two, two and single energy states in GQW structure for $x = 0.1, x = 0.2$ and $x = 0.3$, respectively. Although the depth of the Gaussian potential is large for $x = 0.3$ value, there is only one energy level due to its narrower width. As the height and width of the Gaussian potential profile changes depending on the concentration ratio, both the bound state energy levels and the probability densities of electrons at these energy levels change.

For (both $p = 2$ and $p = 6$ number) $\beta = 0.5$ and $\beta = 1$ value, the resulting bounded state energy levels corresponding to the change in the concentration ratio between $x = (0.10 - 0.3)$ are given in Fig. 4a and Fig. 4b, serially. As the x -value increases, the ground and second energy levels increase. As the β -value shrinks, the Gaussian potential profile narrows and energy levels rise. For $\beta = 0.5$, the change of E_1 and E_2 level versus x -number is faster than $\beta = 1$. So, for $\beta = 0.5$, the E_2 level for $x > 0.28$ values is outside the Gaussian potential well, whereas for both $p = 2$ and $p = 6$, these energies are almost at the same level for $x \leq 0.28$. As the number p increases, its potential profile gradually resembles a square well. As a result, for $p = 6$, both energies and these energy changes depending on the x -parameter are smaller compared to $p = 2$. This seems to be more obvious than the graphs drawn for $\beta = 1$.

For GQW, we give in Fig. 5 and 6 the first two energy levels as a function of the x and p -parameter for $\beta = 0.5$ and $\beta = 1$ rate, respectively. Considering the E_1 and E_2 variations plotted against the increasing x and p parameters at the same rates, it was seen that the energy levels were smaller for $\beta = 1$. As seen from Fig. 5b, for $\beta = 0.5$, the E_2 level at $x > 0.28$ is not within the Gaussian potential. For $\beta = 0.5$ the sensitivity of the energy levels to the x -concentration ratio appears to be higher than $\beta = 1$. Thus, we suggest that the potential shape affects the confinement and localization. These figures are different from Fig. 4 since both x and p -factors change together in Fig. 5 and Fig. 6.

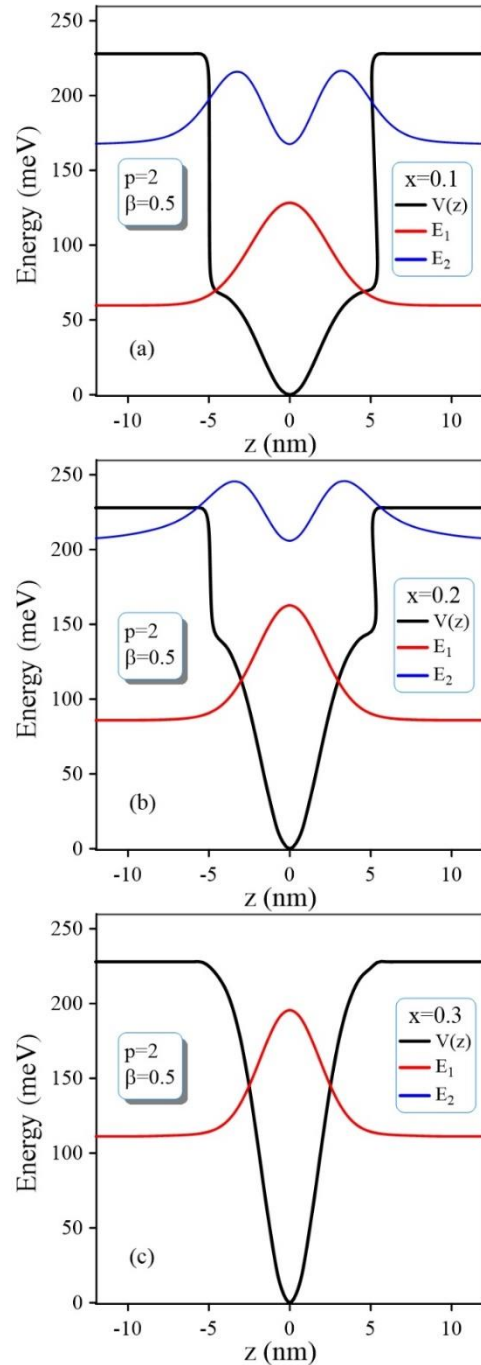


Figure 3. For $\beta = 0.5$ and $p = 2$, the confined potential and the bound energy levels with their squared wave functions for a) $x = 0.1$, b) $x = 0.2$, c) $x = 0.3$.

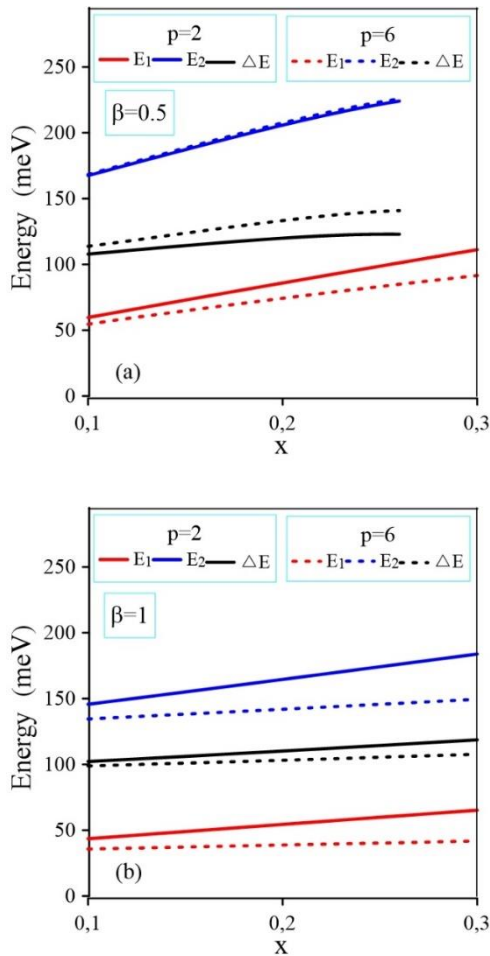


Figure 4. For $p = 2$ and $p = 6$ number, the variation of the bound energy levels and the energy difference versus the x-concentration ratio values for a) $\beta = 0.5$, b) $\beta = 1$.

4. Conclusions

In present work, the electronic qualities of Gaussian quantum well have been examined as dependent on the parameters such as the concentration ratio (x), the even power parameter (p) and Gaussian potential range (β). We analyzed the potential height and the bound energy levels in GQW. In particular, we have considered the potential shape, the eigen-energies and the eigen-functions for these parameters. It is found that depending on the x-concentration value of the electronic features of GQW varies for both β and p -factors. Thus, if it is desired to obtain narrower Gaussian potential depending on x-concentration value, small β and p -values should be preferred. These features could be crucial in the improvement of continual wave operation of GQW semiconductor devices. So, we think that these consequences will supply a development in the electro-optical semiconductor devices applications, for proper selection of the structural parameters.

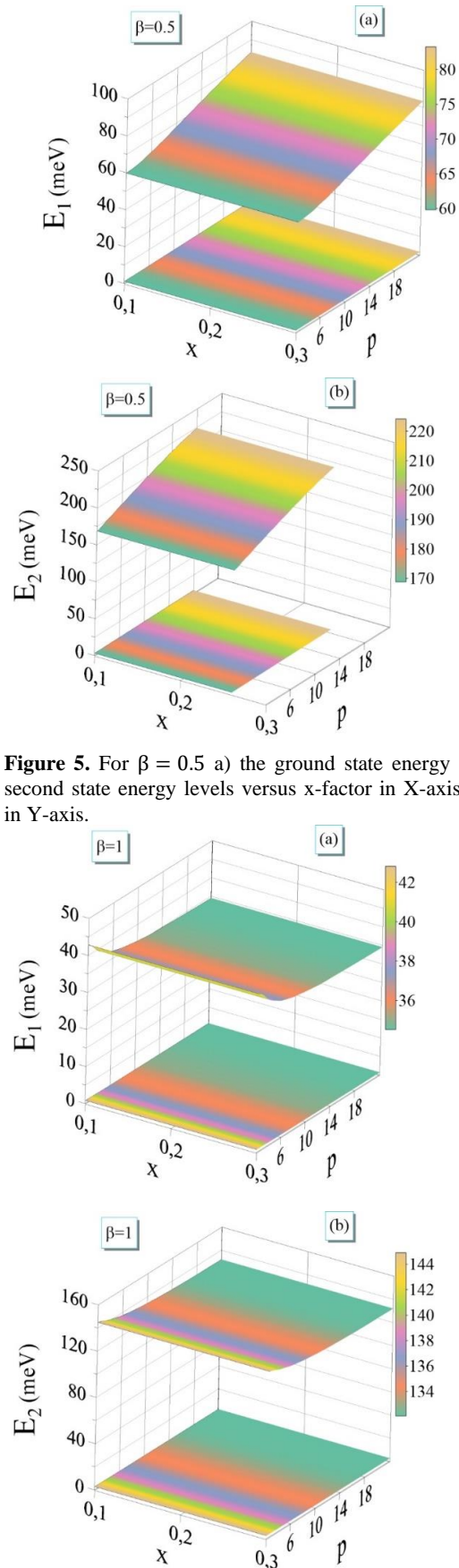


Figure 5. For $\beta = 0.5$ a) the ground state energy levels, b) the second state energy levels versus x-factor in X-axis and p-factor in Y-axis.

Figure 6. For $\beta = 1$ a) the ground state energy levels, b) the second state energy levels versus x-factor in X-axis and p-factor in Y-axis.

Conflicts of interest

There is no conflict of interest.

References

- [1] Enders B.G., Lima F.M.S., Nunes O.A.C., Fonseca A.L.A., Agrello D.A., Qu F., DaSilva J.E. F., Freire V.N., Electronic properties of a quasi-two dimensional electron gas in semiconductor quantum wells under intense laser fields, *Phys. Rev. B* 70 (3) (2004) 035307-035315
- [2] Radu A., Niculescu E. C., Cristea M., Laser dressing effects on the energy spectra in different shaped quantum wells under an applied electric field, *J. Optoelectron. Adv. Mater.* 10 (2008) 2555-2563
- [3] Raigoza N., Morales A. L., Duque C. A., Effects of hydrostatic pressure on donor states in symmetrical GaAs-Ga_{0.7}Al_{0.3}As double quantum wells, *Physica B* 363 (2005) 262-270.
- [4] Peter A. J., Navaneethakrishnan K., Simultaneous effects of pressure and temperature on donors in a GaAlAs/GaAs quantum well, *Superlatt. Microstruct.* 43 (2008) 63-71.
- [5] Ozturk E., Simultaneous effects of the intense laser field and the electric field on the nonlinear optical properties in GaAs/GaAlAs quantum well, *Opt. Commun.* 332 (2014) 136-143.
- [6] Zhao G. J., Liang X. X., Ban S. L., Binding energies of donors in quantum wells under hydrostatic pressure, *Phys. Lett. A* 319 (2003) 191-197.
- [7] Ozturk E., Sokmen I., Nonlinear intersubband absorption and refractive index changes in square and graded quantum well modulated by temperature and hydrostatic pressure, *J. Lumin.* 134 (2013) 42-48.
- [8] Kasapoglu E., Duque C. A., Mora-Ramos M. E., Restrepo R. L., Ungan F., Yesilgul U., Sari H., Sokmen I., Combined effects of intense laser field, electric and magnetic fields on the nonlinear optical properties of the step-like quantum well, *Materials Chemistry and Physics*, 154 (2015) 170-175.
- [9] Ozturk O., Ozturk E., Elagoz S., Linear and nonlinear optical absorption coefficient and electronic features of triple GaAlAs/GaAs and GaInAs/GaAs quantum wells depending on barrier widths, *Optik* 180 (2019) 394-405.
- [10] Lin C. Y., Ho Y. K., Photoionization cross sections of hydrogen impurities in spherical quantum dots using the finite-element discrete-variable representation, *Phys. Rev. A* 84 (2011) 023407-023415.
- [11] Xie W.F., Two interacting electrons in a spherical Gaussian confining potential quantum well, *Commun. Theor. Phys.* 42 (2004) 151-154.
- [12] Sari H., Ungan F., Sakiroglu S., Yesilgul U., Kasapoglu E., Sokmen I., Electron-related optical responses in Gaussian potential quantum wells: Role of intense laser field, *Physica B* 545 (2018) 250-254 .
- [13] Niculescu E. C., Eseanu N., Spandonide A., Laser field effects on the interband transitions in differently shaped quantum wells, *U.P.B. Sci. Bull. Series A*, 77 (4) (2015) 281-292.
- [14] Boda A., Boyacioğlu B., Chatterjee A., Ground state properties of a two-electron system in a three-dimensional GaAs quantum dot with Gaussian confinement in a magnetic field, *Journal of Applied Physics* 114 (2013) 044311-044317.
- [15] Zorrry P. S. Jr., *Quantum well lasers*, Academic Press, Boston, p.79 (1993).
- [16] [Doncev V., Saraydarov M., Shtinkov N., Germanova K., Vlaev S. J., Diffused GaAs/AlGaAs quantum wells with equidistant electronic states, *Mat. Sci. Engin. C* 19 (1-2) (2002) 135-138.
- [17] [Xie W., Potential-shape effect on photoionization cross section of a donor in quantum dots, *Superlatt. Microstruct.* 65 (2014) 271-277.



A matching model to measure compliance between department and student

Hidayet TAKCI¹ Kali GÜRKAHRAMAN¹ Emre ÜNSAL^{2,*} Ahmet Fırat YELKUVAN¹

¹Department of Computer Engineering, Faculty of Engineering, Sivas Cumhuriyet University, 58140, Sivas/ TURKEY

²Department of Software Engineering, Faculty of Technology, Sivas Cumhuriyet University, 58140, Sivas/ TURKEY

Abstract

The aim of all education systems is to train students who are equipped with knowledge. In that case, that student is able to determine the most suitable profession for him/her success in education and career that are related to this profession will be higher. Studies done up to this day have been focused on finding out the factors affecting the career choice of the student, but they have not suggested any method for determining the most suitable profession. It is not possible to obtain satisfying results from a system that does not lead students to appropriate higher education departments. In this context, a student- department matching system is proposed which aims to increase the success of the education systems in our study. The department of computer engineering was dealt with as a sample department and the proposed study was examined to determine whether a student was suitable for computer engineering or. The required data was obtained with the help of the questionnaire, and then a model of successful and unsuccessful students was created. Data mining algorithms such as C4.5, C-SVC, MLP, and Naïve Bayes are used during the test of the generated model. The best result was obtained by the C-SVC algorithm and the second best result by Naive Bayes. The lowest error rate achieved was 0.2700 and the highest accurate recognition rate was 73.00%.

Article info

History:

Received:29.03.2018

Accepted:22.04.2020

Keywords:

Matching system,
Data mining,
Predictive Models.

1. Introduction

Individuals begin to receive education from the moment that they born. The education, which starts at the family passes through the various steps and moves towards the final destination. At these steps, the transition from a lower to a higher education institution often takes place based on the test score rankings. However, evaluation and transposition based on test score ranking are far from being the right approach. Although the test score is an important factor, it cannot provide the complete information on which educational institution is better individually.

Nowadays, it is a necessity to take into account additional factors, because the test scoring based approaches only evaluate cognitive skills. For instance, it is possible that a student will be unhappy first and then unsuccessfully when he or she goes to a school with only his test score. Although the student completes the school with the family enforcement or even have a business owner in that area, the unhappiness continues. The schools that have gone incorrect and the profession obtained will cause low workforce in the future. This situation may be one of the biggest but most overlooked problems today. Even

if it is not possible to overcome this problem, it may be a better solution to take the other factors apart from the test scores.

In this study, a matching model is presented for students to choose the right academic education or profession. The aim of the model is to fulfill the match between the students and the department based on the ability, expectations, and interests. The reason for working with these categories is that a student cannot succeed if he or she is not interested or talented in a profession. In addition, it is also an important factor for a department/profession to meet student expectations.

2. Previous Studies

The proposal confessed in this study is novel; therefore, there are not any previous studies that will overlap with the study. For this reason, similar studies will be considered as previous studies and the differences will be revealed.

The studies have been dealt with the title of factors that affect the selection of professions until now. In 2014, Çelik and Üzmez [1] presented a comprehensive study on this subject. In the related study, the factors such as

*Corresponding author. Email address: eunsal@cumhuriyet.edu.tr

<http://dergipark.gov.tr/csj> ©2020 Faculty of Science, Sivas Cumhuriyet University

teaching, medicine, nursing, accounting, information technology, textile ready-to-wear program, tourism management and many fields were studied. As a result of this study, the factors affecting the selection of profession include family approval, social benefit, social expectations, career opportunity, salary, job security and interest. In addition, it would not be misleading to say that one of the factors influencing students' career choice is guidance units. One of the valuable studies about this subject is the study related to random departments by Sarıkaya and Korshid [2] in 2009. In this study, it was revealed that factors such as interest, helplessness, occupational advantage, recommendations, family factors, grades and personal characteristics had an effect on career choice. The last study about the factors influencing the choice of profession was presented in 2011 by Sathapornvajana and Watanapa [3]. This study was conducted on the students who selected areas related to information technologies. The key factors who choose this area are self-sufficiency, self-criticism, self-consciousness, social outlook, career, reputation, ease of professionalism and innovation.

Although there are many factors which affecting the choice of profession are handled one by one; it can be categorized as skills, expectations, and interests. Therefore, the sub-elements of these categories will be revealed, and data collection and data analysis with the correct tools will be contributed solving the problem. Surveys record what people say, and sometimes the questionnaire participant can give misleading or incorrect information. Moreover, the use of psychometric tests will be valuable. Psychometry is a science that evaluates the characteristics and qualities of people. Psychometric tests measure the relevance of person's abilities and skills, abilities he or she needs to perform required by the job [4]. The goal is to guide people to the profession in accordance with their abilities and qualifications. Psychometric tests have been used in the recruitment of candidates, evaluation of working personnel, the decision of promotion, analysis studies and career counseling.

In this work, data mining techniques will be used for data analysis. Data mining is an interdisciplinary way of discovering new and potentially useful information from huge amounts of data [5] which is applied in many sectors such as banking, finance, marketing, insurance, and medicine, also includes appropriate techniques for the education field. For example, students can be divided into categories by using the classifier [6] and prediction models can show whether students will pass a course or fail [7] by using prediction models. Moreover, students could be classified into similar groups with the help of

clustering analysis [8]. Additionally, in order to increase student participation, sample works have been done, recently such as merging educational software and student information [9].

3. Materials and Methods

In this study, a machine learning based system design will be proposed, in order to place the students in the correct educational departments. One side of the system will contain student information, the other side will contain section information, and the black box of the system will measure the compatibility between the two sides. The output of this compatibility analysis can be labeled as "Appropriate" or "Not Appropriate", so that if the compatibility between the student and the department is positive, then the output of the system labeled as "Appropriate", otherwise it labeled as "Not Appropriate". The proposed matching system design is demonstrated in Figure 1.

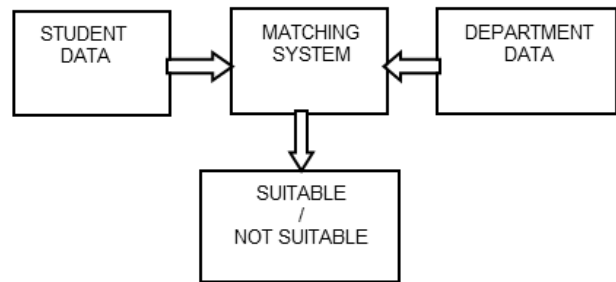


Figure 1. Proposed matching system diagram.

The proposed system will be a system based on predictive models. Therefore, first, the system will be trained with training data, and then the trained system will predict the results for new examples. In this context, some studies have been carried out in accordance with the stages of data mining, and the parameters of the predictive model have been revealed. The data source of the model to be created will be the data obtained from the survey applied to the students who study at the department of computer engineering.

The matches between student information and departmental information will be performed with the help of a predictive model. Before processing the data obtained from the survey, a pre-process is required. In this context, in the first step, the missing, inconsistent, meaningless data in the dataset should be deleted. Subsequently, the survey data will be digitized and transformed, so that data mining methods can be performed. The numerical data which is obtained from the survey will be presented in the vector space model [10], and the data will be presented as a vector for each student. In the data mining phase, a part of the data

obtained from the survey will be defined as training data and the other part used as test data. Models will be built for Successful and Unsuccessful students, through the part of the training data. In the test phase, students whose class is unknown will be tested whether successful or unsuccessful.

If we look at the problem regardless of the data mining process, the performed operations can be expressed simply as follows. The data of the students, that currently studying in the computer engineering department, are collected from the survey. The class label of the students is given based on the transcript information so that the model can be built for the successful student as well as for the unsuccessful student. After that, the survey is applied to other students and it is measured using the previously collected data that the new students will or will not be successful in the computer engineering department. As a result, if the survey profile of a new student is similar to the profiles of the students who are now successfully studying in the department, it can be said that the new student is appropriate, otherwise, the new student is not appropriate.

4. Experimental Work

This section includes studies that we have undertaken within the scope of the proposed system model for students to be placed in the appropriate department.

4.1. Data set

The proposed model test was performed on the data collected by the researchers. The survey was chosen as a measurement tool for data collection, and 210 students participated. A part of this survey was taken from the study of the academic self-concept scale presented by Kuzgun [11]. There are four main categories and several sub-categories of the survey study. The details about the survey are given in Table 1.

Table 1. Distribution of The Applied Survey Questions

Main Category	Sub Categories	Question Count
Ability	Literature, science, shape	16
	space and hand-eye coordination	
Expectations	Professional expectations	14
Demographic data	Demographic and registration data	10
Interest	Science, mechanic, hobbies, social, welfare, foreign language etc.	75

We have used the likert scale corresponding to five different values which are between 1 and 5. These

values are strongly disagree, disagree, neutral, agree, strongly agree. Besides, the answers of some questions are in the case of 1 and 0.

The developed survey was applied to the students who are studying in Cumhuriyet University, Computer Engineering Department in two stages as pre-application and the main application. Sub-dimensions of the scales were determined by applying Exploratory Factor Analysis (EFA) to the data obtained from the pre-application. In the main application, Confirmatory Factor Analysis (CFA) was used to verify both the outputs of the preliminary application and the suitability of the data to the sample group. Students who participated in the survey were selected from 2, 3 and 4 classes. The distribution of the students according to their classes, and label distributions are given in Table 2.

Table 2. Data Characteristics

Data Source	Students of Computer Engineering Department of Cumhuriyet University
Sample Count	210
Record Distribution	76 (4. Class), 76 (3. Class) and 58 (2. Class)
Class Distribution	Successful (141), Unsuccessful (69)

At the end of the main application, 4 of the 210 students survey records were eliminated because of a determined problem in the survey records. Therefore, the experimental study can be done only with 206 survey records of the students.

4.2. Experimental design

For the accordance of predictive modeling, two different labeling studies have been carried out on collected data. In the first case, transcript grades of the students are directly taken into account and, the grade of the students 2.0 and above are labeled Successful the rest of them labeled Unsuccessful. In the second case, not only the transcript grades but also the opinions of the instructors are also taken into account. Successful and unsuccessful labels were obtained from the opinions of the 5 lecturers who entered the course of the students who participated in the survey and the labeling was made accordingly. After that, decision trees (C4.5), support vector machines (C-SVC), artificial neural networks (MLP) and naive Bayes continuous classification algorithms, which are frequently used in past studies, were used to test our recommendation. The success of the algorithms was tested using the Tanagra [12] named machine learning software for the model tests.

Each algorithm was evaluated with optimum parameters and 10-fold cross-validation method was used for model evaluation.

4.3. Experiment results

In the classification experiments to be performed on the data, the results are presented as error rates. In the first step, the obtained results on the labeled data based on the transcript grades represented in terms of all, ability Test, expectancy test, and interests test rates. The test results are given in Table 3.

Table 3. Classification errors from labeling according to transcript grades

Algorithm	All	Ability Test	Expectancy test	Interests Test
<i>C4.5</i>	0.5450	0.4750	0.4550	0.5700
<i>C-SVC</i>	0.4900	0.4300	0.5200	0.4500
<i>MLP</i>	0.4800	0.5050	0.5350	0.5150
<i>Naive Bayes</i>	0.5050	0.5200	0.5750	0.5050

However, in the second stage, the results of the classification errors are obtained from the opinions of the instructors are examined as given in Table 4.

Table 4. Classification errors obtained from the opinions of the instructors

Algorithm	All	Ability Test	Expectancy test	Interests Test
<i>C4.5</i>	0.4550	0.4000	0.4050	0.4400
<i>C-SVC</i>	0.4050	0.2700	0.3350	0.4400
<i>MLP</i>	0.4250	0.3000	0.4300	0.4650
<i>Naive Bayes</i>	0.3650	0.3100	0.3800	0.4200

When the C4.5 algorithm gave an error rate of 0.5450 in the experiments with the questions of the survey completely, the ability test obtained with 16 questions gave 0.4750 error rate, and a better result was obtained. Similarly, the values dropped from 0.4900 to 0.4300 for the C-SVC algorithm. Unlike the other two methods, the error rate of MLP and Naive Bayes algorithms is increased. The error rate of 0.4800 for MLP has increased to 0.5050, and, it rose from 0.5050 to 0.5200 for Naive Bayes.

The second subcategory is the category of occupational expectations which is measured by the Expectancy test. In this category, the C4.5 algorithm yielded better results than both of the previous test results. However, the C-SVC algorithm, in contrast to the other two experiments, gave the most unsuccessful result in the category of occupational expectations. Likewise, the MLP and Naive Bayes algorithm also yielded unsuccessful results in this category. As a result, occupational expectations carry valuable information

for the decision tree classifier but give lower results for others.

Finally, experiments based on areas of interest were carried out and the results are obtained. The results of the Interest test gave values close to the error results as in the Expectancy test. In addition, another remarkable detail is that the C-SVC algorithm yields similar results to the ability test. This situation can be interpreted as a relationship between interests and abilities.

Generally, it can be said that the data set of the second experiment gave the better test results when compared with the first one.

5. Discussion

The transition of the current education system to a higher education institution by exam makes the exam scores significant. While exam scores provide information about the students relatively, in fact, more information can be obtained by assessing the skills. A student who is more intelligent but has less financial facility may not win good department, in contrast, less intelligent, have better financial status, and the hardworking student may win that department. This is an anomaly and does not fit into equal opportunity. In that vein, there are many departments that can be reached with an exam score when the student makes a preference with an exam score alone. For example, a student may prefer computer engineering or mine engineering in terms of test scores. However, there are very different professions than each other, although both departments are found in engineering faculty. As it can be seen from the example, evaluation of the students by exam score alone is not enough; in addition to that, there should be a selection process with more factors. So that, there is a need to collect additional student information and analyze this data correctly for a better evaluation.

For this aim, 210 students from Computer Engineering Department of Cumhuriyet University is selected and asked to fill a survey consist of 115 questions, in order to create a dataset in this study. A matching system based on classification algorithms was established and experiments were carried out with the collected dataset. The class label for student data is given first by reference to the transcript grade. Students with transcript grade 2.00 and above were tagged successfully the rest of them tagged unsuccessfully, and some results were obtained. After that, a labeling was made according to the opinions of the instructors for the students who participated in the survey, and the experiments were repeated with this data. As a result

of the repeated experiments, it was observed that the second data set gave better results. This is because the transcript grades are not enough alone for extracting a good student profile.

The success rate being around 75% is not a value that falls behind the literature. Since the problem we are trying to solve is based on many parameters and the training data obtained is not so much, the average of success are behind the literature. Another reason for the success value to remain relatively low is that it was obtained without pretreatment on the data.

6. Conclusion

The existing education system evaluates the students by only sorting with their exam scores, and ignores the personals skills of the students. This issue causes an anomaly and does not fit into equal opportunity. The university student selection system should be needed to revise with more factors. In this study, a student-department matching system is proposed which aims to increase the success of the existing education systems. For this aim, computer engineering department was selected as the pilot department and the data was collected with a measuring instrument composed of 115 questions on 210 students who were studying in the Department of Computer Engineering of Cumhuriyet University. The proposed model based on predictive models. Two datasets are created from the data obtained from the survey. The first experiment includes only the transcript grades of the students. The second data set consist of both grades and the opinions of the instructors and the experiments were repeated with this data. As a result of the repeated experiments, it was observed that the second data set gave better results. The best result was obtained by the C-SVC algorithm and the second best result by Naive Bayes. The lowest error rate achieved was 0.2700 and the highest accurate recognition rate was 73.00%.

Future studies may investigate the success of the students by adding more factors into the experiment and test with different data mining algorithms.

Acknowledgment

This study was supported by funding from the Scientific and Technological Research Council of Turkey (TÜBİTAK). (Project Number: 115E837).

Conflicts of interest

There is no conflict of interest.

References

- [1] Çelik N, Üzmez U., Evaluation of university students' affecting factors choice of profession. *Electronic Journal of Occupational Improvement and Research (EJOIR)*, 2(1) (2014) 94-105.
- [2] Sarıkaya T., Khorshid L., Üniversite öğrencilerinin meslek seçimini etkileyen etmenlerin incelenmesi: üniversite öğrencilerinin meslek seçimi. *Journal of Turkish Educational Sciences*, 7(2) (2009) 393-423.
- [3] Sathapornvajara S., Watanapa B., Factors affecting student's intention to choose IT program. *Procedia Computer Science*, 13, (2012), 60-67.
- [4] Çoban, A., Psikometrik testler: Available at: http://www.adnancoban.com.tr/psikometrik_testler.html. Retrieved: July 2015.
- [5] Witten I. H., Frank E., Data mining: practical machine learning tools and techniques with Java implementations. 3rd ed. San Francisco CA: Morgan Kaufmann (2002) 76-77.
- [6] Cha H., Kim Y. S., Park. S. H., Yoon T., Jung Y., Lee J. H., Learning styles diagnosis based on user interface behaviors for the customization of learning interfaces in an intelligent tutoring system. *In Proceedings of the 8th International Conference on Intelligent Tutoring Systems*, (2006) 513-524.
- [7] Hämäläinen W., Vinni M., Comparison of machine learning methods for intelligent tutoring systems. *In International Conference on Intelligent Tutoring Systems*, Springer, Berlin (2006) 525-534.
- [8] Perera D., Kay J., Koprinska I., Yacef K., Zaiane O. R., Clustering and sequential pattern mining of online collaborative learning data. *IEEE Transactions on Knowledge and Data Engineering*, 21(6) (2009) 759-772.
- [9] Pardos Z. A., Gowda S. M., Baker S.J.d R., Heffernan N. T., The sum is greater than the parts: ensembling models of student knowledge in educational software. *ACM SIGKDD Explorations Newsletter*, 13(2) (2011) 37-44.
- [10] Salton G., Automatic Text Processing: The Transformation, Analysis, and Retrieval of Information by Computer. Addison-Wesley, (1989).
- [11] Kuzgun Y., Mesleki ve Teknik Öğretim Kurumları ve Meslekler Rehberi. National Education Press, Istanbul, (2006).
- [12] Rakotomalala R., TANAGRA: a free software for research and academic purposes. *Proceedings of EGC'2005, RNTI-E-3*, 2 (2005) 697-702.

Fuzzy control of single-input step-up switched-capacitor- inductor dc-dc converter

Amir Baharlou Houreh¹ , Mohammad Hosein Ershadi^{1*} 

¹Department of Electrical Engineering, Islamic Azad University, Khomeinishahr Branch, Khomeinishahr, Isfahan/IRAN

Abstract

The main objective of this paper is fuzzy control of single-input Step- Up Switched Capacitor-Inductor DC-DC converter. For this purpose, we first introduce the basic structures of capacitor switched converter. Then, a single-input step-up switched capacitor inductor DC-DC converter is investigated. The most important advantage of this category of these converters is that the energy flowing from the source is transmitted directly to the two C1 and L1 elements and is sent directly to the output terminal, thus, they can generate high voltage gain without the need for cascading structures or multiple Floor there. The simulation results show the correctness of the converter's performance.

Article info

History:

Received: 25.10.2018

Accepted: 20.04.2020

Keywords: DC-DC converter, switched - capacitor , single input converter, fuzzy control.

1. Introduction

Capacitor-inductor Switched Converters: In recent years, capacitor switched structures (SCs) have been seemed highly [1-2]. Due to the lack of magnetic elements such as inductors and trans, these converters have a small size, small size, low cost and high efficiency, and they can produce a high gain, both in decreasing form and in increments [19]. The most important problem with these converters is their low power level [14-6].

Recently, many researchers have used a combination of structures for base converters with SC structures to create high-gain converters at higher power levels.

A different category of DC-DC converters, called capacitor-inductor switched, is used in two types of capacitor and inductor switched cells:

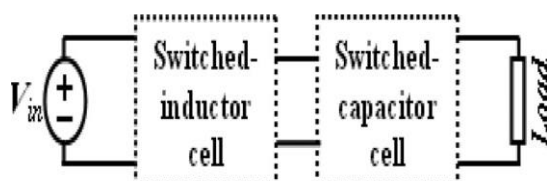


Figure 1. The general structure of inductor-capacitor switched models

The main advantage of this class of converters is that the energy flowing from the source is transmitted directly to L1 and C1 and transmitted directly to the output [9-11]. As a result, they can generate high voltage gain without the need for cascading or multi-store structures. The main objective of this study is to apply fuzzy control to a single-input step-up capacitor-inductor DC-DC converter. The important advantage of using fuzzy control is that it does not need to have a precise mathematical model [20].

2. Single Input Step-up Converter

A family of switched mode converter with different voltage ratios is presented. All family members consist of the same number of electronic components: they include two energy transfer units, for example, one C1 in SC and L1 in a variable inductor, a small LR resonant inductor used to limit the flow of peak flow from SC, three The switch is active or inactive and a filter capacitor output. The most important feature of these converters is

*Corresponding author. Email address: ershadi@iaukhsh.ac.ir
<http://dergipark.gov.tr/csj> ©2020 Faculty of Science, Sivas Cumhuriyet University

that the current energy from the input power supply is directly connected to two components, C1 and L1, and then connected to the output terminal.

For example, these converters are really single-phase converters, such as converters that have received high voltage gain through a cascade method. When the two parts of the energy transition act in parallel in the charging step, then in series during the discharge period, the highest output level can be generated and the members of the increase of the family of converters can be derived. Similarly, the downsizing members are derived by two series of energy transfers during the period of charge and then in the parallel phase at the time of discharge. This principle is not only suitable for the extraction of single-entry converters, but can be used for two-way DC-DC converters commonly used in a two-level DC dual-level renewable energy distribution system. To detect the family of converters from SC / I switches The proposed convertors are called single-step switching inductor / capacitor switched pulse width modulators (SCIs).

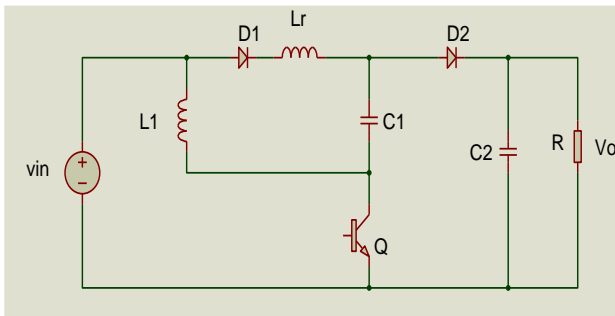


Figure 2. Circuit of single input step-up converter

First state (t_0 to t_1): Q connects and D1 directs and D2 is disconnected:

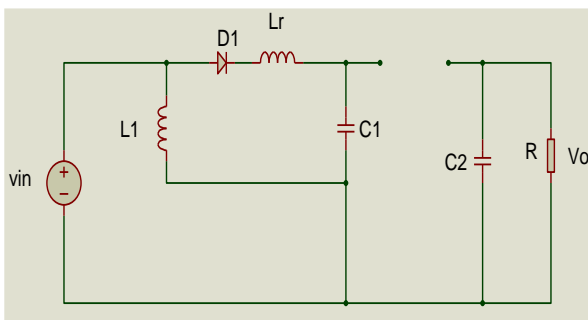


Figure 3. Circuit of figure .2. (t_0 - t_1)

In the case of L_r and C_1 , they form a series of resonant tanks, thereby increasing the capacitor C_1 through zero sinusoidally, and the voltage of the C_1 capacitor begins to increase. The inductor current L_1 increases linearly. In this situation, inductor L_1 current(i_{l1}), capacitor c_1 voltage(v_{c1}):

$$i_{L1} = I_d \sin \omega_0(t - t_0) \quad (1)$$

$$V_{C1} = V_{in} - \frac{\Delta V_{C1}}{2} \cos \omega_0(t - t_0) \quad (2)$$

$$i_{L1} = I_{Lmin} + \frac{V_{in}}{L_1}(t - t_0) \quad (3)$$

$$\omega_0 = \frac{1}{\sqrt{L_r C_1}} = \text{resonance frequency} \quad (4)$$

After half a cycle of resonance, at the instant t_1 , the current of the capacitor C_1 reaches zero and its voltage will be maximized and the diode D_1 will be cut off. The maximum capacitor voltage will be as follows:

$$(V_{C1})_{\max} = V_{in} + \frac{\Delta V_{C1}}{2} \quad (5)$$

Second state (t_1 to t_2): In this situation, Q continues to guide itself, D_1 is cut off, and L_1 is still charged linearly and the capacitor C_1 will remain constant.

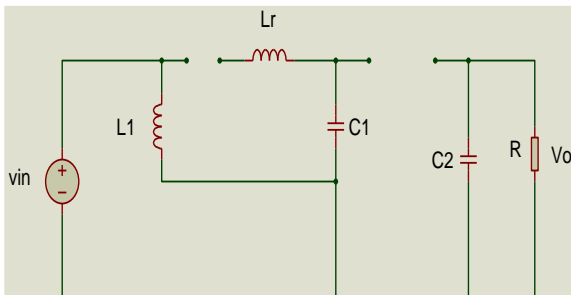


Figure 4. Circuit of figure.2. (t_1 - t_2)

This situation continues until t_2 , at this moment Q will be cut off and the current L_1 will be maximized:

$$(I_{L1})_{\max} = (I_{L1})_{\min} + \frac{V_{in}}{L_1} DT \quad (6)$$

That D is the duty cycle of the switch and T is the keying cycle. Third status (t_2 to t_3): In this situation, Q and D_1 will be cut and D_2 will be directed:

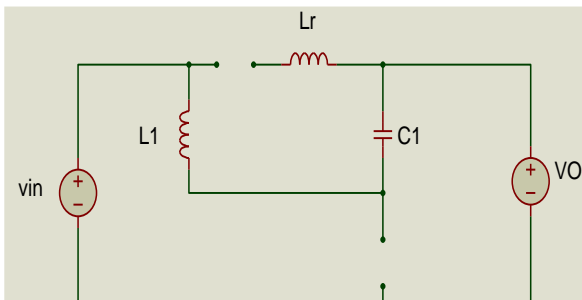


Figure 5. Circuit in state (t_2 - t_3)

In this situation, L_1 and C_1 are in series with the input and output and discharged:

$$i_{L1} = -i_{C1} = (I_{L1})_{\max} - \frac{V_o - V_{in} - V_{C1}}{L_1} (t - t_2) \quad (7)$$

$$V_{C1} = (V_{C1})_{\max} - \frac{I_o}{(1-D)C_1} (t - t_2) \quad (8)$$

At the end of this state, the instant t_3 of the inductor L_1 and the C_1 capacitor voltage reaches its minimum.

$$(I_{L1})_{\min} = (I_{L1})_{\max} - \frac{V_o - V_{in} - V_{C1}}{L_1} (1-D) T \quad (9)$$

$$(V_{C1})_{\min} = (V_{C1})_{\max} - \frac{I_o T}{C_1} \quad (10)$$

At this moment, the switch will be reconnected and will come back to the first position.

3. Calculating of Voltage Relationship

At the time t_0 to t_2 , where the switch is connected (DT), the voltage of the headlamp head $L1$ is equal to V_{in} . However, in the range t_2 to t_0 , the switch is disconnected ($(1-D) T$) The voltage of the inductor $L1$ is $V_{in} + V_{C1} - V_o$. If the voltage of the capacitor $C1$ is approximately equal to V_{in} , the inductor $L1$ will be equal to $2V_{in} - V_o$. Now, if we write the balance of the second Volt $L1$, we will have:

$$(V_{in})(DT) + (2V_{in} - V_o)(1-D) T = 0 \quad (11)$$

as a result:

$$V_{in} D + 2V_{in} - 2DV_{in} - V_o + DV_o = 0 \quad (12)$$

then:

$$V_o = \frac{2-D}{1-D} V_{in} \quad (13)$$

4. Simulation Results

As mentioned, the main purpose of this paper is to use a fuzzy control method to control the capacitor-inductor single-input step-up DC-DC converter. In general, the use of the fuzzy method for various systems has found application. This method has been used in electrical systems and in various branches of electrical engineering, including the following:

- Types of electric drives
- Flexible AC Transmission Systems (FACTS)
- Controlling Electronic Power Controllers
- Electromechanical systems
- Distributed production systems

An important advantage of the fuzzy method is that it can provide proper control for the system without having to know the exact mathematical model of the system..

4.1.Fuzzy control in DC-DC converters

The block diagram of the overall fuzzy control in DC-DC converters is as follows:

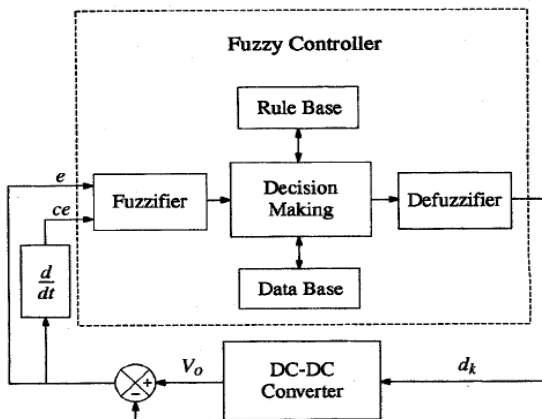


Figure 6. block diagram of the fuzzy control of the converters

As shown in this figure, the error and error derivative are applied as input to the fuzzy controller and the fuzzy controller output determines the duty cycle of the switch. Now, comparing the output of the fuzzy controller with a sawdust waveform, the command signal to the switch is generated, as shown below:

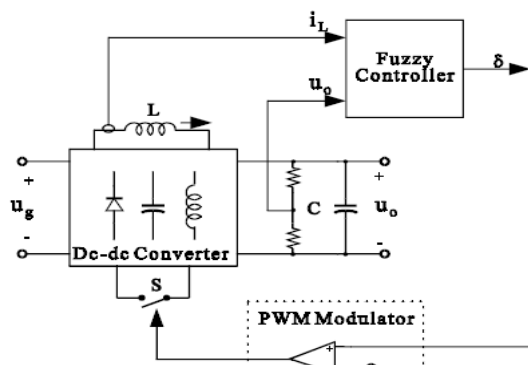


Figure 7. How to generate the command signal to the switch

4.2. Fuzzy control simulation

For this purpose, the fuzzy control toolbox is used in MATLAB software. In this thesis, two inputs for the fuzzy controller are considered, which are voltage error (e) and voltage derivative (ce). The voltage error is obtained from the differential voltage output and reference voltage. The membership functions used for these inputs are as follows:

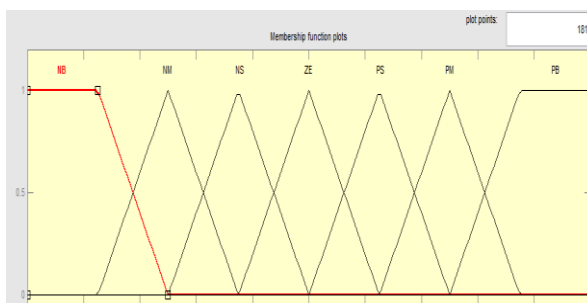


Figure 8. Membership function e

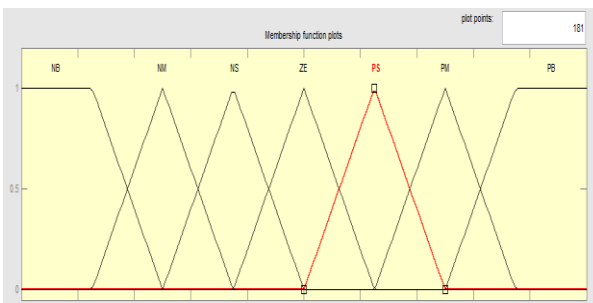


Figure 9. Membership function ce

The controller output membership function is as follows:

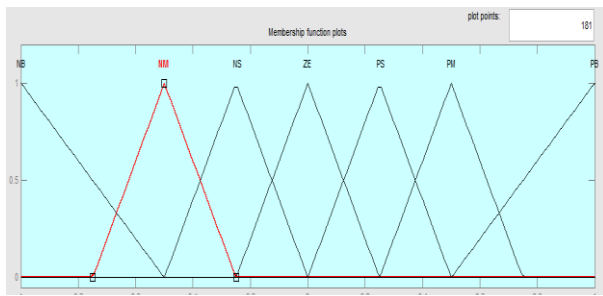


Figure 10. Membership function of output

The fuzzy rules used are as follows:

		error(e)						
		NB	NM	NS	ZE	PS	PM	PB
change in error(ce)	NB	NB	NB	NB	NB	NM	NS	ZE
	NM	NB	NB	NB	NM	NS	ZE	PS
	NS	NB	NB	NM	NS	ZE	PS	PM
	ZE	NB	NM	NS	ZE	PS	PM	PB
	PS	NM	NS	ZE	PS	PM	PB	PB
	PM	NS	ZE	PS	PM	PB	PB	PB
	PB	ZE	PS	PM	PB	PB	PB	PB

Figure 11. Fuzzy rules

The following principles have been used to write the fuzzy rules:

- When the output voltage is far from the reference value, the duty cycle of the switch must be large.
- When the output voltage approaches the reference value, the duty cycle must be small.
- When the output voltage reaches the reference value and remains stable, the duty cycle must remain unchanged.
- When the output voltage reaches the reference value but is still changing and not stable, the duty cycle should be small.

When the output voltage is greater than the reference value, the duty cycle changes must be negative and vice versa.

4.3. Simulation result

The results of the simulation of Fuzzy Control of Single-Input Step-Up Switched Capacitor- Inductor DC-DC Convertor are under the following simulation parameters :

$V_{in} = 22$ (V)

$L_1 = 95$ (uH)

$L_r = 0.3$ (uH)

$C1 = 4.7 \text{ (}\mu\text{F)}$

$C2 = 100 \text{ (}\mu\text{F)}$

$R = 20 \text{ (ohm)}$

$F = 100 \text{ (KHz)}$

In this simulation, the 66 volt reference voltage is applied to the control system to indicate the correct operation of the controller. To reach this voltage, the switch in the converter is switched on at 100 kHz and its duty cycle is 50%. The following figure shows the command signal to the switch:

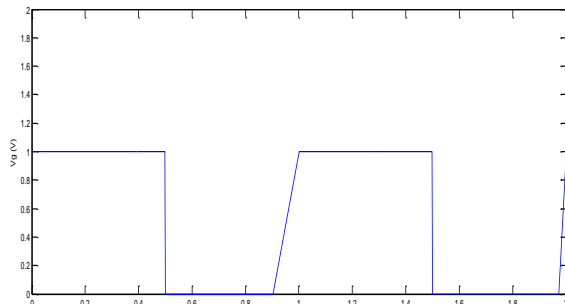


Figure 12. The command signal to switch

In this situation, the output voltage waveform of the converter will be as follows:

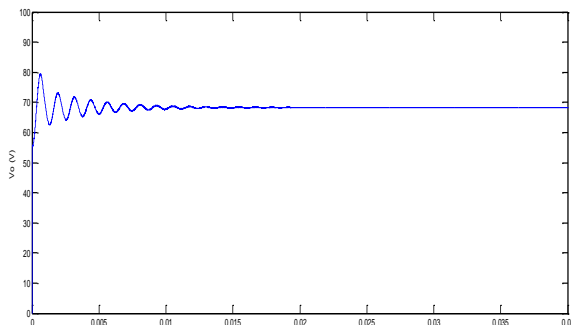


Figure 13. Output voltage

As shown in this figure, the output voltage is about 66 volts and has been able to track the reference value. In this situation, the shape of the capacitor C1 is as follows:

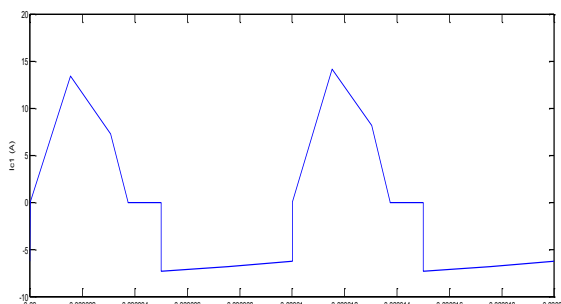


Figure 14. Capacitor c1 current

As shown in this figure, the capacitor C1 has been almost sinusoidally changed in the first state of the circuit, ie, the interval t_0 to t_1 due to the C1 capacitor and the predecessor Lr being serially formed and forming a resonant tank. In the second state of the circuit, ie, the time interval t_1 to t_2 , the capacitor C1 reaches zero and remains at zero in this interval. In the third state of the circuit, ie, the time interval t_2 to t_3 , the C1 capacitor is serially coupled to the inductor L1 and the current of the inductor L1 being discharged will invert the capacitor C1. The voltage waveform of the C1 capacitor is as follows:

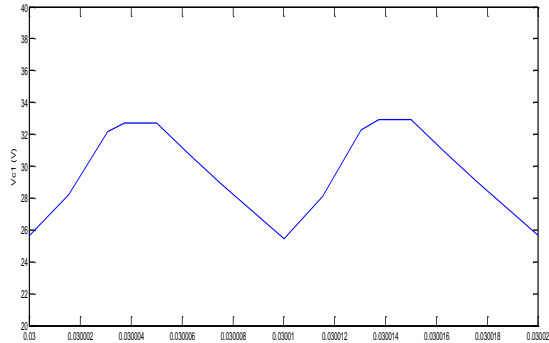


Figure 15.Capacitor c1 voltage

As seen in this figure, in the first state of the circuit,

ie, the time interval t_0 to t_1 , because the capacitor C1 and predecessor Lr are in series and formed a resonant tank, and the current of the capacitor C1 has been changed almost sinusoidally, the voltage The capacitor will change in cosine. In the second state of the circuit, ie, the time interval t_1 to t_2 , the capacitor C1 reaches zero and remains in this range zero, thus, the capacitor C1 voltage remains unchanged.

In the third position of the circuit, ie, the time interval t_2 to t_3 , the C1 capacitor is serially located with the inductor L1 and the current of the inductor L1 being discharged will invert the C1 capacitor. So the C1 capacitor voltage begins to decrease.

The flow pattern of the inductor L1 will be as follows:

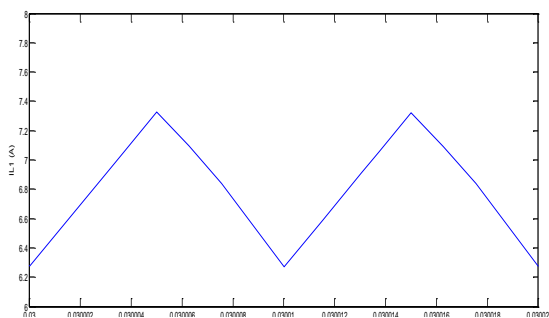


Figure16.Inductor L1 current

As seen in this figure, in the first position of the circuit, ie, the time interval t_0 to t_1 , the inductor L1 starts charging linearly because the switch is connected and the L1 series inductor is placed with the Vin source. In the second state of the circuit, ie, the time interval t_1 to t_2 , the same as the first one, the inductor L1 starts to charge linearly. In the third position of the circuit, ie, the time interval t_2 to t_3 , the C1 capacitor will be serially coupled to the inductor L1 and will be coupled to the output voltage. As a result, the L1 inductor starts to discharge.

The waveform of the switch current will be as follows:

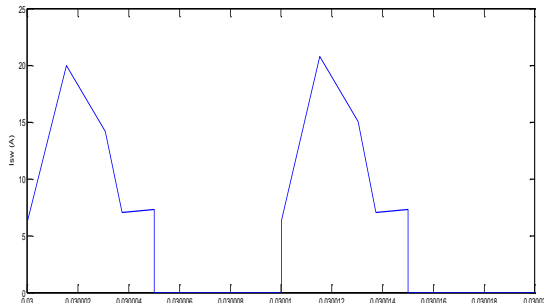


Figure 17. Switch current

As seen in this figure, in the first state of the circuit, ie, the time interval t_0 to t_1 , because the switch is connected and the L1 series follower is placed with the source V2, the switch current will be obtained from the sum of the capacitor C1 and the inductor L1. In the second state of the circuit, ie, the time interval t_1 to t_2 , the same as the first one, the inductor L1 starts to charge linearly, but because in this situation the capacitor current C1 is zero, the switch current will be equal to the inductor L1. In the third position of the circuit, ie, the time interval t_2 to t_3 , the switch is disconnected and therefore the current will be zero. The inductor Lr current waveform, which is actually the same current of the diode D1 (given the circuit shape and the series of these two elements), will be as follows:

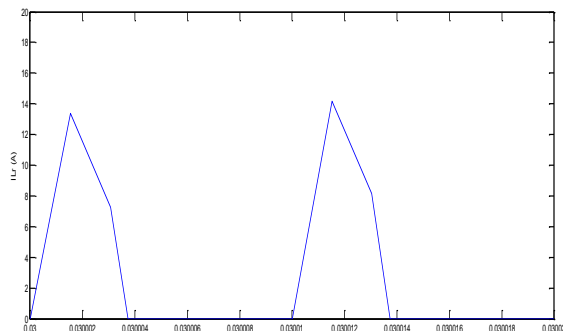


Figure 18. InductorLr current

As it is seen, in the first circuit, the period t_0 to t_1 by connecting switches and diodes D1 and cut D2, because the capacitor C1 and the inductor Lr series and the formation of tanks resonance have , The current of the C1 conduit, which is the current of the inductor Lr, has been roughly sinusoidized. In the second circuit, the period of time t_1 and t_2 , the capacitor C1 to zero and remained in the range of zero. So the diode D1 is disconnected and the current of the inductor Lr will be zero. In the third circuit, the time t_2 and t_3 , similar to the second situation, the diode D1 Lr still cut off and the inductor current is zero.

The waveform of the diode current D2 will be as follows:

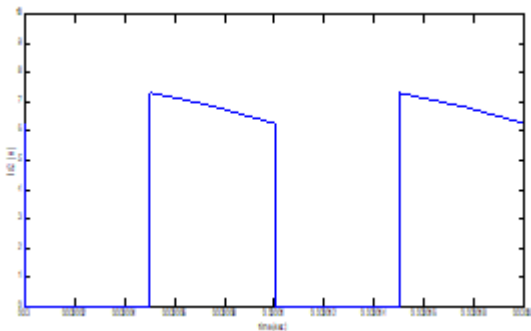


Figure 19.Diode D2 current

As seen in the figure above, in the first and second states of the circuit such as the diode D2, the current is zero and in the third state it will be equal to the inductor L1.

5. Conclusion

The main objective of this paper is to Fuzzy Control of Single-Input Step-Up Switched Capacitor- Inductor DC-DC Converter. For this purpose, first the Single-Input Step-Up Switched Capacitor- Inductor DC-DC Converter was investigated.

The most important advantage of this category of these converters is that the energy flowing from the source is transmitted directly to the two C1 and L1 elements and is sent directly to the output terminal, thus, they can generate high voltage gain without the need for cascading structures or multiple Floor there.

This structure can be generalized not only for single-converter converters, but also for dual-input converters, with two input modes commonly used in non-renewable energies. The simulation results show the accuracy of the converter's performance.

Conflicts of interest

There is no conflict of interest.

References

- [1] Chang, Yuen-Haw. Analysis and Modeling of High-Efficiency Multiphase Switched-Capacitor Converter with Variable-Phase Control. . *ele. power. trans IEEE* 2013
- [2] Choi, Yongsuk .A switched-capacitor DC-DC converter using delta-sigma digital pulse frequency modulation control method. Circuits and Systems (MWSCAS), 2013 *IEEE 56th International Midwest Symposium on*. pp. 356 – 359.2013
- [3]- Rashid M. ,” power electronics handbook ” , ACADEMIC PRESS , 1999.
- [4] M. S. Makowski and D. Maksimovic, Performance limits of switched-capacitor DC-DC converter, *IEEE PESC'95 Conf.* 2. pp. 1215-1221.1995
- [5] Vahidfar N., Ershadi M.H., Sliding mode controller design for DC-DC quasi Z source converter, *Signal Processing and Renewable Energy* 2 (3), 21-26,2018
- [6] C. C. Wang and J.C. Wu, Efficiency Improvement in charge pump circuits, *IEEE J. Solid-State Circuits* 32,pp. 852-860.2016
- [7] H. Chung and A. Ioinovici. Switched-capacitor-based DC-to-DC converter with improved input current waveform, in *Proceedings IEEE Int. Symp. Circuits and Systems, Atlanta, USA.* pp. 541-544.1996
- [8] Weng,g ,You,L , "Fuzzy control design for Luo DC-DC Converter" *IEEE Trans. On Power.elec.* pp.345-353,No.4,Vol.7,2014.

Experimental evaluation and genetic programming based modeling of the compressive strength of concretes produced with various strength classes of cements

Kasım MERMERDAŞ^{1*} , Süleyman İPEK² , Burak BOZGEYİK³ 

¹ Harran University, Civil Engineering Department, Şanlıurfa, Turkey

² Bingöl University, Civil Engineering Department, Bingöl, Turkey

³ Hasan Kalyoncu University, Civil Engineering Department, Gaziantep, Turkey

Abstract

This study aimed to propose a prediction model for estimation of strength of concretes with various cements and mixture proportions. The strength of the samples produced with three different types of cement at different rates of water-to-cement ratios and cement richness were investigated experimentally and evaluated statistically. Three type of cement possessing 28-day strengths of 32.5, 42.5, and 52.5 MPa was used in the production of concretes. The concretes were produced at cement richness values of 300, 400, and 500 kg/m³ and w/c rates at changing levels within the interval of between 0.3 and 0.6. By this way, combined influences of cement strength, amount of cement and w/c ratio was experimentally investigated. Totally 36 mixes were cast then the compressive strength values were examined after specified moist curing periods (7 and 28 day). A statistical study were conducted on the experimental results and the significances of the cement strength, w/c values and amount of cement on the compressive strength of the concretes were assessed. Another crucial focus of the current paper is to generate an explicit expression to predict the compressive strength of the concretes tackled with the current study. To derive an explicit formula for estimation, a soft computing method called gene expression programming (GEP) was benefited. The GEP model was also compared with a less complicated estimation model developed by multi linear regression method. The results revealed that compressive strength of the samples were significantly influenced by cement type and aggregate-to-cement ratio. It was observed that there is a high correlation between experimental and predicted values obtained from the proposed GEP model.

Article info

History:

Received:09.07.2019

Accepted:15.04.2020

Keywords:

Compressive strength,
Gene Expression
Programming,
Multiple Linear
Regression,
Statistical evaluation

1. Introduction

The strength of the cement directly influences the concrete and mortar characteristics especially the compressive strength characteristic [1,2]. During the recent years, different cement strength classes are utilized in diverse construction works. In addition to cement strength class, w/c and cement content are other important factors which affect the performance of concrete. There are many studies evaluating the effects of water and cement content on the strength development of concrete. However, the combined effect of water-to-cement ratio, cement content and strength class of cement on compressive strength of concrete is still insufficient. Mermerdaş et al. [3] modeled compressive strength of metakaolin and

calcined kaolins modified concrete by means of Gene Expression Programming (GEP). They indicated that GEP is a beneficial tool for prediction of the strength of concrete. Sayed [4] investigated the predictability of strength of concrete containing different matrix mixtures by using statistical modeling methods. Eight different parameters of time, water, cement, metakaolin, silica fume, superplasticizer, and fine and coarse aggregates were utilized in the experimental program. According to findings in this research, statistical modeling is capable for prediction the compressive strength of concrete. Deshpande et al. [5] used three different data processing methods called artificial neural networks (ANN), model tree (MT), and non-linear regression (NLR) for prediction of the 28-day strength of recycled aggregate concrete. They reported that with minimum number of inputs, ANN

*Corresponding author. Email address: kasim.mermerdas@harran.edu.tr
<http://dergipark.gov.tr/csj> ©2020 Faculty of Science, Sivas Cumhuriyet University

has a better prediction capability in strength of concretes including reclaimed aggregates than obtained from MT and NLR techniques. However, MT and NLR techniques have advantageous aspects such as MT technique could provide a set of models of discrete complication and precision, and NLR technique could give a single equation which can be easily utilized. Chandwani et al. [6] conducted a study to model strengths of three different types of special concretes which are self-consolidating concrete, high performance concrete, and recycled aggregate concrete. They used ANN for modeling purpose. They used non-destructive test data in the evaluation of the model. According to this study, the ANN is an effective technique that can be used as a predicting tool based on historical data, to estimate the compressive strength of different types of concretes based on mix proportions. More examples can be found in the technical literature regarding the utilization of soft computing based modelling techniques to evaluate mechanical properties of construction materials and structural elements [6].

In the available literature, there has been no study regarding the compressive strength modelling of concretes taking into account the cement classes. A handy tool providing quick interpretation of the compressive strength performance of concretes with different mix compositions and cement types can be obtained through a comprehensive mathematical model. Soft computing techniques are appropriate means for this purpose. GEP can be considered as one of the simplest way among the others. It can yield a simple explicit mathematical expression of physical phenomena. Once this model is transferred via a user friendly software or an interface, the preliminary workload of the researchers can be mitigated.

In this study, the influence of w/c values, amount of cement, and strength class of cement on mechanical property of concrete was experimentally investigated. For this reason, three main concrete mixture groups were determined with respect to cement type of CEM II 32.5, CEM I 42.5 and CEM I 52.5. The cement types were selected regarding to 28-day strength. In each mixture, four different water-to-cement ratios of 0.3, 0.4, 0.5, and 0.6 and three different cement contents of 300, 400, and 500 kg/m³ were considered as experimental parameters. Totally 36 different concrete mixtures were designed and their strengths were tested at the age of 7 and 28 days. After the experimental investigation of the mixtures, the results were used in the modeling of the compressive strength of concrete regarding to input parameters of the cement compressive strength, water-to-cement ratio, aggregate-to-cement ratio, and age by using GEP and multiple linear regression analysis (MLR). The results

indicated that compressive strength of the concrete is directly influenced by water-to-cement ratio, age, and especially the cement compressive strength. Two different models were obtained from GEP and MLR and their results were compared graphically and statistically.

2. Experimental Study

2.1. Materials

CEM II 32.5, CEM I 42.5, and CEM I 52.5 types cements having specific gravities of 3.05, 3.14, and 3.15, which are confirming Turkish Standard requirements, were used in the production of concrete mixtures. Chemical compositions and some critical physical characteristics of the cements are given in Table 1.

Table 1 Chemical compositions and some physical properties of CEM I-52.5, CEM I-42.5, and CEM II-32.5

Item	CEM I 52.5	CEM I 42.5R	CEM II 32.5
SiO ₂ (%)	18.22	18.99	20.31
Al ₂ O ₃ (%)	63.85	3.95	4.96
Fe ₂ O ₃ (%)	3.45	4.65	2.9
CaO (%)	3.65	62.76	60.48
MgO (%)	1.55	2.32	1.65
SO ₃ (%)	2.72	2.75	2.51
Na ₂ O (%)	-	-	0.26
K ₂ O (%)	0.2	-	0.6
Cl ⁻ (%)	0.005	0.0063	0.01
Insoluble residue	0.26	0.34	3.2
Loss on ignition	1.43	0.87	6.3
Free lime (%)	0.78	1.68	-
Specific gravity	3.15	3.14	3.05
Le chatelier (mm)	1	1	1
Blaine surface area (cm ² /g)	4,680	3,520	3,750

The medium and coarse aggregate was river material with a maximum size of 16 mm for the former and 22.5 mm for the latter. The fine aggregate which is natural sand of maximum particle size of less than 4 mm. The specific gravity values were 2.65 for natural sand, 2.71 for medium, and 2.77 for coarse aggregates. The particle size distributions of the aggregates were monitored through the sieve analysis and illustrated in Figure 1.

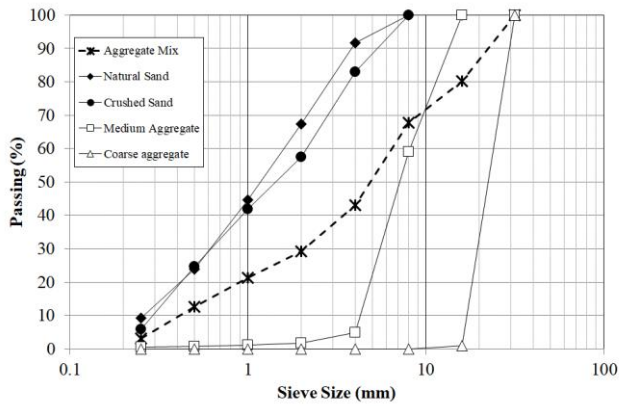


Figure 1. Particle size distribution of the aggregates

2.2. Mixture design

The concrete mixtures were grouped in three according to the cement type utilized in the production of concrete. In each group, the concrete mixtures were manufactured considering various cement contents and water-to-cement ratios. 28-day strengths of cements are 32.5, 42.5, and 52.5 MPa confirming Turkish Standard. The w/c ratios were taken as 0.3, 0.4, 0.5, and 0.6 and cement content as 300, 400, and 500 kg/m³. As results, in each group, twelve mixes were designed and totally, thirty six different concrete groups were cast in the current study. The mix proportions of the concrete mixtures are presented in Table 2.

Table 2. Mix proportions for 1 m³ concrete (in kg/m³)

Cement content (kg/m ³)	Water-to-cement ratio (w/c)	Proportions of Aggregates (Coarse/Medium/Natural)
300	0.3	0.2/0.3/0.5
400	0.4	
500	0.5	
	0.6	

2.3. Concrete casting

In order to provide a consistent and desirable homogeneity as well as uniformity for all mixtures, the same procedure was followed. For preparing the mixes, a laboratory pan mixer was used. At the end of the production process, fresh mixtures were poured into the moulds. After filling the mould, the specimens were covered with plastic sheet to ensure moisture proofing and preventing plastic shrinkage. They left in the temperature controlled laboratory environment for 24 h and 20±1 °C environment. The specimens were taken out of the molds and transferred to lime saturated curing tanks. The curing periods of 7-day and 28-day was applied. Afterwards, they were tested based on the

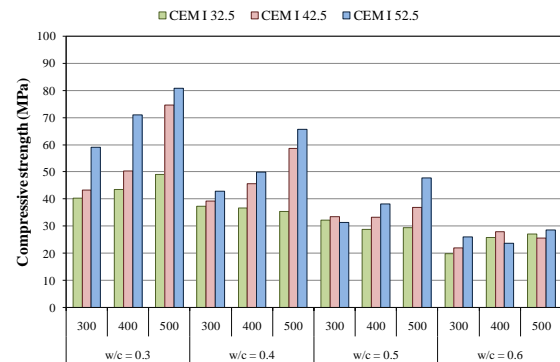
testing procedure proposed ASTM C39 [27] to specify the 7-day and 28-day strengths of the concretes.

3. Results and Discussion

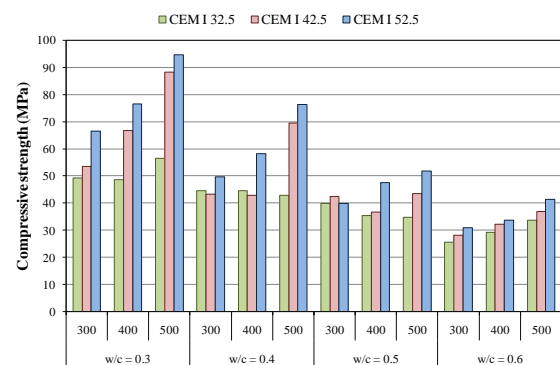
3.1. Experimental results

The compressive strength results of the concretes at the end of 7 and 28 days regarding to cement content and water-to-cement ratio with three different cement types are given in Table 3 and the data provided presented this table were graphically shown in Figure 2.

While the compressive strength values ranged between 19.8 and 80.8 MPa for 7th day compressive strength, the values were determined to be between 25.5 and 94.6 MPa at 28th day. The results indicated that strength of specimens is directly influenced by the cement type and the mix proportions as expected. The highest strength value was obtained for the concrete mixtures produced with CEM I 52.5 cement type regardless the other parameters. Utilization of higher strength cement in concrete improved the quality of the cement paste which in turn is the reason of achieving higher compressive strength.



(a)



(b)

Figure 2. Compressive strength of the concretes a) 7-day and b) 28-day

Table 3. Compressive strength of the concretes

Cement content (kg/m ³)	w/c	Cement type	f _c (MPa)		Cement type	f _c (MPa)		Cement type	f _c (MPa)	
			7-day	28-day		7-day	28-day		7-day	28-day
300	0.3	CEM I 52.5	59.1	66.6	CEM I 42.5	43.3	53.5	CEM II 32.5	40.2	49.3
	0.4		42.8	49.7		39.2	43.2		37.3	44.6
	0.5		31.4	40.0		33.5	42.5		32.1	39.9
	0.6		26.0	30.9		22.0	28.0		19.8	25.5
400	0.3	CEM I 52.5	70.9	76.5	CEM I 42.5	50.2	66.8	CEM II 32.5	43.5	48.6
	0.4		49.8	58.2		45.5	42.8		36.7	44.6
	0.5		38.0	47.5		33.2	36.7		28.8	35.5
	0.6		23.7	33.6		27.8	32.3		25.8	29.3
500	0.3	CEM I 52.5	80.8	94.6	CEM I 42.5	74.6	88.3	CEM II 32.5	48.9	56.4
	0.4		65.7	76.3		58.6	69.6		35.4	42.9
	0.5		47.8	51.7		36.8	43.6		29.3	34.8
	0.6		28.5	41.4		25.5	36.8		27.0	33.6

The amount of water relative to cement content had significant influences on the strength, as w/c ratio is raised from 0.3 to 0.6 a systematic reduction in the strength values at both testing ages were observed. The minimum strength values were noted for the mixtures with water-to-cement ratio of 0.6, almost all of the values were less than 40 MPa. The results also illustrated that there is insignificant change in strength of the concrete mixtures produced including CEM II 32.5 type of cement when the cement content is increased from 300 to 500 kg/m³. At both testing ages, the cement content increasing in the mixtures manufactured with CEM II 32.5 type of cement increased just the strength of the mixture with w/c ratio of 0.6 while in the others no remarkable effect was observed. Contrarily, the effectiveness of cement content on the strength was clearly observed in the mixes with CEM I 52.5 type of cement. Increasing the amount of cement resulted the enhancement of strength especially at low w/c values.

Reducing the water-to-cement ratio from highest ratio to lowest one improved the strength performance. For example, in the concrete series produced with CEM I 52.5 type of cement, the 7th day compressive strength values of concretes produced at 300, 400, and 500 kg/m³ of cement content augmented about 127.3%, 199.0%, and 183.2%, respectively, when w/c is decreased from 0.6 to 0.3. The increment rates in the 28th day compressive strength are 115.4%, 127.6%, and 128.7% for the same concretes. When the w/c values of the concretes were decreased from 0.6 to 0.3, in the concrete series obtained by utilization of cement strengths of 42.5 and 32.5 MPa, the increment rates of the 7th day strengths of the mixtures cast with 300, 400, and 500 kg/m³ richness of cement content were, respectively, 96.8%, 80.6%, and 192.6% and 103.0%, 68.4%, and 81.1% whereas they were, respectively, 90.8%, 106.8%, and 140.0% and 93.3%, 66.1%, and 67.9% for the 28th day strength.

Also, the strengths obtained at 7th and 28th day versus aggregate-to-cement ratio are illustrated in Figures 3a and 3b, respectively. It can apparently be understood from the figures that the strength of the concretes is improved by augmenting of aggregate-to-cement ratio.

4. Statistical evaluation and Multiple Linear Regression (MLR)

Analysis of variance (ANOVA) was used in the evaluation of if the dependent variables are influenced by independent variable. General linear model analysis of variance (GLM-ANOVA), a significant statistical tool, is based on reducing the control variance that helping to assess the effectiveness of parameters. The identification of the statistically significant experimental factor on the strength was determined by analysis at 0.05 level of significance. GLM-ANOVA was applied through a commercial software called "Minitab" to examine the data given in Table 4. The dependent variable was compressive strength while independent variables were the w/c ratio, cement content, and cement compressive strength namely cement type. The general linear model analysis was benefited to determine the effectiveness of the test parameters. Table 4 illustrates the statistical analysis results. The significance of the test parameter on the compressive strength is determined by the p-values. The parameter is acceptable as significant factor on the depended variable if p-value of less than 0.05. Statistical analysis showed that the parameters taken into account have remarkable influences on strength of concrete in both curing ages since the p-values of all parameters are less than 0.05. The contributions of the factors on the measured test results are also presented in Table 4. Analyzing the contribution levels of the independent variables indicated that the most important parameter in strength of the concretes is w/c ratio at both testing ages. The statistical analysis revealed that the contribution of cement compressive

strength, namely cement type, and cement content can be underestimated when compared to contribution of water-to-cement ratio.

Table 4. Statistical evaluation of the compressive strength of the concretes

Dependent Variable	Independent variable	Sequential Sum of Squares	Computed F	P Value	Significance	Contribution (%)
7-day compressive strength	f_{cc}	1064.38	11.90	0.000	Yes	13.05
	w/c	5088.69	37.93	0.000	Yes	62.41
	c	748.08	8.36	0.001	Yes	9.18
	Error	1252.31	-	-	-	15.36
	Total	8153.43	-	-	-	-
28-day compressive strength	f_{cc}	1383.8	12.95	0.000	Yes	13.96
	w/c	5927.3	36.97	0.000	Yes	59.80
	c	1104.4	10.33	0.000	Yes	11.14
	Error	1496.3	-	-	-	15.10
	Total	9911.8	-	-	-	-

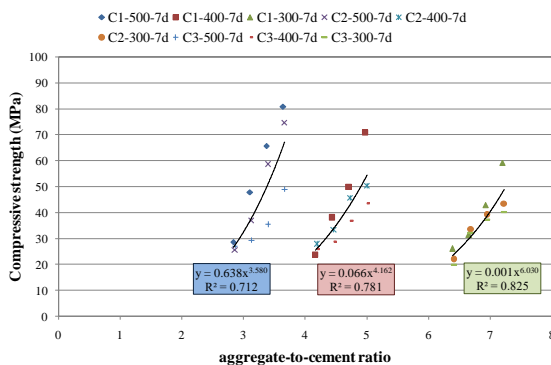
f_{cc} : compressive strength of cement; w/c: water-to-cement ratio; c: cement content

Moreover by using Minitab, a linear equation of observed data was obtained by using multiple linear regression that modeling the relationship between a response variable and two or more descriptor variables.

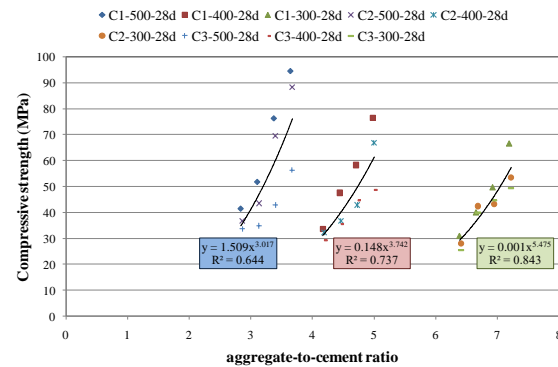
$$F_c = 77.03 + 0.7074 \times f_c - 118.81 \times w - 3.202 \times a + 0.3657 \times t \quad (1)$$

where F_c is the compressive strength of the concrete, f_c , w, a, and t are the compressive strength of the cement, water-to-cement ratio, aggregate-to-cement ratio, and testing age, respectively.

In addition, the results at 7 and 28 days are plotted with respect to compressive strength and aggregate-to-cement ratio on Figure 3a and 3b, respectively. Then, compressive strength results at each testing age were grouped into three according to cement content utilized in the production. Power function fitting was applied on each group. R-square values and power function equations for each group are also illustrated in Figure 3a and 3b. According to the results, the higher R-square values of 0.825 and 0.843 was achieved in the concretes produced with 300 kg/m³ cement content at both ages.



(a)



(b)

Figure 3. Compressive strength values versus aggregate-to-cement ratio with power function fitting at: a) 7-day and b) 28-day

5. Development of Estimation Model

Gene expression programming (GEP), invented by Candida Ferreira [28], uses softwares by statements of the acquired models or presented knowledge [29]. Genetic programming, introduced by Koza [30], is an application of GAs [31]. Solving defined problem by employing a computer program is a commonly used solution. The definition of the problem is the first step in the logic of GP and GAs, and then the program runs to work out the problem in a problem-independent mode [31]. GEP is derived as an enhanced form of aforementioned genetic operators. These three algorithms use almost same genetic operators in the solutions with unimportant differences. Ferreira [28] states that the differences between the three algorithms denoted as “in GAs the individuals are linear strings of fixed length (chromosomes); in GP the individuals are nonlinear entities of different sizes and shapes (parse trees); and in GEP the individuals are encoded as linear strings of fixed length (the genome or chromosomes)

which are afterwards expressed as nonlinear entities of different sizes and shapes (i.e., expression trees (ETs) or simple diagram representations”).

The compressive strength of the cements, water-to-cement ratios, aggregate-to-cement ratios, and testing ages of concretes with experimental results were regulated to achieve a data set. Table 3 presents the data set which was randomly divided into two groups. “Train set” is one of the sub-data set whereas “Test set” is the other. The mathematical model was derived by using a software named GeneXproTools 4.0. The following expression is the prediction model that was achieved from GEP. The sub-expression trees of the prediction model is also depicted in Figure 4.

$$F_c = F_1 + F_2 + F_3 + F_4 + F_5 + F_6 \quad (2)$$

$$F_1 = \arccos(\sin d_2) - \tan(\sqrt{d_1}) - d_0 \times \ln d_1 - 2 \times d_2 \quad (2a)$$

$$F_2 = \sqrt[3]{d_2 - (e^{c_7})^{\ln d_1}} \times \tan(\tan d_0^2) \quad (2b)$$

where $c_7 = -1.6339$

$$F_3 = c_1 + \frac{\sqrt{d_1} \times \log d_3 \times (\arccos d_1 + c_5)}{d_1} \quad (2c)$$

where $c_1 = 0.3216$, $c_5 = 5.3928$

$$F_4 = \frac{\sqrt[3]{c_7 \times d_2}}{d_1} \times \sin((c_3 - d_2) \times \sqrt{c_9}) \quad (2d)$$

where $c_3 = -6.5469$, $c_7 = 1.6151$, $c_9 = 5.384$

$$F_5 = c_2 - d_1 - \arctan(\tan d_0 \times \ln d_1 \times (c_6 + d_2)) \quad (2e)$$

where $c_2 = 6.2143$, $c_6 = -4.1084$

$$F_6 = \sin((\tan d_0^2 + \cos e^{d_3}) \times d_0 \times (c_6 - d_2)) \quad (2f)$$

where $c_6 = -9.6818$

where F_c is the compressive strength of concrete, d_0 , d_1 , d_2 , and d_3 are the compressive strength of the cement, water-to-cement ratio, aggregate-to-cement ratio, and testing age, respectively.

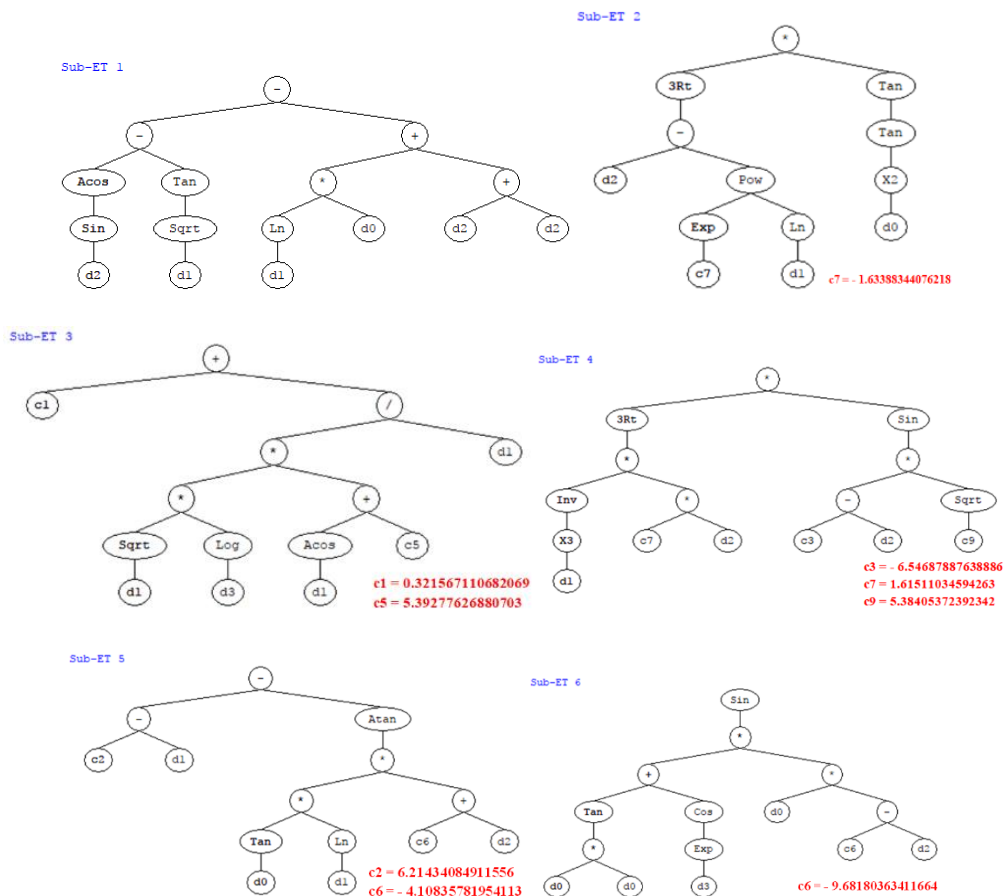
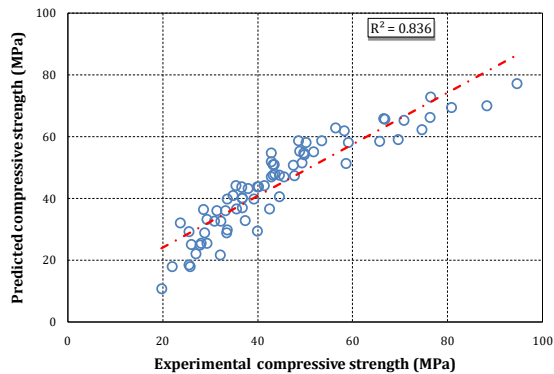


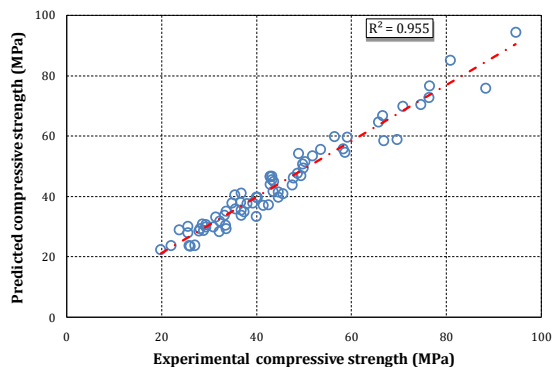
Figure 4. Expression trees for GEP model

6. Correlation between estimated and experimental compressive strength

One of the most popular studies among the researchers is correlation of the experimental data. By this way, it is aimed to assess the results reported. To assess the compressive strength of the mixtures, correlating the estimated compressive strength with the laboratory data was performed. The correlation between laboratory data and the estimation values obtained by Multiple Linear Regression (MLR) and predicted by mathematical model generated by GEP are presented in Figure 5a and 5b, respectively. The coefficient of determination, R^2 , for experimental and predicted compressive strength are also shown on these figures. The higher R^2 values reflects the higher relation between the parameters. Based on R^2 values, it may be determined that there is a strong relation between the estimated and experimental compressive strength for the models achieved by MLR and GEP. But the correlation coefficient of GEP model was higher than that of MLR model. The R^2 value of the proposed GEP model was about 0.955 while it was 0.836 for model obtained by MLR.



(a)



(b)

Figure 5. Predicted versus experimental compressive strength values for a) MLR and b) GEP models

In addition to correlation between the experimental and predicted results, the experimental compressive strength values and predicted values are presented in Figure 6. By this plotting, it was aimed to see that the results achieved by GEP model are closer to the experimental results than obtained by MLR model.

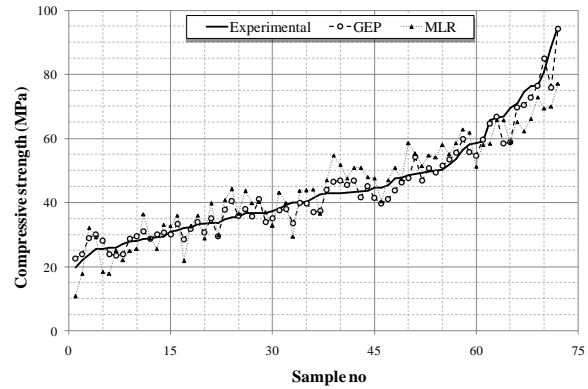


Figure 6. Compressive strengths predicted by MLR and GEP models and experimental compressive strength values versus number of sample

For the purpose of comparison of the predicted and experimental compressive strengths, the strength data obtained from both MLR and GEP model were divided by the corresponding experimental strength values to obtain normalized values. The normalized data versus aggregate-to-cement ratio, cement strength, water-to-cement ratio, and testing age are, respectively, shown in Figure 7a, 7b, 7c, and 7d. When the figures are evaluated, it can be obviously found out that almost all GEP model data are scattered in $\pm 20\%$ limits of the normalized lines whereas some data of MLP model are out of this limit. According to this well distribution of the normalized values, it may be inferred that the prediction formula generated by GEP had an acceptable estimation capability performance.

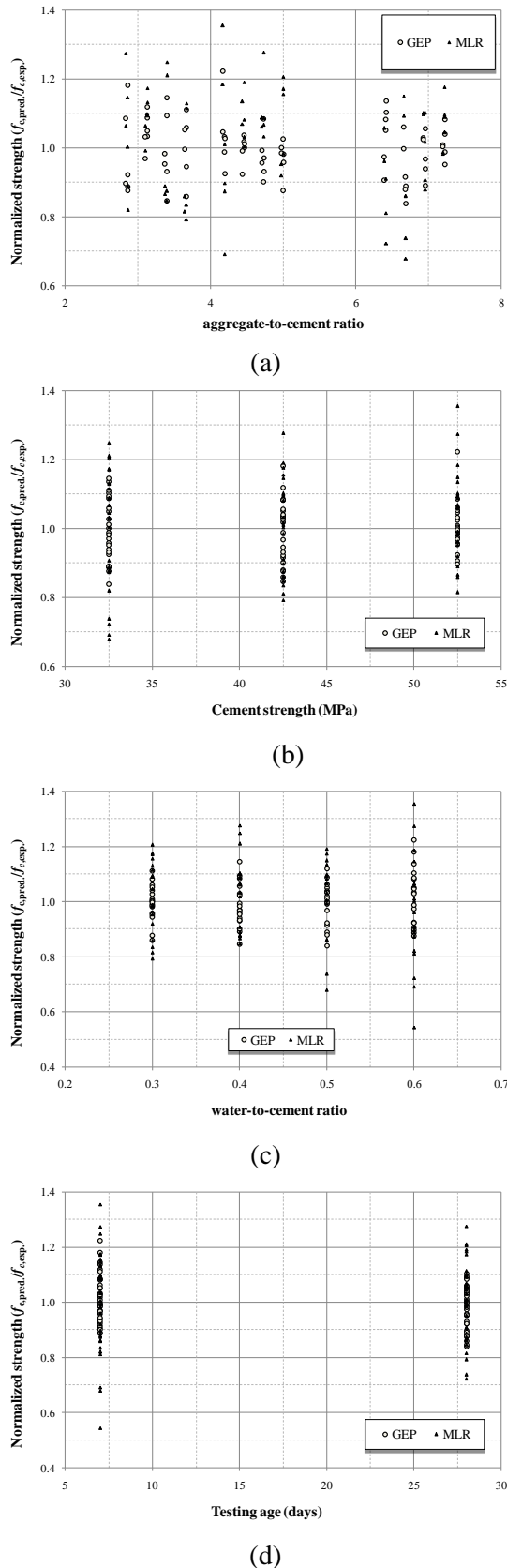


Figure 7. Prediction performance of the GEP model with respect to: a) aggregate-to-cement ratio, b) cement strength, c) water-to-cement ratio, and d) testing age

7. Conclusions

According to the aforementioned discussions, the conclusions below may be reached.

- Reducing the water-to-cement values from 0.6 to 0.3 enhanced the strength performance in all mixture groups.
- Utilization higher strength cement provided higher strength values.
- Cement content has a slight effect on the strength development of the concrete.
- Increasing aggregate-to-cement ratio resulted higher compressive strength of the concrete.
- Statistical analysis revealed that water-to-cement ratio was determined to be the most influential factor on the strength while the cement type and content affected the strength with a lower impact.
- An explicit formula by GEP was proposed using all of the input predictors. It was found out that there is a good correlation between the experimental strength values and those predicted by proposed GEP model. However, the model derived by GEP indicated better estimation performance than MLR model. The high correlation also shows that a reliable analytical model for estimation of strength of concretes produced with different cement types and various mix parameters could be generated by using GEP if there is a plenty of input data.

Conflicts of interest

The authors state that they did not have any conflict of interests.

References

- [1] BS EN 197–1, Cement: Composition, Specifications and Conformity Criteria for Common Cements British Standards Institution, London, 2000.
- [2] Hirschi T., Sika Concrete Handbook Sika Services AG, Zurich, Switzerland, 2005.
- [3] Mermerdaş K., Gesoğlu M., Güneyisi E., Özturan T., Strength development of concretes incorporated with metakaolin and different types of calcined kaolins. *Constr. Build. Mater.*, 37 (2012) 766-774.
- [4] Sayed M. A., Statistical modelling and prediction of compressive strength of concrete. *Concrete. Research Letters*, 3(2) (2003) 452-458.
- [5] Deshpande N., Londhe S., Kulkarni S., Modeling compressive strength of

- recycled aggregate concrete by Artificial Neural Network, Model Tree and Non-linear Regression, *International Journal of Sustainable Built Environment*, 3(2) (2014) 187–198.
- [6] Chandwani V., Agrawal V., Nagar R. Applications of Artificial Neural Networks in Modeling Compressive Strength of Concrete: A State of the Art Review. *International Journal of Current Engineering and Technology*, 4 (2014) 2949-2956.
- [7] Topçu İ.B., Boğa A.R., Hocaoglu FO., Modeling corrosion currents of reinforced concrete using ANN. *Automat. in Constr.*, 18(2) (2009) 145–52.
- [8] Lim C.H., Yoon Y.S., Kim J.H., Genetic algorithm in mix proportioning of high performance concrete. *Cem. Concr. Res.*, 34(3) (2004) 409–20.
- [9] Fairbairn E.M.R., Silvano M.M., Filho R.D.T, Alves J.L.D., Ebecken N.F.F. Optimization of mass concrete construction using genetic algorithms. *Comput. Struct.*, 82(2-3) (2004) 281–99.
- [10] Özcan F., Atis C., Karahan O., Uncuoglu E., Tanyildizi H., Comparison of artificial neural network and fuzzy logic models for prediction of long term compressive strength of silica fume concrete, *Advances in Engineering Software*, 40 (2009) 856–863.
- [11] İnan G., Göktepe A.B., Ramyar K., Sezer A. Prediction of sulfate expansion of PC mortar using adaptive neuro-fuzzy methodology. *Build Environ* 42(3) (2007) 1264–69.
- [12] Shahin M.A., Maier H.R. and Jaksa M.B., Predicting settlement of Shallow Foundations using Neural Networks, *Journal of Geotechnical and Geoenvironmental Engineering*, 128(9) (2002) 785-793.
- [13] Topçu İ.B., Sarıdemir M., Prediction of properties of waste AAC aggregate concrete using artificial neural network. *Comput. Mater. Sci.*, 41(1) (2007) 117–25.
- [14] Topçu İ.B., Sarıdemir M., Prediction of compressive strength of concrete containing fly ash using artificial neural networks and fuzzy logic. *Comput. Mater. Sci.*;41(3) (2008) 305–11.
- [15] Adhikary B.B., Mutsuyoshi H., Prediction of shear strength of steel fiber RC beams using neural networks. *Constr. Build. Mater.*, 20(9) (2006) 801–11.
- [16] Mermerdaş K., Güneyisi E., Gesoğlu M., Özturan T., Experimental evaluation and modeling of drying shrinkage behavior of metakaolin and calcined kaolin blended concretes *Constr. Build. Mater.*, 43 (2013) 337-347.
- [17] Duan Z.H., Kou S.C, Poon C.S., Prediction of compressive strength of recycled aggregate concrete using artificial neural networks. *Constr. Build. Mater.* 40 (2013) 1200–06.
- [18] Tokar, A.S. and Johnson, P.A., Rainfall-Runoff Modeling Using Artificial Neural Networks, *J. Hydrol. Eng.*, 4(3) (1999) 232- 239.
- [19] Ashour, A.F., Alvarez L.F., Toropov, V.V., Empirical modeling of shear strength RC deep beams by genetic programming. *Comput. Struct.*, 81(5) (2003) 331–38.
- [20] Sarıdemir, M., Effect of specimen size and shape on compressive strength of concrete containing fly ash: Application of genetic programming for design, *Materials and Design*, 56 (2014) 297-304
- [21] Lee, S.C. and Han, S.W., Neural-network-based models for generating artificial earthquakes and response spectra. *Computers and Structures* 80 (2002) 1627–1638.
- [22] D'Aniello M., Mete-Güneyisi, E., Landolfo, R., Mermerdaş, K., Predictive Models of the Flexural Overstrength Factor for Steel Thin-Walled Circular Hollow Section Beams, *Thin-Walled Structures*, 94 (2015)67-78.
- [23] Mete-Güneyisi E., Gesoğlu, M., Güneyisi, E., Mermerdaş, K., Assessment of Shear Capacity of Adhesive Anchors for Structures Using Neural Network Based Model, *Materials and Structures*, (2015) DOI 10.1617/s11527-015-0558-x.

- [24] Mete-Güneyisi, E., D'Aniello M., Landolfo, R., Mermerdaş, K., Prediction of the Flexural Overstrength Factor for Steel Beams Using Artificial Neural Network, *Steel and Composite Structures*, 17 (2014) 215-236.
- [25] D'Aniello M., Mete-Güneyisi, E., Landolfo, R., Mermerdaş, K., Analytical Prediction of Available Rotation Capacity of Cold-Formed Rectangular and Square Hollow Section Beams, *Thin-Walled Structures*, 77 (2014) 141-152.
- [26] Gesoğlu M., Mete-Güneyisi E., Güneyisi E., Yılmaz E., Mermerdaş K., Modeling and analysis of the shear capacity of adhesive anchors post-installed into uncracked concrete. *Composites Part B: Engineering*, 60 (2014) 716-724.
- [27] ASTM C39/C39M-12, Standard test method for compressive strength of cylindrical concrete specimens. Annual book of ASTM Standards, 2012.
- [28] Ferreira C., Gene expression programming; a new adaptive algorithm for solving problems. *Complex Syst.*, 12(2) (2001) 87-129.
- [29] Li X., Zhou C., Xiao W., Nelson P.C., Prefix gene expression programming. in Late Breaking Paper at the Genetic and Evolutionary Computation Conference (GECCO), Washington, D.C., 2005.
- [30] Koza J.R. Genetic programming; on the programming of computers by means of natural selection, MIT Press, USA, 1992.
- [31] Gen M, Cheng R. Genetic algorithms and engineering design, Wiley, USA, 1997.

Two lagrangian relaxation based heuristics for vertex coloring problem

Ali İrfan MAHMUTOĞULLARI 

Department of Industrial Engineering, TED University, 06420, Ankara/TURKEY

Abstract

Vertex coloring problem is a well-known NP-Hard problem where the objective is to minimize the number of colors used to color vertices of a graph ensuring that adjacent vertices cannot have same color. In this paper, we first discuss existing mathematical formulations of the problem and then consider two different heuristics, namely HEUR-RA and HEUR-RC, based on Lagrangian relaxation of adjacency and coloring constraints. HEUR-RA does not require solving any optimization problem through execution whereas at each iteration of HEUR-RC another NP-Hard problem, maximal weight stable set problem, is solved. We conduct experiments to observe computational performances of these heuristics. The experiments reveal that although it requires longer running times, HEUR-RC outperforms HEUR-RA since it provides lower optimal gaps as well as upper bound information.

Article info

History:

Received: 02.10.2019

Accepted: 15.06.2020

Keywords:

Vertex coloring problem, Heuristics, Optimization.

1. Introduction

Let $G = (V, E)$ be a graph where V is set of vertices and E is set of edges. Two vertices $i, j \in V$ are called *adjacent* if $e = (i, j) \in E$. A *vertex coloring* of a graph G is a mapping $c: V \rightarrow C$ such that $c(i) \neq c(j)$ whenever i and j are adjacent. The elements of the set C are called *colors*. A graph G is said to be *k-colorable* if there exist a vertex coloring $c: V \rightarrow \{1, \dots, k\}$ and such c is called as *k-coloring* of G . The *vertex coloring problem* (VCP) is to determine *chromatic number*, denoted as $\chi(G)$, of a given graph G where chromatic number of a graph is the smallest number of colors to color it. VCP is an NP-Hard problem according to [1].

Aside from its theoretical importance, VCP has many practical applications in scheduling, timetabling, map coloring etc. For each instance of these problems, we can construct a graph and solve VCP to find the desired solutions. Figure 1 depicts an example graph whose chromatic number is 4.

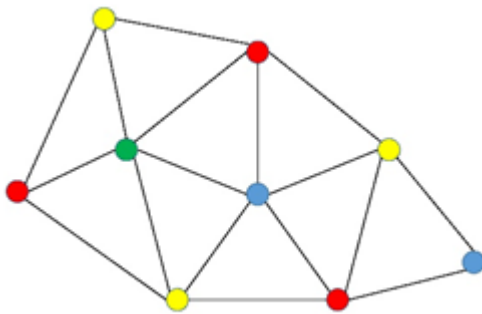


Figure 1. An example of graph G with $\chi(G)=4$.

There are many articles and books (such as [2] from which our notation is adapted) on graph theory that include VCP. However, in this paper, we will provide only studies with operations research perspective. Although first coloring problems were proposed in 19th century, the number of exact approaches of VCP is relatively recent compared to heuristic approaches. First exact approach was proposed by [3]. The idea is based on coloring one vertex at each step and obtain upper and lower bounds for the optimal value. Their approach for VCP can be seen

as an analogous to that of Branch-and-Bound method for solving mixed-integer problems. Later, [4,5] suggested improvements for the method such as tie breaking rules and computing initial upper bounds for the optimal value.

[6] proposed a column generation approach for the problem. Their formulation has exponential number of variables; thus, they solve its continuous relaxation with a subset of variables and then solve a pricing problem to detect that if a negative reduced cost exists. The pricing problem is a weighted independent set problem which is initially solved by a heuristic. If the heuristic does not generate a negative reduced cost values, an exact solution of the problem is performed. When LP relaxation of their model has a fractional solution, they perform a branching operation to recover integrality. This column generation approach solves VCP problems up to random instances of 70 vertices.

[7,8] proposed some extra constraints to eliminate symmetry (see Section 2) and proposed several valid inequalities for the models with these new constraints. With these valid inequalities, they could have solved random instances with more than 80 vertices.

Most of the heuristic approaches for VCP are greedy algorithms, that is ranking vertices (or independent sets) based on some criteria, selecting the one with the highest (or smallest rank) and color it either via color which is already used or a new color. [9-11] are examples of studies that proposed greedy algorithms for VCP. Some metaheuristic approaches were also employed for solving VCP. Local search ([12,13]), tabu search ([14]) and simulated annealing algorithms ([15]) enable us to solve VCP problems with 1000 vertices near-optimally.

VCP lies in the intersection of several disciplines such as graph theory, computer science and optimization. Although it attracts attention of researchers from various disciplines, our study is the first to propose heuristic methods based on different Lagrangian relaxations of a VCP. Therefore, the contribution of this paper is proposal of these methods and a discussion of the results obtained from the computational experiments on randomly generated instances.

The rest of the paper is organized as follows: In Section 2, we provide several existing mathematical models of VCP in the literature and give a detailed discussion on these models. In Section 3, we propose two different Lagrangian relaxations of a VCP model by relaxing adjacency and coloring constraints. We also discuss how to solve these relaxed problems. In Section 4, we propose two heuristics based on the two relaxations discussed in Section 3. In Section 5, we conduct a computational experiment on randomly generated VCP instances to observe the quality of bounds obtained from the proposed heuristics and discuss the results of the experiment. Finally, in Section 6, we present some concluding remarks and possible future extensions of the existing study.

2. Mathematical Models

Let $n = |V|$ be the number of vertices. Since any graph with n vertices is n -colorable (because each vertex can be colored with a different color), number of colors to color a graph is at most n . Moreover, we can label vertices of the graph from 1 to n without loss of generality.

Let $y_h = 1$ if color h is used and, 0 otherwise for all $h \in \{1, \dots, n\}$. Also let $x_{ih} = 1$ if vertex i is colored with color h and, 0 otherwise for all $i \in \{1, \dots, n\}$ and for all $h \in \{1, \dots, n\}$. Then, the following mathematical model VCP-1 solves VCP.

$$(VCP - 1) \text{ minimize } \sum_{h=1}^n y_h \quad (1)$$

$$\text{subject to } \sum_{h=1}^n x_{ih} = 1 \quad \forall i \in \{1, \dots, n\} \quad (2)$$

$$x_{ih} + x_{jh} \leq y_h \quad \forall (i, j) \in E, \forall h \in \{1, \dots, n\} \quad (3)$$

$$x_{ih} \in \{0,1\} \quad \forall i \in \{1, \dots, n\}, \forall h \in \{1, \dots, n\} \quad (4)$$

$$y_h \in \{0,1\} \quad \forall h \in \{1, \dots, n\} \quad (5)$$

Objective function (1) minimizes number of used colors. Constraints (2) and (3) ensure that each vertex is colored exactly with one color and adjacent vertices are colored with different colors, respectively. Constraints (4) and (5) are domain constraints.

VCP-1 has two major drawbacks as stated in [16]. The first one is the symmetry due to fact that colors are indistinguishable. There are $\binom{n}{k}$ possible ways to choose k colors and once k colors are selected, they can be

permutated in $k!$ ways. Thus, given a solution with k colors, there exists $\binom{n}{k} k!$ equivalent solutions. The second drawback is the weakness of LP relaxation of the model. Indeed, LP relaxation of VCP-1 has an optimal value of 2 by letting $x_{i1} = x_{i2} = 1/2$ for all $i \in \{1, \dots, n\}$, $y_1 = y_2 = 1$, $x_{ih} = 0$ for all $i \in \{1, \dots, n\}$, $h > 2$ and $y_h = 0$ for $h > 2$. [7,8] tried to overcome these drawbacks. To eliminate symmetry, they proposed adding some extra constraints to VCP-1. The first one is:

$$y_h \geq y_{h+1} \quad h = 1, \dots, n-1. \quad (6)$$

Constraints (6) ensure that color $h+1$ can be used only if color h is used. An alternative constraint to reduce symmetry is using following constraint:

$$\sum_{i=1}^n x_{ih} \geq \sum_{i=1}^n x_{i,h+1} \quad h = 1, \dots, n-1. \quad (7)$$

Constraints (7) ensure that the number of vertices with color $h+1$ is not greater than the number of vertices with color h .

Finally, following constraints completely eliminate symmetry of VCP-1:

$$x_{ih} = 0 \quad h \geq i+1, \quad (8)$$

$$x_{ih} \leq \sum_{k=h-1}^{i-1} x_{k,h-1} \quad \forall i \in \{2, \dots, n\}, 2 \leq h \leq i-1. \quad (9)$$

Constraints (8) and (9) ensure that independent sets are labeled with the minimum label of its vertices and the vertices in this independent set h are colored with color h .

[6] proposed another formulation of VCP by using independent sets. An *independent (or stable) set* S of a graph $G = (V, E)$ is a subset of V such that whenever $i, j \in S$ then $(i, j) \notin E$. Hence, all vertices in an independent set can be colored with same color. Let \mathcal{S} be collection of all independent sets of G and $z_S = 1$ if all vertices in S are colored with same color, and 0 otherwise for all $S \in \mathcal{S}$. Then, following mathematical model VCP-2 solves VCP.

$$(VCP-2) \quad \text{minimize} \quad \sum_{S \in \mathcal{S}} z_S \quad (10)$$

$$\text{subject to} \quad \sum_{S \in \mathcal{S}: i \in S} z_S \geq 1 \quad \forall i \in \{1, \dots, n\} \quad (11)$$

$$z_S \in \{0,1\} \quad \forall S \in \mathcal{S} \quad (12)$$

Objective function (10) minimizes number of selected independent sets. Constraints (11) ensure that each vertex is included in some independent set and (12) are domain constraints. Although number of variables, that is $|\mathcal{S}|$, is huge, a column generation algorithm can be employed to solve VCP-2. Also, LP relaxation of VCP-2 is as good as LP relaxation of VCP-1 due to [17].

Another mathematical model was proposed in [18] by manipulating constraint (11) in VCP-2. The following *set packing* model VCP-3 solves VCP.

$$(VCP-3) \quad \text{maximize} \quad \sum_{S \in \Omega} (|S| - 1)z_S \quad (13)$$

$$\text{subject to} \quad \sum_{S \in \Omega: i \in S} z_S \leq 1 \quad \forall i \in \{1, \dots, n\} \quad (14)$$

$$z_S \in \{0,1\} \quad \forall S \in \Omega \quad (15)$$

where $\Omega = \{S \in \mathcal{S}: |S| \geq 2\}$. The number of used colors is $n - z^*$ where z^* is optimal value of VCP-3. [18] also showed that LP relaxations of VCP-2 and VCP-3 are equivalent in terms of solution value and proposed valid inequalities for VCP-3. VCP-2 and VCP-3 have exponential number of constraints and hence these models cannot be solved directly even for moderate size instances. These models can only be considered for the solution methods such as column generation and branch-and-cut.

3. Lagrangian Relaxations for VCP

In this section, we propose two different Lagrangian relaxations of VCP.

3.1. Relaxing adjacency constraints

Consider VCP-1 with additional constraints (8):

$$(VCP - 1a) \quad \text{minimize} \quad \sum_{h=1}^n y_h \quad (1)$$

$$\text{subject to} \quad \sum_{h=1}^n x_{ih} = 1 \quad \forall i \in \{1, \dots, n\} \quad (2)$$

$$x_{ih} + x_{jh} \leq y_h \quad \forall (i, j) \in E, \forall h \in \{1, \dots, n\} \quad (3)$$

$$x_{ih} = 0 \quad h \geq i + 1, \quad (8) \quad (4)$$

$$x_{ih} \in \{0, 1\} \quad \forall i \in \{1, \dots, n\}, \forall h \in \{1, \dots, n\} \quad (4)$$

$$y_h \in \{0, 1\} \quad \forall h \in \{1, \dots, n\} \quad (5)$$

Relaxing adjacency constraints (3) in a Lagrangian manner, we get LR1:

$$(LR1) \quad \text{minimize} \quad \sum_{h=1}^n y_h + \sum_{(i,j) \in E} \sum_{h=1}^n u_{ijh} (x_{ih} + x_{jh} - y_h) \quad (16)$$

subject to (2), (4), (5) and (8).

LR1 is a relaxation of VCP-1a for any $u \geq 0$. By rearranging terms of the objective function (16), LR1 becomes:

$$(LR1) \quad \text{minimize} \quad \sum_{h=1}^n (1 - \sum_{(i,j) \in E} u_{ijh}) y_h + \sum_{i=1}^n \sum_{h=1}^n (\sum_{e \in \delta(i)} u_{eh}) x_{ih} \quad (17)$$

subject to (2), (4), (5) and (8).

where $\delta(i) := \{e \in E : e = (i, j) \text{ or } e = (j, i) \text{ for some } j \in \{1, \dots, n\}\}$ is the set of edges adjacent to i .

LR-1 decomposes for each color and vertex. Also, an optimal solution (x^*, y^*) of LR-1 can be found by inspection. Since y variables appear only in objective function, y_h^* takes value 1 only if its objective value coefficient is non-positive for any $h \in \{1, \dots, n\}$. Moreover, constraints (2) and (8) ensures that $\sum_{h=1}^i x_{ih} = 1$. Therefore, the color from set $\{1, \dots, i\}$ with smallest objective value coefficient is used to color vertex $i \in \{1, \dots, n\}$. Hence,

$$y_h^* = \begin{cases} 1, & \text{if } 1 - \sum_{(i,j) \in E} u_{ijh} \leq 0 \\ 0, & \text{otherwise} \end{cases} \quad \forall h \in \{1, \dots, n\} \quad (18)$$

$$x_{ih}^* = \begin{cases} 1, & \text{if } h = \underset{k \in \{1, \dots, i\}}{\operatorname{argmin}} \sum_{e \in \delta(i)} u_{ek} \\ 0, & \text{otherwise} \end{cases} \quad \forall i \in \{1, \dots, n\}, \forall h \in \{1, \dots, n\} \quad (19)$$

3.2. Relaxing coloring constraints

Consider VCP-1: (1)-(5) without anti-symmetry constraints. Relaxing coloring constraints (2) in a Lagrangian manner, we get LR2:

$$(LR2) \quad \text{minimize} \quad \sum_{h=1}^n y_h + \sum_{i=1}^n (1 - \sum_{h=1}^n x_{ih}) v_i \quad (20)$$

subject to (3) – (5).

LR2 is a relaxation of VCP for any choice of Lagrangian multipliers v . By rearranging terms of the objective function (20), LR2 becomes:

$$(LR2) \quad \text{minimize} \quad \sum_{h=1}^n (y_h - \sum_{i=1}^n v_i x_{ih}) + \sum_{i=1}^n v_i \quad (21)$$

subject to (3) – (5).

LR2 decomposes for each color such that:

$$LR2(v) = \sum_{h=1}^n LR2_h(v) + \sum_{i=1}^n v_i \quad (22)$$

where

$$LR2_h(v) = \text{minimize} \quad y_h - \sum_{i=1}^n v_i x_{ih} \quad (23)$$

$$\text{subject to } x_{ih} + x_{jh} \leq y_h \quad \forall (i, j) \in E \quad (24)$$

$$x_{ih} \in \{0, 1\}, y_h \in \{0, 1\} \quad \forall i \in \{1, \dots, n\} \quad (25)$$

The value of $LR2_h(v)$ depends on whether y_h takes value 0 or 1. If $y_h = 0$, then $x_{ih} = 0, \forall i \in V$ due to constraint (24); otherwise $LR2_h(v)$ takes value of following problem:

$$\text{minimize } 1 - \sum_{i=1}^n v_i x_i \quad (26)$$

$$\text{subject to } x_i + x_j \leq 1 \quad \forall (i, j) \in E \quad (27)$$

$$x_i \in \{0, 1\}, \quad \forall i \in \{1, \dots, n\}. \quad (28)$$

which can equivalently be restated as:

$$1 - \text{maximize } \sum_{i=1}^n v_i x_i \quad (29)$$

subject to (27) and (28)

Hence,

$$LR2_h(v) = \min\{0, 1 - f(v)\} \quad (30)$$

where $f(v)$ is the objective of the maximum weight stable set problem

$$(MWSSP) \quad \text{maximize } \sum_{i=1}^n v_i x_i \quad (31)$$

subject to (27) and (28)

Let $\tilde{x}_i, \forall i \in \{1, \dots, n\}$ be an optimal solution of MWSSP. Based on the value that minimum in (30) is attained, an optimal solution of LR2 can be found as:

$$y_h^* = \begin{cases} 0, & \text{if } f(v) \leq 1 \\ 1, & \text{otherwise} \end{cases} \quad \forall h \in \{1, \dots, n\} \quad (32)$$

$$x_{ih}^* = \begin{cases} 0, & \text{if } f(v) \leq 1 \\ \tilde{x}_i, & \text{otherwise} \end{cases} \quad \forall i \in \{1, \dots, n\}, \forall h \in \{1, \dots, n\} \quad (33)$$

Note that in any optimal solution of MWSSP, we have $\tilde{x}_i = 0$ for any $i \in \{1, \dots, n\}$ with $v_i < 0$ since otherwise we can always have feasible solution with a better objective value by changing the value of the variable with a strictly negative coefficient to 0.

4. Heuristics

In this section, we propose two heuristics for VCP based on the Lagrangian relaxations proposed in the previous section. The first **heuristic** is based on the relaxation of adjacency constraint and called as **HEUR-RA**. The outline of HEUR-RA is given below.

HEUR-RA
Initialize: Iteration counter $t \leftarrow 1$, Lagrangian multipliers $u_{ijh}^t = 0$ for all $(i, j) \in E$ and $h \in \{1, \dots, n\}$, step-sizes $\{\mu_t\}_{t=1}^\infty$, lower bound $LB \leftarrow -\infty$.
while some termination criteria is not met do
Compute an optimal solution (x^t, y^t) of the Lagrangian relaxation by (18) and (19).
Update lower bound
$LB_t \leftarrow \sum_{h=1}^n y_h^t + \sum_{(i,j) \in E} \sum_{h=1}^n u_{ijh}^t (x_{ih}^t + x_{jh}^t - y_h^t)$

$LB \leftarrow \max\{LB, LB_t\}$
Update Lagrangian multipliers $u_{ijh}^{t+1} \leftarrow \max\{0, u_{ijh}^t + \mu^t(x_{ih}^t + x_{jh}^t - y_h^t)\}$ for all $(i, j) \in E$ and $h \in \{1, \dots, n\}$
$t \leftarrow t + 1$
end
Return: A lower bound LB and an upper bound UB .

At each iteration of HEUR-RA, an optimal solution of LR1 is found by inspection using equations (18) and (19) and a lower bound for VCP is obtained from this solution. The Lagrangian multipliers are also updated in each iteration. Since adjacency constraints are relaxed in LR1, a solution of the relaxed problem is only an assignment of colors to the vertices. Therefore, it does not provide any information about a feasible coloring and hence an upper bound.

The second **heuristic** is based on relaxation of coloring constraints and hence called as **HEUR-RC**. The outline of HEUR-RC is given below.

HEUR-RC
Initialize: Iteration counter $t \leftarrow 1$, Lagrangian multipliers $v_i^t = 0$ for all $i \in \{1, \dots, n\}$, lower bound $LB \leftarrow -\infty$ and upper bound $UB \leftarrow \infty$.
while some termination criteria is not met do
Solve MWSSP problem given with given $v_i^t, i \in \{1, \dots, n\}$ values and compute an optimal solution (x^t, y^t) of the Lagrangian relaxation by (32) and (33). Update lower bound $LB_{t+1} \leftarrow \max\{LB_t, \sum_{h=1}^n y_h^t + \sum_{i=1}^n (1 - \sum_{h=1}^n x_{ih}^t)v_i\}$ $LB \leftarrow \max\{LB, LB_{t+1}\}$
Let $\bar{x} \leftarrow x^t$ and $\bar{y} \leftarrow y^t$ be a coloring which does not necessarily satisfy coloring constraints (2)
For vertices $i \in \{1, \dots, n\}$ such that $\sum_{h=1}^n \bar{x}_{ih} \geq 2$ only keep the color with smallest index, that is, $\bar{x}_{ih} \leftarrow \begin{cases} 1, & \text{if } h = \min\{k \in \{1, \dots, n\}: \bar{x}_{ik} = 1\} \\ 0, & \text{otherwise} \end{cases}$
For vertices $i \in \{1, \dots, n\}$ such that $\sum_{h=1}^n \bar{x}_{ih} = 0$ assign the color with the smallest index that does not create a conflict, that is, $\bar{x}_{ih} \leftarrow \begin{cases} 1, & \text{if } h = \min\{\{1, \dots, n\} \setminus \mathcal{C}\} \\ 0, & \text{otherwise} \end{cases}$ where $\mathcal{C} := \{h: \bar{x}_{i'h} = \bar{x}_{j'h} = 1 \text{ for some } (i', j') \in \delta(i)\}$ is the set of colors that creates a conflict.
Update used colors $y_h^t \leftarrow \begin{cases} 1, & \text{if } \exists i \in \{1, \dots, n\} \text{ s.t. } x_{ih}^t = 1 \\ 0, & \text{otherwise} \end{cases} \quad \forall h \in \{1, \dots, n\}$
Update upper bound $UB_{t+1} \leftarrow \min\{UB_t, \sum_{h=1}^n y_h^t\}$
Update Lagrangian multipliers $u_{ijh}^{t+1} \leftarrow \max\{0, u_{ijh}^t + \mu^t(x_{ih}^t + x_{jh}^t - y_h^t)\}$ for all $(i, j) \in E$ and $h \in \{1, \dots, n\}$
$t \leftarrow t + 1$
end

Return: A feasible coloring, lower and upper bounds.

At each iteration of HEUR-RC, a solution of LR2 is obtained by solving MWSSP as discussed in the previous section. Unlike LR1, the adjacency requirement is maintained in LR2, it is possible to generate a feasible solution to VCP using x_{ih}^* in equation (33). However, some vertices are colored more than once and some of them are not colored since coloring constraint (2) does not appear in LR2. If a vertex has been colored more than once, only the color with the smallest index is maintained and other colors are discarded. If a vertex has not been colored, then any color which does not violate adjacency requirement can be assigned to that vertex. Such color with the smallest index is used to color any uncolored vertex. Therefore, a feasible coloring and hence an upper bound for VCP is obtained. Finally, Lagrangian multipliers are updated.

5. Computational Study

In order to observe the efficiency of the proposed heuristics, some computational experiments are conducted on randomly generated instances. *Random* class on Java 1.6.023 running on NetBeans IDE 6.9.1 is used to generate random values. IBM ILOG CPLEX Optimization Studio 12.6 is used to solve optimization problems on a PC with specifications Intel(R) Core (TM)2 Duo CPU P7450 2 x 2.13GHz. with 4.00 GB RAM. Five instances are generated for each $|V| = n \in \{10, 20, 30, 40\}$ and edge density coefficient $f \in \{0.2, 0.5, 0.8\}$ pair. Edge density coefficient indicates the probability of existence of an edge between each edge pairs.

The classical subgradient algorithm discussed in [19] is used to solve Lagrangian dual problems with stepsize rule $\mu_t = 1/t$ for HEUR-RA (due to absence of upper bound information) and $\mu_t = \frac{UB - z^t}{||infea||^2}$ for HEUR-RC where $||infea||$ indicates the Euclidean norm of the infeasibility vector of the relaxed constraint, UB indicates current upper bound and z^t is the value of Lagrangian relaxation at iteration t . The algorithm terminates if no improvement is made in last $10n$ iterations in LB so as to prevent memory errors.

Table 1 summarizes optimal values and required CPU seconds for solving VCP-1 with anti-symmetry constraints (8) and (9) of all five instances for each parameter settings (n, f) . Although all instances with $n \leq 30$ are able to be solved less than 10 seconds, instances with $n = 40$ require higher CPU times. For the instances with $n > 40$, memory errors occur due to the fact that the Branch-and-Bound tree is quite large.

Required CPU time and optimality gap percentage of HEUR-RA on each instance are summarized in Table 2. Since LR1 can only be solved by inspection, CPU times are under 36 seconds for all instances. On the other hand, lower bounds obtained by LR1 is not tight with average optimality gap of 40.48%. Also, no upper bound information is obtained during execution of HEUR-RA. Therefore, the optimality gap for these instances are calculated as $Gap \% = 100 \frac{Obj.value - Lower\ bound}{Lower\ Bound}$.

Table 3 summarizes lower and upper bounds, optimality gaps, number of iterations and CPU times of execution of HEUR-RC. For 53 out of 60 instances the heuristic is able to find optimal solution. These instances are indicated with bolded upper bound values in Table 3. For the instances with $n = 40$ and $f = 0.5$ or 0.8 CPU times of Lagrangian dual problem is smaller than CPU times required to solve VCP-1 with constraints (8) and (9). Also, the average optimality gap of the instances in Table 3 is 2%.

HEUR-RC is also tested with larger instances presented in Table 4. For six out of 20 instances, the heuristic yields optimal solutions (these instances are indicated with bolded upper bound values in Table 4). Also, average gap for the instances in Table 4 is 11.18 %. Although, VCP-1 with constraints (8) and (9) cannot find optimal values for the instances in Table 4, the algorithm figures out reasonable bounds even though CPU times are high.

In Tables 3 and 4, the optimality gaps are calculated as $Gap \% = 100 \frac{Upper\ bound - Lower\ bound}{Lower\ bound}$ since both lower and upper bounds are available in HEUR-RC.

6. Conclusion

In this study, two different Lagrangian relaxations of VCP are investigated and then we propose two heuristics based on these relaxations. First, adjacency constraints (3) in VCP-1a are relaxed in Lagrangian manner. Although corresponding relaxed problem can be solved by easily, corresponding lower bounds are not tight. A possible improvement in lower bound can be obtained by adding inequalities that are valid for VCP-1a to LR1. For example,

$$x_{ih} \leq y_h \quad i \in \{1, \dots, n\}, h \in \{1, \dots, n\} \quad (34)$$

or

$$|K| \leq \sum_{h=1}^n y_h \quad (35)$$

where $K \subseteq V$ is a *maximum cardinality clique* of G . Adding (34) and/or (35) to LR1 definitely improves quality of the lower bound. However, solving the relaxed problem with (34) or finding a maximum cardinality clique prohibit color-wise decomposition of LR1. This trade off should be investigated by conducting computational experiments.

Second, coloring constraints (2) are relaxed in Lagrangian manner. The lower bounds obtained by Lagrangian dual problem induced by LR2 are much tighter than the previous relaxation with a computational cost of solving another NP-Hard problem, namely weighted stable set problem, at each iteration. Also, an upper bound can also be obtained by a heuristic whose input is optimal solution of the relaxed problem. Indeed, optimal solution is attained for 58 of 80 instances with average gap is 4%. An improvement for the bound of this relaxation can be achieved solving weighted stable set problem at each iteration more efficiently.

Table 1. Computational performance of VCP-1 with constraints (8) and (9)													
	n	10			20			30			40		
#	f	0.2	0.5	0.8	0.2	0.5	0.8	0.2	0.5	0.8	0.2	0.5	0.8
1	Opt. value	3	3	5	4	5	9	4	7	12	5	8	15
	CPU time	0.016	0.016	0.031	0.031	0.109	0.141	0.764	2.293	3.073	14.274	292.516	656.012
2	Opt. value	3	4	7	3	5	10	4	7	12	5	8	15
	CPU time	0.016	0.046	0.015	0.141	0.156	0.156	0.671	3.417	5.819	11.279	1303.49	647.323
3	Opt. value	3	4	5	4	6	10	4	7	12	5	9	15
	CPU time	0.01	0.312	0.374	0.124	0.203	0.063	0.39	3.026	1.7	0.92	830.14	19.032
4	Opt. value	3	5	6	4	6	10	4	8	13	5	8	16
	CPU time	0.01	0.015	0	0.047	0.109	0.046	0.234	0.562	0.749	4.431	505.581	235.139
5	Opt. value	3	3	5	4	5	10	4	7	13	5	9	14
	CPU time	0.01	0.031	0.031	0.094	0.562	0.125	0.92	7.316	0.858	5.054	632.956	3.37
Average Opt. value		0.012	0.084	0.09	0.087	0.228	0.106	0.596	3.323	2.44	7.192	712.937	312.175
Max CPU time		0.016	0.312	0.374	0.141	0.562	0.156	0.92	7.316	5.819	14.274	1303.49	656.012

Table 2. Computational performance of HEUR-RA													
	<i>n</i>	10			20			30			40		
#	<i>f</i>	0.2	0.5	0.8	0.2	0.5	0.8	0.2	0.5	0.8	0.2	0.5	0.8
1	Opt. Value	3	3	5	4	5	9	4	7	12	5	8	15
	Lower Bound	2	3	4	3	3	5	3	3	5	3	3	4
	Gap %	33.3	0	20	25	40	44.4	25	57.1	58.3	40	62.5	73.3
	CPU time	0.016	0.078	0.047	1.123	0.405	1.201	8.829	1.607	1.467	25.334	5.179	3.759
2	Opt. Value	3	4	7	3	5	10	4	7	12	5	8	15
	Lower Bound	3	3	4	3	3	6	3	3	5	3	3	5
	Gap %	0	25	42.9	0	40	40	25	57.1	58.3	40	62.5	66.7
	CPU time	0.047	0.016	0.016	1.747	0.156	1.185	9.594	1.779	3.916	11.372	2.231	17.971
3	Opt. Value	3	4	5	4	6	10	4	7	12	5	9	15
	Lower Bound	3	3	4	3	3	4	3	3	4	3	3	4
	Gap %	0	25	20	25	50	60	25	57.1	66.7	40	66.7	73.3
	CPU time	0.109	0.063	0.53	0.842	0.562	0.358	1.186	0.936	0.936	23.291	8.643	4.758
4	Opt. Value	3	5	6	4	6	10	4	8	13	5	8	16
	Lower Bound	3	3	4	3	3	6	3	3	4	3	3	5
	Gap %	0	40	33.3	25	50	40	25	62.5	69.2	40	62.5	68.8
	CPU time	0.249	0.016	0.046	0.39	0.328	0.889	1.778	1.076	0.717	10.608	1.794	9.454
5	Opt. Value	3	3	5	4	5	10	4	7	13	5	9	14
	Lower Bound	3	3	4	3	3	4	3	3	4	3	3	5
	Gap %	0	0	20	25	40	60	25	57.1	69.2	40	66.7	64.3
	CPU time	0.25	0.062	0.016	1.06	1.357	0.219	20.031	1.965	2.745	4.836	10.342	35.256
Avg CPU time		0.134	0.047	0.131	1.032	0.562	0.77	8.284	1.473	1.956	15.088	5.638	14.24
Max CPU time		0.25	0.078	0.53	1.747	1.357	1.201	20.031	1.965	3.916	25.334	10.342	35.256
Average Gap %		6.7	18	27.2	20	44	48.9	25	58.2	64.4	40	64.2	69.3
Max Gap %		33.3	40	42.9	25	50	60	25	62.5	69.2	40	66.7	73.3

Table 3. Computational performance of HEUR-RC													
	<i>n</i>	10			20			30			40		
#	<i>f</i>	0.2	0.5	0.8	0.2	0.5	0.8	0.2	0.5	0.8	0.2	0.5	0.8
1	Lower Bound	3	3	5	4	5	9	4	7	12	5	8	14
	Upper Bound	3	3	5	4	5	9	4	7	12	5	8	15
	Gap %	0	0	0	0	0	0	0	0	0	0	0	6.7
	# iter	12	9	16	27	22	39	49	214	299	487	569	49
	CPU time	0.23	0.187	0.234	0.671	0.734	0.84	1.55	20.015	44.444	85.207	210.725	17.394
2	Lower Bound	3	4	7	3	5	10	4	7	12	4	8	15
	Upper Bound	3	4	7	3	5	10	4	7	12	5	9	15
	Gap %	0	0	0	0	0	0	0	0	0	20	11.1	0
	# iter	9	14	14	15	23	35	53	50	48	1346	1032	854
	CPU time	0.03	0.078	0.39	0.093	0.265	0.47	0.66	4.29	4.103	230.29	333.513	467.298
3	Lower Bound	3	4	5	4	6	10	4	7	12	5	9	15
	Upper Bound	3	5	6	4	6	10	4	8	12	5	9	15
	Gap %	0	20	16.7	0	0	0	0	12.5	0	0	0	0
	# iter	12	207	139	95	69	92	35	757	71	40	26	224
	CPU time	0.19	1.342	0.765	1.545	1.248	1.58	0.34	111.74	7.114	1.731	1.779	72.634
4	Lower Bound	3	5	6	4	6	10	4	8	13	5	8	16
	Upper Bound	3	5	6	4	7	10	4	8	13	5	9	16
	Gap %	0	0	0	0	14.3	0	0	0	0	0	11.1	0
	# iter	12	14	22	33	482	38	33	126	418	459	1312	195
	CPU time	0.05	0.078	0.125	0.234	4.103	0.39	0.28	9.142	12.183	55.817	404.166	29.141
5	Lower Bound	3	3	5	4	5	10	4	7	13	5	8	14
	Upper Bound	3	3	5	4	5	10	4	7	13	5	10	14
	Gap %	0	0	0	0	0	0	0	0	0	0	20	0
	# iter	11	10	11	30	22	44	30	444	107	29	625	585
	CPU time	0.02	0.031	0.046	0.14	0.171	0.62	0.42	65.941	7.114	0.843	177.949	214.594
Avg CPU time		0.1	0.343	0.312	0.537	1.304	0.78	0.65	42.226	14.992	74.777	225.626	160.212
Max CPU time		0.23	1.342	0.765	1.545	4.103	1.58	1.55	111.74	44.444	230.29	404.166	467.298
Average Gap %		0	4	3.3	0	2.9	0	0	2.5	0	4	8.4	1.3
Max Gap %		0	20	16.7	0	14.3	0	0	12.5	0	20	20	6.7

Table 4. Computational performance of HEUR-RC on larger instances					
	n	50			60
#	f	0.2	0.5	0.8	0.2
1	Lower Bound	4	9	16	5
	Upper Bound	4	11	19	7
	Gap %	0	18.2	15.8	28.6
	# iter	64	1024	1211	1944
	CPU time	9.02	511.38	474.12	1204.85
2	Lower Bound	5	9	16	7
	Upper Bound	5	11	17	8
	Gap %	0	18.2	5.9	12.5
	# iter	553	812	1763	1603
	CPU time	140.65	380.61	680.82	1574.36
3	Lower Bound	4	10	16	8
	Upper Bound	4	10	19	8
	Gap %	0	0	15.8	0
	# iter	66	526	1018	1056
	CPU time	10.17	244.33	411.79	1008.83
4	Lower Bound	5	6	17	6
	Upper Bound	5	6	19	7
	Gap %	0	0	10.5	14.3
	# iter	236	38	1097	2615
	CPU time	65.83	7.64	462.06	1876.73
5	Lower Bound	5	8	17	6
	Upper Bound	6	11	20	8
	Gap %	16.7	27.3	15	25
	# iter	1153	1268	1040	1862
	CPU time	376.23	584.85	402.54	1755.13
Avg CPU time		120.38	345.76	486.27	1483.98
Max CPU time		376.23	584.85	680.82	1876.73
Average Gap %		3.3	12.7	12.6	16.1
Max Gap %		16.7	27.3	15.8	28.6

Conflicts of interest

There is no conflict of interest.

References

- [1] Karp R. M., Reducibility among combinatorial problems. Springer (1972).
- [2] Diestel R., Graph theory (graduate texts in mathematics). Springer (2005).
- [3] Brown J. R., Chromatic scheduling and the chromatic number problem. *Management Science*, 19 (4) (1972) 456–463.
- [4] Brélaz D., New methods to color the vertices of a graph. *Communications of the ACM*, 220 (4) (1979) 251–256.
- [5] Sewell E., An improved algorithm for exact graph coloring. *DIMACS series in discrete mathematics and theoretical computer science*, 26 (1996) 359–373.
- [6] Mehrotra A. and Trick M. A., A column generation approach for graph coloring. *Inform Journal on Computing*, 80 (4) (1996) 344–354.

- [7] Méndez-Díaz I. and Zabala P., A branch-and-cut algorithm for graph coloring. *Discrete Applied Mathematics*, 1540 (5) (2006) 826-847.
- [8] Méndez-Díaz I. and Zabala P., A cutting plane algorithm for graph coloring. *Discrete Applied Mathematics*, 1560 (2) (2008) 159-179.
- [9] Leighton F. T., A graph coloring algorithm for large scheduling problems. *Journal of research of the national bureau of standards*, 840 (6) (1979) 489–506.
- [10] Bollobás B. and Thomason A., Random graphs of small order. *North-Holland Mathematics Studies*, 118 (1985) 47-97.
- [11] Culberson J. C. and Luo F., Exploring the k-colorable landscape with iterated greedy. *Cliques, coloring, and satisfiability: second DIMACS implementation challenge*, 26 (1996) 245–284.
- [12] Morgenstern C., Distributed coloration neighborhood search. *Discrete Mathematics and Theoretical Computer Science*, 26 (1996) 335–358.
- [13] Chiarandini M., Dumitrescu I., and Stützle T., Stochastic local search algorithms for the graph colouring problem. *Handbook of approximation algorithms and metaheuristics*. Chapman & Hall, CRC (2007).
- [14] Hertz A. and de Werra D., Using tabu search techniques for graph coloring. *Computing*, 390 (4) (1987) 345–351.
- [15] Johnson D. S., Aragon C. R., McGeoch L. A. and Schevon C., Optimization by simulated annealing: An experimental evaluation; part i, graph partitioning. *Operations research*, 370 (6) (1989) 865–892.
- [16] Malaguti E. and Toth P., A survey on vertex coloring problems. *International Transactions in Operational Research*, 170 (1) (2010) 1–34.
- [17] Mehrotra A., Constrained graph partitioning: decomposition, polyhedral structure and algorithms, (1992).
- [18] Hansen P., Labbé M. and Schindl D., Set covering and packing formulations of graph coloring: algorithms and first polyhedral results. *Discrete Optimization*, 60 (2) (2009) 135–147.
- [19] Wolsey L.A., Integer programming. Wiley (1998).

Comparison of functionally graded and ungraded cylinder liners with finite element analysis

Fatih CİVELEK¹ , Cem ERTEK^{1,*} 

¹Department of Manufacturing Engineering, Sivas Cumhuriyet University, 58140 Sivas/ TURKEY

Abstract

In this study, functionally graded and ungraded Al-Si cylinder liners have been compared by the finite element analysis. At the beginning of the study, the most sold gasoline-powered automobiles in recent years have been investigated and the dimensions of the Al-Si cylinder liner have been determined. Al-Si alloy based cylinder liners with a wall-thickness of 6 mm and inner diameter of 74 mm, an outer diameter of 86 mm and a length of 165 mm have been designed. The functionally graded cylinder liner has a twenty-layered structure, and the silicon content of each layer is distinct. Si contents on the inner and the outer surfaces of the functionally graded liner are 32 vol.% and 8.5 vol.%, respectively. The ungraded cylinder liner, on the other hand, has a homogeneous structure and the silicon content of 21 vol.%. The maximum Von Mises stresses reached as a result of thermal loads in the functionally graded and ungraded cylinder liners are determined to be 47.526 MPa and 95.951 MPa, respectively. It has been observed that maximum Von Mises stress decreases by approximately 50% thanks to the functional grading.

Article info

History:

Received: 12.10.2019

Accepted: 27.05.2020

Keywords: Functionally graded material, Finite element method, Al-Si alloys, Thermal stresses.

1. Introduction

Nowadays as an alternative to cast iron, Al-Si alloys are increasingly used to manufacture engine parts. In addition to having a high strength to weight ratio, Al-Si alloys also have excellent thermal conductivity property which is necessary to remove the heat released by combustion [1]. The applications of Al-Si alloys in the automotive industry include engine parts, in particular, cylinder liners, and engine blocks. The use of these alloys reduces engine weight, exhaust gas emissions and fuel consumption [2].

The use of engine blocks made of hypereutectic Al-Si alloy has been contemplated by many companies. Al17Si4CuMg alloy casting to produce cylinder block is a very difficult and expensive process, therefore low-priced hypoeutectic Al-Si alloys are used to manufacture engine blocks. The tribological characteristics of these alloys cannot provide the properties necessary for the combustion chamber surface. Surface coating or use of cylinder liner is required in order to solve this problem [2]. The surface of the cylinder can be coated with Ni/SiC (Nikasil) composite materials to provide the required tribological properties. However, coatings consisting of nickel are extremely sensitive to sulfur; over time, coatings can be broken down when sulfur-containing gasoline is used [3]. Due to economic considerations, cylinder liners used in hypoeutectic Al-Si engine blocks are mostly cast iron. However, the use of cast iron liner causes some problems. The main problems can be summarized as follows. The bond between the cast iron liner and the cylinder block is only mechanical, no metallic bond; this makes the heat conduction difficult. The mismatch in coefficients of thermal expansion of Al-Si alloy and cast iron can cause deformation of the cylinder liner. Besides, cast iron liners bring about an increase in engine weight [3].

Functionally graded materials (FGMs) are an advanced composite type consisting of two or more phases. The gradual structure is formed through the changes in the composition and/or microstructure of the phases within the material in a specific direction. The graded structure reduces local stress concentration, thermal and residual stresses frequently encountered in conventional composites. The centrifugal casting method is one of the simplest methods so that functionally graded material manufacturing can be realized economically. The concentration of the reinforcing particles in the radial direction can be controlled by centrifugal casting. Thus, parts with better thermal dimensional stability and better wear resistance can be manufactured [4].

*Corresponding author. Email address: cemertek@cumhuriyet.edu.tr
<http://dergipark.gov.tr/csj> ©2020 Faculty of Science, Sivas Cumhuriyet University

Liew et al. [5] studied the thermomechanical behavior of functionally graded hollow circular cylinders. They observed that FGMs cannot expand freely in a steady temperature field, unlike homogeneous materials, and this can cause large stresses in FGMs. Also, thermal stresses in the functionally graded cylinder depend on more factors (non-uniform thermal conductivity and linear thermal expansion coefficient, etc.), dissimilar to its homogeneous counterparts, and it is more complicated to estimate. For all cases in this study, it was observed that hoop stress is the dominant stress.

Jabbari et al. [6] presented an analytical solution for the calculation of asymmetric thermal and mechanical stresses in a thick hollow cylinder made of functionally graded material. They designed a material having properties which are depending on the variable r (radius), and material properties were defined as power functions of r . They observed that the magnitude of the radial stress increased when m (power law index) was increased. In this study, it is presented that when $m < 1$, the hoop stress through the radius declined. Because the modulus of elasticity is an increasing function of the radius, the hoop stress increased along the radius, when $m > 1$. Obata and Noda [7] investigated the thermal stresses in a hollow sphere and a hollow circular cylinder made of functionally graded material. They presented that the values and distributions of the hoop stress and axial stress are similar. However, they observed that the distribution of the radial stress is different from them and the magnitude of it is lesser than theirs. Ekici et al. [8] studied the thermal stress behaviors of temperature-dependent functionally graded rectangular plates (FGRPs) using Finite Difference Method (FDM) and Finite Element Method (FEM). They presented that FEM and FDM analyses show very similar results with respect to strain, temperature, and normal stress component levels. In addition, they observed that the distribution characteristics of temperature, strain, displacement, and stress components are highly similar. However, they noted that there are quite differences between the displacement levels of FEM and FDM analyses. They concluded that the finite difference method, which does not lose importance for structures with linear geometry, gives better results than the finite element method. Zhang et al. [9] investigated the mechanical properties and microstructure of functionally graded cup-shaped specimens. The specimens were produced using a backward extrusion process during the semi-solid state of aluminum alloy (A390). They observed that the content of primary Si gradually increased from the upper region to the bottom region of the cup-shaped functionally graded samples, and the hardness values through the axis of the cup-shaped specimen gradually decreased from the bottom region to the upper region. They stated that during the wear test, the weight loss of the upper region is higher than that of the lower region because of the accumulation of numerous Si particles in the bottom region. Lin et al. [10] studied the effects of different process parameters on the particle distributions and the particle segregation ratio of in situ primary Si/Mg₂Si particles in Al-Si-Mg functionally graded tubes produced by centrifugal casting method. They observed that in the functionally graded tubes, many primary Si and Mg₂Si particles segregated in the inner layer, (reinforcement layer), whereas few particles segregated in the outer layer (un-reinforcement layer). They presented that the particle segregation ratios of k (ratio of the width of the reinforcement layer to distance from the inner wall to the outer wall) increased as pouring or mold temperatures increased, but decreased when the mold rotation rate increased. It is stated that when the pouring or mold temperatures or rotation rate were increased, the particle size of primary Si and primary Mg₂Si became smaller. They reported that the largest hardness of HRB 72–75 observed at the middle position of the reinforcement layer of the functionally graded tube.

Although there are many studies on thermal analysis of functionally graded materials in literature, such as those presented above, there are few studies examining thermal stresses in functionally graded cylinder liners and Al-Si based functionally graded materials. It is found that mechanical and microstructural characteristics of the functionally graded cylinder liners are frequently investigated in those studies.

For all these reasons, it was considered that the functionally graded cylinder liner made of Al-Si alloy would bring many benefits in practice. The cylinder liner, which can be manufactured by a centrifugal casting method, will be functionally graded. Since the density of silicon is lower than the density of aluminum, the concentration of silicon by the effect of centrifugal force will be maximum on the inner surface, and it will be minimal on the outer surface of the cylinder liner by gradually decreasing through the radial direction. When compared to cast iron cylinder liner, the functionally graded cylinder liner made of Al-Si alloy will provide the following advantages.

- 1-Reduction of engine weight due to low density,
- 2-Eliminating the problems arising from the mismatch in the coefficients of thermal expansion of the cast iron liner and the aluminum cylinder block,

3-Since the outer surface of the liner will have the same amount of silicon as the cylinder block will, functionally graded liners will be more compatible with the engine block and the wear resistance will increase due to the high silicon content on the inner surface of the cylinder liner.

Thanks to all these advantages, functional graded and ungraded cylinder liners made of Al-Si alloy were analyzed by finite element method and they were evaluated in this study.

2. Material and Methods

Recently, Al-Si alloys have been widely used in cylinder block manufacturing to reduce engine weight. Thus, Al-Si alloy was chosen as the material in this study. A319 and A356 aluminum alloys are the most commonly used materials in engine block manufacturing [1]. A356 aluminum alloy contains 6.5-7.5% (7.45-8.58% volume fraction) silicon. Therefore, the functionally graded cylinder liner was designed as having an outer surface containing 8.5 vol.% silicon to be compatible with engine block and an inner surface with 32 vol.% silicon for better wear resistance. The functionally graded cylinder liner (Fig. 1) was divided into twenty layers, each has a thickness of 0.3 mm. In the ungraded cylinder liner, which was designed for the comparison, the silicon distribution is homogeneous and the volume fraction of silicon is 21%. Cylinder liners were designed with a wall-thickness of 6 mm, an inner diameter of 74 mm, an outer diameter of 86 mm and a length of 165 mm.

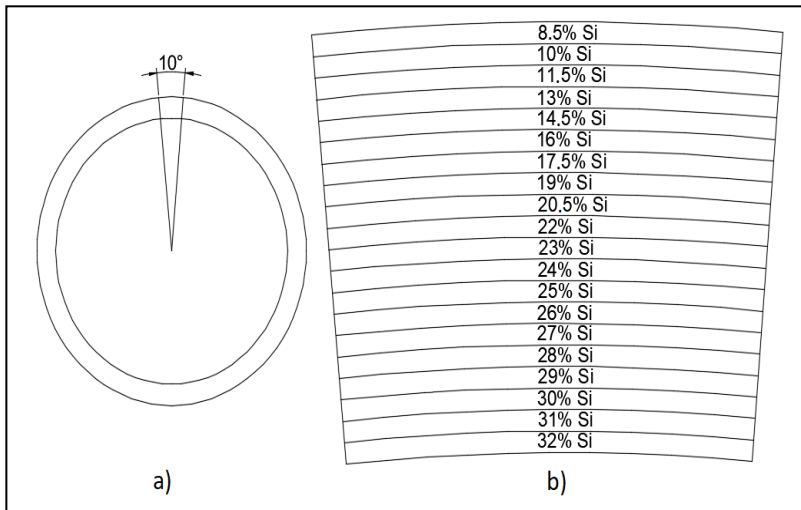


Figure 1. Functionally graded cylinder liner: (a) the entire liner; (b) 20 times magnified view of the 10 ° section, and the silicon content of the layers.

3. Determination Of Material Properties

In this study, the functionally graded cylinder liner has a twenty-layered structure. The silicon content of each layer (alloy) is distinct, so the material properties for each layer must be determined one by one.

3.1. Determination of mechanical properties

Mori-Tanaka method [11] was used to calculate the modulus of elasticity, shear modulus, bulk modulus and Poisson's ratio of the alloys.

The bulk modulus for each layer (alloy) was calculated by using an equation (1).

$$B_{\text{Com}} = B_{\text{Al}} + \frac{(B_{\text{Si}} - B_{\text{Al}}) \cdot v_{\text{Si}}}{1 + \frac{(1-v_{\text{Si}}) \cdot (B_{\text{Si}} - B_{\text{Al}})}{B_{\text{Al}} + \left(\frac{4}{3}\right) \cdot S_{\text{Al}}}} \quad (1)$$

Here, B_{Al} is the bulk modulus of aluminum, B_{Si} is the bulk modulus of silicon, S_{Al} is the shear modulus of aluminum and v_{Si} is the volume fraction of silicon in the alloy.

The shear modulus for each layer was calculated by using an equation (2).

$$S_{Com} = S_{Al} + \frac{(S_{Si} - S_{Al}) \cdot v_{Si}}{1 + \frac{(1-v_{Si})(S_{Si}-S_{Al})}{S_{Al}+f_1}} \quad (2)$$

$$f_1 = \frac{S_{Al} \cdot (9 \cdot B_{Al} + 8 \cdot S_{Al})}{6 \cdot (B_{Al} + 2 \cdot S_{Al})} \quad (3)$$

Here, S_{Si} is the shear modulus of silicon.

The density for each layer was calculated by using an equation (4).

$$d_{Com} = d_{Al} \cdot v_{Al} + d_{Si} \cdot v_{Si} \quad (4)$$

Here, d_{Al} is the density of aluminum, d_{Si} is the density of silicon, and v_{Al} is the volumetric fraction of aluminum in the alloy.

The Poisson's ratio for each layer was calculated by using an equation (5).

$$\nu_{Com} = \frac{1}{2 \cdot (1 + \frac{S_{Com}}{\lambda})} \quad (5)$$

$$\lambda = B_{Com} - \frac{2}{3} S_{Com} \quad (6)$$

The modulus of elasticity for each layer was calculated by using an equation (7).

$$E_{Com} = 3 \cdot (1 - 2 \cdot \nu_{Com}) \cdot B_{Com} \quad (7)$$

The modules of elasticity, Poisson's ratios and densities of aluminum and silicon at 25 °C are given in Table 1.

Table 1. Modulus of elasticity, Poisson's ratio and density of Al and Si elements at 25 °C [12,13].

	Elastic modulus (GPa)	Poisson's ratio	Density (kg/m ³)
Aluminum	70.2	0.345	2700
Silicon	162	0.22	2330

By using equations (8) and (9), bulk modulus and shear modulus of aluminum and silicon were calculated (Table 2)

$$B = \frac{E}{3(1 - 2\nu)} \quad (8)$$

$$S = \frac{E}{2(1 + \nu)} \quad (9)$$

Table 2. Bulk modulus and shear modulus of Al and Si elements at 25 °C.

	Bulk modulus (GPa)	Shear modulus (GPa)
Aluminum	75.48	26.1
Silicon	96.4	66.4

To calculate the mechanical properties at different temperatures, Davoudi's study [14] was used, and Table 3 was formed.

Table 3. Shear modulus and Poisson's ratio of aluminum at 100 °C and 200 °C.

Temperature	Shear modulus (GPa)	Poisson's ratio
100 °C	25.076	0.349
200 °C	23.71	0.355

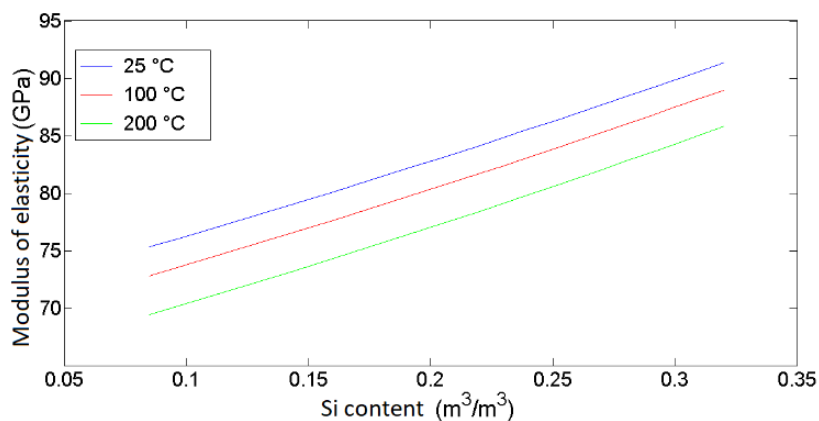
By using the equations (9) and (8), bulk modulus and modulus of elasticity of aluminum at 100 °C and 200 °C were calculated and presented in Table 4.

Table 4. Bulk modulus and modulus of elasticity of aluminum at 100 °C and 200 °C.

Temperature	Bulk modulus (GPa)	Modulus of elasticity (GPa)
100 °C	74.73	67.66
200 °C	74.1	64.274

Since the mechanical properties of silicon had little changes between 20 °C and 200 °C [15], the differences in mechanical properties of silicon were not included in the calculations.

For each Al-Si alloy (layer), the density at 25 °C was calculated by the equation (4), and mechanical properties at 25 °C, 100 °C and 200 °C were calculated using the equations (1), (2), (5) and (7). In addition, the elastic modules and the shear modules of the Al-Si alloys with various silicon content at 25 °C, 100 °C and 200 °C are given in Fig. 2 and Fig. 3.

**Figure 2.** The elastic modules of Al-Si alloys with various silicon content at 25 °C, 100 °C and 200 °C.

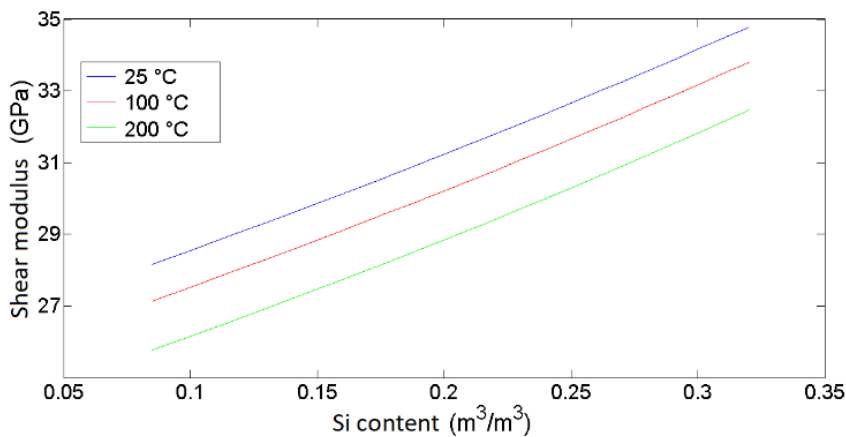


Figure 3. The shear modules of Al-Si alloys with various silicon content at 25 °C, 100 °C and 200 °C.

3.2. Determination of thermal properties

In the study by Huang et al., it was observed that the thermal expansion coefficients of Al-Si alloys obtained with an experimental method were very close to those calculated by using the Turner model [16]. Therefore, the Turner model [17] was used in this study to calculate the coefficients of thermal expansion of the Al-Si alloys, and the equation is shown below.

$$CTE_{Com} = (CTE_{Al}v_{Al}B_{Al} + CTE_{Si}v_{Si}B_{Si})/(v_{Al}B_{Al} + v_{Si}B_{Si}) \quad (10)$$

Here, CTE_{Al} , CTE_{Si} and CTE_{Com} are respectively the thermal expansion coefficient of aluminum, silicon and the Al-Si alloy.

The thermal expansion coefficients of aluminum and silicon at 20 °C, 100 °C and 200 °C are given in Table 5.

Table 5. Linear thermal expansion coefficients of aluminum and silicon at 20 °C, 100 °C and 200 °C [18-20].

	Linear thermal expansion coefficient ($\mu\text{m}/\text{m} \cdot ^\circ\text{C}$)		
	20 °C	100 °C	200 °C
Aluminum	23	24.2	25.7
Silicon	2.5	3	3.4

The coefficients of thermal expansion at 20 °C, 100 °C and 200 °C were calculated for each Al-Si alloy (layer) by using the equation (10) and it is given in Fig. 4.

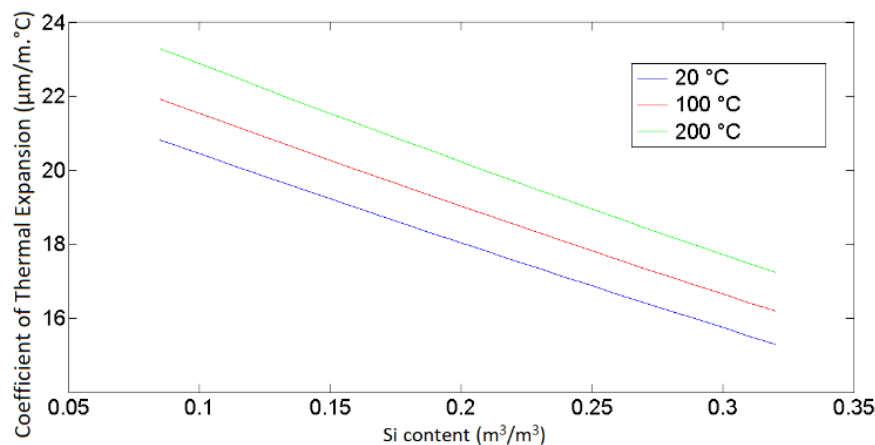


Figure 4. The thermal expansion coefficient of Al-Si alloy at 20 °C, 100 °C and 200 °C versus Si content.

The thermal conductivity coefficients of the Al-Si alloys at 25 °C with Si content of 8.5 vol.%, 15 vol.%, 20.5 vol.%, 30 vol.% and 45.5 vol.% were determined from the study of Sadatomi et al. [21], and are given in Table 6. The thermal conductivity coefficient was assumed to vary linearly between these values.

Table 6. Thermal conductivity coefficients of the Al-Si alloys.

Si content (m ³ /m ³)	Coefficient of Thermal Conductivity (W/m. °C)
0.085	202.94
0.15	180
0.205	166.9
0.3	161.18
0.455	154.4

Every et al.'s study [22] was examined, and the thermal conductivity coefficients of the Al-Si alloys at different temperatures were calculated by using equations (11) and (12). The equation (11) was used for the Al-Si alloys having low silicon content (8.5 vol.%, 15 vol.% and 20.5 vol.%) and the equation (12) was used for the Al-Si alloys with high silicon content (30 vol.% and 45.5 vol.%).

$$\frac{K_{\text{Com}}}{K_{\text{Al}}} = \frac{[K_{\text{Si}}(1 + 2\alpha) + 2K_{\text{Al}}] + 2v_{\text{Si}}[K_{\text{Si}}(1 - \alpha) - K_{\text{Al}}]}{[K_{\text{Si}}(1 + 2\alpha) + 2K_{\text{Al}}] - v_{\text{Si}}[K_{\text{Si}}(1 - \alpha) - K_{\text{Al}}]} \quad (11)$$

$$(1 - v_{\text{Si}})^3 = \left\{ \frac{K_{\text{Al}}}{K_{\text{Com}}} \right\}^{(1+2\alpha)/(1-\alpha)} \times \left\{ \frac{K_{\text{Com}} - K_{\text{Si}}(1 - \alpha)}{K_{\text{Al}} - K_{\text{Si}}(1 - \alpha)} \right\}^{3/(1-\alpha)} \quad (12)$$

Here, K_{Al} , K_{Si} and K_{Com} are respectively the thermal conductivity coefficient of aluminum; silicon and Al-Si alloy.

Thermal conductivity coefficients of aluminum at 25 °C and silicon at 25 °C, 127 °C and 227 °C are given in Table 7.

Table 7. Thermal conductivity coefficients of aluminum and silicon [23-25].

	Coefficient of Thermal Conductivity (W/m. °C)		
	25 °C	127 °C	227 °C
Aluminum	235.2	232.3	229
Silicon	149	105	80

Since the thermal conductivity coefficient of aluminum slightly changes between 20 °C and 200 °C [23], the differences in the coefficients of thermal conductivity of aluminum were not taken into consideration in calculations.

The α values calculated by using the equations (11) and (12) which are given in Table 8.

Table 8. Calculated α values for different Si contents.

Si content (m ³ /m ³)	0.085	0.15	0.205	0.3	0.455
α	-13.8613	-13.4757	-35	3.2995	1.0197

By substituting K_{Si} values at 127 °C and 227 °C and α values into equations (11) and (12), thermal conductivity coefficients at 127 °C and 227 °C were calculated for the Al-Si alloys having various silicon content (8.5 vol.%, 15 vol.%, 20.5 vol.%, 30 vol.% and 45.5 vol.%). It is assumed that the thermal conductivity coefficient has linear changes between these values. The calculated values for each alloy are shown in Table 9.

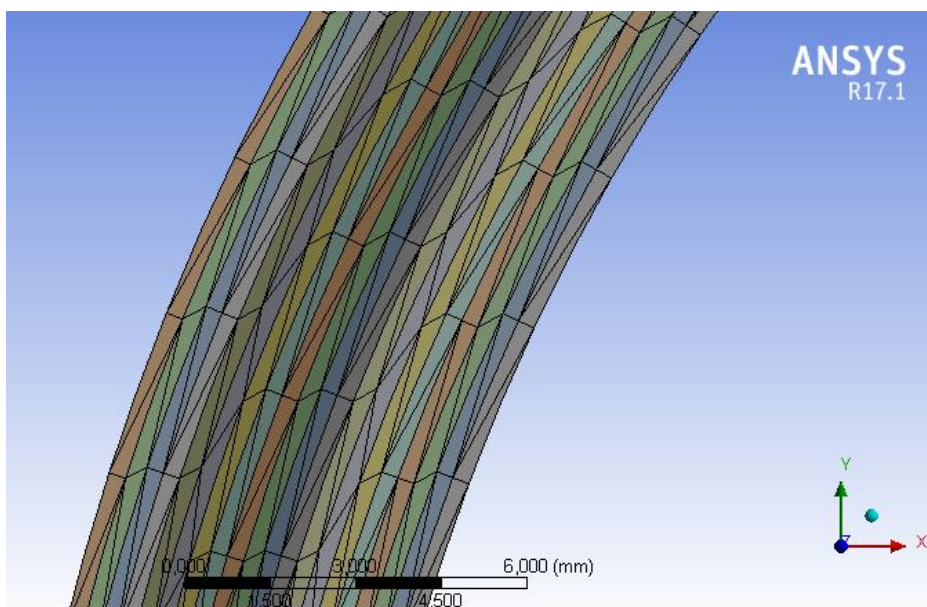
Table 9. Thermal conductivity coefficients of each Al-Si alloy at 25 °C, 127 °C and 227 °C.

Silicon content of Al-Si alloys (m ³ /m ³)	Thermal conductivity coefficient (W/m. °C)		
	25 °C	127 °C	227 °C
0.085	202.940	202.730	202.480
0.1	197.646	197.399	197.108
0.115	192.352	192.068	191.735
0.13	187.058	186.738	186.363
0.145	181.765	181.407	180.991
0.16	177.618	177.305	176.942
0.175	174.045	173.816	173.555
0.19	170.473	170.328	170.167
0.205	166.900	166.840	166.780
0.21	166.599	166.417	166.254
0.22	165.997	165.571	165.201
0.23	165.395	164.724	164.148
0.24	164.793	163.878	163.096
0.25	164.191	163.032	162.043
0.26	163.588	162.185	160.991
0.27	162.986	161.339	159.938
0.28	162.384	160.493	158.885
0.29	161.782	159.646	157.833
0.3	161.180	158.800	156.780
0.31	160.743	157.839	155.465
0.32	160.305	156.879	154.150

4. Thermal Stress Analysis

ANSYS 17.1 Workbench software was used to determine the thermal stresses in the cylinder liners. First, steady state thermal analysis was performed to obtain three-dimensional temperature distribution of the liners.

A twenty-layered geometry consisting of the layers with a thickness of 0.3 mm and a length of 165 mm was formed by using the ANSYS Workbench for the functionally graded cylinder liner. A bonded connection was created between the layers. Then all material properties determined by using mathematical models and experimental data were entered into the program, and material assignment was realized for each layer. After that, a volumetric prismatic finite *element* mesh consisting of 193480 elements, was *generated*. Quadrilateral (3x3 mm) and triangular (0.3x3 mm) elements were used for cylindrical and flat surfaces, respectively. The generated finite element mesh is shown in Fig. 5 and Fig. 6.

**Figure 5.** The finite element mesh on the flat surfaces of the functionally graded cylinder liner.

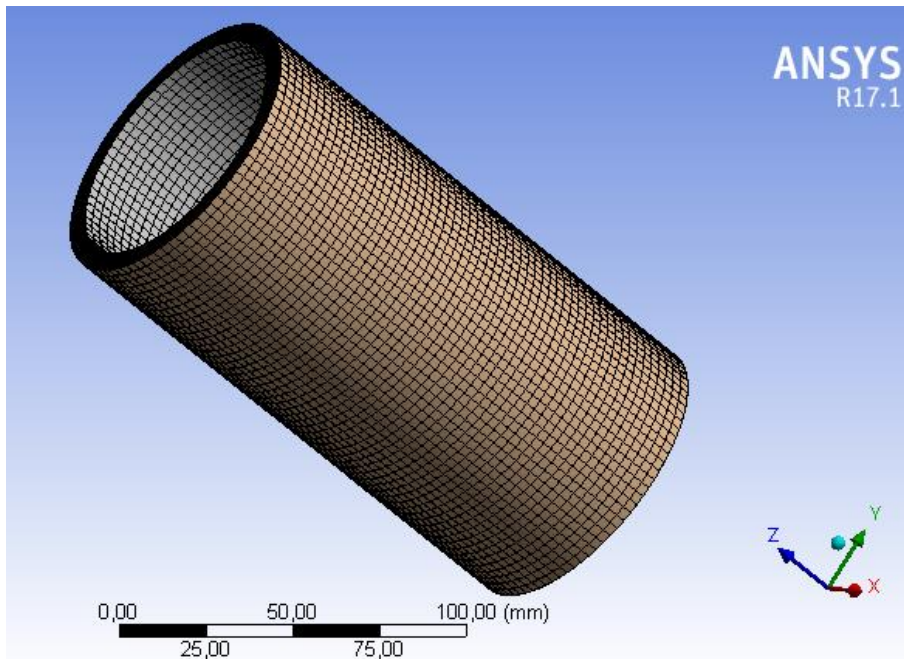


Figure 6. The finite element mesh of the functionally graded cylinder liner.

Wang et al. [26] studied three-dimensional temperature distribution in cylinders of a water-cooled gasoline engine by numerical methods. The average values obtained from this study were entered into the program as the final temperature values of the functionally graded cylinder liner. 180 °C, 120 °C, 110 °C and 85 °C, which were taken from the study of Wang et al., are the temperature values at the upper and lower edges of the inner surface and at the upper and lower edges of the outer surface of the cylinder liner, respectively. A model with an inner diameter of 74 mm, a thickness of 0.3 mm and a length of 165 mm was designed to find the temperature distribution on the inner surface of the liner. Al-Si alloy containing 32% Si was assigned as material for this model, and 180 °C and 120 °C temperature values were respectively entered into the program for the upper and lower surfaces of the model (Fig. 7(a)). The resulting temperature distribution is shown in Fig. 8(a).

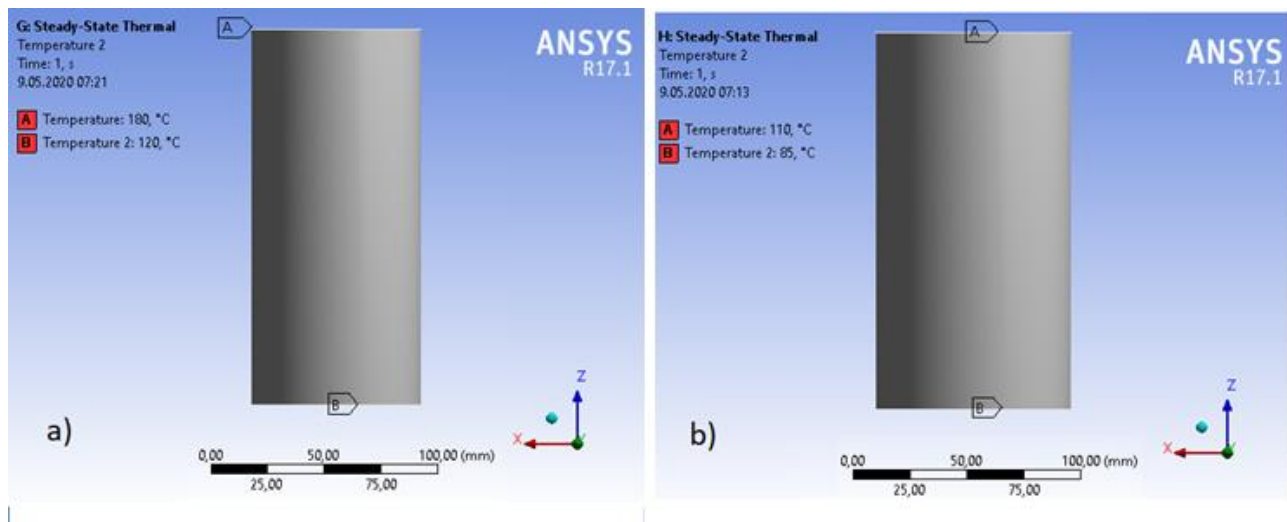


Figure 7. The boundary conditions for the steady-state thermal analysis of the functionally graded cylinder liner: (a) inner surface, (b) outer surface.

A model with an outer diameter of 86 mm, a thickness of 0.3 mm and a length of 165 mm was designed to find the temperature distribution on the outer surface of the functionally graded cylinder liner. Al-Si alloy with an 8.5 vol.% silicon content was assigned as material for this model, and 110 °C and 85 °C temperature values were respectively entered into the program for the upper and lower surfaces of the model (Fig. 7(b)). The temperature distribution on the outer surface of the cylinder liner is given in Fig. 8(b). The temperatures of inner and outer surfaces were taken into the functional graded model and three-dimensional temperature distribution was obtained (Fig. 8(c)).

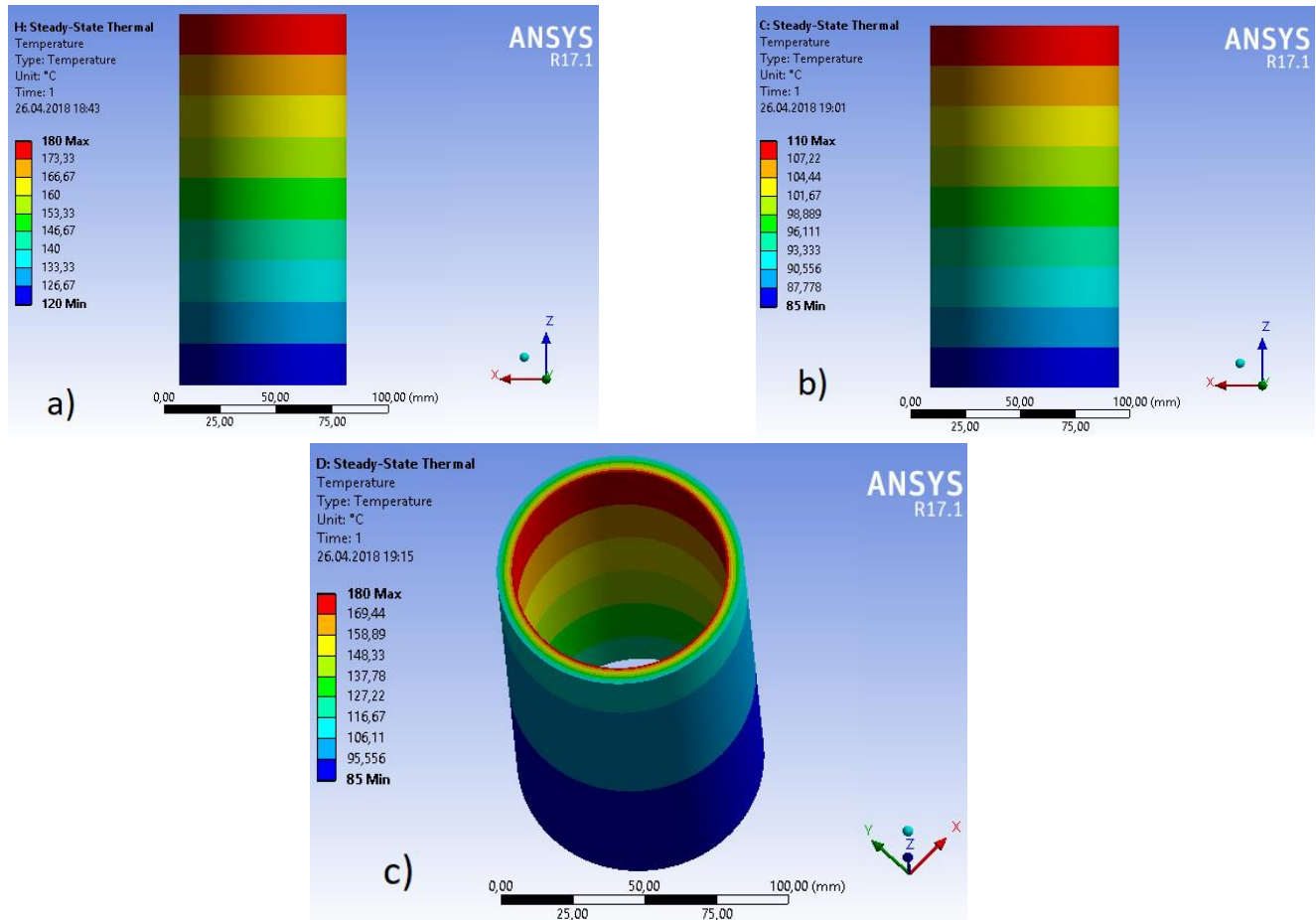


Figure 8. Temperature distribution of the functionally graded cylinder liner: (a) inner surface, (b) outer surface and (c) three-dimensional temperature distribution of the liner.

The temperature change through the thickness of the functionally graded cylinder liner is given in Fig. 9 and Fig. 10.

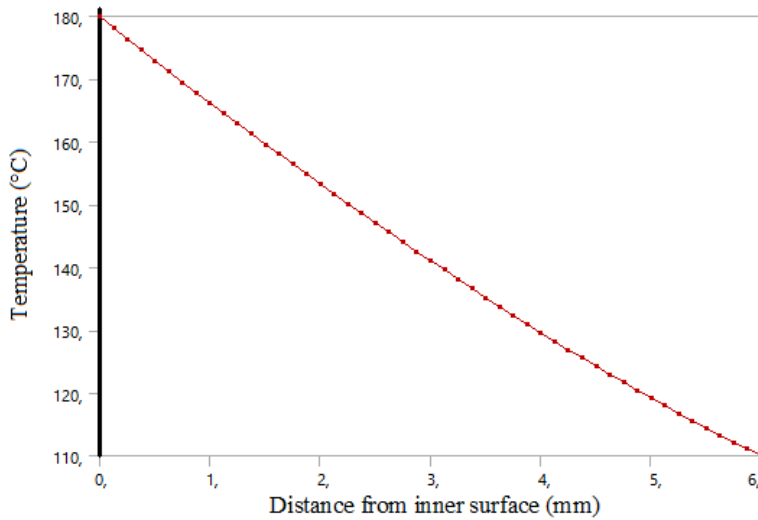


Figure 9. Temperature change through the thickness for the upper surface of the cylinder liner.

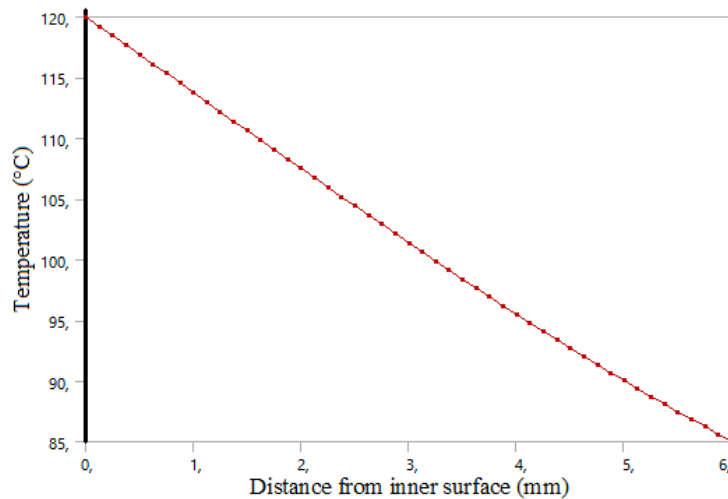


Figure 10. Temperature change through the thickness for the lower surface of the cylinder liner.

For the static structural analysis of the functionally graded cylinder liner, the same geometric model (twenty-layer) was used, and the same finite element mesh used in the thermal analysis was generated, only the element size was changed as 3.5 mm. The three-dimensional temperature distribution, which was obtained from the thermal analysis, was taken into the static analysis and it was applied as a thermal load. In statistical analysis, the ambient temperature entered into the program was 22 °C, and no constraints were applied. During the analysis, some weak springs were automatically applied by the program to restrain the rigid body motion.

The ungraded (homogeneous) cylinder liner with an inner diameter of 74 mm, an outer diameter of 86 mm and a length of 165 mm was designed for the comparison to the functionally graded cylinder liner.

In the thermal analysis, finite element mesh was generated with an average element size of 3mm by 3mm for the ungraded cylinder liner. Al-Si alloy containing 21% Si was assigned as material. The same of the boundary conditions applied to the functionally graded cylinder liner were applied and the three-dimensional temperature distribution of the ungraded cylinder liner (Fig. 11) was found.

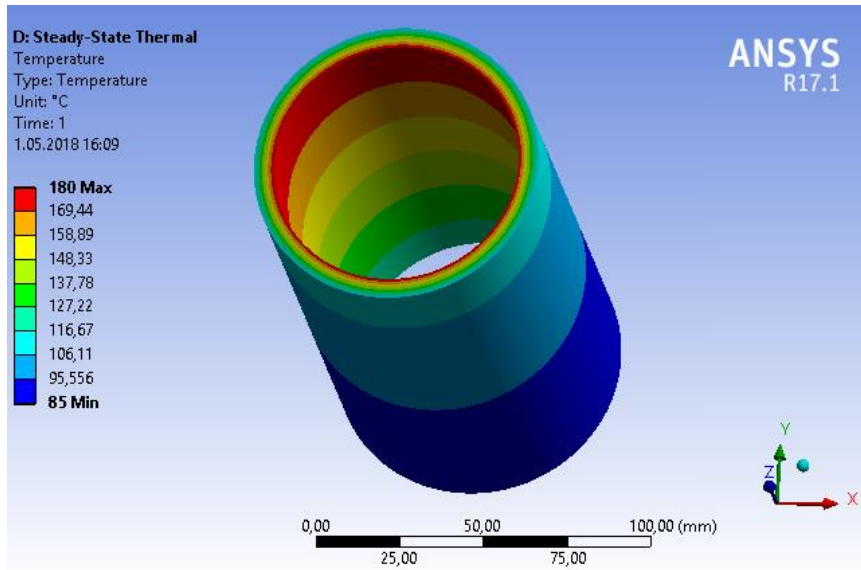


Figure 11. Three-dimensional temperature distribution of the ungraded (homogeneous) cylinder liner.

By respectively using quadrilateral (3.5x3.5 mm) and triangular (0.3x3.5 mm) elements for the cylindrical and flat surfaces, a volumetric prismatic finite element mesh was generated in the statistical structural analysis of the ungraded cylinder liner. The three-dimensional temperature distribution of the ungraded cylinder liner was taken into the static structural analysis and applied as a thermal load. The same boundary conditions in the statistical structural analysis of the functionally graded cylinder liner were applied to the ungraded cylinder liner as well. Von Mises stresses in the functional graded and ungraded cylinder liners obtained from statistical analyzes are given in Fig. 12.

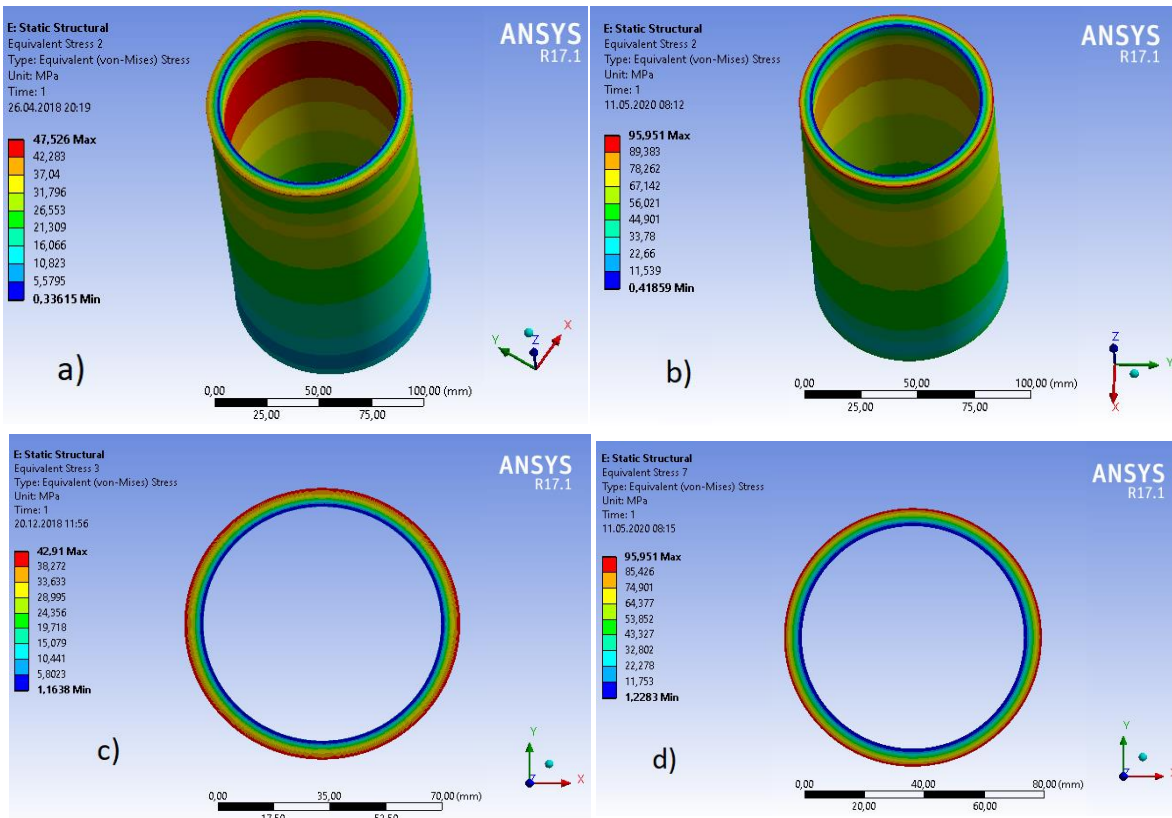


Figure 12. Von Mises stresses in the cylinder liners: (a) functionally graded cylinder liner, (b) ungraded cylinder liner, (c) the upper surface of the functionally graded cylinder liner, (d) the upper surface of the ungraded cylinder liner.

In addition, the statistical structural analysis of the functionally graded cylinder liner was performed by using elements with different sizes in order to see the effect of the element size on the results of the analysis. The maximum Von Mises stresses obtained from these analyses are presented in Table 10.

Table 10. Maximum Von Mises stresses in the functionally graded cylinder liner analyzed by using elements with different sizes.

Element Type	Element Size (mm)	Number of Finite Elements	Maximum Von Mises Stress (MPa)
<i>Triangular Prism</i>	3.5	147024	47.526
	5	76160	47.849
	6	53760	48.199

Table 10 shows that maximum Von Mises stress changed little when element sizes were increased. For instance, when the element size was increased from 3.5 mm to 5 mm, the maximum Von Mises stress increased by 0.68%.

In the literature, no similar study could be found to compare to our study since the results of the analysis vary greatly depending on cylinder liner dimensions, thermal load application, cylinder liner material and boundary conditions.

There are many studies in the literature presenting that thermal stresses are reduced in functionally graded materials. For example, in the study of Tahani [27], it is observed that temperature and thermal stress distributions are improved in the functionally graded shells compared to the classical layered composites.

In addition, Bako et al. [28] studied the simulation of a cast iron cylinder liner. In this study, the interior and the exterior temperatures of the cylinder liner were applied to be 2227 °C and 400 °C respectively, and the maximum compression pressure was applied to be 20 bar. They presented that the maximum Von Mises stress (21.08 MPa) occurred at the inner surface of the cylinder liner, and the minimum Von Mises stress (1.21 MPa) was observed at the outer surface of the cylinder liner. Abdalla et al. [29] investigated the thermo-mechanical stress behaviors in functionally graded (FG) rotating hollow disks with variable thickness. They designed a material as functionally graded in the radial direction. They assumed that materials properties vary along the radius according to a highly accepted power-law model. They designed four different structures: totally metal (TM), totally ceramic (TC), CM (inside is ceramic, outside is metal), and MC (inside is metal, outside is ceramic). The FG structures (MC and CM) were assumed to be a composition of steel and alumina. They assigned the inner and outer surface temperatures to be 300 °C and 100 °C, respectively. They stated that maximum and minimum Von Mises stresses were occurred in the MC and CM structures, respectively. The fact that the functionally graded material with CM structure exhibits the minimum Von Mises stress supports the results of our study.

5. Conclusion

The functionally graded cylinder liner, which can be manufactured by the centrifugal casting of Al-Si alloy containing 21 vol.% silicon, was designed with a silicon content of 32 vol.% on the internal surface and 8.5 vol.% Si on the outer surface. As for the ungraded cylinder liner, it is homogeneous and it contains 21% Si. The Cylinder liners were analyzed by using a finite element method, and the following results were obtained.

Considering the results obtained from the mathematical models and the previous researches in the literature, it was observed that the increase of silicon content in Al-Si alloys increased the modulus of elasticity of the alloy and decreased the thermal expansion and thermal conductivity coefficients. The temperature rises in the Al-Si alloys increased the coefficient of thermal expansion of the alloy but reduced the modulus of elasticity and thermal conductivity coefficient.

As a result of the applied thermal load, thermal stresses were observed in the functional graded and ungraded cylinder liners. The cause of the thermal stresses in the ungraded cylinder liner is the non-uniform temperature distribution. It is seen that not only the non-uniform temperature distribution is a reason for the thermal stresses in the functionally graded cylinder liner, but also it is the silicon content changing.

The maximum Von Mises stresses in the functionally graded and ungraded cylinder liners were determined to be 47.526 MPa and 95.951 MPa, respectively. The maximum Von Mises stress was reduced by approximately 50% due to the functionally grading. The temperature (between 180 °C and 120 °C) of the inner surface of the functionally graded cylinder liner is higher than the temperature (between 110 °C and 85 °C) of the outer surface. The increase of the Si content decreased the thermal expansion coefficient of the alloy. Since the thermal expansion is directly proportional to the product of the temperature difference and the coefficient of thermal expansion, the differences of thermal expansion between regions in the functionally graded cylinder liner are less than that in the ungraded cylinder liner. Therefore, the thermal stresses in the functionally graded cylinder liner are lower.

As a result of the analyses, it was found that the thermal stresses were lower in the functionally graded cylinder liner. Therefore, it is anticipated that the lifetime of the functionally graded cylinder liners will be longer than that of the ungraded liners.

Conflicts of interest

There is no conflict of interest.

References

- [1] Ram S.C., Chattopadhyay K. and Chakrabarty I., High temperature tensile properties of centrifugally cast in-situ Al-Mg₂Si functionally graded composites for automotive cylinder block liners, *Journal of Alloys and Compounds*, 724 (2017) 84-97.
- [2] Santos H.O., Costa I. and Rossi J. L., Mechanical and Microstructural Characterisation of Cylinder Liners, *Materials Science Forum*, 416 (2003) 407-412.
- [3] Javidani M. and Larouche D., Application of Cast Al-Si Alloys in Internal Combustion Engine Components, *International Materials Reviews*, 59(3) (2014) 132-158.
- [4] Jayakumar E., Jacob J.C., Rajan T.P.D., Joseph M.A. and Pai B.C., Processing and Characterization of Functionally Graded Aluminum (A319)-SiC_p Metallic Composites by Centrifugal Casting Technique, *Metallurgical and Materials Transactions A*, 47(8) (2016) 4306-4315.
- [5] Liew K.M., Kitipornchai S., Zhang X.Z. and Lim C.W., Analysis of the thermal stress behaviour of functionally graded hollow circular cylinders, *International Journal of Solids and Structures*, 40(10) (2003) 2355–2380.
- [6] Jabbari M., Sohrabpour S. and Eslami M.R., Mechanical and thermal stresses in a functionally graded hollow cylinder due to radially symmetric loads, *International Journal of Pressure Vessels and Piping*, 79(7) (2002) 493–497.
- [7] Obata Y. and Noda N., Steady thermal stresses in a hollow circular cylinder and a hollow sphere of a functionally gradient material, *Journal of Thermal Stresses*, 17(3) (1994) 471-487.
- [8] Demirbaş M.D., Ekici R. and Apalak M.K., Thermoelastic analysis of temperature-dependent functionally graded rectangular plates using finite element and finite difference methods, *Mechanics of Advanced Materials and Structures*, 27(9) (2020) 707-724.
- [9] Zhang K., Yu H., Liu J., Li Y., Liu J. and Zhang J., Microstructure and property of a functionally graded aluminum silicon alloy fabricated by semi-solid backward extrusion process, *Materials Science & Engineering A*, 624 (2015) 229-238.
- [10] Lin X., Liu C. and Xiao H., Fabrication of Al–Si–Mg functionally graded materials tube reinforced with in situ Si/Mg₂Si particles by centrifugal casting, *Composites: Part B*, 45(1) (2013) 8-21.
- [11] Saunders W. L., Pendley K. and Gutierrez-Miravete E., Modal analysis of functionally graded metal-ceramic composite plates, Proceedings of the 2014 COMSOL Conference, 8-10 October, Boston, (2014).
- [12] Cardarelli F., Background Data for the Chemical Elements. In: Materials Handbook: A Concise Desktop Reference. 2nd ed. London: Springer, 2008; pp 1181-1194.

- [13] Lasagni F. and Degischer H.P., Enhanced Young's Modulus of Al-Si Alloys and Reinforced Matrices by Co-continuous Structures, *Journal of Composite Materials*, 44(6) (2010) 739-755.
- [14] Davoudi K., Temperature dependence of the yield strength of aluminum thin films: Multiscale modeling approach, *Scripta Materialia*, 131 (2017) 63-66.
- [15] Kahn H., Huff M.A. and Heuer A.H., Heating Effects on the Young's Modulus of Films Sputtered onto Micromachined Resonators, Proceedings, Microelectromechanical Structures for Materials Research, Materials Research Society Symposium 518, 15-16 April, San Francisco, (1998) 33-38.
- [16] Ma P., Jia Y., Prashanth K.G., Yu Z., Li C., Zhao J., Yang S. and Huang L., Effect of Si content on the microstructure and properties of Al-Si alloys fabricated using hot extrusion, *Journal of Materials Research*, 32(11) (2017) 2210-2217.
- [17] Ibrahim I.A., Mohamed F.A. and Lavernia E.J., Particulate reinforced metal matrix composites - a review, *Journal of Materials Science*, 26(5) (1991) 1137-1156.
- [18] Frank W.B., Koch G.P. and Mills J.J., Properties of Pure Aluminum. In: Hatch J.E., (Eds). Aluminum Properties and Physical Metallurgy. Ohio: American Society for Metals, 1984; pp 1-24.
- [19] Jia Y.D., Ma P., Prashanth K.G., Wang G., Yi J., Scudino S., Cao F.Y., Sun J.F. and Eckert J., Microstructure and thermal expansion behavior of Al-50Si synthesized by selective laser melting, *Journal of Alloys and Compounds*, 699 (2017) 548-553.
- [20] Kempe V., First-level Packaging. In: Inertial MEMS: Principles and Practice. New York: Cambridge University Press, 2011; pp 205-225.
- [21] Sadatomi N., Hamamoto N., Saigo T. and Yamashita O., Thermal Characterization of Al-Si Materials Prepared by Die Casting Method, *Journal of the Japan Society of Powder and Powder Metallurgy*, 49(9) (2002) 793-798.
- [22] Every A.G., Tzou Y., Hasselman D.P.H. and Raj R., The effect of particle size on the thermal conductivity of ZnS/diamond composites, *Acta Metallurgica et Materialia*, 40(1) (1992) 123-129.
- [23] Jia Y., Cao F., Ma P., Scudino S., Eckert J., Sun J. and Wang G., Microstructure and thermal conductivity of hypereutectic Al-high Si produced by casting and spray deposition, *Journal of Materials Research*, 31(19) (2016) 2948-2955.
- [24] Xiu Z., Chen G., Yang W., Song M. and Wu G., Microstructure and thermal properties of recyclable Si_p/1199Al composites, *Transactions of Nonferrous Metals Society of China*, 19(6) (2009) 1440-1443.
- [25] Masolin A., Bouchard P., Martini R. and Bernacki M., Thermo-mechanical and fracture properties in single-crystal silicon, *Journal of Materials Science*, 48(3) (2013) 979-988.
- [26] Wang G., Chen H., Yuan Z. and Lu W., Numerical Study on Three-Dimensional Steady-State Temperature Field of a Gasoline Engine, *Advanced Materials Research*, 569 (2012) 610-614.
- [27] Tahani M., Analysis of functionally graded cylindrical shells subjected to mechanical and thermal loadings, Proceedings, 12th European conference on composite materials, 29th August-1st September, Biarritz, (2006).
- [28] Bako S., Usman T., Bori I. and Nasir A., Simulation of a Wet Cylinder Liner, *SSRG International Journal of Mechanical Engineering*, 6(4) (2019) 12-17.
- [29] Abdalla H.M.A., Casagrande D. and Moro L., Thermo-mechanical analysis and optimization of functionally graded rotating disks, *The Journal of Strain Analysis for Engineering Design*, (2020).

An efficient method for the plane vibration analysis of composite sandwich beam with an orthotropic core

Sefa YILDIRIM 

Alanya Alaaddin Keykubat University, Mechanical Engineering Department, 07425, Alanya, Turkey

Abstract

The free vibration characteristics of composite sandwich beam is examined using an efficient numerical solution scheme. The simply supported beam is assumed to be composed of two isotropic face sheets and an orthotropic core. The plane elasticity formulations are used to derive the equations of motion and the reduced governing differential equation is solved by Complementary Functions Method. The dimensionless analysis of natural frequencies is done to acquire the high precision along with few divisions. The influences of material and geometric parameters on the natural frequency are also illustrated. The solutions are validated with the results obtained from finite element software and it is shown that presented method is an efficient solution technique for the vibration problems of composite beams with a core.

Article info

History:

Received:17.12.2019

Accepted:10.04.2020

Keywords:

Vibration,
Composites Beams,
Orthotropy,
Plane Elasticity,
Complementary
Functions Method.

1. Introduction

Sandwich composites have been extensively using as a structural member in engineering areas such as automotive, aerospace, computer, biomedical and so on. Sandwich composites have been found in structural systems like beams, plates, annular members. Accordingly, understanding the dynamic behavior of such systems becomes necessary to improve their performance and the mathematical analysis and developing effective numerical methods are important to achieve this aim.

The papers related with the free vibration analysis of cored composited beams are introduced. Arikoglu and Ozkol[1] have studied the vibration behavior of sandwich beam using Differential Transform Method. The experimental and numerical natural frequency analysis of sandwich beam have been conducted by Baba[2]. In his work, the beam made of fiber-glass laminate skins wrapped over polyurethane foam core is subjected to clamped-clamped boundary conditions. The vibration characteristics of layered beam are examined by Lou et. al.[3] where the core material is pyramidal lattice truss. The viscoelastic-core composite beam is investigated by Sadeghnejad et. al.[4] using extended high-order sandwich panel theory. They have considered the effects of transverse shear and core compressibility. The beam with lattice truss core has been studied by Xu and Qui[5] using the

interval optimization method. In their study, the combining theory of Euler–Bernoulli beam and Timoshenko beam is used. Wang and Wang[6] have investigated the free vibration behavior of soft-core layered beams using the extended high-order sandwich panel theory and weak form quadrature element method. Cheng et. al.[7] have examined the vibration analysis of fiber-reinforced polymer honeycomb sandwich beam using refined sandwich beam theory. The shear-deformable Timoshenko porous beam is studied by Chen et. al.[8] where Ritz method in combination with a direct iterative algorithm is employed. The zig-zag beam theory is applied by Khdeir and Aldraihem[9] to the free vibration of soft-core laminated beams. Zhang et. al.[10] have studied the vibration of honeycomb-corrugation hybrid core beam using finite element method. Demir et. al.[11] have investigated natural frequency of curved beam with laminated face sheets and a viscoelastic core using general differential quadrature method. Chanthanumataporn and Watanabe[12] have presented a finite element solution on the free vibration of a layered beam coupling with ambient air where the shear deformation of the sandwich core is considered. The free and forced vibration behavior of sandwich beam having carbon/epoxy face sheets and a magnetorheological elastomer honeycomb core are examined numerically and experimentally by Eloy et. al.[13] where the magnetic field is assumed to be applied on the free end and on the center of the beam.

*Corresponding author. Email address: sefa.yildirim@alanya.edu.tr

Rahmani et. al.[14] have investigated the vibration characteristics of a flexible functionally-graded core beam where the classical beam theory for the face sheets and elasticity theory for core are employed. The natural frequency study has been conducted by Asgari et. al.[15] on the free vibration of simply supported soft-core beam resting on a nonlinear foundation. Xu et. al.[16] have presented a continuous homogeneous theory to derive the governing equations of free vibration problems of sandwich beam with graded corrugated lattice core.

The problem addressed in the present study is to analyze the free vibration of three-layered sandwich beam having an orthotropic core. The plane elasticity formulations are employed and the coupled second-order governing differential equations are reduced to a fourth-order differential equation. The face sheets and core material are assumed to be interconnected through the equilibrium and compatibility. The layers are considered to be in a perfect bond with each other. CFM has been proven to be an accurate and efficient numerical method [17-19] for the present type problem is infused into the analysis.

2. Theoretical Analysis

Consider a rectangular cross-section sandwich beam of length L and depth h . The beam is assumed to be under the conditions of plane stress in the x - z plane hence it has a unit width. The governing equation of motion including faces and core is given as follows:

$$\begin{aligned} \frac{\partial \sigma_{xxi}}{\partial x} + \frac{\partial \tau_{xzi}}{\partial z} &= \rho_i \frac{\partial^2 u_i}{\partial t^2} \\ \frac{\partial \tau_{xzi}}{\partial x} + \frac{\partial \sigma_{zxi}}{\partial z} &= \rho_i \frac{\partial^2 w_i}{\partial t^2} \quad i = b, c, t \end{aligned} \quad (1)$$

where σ and τ are normal and shear stresses, ρ is material density, $u(x, z, t)$ and $w(x, z, t)$ are the axial and transverse displacements, respectively. Here subscripts b , c and t are, respectively, denote bottom face, core and top face.

The constitutive equations are written as follows:

$$\begin{Bmatrix} \sigma_{xxi} \\ \sigma_{zxi} \\ \tau_{xzi} \end{Bmatrix} = \begin{bmatrix} C_{11}^i & C_{13}^i & 0 \\ C_{13}^i & C_{33}^i & 0 \\ 0 & 0 & C_{55}^i \end{bmatrix} \begin{Bmatrix} \varepsilon_{xxi} \\ \varepsilon_{zxi} \\ \gamma_{xzi} \end{Bmatrix} \quad (2)$$

The strain components in the terms of horizontal and vertical displacements:

$$\varepsilon_{xxi} = \frac{\partial u_i}{\partial x}, \quad \varepsilon_{zxi} = \frac{\partial w_i}{\partial z}, \quad \gamma_{xzi} = \frac{\partial u_i}{\partial z} + \frac{\partial w_i}{\partial x} \quad (3)$$

Substituting Eqs. (2, 3) and into Eq. (1) give the following two equations in the axial and transverse displacements:

$$\begin{aligned} \frac{\partial}{\partial x} \left(C_{11}^i \frac{\partial u_i}{\partial x} + C_{13}^i \frac{\partial w_i}{\partial z} \right) + \frac{\partial}{\partial z} \left(C_{55}^i \frac{\partial u_i}{\partial z} + C_{55}^i \frac{\partial w_i}{\partial x} \right) &= \rho_i \frac{\partial^2 u_i}{\partial t^2} \\ \frac{\partial}{\partial x} \left(C_{55}^i \frac{\partial u_i}{\partial z} + C_{55}^i \frac{\partial w_i}{\partial x} \right) + \frac{\partial}{\partial z} \left(C_{11}^i \frac{\partial u_i}{\partial x} + C_{13}^i \frac{\partial w_i}{\partial z} \right) &= \rho_i \frac{\partial^2 w_i}{\partial t^2} \end{aligned} \quad (4)$$

The typical boundary conditions for the simply supported beam are:

$$\begin{aligned} w_i(0, z, t) &= w_i(L, z, t) = 0 \\ \sigma_{xzi}(0, z, t) &= \sigma_{xzi}(L, z, t) = 0 \end{aligned} \quad (5)$$

The displacements satisfying the boundary conditions above are assumed as follows:

$$\begin{aligned} u_i(x, z, t) &= U_i(z) \cos[\xi x] \sin[\omega x] \\ w_i(x, z, t) &= W_i(z) \sin[\xi x] \sin[\omega x] \end{aligned} \quad (6)$$

where $\xi = m\pi/L$ and ω is the natural frequency. Substituting Eq. (6) into Eq. (4) leads to a pair of coupled differential equations for $U(z)$ and $W(z)$:

$$A_1^i U_i'' + A_3^i U_i + A_4^i W_i' = 0 \quad (7)$$

$$B_1^i U_i' + B_3^i W_i'' + B_5^i W_i = 0 \quad (8)$$

where ()' denotes the derivative with respect to transverse coordinate z and

$$\begin{aligned} A_1^i &= C_{55}^i, \quad A_3^i = [\rho_i \omega^2 - C_{11}^i \xi^2], \quad A_4^i = [C_{13}^i \xi + C_{55}^i \xi] \\ B_1^i &= [-C_{13}^i \xi - C_{55}^i \xi], \quad B_3^i = C_{33}^i, \quad B_5^i = [\rho_i \omega^2 - C_{55}^i \xi^2] \end{aligned}$$

These coupled second order equations must be reduced to a simple fourth-order differential equation. In order to obtain an uncoupled governing equation, Eq. is differentiated with respect to z and rearranged as:

$$U_i''' + C_2^i U_i' + C_3^i W_i'' = 0 \quad (9)$$

where $C_2^i = \frac{A_3^i}{A_1^i}$ and $C_3^i = \frac{A_4^i}{A_1^i}$.

The differentiation Eq. (9) gives a fourth order equation as follows:

$$U_i^{iv} + C_2^i U_i'' + C_3^i W_i'' = 0 \quad (10)$$

The first derivative of transverse displacement w can be obtained from Eq. (7). Taking the derivative of obtained equation and substituting it into Eq. (8) gives the followings for transverse displacement function:

$$W_i = \frac{1}{J_4^i} U_i''' + \frac{J_2^i}{J_4^i} U_i' \quad (11)$$

where $J_2^i = C_3^i D_3^i$ and $J_4^i = C_3^i D_2^i$.

Substituting Eq. (9) and its derivatives, the simple forth-order uncoupled governing differential equation may be obtained as:

$$U_i^{iv} + H_2^i U_i'' + H_4^i U_i = 0 \quad (12)$$

where $H_2^i = [D_2^i + C_3^i D_3^i]$ and $H_4^i = [C_2^i D_2^i]$.

The beam is assumed to be composed of three layers, namely bottom, core and top, 12 constants (4 for each layer) are to be determined. The traction-free boundary conditions at the bottom and top surfaces are:

$$\tau_{xz} (x, 0, t) = \left[C_{55}^b \frac{\partial u_b}{\partial z} + C_{55}^b \frac{\partial w_b}{\partial x} \right] = 0 \quad (13)$$

$$\sigma_{zz} (x, 0, t) = \left[C_{13}^b \frac{\partial u_b}{\partial x} + C_{33}^b \frac{\partial w_b}{\partial z} \right] = 0 \quad (14)$$

$$\tau_{xz} (x, h, t) = \left[C_{55}^t \frac{\partial u_t}{\partial z} + C_{55}^t \frac{\partial w_t}{\partial x} \right] = 0 \quad (15)$$

$$\sigma_{zz} (x, h, t) = \left[C_{13}^t \frac{\partial u_t}{\partial x} + C_{33}^t \frac{\partial w_t}{\partial z} \right] = 0 \quad (16)$$

Displacement continuity conditions through lamina interfaces:

$$u_i = u_{i+1} \quad (17)$$

$$w_i = w_{i+1} \quad i = 1, 2, 3 \quad (18)$$

Axial and shear stress continuity conditions through lamina interfaces:

$$\sigma_{zzi} = \sigma_{zzi+1} \quad (19)$$

$$\tau_{xzi} = \tau_{xzi+1} \quad i = 1, 2, 3 \quad (20)$$

Upon substitution of displacements given by Eq. (6), the necessary conditions above may be obtained in the terms of U_i and W_i :

$$\left[C_{55}^b \frac{\partial U_b}{\partial z} + C_{55}^b \xi W_b \right]_{z=0} = 0 \quad (21)$$

$$\left[-C_{13}^b \xi U_b + C_{33}^b \frac{\partial W_b}{\partial z} \right]_{z=0} = 0 \quad (22)$$

$$\left[C_{55}^t \frac{\partial U_t}{\partial z} + C_{55}^t \xi W_t \right]_{z=h} = 0 \quad (23)$$

$$\left[-C_{13}^t \xi U_t + C_{33}^t \frac{\partial W_t}{\partial z} \right]_{z=h} = 0 \quad (24)$$

at the lamina interfaces:

$$U_i = U_{i+1} \quad (25)$$

$$W_i = W_{i+1} \quad (26)$$

$$\left[C_{55}^i \frac{\partial U_i}{\partial z} + C_{55}^i \xi W_i \right] = \left[C_{55}^{i+1} \frac{\partial U_{i+1}}{\partial z} + C_{55}^{i+1} \xi W_{i+1} \right] \quad (27)$$

$$\left[-C_{13}^i \xi U_i + C_{33}^i \frac{\partial W_i}{\partial z} \right] = \left[-C_{13}^{i+1} \xi U_{i+1} + C_{33}^{i+1} \frac{\partial W_{i+1}}{\partial z} \right] \quad i = 1, 2, 3 \quad (28)$$

The stiffness matrix for the isotropic face sheets and orthotropic core are, respectively:

$$C_{jk}^{b,t} = \begin{bmatrix} \frac{E}{1-\nu^2} & \frac{E\nu}{1-\nu^2} & 0 \\ \frac{E\nu}{1-\nu^2} & \frac{E}{1-\nu^2} & 0 \\ 0 & 0 & \frac{E(1-\nu)}{2(1-\nu^2)} \end{bmatrix} \quad (29)$$

$$C_{jk}^c = \begin{bmatrix} \frac{E_1}{1-\nu_{13}\nu_{31}} & \frac{E_3\nu_{13}}{1-\nu_{13}\nu_{31}} & 0 \\ \frac{E_3\nu_{13}}{1-\nu_{13}\nu_{31}} & \frac{E_3}{1-\nu_{13}\nu_{31}} & 0 \\ 0 & 0 & G_{13} \end{bmatrix} \quad (30)$$

CFM is applied to the present problem as an efficient solution method. The laborious mathematical manipulations and moderate tasks such as integral transformation, finite element model or series solution are not required by solutions steps of CFM[20]. CFM transforms the two-point boundary value problem to a

system of initial-value problems which can be solved by a numerical method. In this case, the fifth-order Runge-Kutta(RK-5) is chosen. A-six-digit accuracy is obtained at 4 intervals through the transverse coordinate for each lamina. The theoretical background and detailed solution steps for the present type of problems with CFM are available in the literature[18, 19, 21-23]. Upon the application of CFM to the problem on hand, the complete solution of Eq. is obtained in following form:

$$U_i = \sum_{j=1}^n e^j U_i^j, \quad i = b, c, t \quad n = 4 \quad (31)$$

Applying the boundary conditions prescribed in Eqs. (21-28) for the particular problem on hand results in the following system of algebraic equations for the coefficients e_i^j :

$$[T_{kl}] \{e_i^j\} = 0 \quad k, l = 1, 2, \dots, 12 \quad (32)$$

where $[T_{kl}]$ including the variables z , ω , ξ is the coefficient matrix. The frequencies which make the determinant of coefficients matrix $[T_{kl}]$ zero are the natural frequencies of the composite beam.

3. Results and Discussion

Two different materials for isotropic face sheets and orthotropic core are considered and the material properties are given in Table 1. The thickness of bottom and top face is equal to each other which is taken as 25mm and the thickness of core is 75mm.

The natural frequencies ω are determined from the coefficient matrix given in Eq. (32). It is mainly concentrated on the effectiveness of CFM for the present type of problems. The efficiency and accuracy of the method are compared to the finite element software and results are tabulated in Table 2. As it can be seen that CFM results match quite well with those of finite element software ones. Four divisions through the transverse coordinate for each laminate are sufficient to obtain a-six-digit accuracy. In the finite element model, the structural solid element having quadratic displacement behavior is used. The element has eight nodes with two degrees of freedom at each node which are translations in the nodal x and z axes. The beam is divided into 200 equal elements for each layer. The element has three nodes and six degrees of freedoms based on the first-order shear deformation theory may also be used in the finite element model[24, 25]. The effects of material properties of isotropic face sheets and orthotropic core, wave number and length-to-thickness ratio (L/h) are also examined. Table 3 and 4 show the variation of non-dimensional natural

frequencies of Al face sheets beam with property of core material, wave number and length-to-thickness ratio. As an inspection of these tables, using Glass/Epoxy instead of Graphite/Epoxy as a core material decreases the natural frequency. Also, increasing the wave number and decreasing the length-to-thickness ratio increase the natural frequency. The free vibration results of ceramic face sheet (ZrO_2) composite beam are also obtained and illustrated in Figure 1 and 2 for the first three wave numbers. The results are given in figure form preventing the redundancy to properly compare the differences between Al and ZrO_2 face sheets beams. It is seen that zirconia as face sheets decreases the natural frequency.

Table 1. Elastic properties of the material used in the analysis.

	E_1 (GPa)	E_3 (GPa)	G_{13} (GPa)	ν_{13}	ρ (kg / m ³)
Aluminum (Al)	70	70	-	0.3	2707
Zirconia (ZrO_2)	200	200	-	0.22	5700
Graphite/Ep oxy	181	10.3	7.17	0.28	1600
Glass/Epoxy	38.6	8.27	4.14	0.26	1900

Table 2. Comparison of CFM with ANSYS for the first 5 natural frequencies (Hz)

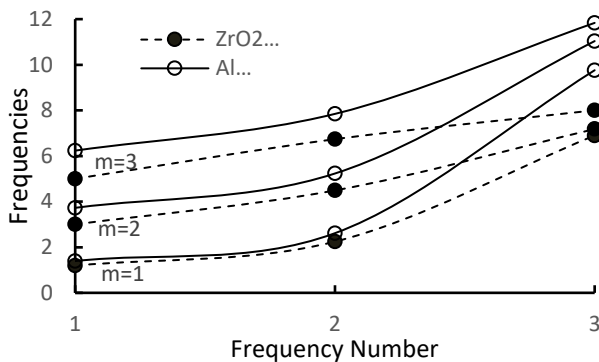
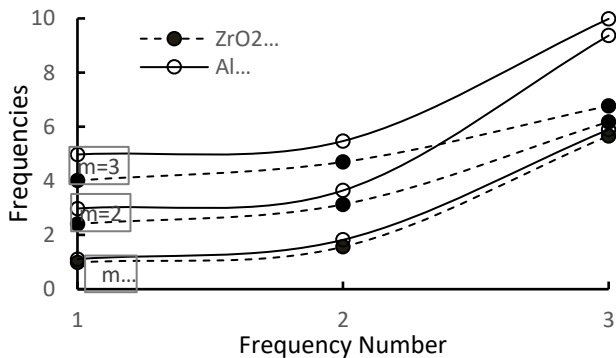
m	CFM	Finite Element
1	1127.67836	1127.68083
2	3015.91541	3015.90980
3	5046.92617	5046.93427
4	7197.83090	7197.83472
5	9462.65677	9462.89252

Table 3. Non-dimensional natural frequencies($\bar{\omega} = \omega \sqrt{\rho_{Al}/E_{Al}}$) of Al-Graphite/Epoxy-Al composite beam for different wave number

L/h	$\bar{\omega}$				
	$m = 1$	$m = 2$	$m = 3$	$m = 4$	$m = 5$
4	1.39335	3.72644	6.23594	8.89358	11.69198
	2.61538	5.23176	7.84614	10.46252	13.07890
	9.76088	11.03734	11.83498	13.22415	15.12607
10	0.28431	0.97403	1.83720	2.76555	3.72644
	1.04675	2.09250	3.13826	4.18401	5.23176
	4.01882	7.90453	10.82299	10.88692	11.03734
15	0.13098	0.48284	0.97403	1.53916	2.14191
	0.69750	1.39400	2.09250	2.78901	3.48751
	2.68761	5.33509	7.90453	10.36411	10.83562

Table 4. Non-dimensional natural frequencies $\bar{\omega} = \omega \sqrt{\rho_{Al}/E_{Al}}$ of Al-Glass/Epoxy-Al composite beam for different wave number

L/h	ω				
	$m = 1$	$m = 2$	$m = 3$	$m = 4$	$m = 5$
4	1.11007	2.97860	4.97436	7.09937	9.11956
	1.82311	3.64722	5.47133	7.29544	9.36666
	5.89605	9.36641	9.98482	11.07141	12.64135
10	0.22439	0.77394	1.46641	2.21098	2.97860
	0.72944	1.45989	2.18833	2.91878	3.64722
	2.36969	4.72858	7.04112	8.91523	9.36641
15	0.10317	0.38195	0.77394	1.22710	1.71103
	0.48663	0.97226	1.45989	1.94552	2.43115
	1.58033	3.15797	4.72858	6.28135	7.77255

**Figure 1.** Non-dimensional natural frequencies($\bar{\omega} = \omega \sqrt{\rho_{Al}/E_{Al}}$) of Graphite/Epoxy core beam for $L/h=4$ **Figure 2.** Non-dimensional natural frequencies($\bar{\omega} = \omega \sqrt{\rho_{Al}/E_{Al}}$) of Glass/Epoxy core beam for $L/h=4$

4. Conclusions

Plane vibration analysis of composite beam with an orthotropic core has been conducted. The governing equation of motion is obtained by plane elasticity theory and readily solved by CFM using very coarse collocation points. The results are obtained in the terms of a non-dimensional frequency parameter in order to accelerate the convergence of study. It is observed that

CFM is very convenient numerical technique for the vibration problems of composite core beams. The influences of laminate properties, geometric parameter and wave number on the natural frequency are also examined. The results show that the core material with low elastic property ratio decreases the natural frequency and increasing the wave number and decreasing the geometric parameter also increase the natural frequency.

Conflicts of interest

The authors stated that did not have conflict of interests.

References

- [1] Arikoglu A. and Ozkol I. Vibration analysis of composite sandwich beams with viscoelastic core by using differential transform method. *Compos. Struct.*, 92(12) (2010) 3031-3039.
- [2] Baba B.O. Free vibration analysis of curved sandwich beams with face/core debond using theory and experiment. *Mech. Adv. Mater. Struc.*, 19(5) (2012) 350-359.
- [3] Lou J., Ma L. and Wu L.Z. Free vibration analysis of simply supported sandwich beams with lattice truss core. *Mat. Sci. Eng. B-Adv.*, 177(19) (2012) 1712-1716.
- [4] Sadeghnejad S., Sadighi M. and Hamedani A. O. An extended higher-order free vibration analysis of composite sandwich beam with viscoelastic core. ASME 2012 11th Biennial Conference on Engineering Systems Design and Analysis, ESDA 2012 2012. p. 75-82.
- [5] Xu M. and Qiu Z. Free vibration analysis and optimization of composite lattice truss core sandwich beams with interval parameters. *Compos. Struct.*, 106(1) (2013) 85-95.
- [6] Wang Y. and Wang X. Free vibration analysis of soft-core sandwich beams by the novel weak form quadrature element method. *J. Sandw. Struct. Mater.*, 18(3) (2016) 294-320.
- [7] Cheng S., Qiao P., Chen F., Fan W. and Zhu Z. Free vibration analysis of fiber-reinforced polymer honeycomb sandwich beams with a refined sandwich beam theory. *J. Sandw. Struct. Mater.*, 18(2) (2016) 242-260.
- [8] Chen D., Kitipornchai S. and Yang J. Nonlinear free vibration of shear deformable sandwich beam with a functionally graded porous core. *Thin-Walled Struct.*, 107(1) (2016) 39-48.
- [9] Khdeir A. A. and Aldraihem O. J. Free vibration of sandwich beams with soft core. *Compos. Struct.*, 154((2016) 179-189.

- [10] Zhang Z. J., Han B., Zhang Q.C. and Jin F. Free vibration analysis of sandwich beams with honeycomb-corrugation hybrid cores. *Compos. Struct.*, 171(1) (2017) 335-344.
- [11] Demir O., Balkan D., Peker R. C., Metin M. and Arikoglu A. Vibration analysis of curved composite sandwich beams with viscoelastic core by using differential quadrature method. *J. Sandw. Struct. Mater.*, 22(3) (2020) 743-770.
- [12] Chanthanumataporn S. and Watanabe N. Free vibration of a light sandwich beam accounting for ambient air. *J. Vib. Control.*, 24(16) (2018) 3658-3675.
- [13] De Souza Eloy F., Gomes G. F., Ancelotti A. C., da Cunha S. S., Bombard A. J. F. and Junqueira D. M. A numerical-experimental dynamic analysis of composite sandwich beam with magnetorheological elastomer honeycomb core. *Compos. Struct.*, 209(1) (2019) 242-257.
- [14] Rahmani O., Khalili S., Malekzadeh K. and Hadavinia H. Free vibration analysis of sandwich structures with a flexible functionally graded syntactic core. *Compos. Struct.*, 91(2) (2009) 229-235.
- [15] Asgari G., Payganeh G. and Fard K. M. Dynamic instability and free vibration behavior of three-layered soft-cored sandwich beams on nonlinear elastic foundations. *Struct. Eng. Mech.*, 72(4) (2019) 525-540.
- [16] Xu G.D., Zeng T., Cheng S., Wang X.-h. and Zhang K. Free vibration of composite sandwich beam with graded corrugated lattice core. *Compos. Struct.*, 229(1) (2019) 335-344.
- [17] Temel B. and Noori A. R. Out-of-plane vibrations of shear-deformable afg cycloidal beams with variable cross section. *Appl. Acoust.*, 155(1) (2019) 84-96.
- [18] Aslan T. A., Noori A. R. and Temel B. Dynamic response of viscoelastic tapered cycloidal rods. *Mech. Res. Commun.*, 92((2018) 8-14.
- [19] Celebi K., Yarimpabuc D. and Tutuncu N. Free vibration analysis of functionally graded beams using complementary functions method. *Arch. Appl. Mech.*, 88(5) (2018) 729-739.
- [20] Yildirim S. and Tutuncu N. Effect of magneto-thermal loads on the rotational instability of heterogeneous rotors. *AIAA J.*, 57(5) (2019) 2069-2074.
- [21] Aktas Z. Numerical solutions of two-point boundary value problems. Ankara, Turkey: METU, Dept of Computer Eng, (1972).
- [22] Roberts S. and Shipman J. Fundamental matrix and two-point boundary-value problems. *J. Optimiz. Theory. App.*, 28(1) (1979) 77-88.
- [23] Tutuncu N. and Temel B. A novel approach to stress analysis of pressurized fgm cylinders, disks and spheres. *Compos. Struct.*, 91(3) (2009) 385-390.
- [24] Temel B. and Noori A.R. Transient analysis of laminated composite parabolic arches of uniform thickness. *Mech. Based Des. Struc.*, 47(5) (2019) 546-554.
- [25] Temel B. and Noori A.R. On the vibration analysis of laminated composite parabolic arches with variable cross-section of various ply stacking sequences, *Mech. Adv. Mater. Struc.* (2018).



Power analysis of robotic medical drill with different control approaches

Yunis TORUN^{1,*} Sefa MALATYALI¹

¹Department of Electrical and Electronics Engineering, ROBOLAB, Faculty of Engineering, Sivas Cumhuriyet University, Sivas/ TURKEY

Abstract

Increasing the efficiency of the systems used in surgical operations has become an important issue. Especially in orthopedic surgery, many surgical systems and instruments are used to reduce the workload of surgeons and increase the success of the operation. Surgical drills, which are one of these systems used in orthopedic surgery, are used in operations such as drilling, cutting and carving in various interventions. Cases such as drill sensitivity and stability are critical to operational success and patient health. In this study, an orthopedic drill design that can be added to a linear motion module or a 6-axis robot manipulator has been realized. Linear Quadratic Regulator (LQR), which is one of the optimal controller methods, Proportional Integral (PI) Controller, which is one of the classical controller methods and Model Predictive Controller (MPC) systems from modern controller systems are designed to perform speed control task of the surgical drill. A drill integrated into the robot manipulator for a constant drilling speed of 120 rad/sec and a robot manipulator were used to provide constant feed rate (1 mm/s) and to drill holes at constant intervals during the drilling experiments. Power analysis is performed in real-time in bone drilling operations for three controllers. Current, and voltage information during drilling are recorded simultaneously in the experimental setup. In particular, it has been observed that the power signal and the force information of the bone in different layers are proportional.

Article info

History:

Received: 19.12.2019

Accepted: 17.04.2020

Keywords: Bone

Drilling, Robotic

Surgery, Power Analysis.

1. Introduction

Bone drilling operations are widely used in the treatment of fractured bones in orthopedic surgery [1-3]. Since it is not possible to intervene with broken plaster for the treatment of broken or shattered bones, screw holes are drilled through surgical drills to fix the nails placed in the bone and treat bone fracture [4]. High sensitivity and stability in bone drilling are crucial to both patient health and surgical success [5,6]. In orthopedic surgical bone drilling operations, drill systems have been transformed into wireless (battery-operated) drill systems over time. In these transformation and development processes, there is an increasing demand for features such as more stable, more efficient, more precise working conditions and long-term use of the drills. Features such as sensitivity and stability directly affect operation success and patient health. In order to make a surgical drill system more efficient, power analysis of that drill can be performed with closed loop control for speed control tasks. The power analysis approach is

primarily for the power efficiency approach for the long-term and stable operation of the devices. Basic information about power efficiency can be obtained in systems where power analysis is performed [7]. Power efficiency directly affects the operating system and performance of the drill. The power irregularity of a surgical drill used in bone drilling procedures in orthopedic surgery may cause the surgical drill to lose some function or to malfunction. This risk may not only shorten device life but also compromise patient health during surgery.

In orthopedic surgery, bones that are pierced and fixed with nails and screws in bone drilling operations consist of three basic bone layers [8]. These layers are the first cortical bone in which the perforation starts, the spongy bone and the second cortical bone layer in which the perforation is terminated [9,10]. These bone layers have different mechanical properties. Due to these differences, the obtained current and voltage signals during the drilling process also change. Based on the change in these quantities, power analysis can be performed.

*Corresponding author. Email address: ytorun@cumhuriyet.edu.tr
<http://dergipark.gov.tr/csj> ©2020 Faculty of Science, Sivas Cumhuriyet University

As a result of the literature research, no studies have been found regarding the power analysis of surgical drills. Only Deng et al., have designed a Fuzzy Force Controller for the vertebral laminated milling process, used the power consumption information to ensure the safety of the operation. They calculated the power consumed by each milling layer by separating the motion in the bone as transverse and longitude motion. They have identified three different situations where power consumption differed by looking at the structure of the bone and they have developed the safety controller according to the stop point of milling [11]. However, drill power optimization with different control approaches has not been developed yet in any study up to our best of knowledge in literature.

In this study, power analyzes of surgical drill used in orthopedic surgical operations are performed. The electrical and mechanical model of the motor of the drill has been extracted. Linear Quadratic Regulator (LQR) which is one of the optimal control methods, Proportional Integral (PI) Controller which is one of the classical controller methods and Model Predictive Controller (MPC) systems from modern controller systems have been applied in real-time. On the bone prototype, which mimics the mechanical properties of the sheep femur, 10 holes are drilled for each bone in equal spacing with constant feed rate and constant rotation speeds. During drilling experiments, power analysis can be performed by taking instant current and voltage. The average power values consumed by the drill during the drilling experiments have calculated using different methods.

In Section II, bone layers and drilling path information, the used drill direct current motor model in the study and controller designs for the power analysis are given. Section III provides information on the experimental setup and equipment to which the study is carried out. The results of the experiments are given in Section IV. Finally, Section V concludes the current research.

2. Material and Methods

In bone drilling operations in orthopedic surgery, the amount of power consumed by the drill varies in different layers of bone. The power consumed when the drill is idle is equal to the amount of power required to rotate the drill. When the drill is in the first and second cortical tissues, the amount of power consumed due to the mechanical properties of the bone is maximum. In order to monitor and analyze these power changes during the drilling process,

firstly the mechanical properties of the bone tissue to be used in the drilling experiments and the drilling path expressing the direction of the drill bit's progression are mentioned. Then, the design of the motor model of the direct current motor to be used in drilling experiments and the design of the proposed controller systems for power analysis in orthopedic surgical drills have implemented.

2.1. Bone layers and drilling path

The bone structure, which is fixed and treated with nails and screws, generally consists of 3 basic bone layers in orthopedic surgery [8]. These bone layers consist of the first cortical bone, spongy bone and the second cortical bone layer [9], [10]. Depending on the type of surgical procedure performed, bone drilling is divided into two steps. These are the perforation process between the two cortical bones (the perforation of the bone from the opposite wall) and the perforation of only one cortical bone (without necessarily passing through the medullary canal) [12], [13]. When the mechanical elastic properties of the bone are examined, the elasticity of an average age human bone is approximately 17 GigaPascal (GPa) in length and 12 GPa in width. The elasticity of cancellous bone is 0.1-4.5 GPa depending on bone density [14]. Furthermore, because of its structure, the cortical bone layer exhibits more strength than the cancellous bone layer [15]. In Figure 1, the bone layers in the orthopedic surgical bone drilling processes and the drilling path, which represent the direction of progress of the drill bit, are given.

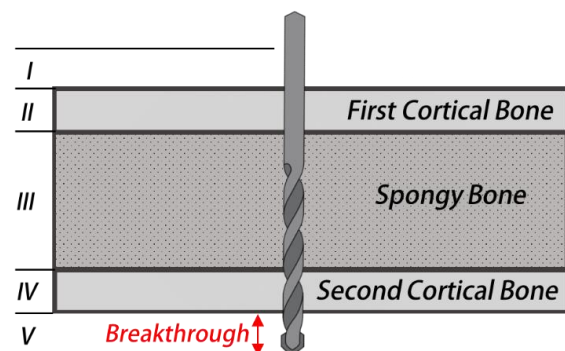


Figure 1: Bone layers and drilling path

Here, the drill does not work before drilling in zone I. Also, the drill does not work after drilling in zone V. Zone II shows the First Cortical Bone layer, where drilling starts. Zone III shows the spongy bone in which drilling is performed. Zone IV refers to the Second Cortical Bone layer. Zone V refers to the breakthrough of the drill bit from the second

cortical layer of the femur bone. The feed distance of the drill bit in Zone V shows the feed distance of the drill bit in tissues such as vessels, nerves, muscles or tendons.

2.2. Direct current (DC) motor model

Direct current motors are widely used in many sectors, especially in industrial applications [16]. It is widely used because the production process is easy and cost-effective. The DC motor mathematical model is less complex than other motor models. This facilitates the formation of the speed/position controller system of the motor is used. Figure 2 shows a model of a direct current motor.

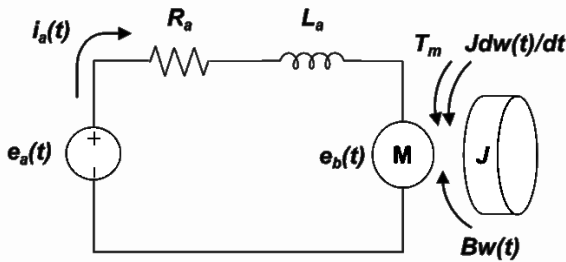


Figure 2: Direct current motor model

In accordance with the above direct current motor model, the electrical parameters of the motor are expressed in Equation 1 as;

$$e_a(t) = i_a(t) \cdot R_a + L_a \cdot \frac{di_a(t)}{dt} + e_b(t) \quad (1)$$

, where e_a is the input voltage, R_a is the motor ohmic resistance, L_a is the motor inductive reluctance, e_b is the counter-electromotive force and i_a is the motor current. DC motor counter electromotive force is given in Equation 2.

$$e_b(t) = K_b \cdot w(t) \quad (2)$$

K_b is the constant of the counter electromotive force and $w(t)$ is the angular velocity (rad/s). The relation of the electrical model and mechanical model is expressed in Equation 3.

$$T_m(t) = K_m \cdot i_a(t) \quad (3)$$

$T_m(t)$ is the shaft rotor torque. DC motor mechanical model is given in Equation 4.

$$T_m(t) = B \cdot w(t) + J \cdot \frac{dw(t)}{dt} + T_L(t) \quad (4)$$

B is the motor friction, J is the rotor inertia and T_L is the load torque. State-space representations of the DC motor are Equation 5 and Equation 6.

$$\begin{bmatrix} \dot{w}(t) \\ \dot{i}_a(t) \end{bmatrix} = \begin{bmatrix} -\frac{B}{J} & \frac{K_m}{J} \\ -\frac{K_b}{L} & -\frac{R}{L} \end{bmatrix} \begin{bmatrix} w(t) \\ i_a(t) \end{bmatrix} + \begin{bmatrix} 0 \\ \frac{1}{L} \end{bmatrix} \cdot e_a(t) \quad (5)$$

$$w(t) = [1 \quad 0] \begin{bmatrix} w(t) \\ i_a(t) \end{bmatrix} \quad (6)$$

The motor used is a geared motor and the total system inertia and friction coefficient vary in the motor model. Total friction and inertia values in the system in Equation 7 and Equation 8, respectively:

$$B_t = B + B_r \cdot red^2 \quad (7)$$

$$J_t = J + J_r \cdot red^2 \quad (8)$$

is expressed as. Here, red is the ratio of the gearbox. In the motor used in bone drilling processes, the ratio of the reducer is constant and $red=1/16$. Parameters of used DC motor previously estimated in our previous work with Nonlinear Least Estimator and Genetic Algorithm.

2.3. Controller methodologies

In this study, Linear Quadratic Regulator (LQR), Proportional-Integral (PI) Controller and Model Predictive Controller (MPC) controller methods, which are frequently used among the controller systems, are used. Although PI control is widely used in many control tasks because of its cost-effective, there are some disadvantages as fine-tuning, wind-up. LQR is another approach to improve the controller performance. However, it needs to know the mathematical model of the physical system and the states of the physical system must measurable. MPC provides to the limitation of controlled signals with predicting the response of the system. In this section, the controller methods used in the study, are LQR, PID, MPC are given.

2.3.1. Linear quadratic regulator (LQR)

The Linear Quadratic Regulator Controller method is a control method based on the Optimal Controller Theory and uses the change of states as feedback [17]. Using this method, the feedback vector can be calculated without manipulation of the poles. The operating system of the LQR controller is based on a minimization of the cost function. Figure 3 is a simple diagram of the LQR controller for the DC motor.

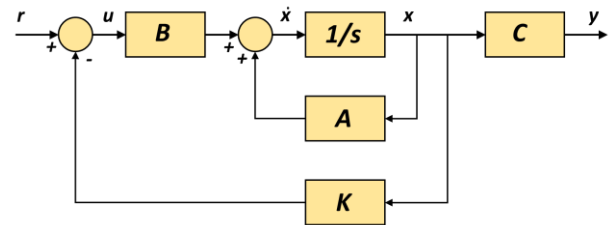


Figure 3: Block diagram of LQR

The K state feedback vector is given in Equation 9 as;

$$u(t) = -Kx(t) \quad (9)$$

where $u(t)$ is the control signal, $x(t)$ is the state of the model. Since LQR is a model-based control method, it calculates the K feedback control coefficient according to the optimal control theory using model state equation coefficients.

In the study, $R=1$ and $Q = \begin{bmatrix} 9400 & 0 \\ 0 & 40 \end{bmatrix}$ were selected and $K = [87.128 \quad -16.283]$ was calculated.

2.3.2. Proportional integral (PI) controller

It is an easy-to-implement closed-loop controller method that enables to control the system using the proportional and integral sums of the PI error signal [18], [19]. Also, a basic PI Controller block diagram is given in Figure 4 in which K_p is the coefficient of proportional and K_i is the coefficient of integral. The error signal is the $e(t)$ represents the difference between the given reference input and the model output. PI minimizes system errors with closed-loop and the system can react to disturbing effects.

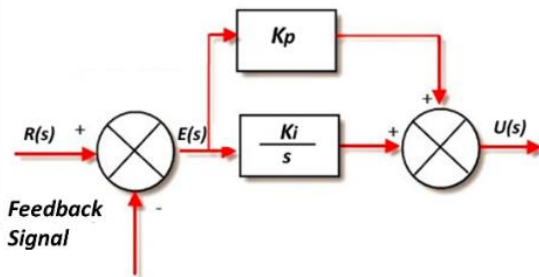


Figure 4: Block diagram of PID

The control parameters $K_p = 0,128$ and $K_i = 0,773$ were determined with MATLAB PID Tuner Toolbox for the PI control system.

2.3.3. Model predictive controller (MPC)

Model Predictive Controller (MPC) is a controller method designed according to the system model to be audited. MPC is a highly successful and advanced controller method in many applications [20]. The MPC calculates the optimal controller signal according to the optimization criterion based on the input and output information and the limits set in the past and present. MPC calculates the future behavior of the system with the control signal to be applied to the system. The Floating Horizon Method is used to generate the controller signal. In this method, the first value of the controller signal calculated at each step is applied to the system [21]. Figure 5 graphically describes the steps and operating

principle of a single output and single input system with MPC.

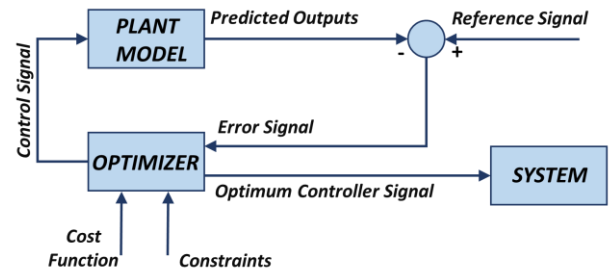


Figure 5: Block diagram of MPC

3. Experimental Setup

In the study, an 18V DC motor was used to provide the torque and rotational movement required for drilling and an encoder was used to measure the rotational speed. In the study, an 18V DC motor was used for drilling and an encoder was used to measure the rotational speed. The DC motor was used for drilling at a constant drilling speed (120 rad/sec). In addition, the KUKA KR900 robot manipulator, Kuka Robot Language (KRL) was programmed with KUKA Programming to ensure a constant plunge speed (1 mm / s) and a constant drilling distance (10 mm). A medical drill bit with a diameter of 3.5 mm and a length of 70 mm was used for drilling. Data acquisition card was used for real-time data collection and drilling speed control. The card output is insulated to protect the data acquisition card from currents and voltages that could damage the card. A load cell with a measuring range of 0-50 N was used to measure the thrust force. Sheep femur bone was used as drilling material. An Acer Aspire 5750G computer with an Intel® Core™ i5-2450M CPU @ 2.50Ghz (4 CPUs), 4096MB RAM, and an NVIDIA GeForce 610M graphics card was used to collect data in real-time and to develop and implement DC motor control systems. A drill holder is designed for robot drilling and is produced with a three-dimensional printer. The holder is designed to be mounted on the load cell intended for use. Drill holder parts and assembled states are shown in Figure 6.

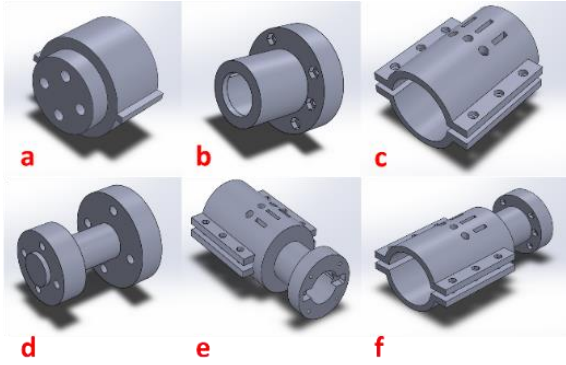


Figure 6: a: Load cell front cover design, b: Load cell outer sheath design, c: Drill motor outer sheath design, d: Load cell and robot attachment design, e: Drill holder design for robot assembled, f: Drill holder design for robot assembled version.

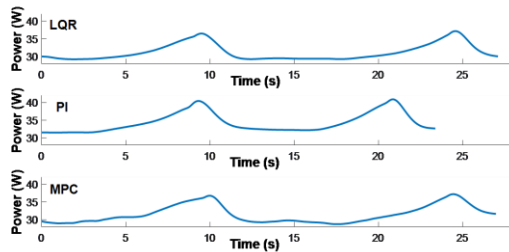


Figure 7: Sheep femur bone with 120 rad / s and 1mm / s Feed Rate

Due to the feature of the bone during drilling, the length of the drilling path is not equal to each other. Therefore, it is necessary to average the power data. The average values of the instantaneous power are given in Table 1.

Table 1: Controller methods for single hole power consumption averages

Controller Methods	Average Consumed Power (W)
LQR	31,2579
MPC	31,5308
PI	34,3473

When the obtained values for instantaneous power are examined, the average power values consumed by the controllers are compared. It is seen that the minimum power consumption is achieved in the drilling experiments performed with the LQR design compared to the drilling tests performed by other methods. MPC power consumption performance was similar to LQR, however, the performance of PI was worse than the other two approaches. Basic

Using the designed drill holder and programmed robot, multiple holes were drilled in the same standard and force, current, voltage, rotation speed and calculated instantaneous power data were collected.

4. Results and Discussions

Bone drilling experiments performed with three controller approaches with drilling 10 holes on sheep femur for each controller. The current and voltage signals were acquired while controlling the drill motor simultaneously. The signals received were also prioritized and examined for the power consumed. The instantaneous power patterns in drilling one hole are shown in Figure 7 with LQR, MPC and PI controller approaches.

Control Voltage, Motor Current and Drill Speed Error signals for LQR control system are given in Figure 8 for a one-hole drilling experiment. Signal waveforms vary according to the stiffness bone being drilled.

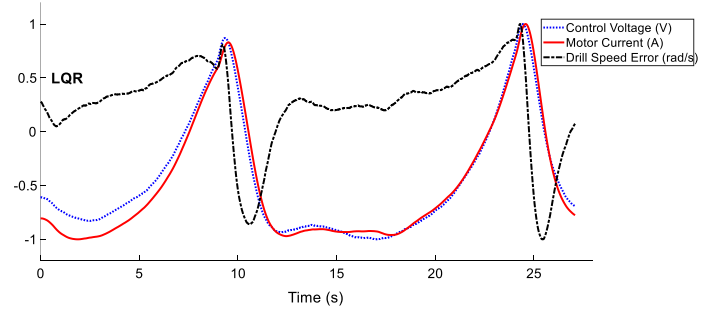


Figure 8: Control voltage (Voltage), motor current (Ampere) and drill speed error (rad/sec) signals for LQR control

5. Conclusion

In this study, an orthopedic drill design that could be adapted to a linear motion module or 6 axis robot manipulators is proposed. Power analyzes of the proposed surgical drill with different controllers were performed. LQR, PI and MPC control approaches were applied to the surgical drill motor in real-time. Power analysis was performed in sheep femur drilling operations in real-time. When performing the power analysis, the current and voltage data during drilling were simultaneously recorded. The result has been analyzed for the instantaneous power analyze based on the current and voltage during the operation of a speed-controlled drill. Improved power analysis accuracy can be improved by further drilling experiments and experiments with human bone.

6. Acknowledgements

This study is financially supported by the Cumhuriyet University Scientific Research Council (CUBAP) with a project number M737. The authors also thank Dr. Özhan Pazarcı for his valuable assistance in bone drilling experiments.

Conflicts of interest

There is no conflict of interest.

References

- [1] Dai Y.Xue Y.and Zhang J., Condition monitoring based on sound feature extraction during bone drilling process, *Proceedings of the 33rd Chinese Control Conference*, (2014) 7317–7322.
- [2] Chung G.B., Lee S.G., Kim S., Yi B.J., Kim W.K., Oh S.M., Kim Y.S., Park J.and Oh S.H., A robot-assisted surgery system for spinal fusion, *IEEE/RSJ International Conference on Intelligent Robots and Systems, IROS*, (2005) 3744–3750.
- [3] Torun Y., Ozturk A., Hatipoglu N.and Oztemur Z., Detection of Bone Excretion with Current Sensor in Robotic Surgery, *UBMK 2018 - 3rd International Conference on Computer Science and Engineering*, (2018) 185-189.
- [4] Duan X., Al-Qwbani M., Zeng Y., Zhang W. and Xiang Z., Intramedullary nailing for tibial shaft fractures in adults, *Cochrane Database of Systematic Reviews*, (2012) CD008241.
- [5] Osa T., Abawi C.F., Sugita N., Chikuda H., Sugita S., Tanaka T., Oshima H., Moro T., Tanaka S.and Mitsuishi M., Hand-Held Bone Cutting Tool with Autonomous Penetration Detection for Spinal Surgery, *IEEE/ASME Transactions on Mechatronics*, 20(6) (2015) 3018–3027.
- [6] Torun Y., Ozturk A., Aksoz A. and Pazarcı O., "Parameters Estimation of Orthopedic Drill," 2019 27th Signal Processing and Communications Applications Conference (SIU), Sivas, Turkey, (2019) 1–4.
- [7] Carroll A. and Heiser G., An Analysis of Power Consumption in a Smartphone., *USENIX annual technical conference*, (2010) 271–285.
- [8] Torun, Y., Öztürk, A., A New Breakthrough Detection Method for Bone Drilling in Robotic Orthopedic Surgery with Closed-Loop Control Approach., *Ann Biomed Eng.*, 48 (2020) 1218–1229.
- [9] Lee W.-Y. and Shih C.-L., Control and breakthrough detection of a three-axis robotic bone drilling system, *Mechatronics*, 2(16) (2006) 73–84.
- [10] Farnworth G.H. and Burton J.A., Optimization of Drill Geometry for Orthopaedic Surgery, *Proceedings of the Fifteenth International Machine Tool Design and Research Conference*, (2015) 227–233.
- [11] Deng Z., Jin H., Hu Y., He Y., Zhang P., Tian W.and Zhang J., Fuzzy force control and state detection in vertebral lamina milling, *Mechatronics*, 35 (2016) 1–10.
- [12] Díaz I., Gil J.J.and Louredo M., Bone drilling methodology and tool based on position measurements, *Computer Methods and Programs in Biomedicine*, 2(112) (2013) 284–292
- [13] Mayer M., Lin H.H., Peng Y.H., Lee P.Y.and Wang M.L., A drill signal detection technology for handheld medical drilling device, *Proceedings - 2014 International Symposium on Computer, Consumer and Control, IS3C 2014*, (2014) 958–961.
- [14] Turner C.H. and Burr D.B., Basic biomechanical measurements of bone: A tutorial, *Bone*, 4(14) (1993) 595–608.
- [15] Zioupos P., Currey J.D., Hamer A.J., The role of collagen in the declining mechanical properties of aging human cortical bone. *J Biomed Mater Res.* 45(2) (1999) 108-116.
- [16] Radcliffe P. and Kumar D., Sensorless speed measurement for brushed DC motors, *IET Power Electronics*, 8(11) (2015) 2223–2228.
- [17] Farrell M., Jackson J., Nielsen J., Bidstrup C. and McLain T., Error-State LQR Control of a Multirotor UAV, *2019 International Conference on Unmanned Aircraft Systems (ICUAS)*, (2019) 704–711.
- [18] Nafea M., Ali A.R.M., Baliah J.and Ali M.S.M., Metamodel-based optimization of a PID controller parameters for a coupled-tank system, *Telkomnika (Telecommunication Computing Electronics and Control)*, 16(4) (2018) 1590–1596.
- [19] Samin R.E., Jie L.M.and Zawawi M.A., PID implementation of heating tank in mini automation plant using programmable logic controller (PLC), *InECCE 2011 - International*

Conference on Electrical, Control and Computer Engineering, (2011) 515–519.

IEEE/CAA Journal of Automatica Sinica, 6(1) (2019) 108–117.

[20] Bai T.Li S. and Zheng Y., Distributed model predictive control for networked plant-wide systems with neighborhood cooperation,

[21] Camacho E.F. and Bordons C. (Carlos), Model predictive control, Springer, 2007; pp 14-46.

Dynamic output-feedback H_∞ control design for ball and plate system

Serdar COŞKUN 

Tarsus University, Faculty of Engineering, Department of Mechanical Engineering, Tarsus/Mersin/TURKEY

Abstract

Ball and plate system is a nonlinear and unstable system, thus introducing great challenges to control scientists and it resembles many complicated real-time systems in several perspectives. There has been a good number of efforts to design a stabilizing controller for this system. This paper presents a dynamic output-feedback H_∞ control strategy for the plate and ball system based on the solution of linear matrix inequalities (LMIs). The discussion involves deriving the equations of motion of the system by using the Lagrange method, linearizing the nonlinear equations, and designing an H_∞ controller to achieve required tracking specifications on the position of the ball. The intent is to show the specified trajectory tracking performance outcomes in time domain via simulation studies conducted using MATLAB/Simulink. A circular and square trajectory following of the designed controller is compared with a baseline PID controller. It is revealed that the proposed controller exhibits an improved tracking performance to following the reference trajectories.

Article info

History:

Received:09.01.2020

Accepted:27.04.2020

Keywords:

Ball and plate system,
 H_∞ control,
Linear matrix
inequalities.

1. Introduction

The plate and ball system is an extension of beam and ball problem. While the latter has two degrees of freedom where a ball rolls on a beam, the first has four degrees of freedom where the ball can roll over a plate freely. Thus the actual system becomes more complicated because of the coupling on the coordinates. The plate rotates around the x and y -axis that requires two perpendicular control inputs to the plate. The control job is to regulate the position of the ball at a certain location in the plate by changing the angle of the plate. This is indeed not an easy task because the ball does not stay in one point on the plate that moves with an acceleration that is proportional to the length of the plate.

The main objective is to design a controller for the ball and plate system and that the controller should be capable of manipulating the position of the ball and tracking a reference path with high accuracy. In a more precise manner, one can stabilize the ball and specify a trajectory then let the ball follow it with the least error and a minimum time. In this regard, there has been a good number of efforts on the designing of tracking controllers from both experimental [1,2] and theoretical perspectives for the plate and ball system. The proportional-integral-derivative (PID) controller is employed in [3], the sliding mode control is

considered in [4,5]. Position of the ball is regulated by a feedback control in [6]. A nonlinear control via input-output linearization is demonstrated in [7]. In more detail, the work in [8] considers the stabilization problem of the plate and ball system by an approximate solution of the matching conditions to derive a stabilizing control law. A sliding mode controller is used and compared with a linear quadratic control for the plate and ball system in [9]. A cost-effective implementation on the Stewart platform with rotary actuators is demonstrated in experiments. Further, in [10], a neural network-based PID control structure is proposed for the nonlinear plate and ball system wherein the controller parameters of PID are adjusted by neural networks during control process.

Unlike the aforementioned rich literature in control techniques applied for the plate and ball system, there are few contributions presented in regards to employing an H_∞ controller for the same problem. For instance, [11] represents a double feedback loop structure where an inner loop is regulated by a DC motor servo controller while outer loop utilizes an H_∞ controller based on the solution of Algebraic Riccati Equations (AREs). Moreover, the work [12] represents AREs-based H_∞ optimal control for the plate and ball system. [13] demonstrates a shaping weighting function method for the loop-shaping that is applied to the plate and ball system for validation.

*Corresponding author. Email address: serdarcoskun@tarsus.edu.tr

<http://dergipark.gov.tr/csj> ©2020 Faculty of Science, Sivas Cumhuriyet University

In most of the cases in control design, sensors have the full state information of the plant, and the state is updated by the model and a state-feedback is performed. In this article, we assume that the states of the system are not directly measurable, which holds a more realistic scenario in real-time applications. The proposed controller directly feeds the plant output to the controller for the next action. The main contributions of this paper are twofold. a) Motivated by the present gap of research in H_∞ control, this study proposes a dynamic output-feedback H_∞ control for reference tracking problem of the plate and ball system first time. b) The output-feedback H_∞ controller gains are computed based on the solution of linear matrix inequalities (LMIs) by MATLAB convex optimization toolbox. The proposed controller is then compared with a baseline PID controller designed via PID tuner in Simulink to reveal the enhanced H_∞ tracking performance.

We start with linearizing the nonlinear plant, hence the linear feedback control methods can be applied and the stability of the open-loop can be determined with the linear model in Section 2. Then the output feedback controller H_∞ synthesis is shown and simulation results are given in Section 3. Lastly, conclusions are drawn in Section 4.

2. Modeling

The mathematical model of the plate and ball system is an important step to describe the main dynamics. There are two ways to derive the equations of motion of the ball and plate system, i.e., by using either the Newtonian method or the Lagrangian method. Each method has some advantages over the other depending on the type of the problem [14]. It is important to fully capture the dynamics of each part by deriving the equation, thus the Lagrangian method is seen more suitable both in terms of simplicity and ability to describe the rotational dynamics within the differential equations.

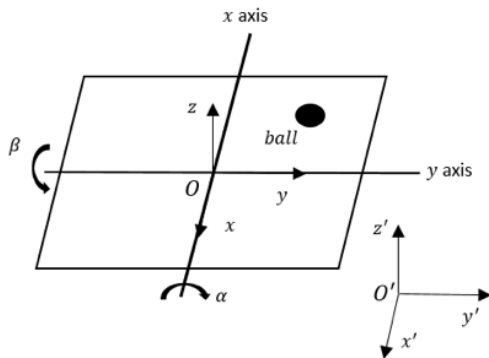


Figure 1. A simplified scheme of ball and plate system.

State variables are chosen as: $x(m)$ is the displacement of the ball along the x -axis, $y(m)$ is the displacement of the ball along the y -axis. The Lagrangian equation of a system is defined as

$$\mathcal{L} = T - P. \quad (1)$$

where T is the kinetic energy and P is the potential energy of the system. The generalized coordinates of the ball and plate system is defined

$$\varphi = \begin{bmatrix} \rho \\ \beta \\ \alpha \end{bmatrix}, \quad (2)$$

ρ is the position of the ball, β is the angle between the x -axis of the plate and horizontal direction, α is the angle between the y -axis of the plate and horizontal direction. Note that time notation t is omitted for simplicity in derivations.

The kinetic energy of the plate is:

$$T_{plate} = \frac{1}{2}J_x\dot{\beta}^2 + \frac{1}{2}J_y\dot{\alpha}^2, \quad (3)$$

where J is the moment of inertia of the ball. The kinetic energy of the ball is given by

$$T_{ball} = \frac{1}{2}J_{ball}\dot{q}_{ball}^2 + \frac{1}{2}mv_{ball}^2, \quad (4)$$

where \dot{q}_{ball} is the angular velocity v_{ball} is the linear velocity of the ball. The \dot{q}_{ball} term is defined as the distance of the ball to the center of the plate divided by its radius. i.e.,

$$\dot{q}_{ball} = \frac{\rho}{r}, \quad (5)$$

where $\rho = \sqrt{x^2 + y^2}$. The linear velocity expression of the ball is $v_{ball}^2 = \dot{x}^2 + \dot{y}^2$.

$$x = \rho \cos \beta + \rho \cos \alpha, \quad (6)$$

$$\dot{x} = \dot{\rho} \cos \beta - \beta \rho \sin \beta + \dot{\rho} \cos \alpha - \beta \rho \sin \alpha, \quad (7)$$

$$y = \rho \sin \beta + \rho \sin \alpha, \quad (8)$$

$$\dot{y} = \dot{\rho} \sin \beta + \beta \rho \cos \beta + \dot{\rho} \sin \alpha + \beta \rho \cos \alpha, \quad (9)$$

$$T_{ball} = \frac{1}{2} \left[\left(m + \frac{J_{ball}}{r^2} \right) (\dot{x}^2 + \dot{y}^2) + J_{ball} (\dot{\beta}^2 + \dot{\alpha}^2) + m(x\dot{\beta} + y\dot{\alpha})^2 \right], \quad (10)$$

Eq. (10) is the said to be the kinetic energy of the ball.

The potential energy of the ball is

$$V_{ball} = mgx \sin \beta + mgy \sin \alpha, \quad (11)$$

The Lagrangian expression of the ball is

$$\mathcal{L} = \frac{1}{2} \left(m + \frac{J_{ball}}{r^2} \right) (\dot{x}^2 + \dot{y}^2) \quad (12)$$

$$+J_{ball}(\dot{\beta}^2 + \dot{\alpha}^2) + m(x\dot{\beta} + y\dot{\alpha})^2 - (mgx\sin\beta + mgy\sin\alpha).$$

The Lagrange equation for both coordinates is

$$\frac{d}{dt}\left(\frac{\partial\mathcal{L}}{\partial\dot{x}}\right) - \frac{\partial\mathcal{L}}{\partial x} = 0, \quad \frac{d}{dt}\left(\frac{\partial\mathcal{L}}{\partial\dot{y}}\right) - \frac{\partial\mathcal{L}}{\partial y} = 0, \quad (13)$$

$$\frac{d}{dt}\frac{\partial\mathcal{L}}{\partial\dot{x}} = \left(m + \frac{J_{ball}}{r^2}\right)\ddot{x}, \quad (14)$$

$$\frac{d}{dt}\frac{\partial\mathcal{L}}{\partial\dot{y}} = \left(m + \frac{J_{ball}}{r^2}\right)\ddot{y}$$

$$\frac{\partial\mathcal{L}}{\partial x} = m\dot{x}\dot{\beta}^2 + m\dot{y}\dot{\beta}\dot{\alpha} - mg\sin\beta, \quad (15)$$

$$\frac{\partial\mathcal{L}}{\partial y} = m\dot{x}\dot{\alpha}^2 + m\dot{y}\dot{\beta}\dot{\alpha} - mg\sin\alpha.$$

Putting the Euler-Lagrange's equation into the equations above, we obtain two decoupled nonlinear differential equations as

$$\left(m + \frac{J_{ball}}{r^2}\right)\ddot{x} - m\dot{x}\dot{\beta}^2 - m\dot{y}\dot{\beta}\dot{\alpha} + mg\sin\beta = 0. \quad (16)$$

$$\left(m + \frac{J_{ball}}{r^2}\right)\ddot{y} - m\dot{x}\dot{\alpha}^2 - m\dot{y}\dot{\beta}\dot{\alpha} + mg\sin\alpha = 0. \quad (17)$$

Then, the Lagrange expression

$$= \frac{1}{2} \left[(J_x\dot{\beta}^2 + J_y\dot{\alpha}^2) + \left(m + \frac{J_{ball}}{r^2}\right)(\dot{x}^2 + \dot{y}^2) + J_{ball}(\dot{\beta}^2 + \dot{\alpha}^2) + m(x\dot{\beta} + y\dot{\alpha})^2 - (mgx\sin\beta + mgy\sin\alpha) \right] \quad (18)$$

The Lagrange equation is for the plate is now given

$$\frac{d}{dt}\left(\frac{\partial\mathcal{L}}{\partial\dot{\beta}}\right) - \frac{\partial\mathcal{L}}{\partial\beta} = \tau_x, \quad (19)$$

$$\frac{d}{dt}\left(\frac{\partial\mathcal{L}}{\partial\dot{\alpha}}\right) - \frac{\partial\mathcal{L}}{\partial\alpha} = \tau_y,$$

$$\left(\frac{\partial\mathcal{L}}{\partial\dot{\beta}}\right) = (J_x + J_{ball} + mx^2)\dot{\beta} + (mxy\dot{\alpha}), \quad (20)$$

$$\left(\frac{\partial\mathcal{L}}{\partial\dot{\alpha}}\right) = (J_x + J_{ball} + mx^2)\dot{\alpha} + (mxy\dot{\beta}),$$

$$\frac{d}{dt}\left(\frac{\partial\mathcal{L}}{\partial\dot{\beta}}\right) = (J_x + J_{ball} + mx^2)\ddot{\beta} \quad (21)$$

$$+ 2m\dot{x}\dot{\beta}\dot{\alpha} + m\dot{y}\dot{\alpha}^2 + m\dot{x}\dot{\alpha}\dot{\beta} + m\dot{y}\dot{\beta}\dot{\alpha}, \quad (22)$$

$$\frac{d}{dt}\left(\frac{\partial\mathcal{L}}{\partial\dot{\alpha}}\right) = (J_x + J_{ball} + my^2)\ddot{\alpha}$$

$$+ 2m\dot{x}\dot{\alpha}\dot{\beta} + m\dot{y}\dot{\beta}^2 + m\dot{x}\dot{\beta}\dot{\alpha} + m\dot{y}\dot{\alpha}\dot{\beta}, \quad (23)$$

$$\frac{\partial\mathcal{L}}{\partial\beta} = -mgx\cos\beta, \quad \frac{\partial\mathcal{L}}{\partial\alpha} = -mgy\cos\alpha.$$

Adding the Euler-Lagrange's equation terms to the plate system

$$(J_x + J_{ball} + mx^2)\ddot{\beta} + 2m\dot{x}\dot{\beta}\dot{\alpha} + m\dot{y}\dot{\alpha}^2 + m\dot{x}\dot{\alpha}\dot{\beta} + m\dot{y}\dot{\beta}\dot{\alpha} + mgx\cos\beta = \tau_x, \quad (24)$$

$$(J_x + J_{ball} + my^2)\ddot{\alpha} + 2m\dot{x}\dot{\alpha}\dot{\beta} + m\dot{y}\dot{\beta}^2 + m\dot{x}\dot{\beta}\dot{\alpha} + m\dot{y}\dot{\alpha}\dot{\beta} + mgy\cos\alpha = \tau_y. \quad (25)$$

Linearization of the ball equations about the plate angle, β and α , assuming $\dot{\beta}$ and $\dot{\alpha}$ are zero, with the small angle condition gives the following linear relations; $\sin\beta = \beta$, $\sin\alpha = \alpha$,

$$\left(m + \frac{J_{ball}}{r^2}\right)\ddot{x} + mg\beta = 0, \quad (26)$$

$$\left(m + \frac{J_{ball}}{r^2}\right)\ddot{y} + mg\alpha = 0. \quad (27)$$

The relation between the plate angle and the angle of the gear can be approximately related

$$\beta = \alpha = \frac{d}{L}\theta. \quad (28)$$

Plugging (28) this into (26,27) and taking the Laplace transform of the decoupled equations with zero initial conditions in x and y axis, the following input-output equations are found

$$\left(m + \frac{J_{ball}}{r^2}\right)X(s)s^2 = -mg\frac{d}{L}\theta(s), \quad (29)$$

$$\left(m + \frac{J_{ball}}{r^2}\right)Y(s)s^2 = -mg\frac{d}{L}\theta(s). \quad (30)$$

by rearranging the terms, the transfer function from the gear angle to the ball position in x and y axis is obtained

$$Q(s) = \frac{X(s)}{\theta(s)} = \frac{Y(s)}{\theta(s)} = -\frac{mgd}{L\left(\frac{J_{ball}}{r^2} + m\right)}\frac{1}{s^2}. \quad (31)$$

One can write the state-space equations of ball and plate system by considering τ_x and τ_y are torques exerted to the plate in x -axis and y -axis respectively [12]. The states variables defined $[x_1, x_2, x_3, x_4, x_5, x_6, x_7, x_8]^T = [x, \dot{x}, \beta, \dot{\beta}, y, \dot{y}, \alpha, \dot{\alpha}]^T$ and $U = [u_x, u_y]^T = [\tau_x, \tau_y]^T$. Then the nonlinear state equations

$$\begin{bmatrix} \dot{x}_1 \\ \dot{x}_2 \\ \dot{x}_3 \\ \dot{x}_4 \\ \dot{x}_5 \\ \dot{x}_6 \\ \dot{x}_7 \\ \dot{x}_8 \end{bmatrix} = \begin{bmatrix} x_2 \\ K(x_1x_4^2 + x_5x_4x_8 - g\sin x_3) \\ x_4 \\ 0 \\ x_6 \\ K(x_5x_8^2 + x_1x_4x_8 - g\sin x_7) \\ x_8 \\ 0 \end{bmatrix} + \begin{bmatrix} 0 & 0 \\ 0 & 0 \\ 0 & 0 \\ 1 & 0 \\ 0 & 0 \\ 0 & 0 \\ 0 & 1 \end{bmatrix} \begin{bmatrix} \tau_x \\ \tau_y \end{bmatrix}. \quad (32)$$

The values $[\tau_x, \tau_y]^T$ are considered to be 0. $K = \frac{m}{(m + \frac{J_{ball}}{r^2})}$, and $J_{ball} = \frac{2}{5}$ for a ball. Then $K = \frac{5}{7}$.

The new state-space equation is:

$$\begin{bmatrix} \dot{x}_1 \\ \dot{x}_2 \\ \dot{x}_3 \\ \dot{x}_4 \\ \dot{x}_5 \\ \dot{x}_6 \\ \dot{x}_7 \\ \dot{x}_8 \end{bmatrix} = \begin{bmatrix} x_2 \\ K(x_1x_4^2 - g\sin x_3) \\ x_4 \\ 0 \\ x_6 \\ K(x_5x_8^2 - g\sin x_7) \\ x_8 \\ 0 \end{bmatrix} + \begin{bmatrix} 0 & 0 \\ 0 & 0 \\ 0 & 0 \\ 1 & 0 \\ 0 & 0 \\ 0 & 0 \\ 0 & 0 \\ 0 & 1 \end{bmatrix} \begin{bmatrix} \tau_x \\ \tau_y \end{bmatrix}. \quad (33)$$

The ball and plate system can be regarded as two individual decoupled systems. Writing the x coordinate state equations in state-space format in (34) with the values yields

$$\dot{x} = A_p x + B_p u$$

$$y = C_p x.$$

where x is being the state vector, u is the control input, and y is the output vector.

$$\begin{bmatrix} \dot{x}_1 \\ \dot{x}_2 \\ \dot{x}_3 \\ \dot{x}_4 \end{bmatrix} = \begin{bmatrix} 0 & 1 & 0 & 0 \\ 0 & 0 & -7 & 0 \\ 0 & 0 & 0 & 1 \\ 0 & 0 & 0 & 0 \end{bmatrix} \begin{bmatrix} x_1 \\ x_2 \\ x_3 \\ x_4 \end{bmatrix} + \begin{bmatrix} 0 \\ 0 \\ 0 \\ 1 \end{bmatrix} \tau_x \quad (34)$$

$$y = [1 \ 0 \ 0 \ 0]x.$$

Note that we omit the time notation. Similar expression can be written for y -axis. As seen, the ball and plate system is an open-loop unstable stable, presenting challenges in control design.

3. Formulations and Results

3.1. PID control

A PID control is designed to compare with H_∞ control for the plate and ball positioning problem in the upcoming section. The gains of the PID is chosen as $K_p=2.38$, $K_i=0.0404$, $K_d=4.16$. The gains are selected based on Matlab's PID control toolbox tuning and successfully stabilize the unstable plate-ball system.

3.2. H_∞ control

In H_∞ control, the design objective is to find a controller that minimizes the worst-case energy amplification over certain frequency ranges. This can be interpreted as minimization of the cost function in the presence of external disturbances. The cost function is given below

$$J = \int_0^\infty [z^T(t)z(t) - \gamma^2 u^T(t)u(t)] dt. \quad (35)$$

where $z(t)$ is the output signal and $u(t)$ is the input signal. The H_∞ norm of a stable transfer function $G(s)$ is the largest input/output root mean square (RMS) gain *i. e.*,

$$\|G\|_\infty = \sup_{\substack{u \in L_2 \\ u \neq 0}} \frac{\|z\|_{L_2}}{\|u\|_{L_2}} = \sup_{\omega} \sigma_{\max}(G(j\omega)). \quad (36)$$

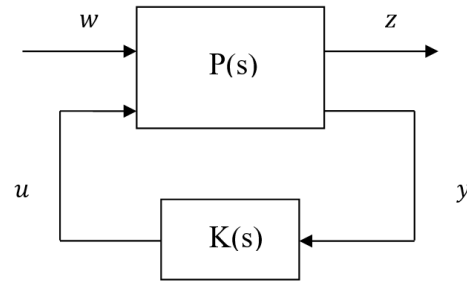


Figure 2. H_∞ controller block diagram.

where $w(t) \in \mathbb{R}^{n_w}$ is the exogenous disturbance with finite energy in the space $L_2[0, \infty)$, $u(t) \in \mathbb{R}^{n_u}$ is the control input vector, $z(t) \in \mathbb{R}^{n_z}$ is the controlled outputs, $y(t) \in \mathbb{R}^{n_y}$ is the measured outputs and $P(s)$ is the augmented plant model with weights and $K(s)$ is being the controller model. The optimal H_∞ controller seeks to minimize $\|F(P, K)\|_\infty$ over all stabilizing LTI controllers $K(s)$.

3.3. L_2 control

The signal $z(t) : [0, \infty) \rightarrow \mathbb{R}^n$ is said to be in the space $L^2_{n_2}[0, \infty)$ or simply L_2 , if

$$\int_0^\infty z^T(t)z(t)dt < \infty. \quad (37)$$

The 2-norm, denoted by $\|z\|_2$, is defined as

$$\|z\|_2 \triangleq \sqrt{\int_0^\infty z^T(t)z(t)dt}. \quad (38)$$

In this section, we use the MATLAB's Control Toolbox to design the controller for the plate and ball system. The proper weighting functions are used such that the regulated outputs remain in specified bound. The weighting error transfer function is chosen such that the output error to be small at lower frequencies, introduces better tracking performance. Similarly, the noise in the system creates high-frequency components that cause the control input to saturate. In order to penalize the input deteriorations at high frequencies, an input weighting function is implemented. We consider Figure 3 for a given closed-loop system where $\tilde{e}, \tilde{u}, \tilde{y}$ represent the weighted outputs of the error, control input and output, respectively. In this design, disturbance (d) and noise (n) are 0.

$$W_e(s) = \frac{1}{s+1}, W_u(s) = \frac{1}{s+10}, W_y(s) = \frac{1}{0.5s+1}.$$

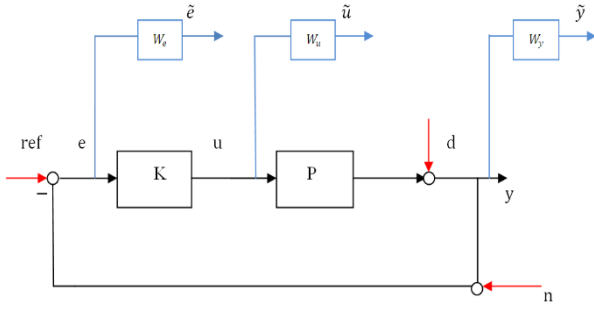


Figure 3. General block diagram for H_∞ synthesis with weighted regulated outputs and disturbances.

In the design of H_∞ control, W_e , W_u , and W_y are used to shape the plant model P in Figure 3. The selection of weighting transfer functions is important that requires experience and skill. We choose them with respect to imposing a reasonable control and enhancing tracking property. The state-space expressions for the weighting functions are:

$$W_e(s) = \begin{bmatrix} A_e & B_e \\ C_e & 0 \end{bmatrix}, W_u(s) = \begin{bmatrix} A_u & B_u \\ C_u & 0 \end{bmatrix},$$

$$W_y(s) = \begin{bmatrix} A_y & B_y \\ C_y & 0 \end{bmatrix},$$

Linear Fractional Transformation (LFT) of the augmented system with omitted time notation t is given as:

$$\begin{bmatrix} \dot{x}_p \\ \dot{x}_y \\ \dot{x}_e \\ \dot{x}_u \end{bmatrix} = \begin{bmatrix} A_p & 1 & 0 & 0 \\ B_y C_p & A_z & 0 & 0 \\ -B_y C_p & 0 & A_e & 1 \\ 0 & 0 & 0 & A_u \end{bmatrix} \begin{bmatrix} x_p \\ x_y \\ x_e \\ x_u \end{bmatrix} \quad (39)$$

$$+ \begin{bmatrix} 0 & B_p \\ 0 & 0 \\ B_e & 0 \\ 0 & 0 \end{bmatrix} \begin{bmatrix} ref \\ u \end{bmatrix}.$$

$$\begin{bmatrix} z_1 \\ z_2 \\ z_3 \\ e \end{bmatrix} = \begin{bmatrix} 0 & C_y & 0 & 0 \\ 0 & 0 & C_e & 0 \\ 0 & 0 & 0 & C_u \\ -C_p & 0 & 0 & 0 \end{bmatrix} \begin{bmatrix} x_p \\ x_y \\ x_e \\ x_u \end{bmatrix} \quad (40)$$

$$+ \begin{bmatrix} 0 & 0 \\ 0 & 0 \\ 0 & 0 \\ 1 & 0 \end{bmatrix} \begin{bmatrix} ref \\ u \end{bmatrix}.$$

where A_p, B_p, C_p are the state-space model of the linearized model. The open-loop generalized plant model with a new state vector is then written with the following state-space equation

$$\begin{aligned} \dot{\tilde{x}}(t) &= A\tilde{x}(t) + B_1 w(t) + B_2 u(t) \\ z(t) &= C_1 \tilde{x}(t) + D_{11} w(t) + D_{12} u(t) \\ y(t) &= C_2 \tilde{x}(t) + D_{21} w(t) + D_{22} u(t) \end{aligned} \quad (41)$$

with $A \in \mathbb{R}^{n \times n}$, $B_1 \in \mathbb{R}^{n \times n_w}$, $B_2 \in \mathbb{R}^{n \times n_u}$, $C_1 \in \mathbb{R}^{n_z \times n}$, $D_{11} \in \mathbb{R}^{n_z \times n_w}$, $D_{12} \in \mathbb{R}^{n_z \times n_u}$, $C_2 \in \mathbb{R}^{n_y \times n}$, $D_{21} \in \mathbb{R}^{n_y \times n_w}$, $D_{22} \in \mathbb{R}^{n_y \times n_u}$. Here, $n = 7$, $n_y = 1$, $n_u = 1$, $n_z = 3$, $n_w = 1$.

We aim to design a dynamic output-feedback controller in the form of

$$\begin{aligned} \dot{x}_c(t) &= A_c x_c(t) + B_c y(t) \\ u(t) &= C_c x_c(t) + D_c y(t) \end{aligned} \quad (42)$$

where $x_c(t) \in \mathbb{R}^n$ is the state of the controller with $A_c \in \mathbb{R}^{n \times n}$, $B_c \in \mathbb{R}^{n \times n_y}$, $C_c \in \mathbb{R}^{n_u \times n}$, and $D_c \in \mathbb{R}^{n_u \times n_y}$. The following theorem is used to construct the output-feedback control gains in terms of a set of LMIs solution.

Theorem [15]: Given the open – loop LFT system governed by (41). Suppose that there exists two symmetric matrices \mathbf{X} , \mathbf{Y} and four data matrices $\hat{\mathbf{A}}$, $\hat{\mathbf{B}}$, $\hat{\mathbf{C}}$ and $\hat{\mathbf{D}}$. The following LMIs give the controller matrices.

$$\begin{bmatrix} \mathbf{X}\mathbf{A} + \hat{\mathbf{B}}\mathbf{C}_2 + (*) & * \\ \hat{\mathbf{A}}^T + \mathbf{A} + \mathbf{B}_2 \hat{\mathbf{D}}\mathbf{C}_2 & \mathbf{A}\mathbf{Y} + \mathbf{B}_2 \hat{\mathbf{C}} + (*) \\ (\mathbf{X}\mathbf{B}_1 + \hat{\mathbf{B}}\mathbf{D}_{21})^T & (\mathbf{B}_1 + \mathbf{B}_2 \hat{\mathbf{D}}\mathbf{D}_{21})^T \\ \mathbf{C}_1 + \mathbf{D}_{12} \hat{\mathbf{D}}\mathbf{C}_2 & \mathbf{C}_1 \mathbf{Y} + \mathbf{D}_{12} \hat{\mathbf{C}} \\ * & * \\ * & * \\ -\gamma I_{n_w \times n_w} & * \\ \mathbf{D}_{11} + \mathbf{D}_{12} \hat{\mathbf{D}}\mathbf{D}_{21} & -\gamma I_{n_z \times n_z} \end{bmatrix} < 0, \quad (43)$$

$$\begin{bmatrix} \mathbf{X} & I_{n \times n} \\ I_{n \times n} & \mathbf{Y} \end{bmatrix} > 0. \quad (44)$$

(*) denotes being symmetric. Then, there exist a controller such that

- i) the closed-loop system is stable
- ii) the induced L_2 -norm of the operator $w \rightarrow z$ is bounded by $\gamma > 0$ (i.e., $\|T_{zw}\|_{i,2} < \gamma$)

Once matrices \mathbf{X} , \mathbf{Y} , $\hat{\mathbf{A}}$, $\hat{\mathbf{B}}$, $\hat{\mathbf{C}}$ and $\hat{\mathbf{D}}$ matrices obtained, the controller matrices are computed in the following steps:

- 1) Solve for \mathbf{N} , \mathbf{M} , the factorization problem $\mathbf{I} - \mathbf{X}\mathbf{Y} = \mathbf{N}\mathbf{M}^T$. (45)

Here, we choose $\mathbf{N} := \mathbf{I} - \mathbf{X}\mathbf{Y}$, $\mathbf{M} := \mathbf{I}$.

2) Compute A_c, B_c, C_c and D_c with

$$A_c = N^{-1}(\hat{A} - \mathbf{X}(A - B_2\hat{D}C_2)\mathbf{Y} - \hat{B}C_2\mathbf{Y} - \mathbf{X}B_2\hat{C})M^{-T}, \quad (46)$$

$$B_c = N^{-1}(\hat{B} - \mathbf{X}B_2\hat{D}), \quad (47)$$

$$C_c = (\hat{C} - \hat{D}C_2\mathbf{Y})M^{-T}, \quad (48)$$

$$D_c = \hat{D}. \quad (49)$$

Then the found controller matrices by LMI Control Toolbox of MATLAB are

$$A_c = \begin{bmatrix} -0.176 & 15.8 & 267 & 97 \\ -2.333 & -2.265 & -21.99 & -7.998 \\ -0.347 & 1.11 & -12.42 & -1.621 \\ 0.0802 & -0.274 & 32.788 & -6.184 \\ 0.0006 & -0.027 & 0.328 & -0.0515 \\ 0.0045 & -0.002 & -0.031 & -0.024 \\ -0.0080 & 0.0335 & -382 & -0.0418 \\ & 13.14 & -9702 & -32501 \\ & -1.101 & 799.1 & 2687.4 \\ & -0.286 & 219.82 & 738.541 \\ & -0.357 & 254.1 & 853.5 \\ & -1.052 & 2.662 & 9.047 \\ & -0.0027 & -6.57 & -21.26 \\ & -0.075 & -3.38 & -10.19 \end{bmatrix},$$

$$B_c = \begin{bmatrix} -0.0004 \\ -0.0073 \\ -10.8287 \\ 67.7571 \\ 0.670 \\ 0.3438 \\ -0.967 \end{bmatrix},$$

$$C_c = [0.962 \quad -17.32 \quad -291.1 \quad 105.8 \quad -14.628 \quad 10581 \quad 35549.5],$$

$$D_c = [-0.0003 \ 0.05].$$

LMI methods have been successfully implemented in the control field in the last decades. The interior-point optimization solver gives the optimal values for controller matrices so that the desired specifications are met. In the above problem, the minimization problem is computed with MATLAB's LMI Toolbox [16] using MATLAB 2018a, and optimal disturbance attenuation value i.e., energy-to-energy norm γ is found as 1.41871. The desired circular reference circle radius is 250 mm and the side length of the square shape reference is set to 500 mm, centered at the origin. Note that the same controller is applied for both x axis and y axis to regulate the ball's position. The obtained results show that the controller design with the LMI approach gives perfect tracking. Notice that the circular trajectory performance in Figure 4 is acceptable whereas the square case possesses significant performance deterioration for square reference in Figure 5.

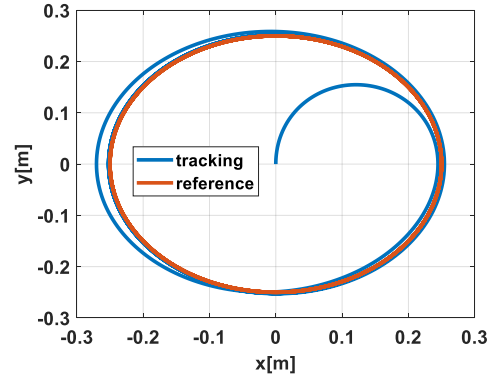


Figure 4. Circular trajectory tracking performance of PID controller.

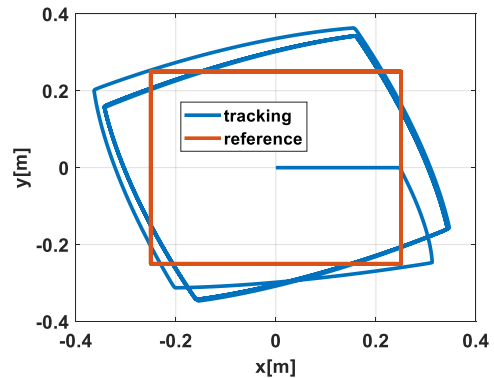


Figure 5. Square trajectory tracking performance of PID controller.

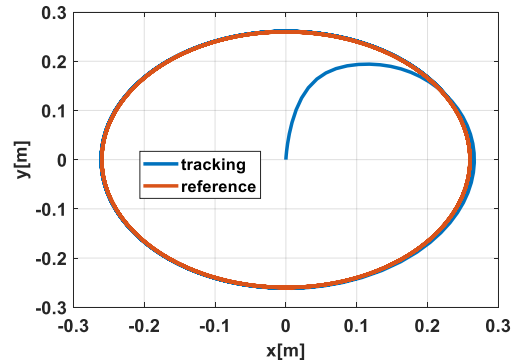


Figure 6. Circular trajectory tracking performance of H_∞ controller.

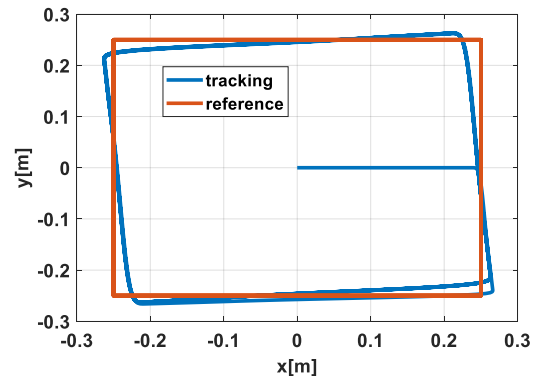


Figure 7. Square trajectory tracking performance of H_∞ controller.

H_∞ controller trajectory tracking of the circular reference from the origin (0,0) of the ball is seen in Figure 6. The tracking problem to make the ball follow the squared path is observed in Figure 7. The ball starts following the reference paths in less than 2 seconds i.e., settling time is less than 2 seconds. To sum up, tracking the references results demonstrate the effectiveness of the proposed solution.

3.4. Performance analysis

The desire of assessing the performance of the controllers is essential due to the need of a reliable and effective application. The closed-loop performance of a control system is measured based on a performance index. Performance index-based analysis is one of the commonly used methods to test whether design requirements are met. To this end, the closed-loop tracking performance of the designed control system is measured with three different performance indices for reference tracking error (of the derived PID and H_∞ controls). The performance indices are:

Integral of the squared value of the error (ISE):

$$ISE = \int_0^\infty e(t)^2 dt. \quad (50)$$

Integral of the absolute value of the error (IAE):

$$IAE = \int_0^\infty |e(t)| dt. \quad (51)$$

Integral of the time-absolute value of the error (ITAE):

$$ITAE = \int_0^\infty t|e(t)| dt. \quad (52)$$

Table 1. Performance comparison of both controllers

Ind.	PID/circ.	PID/sq	H_∞ /circ.	H_∞ /sq.
ISE	1.193	2.5	0.8551	1.466
IAE	6.165	10	5.238	7.157
ITAE	126.6	200	105.8	143.9

Each of these indices is calculated over an interval of time. The simulation is run for 40 seconds. A performance index is a quantitative measure of the performance of a system, thus it is important to determine system specifications i.e., settling time, rise time, peak overshoot and steady-state performance. The steady-state tracking error is vital in our analysis and it is desired to be zero. To quantitatively compare the both controllers' tracking performance for both references, Table 1 is reported. For instance, the ISE index for PID control is obtained as 1.193 while it is 0.8551 for H_∞ controller in circular trajectory case. It

is observed from simulations that since the following square shape reference is a hard task, the tracking performance is deteriorated, proven by numbers. ISE index for PID control is obtained as 2.5 while it is 1.466 for H_∞ controller in square trajectory. Regardless of the tracking shapes and types of performance index, H_∞ controller outperforms.

4. Conclusions

The plate and ball system presents several difficulties in terms of stabilization and control design. This work presents a trajectory tracking control problem for the plate and ball system. We derived the nonlinear model and linearized the plate and ball system that imposes restrictions on the control design step. We use a variety of modern controller design tools to handle the design difficulties. A dynamic output-feedback H_∞ controller is then employed for the presented system based on the solution of linear matrix inequalities. Moreover, the trajectory following performance of the proposed controller is compared with a PID controller to better understand the improvements. It is shown from the simulations that H_∞ controller outperforms on tracking the state variables for both circular and square references.

Acknowledgment

The author thank the anonymous contributors for both conceptual and technical insights.

Conflict of interest

The author declares no conflict of interest.

References

- [1] Dušek F., Honc D. and Sharma K.R. Modelling of ball and plate system based on first principle model and optimal control. *21st International Conference on Process Control (PC)*, (2017) 216-221.
- [2] Knuplez A., Chowdhury A. and Svecko R. Modeling and control design for the ball and plate system. *IEEE International Conference on Industrial Technology*, (2003) 1064-1067.
- [3] Dong X., Zhang Z. and Chen C. Applying genetic algorithm to on-line updated PID neural network controllers for ball and plate system. *Fourth International Conference on Innovative Computing, Information and Control (ICICIC)*, (2009) 751-755.
- [4] Liu H., Liang Y., Trajectory tracking sliding mode control of ball and plate system. *2nd International Asia Conference on Informatics in Control, Automation and Robotics*, (2010) 142-145.

- [5] Liu D., Tian Y. and Duan H. Ball and plate control system based on sliding mode control with uncertain items observe compensation. *IEEE International Conference on Intelligent Computing and Intelligent Systems*, 2 (2009) 216-221.
- [6] Hongrui W., Yantao T., Siyan F. and Zhen S. Nonlinear control for output regulation of ball and plate system. *27th Chinese Control Conference*, (2008) 382-387.
- [7] Hauser J., Sastry S. and Kokotovic P. Nonlinear control via approximate input-output linearization: The ball and beam example. *IEEE Transactions on Automatic Control*, 37(3) (1992) 392-398.
- [8] Yıldız H. A., Gören-Sümer L., Stabilizing of ball and plate system using an approximate model. *IFAC-PapersOnLine*, 50(1) (2017) 9601-9606.
- [9] Bang H., Lee Y. S., Implementation of a ball and plate control system using sliding mode control. *IEEE Access*, 6 (2018) 32401-32408.
- [10] Mohammadi A., Ryu J. C., Neural network-based PID compensation for nonlinear systems: ball-on-plate example. *International Journal of Dynamics and Control*, 8 (2020) 178-188.
- [11] Umar A., Haruna Z., Musa U., Mohammed S. A., and Muyideen M. O. Graphical user interface (GUI) for position and trajectory tracking control of the ball and plate system using H-infinity controller. *Covenant Journal of Informatics and Communication Technology*, 7(1) (2019) 35-56.
- [12] Ghiasi A.R., Jafari H., Optimal robust controller design for the ball and plate system. *9th International Conference on Electronics Computer and Computation*, ICECCO-2012.
- [13] Geng L., Yang Z., and Zhang Y. A weighting function design method for the H-infinity loop-shaping design procedure. *Chinese Control And Decision Conference (CCDC)*, (2018) 4489-4493.
- [14] Bolívar-Vincenty C. G., Beauchamp-Báez G., Modelling the ball-and-beam system from newtonian mechanics and from lagrange methods. *Twelfth LACCEI Latin American and Caribbean Conference for Engineering and Technology*, (2014) 22-24.
- [15] Apkarian P., Adams R.J., Advanced gain-scheduling techniques for uncertain systems. *IEEE Transactions on Control Systems Technology*, 6(1) (1998) 21-32.

Post-op bore profile estimation of workpiece clamped using three-jaw chuck

Fatih GÜVEN 

Hacettepe University, Başkent OSB Vocational School of Technical Sciences, Department of Machinery and Metal Technology, Ankara, Turkey

Abstract

Estimating bore profile is important to select an appropriate tool for precision manufacturing in the process planning stage. Also, it helps in reducing the rejection rate of the process. A manufacturer might not be well-equipped and want to make their best with the resource on hand. Three-jaw chuck allows machining a wide range of workpiece, mostly circular parts in a lathe. However, clamping via a three-jaw chuck distorts the workpiece. In this study, the deformation of the bore profile was investigated numerically for circular parts. Finite element analyses were performed to examine dimensional variation for various materials and different wall thicknesses under fully elastic plane stress conditions. The stressed workpiece had a triangular form. Results showed that wall thickness and materials are important parameters on the triangulation of bore diameter. A simple calculation method based on thick-walled vessel theory was proposed to estimate the tolerance grade of the workpiece. This simple method provides the opportunity to reduce the rejection rate in the mass production of circular parts.

Article info

History:

Received:14.01.2020

Accepted:10.04.2020

Keywords:

Fit,
Cutting,
Machining,
Precision,
Tolerance.

1. Introduction

Machine elements need clearance between mating surfaces of parts in interaction. Form and dimensional tolerances are very important in shrink fits, bush, ball bearings, and plain bearings. In machinery, the workpiece has to be clamped because of the safety issue, however, clamping a workpiece causes its deformation nearby fixture and machining this localized stress zone could yield inaccuracy of dimensions [1]. This phenomenon could cause unbalanced stresses in machine elements such as a shrink fitted hub [2].

Circular parts are mostly clamped via three-jaw chuck for a drilling or a reaming operation. A certain clamping force is needed to fasten the workpiece during operation. During machining operation cutting force, F_c , produces a moment which is resisted by a frictional moment. This moment is a function of the friction coefficient between jaw and workpiece, μ_g , and the clamping force, F_g , needed.

$$F_g = \frac{F_c \cdot S_k}{\mu_g} \cdot \frac{d_m}{d_g} \quad (1)$$

where d_m is the machining diameter, d_g is the clamping diameter, and S_k is the safety factor. The cutting force is the multiplication of the specific cutting force k_c and the cross-sectional area of the chip. The chipping section could be easily calculated using feed rate, f and cutting depth, a .

$$F_c = f \cdot a \cdot k_c \quad (2)$$

This basic formulation is the basis of clamping, however, additional forces come out during machining operation such as centrifugal force, thermal forces, and frictional forces. Besides, clamping force losses are so important for both the accuracy of the process and its safety. Reducing clamping force may contribute to machining accuracy for a thin-walled workpiece in particular [3]. However, the insufficient clamping force could result in the loosening of the workpiece during operation due to centrifugal forces on jaws. It should be noted that clamping system failure could cause serious accidents in manufacturing. The clamping force also causes the deformation of the workpiece elastically or plastically. The bore diameter becomes smaller than its actual size under force and is to return its original diameter after discharging the

clamping force. However, circular parts are no longer round when clamped via three-jaw chuck. Rahman [4] studied a tapered workpiece experimentally and concluded that the workpiece was a triangle from after machining. Brinksmeier et. al. [5] have shown that clamping an elastic ring via chuck leads to a variation of the cutting depth and polygonal form deviations could be observed. Kessler et. al. [6] have measured the out-of-roundness of a circular workpiece and stated that changes could extend up to $60\text{ }\mu\text{m}$. The deformation depends on workpieces' and jaws stiffness as Malluck and Melkote [7] showed. The stiffness of these components also affects dynamic clamping force in high-speed turning [3]. Estrems et. al [8, 9] have investigated the deformation of rings made of aluminum both experimentally and numerically and proposed a mathematical model to calculate total deformation. In another study, Estrems et. al [10] have argued the effect of friction coefficient on clamping force and shape deviation. Bajpai [11] has proposed a diagram concerning the ratio of length to diameter to optimize workpiece size. Length is another parameter for the accuracy of workpiece tolerances. Maračková et. al [12] have examined out-of-roundness of workpieces' open-end showed that clamping force may not affect the open end of the clamped workpiece according to the distance between open-end and chuck jaws. Similarly, Görög and Görögová [13] have examined out-of-roundness of the workpiece along the length of the part and showed the variation in roundness throughout the part length. In this case, it should be kept in mind that other form tolerances are needed due to the discrepancy between the two ends of the workpiece. Shawky et al. [14] have devised ultrasonic sensors to measure thickness variation of part during machining. Beekhuis et al. [15] proposed a method based on controlling the cutting depth of the clamped thin-walled part. Stöbener and Beekhuis [16] have applied an in-situ ultrasonic measuring system to compensates wall thickness variations during turning operations. These methods could reduce wall thickness variation of parts clamped inside, nevertheless, clamping parts outside could prevent accurate measurement of wall thickness due to jaws. Also, one can argue that using mandrel chucks could prevent the triangulation of the workpiece. Nevertheless, the operator needs a wide range of chucks due to the adherence of chuck to a specific dimension.

This study aims to provide a simple calculation method to estimate the degree of deformation due to clamping via tree-jaw chuck to reduce the rejection rate in mass production. In this study, the deformation of the bore profile was investigated numerically for various

materials and different wall thicknesses under fully elastic plane stress conditions to reveal the relation between the triangulation of bore and the material and size of the part machined. A series of finite element analyses were performed to study the relation between dimensional variations and chuck press. A simple calculation method was proposed to estimate the tolerance grade of the workpiece. This simple method provides the opportunity to reduce the rejection rate in the mass production of circular parts.

2. Material and Methods

A series of finite element analyses were performed to investigate the bore profile of the workpiece clamped using a three-jaw chuck. The dimensions of the sample workpiece could be seen in Figure 1.

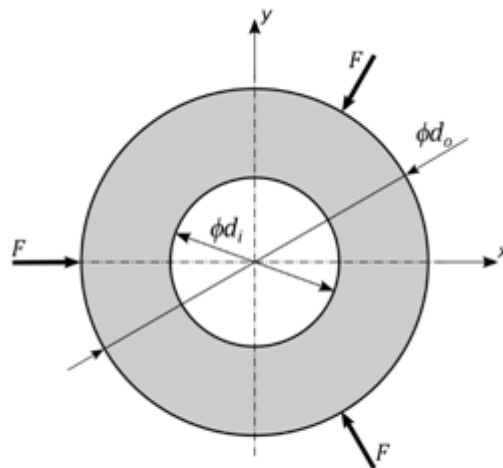


Figure 1. Dimension of workpiece

In the figure, the workpiece with an inner diameter of d_i and an outer diameter of d_o was subject to a force of F on three equidistant points. Cyclic symmetry boundary conditions (frictionless support) were applied on low and high-end of the one-third model as shown in Figure 2. The low end and high end of the model are coincident with the x-axis and the relative direction with an angle of 60° from clamping force, respectively. The model was generated using two-dimensional 8-noded quadrilateral elements with thickness options. It consisted of 2769 nodes and 880 elements smaller than 1 mm. The degrees of freedom of the nodes on symmetry lines were equals to zero for the θ axis in cylindrical coordinate system. Considering the nature of jaw and part in contact, the clamping force applied as a distributed load of 260 N/mm^2 on an arc with a length of 4 mm. The

boundary conditions, applied loads and meshed the model are seen in Figure 2.

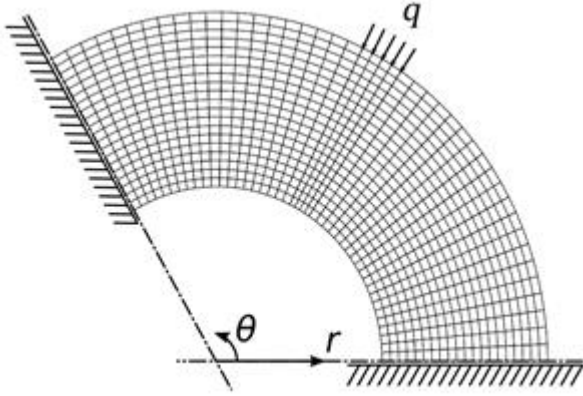


Figure 2. Cyclic sector model of workpiece.

Table 1. elastic properties of materials

Material	Young's Modulus, E (GPa)	Poisson ratio, ν
Steel (cold-rolled)	203	0.287
Bronze (70-30)	109	0.331
Aluminum (6061-T6)	70.0	0.350
Magnesium	44.8	0.350

The deformation of the bore profile was investigated for various materials and different wall thicknesses under fully elastic plane stress conditions. Elastic properties of materials used here are given in Table 1 [17]. The effect of material was examined on samples with a bore diameter of 20 mm, an outer diameter of 40 mm, and a thickness of 10 mm. All other things being equal, only the outer diameter of the workpiece was altered to examine the wall thickness ratio in a range from 0.30 to 0.50.

A negative change in dimension, i.e. the shrinkage of bore, yields an extra amount of chip and a positive change has a reverse situation. When the bore with a diameter of D_b is machined, an amount of material, say S , will be removed, intentionally. After the operation, bore extends to a finishing diameter of D_f as given in Eq. (3). However, the clamping force causes shrinkage of the workpiece and the cutting tool removes an additional chip with a thickness of Δs . When the clamping force is loosened, the dimension of bore extends up to $D_f + \Delta d$ as seen in Eq. (4). It would not be wrong to assume that pre-op shrinkage of bore equals to post-op relaxation of it under fully elastic strain assumption (Eq. (5)).

$$D_b + S = D_f \quad (3)$$

$$(D_b - \Delta s) + S = D_f + \Delta d \quad (4)$$

$$-\Delta s = \Delta d \quad (5)$$

All results are based on this assumption and dimensional variations are gathered in the cylindrical coordinate system. It should be noted that the shrinkage would not be equal throughout the bore diameter since the chuck subjects force on a limited area.

2.1. Verification of model

The aim of the study is figuring out a simple coefficient to estimate the bore profile by modifying known equations. We know the equations governing the fully-pressurized thick-walled vessels. From this point of view, a partially pressurized cylindrical could be calculated by using a modified version of the equation used for fully-pressurized one.

The model has been verified using the formula for a pressurized thick-walled cylinder subjected to constant external pressure. The deformation of a cylindrical vessel is computed using well-known Lamé's Equation. There is no radial stress at the inside of this kind of vessels when pressed at outside and tangential stress, σ_θ , governs the deformation [18].

$$\sigma_\theta = -2p \frac{d_o^2}{d_o^2 - d_i^2} \quad (6)$$

We define the ratio inner diameter to outer diameter denoted as q and rearrange the Equation (6):

$$\sigma_\theta = \frac{-2p}{1 - q^2}; \quad q = \frac{d_i}{d_o} \quad (7)$$

From Hooke's law, dimensional variation, Δd , could be found easily. Substituting into the equation above yields:

$$\Delta d = d \cdot \varepsilon = \frac{d}{E} (\sigma_r - \nu \sigma_\theta) \quad (8)$$

In this study, constant pressure of $p = 260 \text{ N/mm}^2$ was applied to the whole outside diameter of the model to verify the analysis. The finite element analysis showed good agreement with the calculation (Figure

3). The internal tangential stress, σ_θ , was equal to 693.21 N/mm^2 where the calculated was 693.33 N/mm^2 (relative error 0.017%) for the elastic parameters of steel.

3. Results and Discussion

The jaws apply the pressure on contacting the surface of the workpiece and this yields

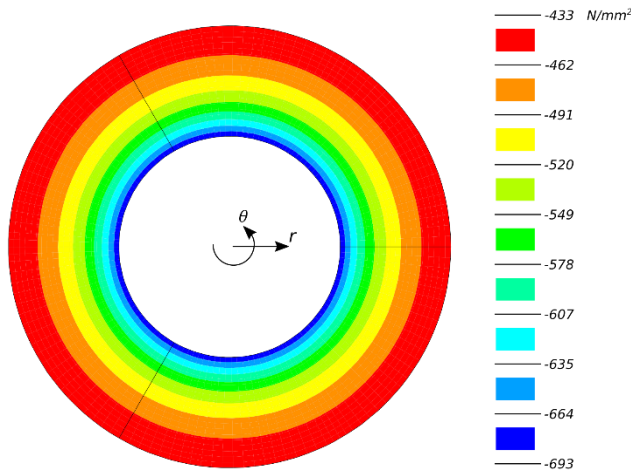


Figure 3. Tangential stress distribution of model under fully-presurized condition.

the clamping force F which holds the workpiece to prevent any convenience during machining operation and stresses the workpiece clutched. The distribution of tangential stresses of the gripped workpiece is shown in Figure 4. The workpiece deforms under this stresses intrinsically. It can be clearly seen that the bore diameter of the workpiece remains elastic under a clamping force of $q = 260 \text{ N/mm}^2$ on the contact area (A) for the materials investigated in this paper. So, the equations are valid for the results presented in this section.

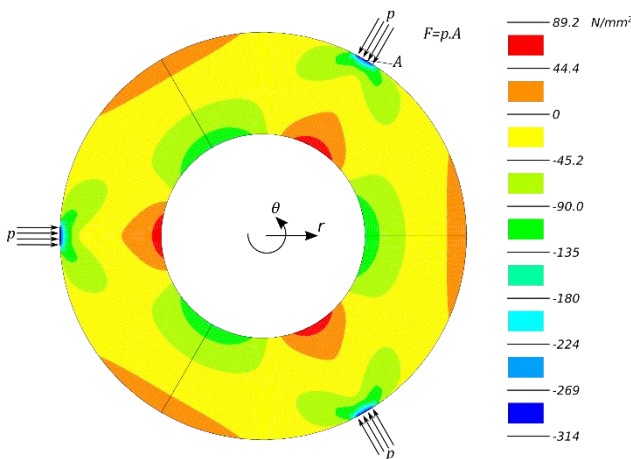


Figure 4. Tangential stress distribution of model under partially-resurized condition.

An exaggerated bore diameter profile of the workpiece made of steel is shown in Figure 5. As shown in the figure, the bore diameter of the clutched workpiece seems triangle. The operation with a circular tool removes an amount of substance that the sum of given chip thickness and displaced material as mentioned earlier. After loosening the workpiece, the bore diameter of the workpiece will expand due to relaxation. For steel material, the biggest size of the bore is $12.7 \mu\text{m}$ greater than the smallest one under given conditions. The overstraining of the workpiece for clamping would affect die tolerance of bore. It stands out in the figure that the size of the bore gets its maximum value in the direction of the clamping force applied. Similarly, its minimum value is in a direction coincident with the symmetry line that has a relative angle of 60° to the clamping force direction.

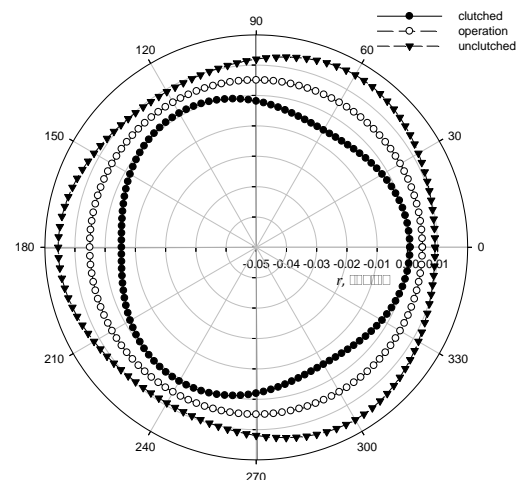


Figure 5. Deformation of bore diameter of steel workpiece before and after clamping.

The degree of deformation depends on the elastic properties of workpiece material. Figure 6 shows post-op bore profiles of unclamped workpieces for different kinds of materials. It could be clearly seen that material plays an important role in the profile of bore. The triangulation of bore is considerably affected by Young's modulus of material. The biggest dimension of the bore is $12.7 \mu\text{m}$, $24.6 \mu\text{m}$, $38.2 \mu\text{m}$ and $59.8 \mu\text{m}$ for steel, bronze, aluminum, and magnesium, respectively. On the contrary, the clamping force direction, the bore size of the clamped workpiece is slightly greater than the free diameter of the bore. This variation and the triangulation of circle become prominent along with a decrease in Young's modulus. It could be concluded that the workpiece made of magnesium, the substance with the smallest Young's modulus among material investigated here, could not be functional under mid- and high-tolerance class.

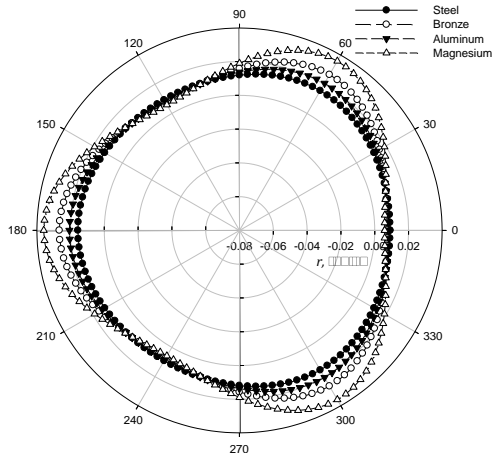


Figure 6. Profile of bore diameter for different materials.

Another parameter investigated here is the ratio of wall thickness to bore diameter (s/d_i). As known, pressure vessels categorized into thin-walled and thick-walled regarding the ratio of wall thickness to bore diameter. This categorization specifies the formulae used for stress calculations in pressure vessels. As a sample, Figure 7 shows the post-op profiles of the unclamped workpiece made of aluminum. Similar to the pressure vessel, the ratio of wall thickness to bore diameter, the ratio affects the degradation level of the bore. As shown in the figure, the biggest size of the bore is $38.2 \mu\text{m}$, $43.4 \mu\text{m}$, $50.6 \mu\text{m}$, $61.1 \mu\text{m}$ and $77.5 \mu\text{m}$ for the s/d_i ratio of 0.30, 0.35, 0.40, 0.45 and 0.50, respectively. This means that the thinner the wall, the more the degradation under pressure. Also, the biggest dimension occurs in the clamping force direction inherently. As mentioned before, the dimension of bore gets bigger when the workpiece clamped. So, the realized bore dimension in the direction coincident with the symmetry line would be smaller than the expected value.

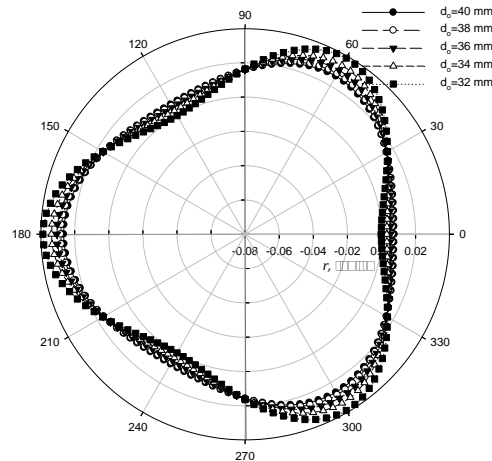


Figure 7. Profile of bore diameter of aluminum workpiece for different Wall thickness.

In machinery, form and dimensional tolerances are specified for a workpiece to be fitted. The degradation level should be within the specified tolerance limit. The dimensional deviations of investigated samples and their corresponding tolerance grade [19] with its value in brackets are seen in Table 2. While circular form tolerance would not pose a problem for steel, a fit part made of aluminum or a material with a similar Young's modulus should be studied carefully. Dimensional tolerances could be challenging in the manufacturing process of fit parts. As known, the lower the grade of tolerance, the more precise the part. A manufactured part that out of tolerance limit could not be functional upon design purpose and ends up as rejected part. Dimensions of parts examined in this paper vary in a wide range. This deviation is not desired for shrink-fitted joint in particular. The reason is that this joint transmits torque from a shaft to a hub, or vice versa, based on frictional force owing to contact pressure between mating surfaces. The clearance of fit designates the contact pressure and consequently the torque to be transmitted. Excessive contact pressure

Table 2. Categorization of post-op dimensions into tolerance classes

Sample		Dimensional deviations (μm)			Tolerance grade (μm)	
Material	s/d_i	SLD	FD	Δd	Form*	Dimension
Steel	0.50	-1.78	11.0	12.7	R (10)	IT7 (22)
Bronze		-3.42	21.1	24.6	S (20)	IT9 (36)
Aluminum		-5.33	32.9	38.2	S (20)	IT10 (58)
Magnesium		-8.32	51.4	59.8	T (60)	IT11 (90)
		-5.33	32.9	38.2	S (20)	IT10 (58)
Aluminum	0.45	-7.20	36.2	43.4	T (60)	IT10 (58)
	0.40	-9.86	40.8	50.6	T (60)	IT10 (58)
	0.35	-13.9	47.3	61.1	T (60)	IT11 (90)
	0.30	-20.3	57.2	77.5	T (60)	IT11 (90)

SLD: Symmetry line direction

FD: Gripping force direction

* Form tolerance $t = \Delta d/2$

could damage parts fitted [20, 21]. So, shrink fitted parts should be manufactured precisely.

Figure 8 shows the correlation between partially pressurized and fully pressurized parts. The maximum dimension of the partially pressurized part is smaller than the fully pressurized one. A correction factor would be useful to estimate the maximum size of the bore. In this situation, the correction factor equals to 0.2 for the same dimensions and different materials. In the figure, it can be clearly seen that wall-thickness is another important parameter to estimate the maximum bore dimension as stated earlier.

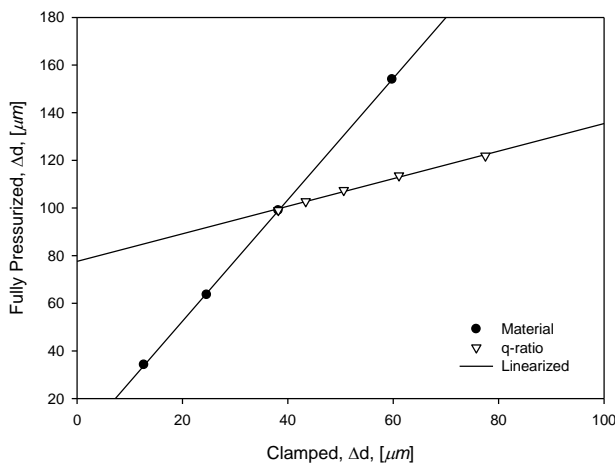


Figure 8. Correlaiton between dimensional variations for partially pressurized and fully pressurized parts.

For thin-walled workpieces, using thin-walled pressurized vessel formula is a more convenient way to calculate deformation rather than using the thickness factor described here. When implementing the correction factor, k_{cr} , and the thickness factor, k_t , in Eq. (8), it yields:

$$\Delta d = \frac{k_{tf} k_{cf} d}{E} (\sigma_r - \nu \sigma_\theta) \quad (9)$$

Eq. (9) allows estimating the maximum dimension of the bore and the tolerance class in which it belongs. The proposed factor should be verified experimentally and could be expanded for further use. This study does not consider residual and thermal stresses caused by the manufacturing process that could also affect the out-of-roundness of the workpiece [22, 23]. The thermal expansion could be neglected under proper cooling conditions. It should be kept in mind that diameter measurement might be erroneous due to the triangulation of part via a linear inside micrometer. The minimum and maximum sizes given in this paper were

accepted as twice the radius assuming that measurements would be gathered using a self-centering inside micrometer.

4. Conclusions

In this paper, two important parameters were studied numerically in order to reduce the rejection rate of the manufacturing process. All results considered, the main conclusion could be drawn as follows:

- The bore profile of the workpiece could be estimated by using the modified formula suggested in this paper.
- Young's modulus affects significantly deformation level of clamped parts. The lower Young's modulus, the more the deformation of the bore. Materials with a low Young's modulus could be out of tolerance limit when clamped by three-jaw chuck. For precise machining, other types of clamping should be considered.
- Another parameter investigated here is the ratio of wall thickness to bore diameter (s/d_i). Thin-walled workpieces are more prone to deformity. Avoiding from overstraining of parts could be useful to improve the quality grade.
- Generally, to reduce the rejection rate and improve the quality grade of dimension with the same equipment, the clamping force should be carefully applied.
- Even if circular form tolerance is acceptable, dimensional tolerance could be still raw. It is not seen possible to achieve high-quality grade (low number) using a three-jaw chuck. The correction factors recommended in this paper should help engineers to estimate bore dimension tolerances.
- From a viewpoint of mass production, a non-controllable clamping force could be responsible for the variation of dimensions among workpiece manufactured under the same circumstances.
- The present study applies clamping force throughout the length of the workpiece. For long parts, clamping force only affects the dimensions of the chuck side. Tolerances of part at free end would vary depending on other manufacturing conditions such as runout.

Nomenclature

a	: Cutting depth
A	: The area of contact
d_g	: Gripping diameter
d_i	: The inner diameter of cylindrical part
d_m	: Machining diameter
d_o	: The outer diameter of cylindrical part
D_b	: The initial bore diameter of workpiece
D_f	: The final bore diameter of workpiece
E	: Young's modulus
f	: Feed rate
F	: Force
F_c	: Cutting force
F_g	: Gripping force
k_c	: Specific cutting force
k_{cf}	: Correction factor
k_{tf}	: Thickness factor
s	: The wall thickness of cylindrical parts
S	: The material machined
S_k	: Safety factor
p	: Pressure
q	: The ratio outer diameter to inner diameter
r	: indicates the radial axis
Δd	: Dimensional variation
Δs	: Additional chip thickness
μ_g	: The friction coefficient between workpiece and jaws
θ	: indicates the tangential axis
σ_θ	: Tangential stress

References

- [1] Li B., Melkote S.N., Fixture clamping force optimisation and its impact on workpiece location accuracy. *Int J Adv Manuf Technol.* 17 (2001) 104–113.
- [2] Güven F., Contact Pressure Losses in Shrink Fitted Assembly Due to Triangular Hub Form. In: 5th International Conference on Advances in Mechanical Engineering. İstanbul (2019) 950–955.
- [3] Feng P.F., Yu D.W., Wu Z.J. and Uhlmann E., Jaw-chuck stiffness and its influence on dynamic clamping force during high-speed turning. *Int. J Mach. Tools Manuf.* 48 (2008) 1268–1275.
- [4] Rahman M., Factors affecting the machining accuracy of a chucked workpiece. *Precis. Eng.* 8 (1986) 34–40.
- [5] Brinksmeier E., Sölter J. and Grate C., Distortion engineering - identification of causes for dimensional and form deviations of bearing rings. *CIRP Ann. – Manuf. Technol.* 56 (2007) 109–112.
- [6] Kessler O., Prinz C., Sackmann T., Nowag L., Surm H., Frerichs F., Lübken Th. and Zoch W., Experimental Study of Distortion Phenomena in Manufacturing Chains. *Mat.-wiss. u. Werkstofftech.*, 37 (2006) 11–18. DOI: 10.1002/mawe.200500975.
- [7] Malluck J.A., Melkote S.N., Modeling of Deformation of Ring Shaped Workpieces Due to Chucking and Cutting Forces. *J. Manuf. Sci. Eng.* Feb 126(1) (2004) 141–147
- [8] Estrems M., Arizmendi M., Cumbicus W.E. and López A., Measurement of Clamping Forces in a 3 Jaw Chuck through an Instrumented Aluminium Ring. *Procedia Eng.* 132 (2015) 456–463.
- [9] Estrems M., Arizmendi M., Zabaleta A.J., and Gil A., Numerical Method to Calculate the Deformation of Thin Rings during Turning Operation and its Influence on the Roundness Tolerance. *Procedia Eng.* 132 (2015) 872–879.
- [10] Estrems M., Carrero-Blanco J., Cumbicus W.E., de Francisco O. and Sánchez H.T., Contact mechanics applied to the machining of thin rings. *Procedia Manuf.* 13 (2017) 655–662.
- [11] Bajpai S., Optimization of workpiece size for turning accurate cylindrical parts. *Int J Mach. Tool Des. Res.* 12 (1972) 221–228.
- [12] Maračeková M., Zvončan M. and Görög A. Effect of clamping pressure on parts inaccuracy in turning. *Teh. Vjesn.* 19(3) (2012) 509–512.
- [13] Görög A., Görögová I., Research of the Influence of Clamping Forces on the Roundness Deviations of the Pipes Turned Surface. *Res. Pap. Fac. Mater. Sci. Technol. Slovak Univ Technol* 26(42) (2018) 47–54.
- [14] Shawky A., Rosenberger T. and Elbestawi M., In-process monitoring and control of thickness error in machining hollow shafts. *Mechatronics* 8 (1998) 301–322.
- [15] Beekhuis B., Stöbener D. and Brinksmeier E., Adapted Non-Circular Soft Turning of Bearing rings – Impact of process machine interactions on compensation potential. *Procedia CIRP* 1 (2012) 540–545.
- [16] Stöbener D., Beekhuis B., Application of an in situ measuring system for the compensation of wall thickness variations during turning of thin-walled rings. *CIRP Annals* 62(1) (2013) 511–514.
- [17] Jones F.D., Oberg E. and Horton H.L. and Henry H.R., Machinery's handbook 27th Eds. Industrial Press, (2004).
- [18] Schmid S.R., Hamrock B.J. and Jacobson B.O., Fundamentals of machine elements. 3rd ed. Boca Raton: CRC Press, 2013.

- [19] Norm ISO 286-1:2010. Geometrical product specifications (GPS) — ISO code system for tolerances on linear sizes — Part 1: Basis of tolerances, deviations and fits. 2010.
- [20] Güven F., Rende H., Influence of Contact Pressure on Surface Roughness Losses in Shrink Fitted Joints. In: 8th International Advanced Technologies Symposium. (2017) 3115–3119.
- [21] Rende H., Güven F., Sıkı geçme bağlantılarında malzemeye bağlı yüzey pürüzlülüğü kayıp katsayısının belirlenmesi. Mühendis ve Makina 665 (2015) 46–52.
- [22] Volkmuth J., Lane S., Jung M. and Sjöblom U., Uneven residual stresses in bearing rings prior to hardening and their effect on shape changes after hardening. HTM - Haerterei-Technische Mitteilungen. 60 (2005) 317-322.
- [23] Neslušan M., Mrkvica I., Čep R., Kozak D., and Konderla R., Deformations after heat treatment and their influence on cutting process. Teh Vjesn 18 (2011) 601–608.

Speciation of chromium in beverages and seasoning samples by magnetic solid-phase extraction and microsample injection system flame atomic absorption spectrometry

Şükrü Gökhan ELÇİ 

Pamukkale University, Technology Faculty, Biomedical Engineering Department, 20017 Denizli-Turkey

Abstract

In this research, a magnetic solid phase extraction based on the use of magnetic polyaniline-polythiophene copolymer ($\text{Fe}_3\text{O}_4@\text{coPANI-PTH}$) nanoparticles is applied for chromium speciation from water, beverages and seasoning samples followed by microsample injection system-flame atomic absorption spectrometry(MIS-FAAS) analysis. The selective adsorption of Cr(III) in presence of Cr(VI) by $\text{Fe}_3\text{O}_4@\text{coPANI-PTH}$ in the pH range of 9.0-10.5 was obtained and the total Cr, after reduction of chromium(VI) to chromium(III) by adding 0.5 mL of concentrated H_2SO_4 and 10 mL of 5% (w/v) hydroxylamine hydrochloride, was determined. The detection limit, enhancement factor, and repeatability of the optimized method for Cr(III) were calculated to be $1.5 \mu\text{g L}^{-1}$, 38.5, and 1.78%, respectively. The method was validated by the analysis of TMDW-500 drinking water and LGC7162 Strawberry Leaves as certified reference materials. The relative error for total chromium was found to be lower than 4.6%. Recoveries were obtained quantitatively using this method ($\geq 95\%$).

Article info

History:

Received:07.04.2020

Accepted:04.06.2020

Keywords:

$\text{Fe}_3\text{O}_4@\text{coPANI-PTH}$, chromium, speciation, water, beverages.

1. Introduction

Chromium is one of the commonly employed elements in various industries, such as leather, textile, paint, battery, ceramic, glass, metal, catalyst, and fungicide[1,2]. Therefore, large amounts of chromium species are emitted or discharged to the environment as waste. This leads to the pollution of farmlands and the pollution of irrigation and drinking water resources. Then, these species are gradually taken up by plants and they reach the human's body through the food chain.

Chromium is typically found in the environment in two oxidation forms: trivalent chromium, Cr(III), and hexavalent chromium, Cr(VI). The naturally occurring Cr(III) is a less toxic and essential ion for the body and it plays a role in glucose and lipid metabolism[3,4]. While certain amounts of Cr(III) is essential, an excess amount of Cr(III) could create toxicity[3,4]. Then, this toxicity may cause some diseases such as cancer or damage to the nervous system[3,4]. On the contrary, Cr(VI) is highly toxic due to its carcinogenic and mutagenic properties[5,6]. Also, Cr(VI) is highly soluble and mobile in groundwater and surface water that could create problems for human health[7]. Thus,

EPA and WHO recommend the threshold value for total chromium as $100 \mu\text{g L}^{-1}$ and Cr(VI) as $50 \mu\text{g L}^{-1}$ in drinking water, respectively[8,9]. Chromium is mostly found in meat, fruit, vegetables, grains, and legumes. Cr(VI) content in many food samples is less than the content of Cr(III)[10]. Taking into account the potential toxicity of Cr(III) and the high toxicity of Cr(VI), it is important to monitor their concentrations in various samples. In real samples, low concentrations of both chromium ions and the complexity of matrix make the determination of these ions challenging. For this reason, an accurate quantification method including preconcentration/separation procedure is required to develop for speciation studies[11].

It is well known that flame atomic absorption spectrometry(FAAS) is widely used for the determination of the total concentration of a metal ion in aqueous samples. Nevertheless, due to its low sensitivity, this technique is not used directly for the determination of total chromium. Also, it lacks ion selectivity for speciation of the different oxidation states of chromium. For overcoming these problems, the speciation analysis is required by combining FAAS with ion selective preconcentration method. Many chromium speciation methods coupled with FAAS

*Corresponding author. Email address: gelci@pau.edu.tr

<http://dergipark.gov.tr/csj> ©2020 Faculty of Science, Sivas Cumhuriyet University

such as solid phase extraction[12,13], coprecipitation[14,15], cloud point extraction (CPE)[16,17] and dispersive liquid-liquid microextraction (DLLME)[18,19] have been developed to simplify analytical approaches. Among these, solid-phase extraction (SPE) based on column technique is generally found to be a more efficient one with high preconcentration factor, easy automation, and commonly available commercial solid phase materials. However, it has some drawbacks like time consuming processes, relatively complicated operation, and slightly toxic organic solvent use. These drawbacks of conventional SPE technique have been avoided by using nanostructured magnetic adsorbents and nowadays, magnetic solid phase extraction(MSPE) have become more popular in preconcentration studies. The magnetic adsorbents have advantages such as easy preparation procedures, faster adsorption and desorption properties, low-cost, environmental friendliness and high surface area that makes them effective adsorbent in SPE. Additionally, by an external magnetic field, the magnetic adsorbent can be simply removed from the analysis solution that it is added. The core-shell magnetic nanoparticles such as Fe_3O_4 , $\gamma\text{-Fe}_2\text{O}_3$, and some ferrites (MFe_2O_4 (M: Cu, Ni, Mn, Mg, etc.)) can be functionalized with various complexing agents on the particle surface to increase the specificity towards metal ions[20,21,22]. For this purpose, conductive polymers (CPs) with sulfur, oxygen, or nitrogen groups complexing with metal ions are promising for selective preconcentration of heavy metal ions without the need for any complexing agent[21]. Additionally, they are preferred due to their highly stable nature at different pH ranges, nontoxic properties, and rapid synthesis procedures. Various CPs, polyaniline(PANI) [23], polypyrrole(PPY) [24,25], polythiophene (PTH) [26,27] and their derivatives[28] have been applied in removal and preconcentration studies of heavy metal ions. In most of these works, only a single type of polymer is used except in a few examples copolymers such as PPY-PTH, PANI-PPY, and so on are used [29-32]. According to the literature search, there is no report seen on the use of PANI-PTH copolymer coated Fe_3O_4 NPs ($\text{Fe}_3\text{O}_4\text{@coPANI-PTH}$) for chromium speciation.

Herein, I synthesized $\text{Fe}_3\text{O}_4\text{@coPANI-PTH}$ nanoparticles and successfully applied them as a nanosorbent for the MSPE of chromium speciation in real samples. Following the speciation, MIS-FAAS was used for chromium detection.

2. Materials and Methods

2.1. Instrumentation and apparatus

A flame atomic absorption spectrometer (Perkin Elmer AAnalyst 200, Norwalk, CT, USA) equipped with a chromium hollow cathode lamp was used with a handmade microsample injection system (MIS) installed on it. The spectrometer was set as recommended in the manufacturer's manual. The MIS provides acceptable absorbance to be obtained with 100 μL sample volume injected with a micropipette into the spectrometer nebulizer[14]. A pH meter (WTW pH720 model, Weilheim, Germany), a heating magnetic stirrer (Velp Scientifica ARE, Usmate, Italy), and an ultrasonic bath (Ultrasound Bendelin Electronic, Berlin, Germany) were used when necessary. The ultrapure (UP) quality water (resistivity, 18.2 $\text{M}\Omega\text{ cm}^{-1}$) was obtained with the reverse osmosis system (Human Corp., Seoul, Korea).

2.2. Reagents and solutions

All reagents used in this work were at least analytical reagent grade. Ferric chloride ($\text{FeCl}_3 \cdot 6\text{H}_2\text{O}$, Sigma Aldrich, St. Louis, MO, USA), ferrous sulfate ($\text{FeSO}_4 \cdot 7\text{H}_2\text{O}$, Panreac, Barcelona, Spain), aniline and thiophene (analytical grade, Merck, Darmstadt, Germany) were used in the synthesis of $\text{Fe}_3\text{O}_4\text{@coPANI-PTH}$. Nitric acid (65%,v/v), hydrochloric acid (37%,v/v), phosphoric acid (85%), acetic acid(glacial), sodium hydroxide, ammonia solution (25%) were purchased commercially (E. Merck, Darmstadt, Germany). Standard stock solutions of Cr(III) (LGC, Manchester, USA) and Cr(VI) (High Purity, North Charleston, USA) as 1000 mg L^{-1} , were used to prepare the daily test and calibration standard solutions. The pH adjustments of test and sample solutions were carried out using an $\text{H}_2\text{PO}_4^-/\text{H}_3\text{PO}_4$ buffer to pH 2, $\text{CH}_3\text{COO}^-/\text{CH}_3\text{COOH}$ buffers to pH 4-6, with $\text{H}_2\text{PO}_4^-/\text{HPO}_4^{2-}$ buffers to pH 6.5-7.5 and $\text{NH}_4^+/\text{NH}_3$ buffers to pH 8-11.

Drinking water (TMDW-500) and Strawberry Leaves(LGC7162) were used to check the accuracy as the certified reference materials. The analyzed real samples were purchased from local markets in Denizli/Turkey.

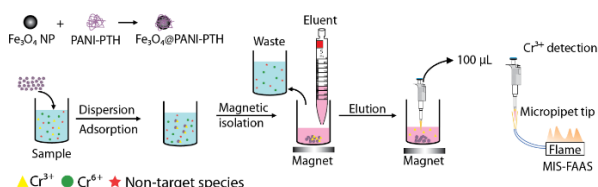
2.3. Synthesis of $\text{Fe}_3\text{O}_4\text{@coPANI-PTH}$

$\text{Fe}_3\text{O}_4\text{@coPANI-PTH}$ nanoparticles as a magnetic adsorbent were prepared via in-situ chemical oxidative polymerization of aniline and thiophene monomers by using FeCl_3 in the presence of Fe_3O_4 , by modifying the

procedure from previous works [29,30-34]. The detail of the synthesis process and characterization data was reported in my earlier work [35]. However, after each synthesis of the magnetic copolymer, Fe_3O_4 and $\text{Fe}_3\text{O}_4@\text{coPANI-PTH}$ IR spectra recorded by ATR-IR instrument (UATR two model, PerkinElmer, Waltham, MA, USA) and the results were compared. Once the peaks belonging to Fe_3O_4 -Polyaniline and Fe_3O_4 -Polythiophene recognized in synthesized $\text{Fe}_3\text{O}_4@\text{coPANI-PTH}$, these $\text{Fe}_3\text{O}_4@\text{coPANI-PTH}$ nanoparticles were used as magnetic solid phase throughout the study.

2.4. General procedure using $\text{Fe}_3\text{O}_4@\text{coPANI-PTH}$ magnetic nanoparticles

Particular volumes of Cr(III) solutions (5-100 mL) with concentrations from 10 to 100 $\mu\text{g L}^{-1}$ were placed into a beaker and buffered to desired pHs in the range of 2-12. 100 mg of $\text{Fe}_3\text{O}_4@\text{coPANI-PTH}$ nanoparticles was added into the beaker and the resulting mixture was shaken by hand for 5 min to ensure the quantitative extraction of Cr(III) ions by the nanosorbent. After that, by applying an external magnet, the liquid is discarded. The remaining magnetic nanoparticles loaded with Cr(III) at the bottom of the beaker were treated with 0.5-5.0 mL of 0.2% thiourea solution in a mixture of 2 mol L^{-1} HCl and 1 mol L^{-1} HNO_3 and sonicated for 5 min. Then, the $\text{Fe}_3\text{O}_4@\text{coPANI-PTH}$ nanoparticles were magnetically collected at the bottom of beaker, and the recovered Cr(III) ions in the clear solution were determined by a microsample injection system-flame atomic absorption spectrometry (MIS-FAAS) to investigate the adsorption behavior of the nanoparticles (Scheme 1).



Scheme 1. Magnetic solid phase extraction of Cr(III) ions using $\text{Fe}_3\text{O}_4@\text{coPANI-PTH}$

2.5. Cr(III) and Cr(VI) determination in real samples

The analyzed local beverages and seasoning samples were prepared according to a simplified and modified version of previous publications [36,37]. 0.6 mL conc. HNO_3 was added to a 40 mL sample in a 50 mL centrifuge tube (Isolab, Eschau, Germany) and the tube was carefully shaken and then centrifuged for 10 min at 10,000 rpm to remove solid particles. The acidic

supernatant solutions were buffered to pH 10 by adding conc. NH_3 dropwise by controlling pH values with a pH meter. Cr(III) concentration in the buffered sample solution was determined by the general procedure presented in Section 2.4.

After reducing Cr(VI) to Cr(III) by adding 1.0 mL of concentrated H_2SO_4 and 5.0 mL of 5% (w/v) hydroxylamine hydrochloride [38,39,40], total chromium concentration (Cr_T) was determined as Cr(III) by the procedure in Section 2.4. The given volumes of concentrated H_2SO_4 and 5% hydroxylamine hydrochloride were added into a 40 mL sample without any pretreatment in a 100 mL beaker and the solution was boiled for 30 min. Then, the solution was cooled to room temperature, and the pH of the solution was adjusted to 10 by adding conc. NH_3 dropwise. After pH adjustment, Cr_T was determined following the procedure given in Section 2.4. The Cr(VI) concentration was calculated by subtracting concentration of Cr_T from the concentration of Cr(III).

The dried and powdered LGC7162 Strawberry Leaves were weighed as 0.50 g into a beaker and treated with 4.0 mL of aqua regia for 3 h at 85 °C on a hot plate to extract chromium species from the sample [38]. To remove undissolved parts, the resulting solutions were filtered through a filter paper. 0.5 mL of conc. H_2SO_4 and 10 mL of 5% (w/v) hydroxylamine hydrochloride added filtrate were boiled for 30 min to ensure that Cr(VI) is completely reduced to Cr(III) [38,39,40]. The final solution cooled to room temperature was buffered to pH 10 by adding conc. NH_3 dropwise and then the procedure given in Section 2.4 was followed to determine Cr_T .

3. Results and Discussion

3.1. Effect of pH

A suitable pH can improve the efficiency and selectivity of adsorbent as it influences both the surface chemistry of adsorbent and the solution chemistry of chromium ions. So, the pH optimization of the analyzed solution is primarily performed in the development of speciation/preconcentration methods based on solid phase extraction. So, the effect of pH on the adsorption of Cr(III) and Cr(VI) ions was controlled over a pH range of 2 to 12. The data in Figure 1 showed quantitative adsorption (recovery $\geq 95\%$) of Cr(III) ions over the pH ranges of 9–10.5. At the same pH range, the recovery values for Cr(VI) ions were found to be $\leq 10\%$. It was concluded that the suitable pH is 10 for distinguishing Cr(III) and Cr(VI) and this pH is chosen for the subsequent experiments.

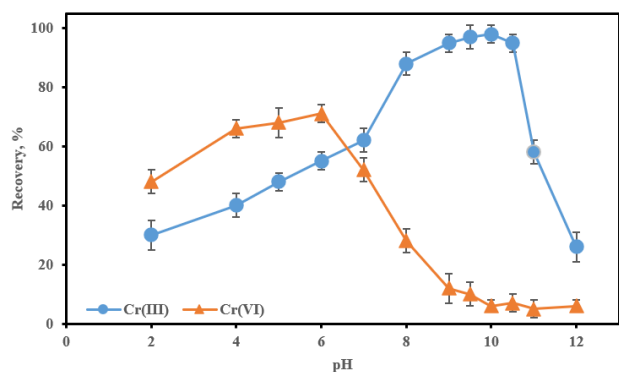


Figure 1. Effect of pH on recovery of Cr(III) and Cr(VI) ions using 100 mg $\text{Fe}_3\text{O}_4@\text{coPANI-PTH}$ (n:3, Sample vol.: 40 mL, Analyte conc.: $25 \mu\text{g L}^{-1}$, Eluent vol.: 2 mL)

The increase in the recovery of Cr(III) from pH 2 to 8 can be explained by the deprotonation of nitrogen and sulfur atoms on the surface of $\text{Fe}_3\text{O}_4@\text{coPANI-PTH}$. As a result of this deprotonation at pH 8 and beyond, the complex formation can be achieved between Cr(III) species ($\text{Cr}(\text{H}_2\text{O})_2(\text{OH})^{2+}$ or $\text{Cr}(\text{H}_2\text{O})(\text{OH})_2^+$) and the surface[41]. Below pH 8, since the ions are positively charged and the surface is protonated, a repulsion of charges is present. The decrease in the recovery of Cr(VI) above pH 6 can be explained by repulsion of Cr(IV) species due to the deprotonation of the surface[28]. Based on this behavior of the two chromium ions, pH 10 was selected for the analysis.

3.2. Effect of $\text{Fe}_3\text{O}_4@\text{coPANI-PTH}$ Amount

The amount of adsorbent required to achieve efficient extraction is an important factor in preconcentration studies. Compared to the conventional adsorbents, the surface area of nanoparticle adsorbents is larger. Thus, quantitative recovery of analytes is expected to be achieved with a smaller amount of nanoparticle adsorbents. The influence of $\text{Fe}_3\text{O}_4@\text{coPANI-PTH}$ amount as a magnetic adsorbent on the recovery of Cr(III) at pH 10 was investigated over the range of 50 to 200 mg for preconcentration of $100 \mu\text{g L}^{-1}$ Cr(III) from 20 mL solution. The quantitative recovery was obtained at 100 mg $\text{Fe}_3\text{O}_4@\text{coPANI-PTH}$ (Table 1). A similar amount of nano-adsorbent use is recorded by other groups as well [27,35,40]. The low recoveries achieved below and above 100 mg could possibly be attributed to the insufficient adsorbent amount and eluent volume, respectively.

Table 1. Effect of $\text{Fe}_3\text{O}_4@\text{coPANI-PTH}$ amount on extraction efficiency of Cr(III) (eluent: 2 mL of 0.2% thiourea solution prepared by $1 \text{ mol L}^{-1} \text{HNO}_3$ and $2 \text{ mol L}^{-1} \text{HCl}$, n:3)

$\text{Fe}_3\text{O}_4@\text{coPANI-PTH}$, mg	Recovery, %
50	44.9 ± 6.5
75	82.3 ± 4.1
100	96.0 ± 4.3
125	65.5 ± 7.5
200	58.7 ± 2.0

3.3. Sample volume

To attain a high preconcentration factor, it is important to work with a maximum sample volume that ensures quantitative adsorption of an analyte by an adsorbent. Effect of sample volume on the adsorption efficiency of Cr(III) ion was studied by extraction of the analytes from 10 to 100 mL of $100 \mu\text{g L}^{-1}$ Cr(III) solution in the presence of 100 mg of $\text{Fe}_3\text{O}_4@\text{coPANI-PTH}$. The largest volume in which the quantitative recovery was obtained was found to be 80 mL (Table 2).

Table 2. Effect of varying sample volumes on recovery values of Cr(III) ions (eluent vol.: 2 mL, n:3)

Sample volume, mL	Recovery, %
5	98.5 ± 2.6
10	100.1 ± 1.7
25	99.1 ± 2.8
40	95.9 ± 3.7
80	96.4 ± 4.1
100	56.5 ± 3.8

3.4. Eluent type and volume

From the data in Figure 1, it can be estimated that quantitative elution would be possible to attenuate the polythiophene-Cr(III) interaction using a highly acidic eluent. Cr(III) as a hard acid is well known to preferentially bind to nitrogen (hard acid) and sulfur (soft acid) containing ligands such as thiourea. Therefore, the elution of preloaded Cr(III) from $\text{Fe}_3\text{O}_4@\text{coPANI-PTH}$ was controlled using 5.0 mL of thiourea solutions prepared with diluted HCl, HNO_3 , and their mixtures (Table 3). The best elution efficiency was obtained with 0.2% thiourea in 1 M $\text{HNO}_3 + 2 \text{ M HCl}$.

Table 3. Recoveries founded at various eluent volumes (sample vol.: 40 mL, $100 \mu\text{g L}^{-1}$ Cr(III), n:3)

Eluent volumes, mL	Recovery, %
5	95.3 ± 3.6
2	97.1 ± 4.1
1	67.2 ± 3.3
0.5	58.9 ± 3.8

To achieve the high preconcentration factor (PF), the elution efficiency of smaller volumes of this eluent was examined over the range of 0.5 to 5 mL. 2.0 mL of 0.2% thiourea in 1 M HNO₃ + 2 M HCl provided the quantitative elution of Cr(III) as the smallest required eluent volume. The ratio of the maximum sample volume (80 mL) to minimum eluent volume (2.0 mL) defines the PF and based on that PF was calculated to be 40.0.

3.5. Extraction time for Cr(III)

Another factor that requires to be optimized is the extraction time including adsorption and desorption times. Adsorption time is defined as the time required for complete adsorption of Cr(III) on the adsorbent surface. The effect of adsorption time was changed over the range of 2 to 15 min (Table 4). At 5 min, the recovery values for Cr(III) achieved to be quantitative ($\geq 95\%$), after that there is no remarkable change in the recovery of Cr(III). This short time can be attributed to the attractive surface properties of the adsorbent for rapid adsorption of Cr(III) from solution under operating conditions. Hence, 5 min was chosen as the adsorption time. A similar study was carried out for desorption time (elution time) by fixing the adsorption time to 5 min. It was also found to be 5 min. This fast extraction time can be explained by the fast adsorption kinetic between the surface and the analyte.

Table 4. Recovery changes found with varying adsorption and desorption times (sample vol.:80 mL, eluent vol.: 2 mL, Cr(III) conc.: 100 $\mu\text{g L}^{-1}$, n:3)

Time, min	Recovery, %	
	Adsorption ^a	Desorption ^b
2	36.2 \pm 3.6	42.2 \pm 4.2
4	85.7 \pm 4.1	79.1 \pm 3.8
5	96.9 \pm 3.4	97.7 \pm 3.2
10	98.9 \pm 3.9	96.8 \pm 4.2
15	97.2 \pm 2.9	96.2 \pm 3.6

^a at fixed desorption time of 5 min. ^b at fixed adsorption time of 5 min.

3.6. Cr(III) and Cr_T determination in sample solution

The usability of described methods in Section 2.4 and 2.5 were checked for the determination of Cr(III) and total chromium(Cr_T) in a solution mixed with Cr(III) and Cr(VI)(Table 5). Cr(III) ions from the solution containing Cr(III) and Cr(VI) were quantitatively adsorbed on Fe₃O₄@coPANI-PTH while Cr(VI) ions remained almost completely in the supernatant solution. On the other hand, Cr_T was determined after the reduction of Cr(VI) to Cr(III) by adding 0.5 mL of concentrated H₂SO₄ and 10 mL of 5% (w/v) hydroxylamine hydrochloride to a 40 mL sample solution containing Cr(III) and Cr(VI) at different amounts. Cr_T was quantitatively recovered. Cr(VI) amount was calculated by subtracting Cr(III) amounts from Cr_T amounts.

Table 5. Determination of Cr(III) ions and total chromium in the mixture of Cr(III) and Cr(VI) ions (Sample volume:40 mL, eluent vol. 2 mL, n:3)

Added, μg			Found, μg ; Recovery%		
Cr(III)	Cr(VI)	Cr _T	Cr(III) ^a	Cr(VI) ^b	Cr _T ^c
5	5	10	4.8 \pm 0.1; 96.0	4.7 \pm 0.2; 94.0	9.6 \pm 0.2; 96.0
5	20	25	4.7 \pm 0.1; 94.0	19.5 \pm 0.2; 97.5	24.2 \pm 0.2; 96.8
10	5	15	9.9 \pm 0.1; 99.0	4.8 \pm 0.2; 96.0	14.7 \pm 0.2; 98.0
20	5	25	19.9 \pm 0.4; 99.5	5.0 \pm 0.4; 100.0	24.9 \pm 0.2; 99.6

^aCr(III): Determined amount of Cr(III) in presence of Cr(VI), ^bCr(VI): Amount of Cr(VI) ions founded by subtracting Cr(III) amount from Cr_T amount. ^c Cr_T: determined after reducing Cr(VI) to Cr (III) ions in sample solutions

3.7. Analytical performance figures

Analytical performance figures of the established MSPE method, combined with MIS-FAAS were evaluated under the optimum conditions (pH 10.0, 100 mg of Fe₃O₄@coPANI-PTH, 80.0 mL sample volume, 2 mL eluent volume and 10 min extraction time). The linear calibration equation in a range of 5-15 $\mu\text{g L}^{-1}$ was $A = 0.2272 C_{\text{Cr(III)}} - 0.0009$ ($R^2=0.997$), where A and $C_{\text{Cr(III)}}$ are the absorbance of chromium and

concentration of chromium ion in $\mu\text{g L}^{-1}$, respectively. The established calibration equation without the preconcentration was $A=0.0059 C_{\text{Cr(III)}}-0.0003$ ($R^2=0.996$) in range of 0.2-5.0 $\mu\text{g mL}^{-1}$ for Cr(III) ions. The enhancement factor (EF) was calculated to be 38.5 from the ratio of the slope of the calibration equation after preconcentration to that without preconcentration. The preconcentration factor(PF) was 40. The close PF and EF values confirm the accuracy of the method with the quantitative sorption and

elution cycle of the analyte recovered as 96.2% which is calculated as the ratio of the preconcentration factor to the enrichment factor. Nevertheless, the accuracy of the optimized method for real sample analysis was checked by applying to TMDW-500 drinking water and LGC7162 Strawberry Leaves as certified reference materials (Table 6). The student t-test was applied; the obtained t_{test} values (1.667 for TMDW-500 and 2.474 for LGC7162) is lower than the $t_{\text{critical}}=4.303$ ($n:3$ and 95% confidence level); therefore, there is no significant difference between certified and found values, and the presented method is applicable for real sample analysis.

Table 6. Analysis of certificated reference materials using proposed method (TMDW-500 vol.: 50 mL, LGC7162 Strawberry Leaves: 0.5 g, $n:3$)

Certified reference materials	Total chromium conc., mean \pm standard deviation		Error, %; RSD, %
	Certified	Found	
TMDW-500 Drinking water, $\mu\text{g L}^{-1}$	20.0 \pm 0.1	19.3 \pm 0.6	-3.5; 3.1
Strawberry Leaves, $\mu\text{g g}^{-1}$	2.15 \pm 0.34	2.05 \pm 0.07	-4.6; 3.4

The reproducibility of the overall preconcentration method was calculated to be 1.85% ($n=7$).

Table 7. Analysis of water, fruit juice, soft drink and vinegar samples spiked with Cr(III) and Cr(VI) ions ($n:3$)

Samples	Added, $\mu\text{g L}^{-1}$		Found ^a , $\mu\text{g L}^{-1}$		Cr_T	Recovery, %		
	Cr(III)	Cr(VI)	Cr(III)	Cr(VI)		Cr(III)	Cr(VI)	Cr_T
Bottled mineral water	0	0	n.d. ^b	n.d.	n.d.	-	-	-
	50	50	50.4 \pm 3.7	50.8 \pm 3.9	101.2 \pm 1.2	100.8	101.6	101.2
Spicy-turnip juice	0	0	8.6 \pm 0.8	$\leq\text{LOQ}^c$	9.4 \pm 0.6	-	-	-
	50	50	62.4 \pm 6.8	48.6 \pm 9.9	110.0 \pm 9.7	107.6	97.2	100.6
Non-spicy turnip juice	0	0	10.5 \pm 1.2	$\leq\text{LOQ}$	12.8 \pm 0.9	-	-	-
	50	50	60.8 \pm 0.8	50.4 \pm 8.5	111.2 \pm 3.8	100.6	100.8	98.4
Apple juice	0	0	n.d.	n.d.	n.d.	-	-	-
	50	50	46.2 \pm 6.3	48.2 \pm 6.6	94.4 \pm 2.1	92.4	96.4	94.4
Apple vinegar	0	0	n.d.	n.d.	n.d.	-	-	-
	50	50	48.4 \pm 3.3	50.8 \pm 4.1	99.2 \pm 2.4	96.8	101.6	99.2
Grape vinegar	0	0	14.3 \pm 3.6	$\leq\text{LOQ}$	16.5 \pm 4.2	-	-	-
	50	50	64.1 \pm 3.5	49.2 \pm 4.4	113.3 \pm 3.7	99.6	98.4	96.8

^a Mean \pm standard deviation, ^b Not detected, ^c lower than limit of quantitation ($5.0 \mu\text{g L}^{-1}$), ^d Cr_T : total chromium

recovery%:97.5, $s=1.78$) in terms of RSD% based on recoveries obtained for different samples and eluent volumes in Table 2 and 3. The limit of detection and limit of quantitation based on $3s_b/m$ and $10s_b/m$ was found to be as 1.5 and $5.0 \mu\text{g L}^{-1}$, respectively.

3.8. Real sample analysis

The applicability of the proposed MSPE method was also controlled by Cr(III) and Cr(VI) spiking analysis of commercially available mineral water, apple juice, turnip juice, and vinegar samples. The recoveries for both ions from the real samples spiked with Cr(III) and Cr(VI) ions were achieved as above 95% (Table 7). The quantitative recovery values indicate that the proposed method is free from interferences and applicable.

On the other hand, the found contents of Cr(III) and Cr(VI) in water, fruit juice, and vinegar samples were evaluated relative to values for drinking water set out by EPA [8] and WHO [9], respectively. The concentrations of Cr(III) and Cr(VI) were both below the maximal permissible levels as $100 \mu\text{g L}^{-1}$ total chromium and $50 \mu\text{g L}^{-1}$ Cr(VI) (Table 7). Therefore, it can be concluded that the consumption of analyzed real samples cannot cause any adverse effects on human health.

4. Conclusions

The proposed magnetic solid phase extraction method for the preconcentration and speciation of chromium is simple, selective, and accurate. The recovery of Cr(III) from real samples and test solutions in the presence of Cr(VI) is quantitative at $\geq 95\%$. The extraction time was fairly short as 10 minutes. Due to the use of $\text{Fe}_3\text{O}_4@\text{coPANI-PTH}$ MNPs as adsorbent, Cr(III) ions were conveniently and rapidly collected on the adsorbent surface and then quickly desorbed from the adsorbent isolated with an external magnetic field. The method for selective determining Cr(III) revealed good analytical figures such as low LOD ($1.5 \mu\text{g L}^{-1}$), high precision (1.85%), and good preconcentration factor (40). Compared to the other research conducted in the literature, this method allows rapid extraction, low RSD, and comparable or higher PF [28,29,40,42-44]. Also, the figure of merits showed that the proposed MSPE-MIS-FAAS method was suitable for the rapid preconcentration, speciation, and determination of chromium in other beverages and various plant leaves.

Acknowledgment

The author thanks to Pamukkale University, Faculty of Art and Sciences, Chemistry Department, Analytical Chemistry Research laboratory for allowing use of instrument and lab space.

Conflicts of interest

The authors state that did not have conflict of interests

References

- [1] Dognani, G., Hadi P., Ma, H., Cabrera, F. C., Job, A. E., Agostini, D. L.S. and Hsiao, B. S. Effective chromium removal from water by polyaniline-coated electrospun adsorbent membrane. *Chem. Eng. J.*, 372 (2019) 341-351.
- [2] Rakhunde, R., Deshpande, L. and Juneja, H. D., Chemical Speciation of Chromium in Water: A Review. *Crit. Rev. Env. Sci. Tec.*, 42(2012) 776-810.
- [3] Anderson, R.A, Chromium, glucose tolerance, diabetes and lipid metabolism. *J. Advancement Med.*, 8 (1995) 37-49.
- [4] Shirani, M., Salari, F., Habibollahi, S. and Akbari, A. Needle hub in-syringe solid phase extraction based a novel functionalized biopolyamide for simultaneous green separation/ preconcentration and determination of cobalt, nickel, and chromium(III) in food and environmental samples with micro sampling flame atomic absorption spectrometry. *Microchem. J.*, 152 (2020) 340-347.
- [5] Office of Dietary Supplements: National Institute of Health. (2013). Dietary Supplement Fact Sheet: Chromium. In).
- [6] Hamilton, E.M., Young, S.D., Bailey, E.H. and Watts, M.J. Chromium speciation in foodstuffs: A review. *Food Chem.*, 250 (2018) 105-112.
- [7] Pan, C., Troyer, L.D., Liao, P., Catalano, J. G., Li, W. and Giammar, D. E. Effect of Humic Acid on the Removal of Chromium(VI) and the Production of Solids in Iron Electrocoagulation. *Environ. Sci. Tech.*, 51 (2017) 6308-6318.
- [8] US EPA. Report No. EPA/570/9-76/003; Washington, DC, 1976.
- [9] Code of Federal Regulation. Protection of Environment. Section 141, 80, p. 425, 2011.
- [10] Hernandez, F., Séby, F., Millour, S., Noël, L. and Guérin, T. Optimisation of selective alkaline extraction for Cr(VI) determination in dairy and cereal products by HPLC-ICPMS using an experimental design. *Food Chem.*, 214 (2017) 339-346.
- [11] Arain, M.A., Ali, I., Yilmaz, E. and Soylak, M. Nanomaterials based chromium speciation in environmental samples: A review. *Trac-Trend Anal. Chem.* 103 (2018) 44-55.
- [12] Aksoy, E., Elci, S. G., Siyal, A. N. and Elci, L. Chromium speciation using an aminated amberlite XAD-4 resin column combined microsample injection-flame atomic absorption spectrometry. *Acta Chim. Slov.*, 65 (2018) 512-520.
- [13] Sacmaci, S., Kartal, S. and Kumsuz, S. Chromium speciation in environmental samples by solid- phase extraction using lewatis ionac SR-7 resin and flame atomic absorption spectrometry. *J. AOAC Int.*, 97 (2014) 1719-1724.
- [14] Baig, J. A., Hol, A., Akdogan, A., Arslan Kartal, A., Divrikli, U., Gul Kazi, T. and Elci, L. A novel strategy for chromium speciation at ultra-trace level by microsample injection flame atomic absorption spectrophotometry. *J. Anal. At. Spectrom.*, 27 (2012) 1509-1517.
- [15] Karatepe, A., Korkmaz, E., Soylak, M. and Elci, L. Development of a coprecipitation system for the speciation/preconcentration of chromium in tap waters. *J. Hazard. Mater.*, 173 (2010) 433-437.

- [16] Matos, G.D., dos Reis, E.B., Costa, A.C.S. and Ferreira, S.L.C. Speciation of chromium in river water samples contaminated with leather effluents by flame atomic absorption spectrometry after separation/preconcentration by cloud point extraction. *Microchem. J.*, 92 (2009) 135-139.
- [17] Lu, J., Tian, J., Wu, H. and Zhao, C. Speciation determination of chromium(VI) and chromium(III) in soil samples after cloud point extraction. *Anal. Lett.*, 42 (2009) 1662-1677.
- [18] Shirkhanloo, H., Ghazaghi, M. and Mousavi, H. Z. Chromium speciation in human blood samples based on acetyl cysteine by dispersive liquid-liquid biomicroextraction and in-vitro evaluation of acetyl cysteine/cysteine for decreasing of hexavalent chromium concentration. *J. Pharmaceut. Biomed.*, 118 (2016) 1-8.
- [19] Hol, A., Arslan Kartal, A., Akdogan, A., Elci, A., Arslan, T. and Elci, L. Ion pair-dispersive liquid-liquid microextraction coupled to microsample injection system-flame atomic absorption spectrometry for determination of gold at trace level in real samples. *Acta Chim. Slov.*, 62 (2015) 196-203.
- [20] Li, Y., Huang, L., He, W., Chen, Y. and Lou, B. Preparation of functionalized magnetic Fe₃O₄@Au@polydopamine nanocomposites and their application for copper(II) removal. *Polymers*, 10 (2018) 570-585.
- [21] Hemmati, M., Rajabi, M. and Asghari, A. Magnetic nanoparticle based solid-phase extraction of heavy metal ions: A review on recent advances. *Microchim. Acta*, 185 (2018) 160.
- [22] Yavuz, E., Tokalioglu, S. and Patat, S. Core-shell Fe₃O₄ polydopamine nanoparticles as sorbent for magnetic dispersive solid-phase extraction of copper from food samples. *Food Chem.*, 263 (2018) 232-239.
- [23] Rezvani, M., Asgharinezhad A.A., Ebrahimzadeh, H. and Shekari, N. A polyaniline-magnetite nanocomposite as an anion exchange sorbent for solid-phase extraction of chromium(VI) ions. *Microchim. Acta*, 181 (2014) 1887-1895.
- [24] Abolhasani, J., Khanmiri, R.H., Ghorbani-Kalhor, E., Hassanpour, A., Asgharinezhad, A.A., Shekari, N. and Fathi, A. An Fe₃O₄@SiO₂@polypyrrole magnetic nanocomposite for the extraction and preconcentration of Cd(II) and Ni(II). *Anal. Methods*, 7 (2015) 313-320.
- [25] Mehdinia, A., Asiabi, M. and Jabbari, A. Trace analysis of Pt (IV) metal ions in roadside soil and water samples by Fe₃O₄/graphene/polypyrrole nanocomposite as a solid-phase extraction sorbent followed by atomic absorption spectrometry. *Intern. J. Environ. Anal. Chem.*, 95 (2015) 1099-1111.
- [26] Tahmasebi, E. and Yamini, Y. Polythiophene-coated Fe₃O₄ nanoparticles as a selective adsorbent for magnetic solid-phase extraction of silver(I), gold(III), copper(II) and palladium(II). *Microchim. Acta*, 181 (2014) 543-551.
- [27] Elyas Sodan, N., Hol, A., Caylak, O. and Elci, L. Use of Fe₃O₄ magnetic nanoparticles coated with polythiophene for simultaneous preconcentration of Cu(II), Co (II), Cd (II), Ni (II) and Zn(II) ions prior to their determination by MIS-FAAS. *Acta Chim. Slov.*, 67, 2020, 375-385.
- [28] Hena, S. Removal of chromium hexavalent ion from aqueous solutions using biopolymer chitosan coated with poly 3-methyl thiophene polymer. *J. Hazard. Mater.*, 181 (2010) 474-479.
- [29] Molaei, K., Bagheri, H., Asgharinezhad, A. A., Ebrahimzadeh, H. and Shamsipur, M. SiO₂-coated magnetic graphene oxide modified with polypyrrole-polythiophene: A novel and efficient nanocomposite for solid phase extraction of trace amounts of heavy metals. *Talanta*, 167 (2017) 607-616.
- [30] Jalilian, N., Ebrahimzadeh, H., Asgharinezhad, A. A. and Molaei, K. Extraction and determination of trace amounts of gold(III), palladium(II), platinum(II) and silver(I) with the aid of amagnetic nanosorbent made from Fe₃O₄-decorated and silica-coated graphene oxide modified with a polypyrrole-polythiophene copolymer. *Microchim. Acta*, 184 (2017) 2191-2200.
- [31] Kera, N.H., Bhaumik, M., Pillay, K. Ray, S.S. and Maity, A. Selective removal of toxic Cr(VI) from aqueous solution by adsorption combined with reduction at a magnetic nanocomposite surface. *J. Colloid Interf. Sci.*, 503 (2017) 214-228.
- [32] Bhaumik, M., Arjun Maity, A., Srinivasu, V. V. and Onyango, M. S. Removal of hexavalent chromium from aqueous solution using polypyrrole-polyaniline nanofibers. *Chem. Eng. J.*, 181(2012) 323-333.
- [33] Martin, M., Salazar, P., Villalonga, R., Campuzano, S., Pingarron, J. M. and Gonzalez-Mora, J. L. Preparation of core-shell Fe₃O₄@poly(dopamine) magnetic

- nanoparticles for biosensor construction. *J. Mater. Chem. B*, 2 (2014) 739-746.
- [34] Liu, X., Ma, Z., Xing, J. and Liu, H. Preparation and characterization of amino-silane modified superparamagnetic silica nanospheres. *J. Magn. Magn. Mater.*, 270 (2004) 1-6.
- [35] Elci, S. G. A magnetic solid-phase extraction method using Fe₃O₄@coPANI-PTH for microsample injection system-flame atomic absorption spectrometric determination of nickel and copper in soft drinks and spice samples. *Intern. J. Environ. Anal. Chem.*, Published (2020) DOI: 10.1080/03067319.2020.1747615.
- [36] [36] Szymczycha-Madeja A. and Welna, M. Evaluation of a simple and fast method for the multi-elemental analysis in commercial fruit juice samples using atomic emission spectrometry. *Food Chem.*, 141 (2013) 3466-3472.
- [37] Elci, S. G., Yan, B., Kim, S. T., Saha, K., Jiang, Y., Klemmer, G. A., Moyano, D. F., Yeşilbag Tonga, G., Rotello, V. M. and Vachet, R. W. Quantitative imaging of 2 nm monolayer-protected gold nanoparticle distributions in tissues using laser ablation inductively-coupled plasma mass spectrometry (LA-ICP-MS). *Analyst*, 141 (2016) 2418-2425.
- [38] [38] Tuzen, M., Determination of heavy metals in soil, mushroom and plant samples by atomic absorption spectrometry. *Microchem. J.*, 74 (2003) 289-297.
- [39] F. Aydın (Supervisor: Mustafa Soylak), Preconcentration of some heavy metal ions by using coprecipitation and solid phase extraction methods, PhD Thesis, Erciyes University, Graduate School of Natural and Applied Sciences, (2008), Kayseri, Türkiye.
- [40] Elyas Sodan, N., Elci, S. G., Arslan Kartal, A., Hol, A. and Elci, L. Chromium speciation in food, biological and environmental samples using magnetic polythiophene nanoparticles, followed by microsample injection system-flame atomic absorption spectrometric determination. *Microchemical Journal*, Under review, 2020.
- [41] Peng, H., Zhang, N., He, M., Chen, B., Hu, B. Simultaneous speciation analysis of inorganic arsenic, chromium and selenium in environmental waters by 3-(2-aminoethylamino) propyltrimethoxysilane modified multi-wall carbon nanotubes packed microcolumn solid phase extraction and ICP-MS. *Talanta*, 131 (2015) 266–272.
- [42] K.M.Diniz, C.R.T.Tarley, Speciation analysis of chromium in water samples through sequential combination of dispersive magnetic solid phase extraction using mesoporous amino functionalized Fe₃O₄/SiO₂ nanoparticles and cloud point extraction, *Microchem. J.*, 123 (2015) 185-195.
- [43] M. Manoochehri, L.A. Naghibzadeh, Nanocomposite based on dipyrildylamine functionalized magnetic multiwalled carbon nanotubes for separation and preconcentration of toxic elements in black tea leaves and drinking water, *Food Anal. Methods*, 10(2017)1777-1786.
- [44] M.Babazadeh, R. Hosseinzadeh-Khanmiri, J. Abolhasani, E. Ghorbani-Kalhor, A. Hassanpour, A. Solid phase extraction of heavy metal ions from agricultural samples with the aid of a novel functionalized magnetic metal-organic framework. *RSC Advances*, 5(2015) 19884-19892.

Ferroelectricity of $\text{Ca}_9\text{Fe}(\text{PO}_4)_7$ and $\text{Ca}_9\text{Mn}(\text{PO}_4)_7$ ceramics with polar whitlockite-type crystal structure

Umut ADEM 

Department of Materials Science and Engineering, Izmir Institute of Technology, 35430, Urla, Izmir, TURKEY

Abstract

$\text{Ca}_9\text{Fe}(\text{PO}_4)_7$ is a member of the double phosphate family having polar whitlockite-type crystal structure. The phase transition from the room temperature polar $R3c$ to the high temperature non-polar $R\bar{3}c$ phase has been called a ferroelectric phase transition using complementary experiments such as temperature dependent second harmonic generation and dielectric constant measurements however no ferroelectric hysteresis measurement has been reported. In order to be able to call these polar materials ferroelectric, measurement of a saturated ferroelectric hysteresis loop is necessary to demonstrate that the electrical polarization of these materials is switchable. In order to realize this goal, we have synthesized $\text{Ca}_9\text{Fe}(\text{PO}_4)_7$ as well as structurally identical $\text{Ca}_9\text{Mn}(\text{PO}_4)_7$ using solid state synthesis. Crystal structure of the ceramics were confirmed using Rietveld refinement of the x-ray diffraction (XRD) patterns. Differential scanning calorimetry (DSC) measurements revealed phase transition temperatures of 848 and 860 K for $\text{Ca}_9\text{Fe}(\text{PO}_4)_7$ and $\text{Ca}_9\text{Mn}(\text{PO}_4)_7$, respectively. Our ferroelectric hysteresis measurements and current electric field loops (I-E) derived from the hysteresis loops showed that the loops cannot be saturated and the direction of the electrical polarization of both materials cannot be switched up to the largest applied electric field of 100 kV/cm. Possible origins of this behaviour are discussed.

Article info

History:

Received:20.04.2020

Accepted:31.05.2020

Keywords:

Ferroelectricity,
Phosphates, Rietveld
refinement,
Phase transitions.

1. Introduction

Calcium phosphate and vanadate compounds have been studied a lot as biomaterials [1-2] or for their luminescence properties [3-6]. Among them, double phosphates $\text{Ca}_9\text{R}^{3+}(\text{PO}_4)_7$ ($\text{R}^{3+}=\text{Al, Fe, Cr, Ga, Sc, In}$) are known to crystallize in polar whitlockite structure with $R3c$ space group [7-9]. There have been quite a few studies that focus on the ferroelectric nature of the phase transition between the polar low temperature and non-polar high temperature phases in both phosphates and vanadates [7-10]. Ferroelectric nature of this phase transition has been shown indirectly using x-ray diffraction, second harmonic generation, DSC, dielectric constant and electron diffraction experiments for example for $\text{Ca}_9\text{Fe}(\text{PO}_4)_7$ [8] among others. All these experiments on $\text{Ca}_9\text{Fe}(\text{PO}_4)_7$ point out to a phase transition from room temperature polar $R3c$ phase to a non-polar $R\bar{3}c$. However, strictly speaking, in order to be able to call these materials ferroelectric, switching of the electrical polarization of these samples must be demonstrated using ferroelectric hysteresis measurements. Otherwise, they can only be called

pyroelectric. In polar $\text{Ca}_9\text{Fe}(\text{PO}_4)_7$ structure, which is based on the whitlockite-type structure, there are six sites that Ca^{2+} and Fe^{3+} can occupy. M1-M3 sites are occupied by Ca^{2+} ions, Fe^{3+} occupies the M5 site of the whitlockite structure and M4 and M6 sites are unoccupied^{7,9}. A phase transition was reported to occur from polar $R3c$ phase to non-polar $R\bar{3}c$ phase at 890 K as shown by DSC measurements [8]. A peak in the dielectric constant was also reported around the same temperature. And the second harmonic generation signal disappears above the same temperature. All these experiments provide evidence to a polar-nonpolar phase transition. The phase transition into the non-polar phase was reported to involve disordering of the Ca^{2+} ions and orientational disordering of the PO_4 tetrahedra [8]. No literature on $\text{Ca}_9\text{Mn}(\text{PO}_4)_7$ could be found. As Mn^{3+} has a very similar ionic radius to other R^{3+} ions already studied in the family of $\text{Ca}_9\text{R}^{3+}(\text{PO}_4)_7$ ($\text{R}^{3+}=\text{Al, Fe, Cr, Ga, Sc, In}$), we have attempted to synthesize $\text{Ca}_9\text{Mn}(\text{PO}_4)_7$ and study its structural and ferroelectric properties as a comparison to $\text{Ca}_9\text{Fe}(\text{PO}_4)_7$.

In this manuscript, following the synthesis and structural characterization of the samples,

*Corresponding author. Email address: umutadem@iyte.edu.tr

<http://dergipark.gov.tr/csj> ©2020 Faculty of Science, Sivas Cumhuriyet University

ferroelectric hysteresis loops of $\text{Ca}_9\text{Fe}(\text{PO}_4)_7$ and $\text{Ca}_9\text{Mn}(\text{PO}_4)_7$ are reported for the first time in order to clarify whether the polarization is switchable in these polar materials with a high temperature polar-non polar phase transition.

2. Materials and Methods

$\text{Ca}_9\text{Fe}(\text{PO}_4)_7$ was synthesized using solid state synthesis following the method in [8]. Fe_2O_3 , CaCO_3 and $\text{Ca}_2\text{P}_2\text{O}_7$ powder were mixed using a mortar and a pestle in acetone medium and pressed into pellets of 13 mm diameter using a hydraulic press. The pellets were placed in alumina crucible and sintered at 1000°C for 6 hours in air. In order to obtain a pure phase, resulting pellets were crushed, ground, pelletized and sintered again under the same conditions. $\text{Ca}_9\text{Mn}(\text{PO}_4)_7$ was also synthesized using the same process from Mn_2O_3 , CaCO_3 and $\text{Ca}_2\text{P}_2\text{O}_7$ precursors. X-ray diffraction (XRD) patterns of the samples were collected using a Panalytical Empyrean diffractometer employing $\text{Cu K}\alpha$ source. Rietveld refinements of the collected XRD data were carried out using GSAS [11]. Differential Scanning Calorimetry (DSC) measurements were done using a Shimadzu DSC-60 Plus between room temperature and 600°C in the nitrogen atmosphere and using 5°C/min heating rate. Ferroelectric hysteresis measurements were done at room temperature using an Aixact TF Analyzer 1000. Dielectric properties were measured at room temperature using a Keysight E4980AL LCR Meter. For the electrical measurements, both surfaces of the pellets were coated with Ag epoxy and cured at 120°C for 20 minutes.

3. Results and Discussion

In Fig.1, refined XRD patterns of both $\text{Ca}_9\text{Fe}(\text{PO}_4)_7$ and $\text{Ca}_9\text{Mn}(\text{PO}_4)_7$ collected at room temperature are shown. For the refinements, crystallographic information files from the Materials Project [12] were used as the reference structure. All peaks belong to the whitlockite-type structure with the space group $R\bar{3}c$ and no impurity peaks could be detected. Good quality of the fits can be observed from the difference curve and low R_{wp} values for the samples: $R_{\text{wp}} = 5\%$ and 7.73% for $\text{Ca}_9\text{Fe}(\text{PO}_4)_7$ and $\text{Ca}_9\text{Mn}(\text{PO}_4)_7$, respectively. Refined lattice parameters are $a=10.3461(1)\text{ \AA}$, $c=37.191(1)\text{ \AA}$ and $a=10.3704(2)\text{ \AA}$, $c=37.2166(9)\text{ \AA}$ and for $\text{Ca}_9\text{Fe}(\text{PO}_4)_7$ and $\text{Ca}_9\text{Mn}(\text{PO}_4)_7$, respectively. Slightly larger lattice parameters of the $\text{Ca}_9\text{Mn}(\text{PO}_4)_7$ might be due to the presence of Mn^{2+} in the samples, in addition to the

expected Mn^{3+} . Mn^{2+} has a larger ionic radius [13] compared to Mn^{3+} and Fe^{3+} .

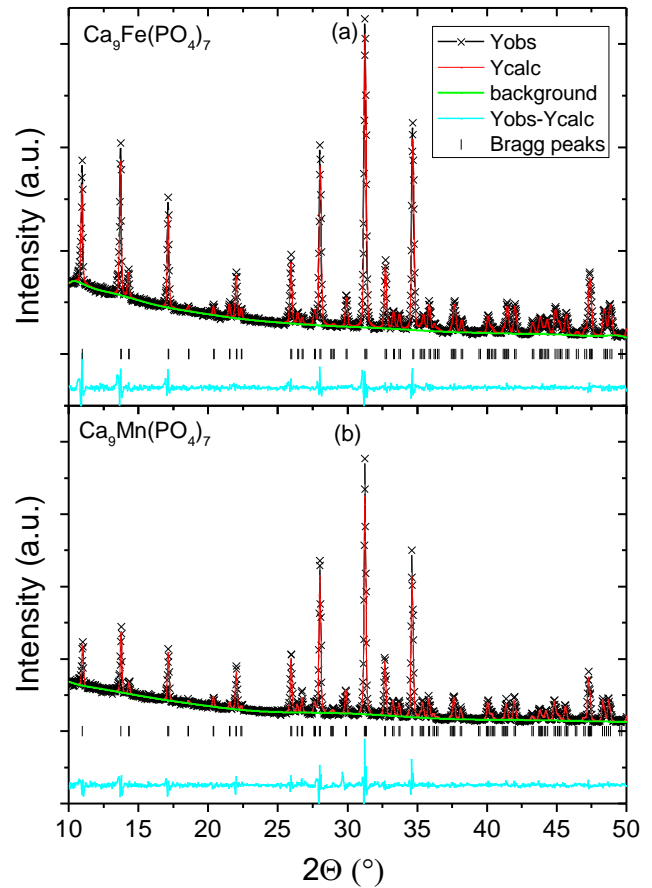


Figure 1. Refined x-ray diffraction patterns of (a) $\text{Ca}_9\text{Fe}(\text{PO}_4)_7$ and (b) $\text{Ca}_9\text{Mn}(\text{PO}_4)_7$. Black triangular symbols represent the collected data from the experiments, red solid lines show the calculated intensity, green lines show the background fits and light blue lines show the difference of experimentally observed and calculated intensities. Peak positions are marked with ticks.

In Figure 2, DSC curves of $\text{Ca}_9\text{Fe}(\text{PO}_4)_7$ and $\text{Ca}_9\text{Mn}(\text{PO}_4)_7$ are shown. In both materials, clear endothermic peaks are observed which correspond to the ferroelectric to paraelectric phase transition [9]. Estimated transition temperatures from DSC measurements are 848 and 860 K for $\text{Ca}_9\text{Fe}(\text{PO}_4)_7$ and $\text{Ca}_9\text{Mn}(\text{PO}_4)_7$, respectively. Transition temperature measured for $\text{Ca}_9\text{Fe}(\text{PO}_4)_7$ is slightly lower than the previously reported value (886 K) [8] whereas no previous studies could be found for $\text{Ca}_9\text{Mn}(\text{PO}_4)_7$. Dielectric constant and dielectric loss measured at RT and 1 kHz are tabulated in Table 1. Both samples have relatively low dielectric constant and loss, similar to the polar double phosphates with whitlockite-type structure reported in the literature [7-8]. Dielectric loss of $\text{Ca}_9\text{Mn}(\text{PO}_4)_7$ is slightly lower

than that of $\text{Ca}_9\text{Fe}(\text{PO}_4)_7$ which is reflected in the hysteresis loop measurements as we discuss below.

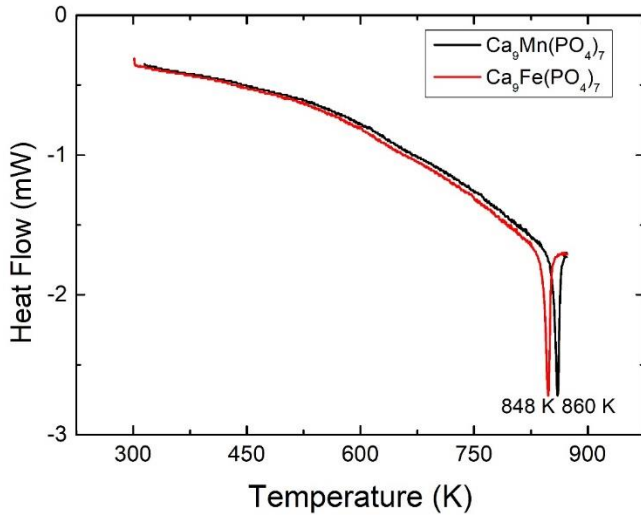


Figure 2. Temperature dependence of heat flow of $\text{Ca}_9\text{Fe}(\text{PO}_4)_7$ and $\text{Ca}_9\text{Mn}(\text{PO}_4)_7$.

Figure 3 shows the ferroelectric hysteresis loops of $\text{Ca}_9\text{Fe}(\text{PO}_4)_7$ as a function of applied voltage collected at 100 kHz. The loops show no saturation up to the largest applied electric field and preserve its linear behaviour with increasing voltage. Polarization value reaches around $0.5 \mu\text{C}/\text{cm}^2$ at the highest applied field of $\approx 85 \text{ kV}/\text{cm}$ which is smaller than the predicted value ($2\text{-}3 \mu\text{C}/\text{cm}^2$) based on the second harmonic generation experiments [8]. In the inset of Figure 3, frequency dependence of the hysteresis loop recorded at the highest applied voltage is shown. Significant frequency dependence could be observed: the loops transform from cigar-like shape at 1 Hz to almost linear shape at 100 kHz. Such relatively strong frequency dependence suggests conductivity contribution to the electrical polarization [14].

Table 1. Dielectric constant and dielectric loss values of $\text{Ca}_9\text{Fe}(\text{PO}_4)_7$ and $\text{Ca}_9\text{Mn}(\text{PO}_4)_7$ measured at room temperature and 1 kHz.

Material	Dielectric constant	Dielectric loss ($\tan\delta$)
$\text{Ca}_9\text{Fe}(\text{PO}_4)_7$	13	0.03
$\text{Ca}_9\text{Mn}(\text{PO}_4)_7$	7	0.023

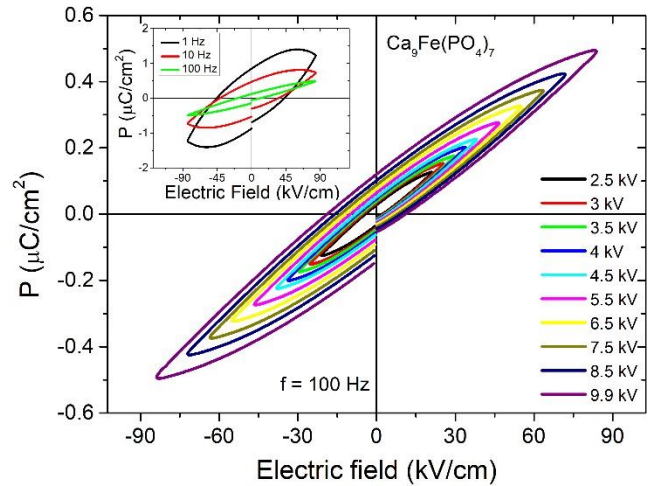


Figure 3. Ferroelectric hysteresis loops of $\text{Ca}_9\text{Fe}(\text{PO}_4)_7$ as a function of applied voltage at 100 Hz. Inset shows the frequency dependence of the polarization.

In Fig.4(a), hysteresis loops of $\text{Ca}_9\text{Mn}(\text{PO}_4)_7$ as a function of applied voltage are shown. Similar to $\text{Ca}_9\text{Fe}(\text{PO}_4)_7$, the loops measured at 10 kHz are not saturated and the polarization increases linearly with increasing voltage. In the inset of Fig.4(a), hysteresis loops measured at 1 and 10 Hz at the largest applied electric field are compared. Again similar to $\text{Ca}_9\text{Fe}(\text{PO}_4)_7$, electrical polarization is frequency dependent. Hysteresis loop has a cigar-like shape at 1 Hz, which changes to a slim linear behaviour at 10 Hz. Since the loops of $\text{Ca}_9\text{Fe}(\text{PO}_4)_7$ reach linear behaviour at lower frequencies compared to those of $\text{Ca}_9\text{Mn}(\text{PO}_4)_7$ (at 100 vs 10 Hz, respectively), we can conclude that the conductivity contribution to the electrical polarization is lower in $\text{Ca}_9\text{Mn}(\text{PO}_4)_7$ [14].

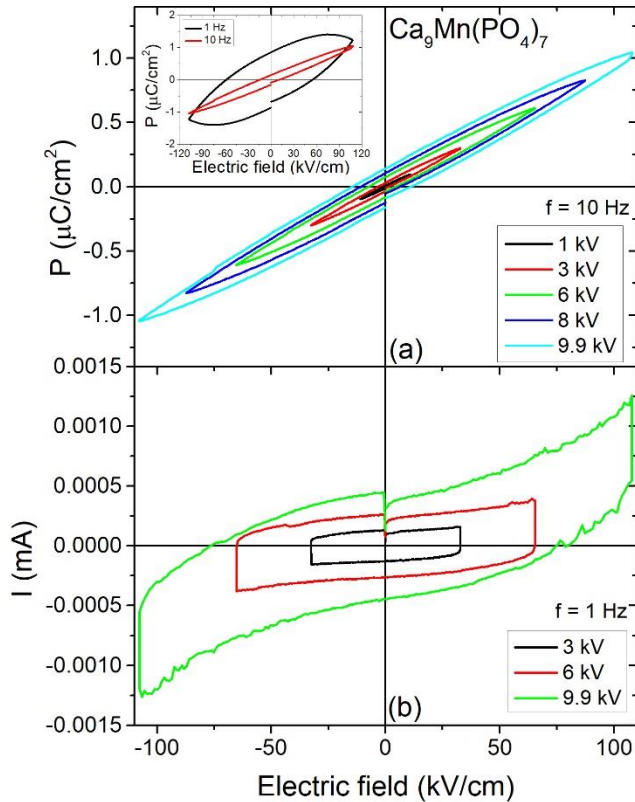


Figure 4. (a) Ferroelectric hysteresis loops of $\text{Ca}_9\text{Mn}(\text{PO}_4)_7$ as a function of applied voltage at 10 Hz. Inset shows the frequency dependence of the polarization compared at 1 and 10 kHz. (b) Current-electric field (I-E) curves of $\text{Ca}_9\text{Mn}(\text{PO}_4)_7$ at three different voltage values and 1 Hz.

In Fig.4(b), current-electric field (I-E) curves at three different voltage values are plotted. These curves can be extracted from hysteresis measurements and can be used together with the hysteresis loops, to assess switching of the electrical polarization and thus ferroelectricity. When the direction of the electric field changes, electrical polarization changes sign and this gives rise to a current peak for a ferroelectric. However, dielectric permittivity and electrical conductivity also contribute to the electrical current and may mask any peaks due to switching of the electrical polarization [15]. In our measurement, no current peaks can be observed in the curves obtained under 3 and 6 kV. In contrast, at 9.9 kV, which is the highest applied voltage, an emerging peak can be observed at the highest voltage. This emerging peak cannot be used as evidence for ferroelectricity as a proper peak is expected before the maximum electric field is reached for ferroelectric switching, but might still indicate that possible switching could be observed if larger electric field/voltage could have been applied [15].

Lack of ferroelectric switching is quite common in polar insulators. Two most common causes that prevent the observation of switching are (1) high activation energy for switching [16-18] and (2) large conductivity contribution masking the switching, due to the poor insulating nature of the material [15]. The former cause i.e. crystallographic switching path(s) for the ion(s) requiring a lot of energy typically leads to a very large coercive field and might cause dielectric breakdown to occur before the switching takes place. The latter cause is also quite common especially in multiferroic materials, most of which are poor electrical insulators [19-21]. In the case of calcium phosphates that we study here, both causes might be playing a role. Strong frequency dependence of the hysteresis loops points out that conductivity contribution is significant in these materials as we discussed above. Nevertheless, the emerging peak at the highest possible applied electric field/voltage for $\text{Ca}_9\text{Mn}(\text{PO}_4)_7$ might be a sign for possible switching at even larger electric fields, suggesting that the switching path is energetically costly. Further experiments on ceramics at higher fields or measurements on thin films (no thin films of double phosphates or vanadates have been reported so far) might be useful to clarify. In the literature of polar phosphates and vanadates, only one report showing hysteresis measurements can be found for $\text{Ca}_3(\text{VO}_4)_2$ [22], which is also isostructural to polar double phosphates and vanadates according to an early report [23]. Reported hysteresis loops are not saturated and hence no switching could be demonstrated. The lack of switching was attributed to the high coercive field of the material [22], similar to our case.

4. Conclusion

In conclusion, we attempted to clarify the ferroelectricity of polar double phosphates $\text{Ca}_9\text{Fe}(\text{PO}_4)_7$ and $\text{Ca}_9\text{Mn}(\text{PO}_4)_7$ with the whitlockite-type structure. Refined XRD patterns confirmed the crystal structure of the materials and DSC measurements yielded phase transition temperatures of 848 and 860 K for $\text{Ca}_9\text{Fe}(\text{PO}_4)_7$ and $\text{Ca}_9\text{Mn}(\text{PO}_4)_7$, respectively. Ferroelectric hysteresis measurements showed that the electrical polarization of both materials cannot be saturated up to the highest possible applied field and the polarization is also not switchable which can be evidenced from the lack of a peak in current-electric field (I-E) loops. Based on these results, strictly speaking, polar double phosphates $\text{Ca}_9\text{Fe}(\text{PO}_4)_7$ and $\text{Ca}_9\text{Mn}(\text{PO}_4)_7$ are pyroelectric rather than ferroelectric.

Acknowledgments

This work is supported by İzmir Institute of Technology (IZTECH) via BAP Project with the project number 2015İYTE29. We thank the IZTECH Department of Chemical Engineering for the DSC experiments and Celal Bayar University's DEFAM for the use of XRD.

Conflicts of interest

The author declares that he has no conflict of interests.

References

- [1] Dorozhkin S.V., Calcium orthophosphates in nature, biology and medicine, *Materials (Basel)*, 2 (2009) 399-498.
- [2] Engin N.Ö. and Taş A.C., Preparation of Porous $\text{Ca}_{10}(\text{PO}_4)_6(\text{OH})_2$ and $\beta\text{-Ca}_3(\text{PO}_4)_2$ Bioceramics, *J. Am. Ceram. Soc.*, 83 (2000) 1581-1584.
- [3] Zhu G., Li Z., Wang C. et al., Highly Eu^{3+} ions doped novel red emission solid solution phosphors, $\text{Ca}_{18}\text{Li}_3(\text{Bi},\text{Eu})(\text{PO}_4)_{14}$: Structure design, characteristic luminescence and abnormal thermal quenching behavior investigation, *Dalt. Trans.*, 48 (2019) 1624-1632.
- [4] Huang C.H., Chen T.M., Liu W.R., Chiu Y.C., Yeh Y.T. and Jang S.M., A single-phased emission-tunable phosphor $\text{Ca}_9\text{Y}(\text{PO}_4)_7:\text{Eu}^{2+},\text{Mn}^{2+}$ with efficient energy transfer for white-light-emitting diodes, *ACS Appl. Mater. Interfaces*, 2 (2010) 259-264.
- [5] Liang S., Dang P., Li G. et al. Controllable two-dimensional luminescence tuning in Eu^{2+} , Mn^{2+} doped $(\text{Ca},\text{Sr})_9\text{Sc}(\text{PO}_4)_7$ based on crystal field regulation and energy transfer, *J. Mater. Chem. C*, 6 (2018) 6714-6725.
- [6] Chen M., Xia Z., Molokeev M.S., Wang T. and Liu Q., Tuning of Photoluminescence and Local Structures of Substituted Cations in $x\text{Sr}_2\text{Ca}(\text{PO}_4)_2-(1-x)\text{Ca}_{10}\text{Li}(\text{PO}_4)_7:\text{Eu}^{2+}$ Phosphors, *Chem. Mater.* 29 (2017) 1430-1438.
- [7] Morozov V.A., Belik A.A., Stefanovich S.Y. et al., High-temperature phase transition in the whitlockite-type phosphate $\text{Ca}_9\text{In}(\text{PO}_4)_7$, *J. Solid State Chem.*, 165 (2002) 278-288.
- [8] Lazoryak B.I., Morozov V.A., Belik A.A. et al., Ferroelectric phase transition in the whitlockite-type $\text{Ca}_9\text{Fe}(\text{PO}_4)_7$; crystal structure of the paraelectric phase at 923 K, *Solid State Sci.*, 6 (2004) 185-195.
- [9] Deineko D.V., Stefanovich S.Y., Mosunov A.V., Baryshnikova O.V. and Lazoryak B.I., Structure and properties of $\text{Ca}_{9-x}\text{Pb}_x\text{R}(\text{PO}_4)_7$ ($\text{R} = \text{Sc}, \text{Cr}, \text{Fe}, \text{Ga}, \text{In}$) whitlockite-like solid solutions, *Inorg. Mater.* 49 (2013) 507-512.
- [10] Belik A.A., Deyneko D.V., Baryshnikova O.V., Stefanovich S.Y. and Lazoryak B.I., $\text{Sr}_9\text{In}(\text{VO}_4)_7$ as a model ferroelectric in the structural family of $\beta\text{-Ca}_3(\text{PO}_4)_2$ -type phosphates and vanadates, *RSC Adv.*, 10 (2020) 10867-10872.
- [11] Larson A.C. and Von Dreele R.B., General Structure Analysis System (GSAS), *Los Alamos National Laboratory Report LAUR*, (2004) 86-748.
- [12] Jain A., Ong S.P., Hautier G. et al., Commentary: The Materials Project: A materials genome approach to accelerating materials innovation, *APL Mater.*, 1 (2013) 011002.
- [13] Shannon R.D., Revised effective ionic radii and systematic studies of interatomic distances in halides and chalcogenides, *Acta Crystallogr. Sect. A*, 32 (1976) 751-767.
- [14] Jin L., Li F. and Zhang S.J., Decoding the Fingerprint of Ferroelectric Loops: Comprehension of the Material Properties and Structures, *J. Am. Ceram. Soc.*, 97 (2014) 1-27.
- [15] Yan H., Inam F., Viola G. et al., the Contribution of Electrical Conductivity, Dielectric Permittivity and Domain Switching in Ferroelectric Hysteresis Loops, *J. Adv. Dielectr.*, 01 (2011) 107-118.
- [16] Song S., Jang H.M., Lee N.S. et al., Ferroelectric polarization switching with a remarkably high activation energy in orthorhombic GaFeO_3 thin films, *NPG Asia Mater.*, 8 (2016) e242.
- [17] De C. and Sundaresan A., Nonswitchable polarization and magnetoelectric coupling in the high-pressure synthesized doubly ordered perovskites NaYMnWO_6 and NaHoCoWO_6 , *Phys. Rev. B*, 97 (2018) 214418.
- [18] Garrity K.F., High-throughput first-principles search for new ferroelectrics, *Phys. Rev. B*, 97 (2018) 024115.
- [19] Buurma A.J.C., Blake G.R., Palstra T.T.M. and Adem U., Multiferroic Materials: Physics and

Properties, *Reference Module in Materials Science and Materials Engineering*: <https://www.sciencedirect.com/science/article/pii/B9780128035818092456>, Elsevier Ltd., (2016).

- [20] Li M-R., Adem U., McMitchell S.R.C. et al., A polar corundum oxide displaying weak ferromagnetism at room temperature, *J. Am. Chem. Soc.*, 134 (2012) 3737-3747.
- [21] Catalan G. and Scott J.F., Physics and applications of bismuth ferrite, *Adv. Mater.*, 21 (2009) 2463-2485.
- [22] Ning H.P., Yan H.X. and Reece M.J., A High Curie Point Ferroelectric Ceramic $\text{Ca}_3(\text{VO}_4)_2$, *Ferroelectrics*, 487 (2015) 94-100.
- [23] Teterskii A.V., Morozov V.A., Stefanovich S.Y. and Lazoryak B.I., Dielectric and nonlinear optical properties of the $\text{Ca}_9\text{R}(\text{PO}_4)_4$ ($\text{R}=\text{Ln}$) phosphates, *Russ. J. Inorg. Chem.* 50 (2005) 986-989.

AUTHOR GUIDELINES

Thank you for choosing to submit your paper to Cumhuriyet Science Journal. The following instructions will ensure we have everything required so your paper can move through pre-evaluating, peer review, production and publication smoothly. Please take the time to read and follow them as closely as possible, as doing so will ensure your paper matches the journal's requirements.

Submission

Cumhuriyet Science Journal is an international, peer-reviewed, free of charge journal covering the full scope of both natural and engineering sciences. Manuscripts should be submitted by one of the authors of the manuscript as online submission after registration to the Cumhuriyet Sciences Journal. Microsoft Word (.doc, .docx, .rtf), files can be submitted. There is no page limit. If there is a problem while uploading the files of manuscript, please try to reduce their file size, especially manuscripts including embedded figures. Submissions by anyone other than one of the authors will not be accepted. The submitting author takes responsibility for the paper during submission and peer review. If for some technical reason submission through the online submission system is not possible, the author can contact csj@cumhuriyet.edu.tr for support.

Submission or processing charges

Cumhuriyet Science Journal does not charge any article submission, processing charges, and printing charge from the authors.

Terms of Submission

Papers must be submitted on the understanding that they have not been published elsewhere (except in the form of an abstract or as part of a published lecture, review, or thesis) and are not currently under consideration by another journal. The submitting author is responsible for ensuring that the article's publication has been approved by all the other coauthors. It is also the authors' responsibility to ensure that the articles emanating from a particular institution are submitted with the approval of the necessary institution. Only an acknowledgment from the editorial office officially establishes the date of receipt. Further correspondence and proofs will be sent to the author(s) before publication unless otherwise indicated. It is a condition of submission of a paper that the corresponding author permit editing of the paper for readability. All enquiries concerning the publication of accepted papers should be addressed to csj@cumhuriyet.edu.tr. Please note that Cumhuriyet Science Journal uses iThenticate software to screen papers for unoriginal material. By submitting your paper to Cumhuriyet Science Journal are agreeing to any necessary originality checks your paper may have to undergo during the peer review and production processes. Upon receiving a new manuscript, the Editorial office conducts initial pre-refereeing checks to ensure the article is legible, complete, correctly formatted, original, within the scope of the journal in question, in the style of a scientific article and written in clear English. Any article that has problems with any of the journal criteria may be rejected at this stage.

Peer Review

This journal operates a single blind review process. All contributions will be initially assessed by the editor for suitability for the journal. Papers deemed suitable are then typically sent to a minimum of two independent expert reviewer to assess the scientific quality of the paper. The author is required to upload the revised article to the system within 15 days by making the corrections suggested by the referee. The article will be rejected if there are no fixes in it. The Editor is responsible for the final decision regarding acceptance or rejection of articles. The Editor's decision is final

Title and Authorship Information

The following information should be included

Paper title

Full author names

Full institutional mailing addresses

Corresponding address

Email address

Abstract

The manuscript should contain an abstract. The researchers who are native speakers of Turkish have to add Turkish title and abstract as well. The abstract should be self-contained and citation-free and should be 250-300 words.

Keywords

Keywords of the scientific articles should be selected from the web address of www.bilimadresleri.com

Introduction

This section should be succinct, with no subheadings.

Materials and Methods

This part should contain sufficient detail so that all procedures can be repeated. It can be divided into subsections if required.

Conflicts of interest

Sample sentence if there is no conflict of interest: The authors stated that did not have conflict of interests.

Acknowledgements

Sample sentences for acknowledgements: The work was supported by grants from CUBAP (T-11111). We would like to acknowledge Prof. Mehmet Sözer, MD, for his precious technical and editorial assistance. We would like to thank

References

References to cited literature should be identified by number in the text in square brackets and grouped at the end of the paper in numerical order of appearance. Each reference must be cited in the text. Always give inclusive page numbers for references to journal articles and a page range or chapter number for books. References should be styled and punctuated according to the following examples

[1] Keskin B. and Ozkan A.S., Inverse Spectral Problems for Dirac Operator with Eigenvalue Dependent Boundary and Jump Conditions, *Acta Math. Hungar.*, 130-4 (2011) 309– 320.

[2] National Cancer Institute, Surveillance Epidemiology and End Results. Cancer of the Corpus and Uterus, NOS. Available at: http://seer.cancer.gov/statfacts/html/corp.html?statfacts_page=corp. Retrieved March 2, 2008. (Sample reference of website)

[3] Isaacson K.B., Endometrial ablation. In: UpToDate, Basow, DS (Ed), UpToDate, Waltham, M.A., 2008. (Sample reference of Uptodate topics)

[4] Speroff L., Fritz M.A., Anovulation and The Polycystic Ovary. In. Speroff L., Fritz M.A., (Eds). *Clinical Gynecologic Endocrinology and Infertility*. 7th ed. Philadelphia, Pa: Lippincott Williams and Wilkins; 2005: chap 12. (Sample reference of online book chapters found in websites).

[5] Mazur M.T., Kurman R.J., Dysfunctional Uterine Bleeding. In: Mazur M.T., Kurman R.J., (Eds). *Diagnosis of endometrial biopsies and curettings. A practical approach*. 2nd ed. Berlin: Springer, 2005; pp 100-120. (Sample reference of printed book chapters)

Preparation of Figures

Each figure can be integrated in the paper body or separately uploaded and should be cited in a consecutive order. Figure widths can be 4-6 inch as 300 dpi. The labels of the figures should be clear and informative. The name and the subtitles of the figures must be 9-point font.

Preparation of Tables

Tables should be cited consecutively in the text. Every table must have a descriptive title and if numerical measurements are given, the units should be included in the column heading. Tables should be simple with simple borders and text written as left text. The name and the subtitle of the tables must be 9-point font

Proofs

Corrected proofs must be returned to the publisher within 2 weeks of receipt. The publisher will do everything possible to ensure prompt publication. It will therefore be appreciated if the manuscripts and figures conform from the outset to the style of the journal.

Copyright

Open Access authors retain the copyrights of their papers, and all open access articles are distributed under the terms of the Creative Commons Attribution license, which permits unrestricted use, distribution and reproduction in any medium, provided that the original work is properly cited.

The use of general descriptive names, trade names, trademarks, and so forth in this publication, even if not specifically identified, does not imply that these names are not protected by the relevant laws and regulations.

While the advice and information in this journal are believed to be true and accurate on the date of its going to press, neither the authors, the editors, nor the publisher can accept any legal responsibility for any errors or omissions that may be made. The publisher makes no warranty, express or implied, with respect to the material contained herein.

Ethical Guidelines

New methods and ethically relevant aspects must be described in detail, bearing in mind the following:

Human Experiments. All work must be conducted in accordance with the Declaration of Helsinki (1964). Papers describing experimental work on human subjects who carry a risk of harm must include:

A statement that the experiment was conducted with the understanding and the consent of the human subject.

A statement that the responsible Ethical Committee has approved the experiments.

Animal Experiments. Papers describing experiments on living animals should provide:

A full description of any anaesthetic and surgical procedure used.

Evidence that all possible steps were taken to avoid animal suffering at each stage of the experiment. Papers describing experiments on isolated tissues must indicate precisely how the donor tissues were obtained.

Submission Preparation Checklist

As part of the submission process, authors are required to check off their submission's compliance with all of the following items, and submissions may be rejected that do not adhere to these guidelines.

The submission has not been previously published, nor is it before another journal for consideration (or an explanation has been provided in Comments to the Editor).

The submission file is in Microsoft Word document file (Times New Roman) format.

Where available, URLs for the references have been provided.

The text is single-spaced; uses a 11-point font; employs italics, rather than underlining (except with URL addresses); and all illustrations, figures, and tables are placed within the text at the appropriate points, rather than at the end.

The text adheres to the stylistic and bibliographic requirements outlined in the Author Guidelines, which is found in About the Journal.

If submitting to a peer-reviewed section of the journal, the instructions in Ensuring a Double-Blind Review have been followed.